Author:
Pau, V. H

Title:
An investigation of a three-dimensional natural convection problem using an adapted multigrid method

An investigation of a three-dimensional natural convection problem using an adapted multigrid method

Vipinkumar Haridas Pau

March 1988

A thesis submitted to the University of Bristol for the degree of Doctor of Philosophy in the Faculty of Engineering, Department of Computer Science in March 1988.

Abstract

The research undertaken is concerned with the study of natural convection in closed cavities with differential heating across the vertical side walls. The objective of the study was to obtain three-dimensional numerical solutions for the window cavity problem in a computationally efficient manner.

This problem has many important applications, the best known of these being double glazing. It is also of great importance in other areas. For example the cooling of electronic equipment, stellar convection, crystal growth in liquid metals, cooling of irradiated nuclear fuel pins and reactor insulation. Three-dimensional numerical solutions of this problem are very rare and the effect of the third dimension upon the physical instabilities is not completely understood. The influence of the end walls could radically change the currently understood two-dimensional solution structure.

Three-dimensional computations are in general expensive to perform using conventional numerical methods. A relatively new method, the multigrid method, is used which produces considerable savings in computation time and is easily incorporated into existing software.

The study demonstrates the applicability of multigrid methods to two- and three-dimensional fluid flow problems, particularly for use in natural convection problems. The multigrid method is applied to equations derived from the SIMPLE algorithm [47] using the control volume approach. This manner of applying the mulitigrid method does not appear to have been discussed elsewhere. In order to solve equations which have been derived using the control-volume discretization, the multigird method has been adapted. The efficiency of the multigrid methods with the use of the CRAY-XMP supercomputer has permitted a wide ranging parameter study of the three-dimensional window cavity problem. The problem has been studied with low and moderate Prandtl number fluids, the liquid metal cerrobase and air respectively, for low to moderately high Rayleigh numbers in shallow, square and tall cross-section window cavities.

An extensive study of three dimensional convection in low Prandtl number fluids has not appeared before and it is hoped that the general trends described in this study will help to focus any future investigations. Limited studies of the effect of mesh refinement have also been performed. The complex fluid flow structure, heat transfer

and the minimum length of the window cavity required for two-dimensional flow to exist are described for various fluid flow parameters investigated.

Dedicated to my late parents

Haridas Gokaldas Pau

and

Saker Haridas Pau

Acknowledgements

I would like to thank my supervisors Dr. Eric Lewis (University of Bristol) and Dr. Ian Jones (AERE Harwell) for their guidance and support throughout this work. I would also like to thank those who have provided help and friendship over the time of this thesis, especially Ross Hughes (University of Bristol) and Jim Keightley (AERE Harwell). My gratitude is also extented to Steve Hurst (STL Harlow) for the use of word processing facility and friends at Harlow for their help and constant support.

I would also like to thank the Atomic Energy Research Establishment Harwell, who sponsored this study, for the generous use of their computing facilities and for participating in the Science and Engineering Research Council's CASE scheme. The financial support, from Oct. 1983 to Sept. 1986, from the AERE Harwell and the SERC is gratefully acknowledged.

Finally, I would like to thank my wife Krutika for all her support throughout the course of this work.

Statement

No portion of this work referred to in this thesis has been submitted in support of an application for another degree or qualification of this or any other institution of learning.

Contents

Contents

Contents

List of figures

List of tables

Chapter 1

Introduction

The problem of natural convection in closed cavities with differential heating across the vertical side walls has many important applications, the best known of these being double glazing. The problem also has further applications in other areas. For example the cooling of electronic equipment, stellar convection, crystal growth in liquid metals, cooling of irradiated nuclear fuel pins and reactor insulation. The last of these is being investigated at AERE Harwell in connection with thermal insulation of a liquid metal cooled fast breeder reactor (LMFBR). Also an exhaustive program of work both theoretical and experimental has been undertaken there.

The double glazing problem has also attracted great interest academically due to its complex solution structure, particularly in liquid metals, and the simple geometry makes it an ideal problem to study. Due to its complex solution structure the problem is regarded as an excellent test problem for fluid flow prediction codes.

The problem is now reasonably well understood in two-dimensions for high Prandtl number fluids such as oils, water and common gases, and many prediction codes are able to routinely tackle this problem. However, very few results exist for low Prandtl number fluids. Therefore, the low Prandtl number fluid flows need to be investigated especially as liquid metals have recently become of great interest due to their use in LMBFR's.

The practical industrial problems are three-dimensional in nature yet very few three-dimensional numerical solutions of this problem exist. The effect of the third dimension upon the physical instabilities is not completely understood. The influence of the end walls in the three dimensional problem could radically change the currently understood two-dimensional solution structure. Prior to the commencement of this

study, the effects of the end walls upon low Prandtl number fluids had not been investigated.

The computation of industrial fluid flow problems, particularly those incorporating three-dimensional incompressible flows are dominated by finite difference methods based on velocity-pressure formulation. The computational cost of these methods are dependent on solutions of linearised equations, a pressure correction equation for the conservation of mass and transport equations for the conservation of momentum and energy. Three-dimensional computations are in general expensive to perform using conventional numerical methods. For this reason, gains in the efficiency of obtaining solutions to these equations is highly desirable, especially if they can be translated into existing industrial prediction codes with ease.

Such a method to emerge is the multigrid method. The multigrid method promises considerable savings in computation time and in its ease of implementation to existing software. However, many of the difficulties with new methods do not emerge on very simple problems. They need to be tried and tested on realistic problems for their advantages and disadvantages to emerge fully.

The principal aims of this study are to demonstrate the applicability of multigrid methods to a two- and three-dimensional fluid flow problem, particularly for use in natural convection problems and then to utilise the resulting software for investigating a three-dimensional natural convection problem, the window cavity problem. The efficiency of the multigrid methods with the use of the CRAY-XMP supercomputer and generous allocations of computer time (from AERE Harwell) has permitted a wide ranging parameter study of the three-dimensional window cavity problem, enabling future studies to concentrate on regions of particular interest in the parameter space.

Chapter 2 describes the SIMPLE (Semi-Implicit Method for Pressure Linked Equations) algorithm of Patankar and Spalding, [46]. The algorithm has been demonstrated to be very efficient at solving fluid flow problems and has thus been used in industry for over a decade. The algorithm is based on pressure-velocity formulation as the principal interest of engineers lies in obtaining solutions in terms of the primitive variables rather than in terms of stream-function and vorticity. Some of the other advantages are that three-dimensional fluid flows and variable viscosity flows can be modelled and boundary conditions for turbulent flows can be implemented. The transport equations and the continuity equation are discretized over finite control volumes, as this approach leads to the preservation of mass, momentum and energy. The first

order upwind differencing scheme is used when discretizing the differential equations. The use of the upwinding scheme results in producing diagonally dominant matrices, ensuring convergence of the iterative process when solving the set of simultaneous equations. The price paid for guaranteed convergence is that the upwinding scheme augments the true diffusion term hence generating false diffusion. It is felt that the first order upwinding scheme is sufficient for this investigative study, where the aim has been to identify general trends and regions of the parameter space worthy of further detailed study. The iterative process used is the line Gauss Seidel solver. The SIMPLE algorithm has been applied to a two-dimensional natural convection test problem, commonly referred to as 'the double glazing problem'. Comparisons of the results obtained for the double glazing problem using the SIMPLE algorithm are made with other methods. These results are also used to compare values against those obtained with the three-dimensional problem.

In order to obtain a converged solution for a system of coupled equations the discretized equations in the SIMPLE algorithm have to be under-relaxed, as is the normal practice with most fluid flow algorithms. The under-relaxation parameters are chosen arbitrarily and may not necessarily lead to a converged solution. An investigation of the effects of varying the under-relaxation parameters is presented in section 2.8 and it reveals the importance of solving the pressure correction equation (which conserves mass) accurately as this makes the algorithm much less sensitive to the under-relaxation parameters.

Finally it is shown that the revised versions of the SIMPLE algorithm have the same difficulty as the SIMPLE algorithm itself, that is, the problem posed by the under-relaxation parameters.

Chapter 3 is an introduction of the multigrid method, from a practical point of view, based on that of Stuben and Trottenberg [60]. The introduction to multigrid methods by Stuben and Trottenberg and by others is presented using the finite difference approach. Multigrid methods have been rarely applied to discretized equations which have been derived using the control volume approach, see [4]. In this chapter, the consequence of using the multigrid methods with the finite difference and control volume approach is discussed. The two approaches are compared and their differences and relative merits are described, especially those arising when obtaining the restriction and prolongation operators for the two approaches. Multigrid cycles and the full multigrid algorithm are introduced and discussed. Although these exist in

the current multigrid literature they are nevertheless presented here for completeness. The non-linear multigrid method which is not used in this study is also presented for completeness.

Chapters 4 and 5 describe the adapted multigrid method to be used when solving discretized equations which have been derived using the control volume approach. The savings obtained when applying the adapted multigrid method to a two- and three-dimensional pressure-correction equation with Dirichlet boundary conditions and also to a three-dimensional temperature equation with Neumann boundary conditions are also presented. The chapters clearly demonstrate the importance of applying the multigrid method to a discrete equation which must be derived from a differential equation and not from combinations of other discrete equations. Chapter 4 introduces two prolongation schemes (non-weighted and weighted), and discusses their relative merits in terms of the computational work done and the rate of convergence. Chapter 5 also demonstrates how improper coarsening can lead to the deterioration of the multigrid method. It is hoped that the material presented in chapters 3, 4 and 5 will be a useful contribution to the existing multigrid literature.

Chapter 6 describes the three-dimensional window cavity study performed using the SIMPLE algorithm with the adapted multigrid methods. This chapter demonstrates the ease of extending the SIMPLE algorithm to three-dimensions, the savings made by using the adapted multigrid method and describes general trends obtained with low and moderate Prandtl number fluids (the liquid metal cerrobase and air respectively), for low to moderately high Rayleigh numbers in shallow, square and tall cross-section window cavities. The complex fluid flow structure, heat transfer results and the minimum cavity length aspect ratio required for two-dimensional flow to exist are presented for the wide range of parameters investigated. An extensive study of the three-dimensional natural convection for low Prandtl number fluids has not appeared before to the author's knowledge and it is hoped that the general trends described will help to direct any future investigations. Also the trends for air in shallow cross section cavities has not been studied before. Limited studies of the effect of the mesh refinements has also been performed and presented. A wide range of parameter investigation producing valuable solutions has been possible due to using the multigrid method, without which the solutions obtained would have been much more time consuming, very expensive and would have reduced the scope of the study. The solutions have been obtained using fine grids ranging from 16x16x16 to 16x40x40. For multigrid

purposes the maximum number of coarse grids possible with standard coarsening have been used.

Extensive literature reviews of the two- and three-dimensional problem are presented in section 6.3 and 6.4 respectively. The results for the square, shallow and tall cross section window cavity problems are presented in sections 6.6, 6.7 and 6.8 respectively. The results obtained with this study for air in square and tall cross section window cavities show similar trends to those obtained by Mallinson and de Vahl Davis [39]. These authors have carried out the most in-depth study of this problem so far. Their work concentrates on fluids with Prandtl numbers which are moderate to high and on window cavities with square and tall cross sections. As a result of studying solutions for isolated parameter values their work covers a broad range.

The fluids studied in the square, shallow and tall window cavities are air at $Ra=10^3$, air at $Ra=10^5$, cerrobase at $Ra=10^3$ and cerrobase at $Ra=5\times10^3$ in three length aspect ratios Hy=1, 2 and 5. The height aspect ratios investigated are Hz=0.5 which is representative of the shallow cross-section window cavity, Hz=1.0 the square cross-section window cavity and Hz=5.0 which is representative of the tall cross-section window cavity. In order to investigate the effect of the truncation error a fine mesh study of 32x32x32 has been performed for air and cerrobase in the square cross-section window cavity with length aspect ratio Hy=1.0. The axial velocity along the centre of the window cavity and the heat transfer values for the fine grid have been compared with those obtained by using the coarse grid 16x16x16.

The effect of the three-dimensional motion on the heat transfer with the shallow, square and tall cross-sections are also presented in sections 6.6.5, 6.7.5 and 6.8.5 respectively. The maximum stream function obtained at the symmetry plane, where two-dimensional flow exists, have been obtained and compared with those obtained from the two-dimensional double glazing problem.

A summary of the square, shallow and tall cross-sections is presented at the end of sections 6.6, 6.7 and 6.8 respectively. Overall conclusions of the shallow, square and tall cross-section window cavity problems are presented in section 6.9.

This study has been performed at the request of the sponsor whose primary interest lies in obtaining the characteristics of liquid metal flows driven by natural convection in three-dimensions. In order to make this a comprehensive study of the window cavity problem, as much information as possible in the form of graphical output has been presented.

Chapter 2

Review of the SIMPLE algorithm

2.1 Introduction

Fluid flow problems governed by the Navier-Stokes equations can be solved numerically using either the stream function - vorticity method or the primitive variable methods. In industry the primitive variable approach is preferred since the quantities measured or specified are usually in terms of pressure and velocities. However the primitive variable methods are at a disadvantage when used to solve two-dimensional problems, as one extra equation has to be solved compared to the stream function vorticity method but the situation is reversed for three-dimensional problems. For three-dimensional problems the primitive variable methods require four fewer equations to be solved compared to the vorticity velocity-potential method. This advantage enables computational fluid dynamicists to obtain detailed numerical solutions for three-dimensional industrial fluid flow problems. There are three widely used primitive variable algorithms SIMPLE, MAC and SOLA. Their advantages and disadvantages are discussed by Roach [54]. They basically operate by solving the momentum equations and a pressure/pressure-correction equation, the latter being derived from the continuity equation. The method used at AERE Harwell is the *Semi-Implicit Method for Pressure Linked Equations*, the SIMPLE algorithm of Patankar and Spalding [46]. This algorithm has been used to solve steady/unsteady, laminar/turbulent, incompressible/compressible fluid flow problems for the last fifteen years. The SIMPLE algorithm is presented in this chapter for the sake of clarity and completeness. The description presented is a summary of a more thorough treatment given in [47]. Here the algorithm is described via application to a two-dimensional steady state test problem in

Cartesian coordinates. The test problem considered is a natural convection problem, namely *the double glazing problem for an aspect ratio 1*, the flow being assumed to be laminar and incompressible.

2.2 The test problem

The double-glazing problem aspect ratio 1

The flow in the cavity, aspect ratio 1.0, is a simple recirculation induced by the differentially heated side walls, see Figure 2.1.

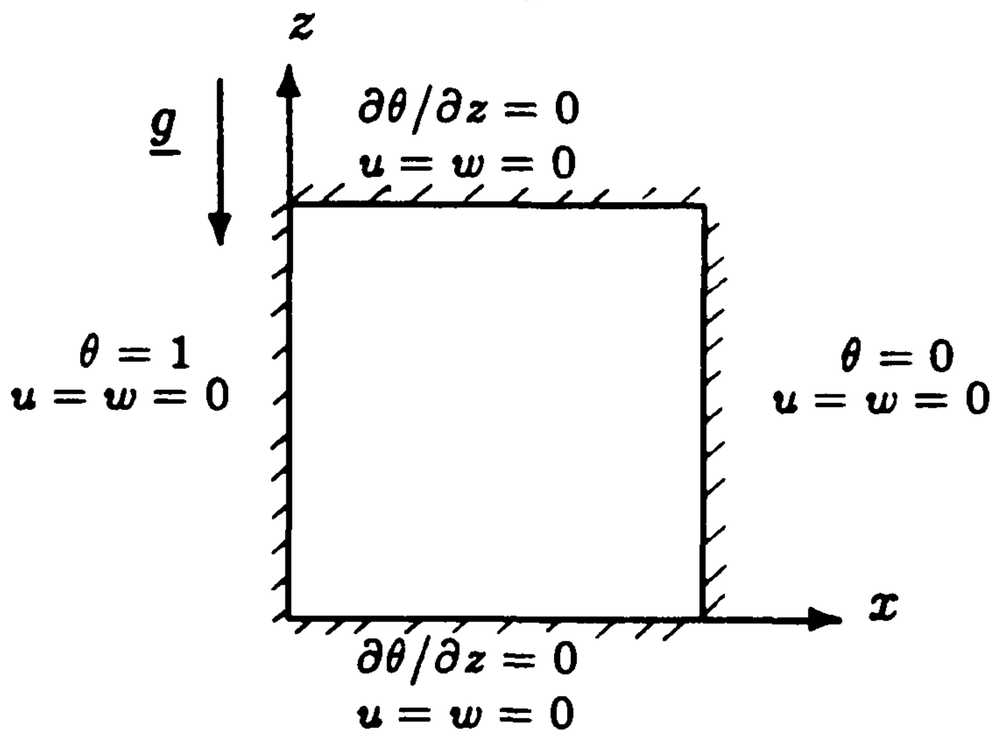

Figure 2.1: Geometry of the Double-Glazing problem

The problem is also regarded as an ideal test problem since many bench-mark results exist (see [11], [12] and [28]). The problem has been reviewed in depth in chapter 6 where the three-dimensional window cavity problem is treated.

The equations can be considerably simplified by adopting the Boussinesq approximation, that is the density of the fluid is assumed constant except in the buoyancy term.

In the usual notation the problem is governed by the non-dimensional equations :

$$\frac{\partial(u^2)}{\partial x} + \frac{\partial(uw)}{\partial z} = \frac{\mathrm{Pr}}{\mathrm{Ra}}\left(\frac{\partial^2 u}{\partial x^2} + \frac{\partial^2 u}{\partial z^2}\right) - \frac{\mathrm{Pr}}{\mathrm{Ra}}\frac{\partial p}{\partial x} \tag{2.1}$$

$$\frac{\partial(uw)}{\partial x} + \frac{\partial(w^2)}{\partial z} = \frac{\mathrm{Pr}}{\mathrm{Ra}}\left(\frac{\partial^2 w}{\partial x^2} + \frac{\partial^2 w}{\partial z^2}\right) - \frac{\mathrm{Pr}}{\mathrm{Ra}}\frac{\partial p}{\partial z} + \frac{\mathrm{Pr}}{\mathrm{Ra}}(\theta - \theta_0) \tag{2.2}$$

$$\frac{\partial u}{\partial x} + \frac{\partial w}{\partial z} = 0 \tag{2.3}$$

$$\frac{\partial(u\theta)}{\partial x} + \frac{\partial(w\theta)}{\partial z} = \frac{1}{R_\lambda}\left(\frac{\partial^2 \theta}{\partial x^2} + \frac{\partial^2 \theta}{\partial z^2}\right) \tag{2.4}$$

where $g\beta(T_h - T_c)L^2/\nu$, $(T_h - T_c)$, L, g, $\rho g\beta(T_h - T_c)L$ are the non-dimensionalizing

factors for velocity, temperature, distance, gravity and pressure respectively. The parameters $\mathrm{Ra} = g\beta(T_h - T_c)L^3/\nu\kappa$ and $\mathrm{Pr} = \nu/\kappa$ are the non-dimensional Rayleigh and Prandtl numbers respectively. The boundary conditions are as shown in Figure 2.1.

2.3 The control volume approach

The SIMPLE algorithm is based on the control volume approach, which lends itself directly to physical interpretation. The calculation domain is divided into non-overlapping control volumes. The differential equation is then integrated over each control volume to obtain the discretized equation. The discretized equation obtained expresses the conservation principle for the finite control volume just as the differential equation expresses it for an infinitesimal control volume. Thus the resulting solution would imply that the conservation of quantities such as mass, momentum and energy is exactly satisfied over any group of control volumes and of course over the whole calculation domain. As a result, solutions obtained on coarse grids are also physically realistic.

The derivation of discrete analogues of the partial differential equation via the control volume approach or Taylor series expansions lead to the same expressions. The advantage of the control volume approach is that it always preserves the conservation property of the differential equation, whilst the Taylor series expansion based on continuum mathematics does not, especially with compressible fluids in which shock waves exist (see [48]).

2.4 Staggered grids

The need for staggered grids can be best illustrated by considering the following :

Integrating the pressure term $-\partial p/\partial x$ in a one-dimensional momentum equation over the shaded control volume centred at point P, as depicted in Figure 2.2, with the

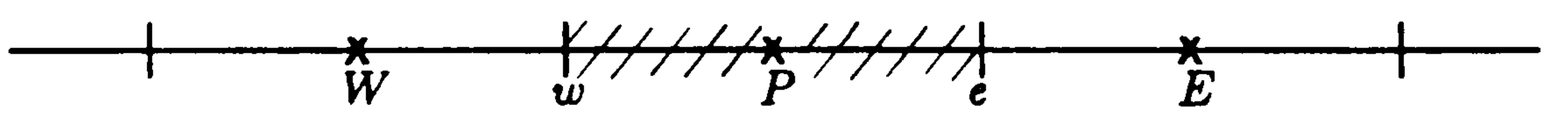

Figure 2.2: One-dimensional grid.

velocities and pressures centered at x, one obtains :

$$
\begin{aligned}
-\int_w^e \frac{\partial p}{\partial x} dx &= -(P_e - P_w) \\
&= \frac{P_W + P_P}{2} - \frac{P_P + P_E}{2} \\
&= \frac{P_W - P_E}{2}.
\end{aligned} \tag{2.5}
$$

The result is a pressure drop between two alternate points and not two adjacent points. This of course diminishes the accuracy of the solution but, worse still, consider a non-realistic zig-zag pressure field, as in Figure 2.3.

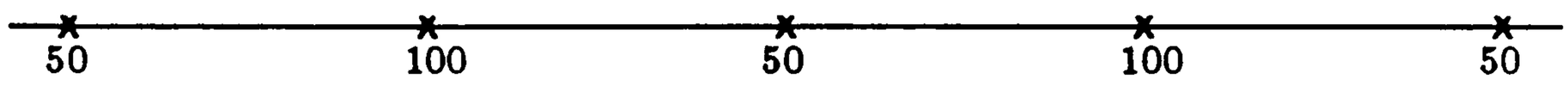

Figure 2.3: A zig-zag pressure field.

For any grid point P in Figure 2.3, the corresponding $P_W - P_E$ can be seen to be zero. Hence such an unrealistic pressure field will appear like a uniform pressure field to the momentum equation. Should such a pressure field arise during the iterative solution procedure there would be nothing to stop it from being preserved till convergence, since the momentum equation would be oblivious to its presence. Also if a certain smooth pressure field is obtained as a solution then any number of additional solutions can be constructed by adding a zig-zag pressure field to that solution. The momentum equation would remain unaffected by the addition since the zig-zag field implies zero pressure force. This behaviour is of course undesirable.

Similar problems arise when constructing the discretized equation for the continuity equation. An unrealistic velocity field as described above would satisfy the discretized continuity equation.

These difficulties can be resolved by recognizing that all the variables do not have to be solved at the same grid points. By solving different variables at different locations a staggered grid is created. Such a grid was first used by Harlow and Welch (1965) in their MAC (Marker And Cell) method [54],[24].

By locating the velocities at the control volume faces and the pressure and any other variables at the control volume centres the above problems can be overcome. With the velocities lying on the control volume faces the mass volume flow rates across the control volume faces can be calculated without any interpolation for the relevant velocity components. But the more important advantages are:

1. The discretized continuity equation contains the differences of adjacent velocity components and this prevents unrealistic velocity fields such as a zig-zag velocity field from satisfying the continuity equation.

2. The pressure difference between two adjacent grid points now becomes the natural driving force for the velocity component located between these grid points. Consequently zig-zag pressure fields will no longer appear uniform and thus cannot arise as a pressure solution.

So integrating the pressure term $-\partial p/\partial x$ over the staggered control volume, Figure 2.5, which is part of the one-dimensional staggered grid, Figure 2.4, with the

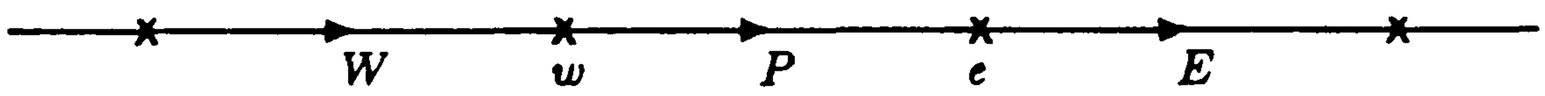

Figure 2.4: One-dimensional staggered grid.

velocities located at ▶ and pressures centered at x, gives,

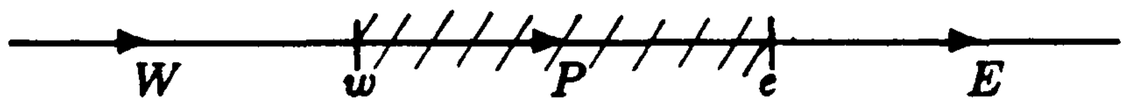

Figure 2.5: One-dimensional control volume for the velocity.

$$-\int_w^e \frac{\partial p}{\partial x} dx = -(P_e - P_w) \tag{2.6}$$

and of course the pressures are now defined at points e and w.

Figure 2.6 depicts the positions of the velocities and pressure for a two-dimensional staggered grid.

2.5 The SIMPLE algorithm

In this section the control volumes used to discretize the momentum and pressure equations are presented and the equations governing the double-glazing problem discretized. The SIMPLE algorithm is then derived.

When discretizing the momentum and temperature equations the convection and diffusion terms are integrated in the normal fashion, after which the upwinding scheme of Courant, Isaacson and Rees(1952) is used on the resulting integrated convective terms and the central difference scheme is used on the integrated diffusion terms. The central difference scheme for the integrated convective term is not preferred since it

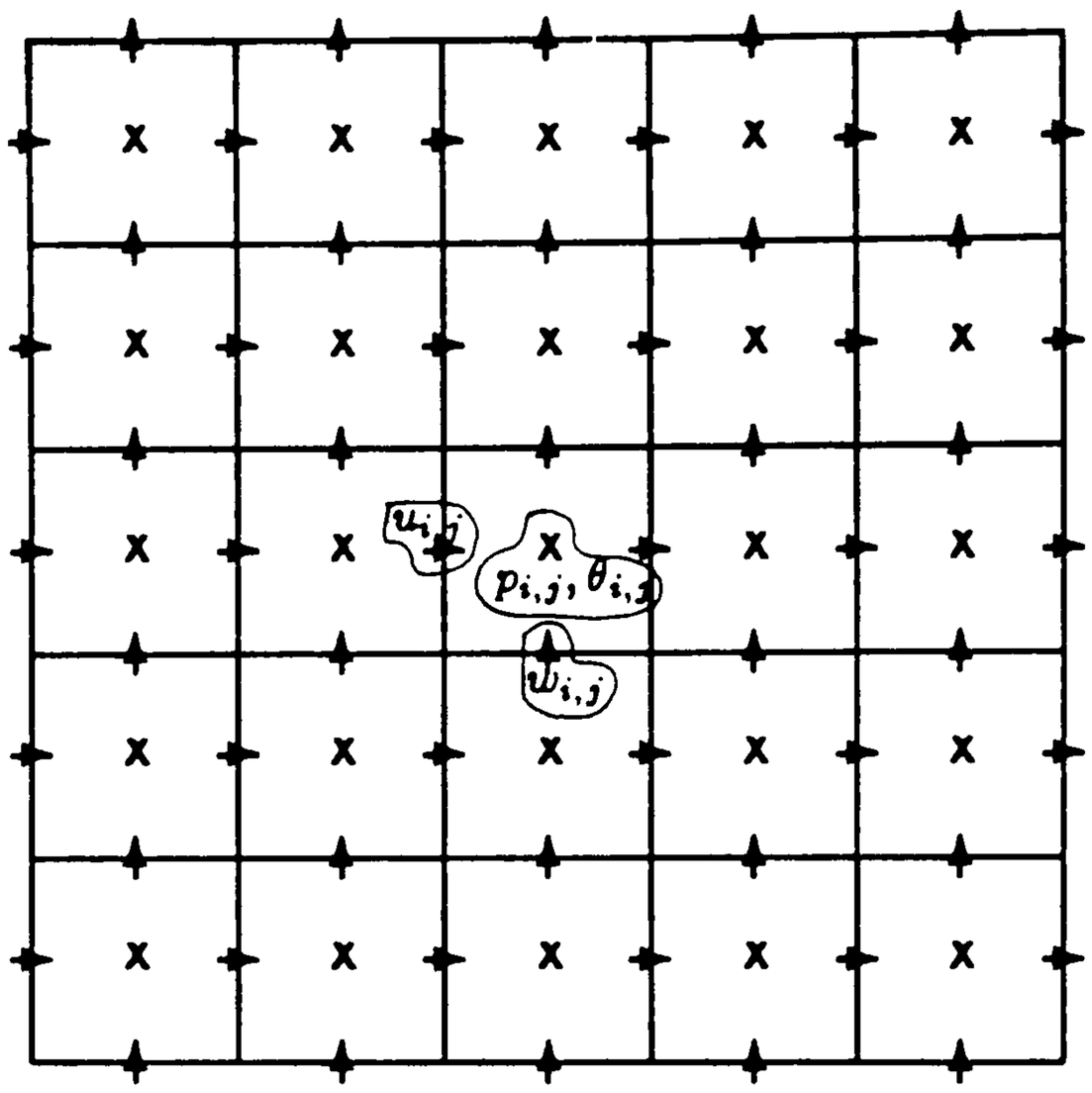

Figure 2.6: A uniform staggered grid in two-dimensions.

is unstable for cell Reynolds number, Rc, greater than 2.0. Rc is defined as $U_h h/\alpha$ where h is the mesh size, U_h is the characteristic velocity and α is the diffusion coefficient (here Pr/Ra). The upwinding scheme, however, is unconditionally stable for all cell Reynolds number (see [54]). The nature of the upwinding scheme results in augmenting the true diffusion term and hence generating false diffusion. For a large α, diffusion effects dominate the convective effects and the additional diffusion term in comparison is then quite small. Hence the upwind scheme will still produce fairly accurate results. For large α it may be possible to use the central difference scheme as Rc may be less than 2.0. For small α, when convection starts to dominate diffusion, the central differencing scheme becomes unstable and so the alternative then left is the upwinding scheme (see [46] and [54] for further discussion).

2.5.1 Discretized equations for the double-glazing problem.

W-momentum equation

Consider first the approximation to the equation:

$$\frac{\partial(u\phi)}{\partial x} + \frac{\partial(w\phi)}{\partial z} = -\frac{\mathrm{Pr}}{\mathrm{Ra}}\frac{\partial p}{\partial z} + \frac{\mathrm{Pr}}{\mathrm{Ra}}\left(\frac{\partial^2\phi}{\partial x^2} + \frac{\partial^2\phi}{\partial z^2}\right) + \frac{\mathrm{Pr}}{\mathrm{Ra}}(\theta - \theta_0)\,. \tag{2.7}$$

This is equivalent to the w-momentum equation where $\phi = w$.

Integrating equation 2.7 over the uniform control volume in Figure 2.7,

$$\int_w^e \int_s^n \left(\frac{\partial(u\phi)}{\partial x} + \frac{\partial(w\phi)}{\partial z}\right) dxdz \;=\; -\frac{\mathrm{Pr}}{\mathrm{Ra}}\int_w^e \int_s^n \left(\frac{\partial p}{\partial z}\right) dxdz + \frac{\mathrm{Pr}}{\mathrm{Ra}}\int_w^e \int_s^n \left(\frac{\partial^2\phi}{\partial x^2} + \frac{\partial^2\phi}{\partial z^2}\right) dxdz$$

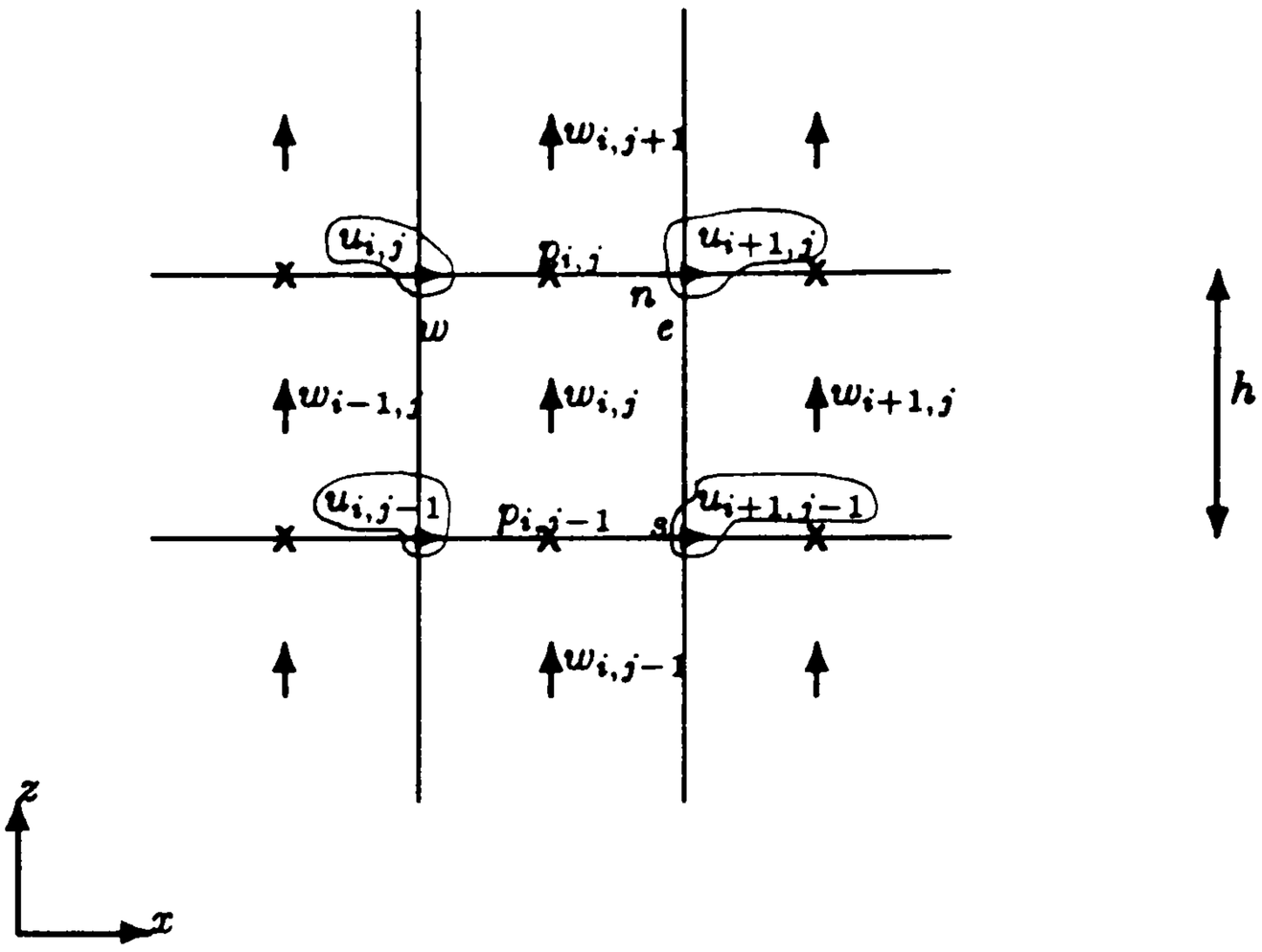

Figure 2.7: Control volume for the w-velocity.

$$+ \frac{\mathrm{Pr}}{\mathrm{Ra}} \int_w^e \int_s^n (\theta - \theta_0) dx dz \tag{2.8}$$

$$[(u\phi)_e - (u\phi)_w + (w\phi)_n - (w\phi)_s]\, h = \frac{\mathrm{Pr}}{\mathrm{Ra}}(P_{i,j-1} - P_{i,j})h + \frac{\mathrm{Pr}}{\mathrm{Ra}}\left[\left.\frac{\partial\phi}{\partial x}\right|_e - \left.\frac{\partial\phi}{\partial x}\right|_w + \left.\frac{\partial\phi}{\partial z}\right|_n - \left.\frac{\partial\phi}{\partial z}\right|_s\right] h$$

$$+ \frac{\mathrm{Pr}}{\mathrm{Ra}}\left(\frac{\theta_{i,j} + \theta_{i,j-1}}{2} - \theta_0\right) h^2 \tag{2.9}$$

Then using the upwinding scheme on the convective terms gives,

$$\begin{aligned}
(u\phi)_e &= \phi_{i,j}\,|u_e, 0| - \phi_{i+1,j}\,|-u_e, 0| \\
&= \phi_{i,j}\left|\frac{u_{i+1,j} + u_{i+1,j-1}}{2}, 0\right| - \phi_{i+1,j}\left|-\frac{u_{i+1,j} + u_{i+1,j-1}}{2}, 0\right| \\
(u\phi)_w &= \phi_{i-1,j}\,|u_w, 0| - \phi_{i,j}\,|-u_w, 0| \\
&= \phi_{i-1,j}\left|\frac{u_{i,j} + u_{i,j-1}}{2}, 0\right| - \phi_{i,j}\left|-\frac{u_{i,j} + u_{i,j-1}}{2}, 0\right| \\
(w\phi)_n &= \phi_{i,j}\,|w_n, 0| - \phi_{i,j+1}\,|-w_n, 0| \\
&= \phi_{i,j}\left|\frac{w_{i,j} + w_{i,j+1}}{2}, 0\right| - \phi_{i,j+1}\left|-\frac{w_{i,j} + w_{i,j+1}}{2}, 0\right| \\
(w\phi)_s &= \phi_{i,j-1}\,|w_s, 0| - \phi_{i,j}\,|-w_s, 0| \\
&= \phi_{i,j-1}\left|\frac{w_{i,j-1} + w_{i,j}}{2}, 0\right| - \phi_{i,j}\left|-\frac{w_{i,j-1} + w_{i,j}}{2}, 0\right|
\end{aligned} \tag{2.10}$$

where $|a, b|$ denotes the maximum of a and b, and substitution in equation 2.9 gives,

$$a^w_{i,j}\phi_{i,j} = a^w_{i+1,j}\phi_{i+1,j} + a^w_{i-1,j}\phi_{i-1,j} + a^w_{i,j+1}\phi_{i,j+1} + a^w_{i,j-1}\phi_{i,j-1}$$

$$+ \frac{h\mathrm{Pr}}{\mathrm{Ra}}(P_{i,j-1} - Pi,j) + b_{i,j} \tag{2.11}$$

where

$$a^w_{i,j} = h\left[\left|\frac{u_{i+1,j}+u_{i+1,j-1}}{2},0\right|+\left|-\frac{u_{i,j}+u_{i,j-1}}{2},0\right|+\left|\frac{w_{i,j}+w_{i,j+1}}{2},0\right| + \left|-\frac{w_{i,j-1}+w_{i,j}}{2},0\right|\right]+\frac{4\mathrm{Pr}}{\mathrm{Ra}} \quad (2.12)$$

$$a^w_{i+1,j} = h\left|-\frac{u_{i+1,j}+u_{i+1,j-1}}{2},0\right|+\frac{\mathrm{Pr}}{\mathrm{Ra}} \quad (2.13)$$

$$a^w_{i-1,j} = h\left|\frac{u_{i,j}+u_{i,j-1}}{2},0\right|+\frac{\mathrm{Pr}}{\mathrm{Ra}} \quad (2.14)$$

$$a^w_{i,j+1} = h\left|-\frac{w_{i,j}+w_{i,j+1}}{2},0\right|+\frac{\mathrm{Pr}}{\mathrm{Ra}} \quad (2.15)$$

$$a^w_{i,j-1} = h\left|\frac{w_{i,j-1}+w_{i,j}}{2},0\right|+\frac{\mathrm{Pr}}{\mathrm{Ra}} \quad (2.16)$$

$$b^w_{i,j} = \frac{h^2\mathrm{Pr}}{\mathrm{Ra}}\left(\frac{\theta_{i,j}+\theta_{i,j-1}}{2}-\theta_0\right) \quad (2.17)$$

and

$$a^w_{i,j} = a^w_{i+1,j}+a^w_{i-1,j}+a^w_{i,j-1}+a^w_{i,j+1} + h\left[\frac{u_{i+1,j}+u_{i+1,j-1}}{2}-\frac{u_{i,j}+u_{i,j-1}}{2}+\frac{w_{i,j}+w_{i,j+1}}{2}-\frac{w_{i,j-1}+w_{i,j}}{2}\right]. \quad (2.18)$$

Similarly the u-momentum equation can be written as

$$a^u_{i,j}\phi_{i,j} = a^w_{i+1,j}\phi_{i+1,j}+a^u_{i-1,j}\phi_{i-1,j}+a^u_{i,j+1}\phi_{i,j+1}+a^u_{i,j-1}\phi_{i,j-1} + \frac{h\mathrm{Pr}}{\mathrm{Ra}}(P_{i-1,j}-Pi,j) \quad (2.19)$$

where

$$a^u_{i,j} = a^u_{i+1,j}+a^u_{i-1,j}+a^u_{i,j-1}+a^u_{i,j+1}+h\left[\frac{u_{i+1,j}+u_{i,j}}{2}- \frac{u_{i,j}+u_{i-1,j}}{2}+\frac{w_{i-1,j+1}+w_{i,j+1}}{2}-\frac{w_{i-1,j}+w_{i,j}}{2}\right] \quad (2.20)$$

with the coefficients a^u's being derived in the same manner as a^w's. Hence the discrete momentum equations can be written as

$$a^u_{i,j}u_{i,j} = \sum a^u_{nb}u_{nb} + \frac{h\mathrm{Pr}}{\mathrm{Ra}}(P_{i-1,j}-P_{i,j}) \quad (2.21)$$

$$a^w_{i,j}w_{i,j} = \sum a^w_{nb}w_{nb} + \frac{h\mathrm{Pr}}{\mathrm{Ra}}(P_{i,j-1}-P_{i,j})+b^w_{i,j} \quad (2.22)$$

where the summation is over the four neighbouring control volumes.

The discrete momentum equations can only be solved when the pressure field is given or somehow estimated. Unless the correct pressure field is known, the resulting

velocity field from the momentum equations will not satisfy the continuity equation. Let u^* and w^* denote the imperfect velocity field resulting from the momentum equations based on a guessed pressure field p^*. That is

$$a^u_{i,j}u^*_{i,j} = \sum a^u_{nb}u^*_{nb} + \frac{h\mathrm{Pr}}{\mathrm{Ra}}(P^*_{i-1,j} - P^*_{i,j}) \tag{2.23}$$

$$a^w_{i,j}w^*_{i,j} = \sum a^w_{nb}w^*_{nb} + \frac{h\mathrm{Pr}}{\mathrm{Ra}}(P^*_{i,j-1} - P^*_{i,j}) + b^w_{i,j}. \tag{2.24}$$

The aim of the SIMPLE algorithm now is to improve the guessed pressure field p^* such that the resulting starred velocities will progressively get closer to satisfying the continuity equation. Let the correct pressure p be obtained from

$$p = p^* + p' \tag{2.25}$$

where p' is the pressure-correction. The corresponding velocity corrections u', w' can be introduced in a similar manner

$$u = u^* + u' \tag{2.26}$$

$$w = w^* + w'. \tag{2.27}$$

Subtracting equation 2.23 from equation 2.21 gives

$$a^u_{i,j}u'_{i,j} = \sum a^u_{nb}u'_{nb} + \frac{h\mathrm{Pr}}{\mathrm{Ra}}(P'_{i-1,j} - P'_{i,j}) \tag{2.28}$$

The assumption made here is that the coefficients $a^u_{i,j}$ are exact and known. Dropping the summation term in equation 2.28 gives

$$u'_{i,j} = \frac{h\mathrm{Pr}}{\mathrm{Ra}a^u_{i,j}}(P'_{i-1,j} - P'_{i,j}) \tag{2.29}$$

which can be rewritten as

$$u_{i,j} = u^*_{i,j} + \frac{h\mathrm{Pr}}{\mathrm{Ra}a^u_{i,j}}(P'_{i-1,j} - P'_{i,j}). \tag{2.30}$$

Equation 2.30 is known as the velocity-correction formula. A similar velocity-correction formula can be obtained for the velocities in the z-direction

$$w_{i,j} = w^*_{i,j} + \frac{h\mathrm{Pr}}{\mathrm{Ra}a^w_{i,j}}(P'_{i,j-1} - P'_{i,j}). \tag{2.31}$$

The velocity-correction formulae show how the starred velocities are to be corrected in response to the pressure-corrections p' to produce the corrected velocities which should satisfy the continuity equation slightly better.

The equation to calculate the pressure-corrections is obtained via the continuity equation by integrating it over the pressure control volume depicted in Figure 2.8 and then substituting the velocity-correction formulae for the velocities.

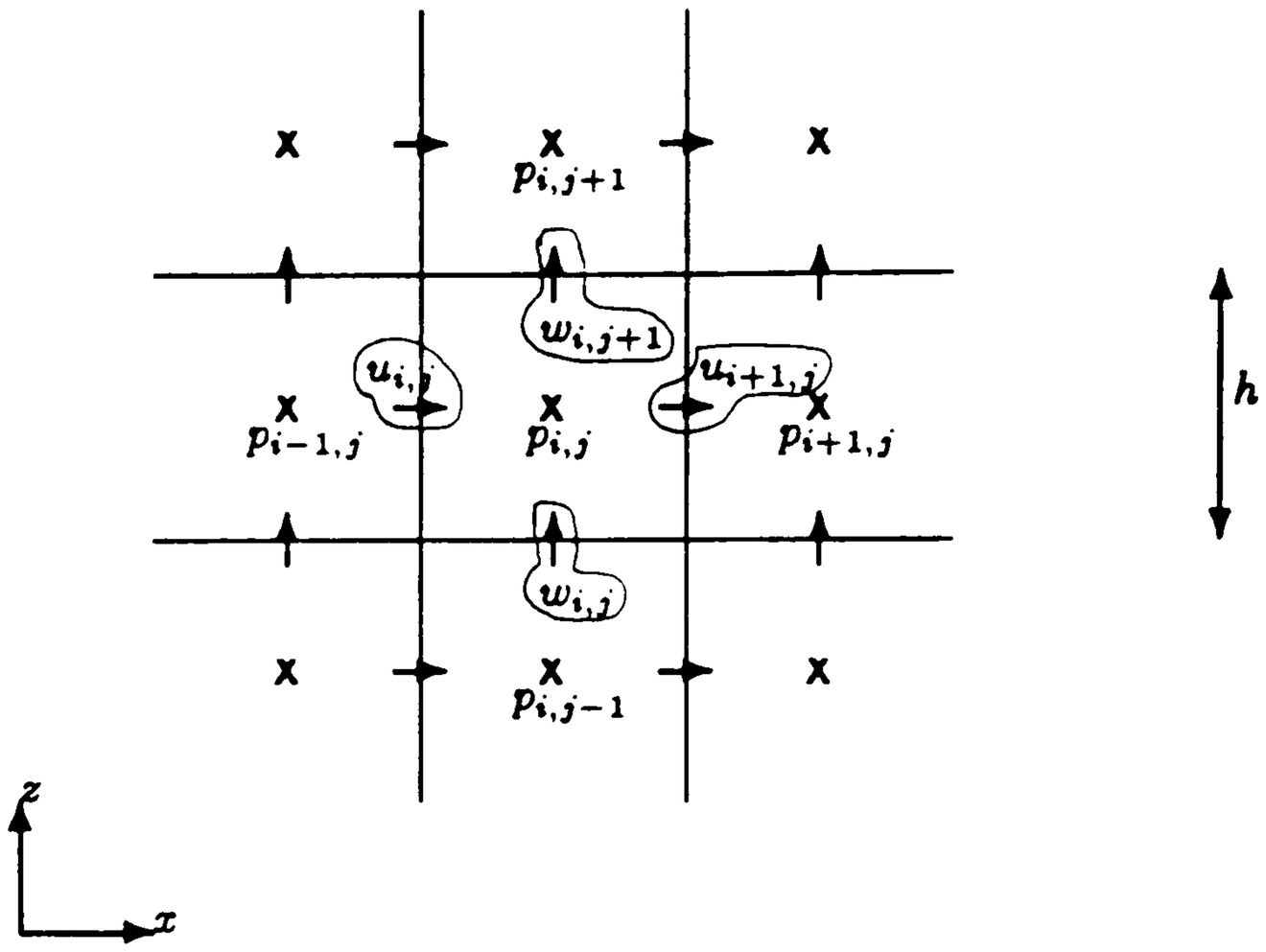

Figure 2.8: Control volume for the pressure.

Hence

$$\int_{u_{i,j}}^{u_{i+1,j}} \int_{w_{i,j}}^{w_{i,j+1}} \left(\frac{\partial u}{\partial x} + \frac{\partial w}{\partial z} \right) dx dz = 0 \tag{2.32}$$

$$(u_{i+1,j} - u_{i,j} + w_{i,j+1} - w_{i,j})h = 0 \tag{2.33}$$

and substituting equations 2.30 and 2.31 into equation 2.33 gives

$$a^p_{i,j} p'_{i,j} = a^p_{i+1,j} p'_{i+1,j} + a^p_{i-1,j} p'_{i-1,j} + a^p_{i,j+1} p'_{i,j+1} + a^p_{i,j-1} p'_{i,j-1} + b^p_{i,j} \tag{2.34}$$

where

$$a^p_{i,j} = \frac{h\mathrm{Pr}}{\mathrm{Ra}} \left(\frac{1}{a^u_{i+1,j}} + \frac{1}{a^u_{i,j}} + \frac{1}{a^w_{i,j+1}} + \frac{1}{a^w_{i,j}} \right) \tag{2.35}$$

$$a^p_{i+1,j} = \frac{h\mathrm{Pr}}{\mathrm{Ra}} \frac{1}{a^u_{i+1,j}} \tag{2.36}$$

$$a^p_{i-1,j} = \frac{h\mathrm{Pr}}{\mathrm{Ra}} \frac{1}{a^u_{i,j}} \tag{2.37}$$

$$a^p_{i,j+1} = \frac{h\mathrm{Pr}}{\mathrm{Ra}} \frac{1}{a^w_{i,j+1}} \tag{2.38}$$

$$a^p_{i,j-1} = \frac{h\mathrm{Pr}}{\mathrm{Ra}} \frac{1}{a^w_{i,j}} \tag{2.39}$$

$$b^p_{i,j} = u^*_{i,j} - u^*_{i+1,j} + u^*_{i,j} - w^*_{i,j+1} \tag{2.40}$$

$$a^p_{i,j} = a^p_{i+1,j} + a^p_{i-1,j} + a^p_{i,j+1} + a^p_{i,j-1}. \tag{2.41}$$

Pressure-corrections are of course located at the same point as the pressures. The term $b^p_{i,j}$ in the pressure-correction equation is essentially the negated left hand side of

the discretized continuity equation evaluated in terms of the starred velocities. Hence the term $b^p_{i,j}$ represents the mass source term, which if equal to zero implies that the starred velocities satisfy the continuity equation and no pressure-corrections are required.

Temperature equation

Integrating the temperature equation 2.4 over the control volume depicted below:

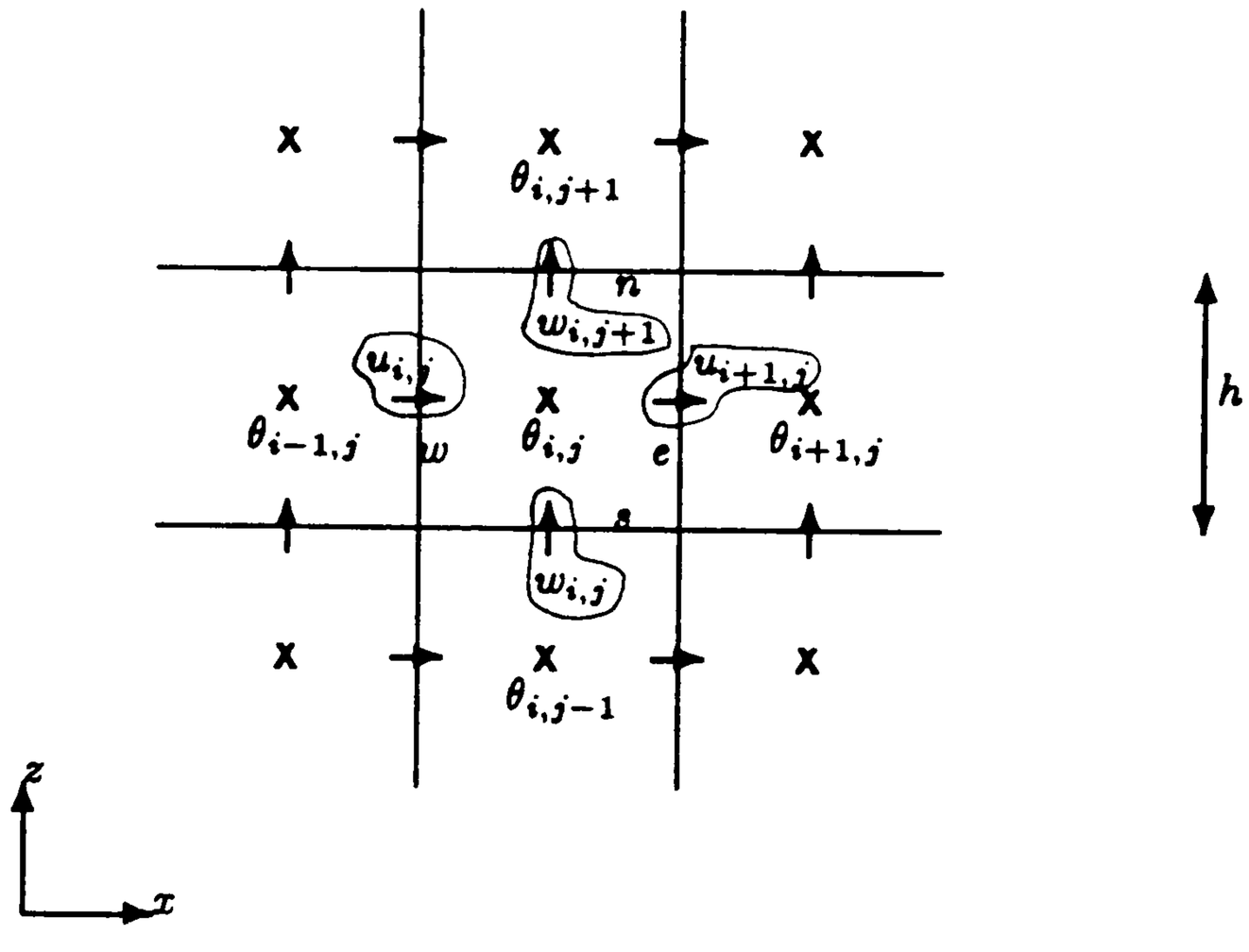

Figure 2.9: Control volume for the temperature.

gives

$$\int_w^e \int_s^n \left(\frac{\partial(u\theta)}{\partial x} + \frac{\partial(w\theta)}{\partial z} \right) dxdz = \frac{1}{\mathrm{Pr}} \int_w^e \int_s^n \left(\frac{\partial^2\theta}{\partial x^2} + \frac{\partial^2\theta}{\partial z^2} \right) dxdz \tag{2.42}$$

$$[(u\theta)_e - (u\theta)_w + (w\theta)_n - (w\theta)_s]\, h = \frac{1}{\mathrm{Pr}} \left[\left.\frac{\partial\theta}{\partial x}\right|_e - \left.\frac{\partial\theta}{\partial x}\right|_w + \left.\frac{\partial\theta}{\partial z}\right|_n - \left.\frac{\partial\theta}{\partial z}\right|_s \right] h. \tag{2.43}$$

Using the upwinding scheme on the convective terms gives,

$$\begin{aligned}
(u\theta)_e &= \theta_{i,j} \left| \frac{u_{i+1,j}}{2}, 0 \right| - \theta_{i+1,j} \left| -\frac{u_{i+1,j}}{2}, 0 \right| \\
(u\theta)_w &= \theta_{i-1,j} \left| \frac{u_{i,j}}{2}, 0 \right| - \theta_{i,j} \left| -\frac{u_{i,j}}{2}, 0 \right| \\
(w\theta)_n &= \theta_{i,j} \left| \frac{w_{i,j+1}}{2}, 0 \right| - \theta_{i,j+1} \left| -\frac{w_{i,j+1}}{2}, 0 \right| \\
(w\theta)_s &= \theta_{i,j-1} \left| \frac{w_{i,j}}{2}, 0 \right| - \theta_{i,j} \left| -\frac{w_{i,j}}{2}, 0 \right|
\end{aligned}$$

and thus equation (2.43) can be written as

$$a^\theta_{i,j}\theta_{i,j} = a^\theta_{i+1,j}\theta_{i+1,j} + a^\theta_{i-1,j}\theta_{i-1,j} + a^\theta_{i,j+1}\theta_{i,j+1} + a^\theta_{i,j-1}\theta_{i,j-1} \tag{2.44}$$

where

$$a^{\theta}_{i,j} = h\left[\left|\frac{u_{i+1,j}}{2},0\right| + \left|-\frac{u_{i,j}}{2},0\right| + \left|\frac{w_{i,j+1}}{2},0\right| + \left|-\frac{w_{i,j}}{2},0\right|\right] + \frac{4}{\mathrm{Pr}} \tag{2.45}$$

$$a^{\theta}_{i+1,j} = h\left|-\frac{u_{i+1,j}}{2},0\right| + \frac{1}{\mathrm{Pr}} \tag{2.46}$$

$$a^{\theta}_{i-1,j} = h\left|\frac{u_{i,j}}{2},0\right| + \frac{1}{\mathrm{Pr}} \tag{2.47}$$

$$a^{\theta}_{i,j+1} = h\left|-\frac{w_{i,j+1}}{2},0\right| + \frac{1}{\mathrm{Pr}} \tag{2.48}$$

$$a^{\theta}_{i,j-1} = h\left|\frac{w_{i,j}}{2},0\right| + \frac{1}{\mathrm{Pr}} \tag{2.49}$$

and

$$a^{\theta}_{i,j} = a^{\theta}_{i+1,j} + a^{\theta}_{i-1,j} + a^{\theta}_{i,j-1} + a^{\theta}_{i,j+1} + h\left[u_{i+1,j} - u_{i,j} + w_{i,j+1} - w_{i,j}\right]. \tag{2.50}$$

The steps involved in the SIMPLE algorithm are:

1. guess the pressure field p^*.

2. solve the momentum equations 2.23 and 2.24.

3. check the residual of the continuity equation.
   (which is the convergence criterion for the SIMPLE algorithm)

4. solve the pressure-correction equation 2.34.

5. update the pressure field p^* by p', equation 2.25.

6. solve other discrete equations
   (with the double glazing problem solve for θ, equation 2.43).

7. treat the corrected pressures as new guessed pressures
   and repeat from step 2.

The derived pressure-correction equation can lead to slow convergence or even divergence. This is due to neglecting neighbouring velocity correction terms in the velocity-correction formulae. In order to ensure convergence of the SIMPLE algorithm the pressure-corrections have to be under-relaxed. That is the updating in step 5 is performed by

$$p_{i,j} = p^*_{i,j} + \alpha p'_{i,j} \tag{2.51}$$

where $0 < \alpha \leq 1$ is the pressure-correction under-relaxation parameter. The velocity correction equations 2.26 and 2.27 are not under-relaxed. Instead velocities derived from the momentum equations are under-relaxed, namely

$$u_{i,j}^{new} = u_{i,j}^{old} + \beta(u_{i,j}^{calculated} - u_{i,j}^{old}) \tag{2.52}$$

where $0 < \beta < 1$ is the velocity under-relaxation parameter. Optimum relaxation parameters α and β generally depend on the fluid flow problem being solved and are obtained by trial and error.

2.6 Boundary conditions

For the test problem considered the following boundary conditions exist:

- Dirichlet velocity conditions,
- Dirichlet and Neumann temperature conditions.

The pressure boundary conditions are unknown.

When solving the discrete momentum equations at or near the boundaries no difficulties arise since the velocities are known at the boundaries and with the pressure and temperature locations lying in the interior no boundary information about them is required. However when solving the pressure-correction equation at the boundaries there appears to be some difficulty since the pressure boundary conditions are unknown. When deriving the pressure-correction equation this difficulty is easily overcome by expressing the flow rate across the boundary faces in terms of the known velocity boundary conditions rather than the estimated velocity and its corresponding correction (i.e. substituting u into equation 2.30 rather than $u^* + u'$). This then eliminates the need for pressure or pressure-correction boundary conditions. So the pressure-correction equation for a cell with one boundary face results in a 4-pt discrete equation and for a corner cell in a 3-pt discrete equation.

It should be noticed that if the pressure is not specified at a boundary or at an interior location then the pressure-correction equation is left without any means of establishing the absolute value of the pressure-corrections. Since the important quantity is the pressure gradient, pressure is then a relative variable and not an absolute one. Hence only pressure differences are meaningful and these are not altered by an arbitrary constant added to the pressure-correction field. It also appears to be more

computationally economical for the pressure-correction to seek its own value rather than fixing it at a particular grid point [63].

For the temperature a Neumann boundary condition is given at the top and bottom walls and a Dirichlet boundary condition at the side walls. When deriving the temperature equation for a cell at the top or bottom wall the Neumann condition can be substituted for the integrated diffusion terms and the convective terms can be eliminated due to zero velocities at the boundary. When deriving the temperature equation for a cell at the side walls, the convective terms can again be eliminated due to zero velocities and the forward and backward differences are used for the diffusion terms at the left and right side walls respectively.

2.7 Solving the discretized equations

The method chosen to solve the discretized equations is the line Gauss-Seidel method. This method is a combination of a direct and an iterative method and is efficient in terms of computer storage, programming complexity and convergence. In one-dimension this method becomes a direct method, solving a system of linear equations (a tridiagonal matrix) via forward and backward substitution, (the tridiagonal matrix algorithm). In two-dimensions, lines of unknowns are solved using the tridiagonal matrix algorithm marching first in one direction and then the other. That is first solving vertical lines marching from left to right and then solving horizontal lines marching from top to bottom. This is called a double relaxation sweep.

When solving a non-linear system of equations such as the discretized Navier-Stokes equations it is unnecessary to solve each equation to final convergence for a fixed set of coefficient values. With a given set of these values a few iterations of the solver, line Gauss-Seidel, are sufficient before updating of the coefficients is performed. In general there should be a balance between the effort required to calculate the coefficients and the time spent on solving these equations. Basically it is unwise to spend an excessive amount of computational effort in solving equations that are based on tentative coefficients.

The recommended number of double sweeps of the line Gauss-Seidel solver are one for the momentum equations, four to six for the pressure-correction equation and one for the other equations, such as the temperature equation, see [7], [46], [47], [53] and [63].

Other methods such as ADI, Stones strongly implicit method, conjugate gradient methods and multigrid methods can be used to solve the discretized equations.

2.8 Optimum relaxation parameters

As indicated above, the convergence of the SIMPLE algorithm is very much dependent on how well the pressure-correction is solved. The approximations made in deriving the pressure-correction requires the pressure and velocities to be under-relaxed. These under-relaxation parameters have to be chosen by trial and error. As there is no guide for choosing these parameters a study has been carried out to analyse the behaviour of the relaxation parameters. Two further parameters have also been investigated, these being the number of double relaxation sweeps performed on the momentum and the pressure-correction equations.

The fluid flow problem studied is the double-glazing problem for air($Pr = 0.71$) and cerrobase($Pr = 0.035$) at $Ra = 10^3$ on 8x8, 16x16 and 24x24 mesh sizes. Temperatures are not under-relaxed. Pressure is under-relaxed when updating the pressure with the pressure-correction, that is:

$$\text{new pressure} = \text{old pressure} + \alpha(\text{pressure-correction})$$

$$p_{i,j} = p^*_{i,j} + \alpha p'_{i,j} \tag{2.53}$$

where $0 < \alpha \leq 1$. The velocities are under-relaxed after the tridiagonal matrix algorithm has been performed on each grid line of the solution domain, that is,

$$u^{new}_{i,j} = u^{old}_{i,j} + \beta(u^{calculated}_{i,j} - u^{old}_{i,j}) \tag{2.54}$$

where $0 < \beta < 1$. For each grid considered, four combinations of double relaxation sweeps were applied to the momentum and pressure-correction equations. See Table 2.1.

Combination	Number of double-relaxation sweeps	
	momentum equation	pressure-correction equation
2m:2pc	2	2
1m:2pc	1	2
1m:3pc	1	3
1m:10pc	1	10

Table 2.1: Combination of double relaxation sweeps

The optimum combination of relaxation parameters, (α, β), for a particular combination of double relaxation sweeps is the one that results in producing the fluid flow solution with the smallest amount of computational cost. The convergence criterion for the SIMPLE algorithm was to reduce the residual of the continuity equation by 10^{-5} .

2.8.1 Results

A pilot study for finding the optimum combination of α and β was performed with α fixed at a particular value and β varied from 0.1 to 0.9 in steps of 0.1. It was found that as β was increased from 0.1 to 0.9 the number of global iterations required for the SIMPLE algorithm to converge to the specified tolerance started to decrease, reached a minimum, then started to increase and finally for larger β divergence resulted. When the final study was performed with values of α varying from 0.1 to 0.9 in steps of 0.1, β was varied from 0.1 by steps of 0.1 until the minimum number of global iterations to converge was obtained. The maximum number of global iterations allowed per combination of α and β was 200. The total number of global iterations and the total c.p.u. time taken to converge are tabulated in Tables 2.2 - 2.7. As the finer mesh solutions are more computationally expensive fewer combinations of α and β have been tried. The computations have been performed on the Honeywell Multics Computer. The key n/c in the tables denotes that the SIMPLE algorithm did not converge. The minimum amount of c.p.u. time taken to converge for each combination of the double relaxation sweep has been underlined in the tables.

α	β								
	0.1	0.2	0.3	0.4	0.5	0.6	0.7	0.8	0.9
0.1	ITS 184	119	98	89	85	83	83	83	83
	CPU 227	148	121	115	107	103	103	103	103
0.2	90	59	48	45	46				
	113	75	61	58	59				
0.3	59	40	47						
	75	52	60						
0.4	44	41	75						
	57	53	94						
0.5	37	62							
	48	79							
0.6	39	94							
	51	117							
0.7	42	164							
	54	204							
0.8	51	200+							
	65	251+							
0.9	63	200+							
	80	251+							
1.0	87	200+							
	109	251+							

Table 2.2: Grid 8x8, double sweep combination 2m:2pc

α	β								
	0.1	0.2	0.3	0.4	0.5	0.6	0.7	0.8	0.9
0.1	ITS 200+	176	133	111	98	90	85	83	83
	CPU 165+	145	110	93	82	76	72	70	70
0.2	144	86	65	54	48	46	45	46	
	119	73	56	47	42	40	39	40	
0.3	94	57	43	39	44				
	79	49	38	35	39				
0.4	69	42	39	54					
	59	37	35	47					
0.5	59	37	51						
	51	33	48						
0.6	54	39	69						
	47	35	59						
0.7	52	52	98						
	45	45	82						
0.8	50	61							
	43	52							
0.9	51	76							
	44	65							
1.0	51	93							
	44	78							

Table 2.3: Grid 8x8, double sweep combination 1m:2pc

α	β								
	0.1	0.2	0.3	0.4	0.5	0.6	0.7	0.8	0.9
0.1	ITS 200+	176	133	111	98	90	85	83	83
	CPU 418+	368	278	233	206	189	179	175	175
0.2	144	86	65	54	48	44	42	41	41
	302	181	137	114	102	93	89	87	87
0.3	94	56	43	36	31	29	27	27	27
	197	118	91	77	66	62	58	58	58
0.4	69	42	31	26	23	21	20	20	20
	145	89	67	57	50	46	44	44	44
0.5	59	33	25	23	18	17	16	19	
	126	71	54	44	40	38	35	42	
0.6	54	29	20	17	15	13	21		
	115	63	44	38	33	29	46		
0.7	52	27	18	14	12	17			
	110	58	39	31	27	38			
0.8	50	25	17	13	13	50			
	106	54	37	29	29	106			
0.9	50	25	16	12	21				
	106	45	35	27	46				
1.0	50	25	16	12	59				
	106	54	35	27	124				

Table 2.5: Grid 8x8, double sweep combination 1m:10pc

α	β								
	0.1	0.2	0.3	0.4	0.5	0.6	0.7	0.8	0.9
0.1	ITS 200+	176	133	111	98	90	90	85	83
	CPU 197+	173	132	110	97	90	90	85	83
0.2	144	86	65	54	48	44	42	41	41
	141	86	66	55	49	46	43	42	42
0.3	94	43	36	32	31	32			
	94	45	37	33	32	33			
0.4	69	42	31	29	30				
	69	43	32	30	31				
0.5	59	33	29	30					
	60	34	30	31					
0.6	54	29	28	39					
	55	30	29	40					
0.7	52	27	35						
	53	28	37						
0.8	50	29	39						
	51	30	41						
0.9	50	31	48						
	51	32	49						
1.0	50	33	56						
	51	34	57						

Table 2.4: Grid 8x8, double sweep combination 1m:3pc

Figure 2.10 Random point contour plot for 8x8 and 2m:2pc

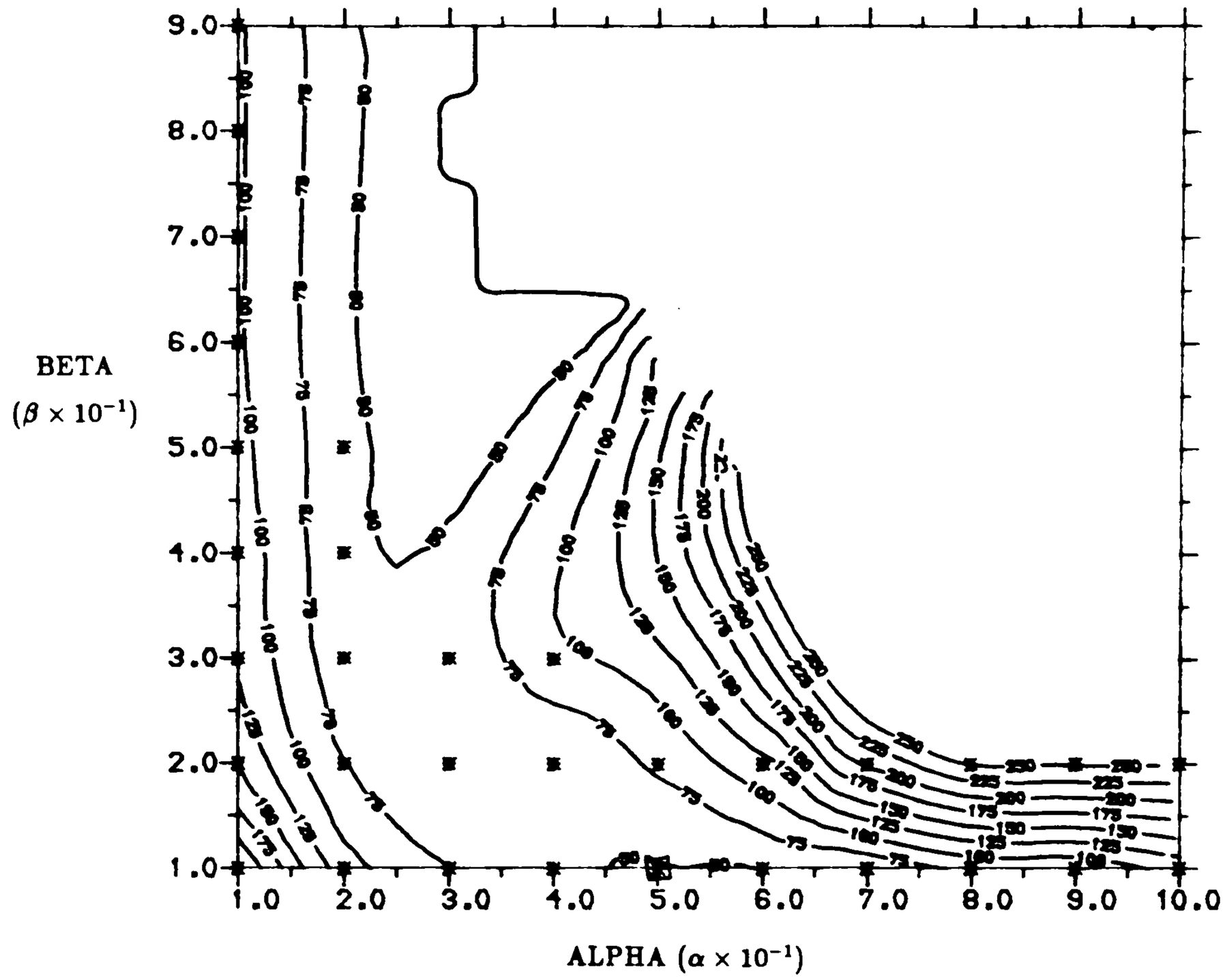

Figure 2.11 Random point contour plot for 8x8 and 1m:2pc

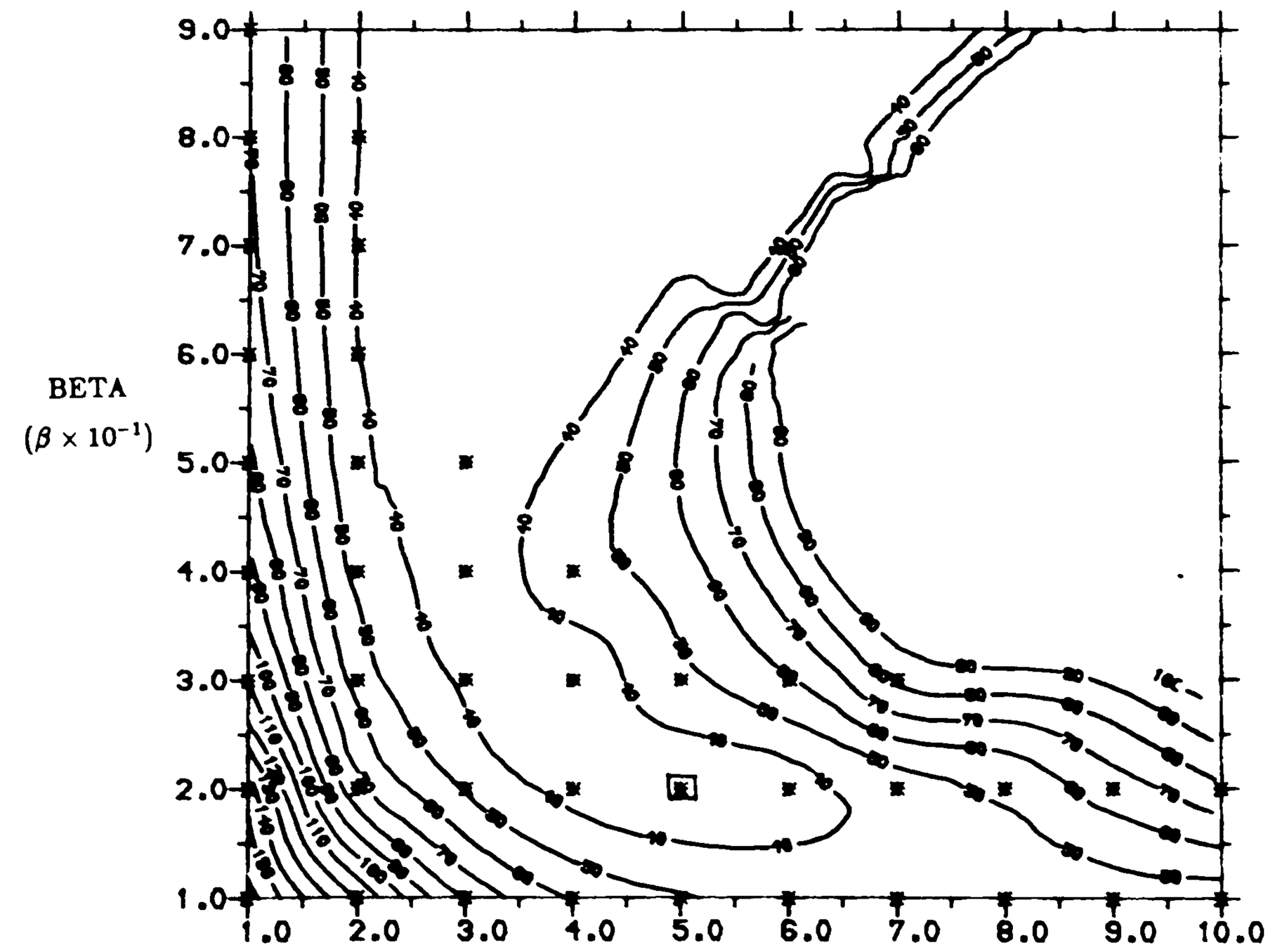

Figure 2.12 Random point contour plot for 8x8 and 1m:3pc

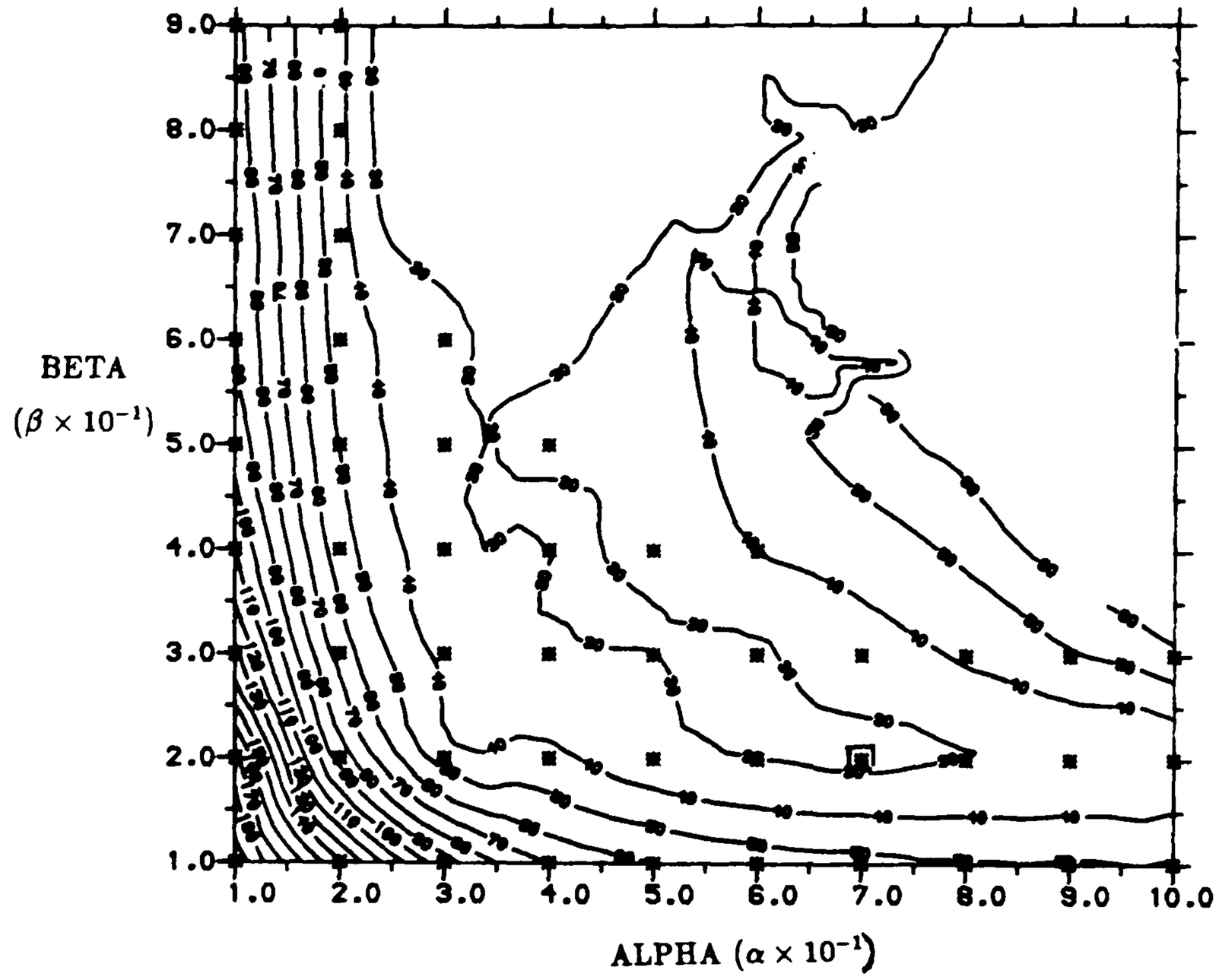

Figure 2.13 Random point contour plot for 8x8 and 1m:10pc

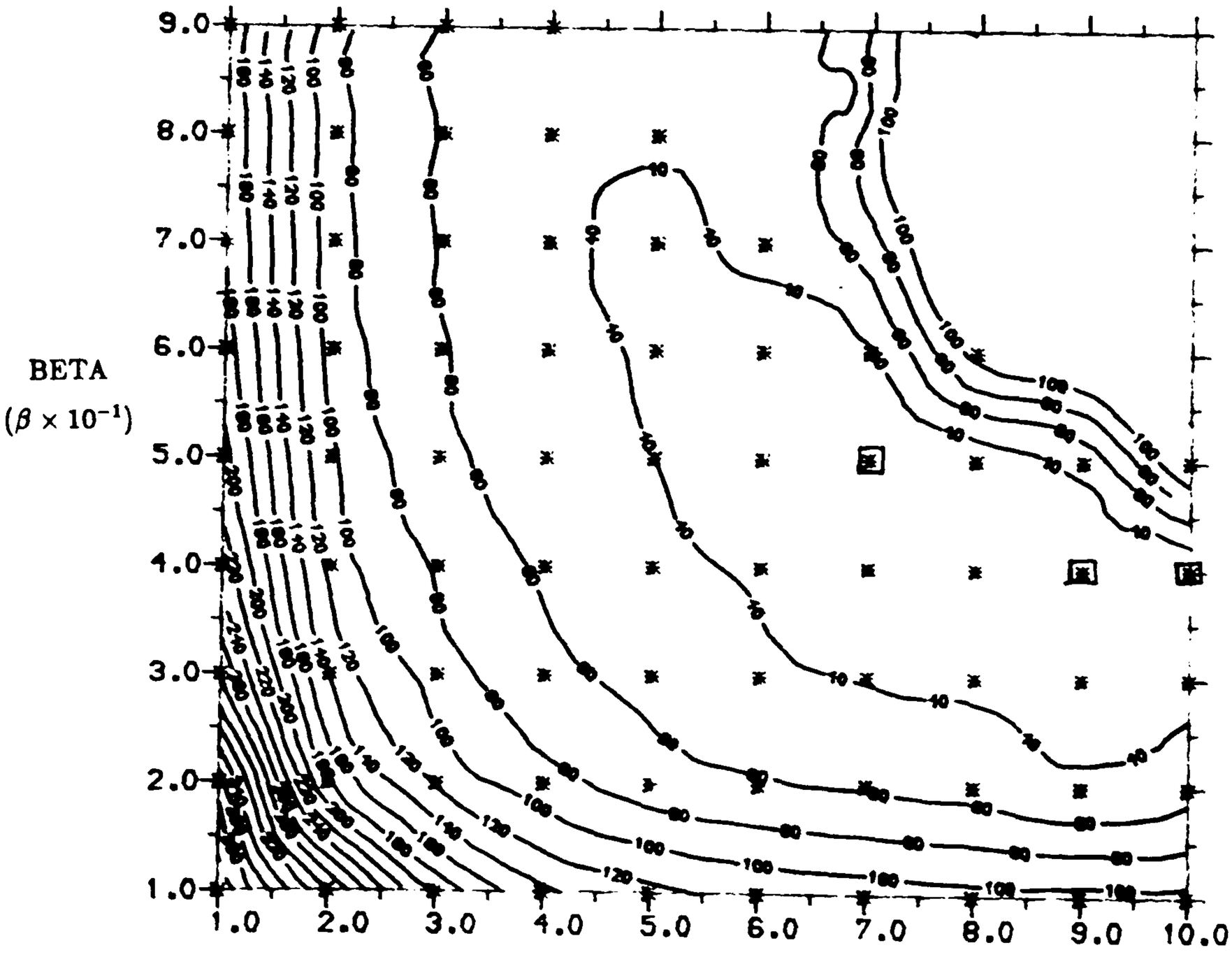

Key:	α	β									
		0.1		0.3		0.5		0.7		0.9	
m:pc		ITS	CPU	ITS	CPU	ITS	CPU	ITS	CPU	ITS	CPU
2:2	0.1	184	975	200+	1060						
1:2		200+	697	136	474	200+	697				
1:3		200+	827	133	550	115	477	200+	827		
1:10		200+	1732	133	1152	98	852	85	741	83	723
2:2	0.3	200+	1060								
1:2		127	443	200+	697						
1:3		99	415	200+	827						
1:10		99	861	44	387	43	379	100	878		
2:2	0.5	n/c									
1:2		200+	697								
1:3		120	500	n/c							
1:10		101	878	46	405	66	580				
2:2	0.7	n/c									
1:2		n/c									
1:3		199	832	n/c							
1:10		101	878	60	526	200+	1738				
2:2	0.9	n/c									
1:2		n/c									
1:3		n/c									
1:10		102	910	152	1327	n/c					

Table 2.6: Grid 16x16

Key:	α	β									
		0.1		0.3		0.5		0.7		0.9	
m:pc		ITS	CPU	ITS	CPU	ITS	CPU	ITS	CPU	ITS	CPU
2:2	0.1	200+	2422	n/c							
1:2		200+	1593	200+	n/c	n/c					
1:3		200+	1885	200+	n/c	n/c					
1:10		200+	3959	134	2653	99	1865	115	2277		
1:10	0.3	130	2577	84	1679	180	3577				
1:10	0.5	132	2669	200+	3959						
1:10	0.7	129	2557								
1:10	0.9	154	3045	200+	3959						

Table 2.7: Grid 24x24

Notice that with the 24x24 grid convergence for the 1m:2pc, 1m:3pc and 2m:2pc combination of double sweeps was not obtained within 200 iterations. The fastest convergence times obtained for the four combinations of the double sweeps are listed in Table 2.8.

Key:	8x8 Grid		16x16 Grid		24x24 Grid	
m:pc	ITS	CPU	ITS	CPU	ITS	CPU
2:2	37	48	184	975	200+	2422
1:2	37	33	127	443	200+	1393
1:3	27	28	92	389	200+	1885
1:10	12	27	38	336	84	1679

Table 2.8: Best results obtained with the α and β tried.

Contour plots of the amount of c.p.u. time taken to converge for a combination of (α, β) for each combination of double relaxation sweep are presented in Figures 2.10-2.13. The plots have been produced using the Gino-F random point contours plotting routine which uses a least squares fit to obtain the contours. With the 1m:10pc combination of double sweeps there is not just one optimum combination of α and β but three. There appears to be a region of optimum relaxation factors, see Figure 2.13, the optimum region is not described but the optimum combinations have been indicated by drawing a square around them.

The gradient of contours above the optimum region is steeper than that below the optimum region. Thus trial combinations of (α, β) above the optimum region leads to large increase in the c.p.u. time taken to converge and even leads to the possibility of divergence whereas those below the optimum region lead to small increase in c.p.u. time taken to converge and always guarantee convergence. With the 1m:10pc double sweep combination the region of optimum relaxation parameter is large. Thus a slight deviation from the optimum region only increases the number of iterations slightly compared to the 1m:2pc combination, implying the algorithm is less sensitive to the relaxation parameters when the pressure-correction equation is solved more accurately.

From the graphs in Figures 2.10 to 2.13 and Tables 2.2 to 2.7 it can be concluded that:

1. if α *or* β are near 1.0 then either a large number of iterations are required for convergence or divergence results.

2. the more double sweeps that are applied on the pressure-correction equation the less sensitive the SIMPLE algorithm is to the relaxation parameters.

3. As the mesh is refined the number of iterations required for convergence increases. The algorithm also becomes more sensitive to the relaxation parameters. That is, a slight deviation from the optimum region dramatically increases the number of iterations required for convergence and hence the c.p.u. time increases. (see tables).

4. With the finer mesh the optimum region is approximately defined by $0.3 < \alpha < 0.5$, $0.3 < \beta < 0.5$, see tables 2.6-2.7. If the number of double sweeps were increased the optimum region could be defined by the larger area $0.5 < \alpha < 1.0$, $0.25 < \beta < 0.7$ with the algorithm becoming less sensitive to the relaxation factors as with the smaller mesh size.

5. Combinations of (α, β) chosen below the optimum region always results in convergence. This cannot be guaranteed for combinations chosen above the optimum curve.

From Table 2.8 it can be seen that 1m:10pc is the most efficient combination of double sweeps. Note that with the line Gauss-Seidel solver the most gain in residual reduction is obtained with the first five to six double sweeps. So the 1m:6pc combination would have been more efficient than 1m:10pc with the 8x8 grid at least.

The 2m:2pc combination of double sweep performs quite poorly compared to the other combinations. This justifies the suggestion made in [46], [53] and [63] of applying only one double sweep on the momentum equations.

The main conclusion from this study is that the pressure-correction equation needs to be solved fairly accurately for the SIMPLE algorithm to converge faster and be less sensitive to the under-relaxation parameters, especially for large grid sizes. Thus a computationally cheap solver for the pressure-correction is extremely desirable.

2.8.2 Results obtained for the double-glazing problem in a square cavity

In this section results using the SIMPLE algorithm for a two-dimensional natural convection problem, namely the double-glazing problem in a square cavity, are presented. The grid used is a uniform one of size 24x24 with 1 double sweep applied to the momentum and temperature equations and 6 double sweeps applied to the pressure-correction equation. The convergence criterion of the algorithm is based on the continuity equation and a reduction of it by 10^{-6} is sought. Results have been obtained for the moderate Prandtl number fluid, air, (Pr = 0.71) with Rayleigh numbers 10^3 and 10^5 and the low Prandtl number fluid, cerrobase, (Pr = 0.035) with Rayleigh numbers 10^3 and $5x10^3$. The streamline and isotherm plots are not presented as they do not contribute any new information. The Nusselt number along the wall and the maximum stream functions for the four combinations of Rayleigh and Prandtl numbers are tabulated in Table 2.9 and have been compared with those obtained by Winters [70] and Jones [27]. Winters obtained his results using the finite-element approximation on a 37x37 irregular mesh while Jones obtained his results using the finite-difference approximation on a 50x50 regular mesh using the stream-vorticity formulation.

Pr	Ra	Nu	ψ_{max}	Nu	ψ_{max}
0.71	10^3	1.142	1.25	1.12*	1.17*
0.71	10^5	5.229	11.90	4.53*	10.00*
0.035	10^3	1.107	0.17	1.11+	0.19+
0.035	$5x10^3$	1.632	0.22	1.68+	0.25+

Table 2.9: Comparisons of Nu and ψ_{max} *K.Winters +I.P.Jones

An interesting observation is that the SIMPLE algorithm over predicts the results

for air (moderate Pr = 0.71) and under predicts the results for cerrobase (low Pr = 0.035).

For further comparison the u-velocity profiles along the mid-vertical plane for air have been plotted against those of Winters and are presented in Figures 2.14 and 2.15. With the low Rayleigh number flow the agreement of the velocity profiles is very good. With the high Rayleigh number flow, the velocity profile obtained with the SIMPLE algorithm over shoots at the velocity peaks. This is due to using a uniform coarse grid which does not model the flow in the boundary layer very well, where the peak velocities for high Rayleigh number occur. Winters has obtained his results using a 37x37 irregular mesh which models the boundary layer well. The Nusselt number and the maximum stream function for low Prandtl number obtained with the SIMPLE algorithm agree very well with the results obtained by Jones.

Winters[70]
: SIMPLE algorithm

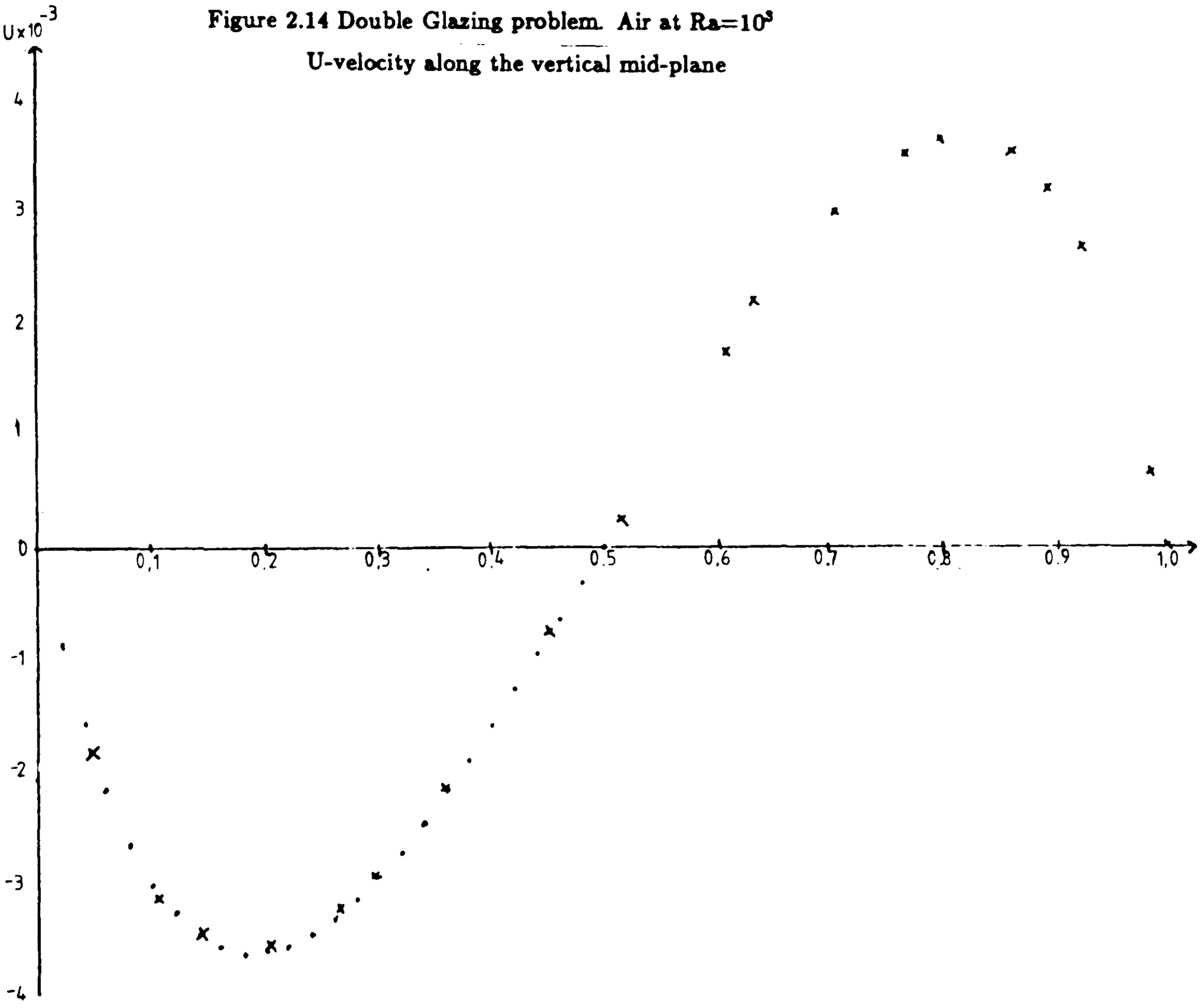

Figure 2.14 Double Glazing problem. Air at Ra=10^3

U-velocity along the vertical mid-plane

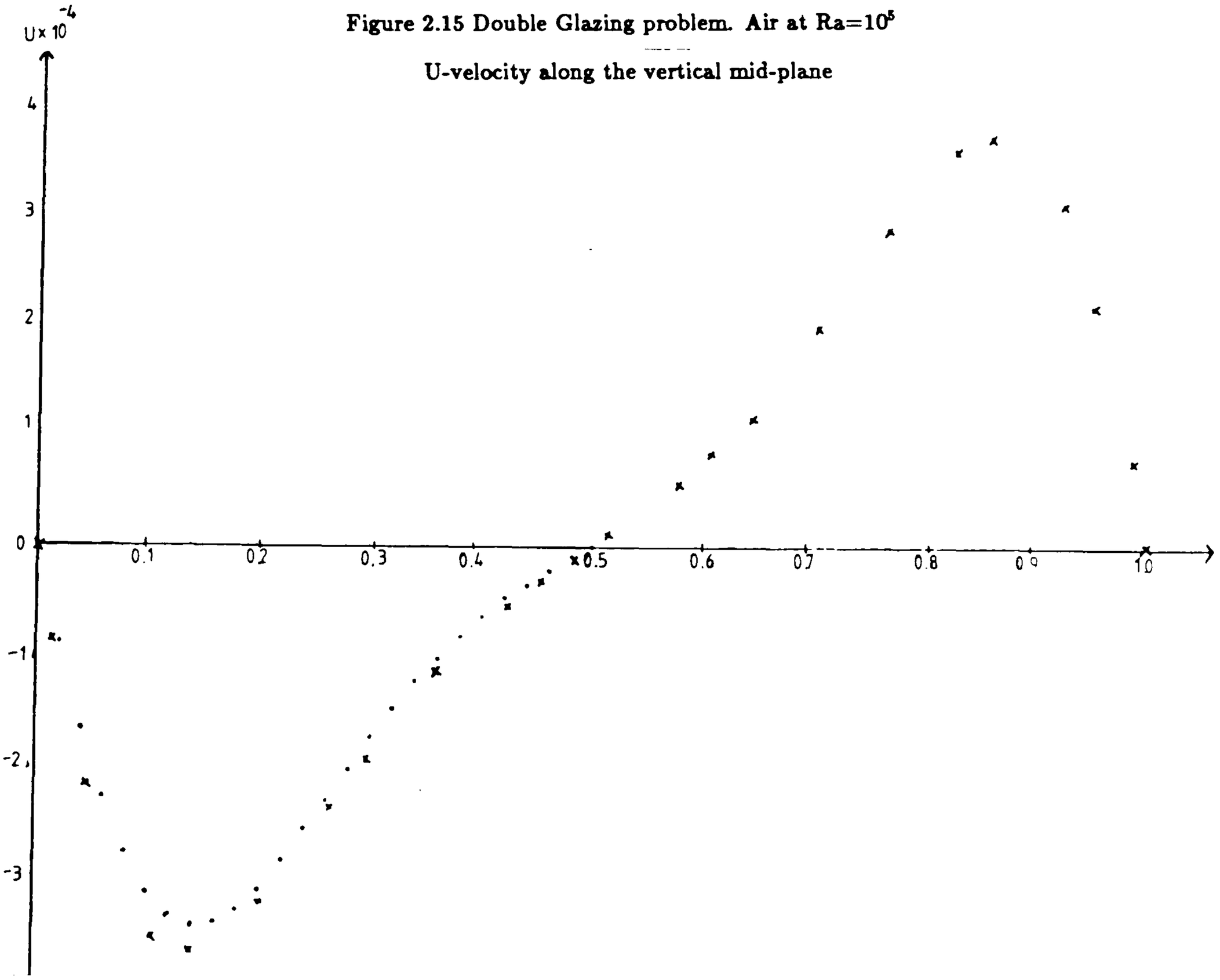

Figure 2.15 Double Glazing problem. Air at Ra=10^5

U-velocity along the vertical mid-plane

2.9 Revisions of the SIMPLE algorithm

The coarse approximation made in deriving the pressure-correction equation in the SIMPLE algorithm has lead to revised versions of SIMPLE .

A revised version of SIMPLE is SIMPLEC presented by Van Doormal and Raithby [63]. It stands for SIMPLE Corrected and is based on the inconsistency which arises from dropping the term $\sum a^u_{nb} u'_{nb}$ on the right hand side of the velocity-correction formula.

$$a^u_{i,j} u'_{i,j} = \sum a^u_{nb} u'_{nb} + \frac{h\mathrm{Pr}(P'_{i-1,j} - P'_{i,j})}{\mathrm{Ra}}. \tag{2.55}$$

The inconsistency lies in dropping the first term on the right hand side when a term of similar magnitude is retained on the left hand side, that is,

$$a^u_{i,j} = \sum a^u_{nb}. \tag{2.56}$$

To introduce a consistent approximation, the term $\sum a^u_{nb} u'_{nb}$ is subtracted from both sides of the above equation 2.55,

$$(a^u_{i,j} - \sum a^u_{nb}) u'_{i,j} = \sum a^u_{nb}(u'_{nb} - u'_{i,j}) + \frac{h\mathrm{Pr}(P'_{i-1,j} - P'_{i,j})}{\mathrm{Ra}} \tag{2.57}$$

and then the first term on the right hand side neglected. This approximation in theory should not produce exaggerated pressure-correction field but under-relaxation is still required.

Another revised version of the SIMPLE algorithm is the 13-pt pressure-correction method presented by Raithby and Schneider[53]. This method also focuses on the dropped neighbouring velocity-correction terms in the velocity-correction formula. This method retains the neighbouring velocity-corrections, giving

$$a^u_{i,j} u'_{i,j} = a^u_{i+1,j} u'_{i+1,j} + a^u_{i-1,j} u'_{i-1,j} + a^u_{i,j+1} u'_{i,j+1} + a^u_{i,j-1} u'_{i,j-1} + \frac{h\mathrm{Pr}(P'_{i-1,j} - P'_{i,j})}{\mathrm{Ra}} \tag{2.58}$$

introducing the relationship

$$a^u_{i+1,j} u'_{i+1,j} = \frac{h\mathrm{Pr}(P'_{i,j} - P'_{i+1,j})}{\mathrm{Ra}}. \tag{2.59}$$

The above equation is really the velocity correction formula at point $u_{i+1,j}$ with the summation term dropped. Effectively the summation term is dropped at a distance two mesh points away from the point (i,j) instead of the neighbouring points. Similar relationships for the w-velocity-correction formula can be calculated and when substituted into the discrete continuity equation, they lead to a 13-point pressure-correction equation. This method has too many disadvantages, viz.

1. Boundary conditions require special attention, that is, near the boundaries the accuracy obtained is lost with the method reverting back to the SIMPLE algorithm

2. the method seems to improve convergence and stability but this is offset by the additional complexities, especially with three-dimensional problems.

3. It is necessary to resort to pointwise-relaxation schemes to solve for the 13-point operator.

Finally another revised version of the SIMPLE algorithm is the SIMPLER algorithm presented by Patankar [46]. SIMPLER stands for SIMPLE Revised. As mentioned in the last section, the pressure-correction field does a good job of correcting the velocities but a rather poor job of correcting the pressure field. This is due to dropping the neighbouring velocity-correction formulas. The SIMPLER algorithm derives a pressure equation in order to calculate a better pressure field. The pressure field is obtained as follows. The momentum equation is,

$$u_{i,j} = \frac{\sum a^u_{nb} u_{nb}}{a^u_{i,j}} + \frac{h\mathrm{Pr}(P'_{i-1,j} - P'_{i,j})}{\mathrm{Ra} a^u_{i,j}} \tag{2.60}$$

which, by defining the pseudo velocity $\hat{u}_{i,j}$ by

$$\hat{u}_{i,j} = \frac{\sum a^u_{nb} u_{nb}}{a^u_{i,j}} \tag{2.61}$$

can be written as

$$u_{i,j} = \hat{u}_{i,j} + \frac{h\mathrm{Pr}(P'_{i-1,j} - P'_{i,j})}{\mathrm{Ra} a^u_{i,j}}. \tag{2.62}$$

Then substitution of equation 2.62 into the discrete continuity equation 2.33 yields

$$A_{i,j} P_{i,j} = A_{i,j} P_{i,j} + A_{i,j} P_{i,j} + A_{i,j} P_{i,j} + A_{i,j} P_{i,j} + B_{i,j} \tag{2.63}$$

where

$$A_{i+1,j} = \frac{h\mathrm{Pr}}{\mathrm{Ra} a^u_{i+1,j}} \tag{2.64}$$

$$A_{i-1,j} = \frac{h\mathrm{Pr}}{\mathrm{Ra} a^u_{i,j}} \tag{2.65}$$

$$A_{i,j+1} = \frac{h\mathrm{Pr}}{\mathrm{Ra} a^w_{i,j+1}} \tag{2.66}$$

$$A_{i,j-1} = \frac{h\mathrm{Pr}}{\mathrm{Ra} a^w_{i,j}} \tag{2.67}$$

$$A_{i,j} = \frac{h\mathrm{Pr}}{\mathrm{Ra}} \left(\frac{1}{a^u_{i+1,j}} + \frac{1}{a^u_{i,j}} + \frac{1}{a^w_{i,j+1}} + \frac{1}{a^w_{i,j}} \right) \tag{2.68}$$

$$B_{i,j} = \hat{u}_{i,j} - \hat{u}_{i+1,j} + \hat{w}_{i,j} + \hat{w}_{i,j+1}. \tag{2.69}$$

The expression for $B_{i,j}$ is the only difference between the pressure and the pressure-correction equations. No approximations have been introduced in the derivation of the

pressure equation. Thus if a correct velocity field were used to calculate the pseudo velocities the pressure equations would at once give the correct pressures.

The steps involved in the SIMPLER algorithm are:

1. start with guessed velocity field u^* and w^*

2. calculate momentum equation coefficients and $\hat{u}, \hat{w}$

3. calculate pressure coefficients and solve for pressure

4. treat pressure as p^* and solve momentum equation to obtain u^* and w^*

5. solve the pressure-correction equation

6. correct velocities using velocity-correction formulas but DO NOT correct the pressure i.e $(p = p^* + p')$

7. solve for other discrete equations such as for θ

8. repeat from step 2 until convergence

The convergence criterion for the SIMPLER algorithm is the same as for the SIMPLE algorithm, namely the residual of the continuity equation satisfying some tolerance. The SIMPLER algorithm requires 30% greater computational effort than the SIMPLE algorithm. This extra effort results from solving the pressure equation. In a comparison study of the SIMPLE, SIMPLEC and SIMPLER algorithms, performed by Van Doormal and Raithby [63] on the driven flow in a square cavity (20x20 grid), it has been shown that SIMPLEC performed better than SIMPLER and that SIMPLER performed better than SIMPLE . In this study the momentum equations with all three algorithms were not under-relaxed but SIMPLE has optimal behaviour when momentum equations are under-relaxed along with the pressure-correction equation, see section 2.9.

The important point to note with all these algorithms and those like MAC and SOLA, is that the pressure-correction uses the bulk of the c.p.u. time, approximately 70%, since it has to be solved fairly accurately in order to obtain convergence of the algorithms. If an efficient method of solving the pressure-correction equation could be found all these algorithms would become robust.

Chapter 3

The linear multigrid method

3.1 Introduction

Results in the last chapter indicated that with the SIMPLE algorithm it is important to solve the pressure-correction equation accurately at every outer iteration, as this determines the sensitivity of the under-relaxation parameters and more significantly, it determines the number of outer iterations required for convergence, [30]. This is demonstrated in Figure 3.1 which is a graph of *global iterations of the SIMPLE algorithm against log of the mass-continuity residual.* The dashed line is the result obtained when the residual of the pressure-correction equation is reduced by 0.8 at every global iteration and the solid line is the result obtained when the residual of the pressure-correction equation is reduced by 10^{-3}. The benefit of solving the pressure-correction equation accurately can be clearly seen. Since the majority of the computational effort, about 80% with two-dimensional problems and more with three-dimensional problems, is taken up by the pressure-correction equation, it is clearly advantageous to find a method which solves the equation accurately and "cheaply".

The multigrid principle provides a general concept for solving the discrete elliptic partial differential equations very efficiently. In this chapter the linear multigrid method is presented from a practical point of view and a brief introduction of the non-linear multigrid method is also presented for the sake of completeness. An in-depth look at multigrids can be found in [4], [5], [16], [20], [23], [29], [58], [60], [66], [68]. Elsewhere multigrid methods have been presented in terms of the finite difference approach, here it is presented in terms of the control volume approach. In chapter 4 and 5 it is shown that the multigrid method produces accurate solutions

to the pressure-correction equation in two- and three-dimensions respectively with a fast rate of convergence. The method is also relatively easy to incorporate into existing production codes. This last point should not be lightly dismissed since industry has invested large amounts of time and money developing fluid flow programs and companies will be reluctant to discard their investment unnecessarily. It is therefore asserted that the codes based on the SIMPLE algorithm could be greatly improved with little cost in terms of man effort by using the multigrid method to solve the pressure-correction equation.

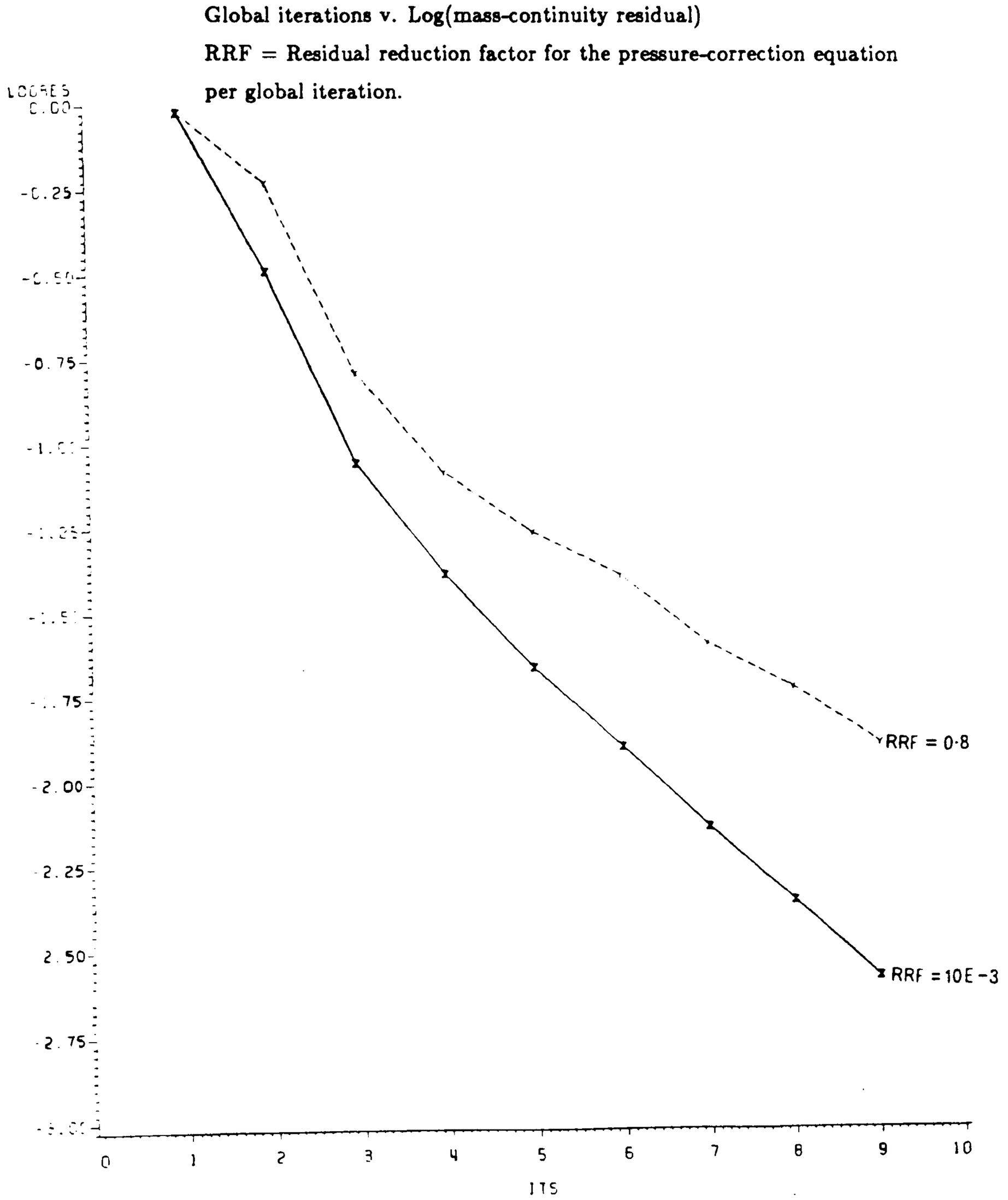

Figure 3.1 Double Glazing problem. Air at Ra=10^5, grid=64x64

3.2 Multigrid Ideology

The description of the multigrid method in this and the following sections is largely based upon that given by Stuben and Trotenberg. [60]. Although only the linear multigrid method is used in this study the following general principle of the multigrid method applies equally to the non-linear multigrid method. The multigrid principle for the discrete elliptic boundary value problem is extremely simple. Its description follows.

Approximations with smooth errors for the elliptic boundary value problem are obtained efficiently by applying suitable relaxation methods. Corrections of these approximations can then be calculated on coarser grids where the smooth errors no longer appear smooth and thus can be eliminated using the suitable relaxation methods. This basic idea can be used recursively on coarser and coarser grids. This leads to asymptotically optimum iterative methods, that is, methods for which the computational work required for achieving a fixed accuracy is proportional to the number of discrete unknowns. If the multigrid principle is then combined with the idea of nested iteration, that is, the use of coarser grids to obtain good initial approximations on finer grids, it can lead to a method for which the computational work required for achieving the discretization accuracy is still proportional to the number of unknowns. Thus there are three stages:

1. error smoothing by relaxation

2. calculation of corrections on coarser grids

3. combination with nested iteration.

The combination of stages 1, 2 and 3 and its efficiency was first recognized by Brandt.A (1970), [5]. His essential contributions were the introduction of the non-linear multigrid method (FAS) and the provision of the tool of the 'local Fourier analysis' for theoretical investigation and method optimization.

Multigrid methods are at least as efficient as the direct fast solvers such as Buneman's algorithm. In fact in two-dimensions, the MG00 code for solving a Poisson equation on a rectangular domain developed by Foerster and Witsch [16] is more efficient than Buneman's algorithm, see [59]. The decisive advantage of the multigrid method is, however, that it can be easily applied to problems that do not fully meet the requirements demanded by the direct fast solvers [16].

A general convergence theory of multigrid methods has been presented by Hackbush.W(1981). [19].[20]. The abstract theories for multigrid convergence are often pessimistic and do not really provide constructive criteria for the construction of optimal methods for concrete situations. Only the 'model problem analysis', that is the analysis of the Poisson equation in a unit square, and local Fourier analysis yield quantitative results to be used for the conclusions of the multigrid algorithms. These do have disadvantages. The 'model problem analysis' can only be applied to a small class of problems and local Fourier analysis is based on idealising assumptions, such as that the solution is derived on an infinite grid, see [60].

Non-elliptical problems are attracting more and more interest. Application of multigrid methods on vector and parallel computers are also attracting more interest [5]. In order to apply multigrid methods in the most efficient manner computers with pyramidical processor architecture are being developed at GMD.

The convergence properties of classical relaxation methods, such as the Jacobi, Gauss-Seidel and SOR, applied to h-discrete elliptic equation are known to become very bad as $h \rightarrow 0$. For the Poisson equation on a unit square for instance, the spectral radius of the Jacobi and Gauss-Seidel methods behaves *like* $1\text{-}O(h^2)$. SOR with optimal over-relaxation parameter has a spectral radius of $1\text{-}O(h)$. The error reducing properties of these methods can be analyzed by expanding the errors, v_h , into discrete Fourier series. In terms of this Fourier expansion one can distinguish between SMOOTH (low frequency) and NON-SMOOTH (high frequency) error components. It is well known from investigations of the classical relaxation methods that the smooth error components are responsible for the slow convergence. On the other hand, these relaxation methods are very efficient in smoothing the errors, that is, in reducing high frequency error components, as shown, in Figure 3.2.

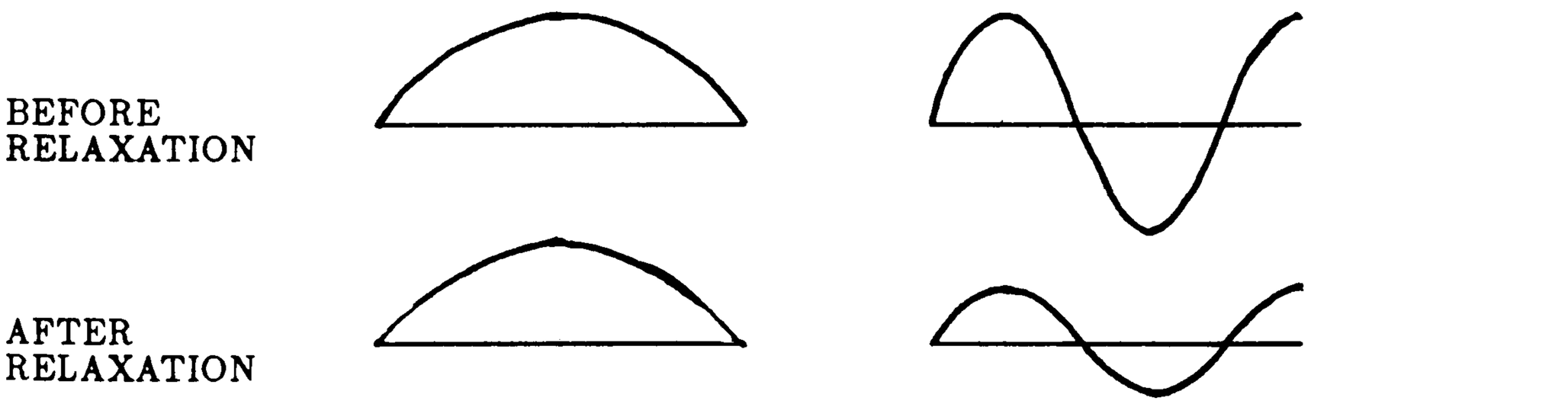

Figure 3.2: Low and high frequency errors before and after relaxation

Smocthing properties of the relaxation methods are measured by the SMOOTHING FACTOR , that is the largest factor by which the high frequency error components are reduced per relaxation sweep. This factor refers to the high frequency error components in the same manner as the spectral radius refers to all error components. Stuben and Trotenberg [60] have shown that the above relaxation methods are characterised by smoothing factors which are smaller than 0.5, independent of h, the mesh size. The important thing to note is that these smooth errors which cannot be reduced by the relaxation methods on a grid with mesh size $\omega_h$become non-smooth errors (high frequency errors) on some coarser grid ω_H, see Figure 3.3. Let H=2h, then the error components described by $sin(n\pi x)$ for $n = 1, 7$ on (0,1) appear as depicted in Figure 3.3.

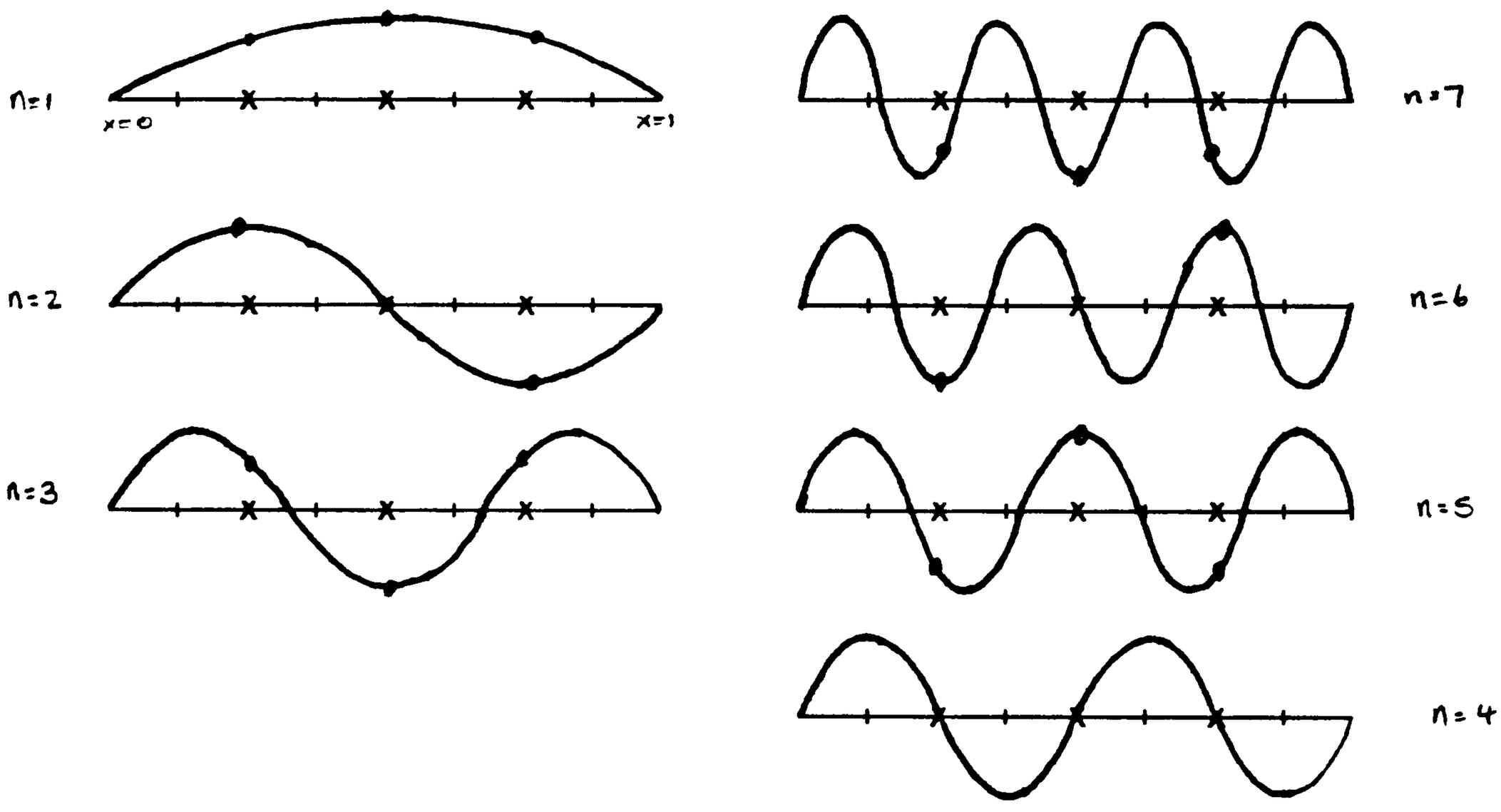

Figure 3.3: Low(n=1,2,3) and High(n=4,5,6,7) frequency components for h=1/8 and H=1/4

The low frequency errors on the left hand side cannot be reduced by the classical relaxation methods. These low frequency errors become high frequency errors on a coarser grid and can then be reduced on the coarser grid by applying suitable classical relaxation methods. Note the terms 'high' and 'low' have to be related to the given h and H-grids.

This leads to the basic multigrid procedure:

1. solve the problem on the fine grid h,

2. transport the problem in some form to the coarse grid H,

3. solve the problem on the coarse grid H,

4. transport the solution obtained on the coarse grid in some suitable form to the fine grid h.

Although the multigrid idea is simple, the complications arise when the details are filled in. Firstly how is the problem to be transported onto the coarse grid, which will be referred to as the restriction process. Secondly, how to choose the most efficient coarse grid?. Thirdly what problem is going to be solved on the coarse grid and how will the coarse grid problem relate to the fine grid problem, that is, how is the coarse grid difference operator to be chosen. Fourthly, how is the solution from the coarse grid problem to be interpolated onto the fine grid, which will be referred to as the prolongation process. The above four questions are answered below from a practical point of view.

3.3 Choosing the coarse grid

When the fine grid with mesh size h is given, the choice of the coarse grid with mesh size H is often straightforward. The coarsening ratio $H/h = 2$ is usually optimal. It is the smallest recursive convenient number and it is already big enough to make the amount of work performed on the coarse grid quite small relative to that performed on the fine grid. Large H/h will not significantly save more work but will significantly degrade the smoothing factors since a large range of (low) frequency error will not be resolved on the coarser grids.

When the finite-difference approach is used the coarse grid points are every alternate fine grid point, that is, the coarse grid points form a subset of the fine grid points. When the control-volume approach is used with the discrete variables defined at the centre of the cells, coarsening must be performed in terms of the cells; taking every 2^d fine cells as a coarse cell and then placing the coarse grid variables at coarse cell positions analogous to their positioning in the fine cells, where d refers to the dimension of the problem. With this approach, the coarse grid locations do not form a subset of the fine grid locations, see Figure 3.4. The coarsening used

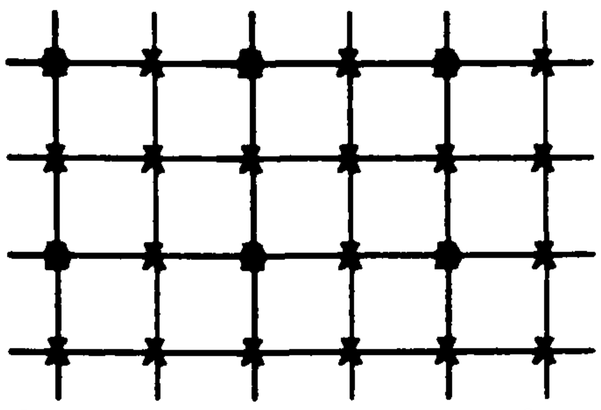

finite difference approach
x fine grid points
o coarse grid points
■ fine and coarse grid points coincide

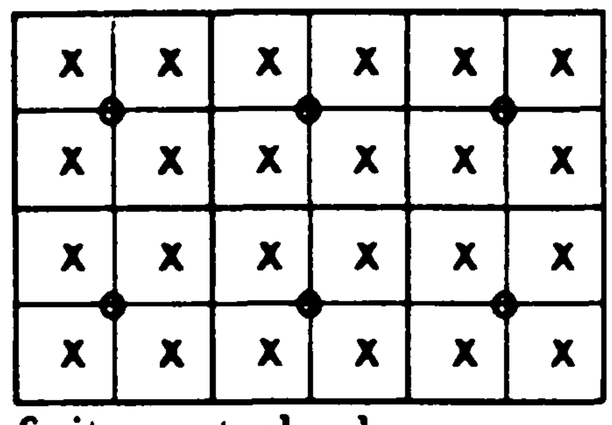

finite control volume approach
x fine grid cell centre
o coarse grid cell centre

Figure 3.4: Fine and coarse grids with the finite difference and the finite control volume approaches

in Figure 3.4 is the standard coarsening. Other types of coarsenings are semi- and red-black coarsening.

Semi-coarsening is the technique of using a grid H which is not coarser than the fine grid h in all coordinate directions. Red-black coarsening is where every red or black point is taken as a coarse grid point with the red-black points ordered as on a chequer board. The idea of partial coarsening, that is non-standard coarsening, may seem contrary to the multigrid ideology, especially, since partial coarsening means somewhat more work on the coarse grid compared to standard coarsening and more importantly the low frequency errors associated with the non-coarsened coordinate are not solved for. Figure 3.5 is an example of semi-coarsening in the x-direction applied to the finite-difference and the finite control volume approaches.

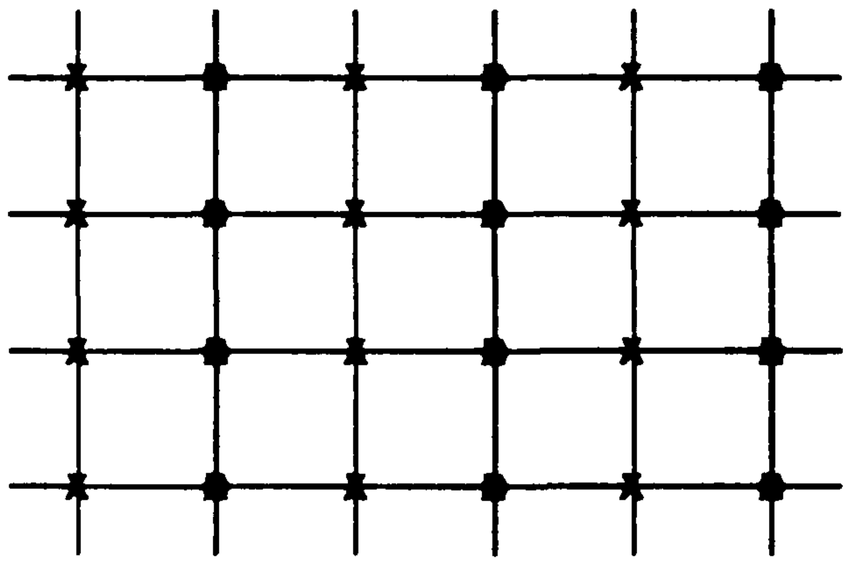

finite difference

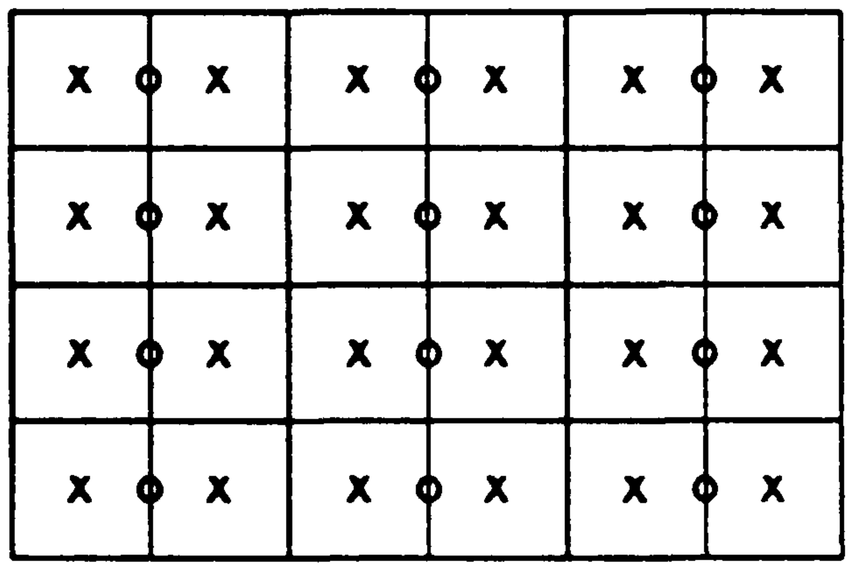

finite control volume

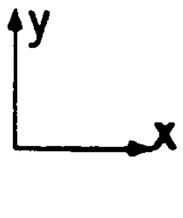

o coarse grid locations, x fine grid locations

Figure 3.5: An example of semi-coarsening in the x-direction with the finite difference and finite control volume approach

Semi-coarsening is efficient when the problem being solved is anisotropic, that is, it is strongly coupled in one direction, for example, $aU_{xx} + bU_{yy} = f$ with $a << b$.

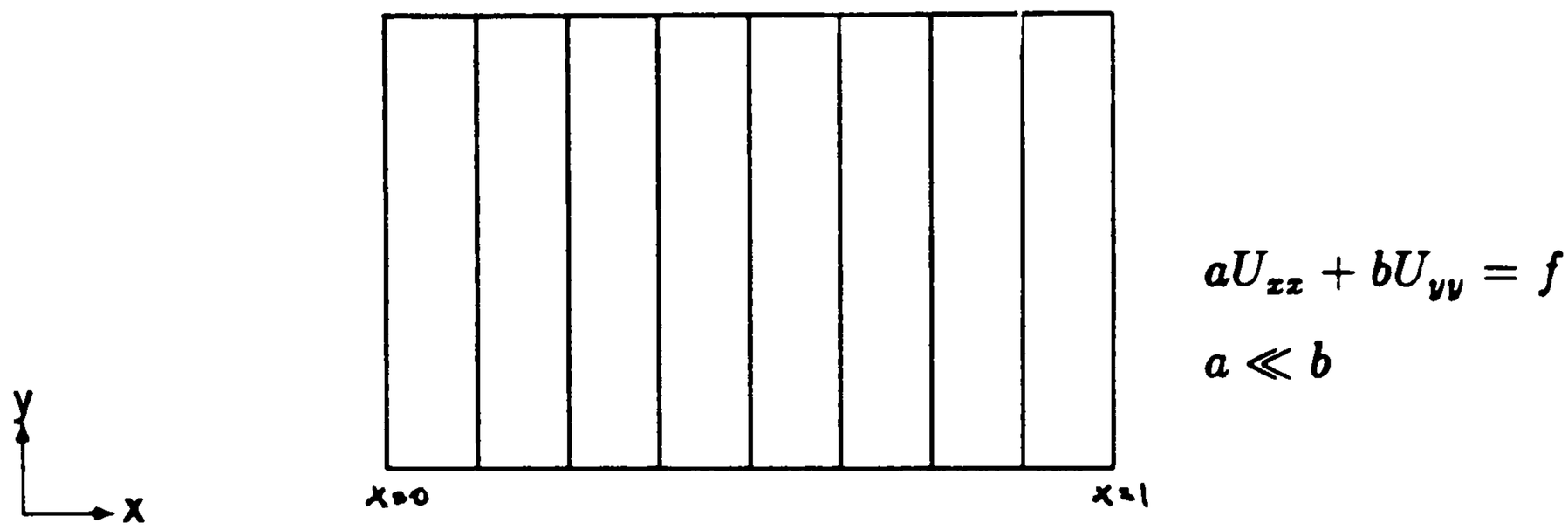

Figure 3.6: Strongly coupled problem in the y-direction

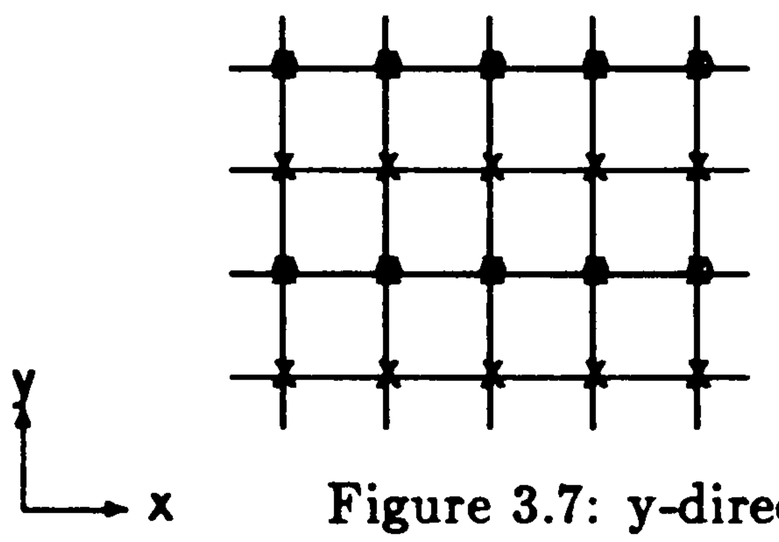

Figure 3.7: y-direction coarsening

This problem is strongly coupled in the y-direction, see Figure 3.6.

The application of line relaxation in the y-direction marching forward from x=0 to x=1 will give very good smoothing rates. Further application of line relaxation with lines in the x-direction marching forward is only going to improve the smoothing rate very slightly due to the weak coupling in the x-direction. This is not worth doing since the improvement obtained in the smoothing of high frequencies is not worth the amount of computer work required (see [29]). Transferring the problem onto a semi-coarsened grid, coarsened in the y-direction only, and then applying line relaxation with lines in the y-direction marching forward from x=0 to x=1 is further going to produce good smoothing rates on the the coarser grid, i.e. reducing any high frequency errors related to this coarser grid which are low frequency errors related to the fine grid.

With this problem one could easily use standard coarsening and apply double sweeps on the coarse-grid and interpolate the corrections onto the fine grid. With the finite difference approach the amount of information transferred between the grids for the semi-coarsening is greater than that transferred for the standard coarsening. The extra information available leads to more accurate prolongation and restriction for the semi-coarsening approach. This benefit is very likely to be offset by the greater number of points that are relaxed on the semi-coarse grid, whereas on the standard coarse grid, only $N/4$ points are relaxed and the prolongation and restriction operators

are constructed from weighted averages of distant neighbouring points. For the control volume approach the problem of the coarse grid unknowns not coinciding with the fine grid unknowns still remains.

It is of course left to the user to decide which coarsening scheme is to be pursued. This decision may depend on many factors, for instance, whether it is easy to predict the direction and strength of the coupling, especially with variable coefficients and particularly in three-dimensions (if the coupling is not predictable then standard coarsening has to be used); or whether the code is for a particular problem, a class of problems or if it is to be a general purpose code. If the code is for a specialised problem then the various multigrid components can be adjusted to obtain a very efficient code. Furthermore the question of whether the code is to be used on scalar, vector or parallel machine needs to be considered. If the code is to be run on only parallel machines then the Jacobi relaxation method can be used as it utilises the parallel processors extremely well, whereas if the code is to be run on scalar and vector machines then the Gauss-Siedel relaxation should to be used, with the odd-even Gauss-Seidel method performing better on vector machines (see [42]). As mentioned above when the strength and direction of the coupling are difficult to predict or likely to change by altering a parameter governing the equations then the most robust scheme would use standard coarsening with line relaxation in all directions. This would of course prove expensive in some situations, for instance, with anisotropic problems.

The red-black coarsening, ratio $H/h = \sqrt{2}$, is as efficient as standard coarsening, trading a larger amount of work per sweep for fewer relaxation sweeps. The grid can be identified with a rotated grid of mesh $\sqrt{h}$. This mesh is recursively convenient with some two-dimensional problems with rotatable operators (see [60]). It is not clear as

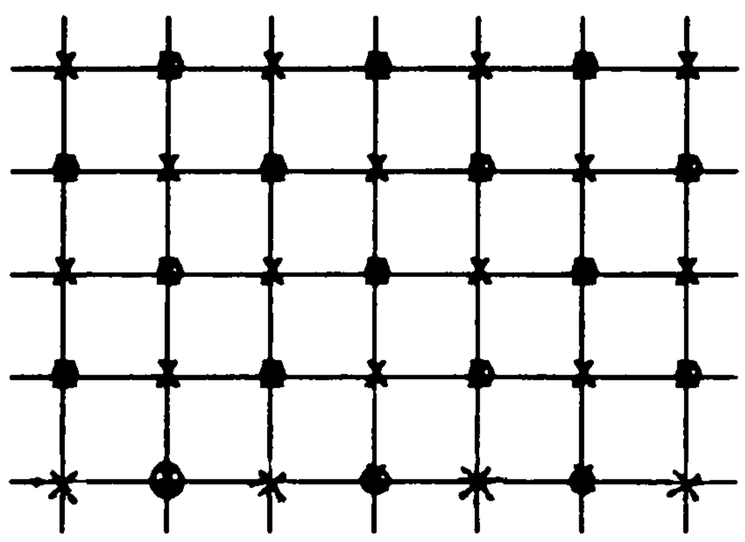

Figure 3.8: Red-black grid with the finite difference approach.

to how the red-black coarsening relates to the control volume approach.

3.4 The restriction operator, I_h^H

Having defined or chosen the type of coarse grid, the next step is to transfer the problem onto it. The multigrid philosophy is to work with the corrections of the fine grid problem. This leads to two steps for transferring the problem onto the coarse-grid, the first step being the formulation of the correction problem on the fine grid and the second step being that of transporting the correction problem onto the coarse grid.

The correction-problem on the fine grid can be described by

$$L_h V_h = r_h \tag{3.1}$$

where

$$r_h = f_h - L_h U_h. \tag{3.2}$$

The process of transferring the residual r_h from the fine grid to the right hand side of the coarse grid problem

$$L_H V_H = r_H \tag{3.3}$$

is known as the restriction process, that is,

$$r_H = I_h^H r_h \tag{3.4}$$

where I_h^H is the restriction operator. The most commonly used restriction operator is the full-weighting (FW) operator,

$$I_h^H = \frac{1}{16}\begin{bmatrix} 1 & 2 & 1 \\ 2 & 4 & 2 \\ 1 & 2 & 1 \end{bmatrix}. \tag{3.5}$$

Others used are the half-weighting (HW) operator

$$I_h^H = \frac{1}{8}\begin{bmatrix} 0 & 1 & 0 \\ 1 & 4 & 1 \\ 0 & 1 & 0 \end{bmatrix} \tag{3.6}$$

and the injection operator

$$I_h^H = [1] \tag{3.7}$$

that is, $r_H = r_h$. Obviously, the restriction operators should be such that when the grid functions (low and high frequency errors) are transferred to the coarse grid the high frequency error components must not increase in amplitude otherwise all the effort of relaxation on the fine grid will have been wasted. So, the high frequency error components should be transferred by high order operators. The low frequency error components transfer does not really matter as they will be smoothed out on the

coarse grid by the chosen relaxation method. The injection operator is of zero order for transferring high frequency error components and infinite order for transferring low frequency error components. The FW operator is of second order for transferring high and low frequency error components (see [60]).

With the control volume approach the residual calculated for an equation represents a physical quantity, the volume integral of a source strength. In the light of this the multigrid method needs to be adapted when solving equations derived from the control volume approach. A restriction strategy for the control volume approach is described in Chapter 4 and Chapter 5 for solving a two- and a three dimensional equation respectively. Note that with the control volume approach the injection operator does not exist since the coarse grid unknowns are not a subset of the fine grid unknowns.

3.5 The coarse-grid difference operator L_H

In principle L_H can be any reasonable coarse grid difference operator approximating the fine grid difference operator L_h with respect to ω_H in a manner analogous to the construction of L_h with respect to ω_h, where ω_H and ω_h are the coarse and fine grids. This is the same as obtaining L_H from the differential operator but on the coarse grid.

Another way of obtaining the coarse grid difference operator is to use the Galerkin approach. Here the restriction operator and prolongation operators I_h^H and I_H^h respectively are used to define the coarse-grid operator L_H,

$$L_H = \hat{L}_H = I_h^H L_h I_H^h. \tag{3.8}$$

The Galerkin operator $\hat{L}_H$ is equivalent to requiring the residuals of the corrected solution $(U_h + I_H^h v^H)$ to vanish when transferred to the coarse grid:

$$I_h^H(f_h - L_h(U_h + I_H^h v_H)) = 0 \tag{3.9}$$

$$I_h^H(r_h - L_h(I_H^h v_H)) = 0 \tag{3.10}$$

$$r_H - I_h^H L_h I_H^h v_H = 0 \tag{3.11}$$

$$r_H - \hat{L}_H v_H = 0 \tag{3.12}$$

where $\hat{L}_H = I_h^H L_h I_H^h$. The Galerkin operator may seem an ideal manner of obtaining the coarse grid operator but a large amount of computer work is required to construct it. Once the Galerkin operator is constructed it is often much more complicated than the ordinary L_H operator, that is it is a 9-pt rather than a 5-pt operator. Thus it also requires a larger amount of storage for storing its coefficients. These problems

increase for an equation in three dimensions. For a "Black-Box" multigrid code the Galerkin Operator is ideal, as the problem $Lu = f$ is treated as a matrix problem and thus the coarse grid problem and boundary conditions are taken care of automatically (see [67]).

3.6 The prolongation operator I_H^h

The process of transferring the corrections calculated on the coarse grid, H, onto the fine grid, h, is known as prolongation, and is defined by

$$U_h^c = I_H^h V^H \tag{3.13}$$

where V^H are the corrections obtained on the coarse grid and I_H^h is the prolongation operator. The most common prolongation operator is the bilinear interpolation operator

$$I_H^h = \frac{1}{4}\begin{bmatrix} 1 & 2 & 1 \\ 2 & 4 & 2 \\ 1 & 2 & 1 \end{bmatrix}. \tag{3.14}$$

Other higher order prolongation operators used are bicubic and biquintic, see [60]. Obviously, the prolongation operator should be such that the interpolation of the low frequency error components from the coarse to the fine grid should not increase in amplitude.

3.7 Treatment at the boundary

The general feeling in the literature is that special care should be taken when multigridding near or at the boundaries, see [5], [59], [60]. Precise residual transfers must be performed near the boundaries since relaxation rarely leaves smooth residuals near the boundary, where the normal relaxation step breaks off, for example in the lexicographic scheme. Precise residual transfers can be best achieved by full residual weighting. The FW operator is slightly more complicated since the distance of fine grid points from the boundary will be different from that of the coarse grid points. Thus the weight used in transferring a residual from a fine grid point to a coarse grid point depends on the distance of both points from the boundary. Near boundary corners the dependence is even more involved. Also, for prolongation, corrections near the boundary should use the coarse grid boundary conditions even when they are not explicitly shown on the grid, (see Chapter 5). Hence, if the grid points on or near

the boundaries are not treated correctly then there can be deterioration of the overall multigrid behaviour.

3.8 Multigrid cycles

Having described the basic two-level multigrid algorithm, the multigrid idea can be further extended by treating the coarse-grid as the new fine grid and solving for the low frequency errors for that grid on a further coarser grid. Hence the recursive multigrid structure is now obvious. There are many different ways of traversing the grids, that is, there are many different forms of the multigrid cycles. The general structure of the multigrid cycles is defined by the flow chart in Figure 3.9, where the boxes labelled 1, 2 and 3 are explained below.

1. Relax$(\nu_1, L_k v_k, r_k)$ is some suitable relaxation scheme applying ν_1 relaxation sweeps on the problem $L_k v_k = r_k$.

2. On the coarsest grid , due to the small number of unknowns one can afford to solve the problem $L_0 v_0 = r_0$ exactly or alternatively apply Relax$(\nu_1 + \nu_2, L_k, v_k, r_k)$.

3. The switching parameter $c(k)$ is used to control traversal between grids.

The simplest multigrid cycle is when $\gamma = 1$, the V-cycle, $\gamma = 2$ gives the W-cycle.

Practically one works with γ =1 or 2. Algorithms with $\gamma = 2$, although slightly more expensive are usually preferable over those with $\gamma = 1$ as they are more robust. The cycle $\gamma > 2$ is never used since it is highly inefficient as the computational work per multigrid cycle becomes proportional to N(logN) rather than N, see [60]. A variant of the V-cycle is the saw-tooth cycle, which is a V-cycle but with $\nu_1 = 0$ and $\nu_2 = 1$. Another cycle is the F(fixed)-cycle, which is depicted in Figure 3.12.

3.8.1 The full multigrid algorithm (FMG)

With the full multigrid algorithm, one starts by solving the problem on the coarsest grid first and then interpolates the full solution onto the next finer grid, where the solution is obtained via the correction cycle; at this stage only one coarse grid is involved. Once the solution on the finer grid has been obtained it is then transferred to the next finer grid and that is corrected using the correction cycle this time involving

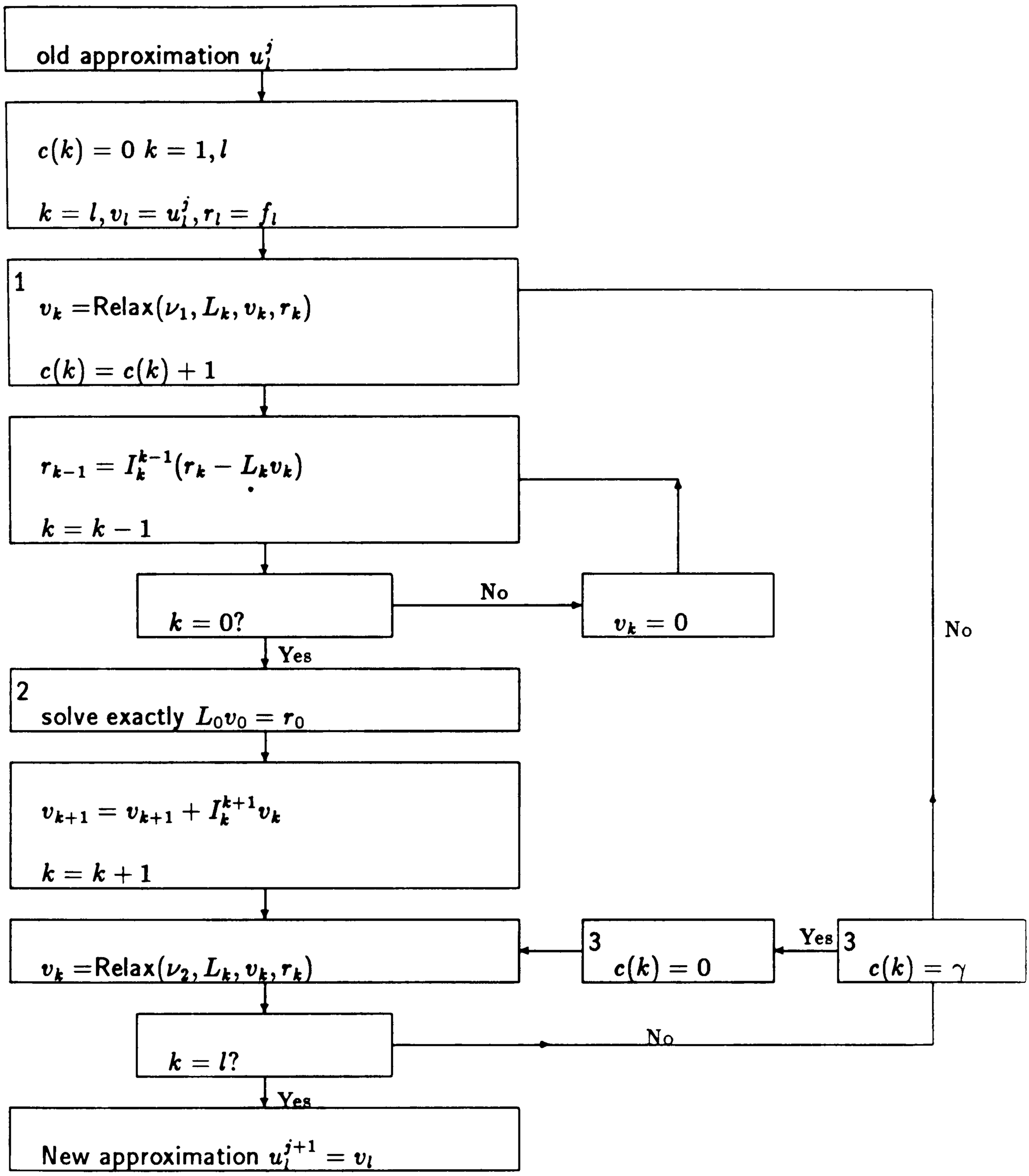

Figure 3.9: Flow chart for one multigrid iteration/cycle

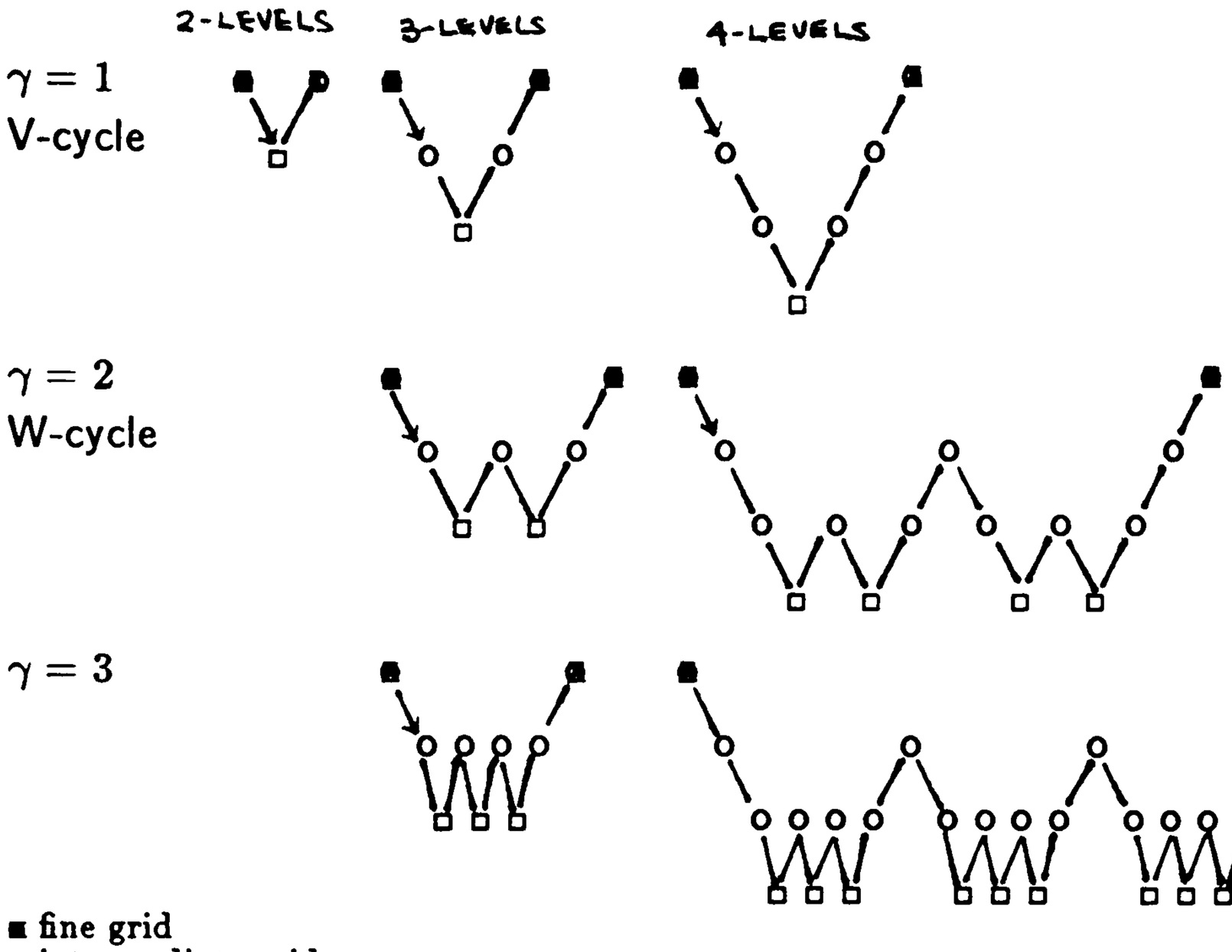

Figure 3.10: V and W cycles with $\gamma = 1, 2, 3$

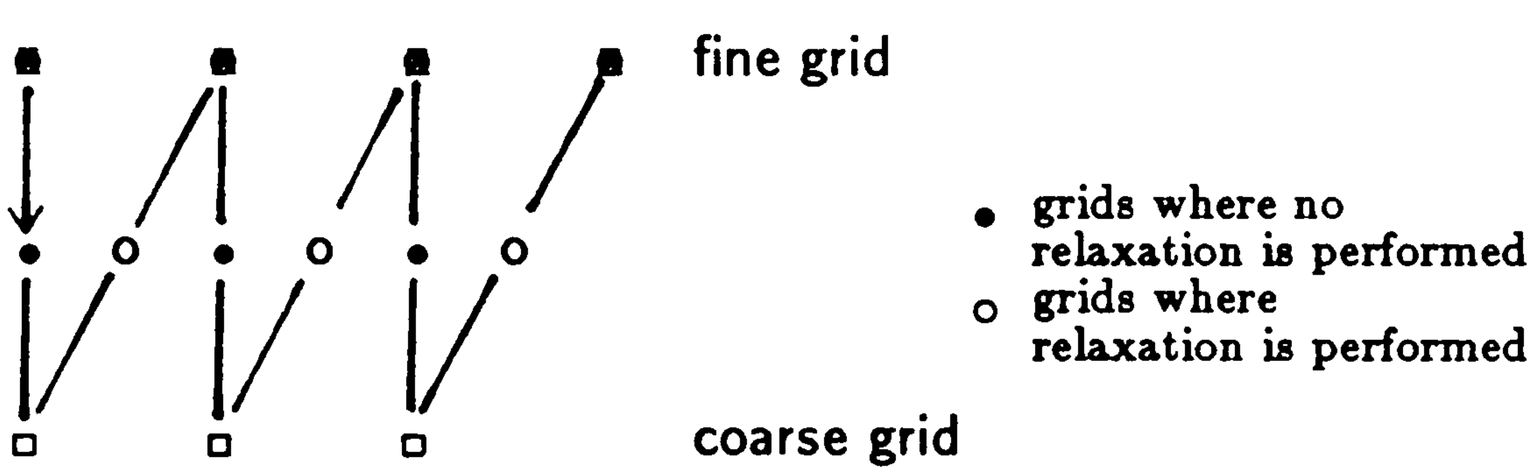

Figure 3.11: Sawtooth cycle for 3 grids

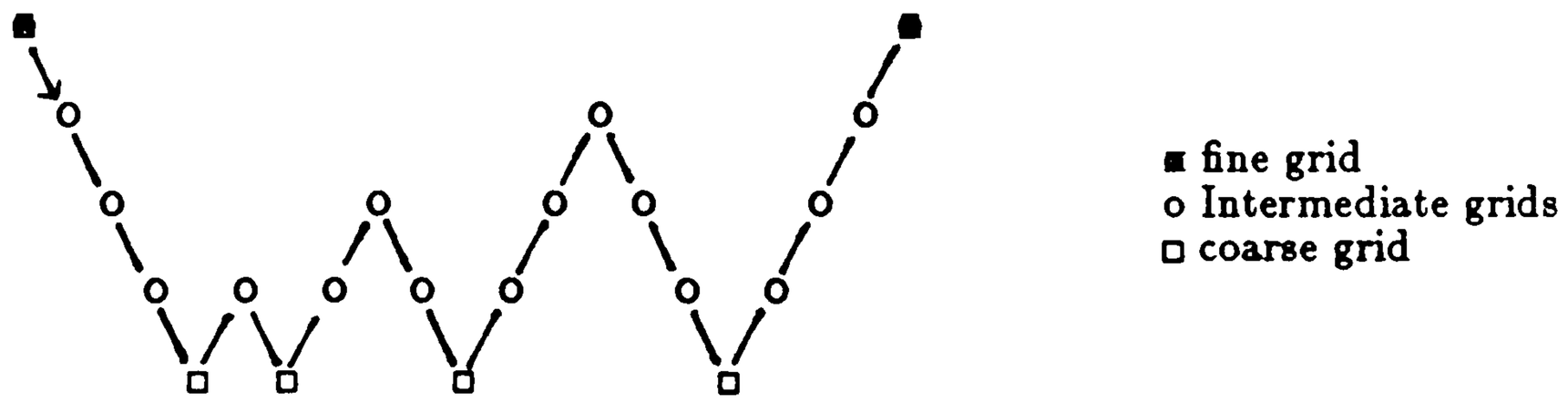

Figure 3.12: F(fixed) cycle

two coarser grids, and so on until the full solution is interpolated onto the finest grid which is then finally corrected using one V-cycle involving all the coarser grids, see Figure 3.13. FMG is regarded as an approximate direct solver, see [60], because

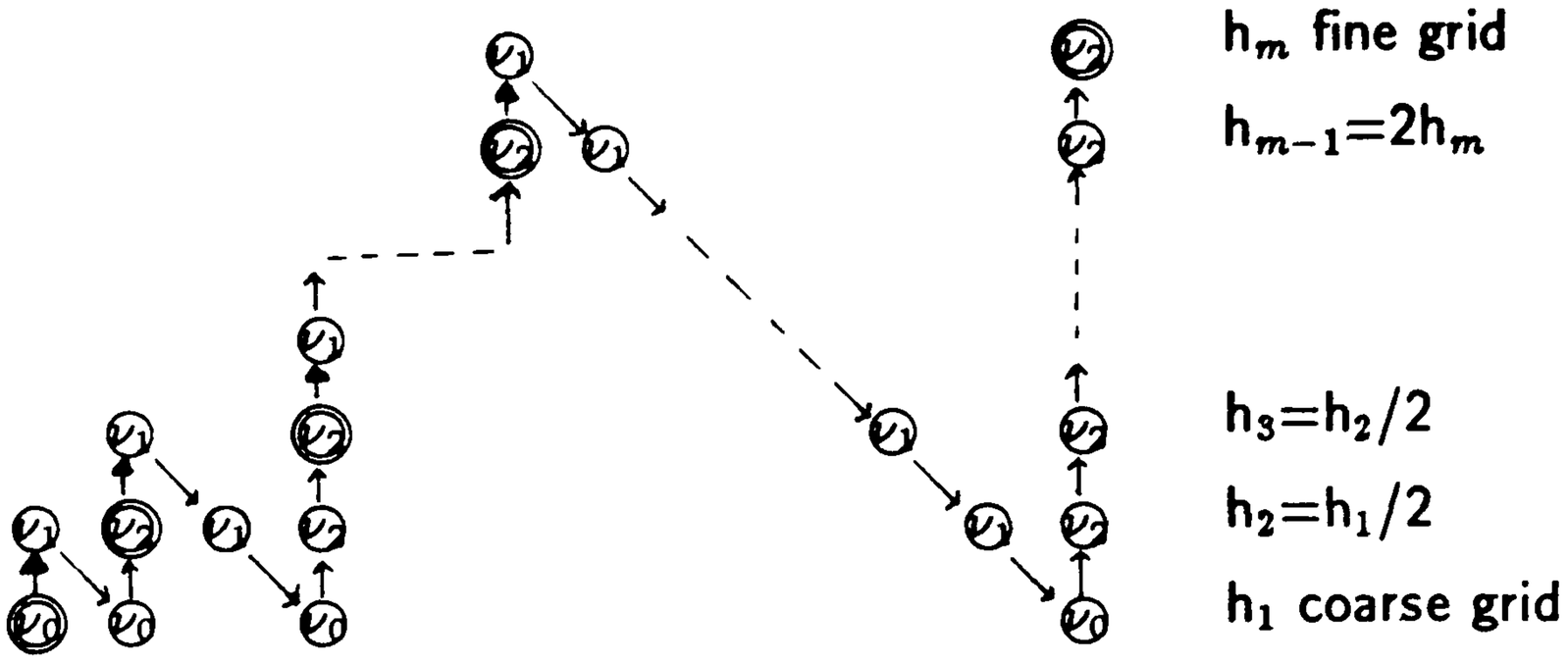

Figure 3.13: FMG Structure

1. the discrete solution U_h is approximately computed up to an error (with respect to the continuous solution u) of about the same magnitude as the discretization error, and

2. the amount of computer work needed is proportional to the number of grid points of ω_h (with only a small constant of proportionality).

3.9 Non-linear multigrid:

The Full Approximation Scheme (FAS)

FAS, although not used here , is briefly introduced for completeness.

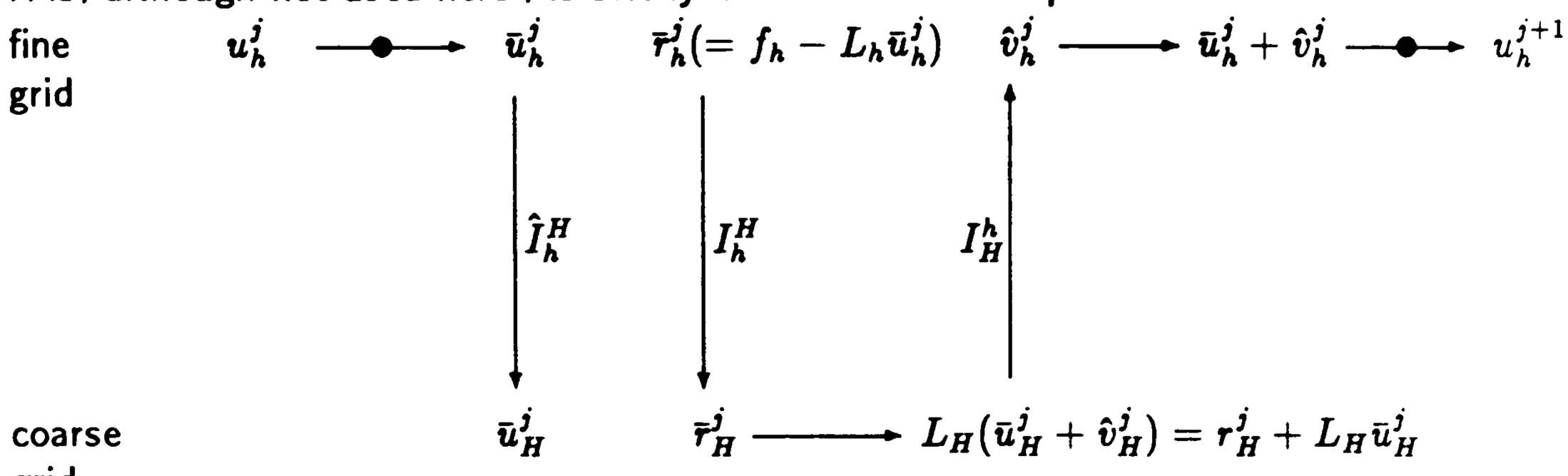

Figure 3.14: The Full Approximation Scheme

With FAS not only the residuals are transferred to the coarse grid by some linear operator I_h^H but also the relaxed approximation $\bar{U}_h^j$ by some linear operator $\hat{I}_h^H$, which may be different from I_h^H. Also on the coarse grid the correction equation is not solved but the full approximation

$$L_H W_H^j = L_H(\bar{U}_H^j + \hat{V}_H^j) \tag{3.15}$$

$$= r_H^j + L_H\bar{U}_H^j \tag{3.16}$$

where $\hat{V}_H^j = W_H^j - \bar{U}_H^j$.

Only the correction, $\hat{V}_H^j$, and not the full approximation W_H^j, is transferred back to the fine grid. This is important since only the correction quantities are smoothed by the relaxation process on the coarse grid. If L_h is a linear operator then FAS is equivalent to the linear multigrid method.

Chapter 4

Application of the multigrid method to the two-dimensional Pressure-Correction equation

As the pressure-correction equation in the SIMPLE algorithm takes the majority of the computation time an adapted multigrid method has been applied to it to enable the SIMPLE algorithm to converge in shorter computation time. Consider the pressure-correction equation derived when solving the double glazing problem in a square cavity, equation (2.1). The pressure-correction equation is first obtained by integrating the continuity equation over the appropriate control volume and then substituting the velocity correction formulae to obtain equation (2.34).

$$h^2 \begin{bmatrix} 0 & \frac{-1}{a^v_{i,j+1}} & 0 \\ \frac{-1}{a^u_{i,j}} & \left(\frac{-1}{a^u_{i,j}} + \frac{-1}{a^u_{i+1,j}} + \frac{-1}{a^v_{i,j}} + \frac{-1}{a^v_{i,j+1}}\right) & \frac{-1}{a^u_{i+1,j}} \\ 0 & \frac{-1}{a^v_{i,j}} & 0 \end{bmatrix} p'_{i,j} = h(u^*_{i,j} - u^*_{i-1,j} + v^*_{i,j} - v^*_{i,j+1}).$$

In applying the multigrid method to the pressure-correction equation one must be careful to obtain the discrete operator in a form suitable for transferring between the various grids, [5]. The pressure-correction (p-c) equation (2.34) in the SIMPLE algorithm is obtained via a series of discretized equations as described in chapter 2. It is therefore important to determine just what differential operator corresponds to the discrete pressure-correction operator given in (2.34). This is most easily done by noticing that the velocity correction formulae (2.30) and (2.31) can be considered to be approximations to:

$$u = u^* + \frac{1}{\alpha}\left(-\frac{\partial p'}{\partial x}\right)$$

$$v = v^* + \frac{1}{\beta}\left(-\frac{\partial p'}{\partial y}\right) \tag{4.1}$$

where α and β are some continuously varying coefficients in the (x,y) domain. Substituting now for u and v in the continuity equation gives

$$\frac{\partial}{\partial x}\left(-\frac{1}{\alpha}\frac{\partial p'}{\partial x}\right) + \frac{\partial}{\partial y}\left(-\frac{1}{\beta}\frac{\partial p'}{\partial y}\right) = -\left(\frac{\partial u^*}{\partial x} + \frac{\partial v^*}{\partial y}\right). \tag{4.2}$$

Integrating over the appropriate control volume gives

$$h\left[-\frac{(p'_{i+1,j} - p'_{i,j})}{\alpha_{i+1,j}h} + \frac{(p'_{i,j} - p'_{i-1,j})}{\alpha_{i,j}h}\right] +$$

$$h\left[-\frac{(p'_{i,j+1} - p'_{i,j})}{\beta_{1,j+1}h} + \frac{(p'_{i,j} - p'_{i,j-1})}{\beta_{i,j}h}\right] = -h[u^*_{i+1,j} - u^*_{i,j} + v^*_{i,j+1} - v^*_{i,j}] \tag{4.3}$$

which, in stencil format, is

$$\begin{bmatrix} & \frac{-1}{\beta_{i,j+1}} & \\ \frac{-1}{\alpha_{i,j}} & (\frac{-1}{\alpha_{i,j}} + \frac{-1}{\alpha_{i+1,j}} + \frac{-1}{\beta_{i,j}} + \frac{-1}{\beta_{i,j+1}}) & \frac{-1}{\alpha_{i+1,j}} \\ & \frac{-1}{\beta_{i,j}} & \end{bmatrix} p'_{i,j} = h(u^*_{i,j} - u^*_{i-1,j} + v^*_{i,j} - v^*_{i,j+1}). \tag{4.4}$$

The right hand side of (4.4) is the integral of the source term $\nabla.u^*$. The coefficients of p' on the left hand side are the discrete approximations to α and β and should be considered independent of the mesh size. In fact on comparing (2.34) and (4.4) we obtain

$$\alpha_{i,j} = \frac{a^u_{i,j}}{h^2} \quad ; \quad \alpha_{i+1,j} = \frac{a^u_{i+1,j}}{h^2} \tag{4.5}$$

$$\beta_{i,j} = \frac{a^v_{i,j}}{h^2} \quad ; \quad \beta_{i,j+1} = \frac{a^v_{i,j+1}}{h^2} \tag{4.6}$$

which appears to contradict the previous statement. However it must be firmly borne in mind that once the fine grid has been given, the coefficients α and β are fixed. In using these coefficients on coarse grids, one should not be misled into changing the fine grid mesh size h to the coarse grid mesh size H, [49],[50].

The pressure-correction equation is a linear equation and so the correction cycle is used to multigrid the equation. The v-correction cycle is used with three different cycles namely, (0,1) the sawtooth cycle, (1,1) and (1,2). In keeping with the control volume formulation of the discretized equations, the coarsening of the grid is performed over pressure cells and not pressure points. A coarse grid cell is obtained by combining four fine grid cells as shown in Figure 4.1. It can be seen that the coarse grid coefficient locations do not coincide with the fine grid coefficient locations. Therefore, in order to obtain the coarse grid coefficients the two adjacent fine grid coefficients are averaged. In view of the fact that the coefficients are of the

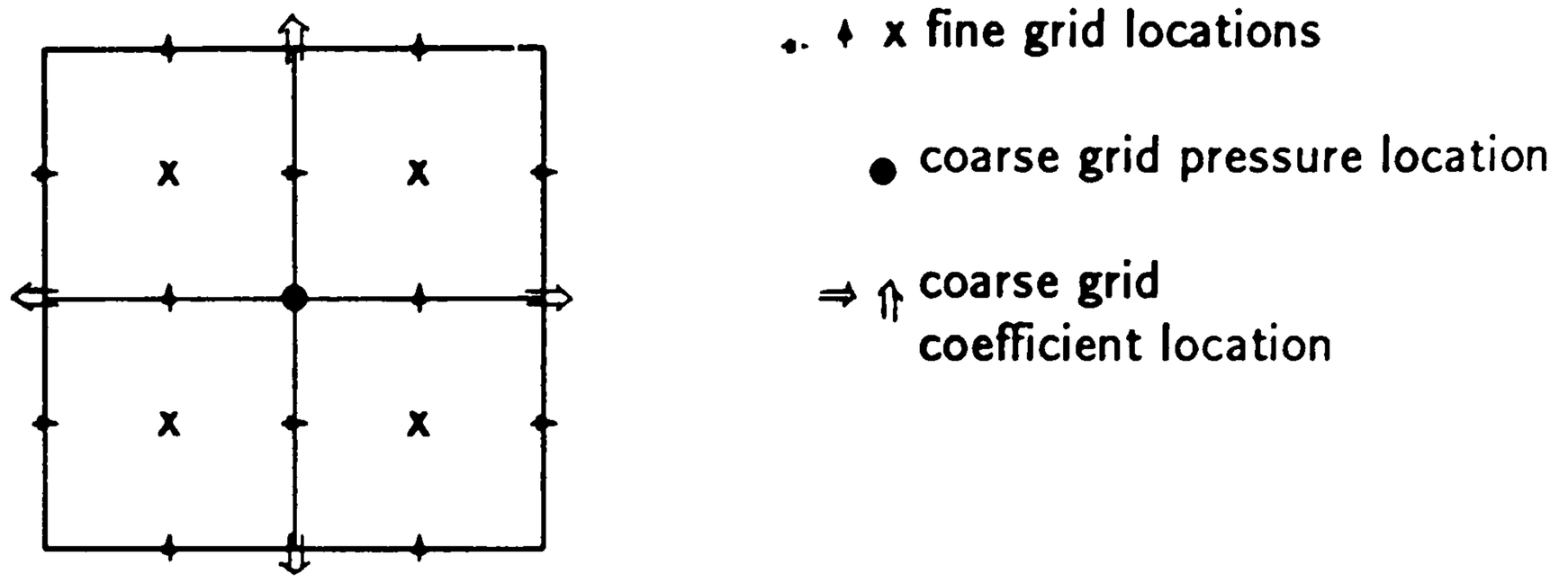

Figure 4.1: Coarse grid pressure cell

form $\alpha_{i,j} = a^u_{i,j}/h^2$ it is tempting to recalculate the coefficients, that is, replacing the fine grid mesh size h by the coarse-grid mesh size 2h and interpolating the velocities necessary in calculating $a^u_{i,j}$. However, this argument has already been shown to be incorrect. Further argument against this approach can also be provided by the fact that it implies that the coarse grid momentum equations are required to derive the coarse grid pressure-correction equation, and this is clearly not the case since the multigrid method is applied to the pressure-correction equation in isolation from the other equations in the SIMPLE algorithm.

The coarse grid equation is of the form

$$L^H v^H = I^H_h r^h \tag{4.7}$$

where $\alpha_{i,j}$ and $\beta_{i,j}$ are obtained as described above. The residuals r^h on the fine grid are calculated from

$$r_h = L^h p'_{i,j} - f^h \tag{4.8}$$

where

$$L^H = \begin{bmatrix} 0 & \frac{-1}{\beta_{i,j+1}} & 0 \\ \frac{-1}{\alpha_{i,j}} & (\frac{-1}{\alpha_{i,j}} + \frac{-1}{\alpha_{i+1,j}} + \frac{-1}{\beta_{i,j}} + \frac{-1}{\beta_{i,j+1}}) & \frac{-1}{\alpha_{i+1,j}} \\ 0 & \frac{-1}{\beta_{i,j}} & 0 \end{bmatrix}. \tag{4.9}$$

The restriction operator I^H_h is described below.

4.1 The restriction operator

In multigrid techniques the restriction operator has to be consistent with the discretization scheme. It is important to note that with the control volume formulation the residuals represent the volume integral of a source strength. Therefore, since four fine grid cells are needed to make one coarse grid cell, the residual on the coarse grid

cell must be the sum of the residuals of the four fine grid cells, Figure 4.2. The lower case subscripts represent fine grid points and the upper case subscripts represent coarse grid points.

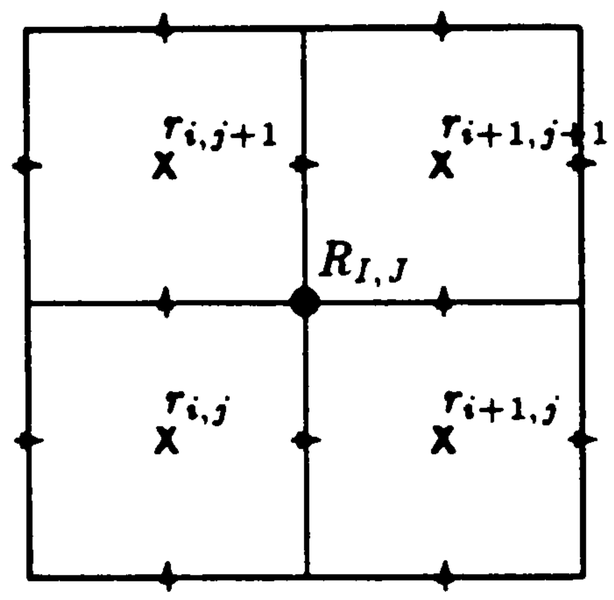

x fine grid locations

coarse grid pressure location

$$R_{I,J} = r_{i,j} + r_{i+1,j} + r_{i,j+1} + r_{i+1,j+1}$$

Figure 4.2: Restriction operator

4.2 The prolongation operator

Two methods of prolongation have been tried and are illustrated in Figure 4.3 and Figure 4.4. One, which has been called the non-weighted operator is defined by,

$$\begin{aligned} p'_{i,j} &= p'_{i,j} + \delta p'_{I,J} \\ p'_{i+1,j} &= p'_{i+1,j} + \delta p'_{I,J} \\ p'_{i,j+1} &= p'_{i,j+1} + \delta p'_{I,J} \\ p'_{i+1,j+1} &= p'_{i+1,j+1} + \delta p'_{I,J} \end{aligned} \tag{4.10}$$

while the other, called the weighted, is a bilinear interpolation using the nearest three coarse grid nodes, namely,

$$p'_{i,j+1} = p'_{i,j+1} + \frac{1}{2}\delta p'_{I,J} + \frac{1}{4}\delta p'_{I-1,J} + \frac{1}{4}\delta p'_{I,J+1} \tag{4.11}$$

with appropriate changes near the boundary, see Figure 4.4. The fine grid pressure-correction are represented by p' and those obtained from the coarse grid by $\delta p'$.

The boundary conditions on the coarse grid do not appear since the boundary considerations have been embedded in the discretized pressure-correction equation.

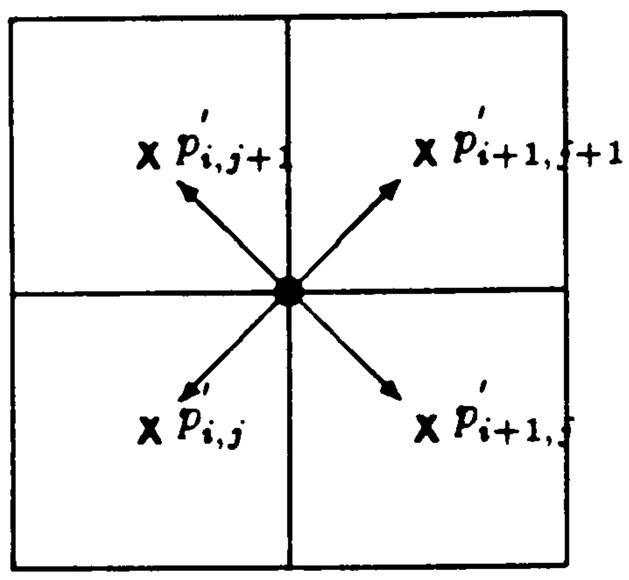

Figure 4.3: The Non-weighted prolongation operator

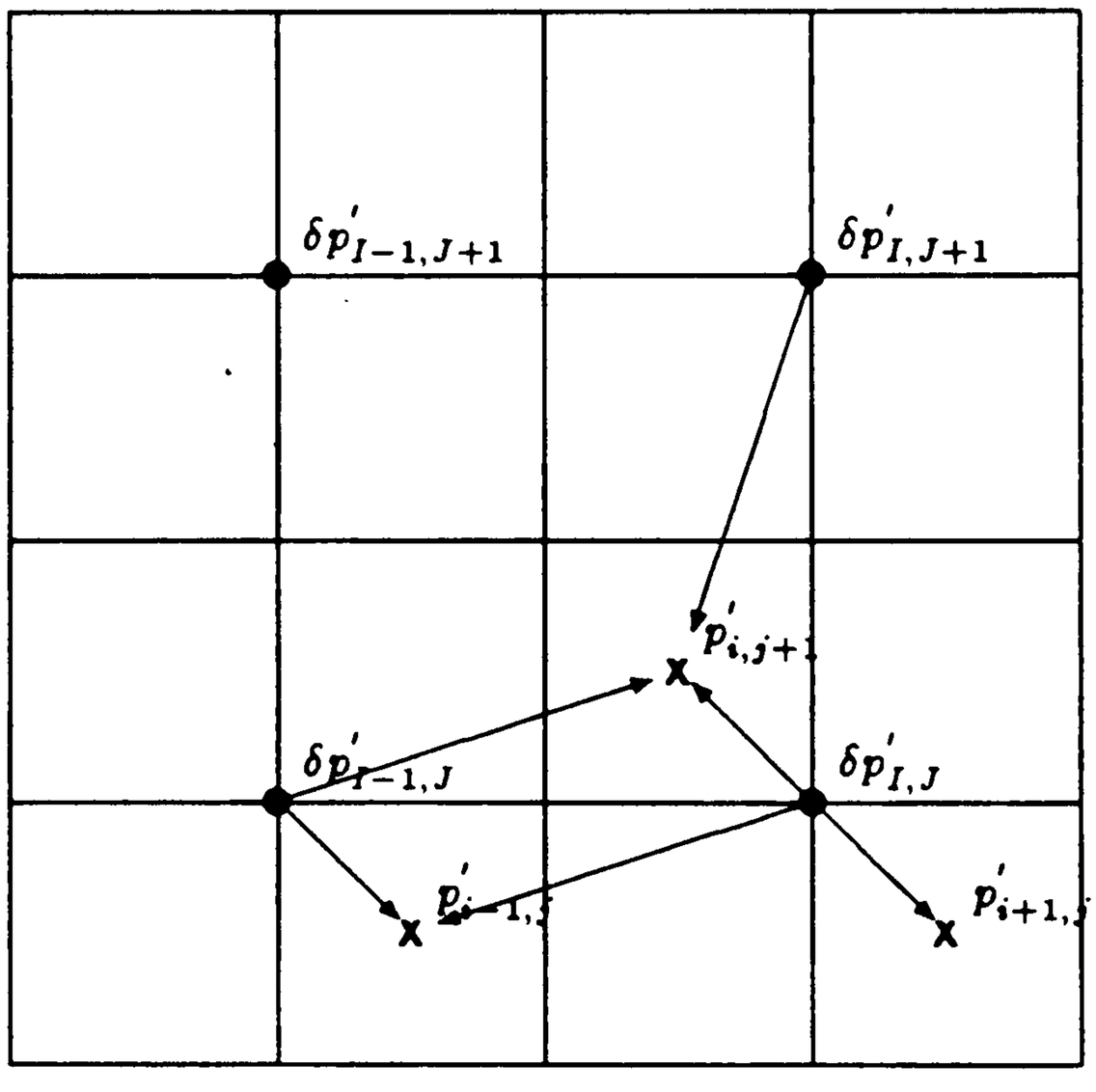

Prolongation for a fine grid corner cell
$p'_{i+1,j} = p'_{i+1,j} + \delta p'_{I,J}$

Prolongation for a fine grid boundary cell
$p'_{i-1,j} = p'_{i-1,j} + \frac{3}{4}\delta p'_{I,J} + \frac{1}{4}\delta p'_{I-1,J}$

Figure 4.4: The weighted prolongation operator

4.3 Results

The smoother used for the multigrid method was the line Gauss-Seidel relaxation procedure, with one iteration on the pressure-correction equation consisting of a single double sweep over the domain and where one double sweep comprised a sweep in the x-direction followed by a sweep in the y-direction. The double glazing problem with aspect ratio one has been used to measure the performance of the multigrid method when solving the pressure-correction equation. Results for air and cerrobase at Ra $= 10^3$ for varying grid sizes have been obtained at several stages of the global iteration process on the CRAY-I vector computer. Three multigrid correction cycles, namely (0,1), (1,1) and (1,2) with both weighted and non-weighted prolongation schemes have been used. For a given fine grid the maximum number of coarser grids possible were used with the coarsest grid being 4x4. Results for the two-level multigrid scheme are also presented. An extra four double sweeps were performed on the coarsest grid in order to solve the problem there accurately.

The graphs that follow show log_{10} of the normalized pressure-correction residuals plotted against the work done in flops (floating point operations per second). It should be noted that one unit of work has been defined to be the number of flops to perform one double sweep of line Gauss Seidel on the fine grid, which is 24N flops, where N is the number of fine grid points. Figures 4.5 and 4.6 are a comparison of the two level multigrid method with weighted interpolation (TLW(ν_1, ν_2)) against ordinary Gauss-Seidel double line sweep (G-S) after the first global iteration for 64x64 and 256x256 grids respectively at Ra $= 10^5$ for air. The behaviour of the two-level scheme is similar to that of the Gauss Seidel relaxation, that is a good rate of convergence with respect to work for the first two correction cycles then the rate of convergence starts to deteriorate. However, the solution with the (TLW(ν_1, ν_2)) scheme is more accurate than those obtained with the Gauss-Seidel relaxation procedure. This is because some of the low frequency errors which existed on the the fine grid have been eliminated on the coarse grid. Since two levels are used, only the low frequency errors with respect to the fine grids (64x64 and 256x256) corresponding to the high frequency errors on the coarse grid (32x32 and 128x128 respectively) have been eliminated. It is thus obvious that in order to get a better performance from multigrid methods the maximum number of possible coarse grids should be used in order to eliminate a larger range of the low frequency errors with respect to the fine grid. The results show that

the (0,1) correction cycle is more efficient than the other two correction cycles.

Figures 4.7 and 4.8 represent the results obtained with the maximum number of levels possible for the problem on the 64x64 and 256x256 grids respectively. That is, four coarser grids are used with 64x64 grid and six coarser grids with 256x256 grid for air at Ra=10^3. The maximum level schemes are the most efficient giving not only better rates of convergence with respect to the work done but also more accurate solutions than two-level multigrid and ordinary Gauss-Seidel schemes.

In view of the superiority of the implementation of the multigrid technique over traditional relaxation methods the results obtained have also been compared with those obtained by using MGD1 [68], a multigrid code developed by P.Wesseling. The code is intended as more of a black box solver whereby the user discretizes the differential equation using 5/7 point difference star and then passes the resulting arrays of coefficients across to the MGD1 code. The prolongation, I_H^h, and the full weighted restriction operator I_h^H are adjoint operators and the coarse grid operators are created using the Galerkin approximation $\hat{L}_H = I_h^H L_h I_H^h$. Smoothing is performed using ILU (incomplete LU factorization) with the (0,1) v-cycle, (the sawtooth cycle). The advantages of this algorithm are; that it is efficient and robust for a wide range of problems; accepts any finite difference star that fits with the 7 point scheme; and generates coarse grid operators automatically once the restriction and prolongation operators have been defined. However, it does have some disadvantages in that it requires a large amount of computer storage and is only usable for two-dimensional problems.

Figure 4.9 is a comparison of the sawtooth cycle for weighted two- and maximum-level schemes, MGD1 and Gauss-Seidel for air at Ra=10^3 on a 256x256 grid. From this figure it can be seen that MGD1 performs better than the other three schemes but not by a large extent. The MGD1 code has been fully optimized for vector computers whereas the code developed at Bristol/Harwell has not.

Figures 4.10 and 4.11 represent results for the non-weighted and weighted interpolation schemes respectively at the first global iteration, for the 64x64 fine grid with the maximum number of coarse grids at Ra $= 10^3$ for cerrobase. The weighted interpolation scheme performs better than the non-weighted. This is expected since the weighted scheme is of a higher order and, hence, more accurate and well behaved. The zig-zag behaviour of the residual reduction with the non-weighted (0,1) scheme is probably due to the low order interpolation operator. Figure 4.12 and 4.13 rep-

	Gauss-Seidel	Weighted (0,1)	MGD1
cpu sec spent on the p-c equation per global iteration	6.75	2.25	1.15
Iterations on the p-c equation	15 double sweeps	2/3 cycles	2cycles
to obtain reduction of	0.1 (at best)	10^{-2}	10^{-2}
Total cpu secs on the p-c equation after 22 global iterations	148	43	26
Savings of cpu time	-	71%	83%
Residual of the continuity equation	3×10^{-4}	1×10^{-4}	1×10^{-4}

Table 4.1: Time spent on solving the pressure-correction (p-c) equation, measured in cpu secs, for cerrobase at Ra $= 10^3$, on a 256x256 grid

resent results of the (0,1) v-cycle for the weighted and non-weighted prolongation schemes using the MGD1 code and the Gauss Seidel solver at the first and fiftieth global iteration respectively for air at Ra=10^3. The reductions obtained by the multigrid methods are similar for both the global iterations presented and this multigrid efficiency is obtained with all global iterations.

Figure 4.14 is that of MGD1 and max-level weighted interpolation scheme at the first global iteration for air at Ra=10^3. The solution is obtained to machine round-off error in 11 correction cycles using 22.5 work units for MGD1 and 28 work units for MLW(0,1), which performs better than (1,1) and (1,2) cycles.

The superiority of multigrid methods is apparent from studying Table 4.1. Using a 256x256 grid with cerrobase at Ra $= 10^3$ and performing 22 global iterations, it can be seen that the multigrid methods can produce savings of $70-80\%$ in cpu time over standard relaxation methods while producing a more accurate solution in the process.

For a 256x256 grid MGD1 code requires storage for almost 10^6 elements of Real*8 array whereas the Bristol/Harwell code requires just over one-third of this, which is at most one-third greater than that required for ordinary Gauss-Seidel relaxation procedure.

4.4 Conclusion

In this chapter the multigrid method has been successfully adapted to solve discretized equations which have been derived from the control volume approach. The results show that multigrid methods can be used to solve the pressure correction equation accurately and efficiently. Since this equation accounts for the majority of the computation with codes based on the SIMPLE algorithm, it is clear that use of the multigrid methods should prove an attractive proposition in such codes.

Figure 4.5 Double Glazing problem. Air at Ra=10^5
G-S and weighted two-level multigird cycles
Grid = 64x64; global iteration = 1

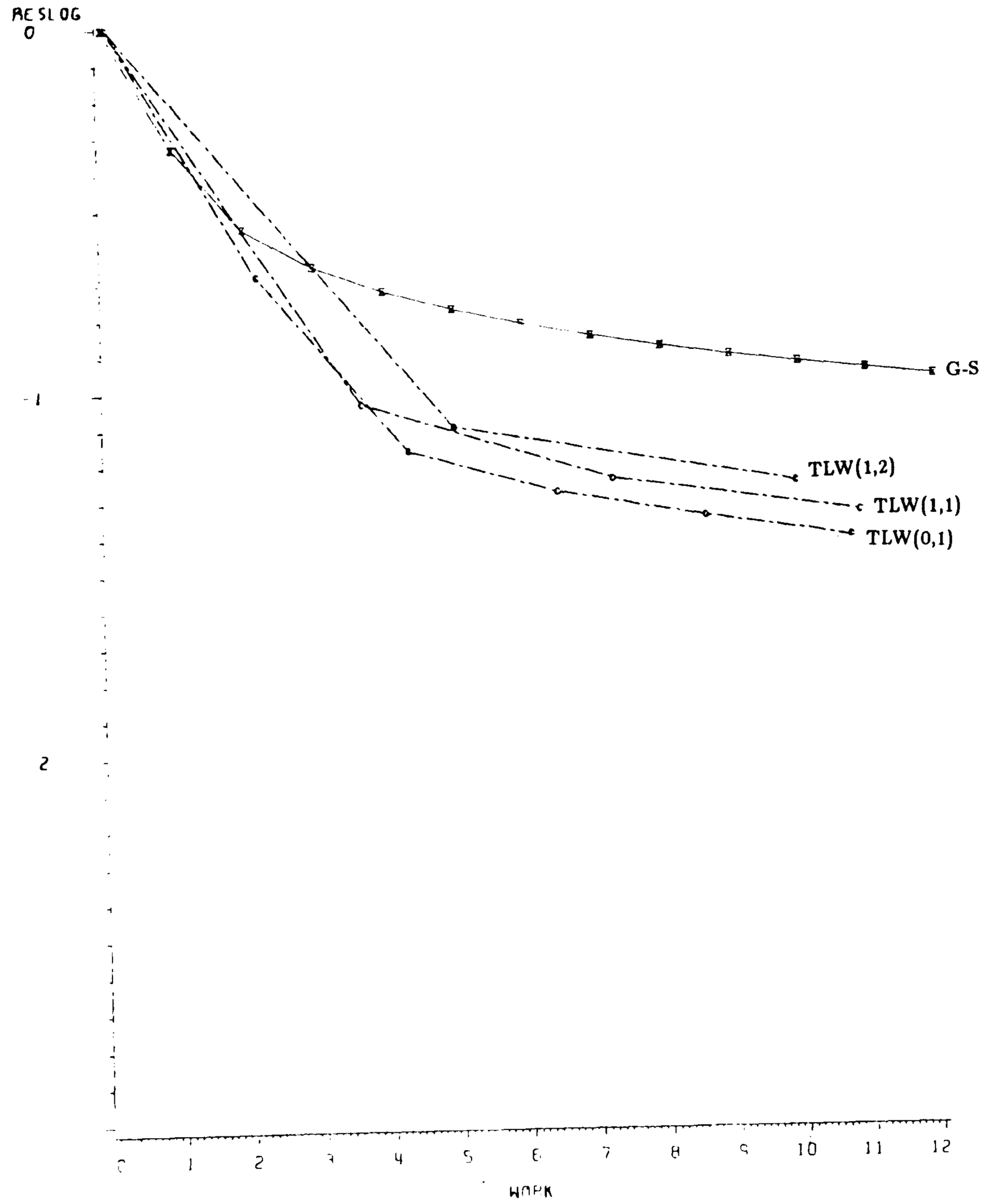

Figure 4.6 Double Glazing problem. Air at Ra=10^5
G-S and weighted two-level multigird cycles
Grid = 256x256; global iteration = 1

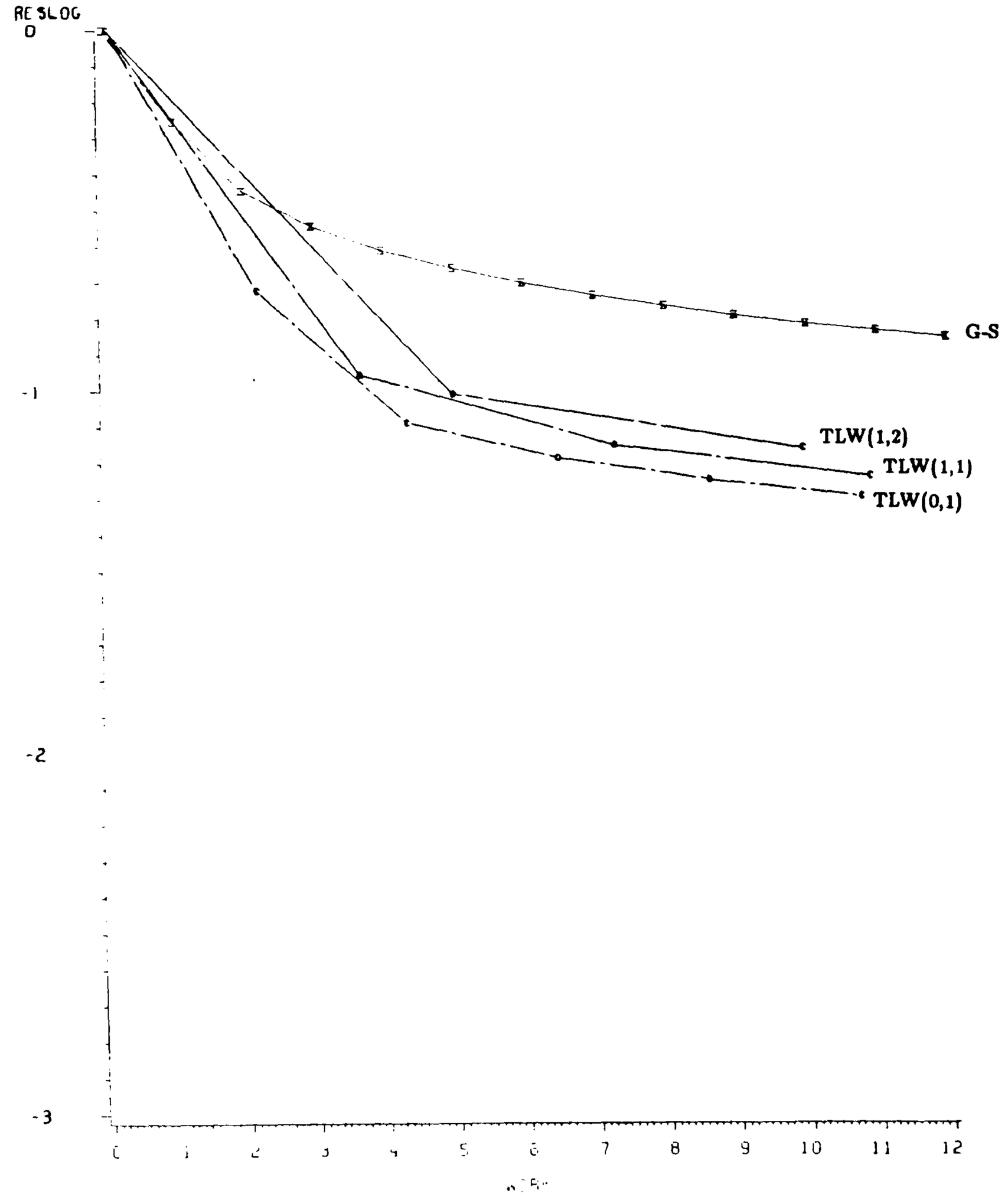

Figure 4.7 Double Glazing problem. Air at Ra=10^3
G-S, weighted two-level and max-level multigird cycles
Grid = 64x64; global iteration = 1

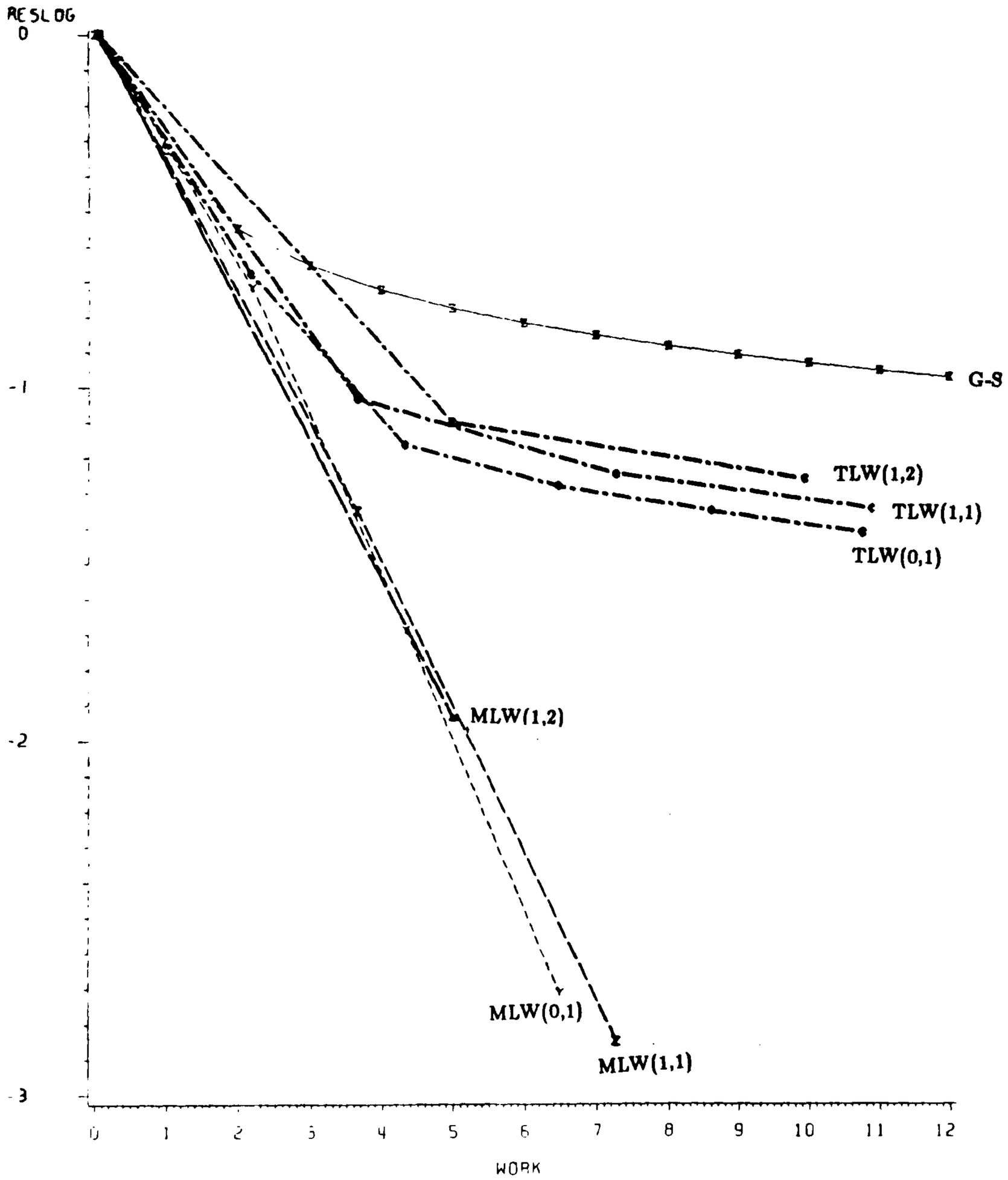

Figure 4.8 Double Glazing problem. Air at Ra=10^3
G-S, weighted two-level and max-level multigird cycles
Grid = 256x256; global iteration = 1

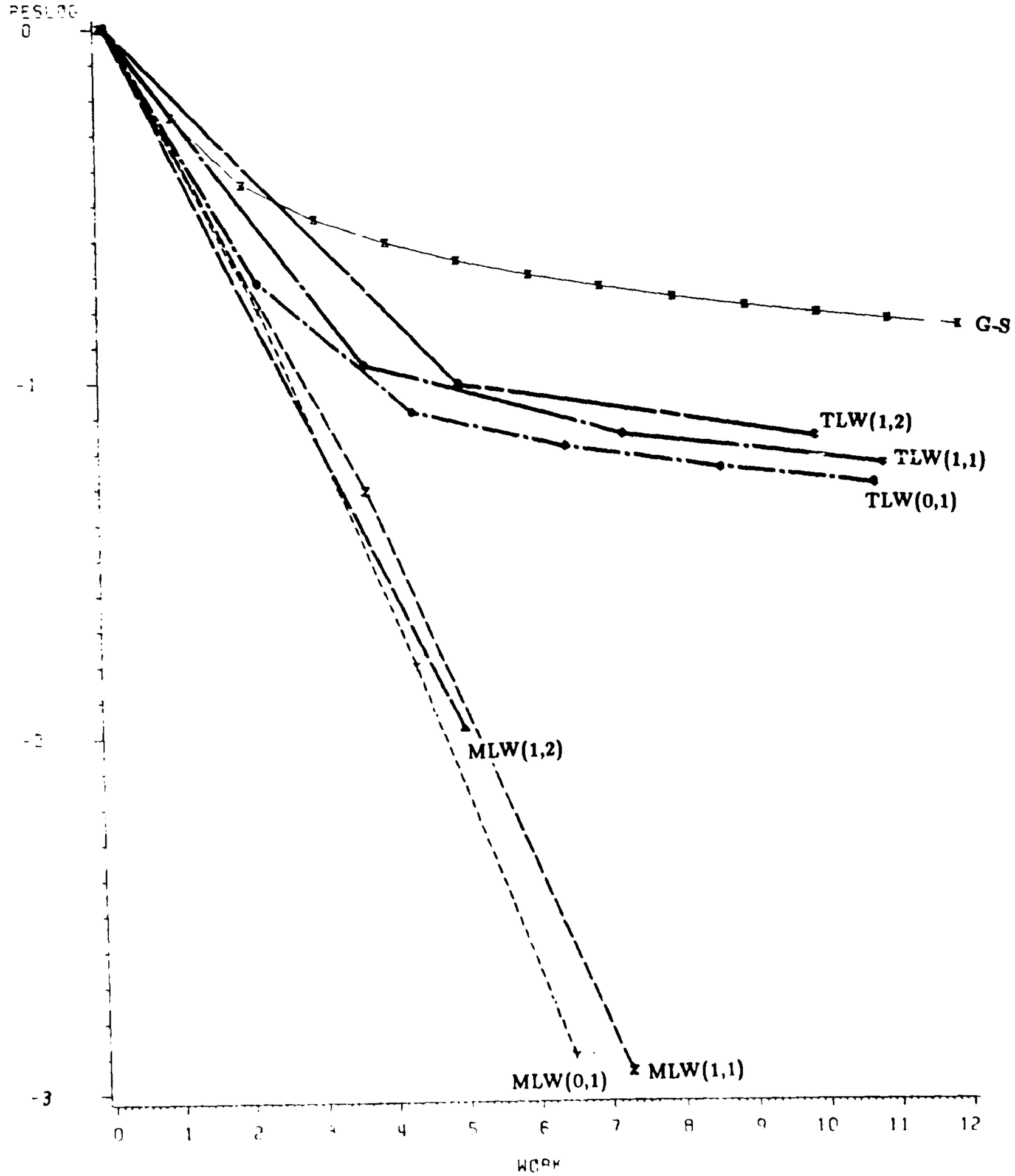

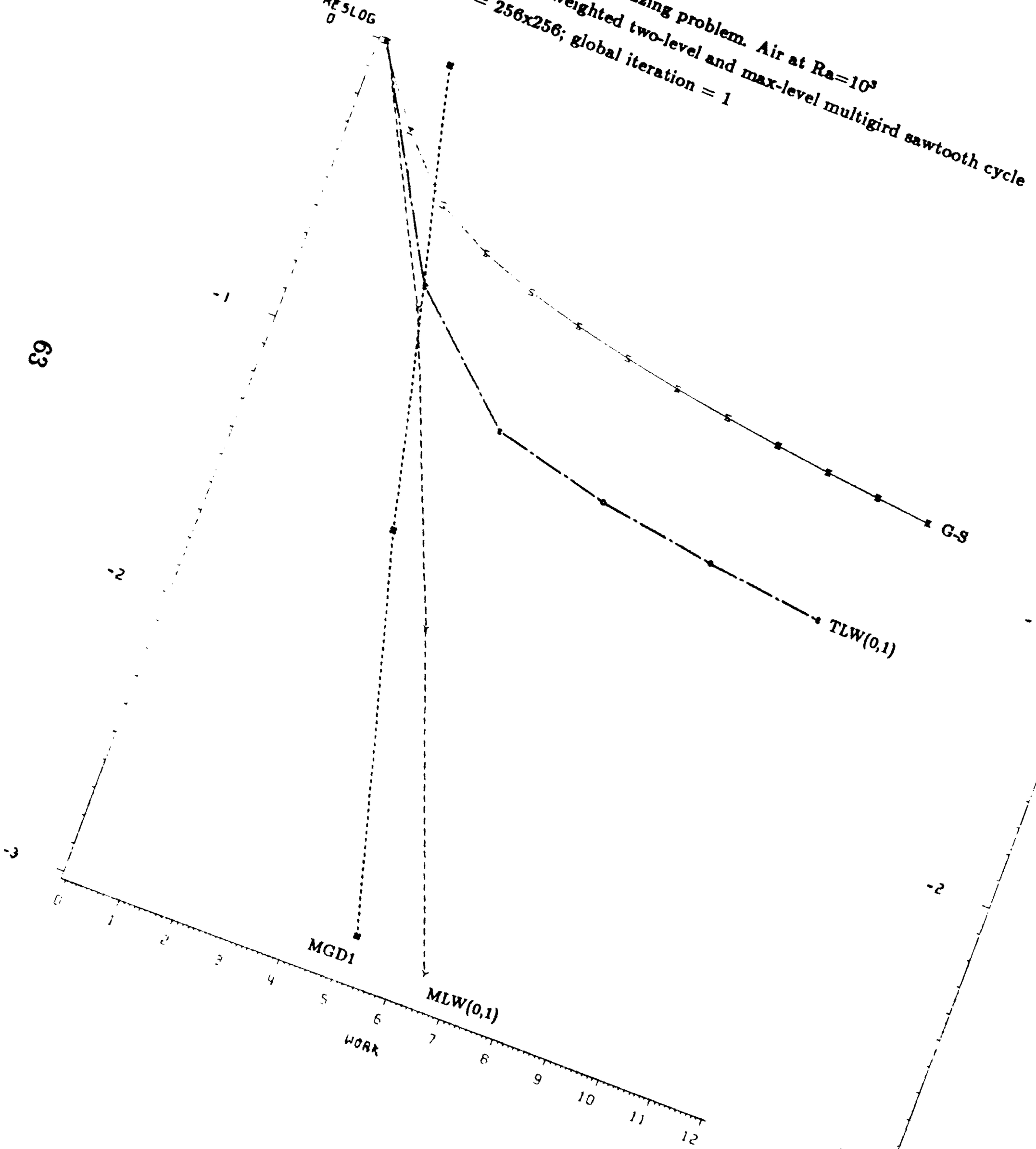

Figure 4.9 Double Glazing problem. Air at $Ra=10^3$
G-S, MGD1, non-weighted two-level and max-level multigird sawtooth cycle
Grid = 256x256; global iteration = 1

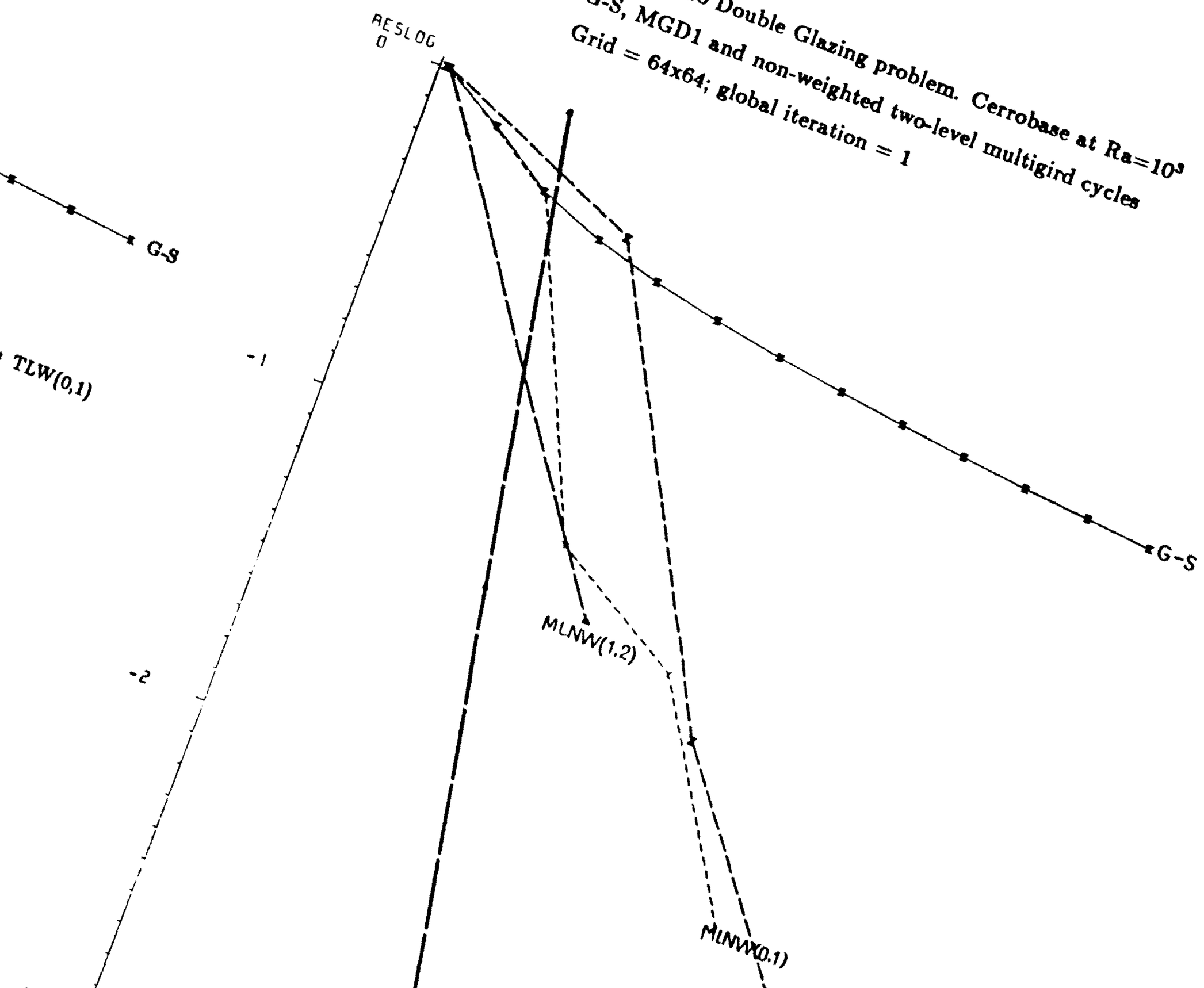

Figure 4.10 Double Glazing problem. Cerrobase at $Ra=10^3$
G-S, MGD1 and non-weighted two-level multigird cycles
Grid = 64x64; global iteration = 1

Figure 4.11 Double Glazing problem. Cerrobase at Ra=10^3
G-S, MGD1 and weighted two-level multigird cycles
Grid = 64x64; glob ' iteration = 1

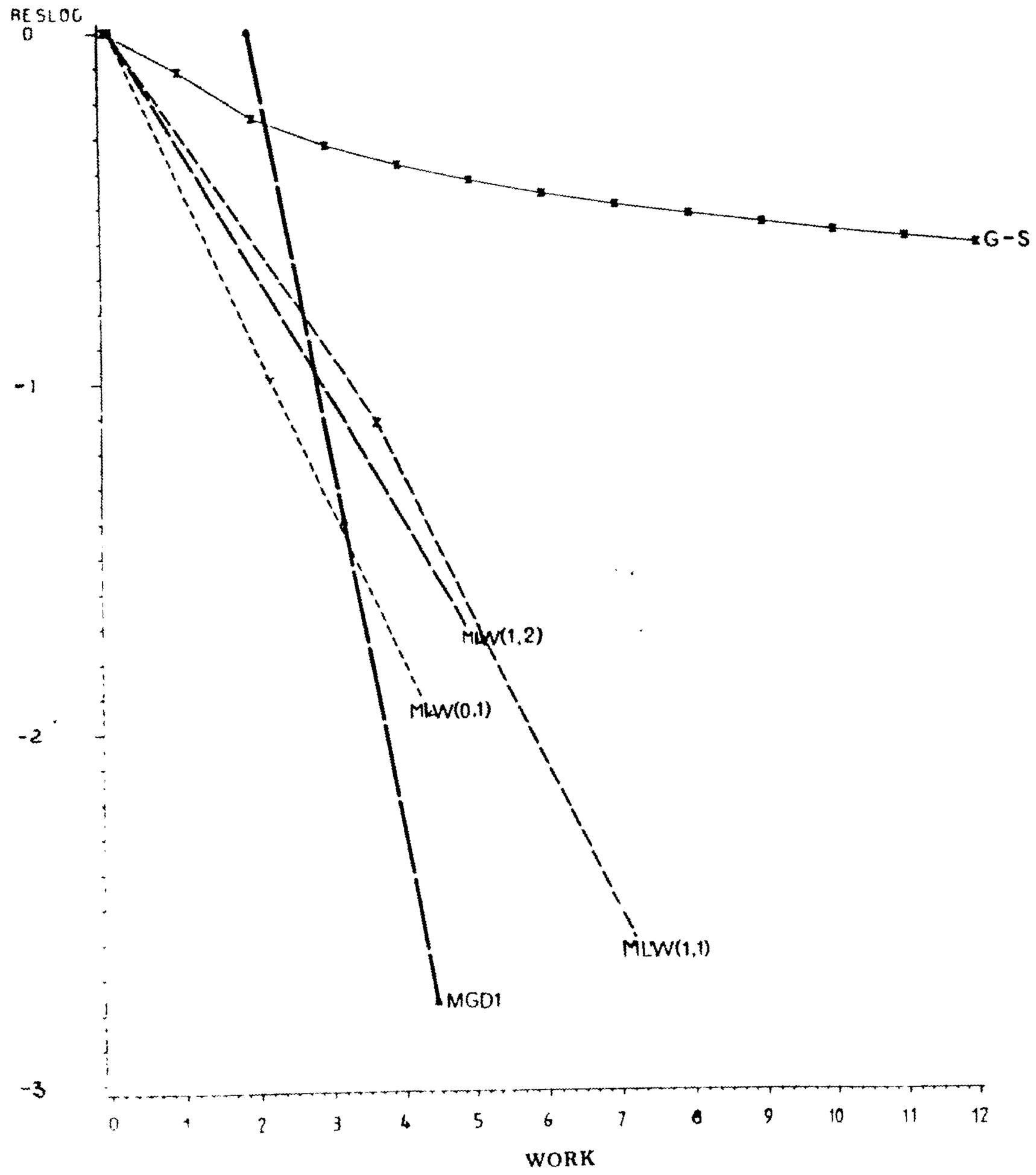

Figure 4.12 Double Glazing problem. Air at Ra=10^3
G-S, MGD1, weighted two-level and max-level multigird sawtooth cycle
Grid = 64x64; global iteration = 1

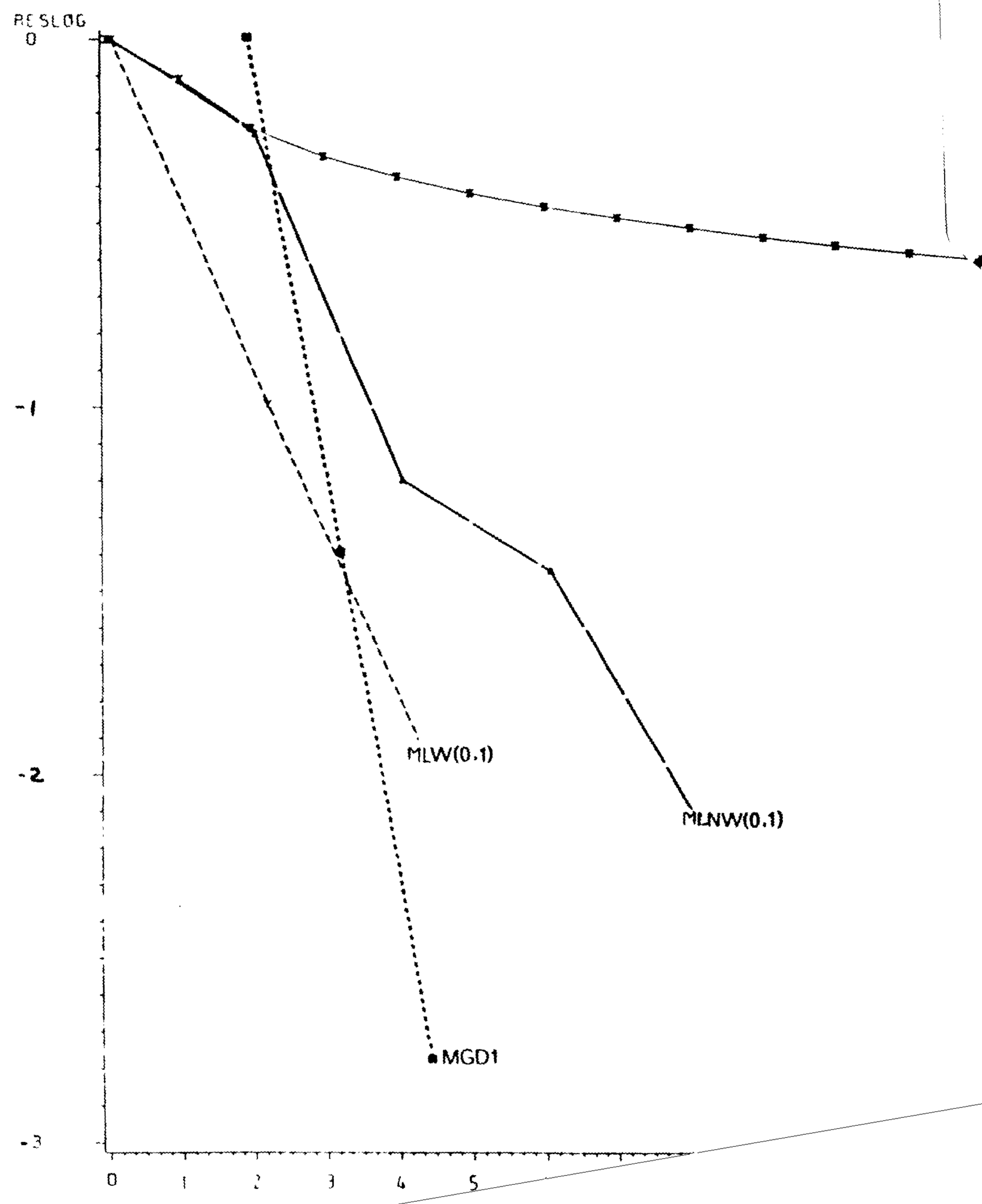

.. Glazing problem. Air at Ra=10^5
.. G, MGD1, weighted two-level and max-level multigird sawtooth cycle
Grid = 64x64; global iteration = 50

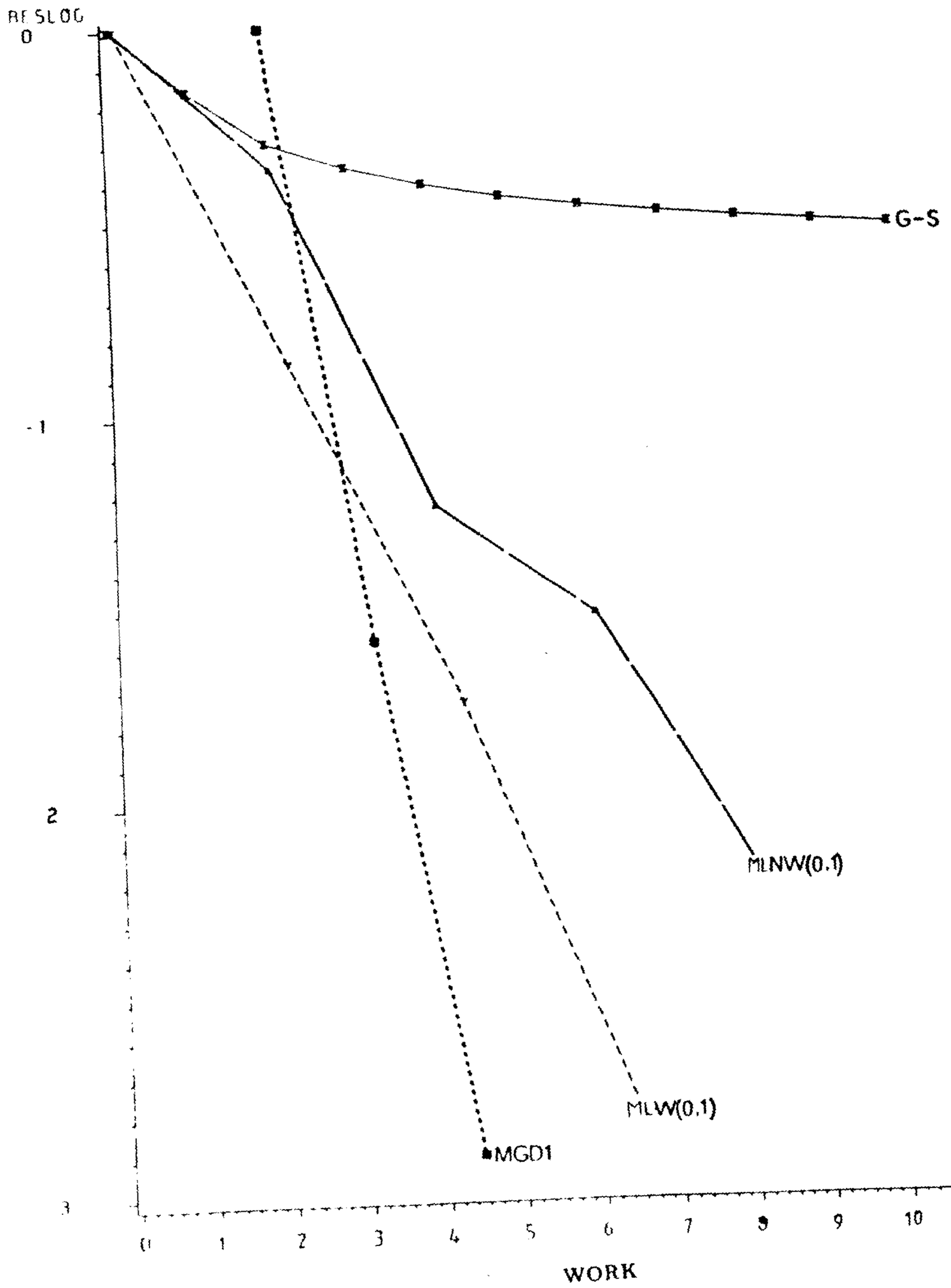

Figure 4.14 Double Glazing problem. Air at Ra=10^5
G-S, and weighted max-level multigird cycles
Grid = 256x6256 global iteration = 1

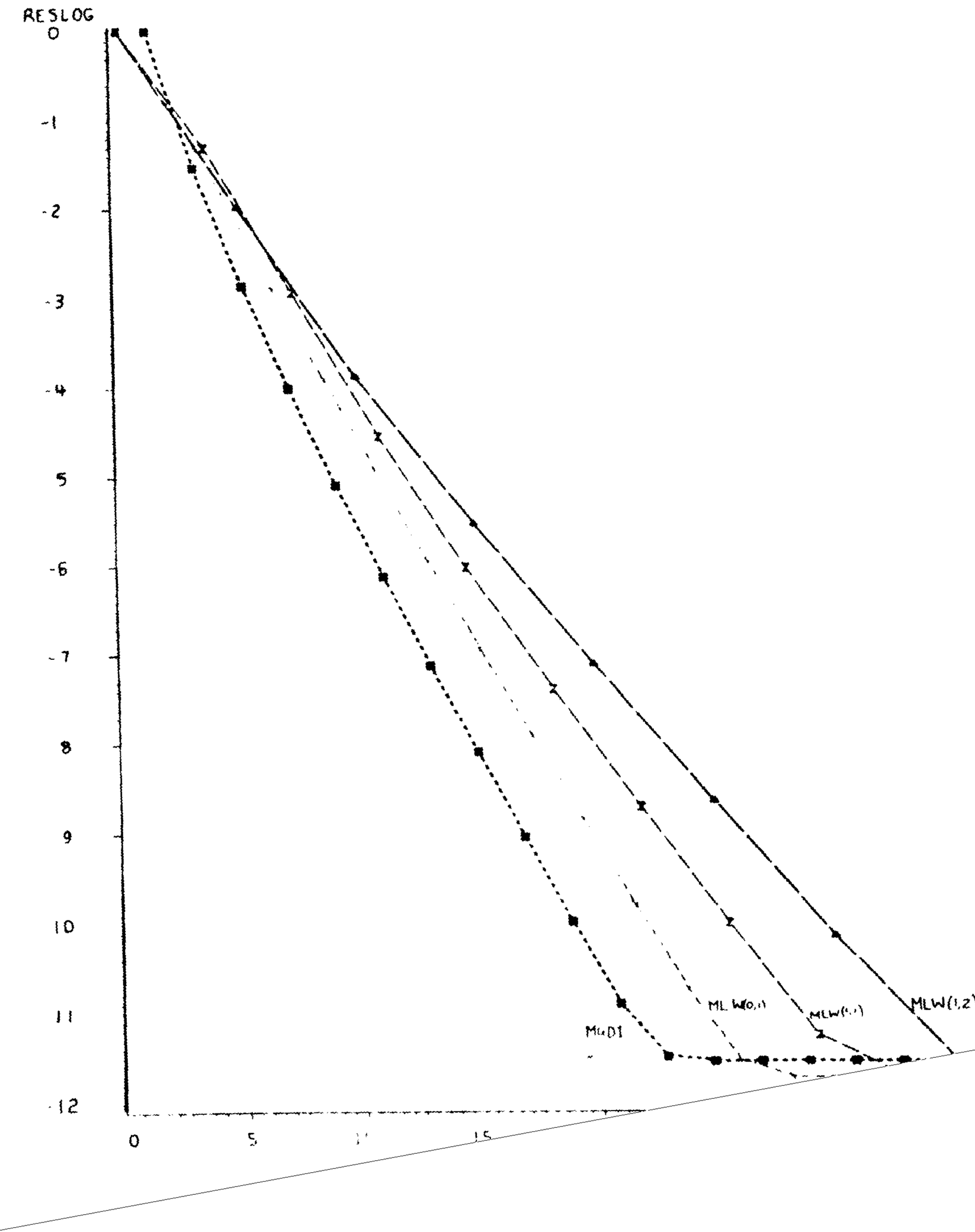

Chapter 5

Application of the multigrid method to equations in three-dimensions

As a natural extension to the last chapter the linear multigrid method is now applied to two three-dimensional equations that arise when the SIMPLE algorithm is used to solve the window-cavity problem (see chapter 6). The linear multigrid method is applied to the three-dimensional pressure-correction equation and the three-dimensional temperature equation, which forms a part of the non-linear system of governing equations. The multigrid method has been applied to the temperature equation because the boundary conditions appear explicitly, unlike with the pressure-correction equation, and so has to be given special treatment. The MGD1 code is not used since it can only solve two-dimensional problems. However, it should be noted that if an MGD1 type code were written for three-dimensional problems the code would require large amounts of storage for the matrix coefficients. It would also be costly in cpu terms since more work would be required in calculating $L_H = I_H^h L_h I_h^H$, as I_H^h and I_h^H would be full weighted operators and thus L_H would be a non-sparse operator requiring the smoother to perform a large amount of work to solve the matrix problem.

When using standard coarsening with multigrid methods in three-dimensions, the extra number of unknowns and hence the extra storage requirement is not more than one seventh of the fine grid unknowns, that is, $N/8 + N/64 + N/256...$ where N is the total number of fine grid unknowns.

The smoother used is the triple line sweep Gauss-Seidel. The triple sweep can be

defined by applying double line sweep on each plane of the third direction. In order to make the code robust the smoother is applied in all three directions as shown in Figures 5.1, 5.2 and 5.3.

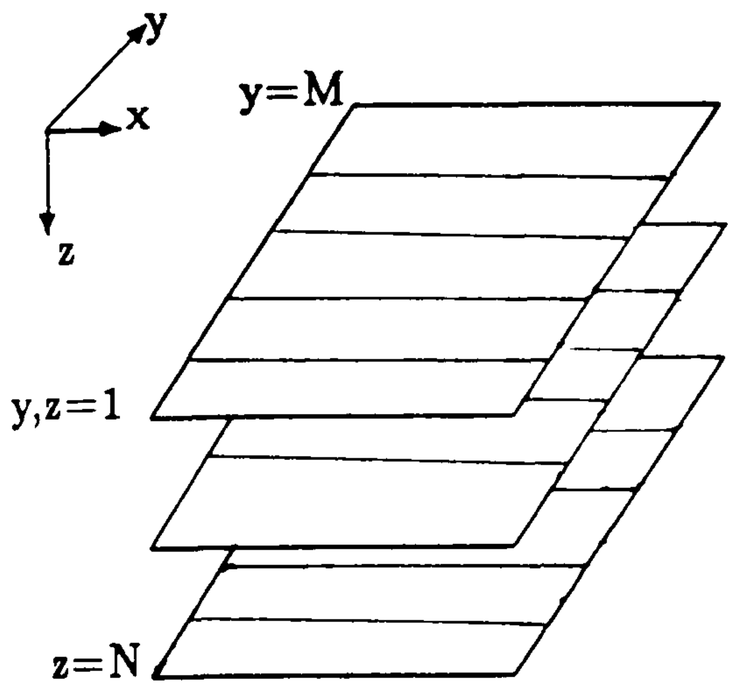


```
Solving for z-planes
  do z=1,N
  do y=1,M
    solve x-lines
  enddo
  enddo
```

Figure 5.1: Sweeping the z-planes

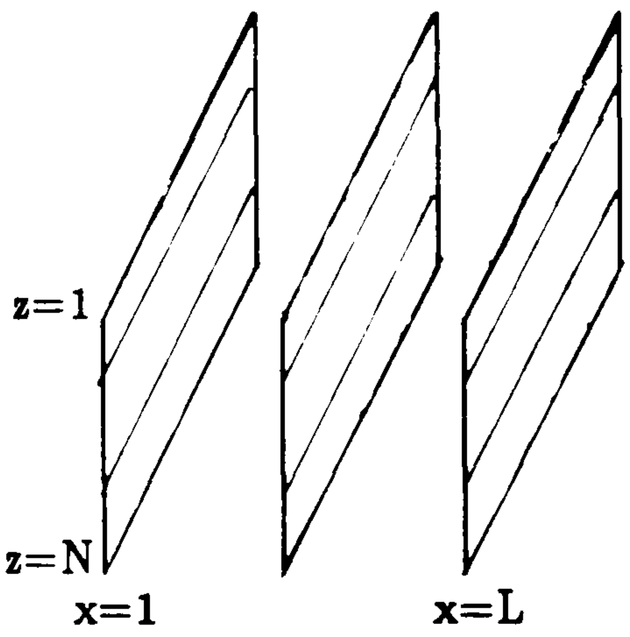


```
Solving for x-planes
  do x=1,L
  do z=1,N
    solve y-lines
  enddo
  enddo
```

Figure 5.2: Sweeping the x-planes

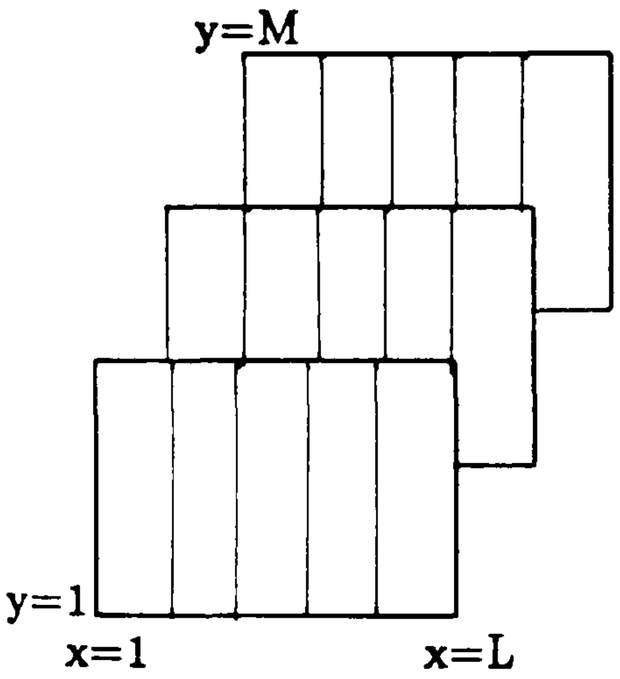


```
Solving for y-planes
  do y=1,M
  do x=1,L
    solve z-lines
  enddo
  enddo
```

Figure 5.3: Sweeping the y-planes.

The three-dimensional coarse grid control volumes are obtained by combining the eight fine grid control volumes, as shown in Figure 5.4. The coarse grid variables are in upper-case. The coarse grid temperature unknowns lie at the same location as the coarse grid pressures. The restriction and prolongation for the pressure-correction and the temperature unknowns are the same except for the special treatment at the boundaries for the temperature unknowns when restricting. The restriction operator is such that the residuals of the eight fine grid control volumes are added to represent

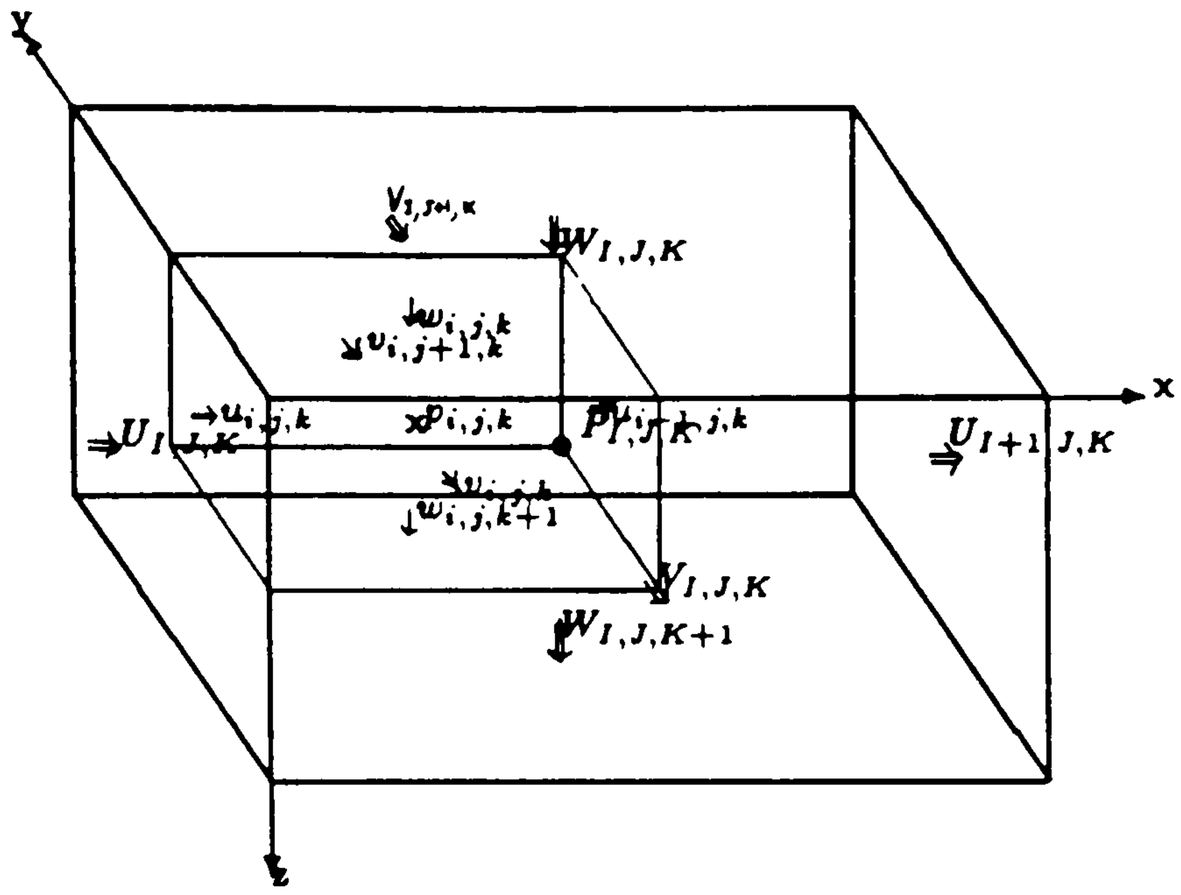

Figure 5.4: Three-Dimensional coarse grid control volume.

the residual on the coarse grid. This is in keeping with the discretization scheme, since with the control volume formulation the residuals represent the volume integral of a source strength. Since eight fine grid cells are needed to form one coarse grid cell, the residual on the coarse grid cell is the sum of the eight fine grid cells, namely

$$\begin{aligned} R_{I,J,K} &= r_{i,j,k} + r_{i+1,j,k} + r_{i,j+1,k} + r_{i,j,k+1} \\ &\quad + r_{i+1,j+1,k} + r_{i+1,j,k+1} + r_{i,j+1,k+1} + r_{i+1,j+1,k+1} \end{aligned} \tag{5.1}$$

where $R_{I,J,K}$ represents the coarse grid residual and $r_{i,j,k}$ the fine grid residuals, see Figure 5.5.

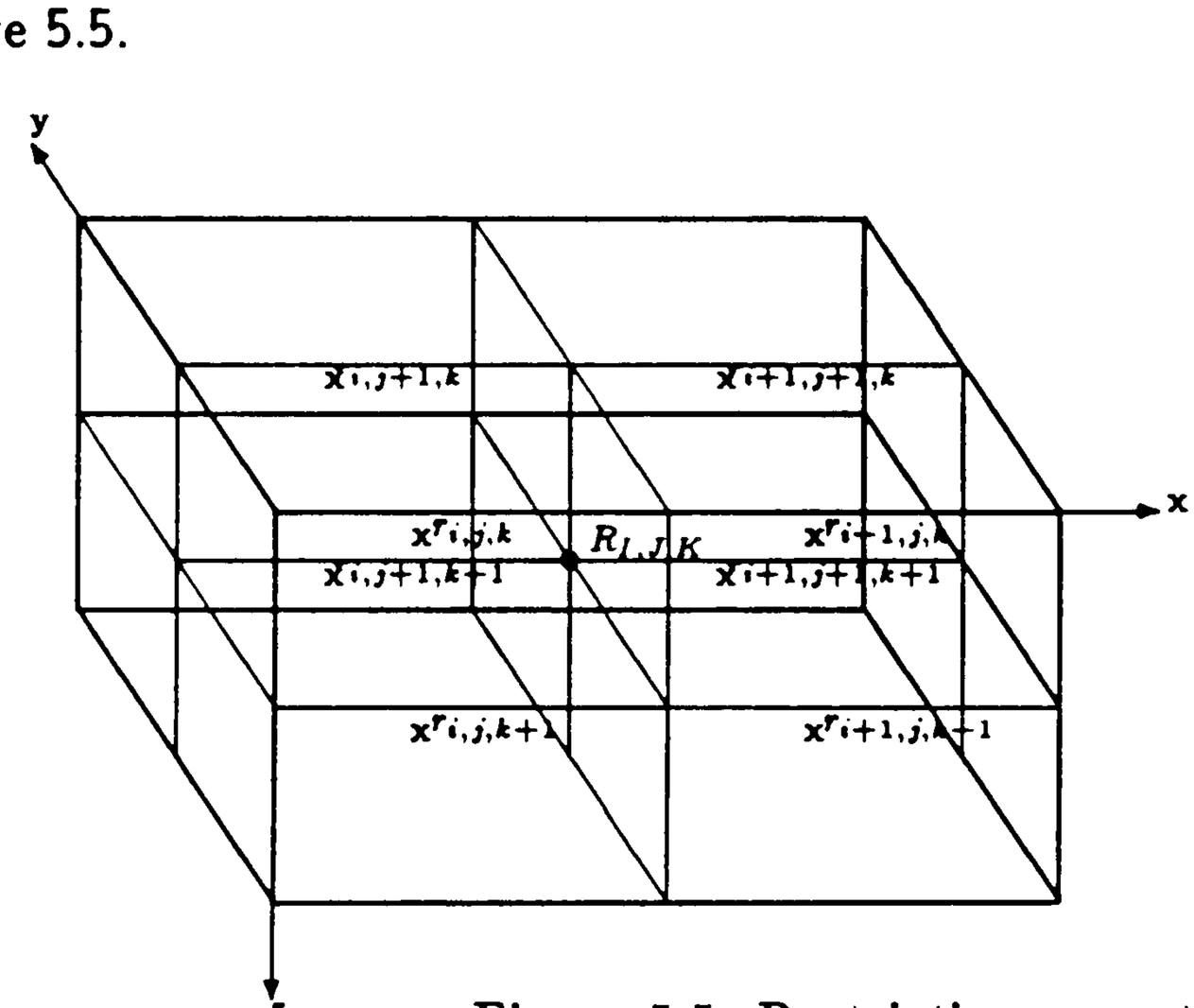

Figure 5.5: Restriction operator.

The three-dimensional prolongation operator is such that the corrections obtained from the coarse grid control volume are passed onto each fine grid control volume that constitutes the coarse grid cell. That is,

$$p'_{i,j,k} = p'_{i,j,k} + \delta p'_{I,J,K} \qquad p'_{i+1,j,k} = p'_{i+1,j,k} + \delta p'_{I,J,K}$$

$$p'_{i,j+1,k} = p'_{i,j+1,k} + \delta p'_{I,J,K} \qquad p'_{i,j,k+1} = p'_{i,j,k+1} + \delta p'_{I,J,K}$$

$$p'_{i,j+1,k+1} = p'_{i,j+1,k+1} + \delta p'_{I,J,K} \qquad p'_{i+1,j+1,k} = p'_{i+1,j+1,k} + \delta p'_{I,J,K}$$

$$p'_{i+1,j,k+1} = p'_{i+1,j,k+1} + \delta p'_{I,J,K} \qquad p'_{i+1,j+1,k+1} = p'_{i+1,j+1,k+1} + \delta p'_{I,J,K} \tag{5.2}$$

where $p'_{i,j,k}$ are the fine grid solutions and $\delta p'_{I,J,K}$ is the coarse grid correction. This prolongation is similar to the two-dimensional non-weighted operator described in the last chapter. A three-dimensional weighted prolongation operator has not been used since it was felt that the benefits derived would be heavily offset by the extra computational work involved.

5.1 The three-dimensional pressure-correction equation

As mentioned before, the pressure-correction equation is obtained via a series of discretized operators but for multigrid purposes the pressure-correction operator must be in a suitable form for inter-grid transfers. Hence the differential operator corresponding to the pressure-correction equation has to be determined. This is done in an analogous fashion to that described in the last chapter. Substituting the differential form of the velocity correction equations (as in 2.30 and 2.31) into the continuity equation and integrating over the appropriate control volume gives the equation:

$$\begin{aligned} p'_{i,j,k}\left[\frac{h_y h_z}{h_x}\left(\frac{1}{\alpha_{i+1,j,k}}+\frac{1}{\alpha_{i,j,k}}\right)+\frac{h_x h_z}{h_y}\left(\frac{1}{\beta_{i,j+1,k}}+\frac{1}{\beta_{i,j,k}}\right)+\frac{h_x h_y}{h_z}\left(\frac{1}{\gamma_{i,j,k+1}}+\frac{1}{\gamma_{i,j,k}}\right)\right]- \\ -\frac{h_y h_z}{h_x \alpha_{i+1,j,k}}p'_{i+1,j,k}-\frac{h_y h_z}{h_x \alpha_{i,j,k}}p'_{-i1,j,k}-\frac{h_x h_z}{h_y \beta_{i,j+1,k}}p'_{i,j+1,k} \\ -\frac{h_x h_z}{h_y \beta_{i,j,k}}p'_{i,j-1,k}-\frac{h_x h_y}{h_z \gamma_{i,j,k+1}}p'_{i,j,k+1}-\frac{h_x h_y}{h_z \gamma_{i,j,k}}p'_{i,j,k-1} \\ = (u^*_{i,j,k}-u^*_{i+1,j,k})h_y h_z+(v^*_{i,j,k}-v^*_{i,j+1,k})h_x h_z+(w^*_{i,j,k}-w^*_{i,j,k+1})h_x h_y. \end{aligned} \tag{5.3}$$

The right hand side of the above equation is the integral of the source term, $\nabla.u^*$. The terms $\alpha_{i,j,k}$, $\beta_{i,j,k}$ and $\gamma_{i,j,k}$ appearing on the left hand side are discrete approximations to α, β and γ and are independent of the mesh size. In comparing the above discrete equation to that normally derived from the SIMPLE algorithm:

$$\alpha_{i+1,j,k} = \frac{a^u_{i+1,j,k}}{h_x h_y h_z} \qquad \alpha_{i,j,k} = \frac{a^u_{i,j,k}}{h_x h_y h_z}$$

$$\beta_{i,j+1,k} = \frac{a^v_{i,j+1,k}}{h_x h_y h_z} \qquad \beta_{i,j,k} = \frac{a^v_{i,j,k}}{h_x h_y h_z}$$

$$\gamma_{i,j,k+1} = \frac{a^w_{i,j,k+1}}{h_x h_y h_z} \qquad \gamma_{i,j,k} = \frac{a^w_{i,j,k}}{h_x h_y h_z}. \tag{5.4}$$

On the coarse grid α, β and γ are obtained by simply averaging them. Note that in the three-dimensional case as with the two-dimensional case the multigrid algorithm does not have to cope with the boundary conditions since they are embedded in the discretized pressure-correction. The coarse grid equation is obtained by formulating the correction problem on the fine grid, that is

$$L^h \delta p'_{i,j,k} = f_{i,j,k} - L^h p'_{i,j,k}, \tag{5.5}$$

and then transporting the correction problem onto the coarse grid by discretizing the differential form of it on the coarse grid, giving,

$$L^H \delta p'_{I,J,K} = R_{I,J,K} \tag{5.6}$$

where $\delta p'_{I,J,K}$ are the corrections to be calculated on the coarse grid, $R_{I,J,K}$ are the restricted residuals and L^H the discretized coarse grid operator.

5.2 The three-dimensional temperature equation

The discretized thermal equation is obtained by integrating

$$\frac{\partial(u\theta)}{\partial x} + \frac{\partial(v\theta)}{\partial y} + \frac{\partial(w\theta)}{\partial z} - \left(\frac{\partial^2\theta}{\partial x^2} + \frac{\partial^2\theta}{\partial y^2} + \frac{\partial^2\theta}{\partial z^2}\right) = 0 \tag{5.7}$$

over the control volume shown in Figure 5.6. The discretized equation, using

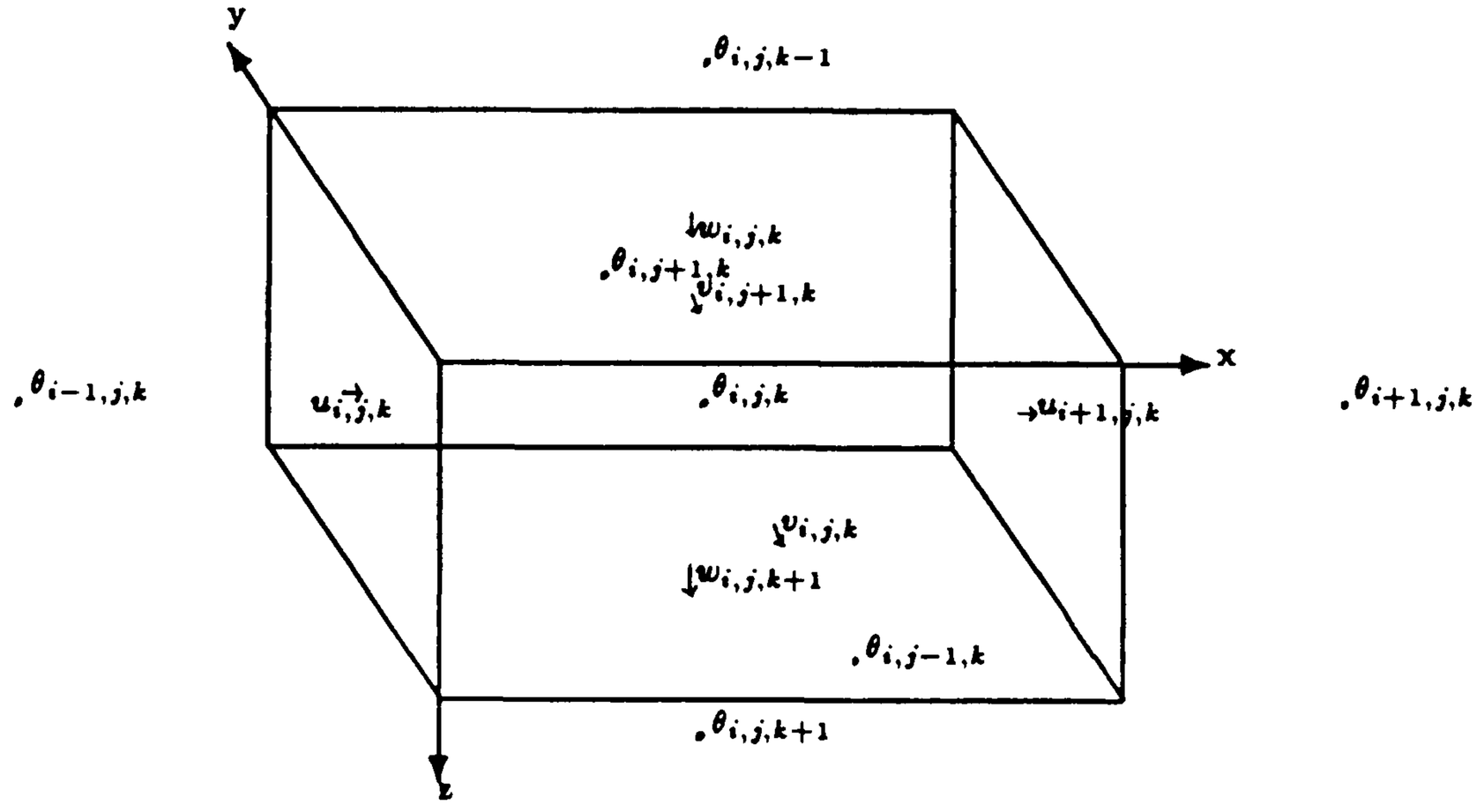

Figure 5.6: Three-Dimensional temperature control volume.

upwinding for θ is,

$$\theta_{i,j,k}[(|U_E,0| + |-U_W,0|)h_y h_z + (|V_N,0| + |-V_S,0|)h_x h_z +$$

$$(|W_B,0| + |-W_T,0|)h_x h_y + 2\frac{(h_y h_z)^2 + (h_x h_z)^2 + (h_x h_y)^2}{h_x h_y h_z}]$$

$$-\theta_{i+1,j,k}[|-U_E,0|+\frac{1}{h_x}]h_yh_z-\theta_{i-1,j,k}[|U_W,0|+\frac{1}{h_x}]h_yh_z-$$

$$\theta_{i,j+1,k}[|V_N,0|+\frac{1}{h_y}]h_xh_z-\theta_{i,j-1,k}[|V_S,0|+\frac{1}{h_y}]h_xh_z-$$

$$\theta_{i,j,k+1}[|W_B,0|+\frac{1}{h_z}]h_xh_y-\theta_{i,j,k-1}[|W_T,0|+\frac{1}{h_z}]h_xh_y \quad = \quad 0 \tag{5.8}$$

which can be put in the form

$$L^h\theta_{i,j,k}=0. \tag{5.9}$$

The coarse grid correction equation is obtained by formulating the correction problem on the fine grid, that is

$$L^h\theta' = f_{i,j,k}-L^h\theta \tag{5.10}$$

and then transferring the correction problem onto the coarse grid by

$$L^H\theta'_{I,J,K}=R_{I,J,K} \tag{5.11}$$

where $\theta'_{i,j,k}$ are the corrections to be obtained on the coarse grid, $R_{I,J,K}$ are the residuals restricted from the fine grid to the coarse, and L^H is the discretized coarse grid operator. Again the coarse grid velocity locations do not coincide with the fine grid velocity locations. To obtain the coarse grid operator L^H the coarse grid velocities required are U^c,V^c and W^c, these are obtained by averaging the fine grid velocities, see below.

$$\theta'_{i,j,k}[((|U^c_E,0|+|-U^c_W,0|)h_yh_z+(|V^c_N,0|+|-V^c_S,0|)h_xh_z+$$

$$(|W^c_B,0|+|-W^c_T,0|)h_xh_y+2\frac{(h_yh_z)^2+(h_xh_z)^2+(h_xh_y)^2}{h_xh_yh_z}]$$

$$-\theta'_{i+1,j,k}[|-U^c_E,0|+\frac{1}{h_x}]h_yh_z-\theta'_{i-1,j,k}[|U^c_W,0|+\frac{1}{h_x}]h_yh_z-$$

$$\theta'_{i,j+1,k}[|V^c_N,0|+\frac{1}{h_y}]h_xh_z-\theta'_{i,j-1,k}[|V^c_S,0|+\frac{1}{h_y}]h_xh_z-$$

$$\theta'_{i,j,k+1}[|W^c_B,0|+\frac{1}{h_z}]h_xh_y-\theta'_{i,j,k-1}[|W^c_T,0|+\frac{1}{h_z}]h_xh_y \quad = \quad R_{I,J,K} \tag{5.12}$$

5.3 The boundary conditions

For the discretized non-dimensional equation governing the thermal flow in the window cavity problem there exist Dirichlet and Neumann boundary conditions.

With the correction problem the Dirichlet conditions are replaced by $\theta' = 0$ on the coarse grid, that is, the Dirichlet boundary conditions do not need to be corrected on the coarser grid.

The Neumann boundary condition is treated as follows. Consider a two-dimensional control volume which has one face on the boundary with the boundary condition as in Figure 5.7 The boundary condition at the top wall is denoted by $\left(\frac{\partial\theta}{\partial z}\right)_{top} = \alpha$, where

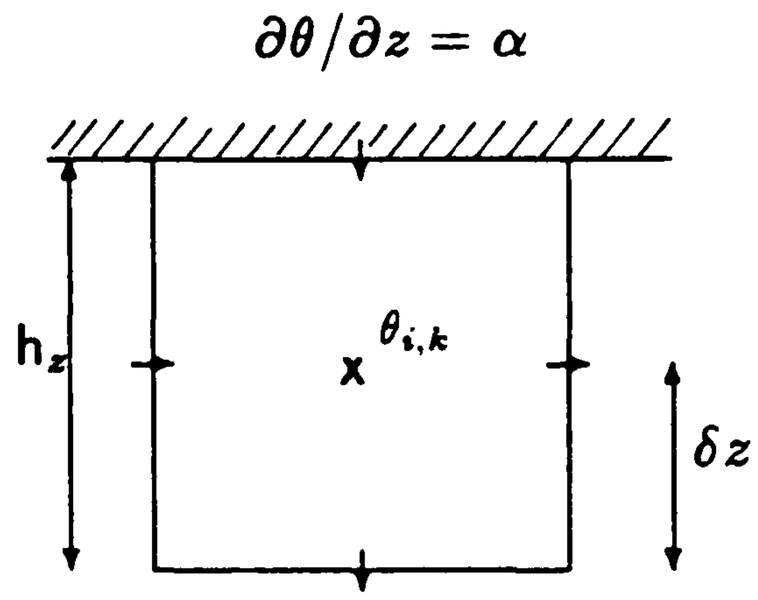

Figure 5.7: A cell at a boundary.

$\alpha = 0$ for the window cavity problem. Let the unknown temperature at the top wall be θ_{top}. Then θ_{top}, if required, can be obtained from the relationship $\frac{\theta_{top}-\theta_{i,k}}{\delta z} = \alpha$, or $\theta_{top} = \delta z\alpha + \theta_{i,k}$. The point $\theta_{i,k}$ is an interior point which starts off as an initial guess and is updated in the iterative process. If one assumes $\theta_{i,k}$ is corrected via the multigrid process by $\theta'_{i,k}$, where $\hat{\theta}_{i,k} = \theta_{i,k} + \theta'_{i,k}$ is the new updated value of $\theta_{i,k}$, then the temperature at the top wall becomes

$$\begin{aligned} \hat{\theta}_{top} &= \delta z\alpha + \hat{\theta}_{i,k} \\ &= \delta z\alpha + \theta_{i,k} + \theta'_{i,k} \\ &= \theta_{top} + \theta'_{i,k} \end{aligned} \tag{5.13}$$

which implies that the correction made at the interior point is also made at the boundary point. This condition leads to the Neumann condition $\left(\frac{\partial\theta'}{\partial z}\right) = 0$ as the boundary condition for the correction problem.

5.4 Results

The benefit obtained from the three-dimensional multigrid method can clearly be seen in Figure 5.8 to 5.13. Residual reductions at only the first global iteration of the SIMPLE algorithm for the window cavity problem are presented, since only at the initial global iteration do the multigrid and non-multigrid methods have the same conditions. Results presented are for Cerrobase with Ra $= 10^3$ in the window cavities (1,1,1), (1,2,1) and (1,5,1) with mesh sizes 16x16x16, 16x16x16 and 16x40x16 respectively. Two types of v-cycles have been tried, the (0,1) sawtooth cycle and the

(1,1) v-cycle. Two graphs, one for the effects of multigrid on the pressure-correction equation and the other for the effects on the temperature equation have been presented for the above three window cavities. The residual reductions obtained with the temperature equation are just as good as for the pressure-correction equation indicating that the Neumann boundary conditions with the temperature equation have been treated correctly. Note the sawtooth cycle is more economical than the (1,1) v-cycle.

With the window cavity (1,5,1) the residual reduction per cycle for the pressure-correction and the temperature equations is not as great as those for the window cavities (1,1,1) and (1,2,1). This is due to the standard coarsening used for the 16x40x16 mesh which gives 4x10x4 as the coarsest mesh. With a 4x10x4 mesh a band of low frequency errors corresponding to $h < \frac{1}{10}$ have not been solved for in the y-direction. A further coarsening of the grid in the y-direction using the semi-coarsening method would give a mesh size of 4x5x4 which would eliminate this band of low frequency errors. Practically, the man-hours required to incorporate semi-coarsening in the code was felt to be unjustifiable compared to the efficiency that would be obtained.

5.5 The Tri-Diagonal Matrix Algorithm, (TDMA)

The basic solver for all the equations in the SIMPLE algorithm is the line Gauss-Seidel solver. This involves solving a tridiagonal system of linear algebraic equations and is solved by forward and backward substitution. Since around 95% of the cpu time in the SIMPLE algorithm is spent on solving sets of tridiagonal algebraic equations it is worthwhile finding an efficient and cost effective way of solving these equations. One approach is to vectorize the TDMA in Fortran but unfortunately it is impossible to vectorize the whole algorithm since it is inherently recursive. However, some parts of the algorithm can be vectorized, see [42]. An efficient manner of solving these sets of algebraic equations is to write the algorithm in machine language, or in this case the CRAY assembler. This is considerably faster than part vectorizing the TDMA routine in Fortran, as illustrated in the Table 5.1. The cpu timings in the table are for Cerrobase with $Ra = 10^3$ in the window cavity (1,1,1) with mesh size 16x16x16. The results are given after 50 global iterations of the SIMPLE algorithm with both the pressure-correction and temperature equations being multigridded. The under-relaxation parameters used for the pressure and the velocity are 0.4 and 0.5

respectively.

	TDMA in Assembler	TDMA part vectorized in Fortran
Total cpu for 50 iterations of the SIMPLE algorithm	32.68	74.82
Total cpu time spent on the p-c equation	16.27	36.53
Total cpu time spent on the temp. equation	10.82	32.13

Table 5.1: Comparison of the TDMA written in Assembler and Fortran.

Figure 5.8 Window cavity problem (1x1x1). Cerrobase at $Ra=10^3$
Pressure-correction equation
G-S and three-level multigrid cycles (0,1) and (1,1)
Grid = 16x16x16; global iteration = 1

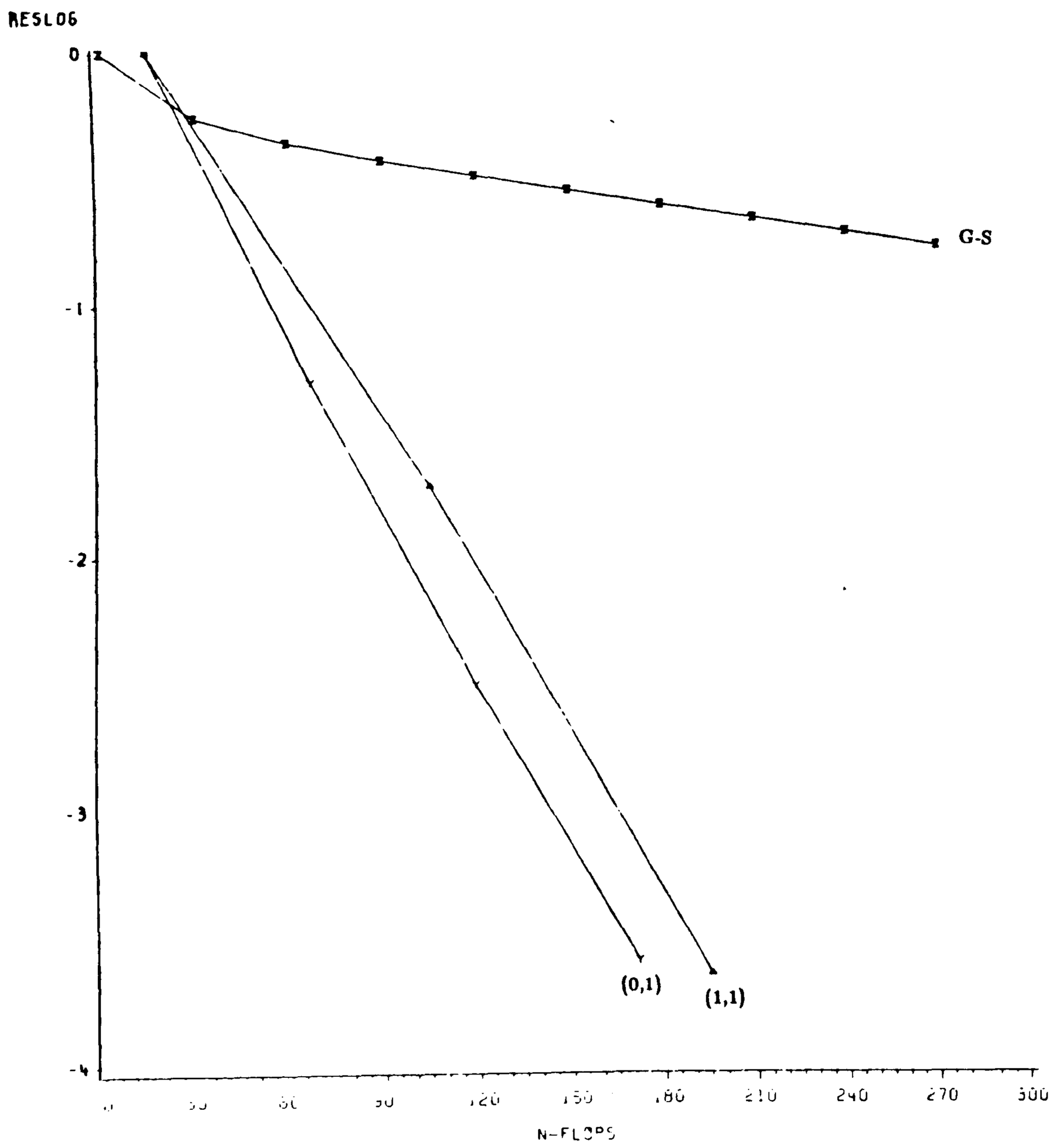

Figure 5.9 Window cavity problem (1x1x1). Cerrobase at $Ra=10^3$
Temperature equation
G-S and three-level multigrid cycles (0,1) and (1,1)
Grid = 16x16x16; global iteration = 1

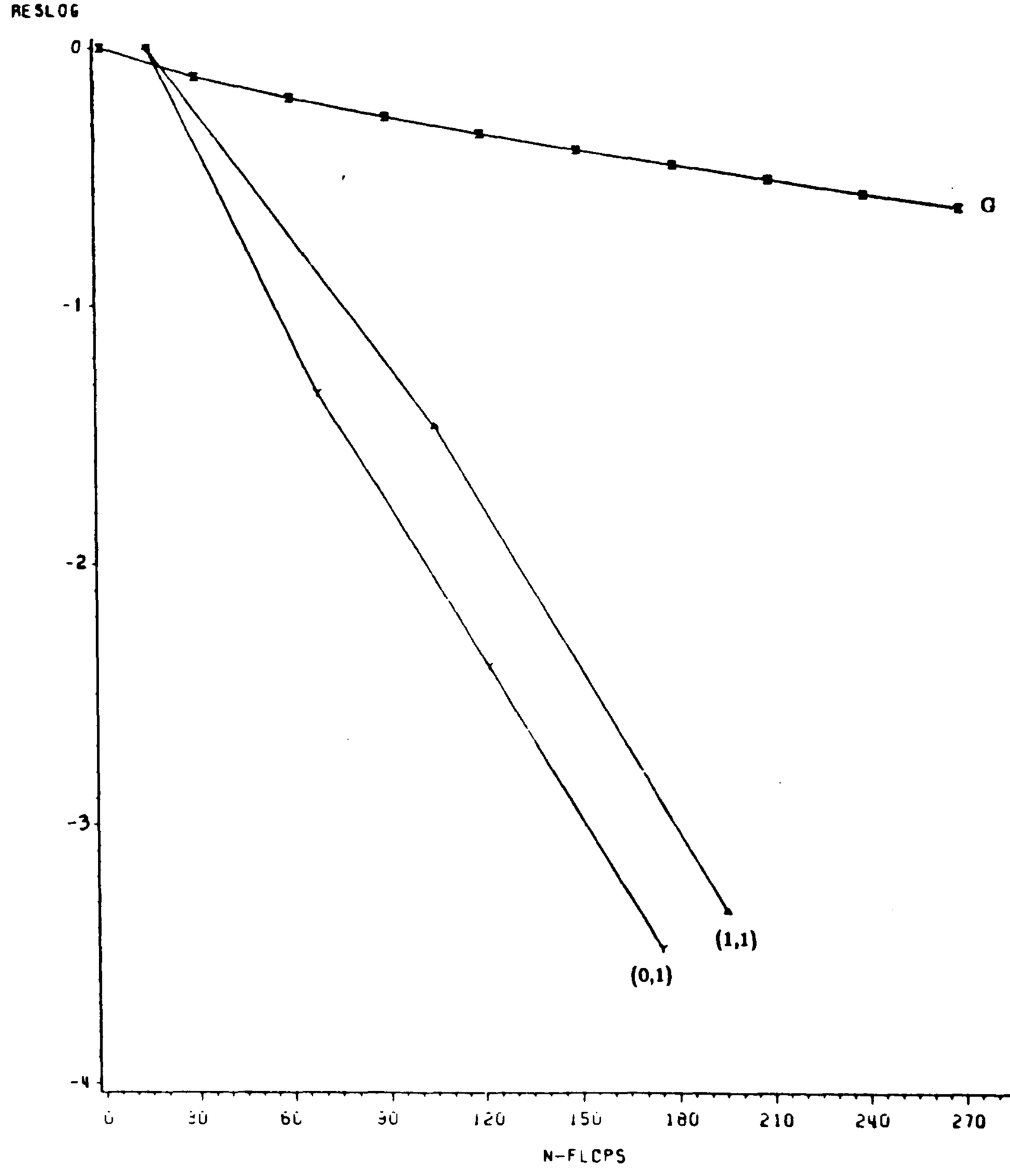

Figure 5.10 Window cavity problem (1x2x1). Cerrobase at Ra=10^3
Pressure-correction equation
G-S and three-level multigrid cycles (0,1) and (1,1)
Grid = 16x16x16; global iteration = 1

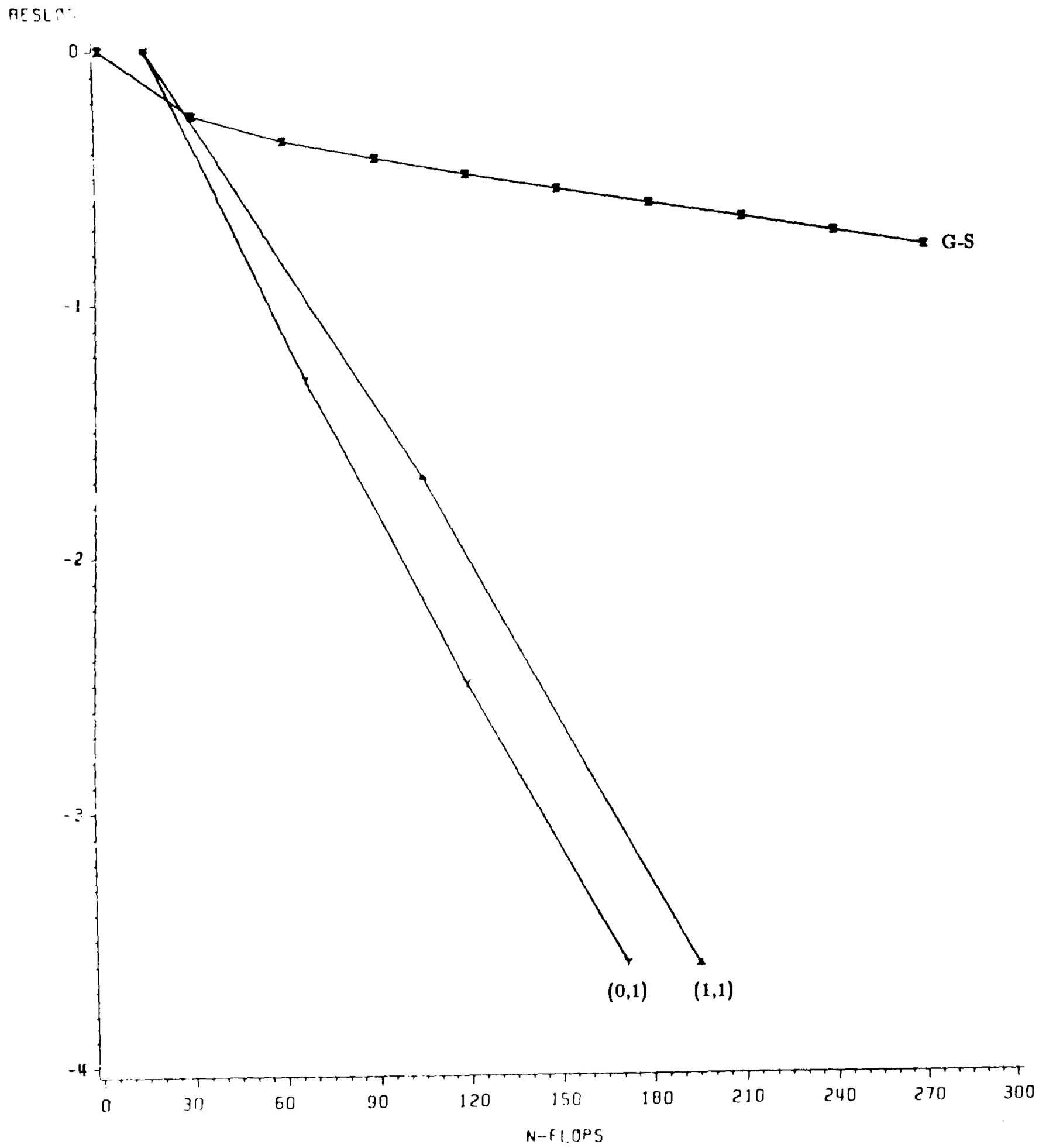

Figure 5.11 Window cavity problem (1x2x1). Cerrobase at Ra=10^3
Temperature equation
G-S and three-level multigrid cycles (0,1) and (1,1)
Grid = 16x16x16; global iteration = 1

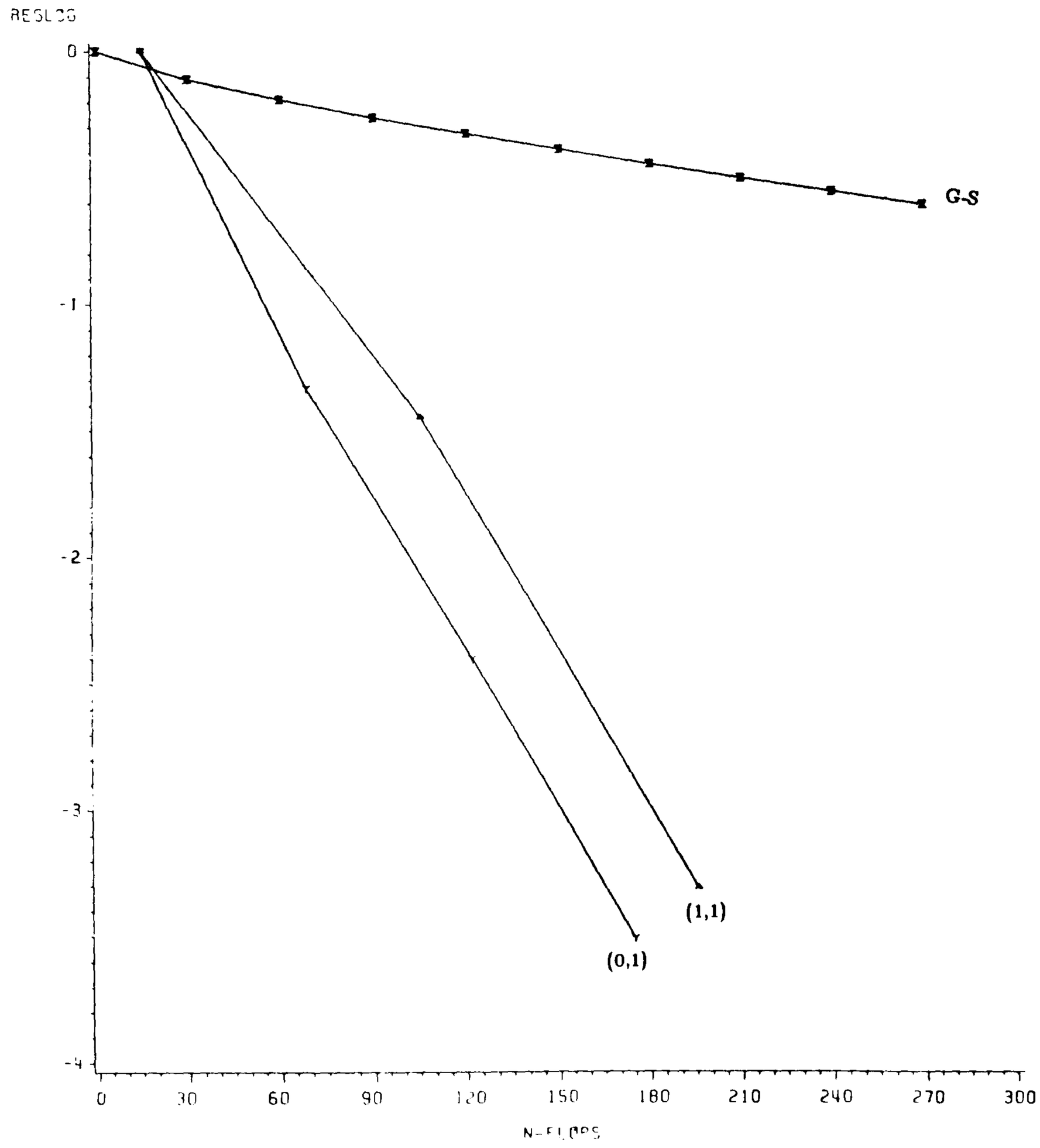

Figure 5.12 Window cavity problem (1x5x1). Cerrobase at Ra=10^3
Pressure-correction equation
G-S and three-level multigrid cycles (0,1) and (1,1)
Grid = 16x40x16; global iteration = 1

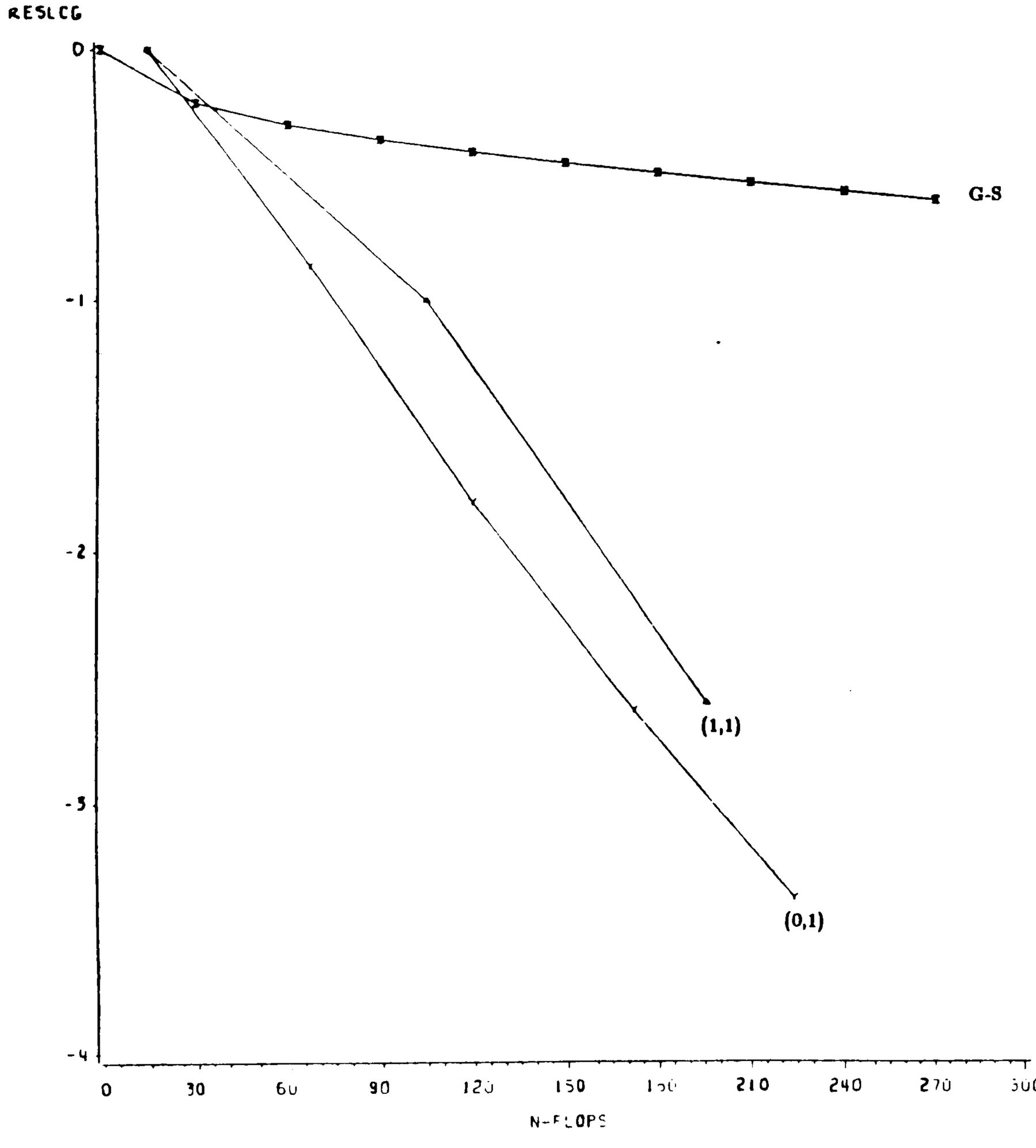

Figure 5.13 Window cavity problem (1x5x1). Cerrobase at Ra=10^3
Temperature equation
G-S and three-level multigrid cycles (0,1) and (1,1)
Grid = 16x40x16; global iteration = 1

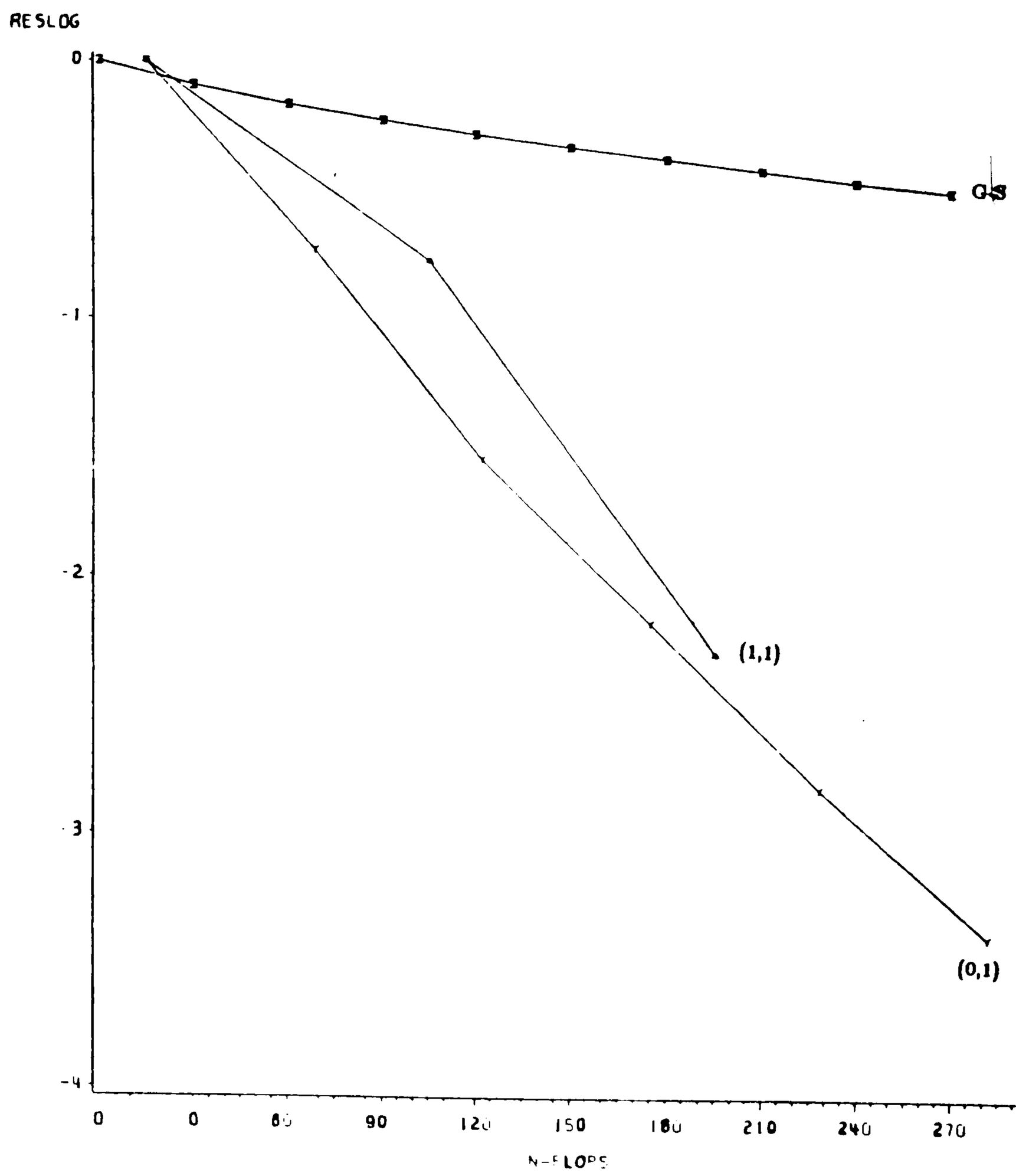

Chapter 6

A three-dimensional numerical study of laminar natural convection in a rectangular cavity

6.1 Introduction

The problem studied is that of steady laminar free convection in a rectangular cavity filled with a viscous heat conducting fluid. The importance of the problem has already been described in chapter 1. The nature of the geometry is such that the fluid motion is induced by keeping two of the vertical walls at different uniform temperatures T_h and T_c ($T_h > T_c$). The remaining four walls are adiabatic with the no-slip boundary condition applying at all walls. The geometry exhibits symmetry about a plane perpendicular to the two isothermal walls half way along the cavity in the y-direction. It is therefore only necessary to obtain solutions over one half of the cavity, the solution cavity, see Figure 6.1.

Choosing l, the length of the cavity in the x-direction, as the scale factor for length, the shape of the cavity is determined by the non-dimensional aspect ratios Hy $= m/l$ and Hz $= n/l$, where m and n are the lengths of the cavity in the y and z direction respectively. The scale factors for velocity and pressure are κ/l and $\rho_0\kappa^2/l^2$ respectively, where κ is the coefficient of thermal diffusivity and ρ_0 is the density of the fluid at a reference temperature, T_0. The non-dimensional temperature is $\theta = (T - T_c)/(T_h - T_c)$, where T is the local temperature of the fluid and T_h and T_c are the temperatures of the hot and cold boundaries respectively. The non-dimensional

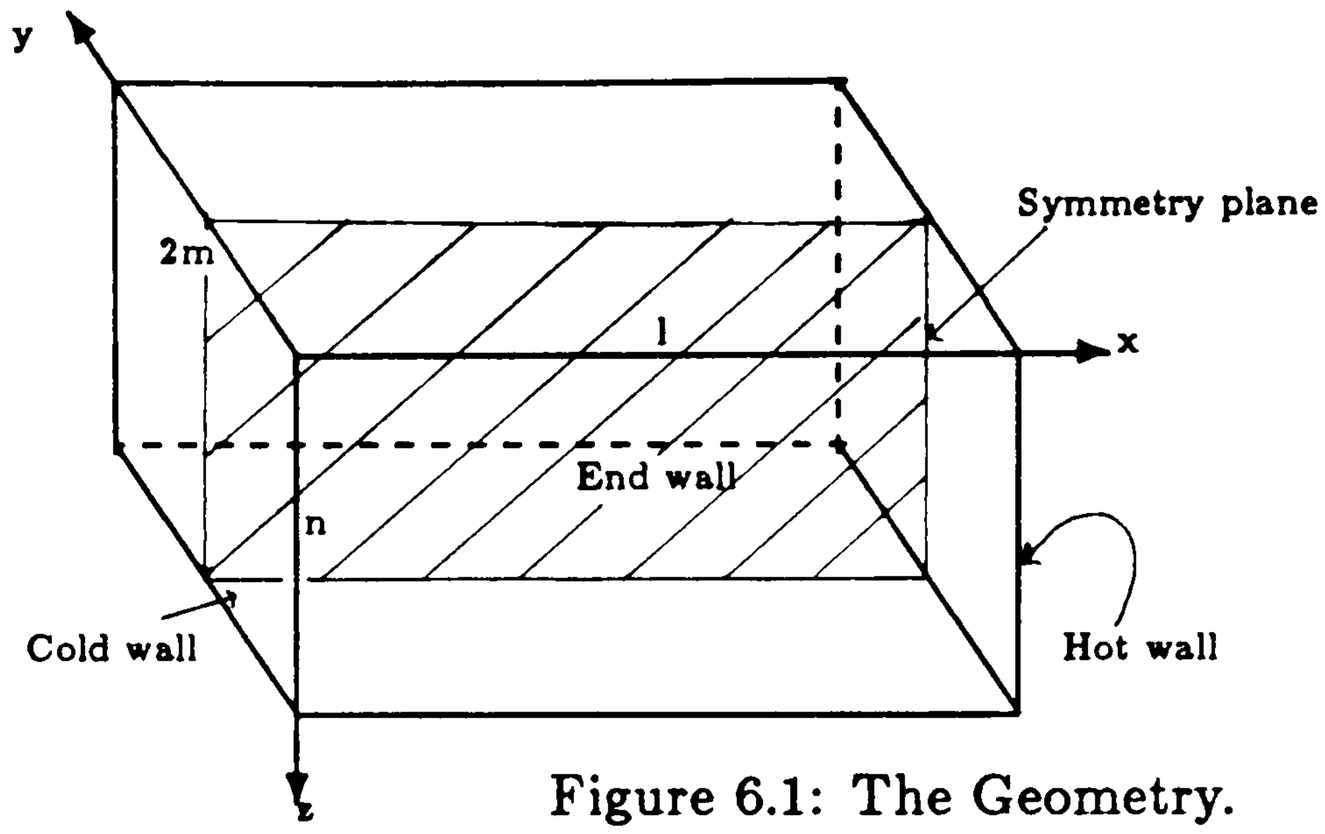

Figure 6.1: The Geometry.

parameters, the Rayleigh and Prandtl numbers, are defined as $\mathrm{Ra} = g\beta(T_h - T_c)l^3/\kappa\nu$ and $\mathrm{Pr} = \nu/\kappa$ respectively, where β is the coefficient of volumetric expansion, ν is the kinematic viscosity and g is the gravitational acceleration in the z direction.

The governing equations are the Navier-Stokes equations, the continuity equation and the temperature equation. These equations are strongly coupled and can be considerably simplified by using the Boussinesq approximation, that is, all fluid properties except density are assumed constant. The fluctuations in density are assumed to be entirely due to thermal (as opposed to pressure) effects and the variations in the density are neglected except in the buoyancy term. This approximation is quite realistic for a small temperature difference across the cavity. With the Boussinesq approximation applied, the non-dimensional forms of the momentum, continuity and temperature equations in three dimensions are:

$$(\bar{u}.\nabla)\bar{u} = -\nabla p + \mathrm{Pr}\nabla^2\bar{u} - \mathrm{RaPr}\theta\bar{k} \tag{6.1}$$

$$\nabla.\bar{u} = 0 \tag{6.2}$$

$$\nabla.(\bar{u}\theta) = \nabla^2\theta \tag{6.3}$$

respectively, where $\bar{u}$ is the velocity vector (u, v, w) in Cartesian coordinates, p is the pressure and $\bar{k}$ is the unit vector in the z-direction. The boundary conditions are $v = 0$ and $\frac{\partial u}{\partial y} = \frac{\partial w}{\partial y} = \frac{\partial \theta}{\partial y} = \frac{\partial p}{\partial y} = 0$ at the symmetry plane; $y = \frac{\mathrm{Hy}}{2}$ and $\bar{u} = 0$ at all the other boundaries; adiabatic temperature conditions at all other walls except the hot and cold walls where $\theta = 1$ and $\theta = 0$ respectively.

Although the problem of free convection in an enclosure has been studied for a simple geometry, it nevertheless has a complex solution structure and provides some insight into more difficult industrial and geophysical problems. For this reason the

problem has been of wide interest and has thus been studied extensively -analytically, experimentally and numerically- for a large range of governing parameters but mostly in two-dimensions. Some direct applications of this problem are the insulation of buildings including nuclear reactor cores, double glazing of windows, design of furnaces and cooling of nuclear fuels. This problem with small height aspect ratio Hz is particularly important in modelling solar collectors, cooling of electronic equipment and thermal circulation in estuaries and lakes. The problem with low Prandtl number fluids is of particular interest to important applications such as LMFBR's, crystal growing, purification of metals and in heat exchangers.

A review of some of the results obtained with the two-dimensional problem is presented in the following section.

6.2 The two-dimensional problem

In two-dimensions the problem is referred to as the double glazing problem. The same boundary conditions for the velocities (u, v) and the temperature θ on the x and z boundaries apply. The equation, boundary conditions and terms related to the third coordinate direction, the y-direction, are now irrelevant. The fluid flow in the two-dimensional cavity has no equilibrium solution. That is, the buoyancy effect is not balanced by the vertical pressure gradients and a recirculating flow results. The fluid near the hot wall rises due to its relatively low density. Similarly the fluid near the cold wall looses heat to its surroundings, increases in density and hence sinks. The rising and sinking fluid entrains fluid along the bottom and top walls respectively, thus completing a cycle around the cavity.

The non-dimensional equations 6.1-6.3 reveal that the flow is uniquely determined by the Prandtl number, Pr, the Rayleigh number, Ra, and the height aspect ratio $\mathrm{Hz} = n/l$.

6.2.1 The Prandtl number

This non-dimensional number, Pr, is a property of the fluid and so plays the part of a governing parameter. It is the ratio of two diffusivities,

$$\mathrm{Pr} = \nu/\kappa, \tag{6.4}$$

ν, the kinematic viscosity, being the diffusivity of momentum and vorticity and κ being the diffusivity of heat.

Gases have values of Pr a little less than 1.0, typically air=0.71. Most liquids have values greater than 1.0, water=6 being typical of the lower end of the range, with oils having values 10-10000. In general the kinematic viscosity varies much more widely than the thermal diffusivity, so the high Prandtl number fluids are the viscous ones. [62]. The important exceptions to these statements are the liquid metals with high thermal diffusivity, giving low Prandtl numbers, e.g. mercury=0.03, Gallium=0.02. The thermal and velocity boundary layers are expected to behave differently for high and low Prandtl fluids. This can be demonstrated by considering free convection around a vertical heated plate. The heat spreads into the fluid via the thermal boundary layer which increases in thickness with height. Velocity is introduced into the flow via the viscous boundary layer which also increases in thickness with height. When the Prandtl number is large (> 1) the velocity boundary layer is thicker than the thermal boundary layer. This is because the heat diffuses slowly away from the wall but the thin hot layer drags much more fluid into motion through the action of viscosity. When the Prandtl number is small (< 1) the thermal boundary layer is thicker due to the high thermal diffusivity of the low Prandtl number fluid, resulting in the velocity and the thermal boundary layers being of similar thickness. From the above considerations, it is expected that for the double glazing problem the thermal behaviour of the low Prandtl number fluids ($\ll 1$) will be different to that of moderate ($O(1)$) and high ($\gg 1$) Prandtl number fluids.

6.3 The two-dimensional fluid flow structure

Batchelor (1953) [2] analytically investigated the heat transfer and flow structure in tall air filled cavities. He obtained estimates of the heat transfer in what are now called the conduction and transition regimes of the flow and a criterion for the change from one flow to the other. He concluded that at sufficiently high Ra, the flow would consist of a core of constant temperature and vorticity surrounded by a continuous boundary layer. He verified his conclusions using heat transfer results from an experimental study performed by Mull and Reither (1930)[2]. Eckert and Carlson (1961) [15] with their experimental investigation supplemented Batchelors analytical results. They categorized various flow regimes found in a tall air filled cavity based on

heat transfer results. For low Rayleigh number they noted that the heat transfer was dominated by conduction, which they called the conduction regime. With increasing Rayleigh number convective effects appeared with both conduction and convection playing important roles. This regime they called the transition regime, which marks the transition between conduction and convection dominated heat transfer. For larger Rayleigh numbers the heat transfer was convection dominated. The flow mainly taking place within the boundary layers with the central core being relatively stagnant with zero horizontal temperature gradients. Hence the heat transfer occurs through the boundary layers and not through the central core. For this reason they called it the boundary layer regime. They also noted that the core temperature varied vertically and was not constant as postulated by Batchelor. These results were further verified by Elder (1965)[14] with an experimental study of tall air filled cavities. Elder also noted that a small increase in Rayleigh number beyond the boundary layer regime resulted in a slight increase of the horizontal temperature profile and appearance of weak secondary rolls in the central core.

The fluid under certain circumstances may not follow these patterns, indeed the low Rayleigh number primary flow may become unstable and exhibit secondary rolls. These instabilities have been the subject of linear stability analysis, see Gill and Davey [18], Vest and Arpaci [64], and Bergholtz [3].

The third governing parameter the height aspect ratio, Hz, can be categorized in terms of tall ($Hz \gg 1$), square ($Hz \approx 1$) and shallow ($Hz \ll 1$) cavities. The fluid flow behaviour in these three categories of enclosure differ considerably in character, as described below. The flow in the tall cavity is described first, followed by that in the square cavity and then finally by that in the shallow cavity.

For Rayleigh numbers in the conduction regime, the primary recirculating flow exists in the tall, square and shallow cavities with all fluids.

In the boundary layer regime and for higher Rayleigh numbers secondary flow develops in tall and square cavities with moderate and high Prandtl number fluids, [14],[64].

The secondary flow occurs in the form of a multicellular flow, commonly referred to as the cat's eye cells. These cells are all stacked on top of each other embedded in, and rotating in the same direction as, the primary base flow. With a further increase in the Ra number the development of a tertiary flow occurs which consists of smaller counter rotating cells in between the earlier developed secondary cells.

The tertiary flow results are due to the strengthening of the secondary flow relative to the primary flow and not as a result of an instability of the secondary flow [14]. Gill and Davey [18] by using linear stability analysis also showed that the instability is buoyancy driven and that the flow for these moderate and high Prandtl number fluids is highly stratified. The effect of stratification is to slow the fluid motion, thus reducing the shearing action between the upward and downward moving streams. This effect has been demonstrated by Lee and Korpela [31]. They detected numerically that for moderate and high Prandtl number fluids, much taller cavities, around Hz=20, were required to produce multicellular flow compared to low Prandtl number fluids, for which multicellular flow occurred for cavities as short as Hz=6. This is attributed to highly stratified fluid flow with moderate and high Prandtl number fluids reducing the shearing action. Hence the instability for moderate and large Prandtl number fluids is buoyancy driven; see Gill and Davey [18] and Bergholtz [3]. However the highly thermal diffusive low Prandtl number fluids reduce stratification and thus for these fluids the motion is not slowed down. Consequently multicellular flow is produced due to the shear instability. Jones [27], in a numerical study, produced multicellular flow with a cavity height aspect ratio as low as Hz=5 for a low Prandtl number fluid ($Pr = 0.035$) with $Ra = 10^3$ and $Ra = 5 \times 10^3$.

Apart from these numerical and linear stability theory results, very little information on low Prandtl number fluids exist. Experiments performed with low Prandtl number fluids have been reported by Lillie and Nottage [32] and MacGregor and Emery [35], [36]. The latter study concluded that for low Prandtl number fluids the high conductivities prevent the formation of a boundary layer flow and the resulting heat transfer is more geometry dependent than normal fluids.

Many studies of the flow in the square cavity exist [9],[11],[12],[13],[27],[28],[33], being some. The secondary flow in the square cavity for moderate to high Pr does not result from an instability of the primary flow but as a direct consequence of the convective distortion of the temperature field. The flow may be regarded as being driven by the generation of vorticity by the horizontal temperature gradients [11],[39]. For low Rayleigh number the horizontal temperature gradients in the cavity are of the same sign. As the Rayleigh number increases, the development of the thermal boundary layer intensifies in the vicinity of the walls and the convection within the layer leads to a change in the sign of the horizontal temperature gradients in the centre of the cross-section. This behaviour generates a vorticity sink. The vorticity sink separates the regions of

concentrated vorticity generation at the isothermal boundaries and provided that the viscous diffusion does not completely smear the distribution of vorticity, secondary flow is generated. Quon [52] showed that the flow structure for moderate and high Prandtl number fluids is similar for this cavity and that the various horizontal boundary conditions make virtually no difference to the main boundary layer flow, although free surface boundaries double the velocity in the boundary layer adjacent to them. Jones [27] has numerically obtained the flow structure for a low Prandtl number fluid (0.035) in a square cavity for Rayleigh number 5×10^3. Secondary flow does exist but not in the form of cells embedded in the primary flow; rather, it occurs in the form of weak reverse eddies appearing in the corner at the top of the hot wall and in the corner at the bottom of the cold wall. These eddies become stronger as the Prandtl number decreases.

Very few experimental results exist for the shallow cavities. The flow in shallow cavities is composed of two major regions, viz (a) a core region with a parallel counter flow, and (b) an end region with length of order Hz turning the parallel counter flow around by 180 degrees, Cormack et al. [10],[25]. The flow with moderate and high Prandtl number fluids is laminar over a large range of Rayleigh number. This is due to the viscous effect dominating the buoyancy effect and the stablizing effect of the strong temperature stratification throughout much of the cavity, Hart [21], Titchy and Godgik [61], Winters[69]. For low Prandtl number fluids there are weak secondary motions in the core for high Ra numbers, Shiralkar and Tien [57]. This has been confirmed by Hart [21] using asymptotic analysis. He showed that the breakdown of the primary circulation is due to the development of shear instability in the core region.

As the Ra number is slowly increased fluid flow in the double glazing problem can generally be categorized as follows. At first a primary state of motion exists. This is followed by a series of secondary motions until unsteadiness occurs and then finally turbulence follows.

One of the earliest experimental studies of the double glazing problem dates back to 1930, see [2]. Many more have been carried out since then due to its important applications and simplicity. Experimental results for the two dimensional problem are obtained by using a cavity which is large in the third direction (y-direction, see Figure 6.1) and all measurements are performed at the symmetry plane where the effects of the third dimension are a minimum. The length of the cavity in the third dimension

and the end wall insulation ultimately hinder visualization of the flow structure. Some fluids are opaque, especially those with low Prandtl numbers and hence the fluid flow structure at the symmetry plane is impossible to visualize.

These conditions have given heat transfer results as the only end product in most studies. Hence comparisons between numerical predictions and experimental studies have been limited to the non-dimensional heat transfer number, the Nusselt number.

The heat flux at the isothermal boundary, $x = 0$, Figure 6.1, is defined by:

$$K\left(\frac{\partial T}{\partial x'}\right)_{x'=0} = \frac{K}{l}\left(\frac{\partial \theta}{\partial x}\right)_{x=0}(T_h - T_c) = H(T_h - T_c) \tag{6.5}$$

where K is the thermal conductivity, T is the dimensional temperature, x' is the dimensional x coordinate and H the local heat transfer coefficient. The non-dimensional local heat transfer coefficient, the local Nusselt number, Nu_l, is defined as

$$\mathrm{Nu}_l = \frac{Hl}{K} = \left(\frac{\partial \theta}{\partial x}\right)_{x=0}. \tag{6.6}$$

The total non-dimensional heat flux at the wall is the overall Nusselt number, Nu,

$$\mathrm{Nu} = \int_0^{Hz}\left(\frac{\partial \theta}{\partial x}\right)_{x=0} dz \tag{6.7}$$

This is the ratio of the total heat transferred across the cavity to that which would be transferred by conduction alone. Since the fluid flow in the double glazing problem is governed by the Ra number, the Pr number and the height aspect ratio, Hz, the Nusselt number is expected to be a function of the three governing parameters. The comparisons between numerical and experimental heat transfer results have in general been good. Some correlations of heat transfer with Ra, Pr and Hz have been provided by Churchill [9] for tall, square and shallow cavities. Heat transfer results using an interferometer in experiments have been published by Brooks [6].

In order to obtain detailed solutions of all variables a numerical study is ideal. Once the numerical predictions have been verified by comparison with the experimental results, the code can be used to calculate more predictions with different Ra numbers, Pr numbers and aspect ratios. Solutions for the variables are calculated at discrete points in the cavity and the graphical output produced to give qualitative and quantitative results. As pointed out earlier, the importance of the double glazing problem is in it being an excellent prototype natural convection problem to test codes which model more complicated free convection problems. Detailed reviews of the two-dimensional problem may also be found in Catton [8] and Ostrach [43].

6.4 The three-dimensional problem review

Fluid motion is inherently three-dimensional and thus the two-dimensional models have their limitations. However, the value of the two-dimensional models must not be degraded, since they can form a good basis for the interpretation and analysis of the more complicated three-dimensional flow.

With the three-dimensional problem, the end walls have a large influence on the fluid flow thus introducing another governing parameter, viz the length aspect ratio, Hy. Very few reported three-dimensional studies of the double glazing problem exist. One of the earlier reported experimental studies is that of Mallinson and Graham (1974) [37]. They observed a complex spiralling motion in air filled cavities with height aspect ratios Hz=1 and 5 and length aspect ratios Hy=2 and 5 for moderate Rayleigh numbers. One of the first numerical studies reported is that by Mallinson and De Vahl Davis (1977) [38], also see [1], who used particle tracks to show that the structure of the air flow was described by a closed spiral for low Ra number ($= 10^4$) in cavities with Hz=1, 5 and Hy=5. They further produced a more detailed study of the problem, [39], by considering moderate and high Prandtl number fluids between(0.1 - 100), $0 \leq \mathrm{Ra} \leq 10^6$, $\mathrm{Hy} = 1$ and $\mathrm{Hz} = 1$ and also with other isolated parameter values. In their study they describe two different types of end effects; one, an inertial action of the rotating fluid against the end wall; two, buoyancy effects generated by longitudinal temperature gradients. They also termed the three-dimensional double-glazing problem, the window-cavity problem. In the same year Morrison and Tran [41] reported experimental results for insulated and uninsulated air filled window cavities with Hz=Hy=5 and $\mathrm{Ra} = 5 \times 10^4$ and confirmed the existence of the spiralling motion. They also concluded by comparing velocities for insulated and uninsulated cavities that, with the insulated walls, the direct influence of the end wall is reduced substantially compared with uninsulated walls. Ozoe et al. (1978)[44] presented experimental and numerical results for the inclined window cavity for $\mathrm{Ra} = 6 \times 10^3$ and $\mathrm{Pr} = 10$ with $\mathrm{Hz} = 1, 2, 3$ and $\mathrm{Hy} = 2, 6$. As the cavity is inclined at various angles to the vertical axis, the spirals start to deform. Schinkel (1980) [55] in an experimental and numerical investigation for air filled window cavity for moderate Ra with Hz=1, showed that the flow at the symmetry plane can be considered two-dimensional if $\mathrm{Hy} > 4$. Linthorst et al., [33],[34] performed experimental studies, for air filled cavities with $0.25 \leq \mathrm{Hz} \leq 7$, $5 \times 10^3 \leq \mathrm{Ra} \leq 2.5 \times 10^5$ with perfectly conducting side

walls. For the upright window cavity they concluded that the value of Hy=5 is great enough to ensure two-dimensional flow at the symmetry plane. Furthermore, the secondary rolls that appear for the double glazing problem also appear with the window cavity problem at increased values of Ra. Viskanta et al. (1986) [65] have recently performed an experimental study for a low Prandtl number fluid, Gallium (Pr = 0.02) with Ra = 10^6, Hz = 1, 0.5 and Hy = 0.5. Due to Gallium being opaque, visualization experiments were carried out with water. Numerical predictions in a window cavity with Hz=Hy=1.0 for Gallium at Ra = 10^6 revealed at the symmetry plane secondary flow in the form of two rotating cells. The percentage difference between average Nusselt number predicted by the double-glazing problem and the window cavity problem is greater for low Pr number fluids than for moderate and high Pr number fluids. The comparison of their numerically predicted thermal solution with the experiment data do not agree well. The authors have associated the discrepancy with errors in measuring the temperatures in the experiment. This seems to be the only three dimensional low Prandtl number fluid study to have been reported.

6.5 Discussion of results

From the review in the above section it can be noted that not many studies have been performed for the three-dimensional problem. Those studies that have been performed have generally concentrated on moderate and high Prandtl number fluids with the cavities having square and tall cross-sections. The prime purpose of this investigation is to study the effect of low Prandtl number fluids in three-dimensional cavities with shallow, square and tall cross-sections. The low Prandtl fluid studied is cerrobase, a lead-bismuth eutectic, used at Harwell (sponsorer of the study) for studies of liquid metal natural convection. The fluid has its Prandtl number close to liquid sodium. Thus it is used as a simulant fluid for studies of coolant flows in liquid metal cooled fast breeder reactors, as experiments using liquid sodium are extremely difficult and expensive. Cerrobase has been studied for Ra = 10^3 and 5×10^3, since in the two-dimensional problem, the flow with Ra = 10^3 is conduction dominated, while with Ra = 5×10^3 convective effects start to appear, Jones [27]. For comparison purposes a moderate Prandtl number fluid, air, has been studied with Ra = 10^3. Results for air with Ra = 10^5 have also been studied to investigate the effects of secondary motion in tall and shallow cross-section window cavities as the fluid flow at this higher Rayleigh

number in the past has only been studied in the square cross-section window cavity.

In the next three sections, numerical fluid flow predictions for low and moderate Prandtl number fluids with the Rayleigh number in the range 10^3 and 10^5 are reported in window cavities of height aspect ratio Hz=0.5, 1 and 5 corresponding to cavities with shallow, square and tall cross-sections respectively. To examine the effect of the end walls, solutions for window cavities of length aspect ratios Hy=1, 2 and 5 have been obtained. In all, 36 combinations of the governing parameters have been studied. The parameters are tabulated below:

Height aspect ratio Hz	a) 0.5 representing a shallow cavity b) 1.0 square cavity c) 5.0 representing a tall cavity
Fluid	a) air (Pr = 0.71) with Ra = 10^3 b) air with Ra = 10^5 c) cerrobase (Pr = 0.035) with Ra = 10^3 d) cerrobase with Ra = 5×10^3
Length aspect ratio Hy	a) 1.0 b) 2.0 c) 5.0

Table 6.1: Combinations of governing parameters studied.

Solutions for the square cavity Hz=1 are presented in section 6.6 with results for air compared with those obtained by Mallinson and de Vahl Davis [39]. Solutions for the shallow cavity, Hz=0.5 and tall cavity Hz=5 are presented in sections 6.7 and 6.8 respectively. The SIMPLE algorithm as described in chapter 2 has been used to obtain the numerical predictions with the pressure-correction and temperature equations solved using the adapted multigrid method as described in chapter 5. Mallinson and de Vahl Davis's [39] results indicate that the behaviour of the flow is complex throughout the whole window cavity and so a uniform mesh has been used to solve the problem. The largest mesh size used is 16x40x40 and the smallest 16x16x16. Further details of mesh sizes with the total number of the SIMPLE algorithm iterations taken to converge are presented in Appendix A. To explore the effect of truncation errors limited finer mesh studies, 32x32x32, have been carried out.

Discussions on the particle path closure, the method used to generate them and general graphical presentation of the results are presented in Appendix B.

For clarity, the particle paths are only presented in one half of the cavity,the solution cavity, which is to be viewed from (-8,-4,-3), unless otherwise stated. The faces of the cavity as seen from the viewing position are drawn in solid lines and the hidden faces are drawn with dashed lines.

Although results have been plotted at all planes, in order to analyze the full three-dimensional flow, only selected plots that convey a large quantity of information are presented here. Three such positions have been chosen: plane A $(x, hy/2, z)$, a plot near the end wall, since the end wall is the cause of the three-dimensional flow; plane B $(x, m - hy/2, z)$, a plot near the symmetry plane, to examine to what extent the flow resembles two-dimensional motion there, and plane C $(0.5 - hx/2, y, z)$, a plot near the mid-vertical axial plane x=0.5, in order to assess how the flow behaves along the cavity, where hx and hy are the meshlengths in the x and y directions respectively. The xz-plane slices presented are to be viewed from $y >$ Hy/2 with the positive y-axis coming out of the paper towards the viewer. The yz-plane slices presented are to be viewed from $x < 0$ with the positive x-axis going into the paper away from the viewer. The key for the interpretation of the velocity vector plots is described in Appendix C.

6.6 Window cavities with a square cross section, Hz=1.0

Results for the two fluids, see Table 6.1, are presented for a window cavity with a square cross-section, Hz=1.0. The extent of the end wall effect is investigated for window cavities with length aspect ratios, Hy=1.0, 2.0 and 5.0. The results for air are presented first which are then followed by results for cerrobase. Comparison of results with those obtained by Mallinson and de Vahl Davis [39] are presented in section 6.6.5 along with a description of the heat transfer results. Comparisons are also made with the finer mesh studies for air and cerrobase at Ra $= 10^3$ with Hy=1.0.

6.6.1 Results obtained for Air (Pr = 0.71) with Ra = 10^3

Window cavity (1,1,1): length aspect ratio Hy=1.0

Particle paths traced for this problem, Figures 6.2, 6.3 and 6.4, reveal the basic form of the flow. The superimposing of the axial flow on the cross sectional flow results in a recirculating roll, the axis of which is perpendicular to the adiabatic end walls. The particles are directed away from the central region of the end wall and spiral towards the symmetry plane. In the vicinity of the symmetry plane the spiral uncoils in the xz-plane until it reaches the boundary layers, after this the particles spiral back towards the end wall. Near the end wall the spiral starts to coil towards the centre of the end wall to form closed particle paths. These paths lie on a torus like surface. The fluid flow behaviour described above is the same as that obtained by other investigators, Mallinson and de Vahl Davis [39], Mallinson and Graham [37], Morrison and Tran [41] and Linthorst et al. [33],[34].

In Figure 6.2 the particle path has been traced from the point $(.45, .10, .35)$ and the half cavity is viewed from $(-8, -4, -3)$. A side view of the same particle has been obtained, Figure 6.3 and shows the penetration of the particle in the y-direction, from a view point $(-5, .25, .6)$. Figure 6.4 shows four particle tracks. Path1 has been traced from the point $(.5, .005, .45)$ near the centre of the end wall. Here the particle rotates about the centre line of the cavity, $(.5, y, .5)$, whilst traversing towards the symmetry plane. It reaches the vicinity of the symmetry plane in approximately fifteen revolutions about the centre line and there the path starts to uncoil. Path2 has been traced from a point $(.2, .49, .2)$, near the symmetry plan where it uncoils with

very small or nil axial velocity. Path3 has been traced from the point (.01, .4, .01). close to the top of the cold wall near the symmetry plane. The particle in this case returns to the vicinity of the end wall in about two revolutions via the boundary layers. Path4 has been traced from the point (.9, .01, .9). near the end wall and coils inwards towards the centre of the end wall. The four paths describe effectively some of the important features of the three-dimensional flow: path1 shows that very strong axial velocities exist near the end wall and how the motion in the y-direction decays as the particle reaches the symmetry plane; path2 shows a particle near the symmetry plane where the flow is more two-dimensional and the cross sectional velocities are directed away from the centre of the symmetry plane; path3 shows the strong return flow and path4 shows the effect of the end wall on a particle with the cross-sectional velocities being directed towards the centre of the end wall.

The core of the fluid moving away from the end wall has been termed the 'inner core' and the core of fluid returning to the end wall has been termed the 'outer core'. In the inner core, the particles near the centre of the core axis reach very near to the symmetry plane and uncoil until they meet the boundary layers in which they return back to the end wall to form closed paths, see Figure 6.4. The particles further away from the core axis do not penetrate the axial direction as much as the particles nearer the core axis. They return well before reaching the symmetry plane spiralling back between the boundary layers and the inner core, see Figure 6.2.

The interaction of a roll with an end wall is similar to the interaction of a rotating mass of fluid with a rigid flat plate normal to the axis of the rotating fluid, Davis, see [39]. The infinite system of rotating fluid motion above a stationary horizontal flat plate was first analytically considered by Bodewadt, see [39]. In this problem the fluid at a large distance above the plate rotates at a constant angular velocity, ω, with the no-slip boundary condition at the plate. The fluid particles which rotate at a large distance from the plate are in equilibrium under the influence of the centrifugal force which is balanced by the radial pressure gradients. The angular velocity of the particle near the stationary wall is small due to the no-slip boundary condition whereas the radial pressure gradients directed towards the axis remains the same. This set of circumstances causes the particles near the plate to flow radially inwards and for reasons of continuity that motion is compensated by an axial flow upwards, Schlichting [56]. The axial flow in the window cavity is produced in a similar manner except the fluid roll is finite and produced by the buoyancy force resulting in a horizontal axial

flow. The end wall effect that generates the three-dimensional flow has been termed by Mallinson and de Vahl Davis [39] as the inertial end effect, that is, the kinematic interaction of the rotating fluid with a stationary plane as modelled by Bodewadt.

In order to assess how tightly the spiralled particle path is wound the contour plots of the ratio of the axial velocity to the cross sectional velocity, $R = v/(u^2 + w^2)^{0.5}$, have been plotted. R is undefined at the boundaries. This ratio represents the distance travelled by the particle in the axial direction to that travelled by the particle in the cross-section for small times. Thus the ratio R can be interpreted as the strength of the end wall effect to that of the buoyancy effect.

If $R < O(1)$ then the spiral is tightly wound since the particle travels a greater distance in the cross-section than in the axial direction, that is, the buoyancy effect is stronger than the end wall effect. If $R > O(1)$ then the spiral is loosely wound since now the particle travels a greater distance in the axial direction than in the cross-section, that is, the end wall effect is stronger than the buoyancy effect. R is only zero in the window cavity if v=0, thus the contours R=0 indicates the turning point of the particles with respect to the axial direction. The contours of R also clearly show the regions of inner and outer core of fluid flow.

Figure 6.5, 6.6 and 6.7 are contour plots of the ratio R at planes A, B and C respectively (planes described at the end of the last section). The inner core indicated by positive R is at the centre. The particles near the centre of the inner core, where the cross sectional velocity is a minimum, wind a looser spiral compared to particles further away from the centre of the inner core. The values of R near the symmetry plane are considerably smaller than those near the end wall indicating that the buoyancy effect has a greater effect near the symmetry plane than near the end wall. The ratio R is larger in the inner core near the centre line of the cavity. This is due to there being no or very small cross sectional flow in the centre of the xz-planes. For instance, in two-dimensions the vertical and horizontal components of the velocity at the centre point are zero. Note the increase in R in the boundary layer as the end wall is approached from the symmetry plane. Near the end wall positive R contours are attached to the four side walls. These would seem to imply the existence of fluid rolls in the corners. This is not so, the positive R contours attached to the walls merely represent slight *undulations* in the axial direction of the particles in the boundary layers. These undulations can be seen in Figure 6.8 which is a plot of a particle path in the boundary layer traced from, $(.9, .45, .9)$, near the symmetry plane. The change of the sign of

the axial flow in the boundary layers is due to prominent axial temperature gradients. Figure 6.9 shows the axial temperature gradients, near the plane x=0, close to the hot wall, for Hy=2. Positive axial temperature gradients predominate in the upper two thirds of the cavity which generate a source of negative vorticity. Figure 6.10 shows the axial temperature gradients at the plane x=1, close to the cold wall, for Hy=2. Negative axial temperature gradients predominate in the lower two thirds of the cavity which generate a source of positive vorticity. These sources of positive and negative vorticities act against the returning flow in the outer core thus creating the undulations in the axial motion of the particles in the boundary layers. This phenomenon has not been reported in previous studies but can be seen when closely examining the results published by Mallinson and de Vahl Davis [39], Figure 5, $Ra=10^4$, Pr=0.2, Hy=2 and Hz=1. Figure 6.11 is a contour plot of the axial temperature gradient $\partial\theta/\partial y$ at plane C, for Hy=1, which shows that the positive $\partial\theta/\partial y$, which leads to a source of negative vorticity, predominates in the upper half of the cavity and the negative $\partial\theta/\partial y$, which leads to a positive source of vorticity, predominates in the lower half of the cavity with maximum $\partial\theta/\partial y$ =0.1008.

Figures 6.12, 6.13 and 6.14 show the velocity vectors at planes A, B and C respectively. The cross-sectional velocities near the end walls are much smaller than those near the symmetry plane. This is due to the no-slip boundary conditions at the end wall. The cross sectional velocities are directed towards the centre of the cross-section near the end wall and towards the side walls near the symmetry plane. Unfortunately this is not easily detectable from Figures 6.12 and 6.13. Figure 6.14, the velocity vectors near the plane C, shows the magnitude of the velocity increasing from the end wall to the symmetry plane. It also clearly shows the boundary between the flow travelling towards the symmetry plane and the returning flow.

Figures 6.15, 6.16 and 6.17 show the isotherms at planes A, B and C respectively. Figure 6.15 and 6.16 represent conduction dominated thermal solution which is as expected for a low Rayleigh number such as $Ra = 10^3$. The solution near the end wall is more conductive than that at the symmetry plane. This is of course due to the slower moving fluid near the end wall which reduces convection. Figure 6.17 shows the variation of the temperature in the axial direction.

The generation of the vorticity sources by the axial temperature gradients is such that they augment the inertial end effect. This is another mechanism by which the three-dimensional flow is induced at the end walls. This mechanism has been termed

the thermal end effect by Mallinson and de Vahl Davis[39]. These authors investigated the thermal end effect by comparing their window cavity results with those obtained for a rotating cylinder with a stationary end wall published by Pao [45]. They also ascertained that the magnitude of the end wall effect for $0.2 \leq Pr \leq 100$ is independent of Pr since the thermal solutions change insignificantly for $Pr \geq 0.2$. Thus the thermal end effect can be deduced from a high Pr solution for which the inertial end effect should be negligible.

Figure 6.18, 6.19 and 6.20 show the pressure contours at planes A, B and C respectively. Strong pressure gradients exist in the corner at the top of the hot wall and in the corner at the bottom of the cold wall. There is a slight difference between the pressure gradients at the end wall and those at the symmetry plane. This difference can be ascertained from Figure 6.20.

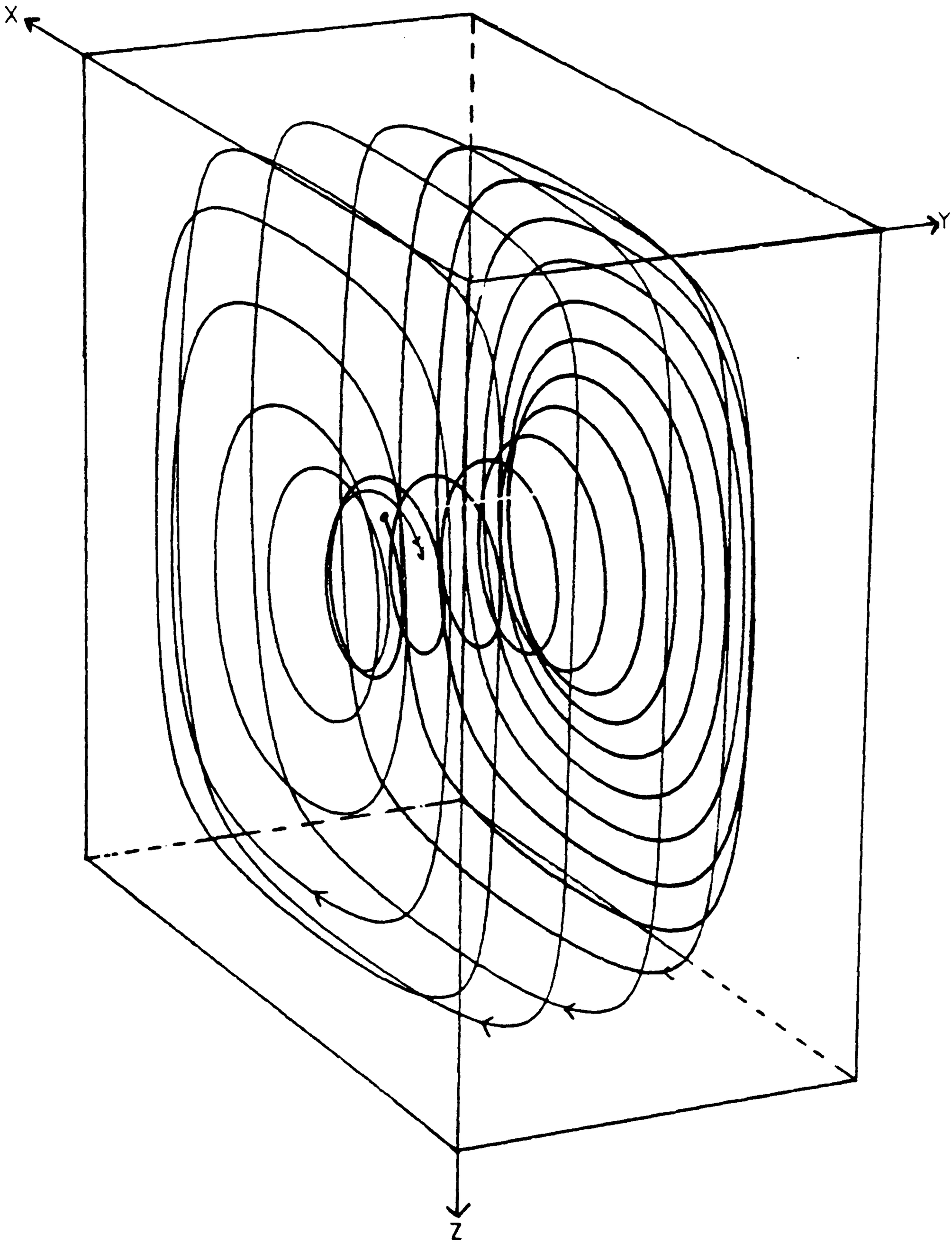

Figure 6.2 Particle track for air at Ra = 10^3, cavity (1,1,1)

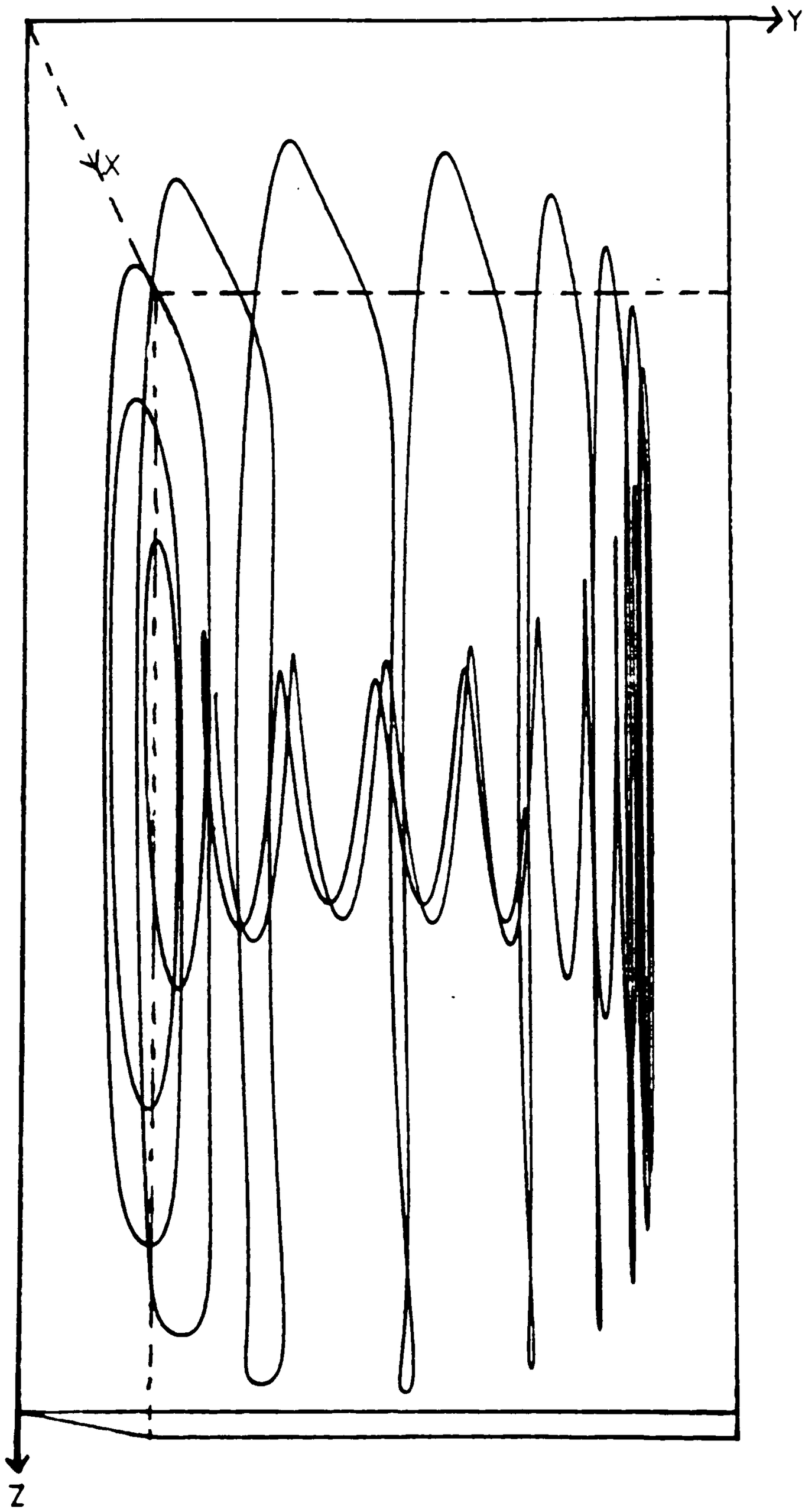

Figure 6.3 Side view of Figure 6.2

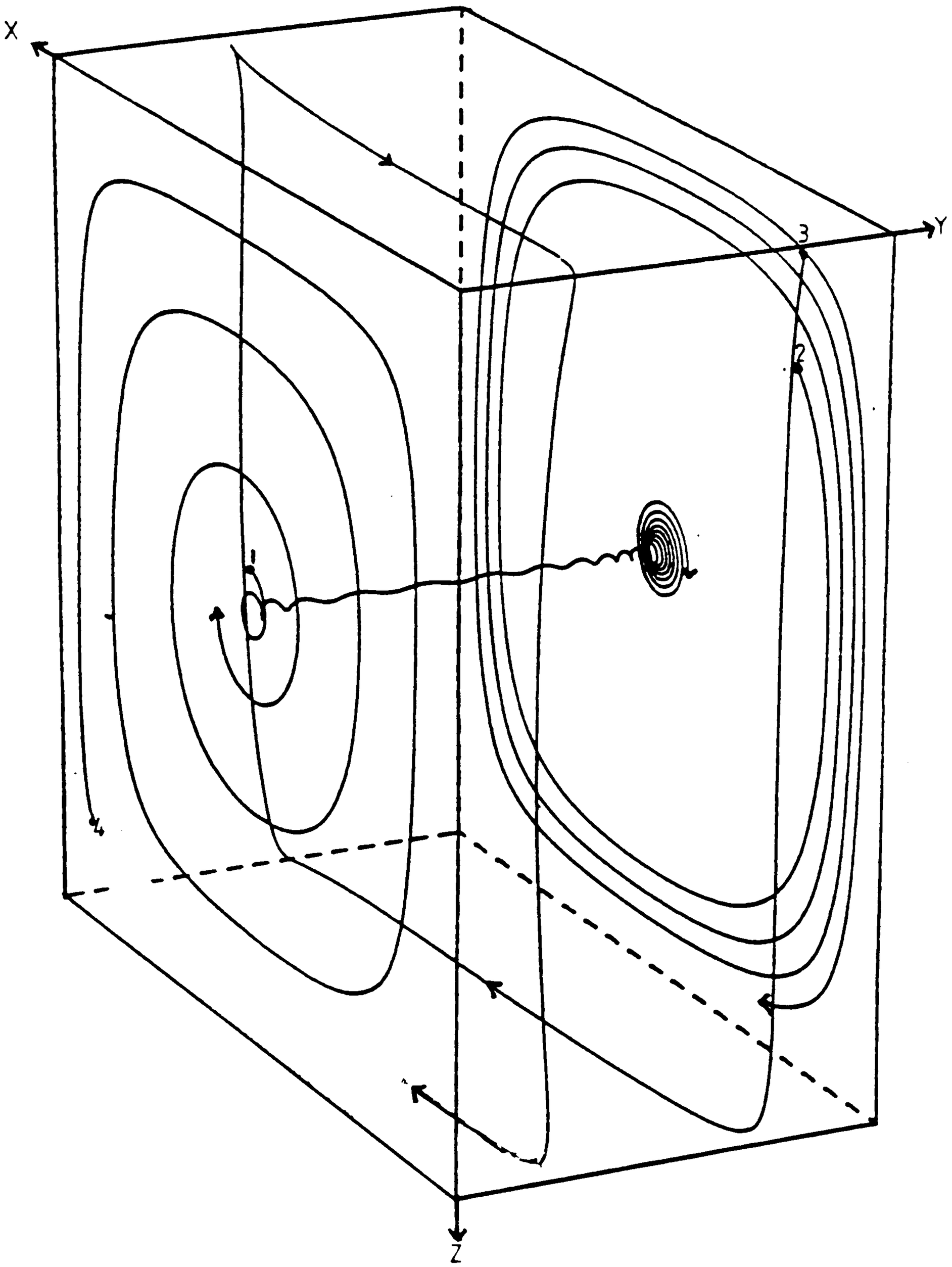

Figure 6.4 Particle tracks for air at Ra = 10^3, cavity (1,1,1)

Fluid = air, Ra = 10^3, Hy=1, Hz=1, grid=16x16x16

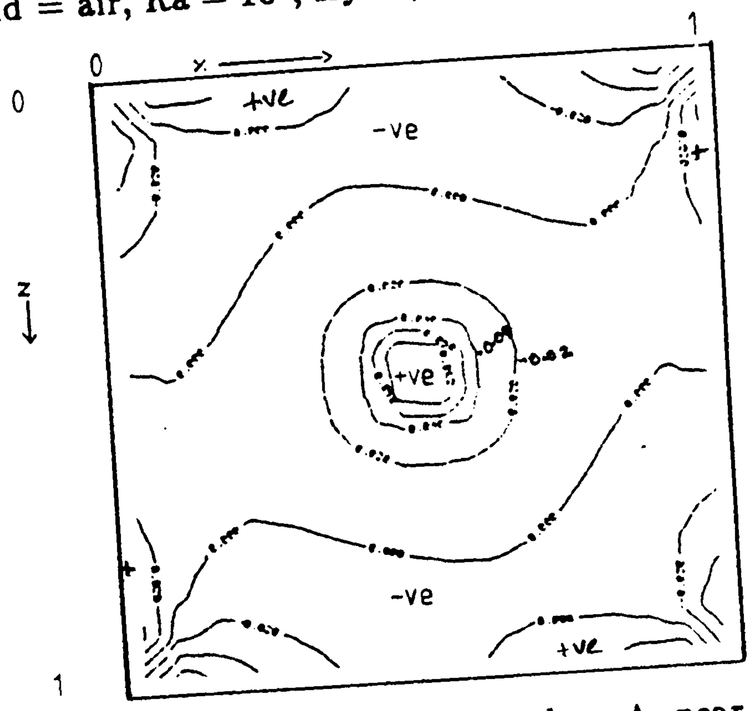

Figure 6.5 Contour plot of ratio R at plane A, near the end wall

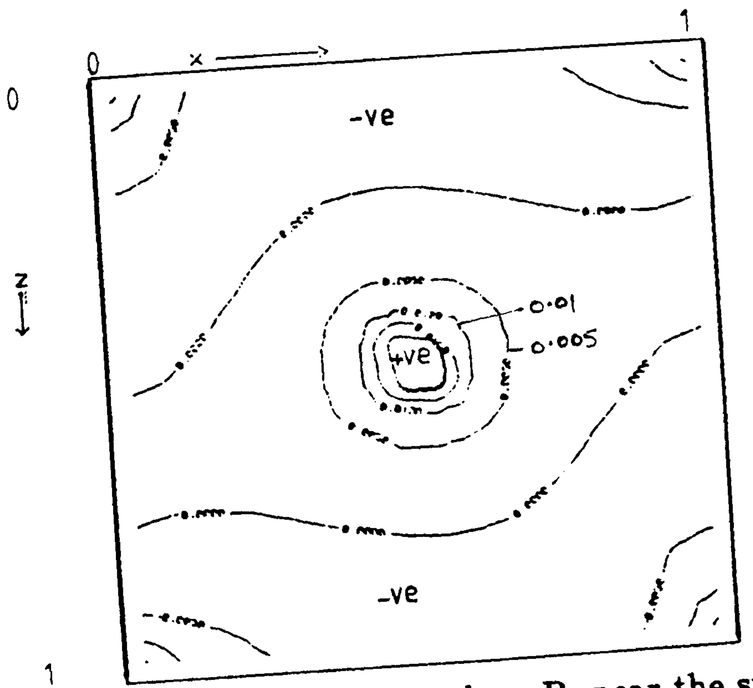

Figure 6.6 Contour plot of ratio R at plane B, near the symmetry plane

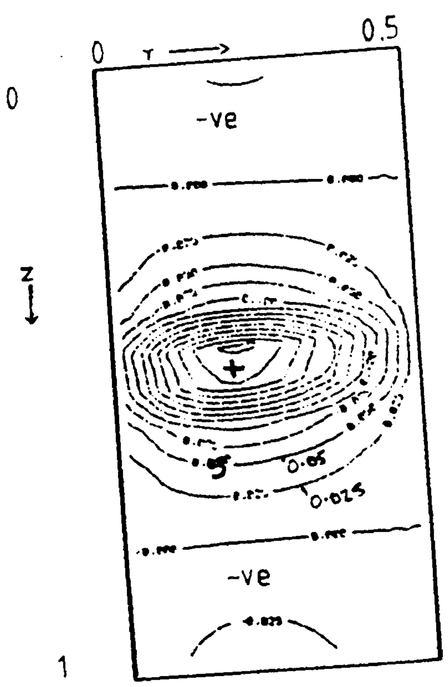

Figure 6.7 Contour plot of ratio R at plane C $(0.5 - hx/2, y, z)$

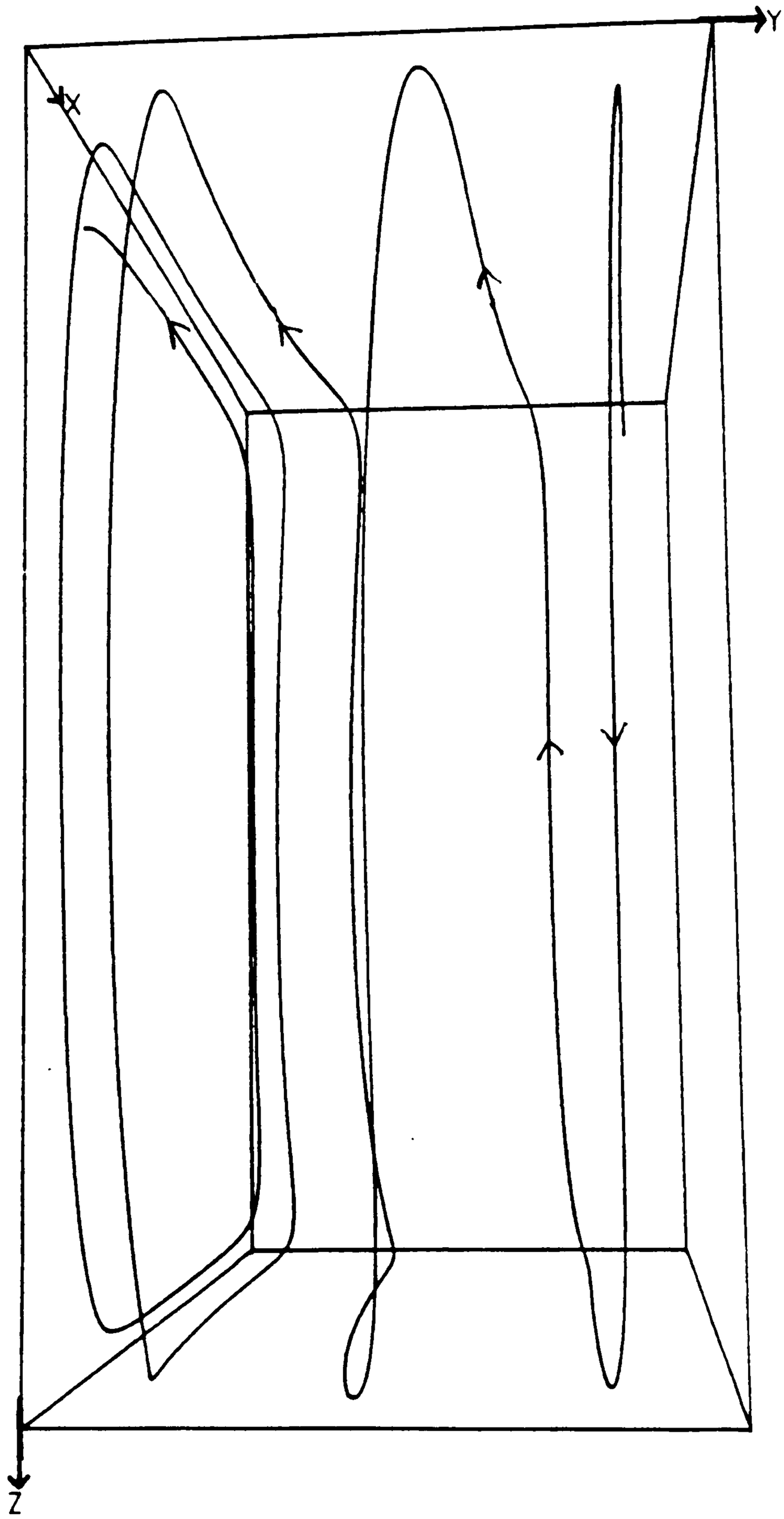

Figure 6.8 Undulations in the particle track

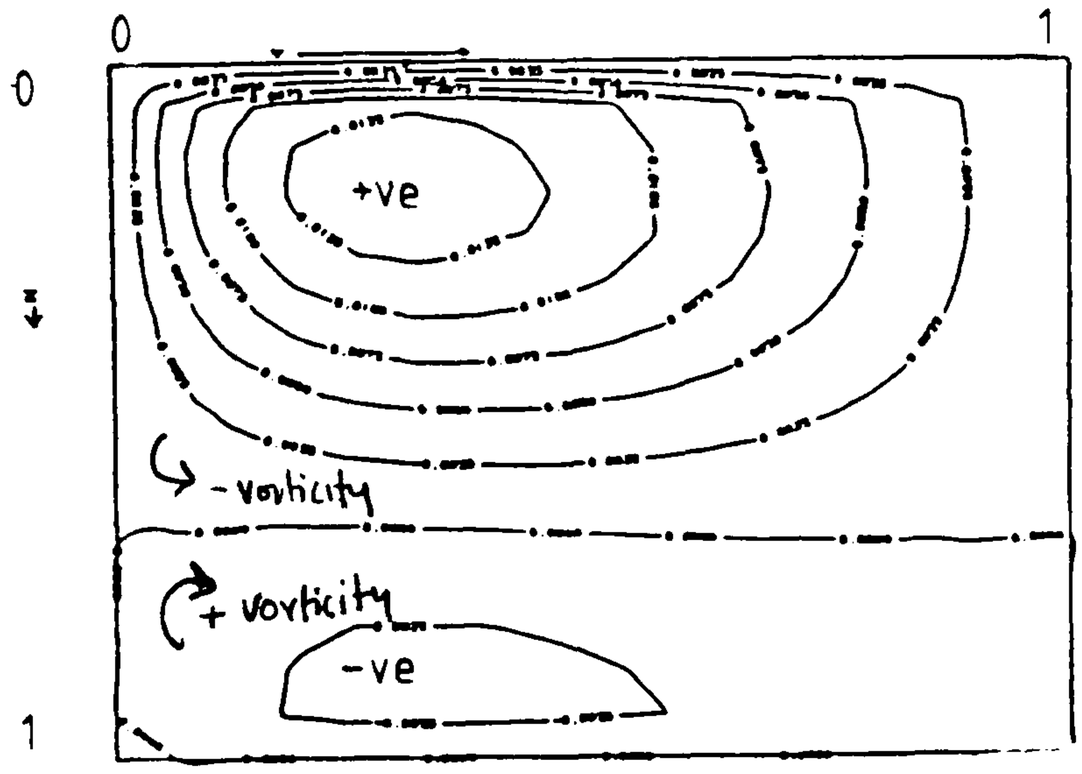

Figure 6.9 Contour plot of $\partial\theta/\partial y$ at plane $(hx/2, y, z)$ near the hot wall, air at Ra = 10^3, cavity (1,2,1)

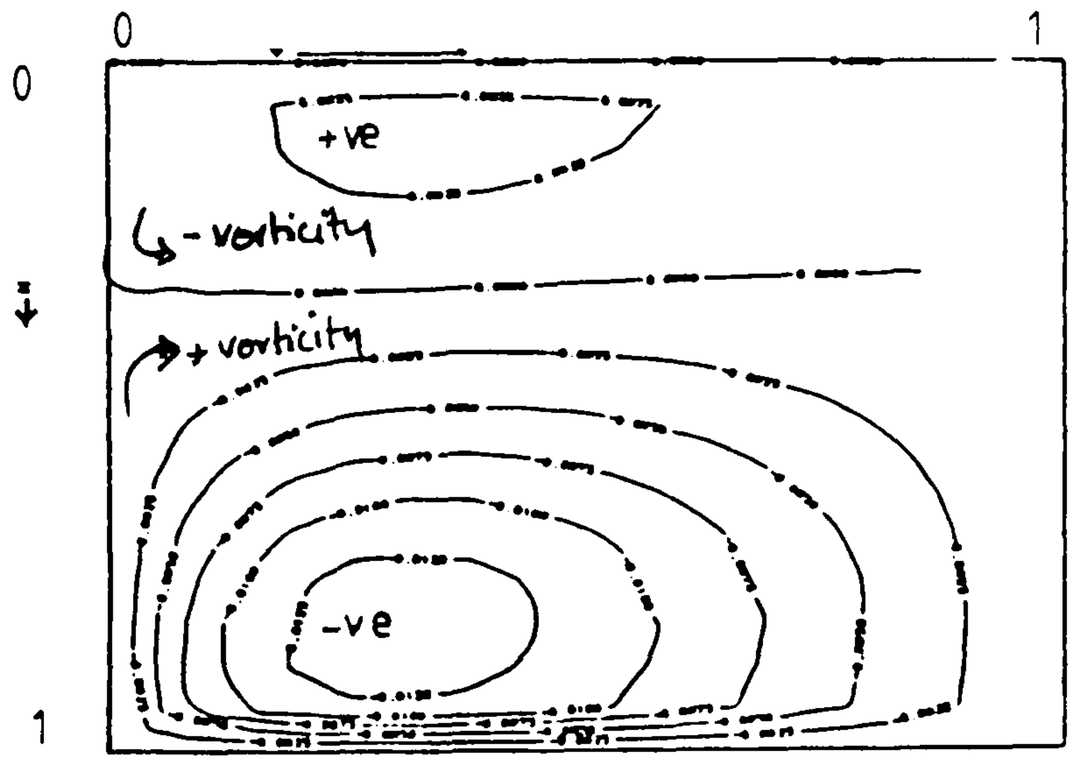

Figure 6.10 Contour plot of $\partial\theta/\partial y$ at plane $(1.0 - hx/2, y, z)$ near the cold wall, air at Ra = 10^3, cavity (1,2,1)

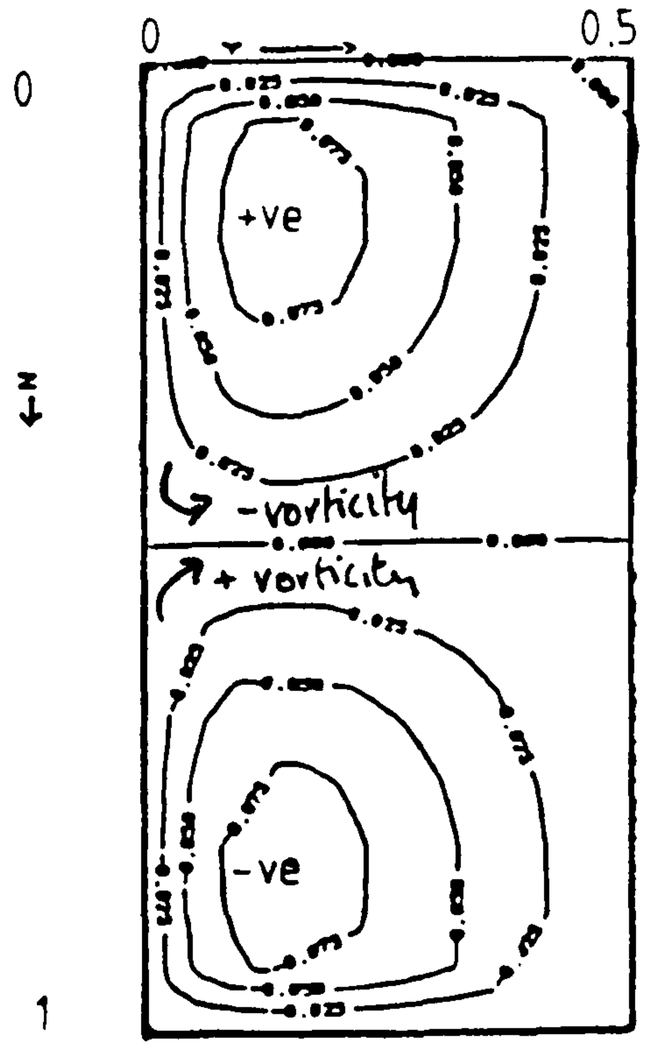

Figure 6.11 Contour plot of $\partial\theta/\partial y$ at plane C $(0.5 - hx/2, y, z)$

Fluid = air, Ra = 10^3, Hy=1, Hz=1, grid=16x16x16

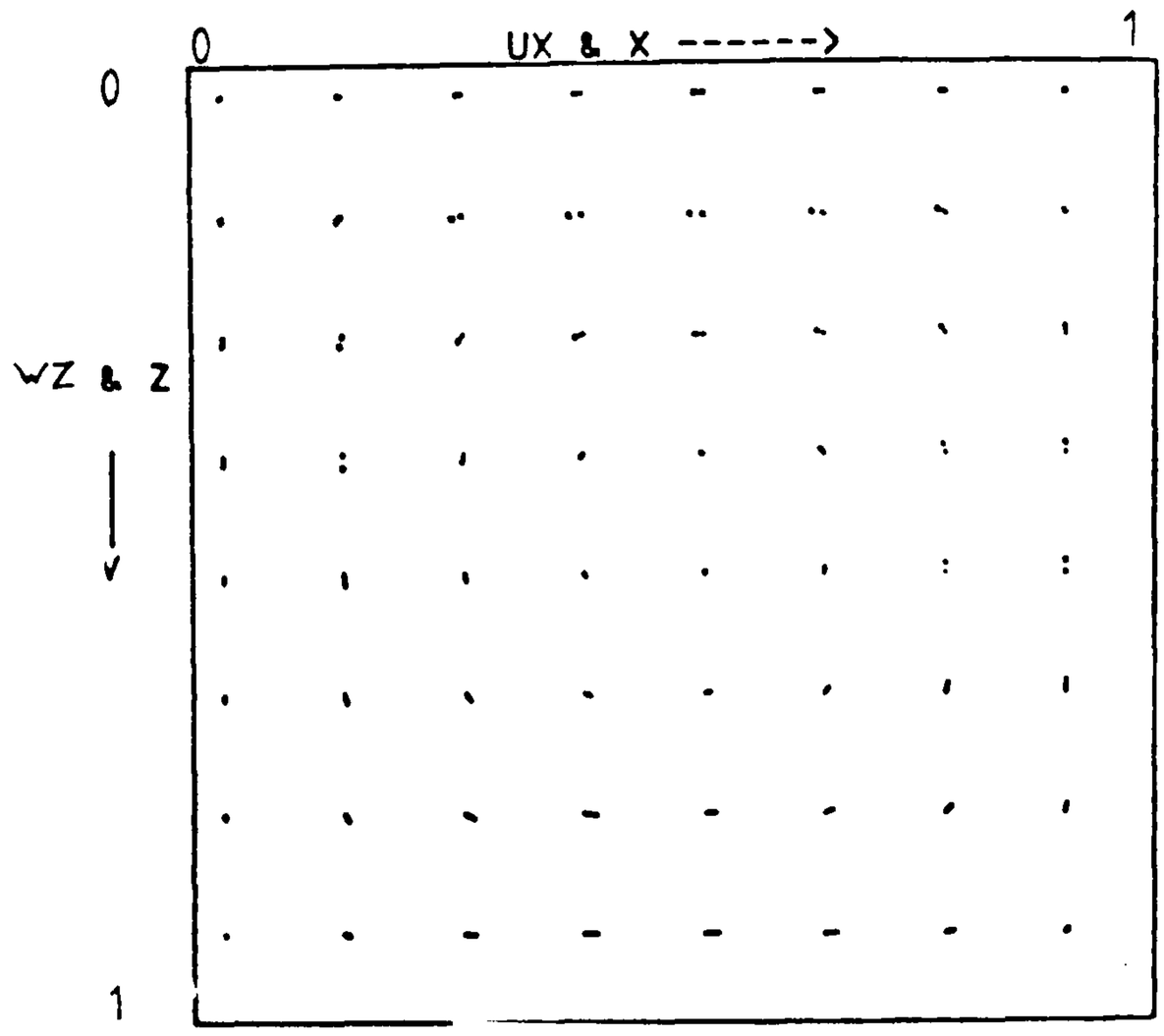

Figure 6.12 Velocity vectors at plane A, near the end wall

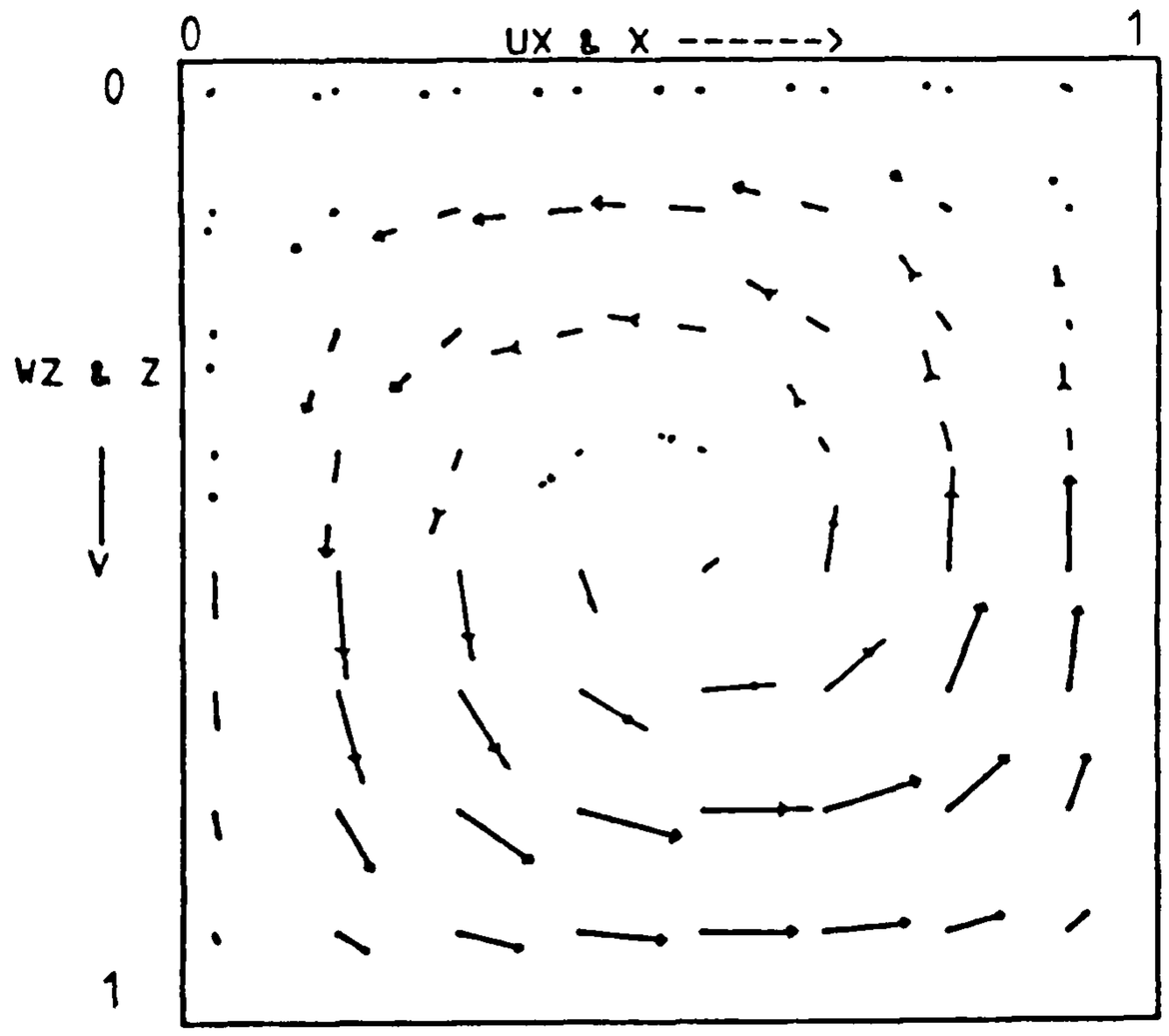

Figure 6.13 Velocity vectors at plane B, near the symmetry wall

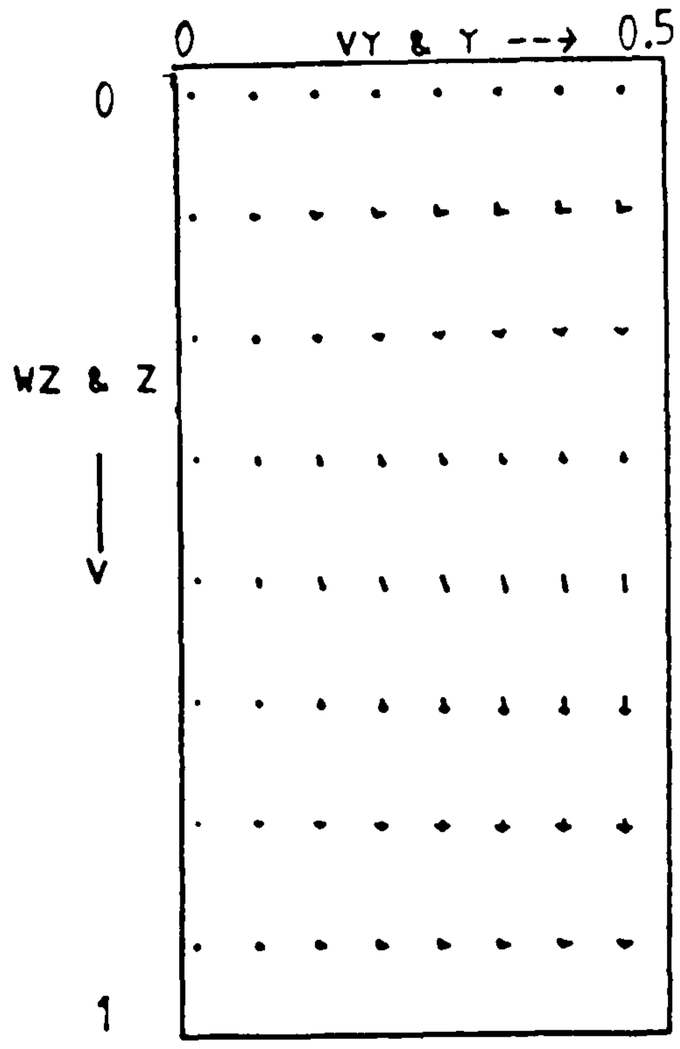

Figure 6.14 Velocity vectors at plane C $(0.5 - hx/2, y, z)$

Fluid = air, Ra = 10^3, Hy=1, Hz=1, grid=16x16x16

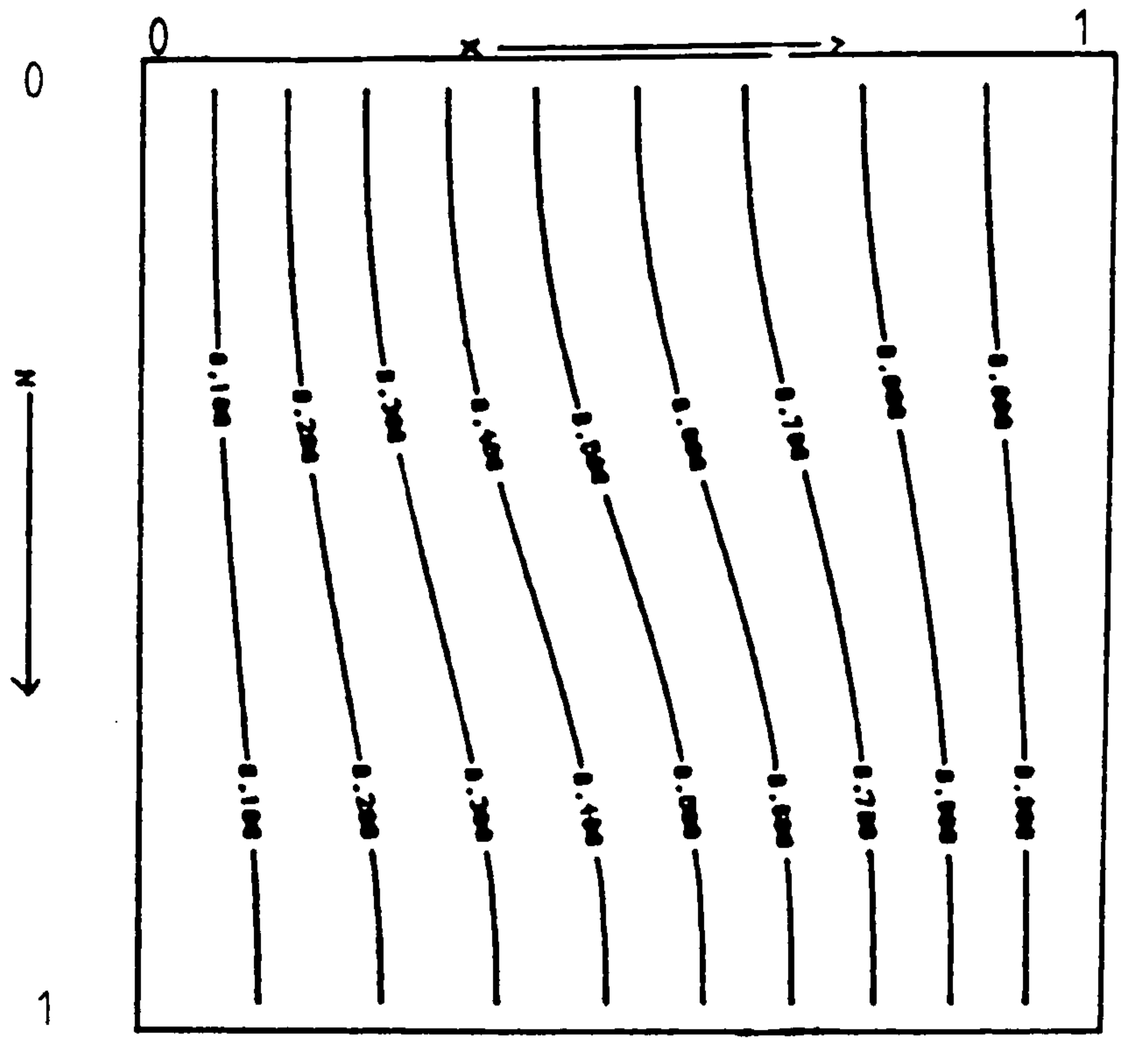

Figure 6.15 Isotherms at plane A, near the end wall

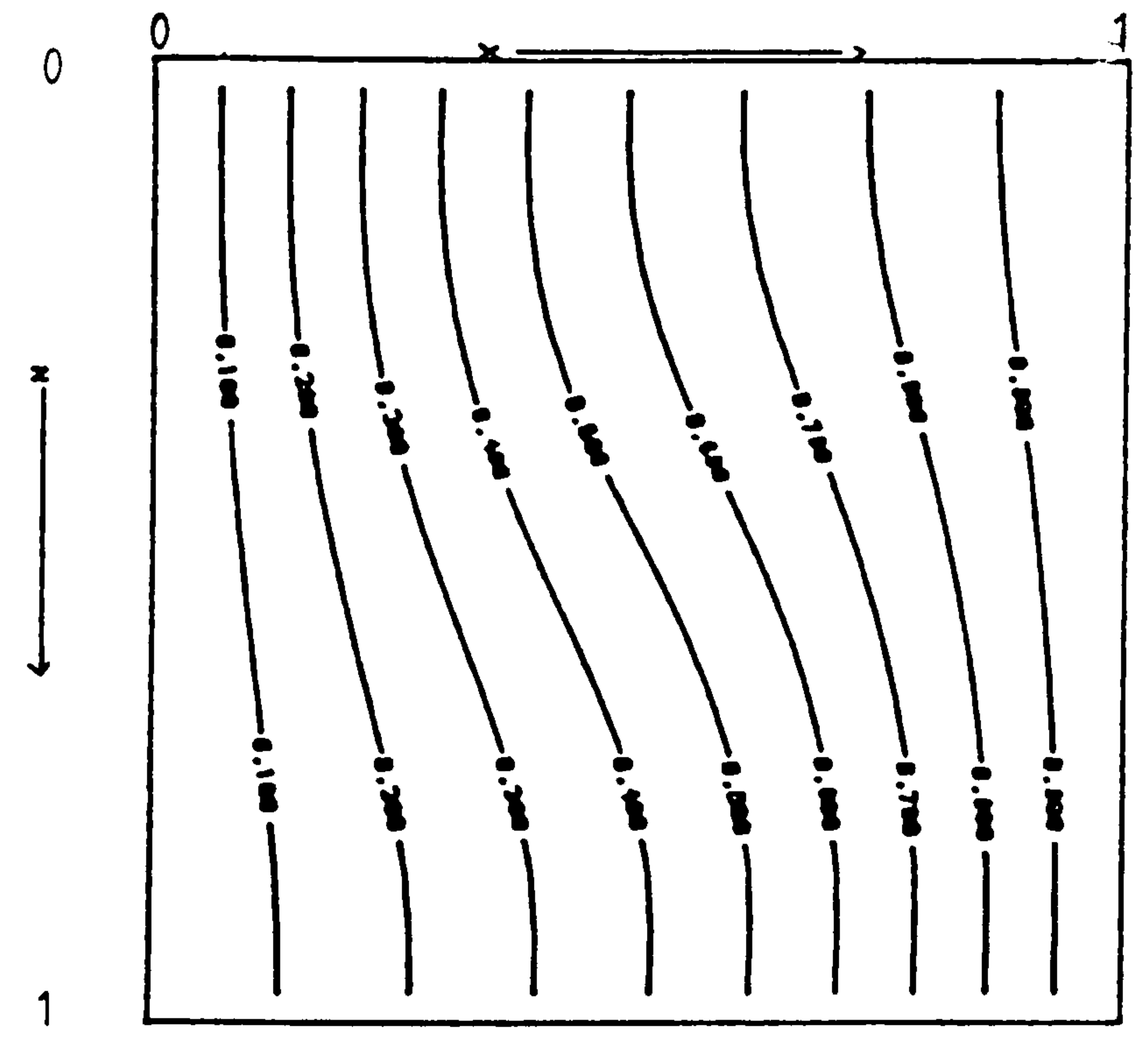

Figure 6.16 Isotherms at plane B, near the symmetry plane

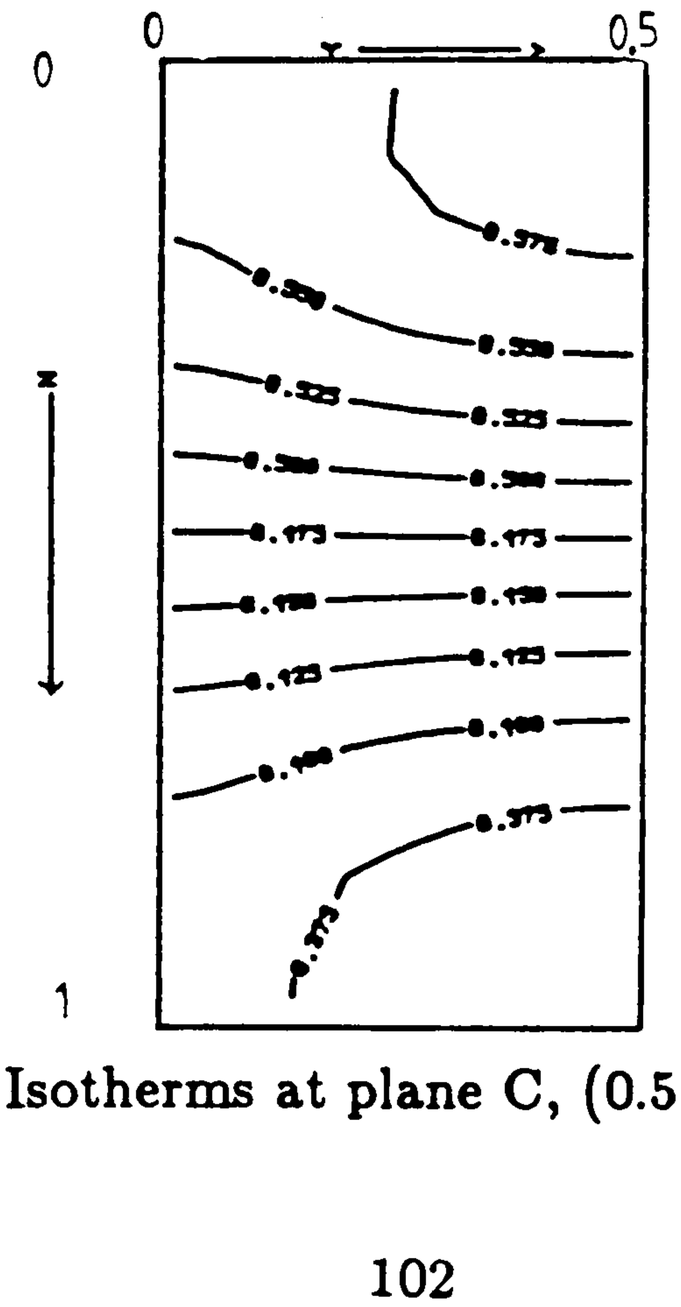

Figure 6.17 Isotherms at plane C, $(0.5 - hx/2, y, z)$

Fluid = air, Ra = 10^3, Hy=1, Hz=1, grid=16x16x16

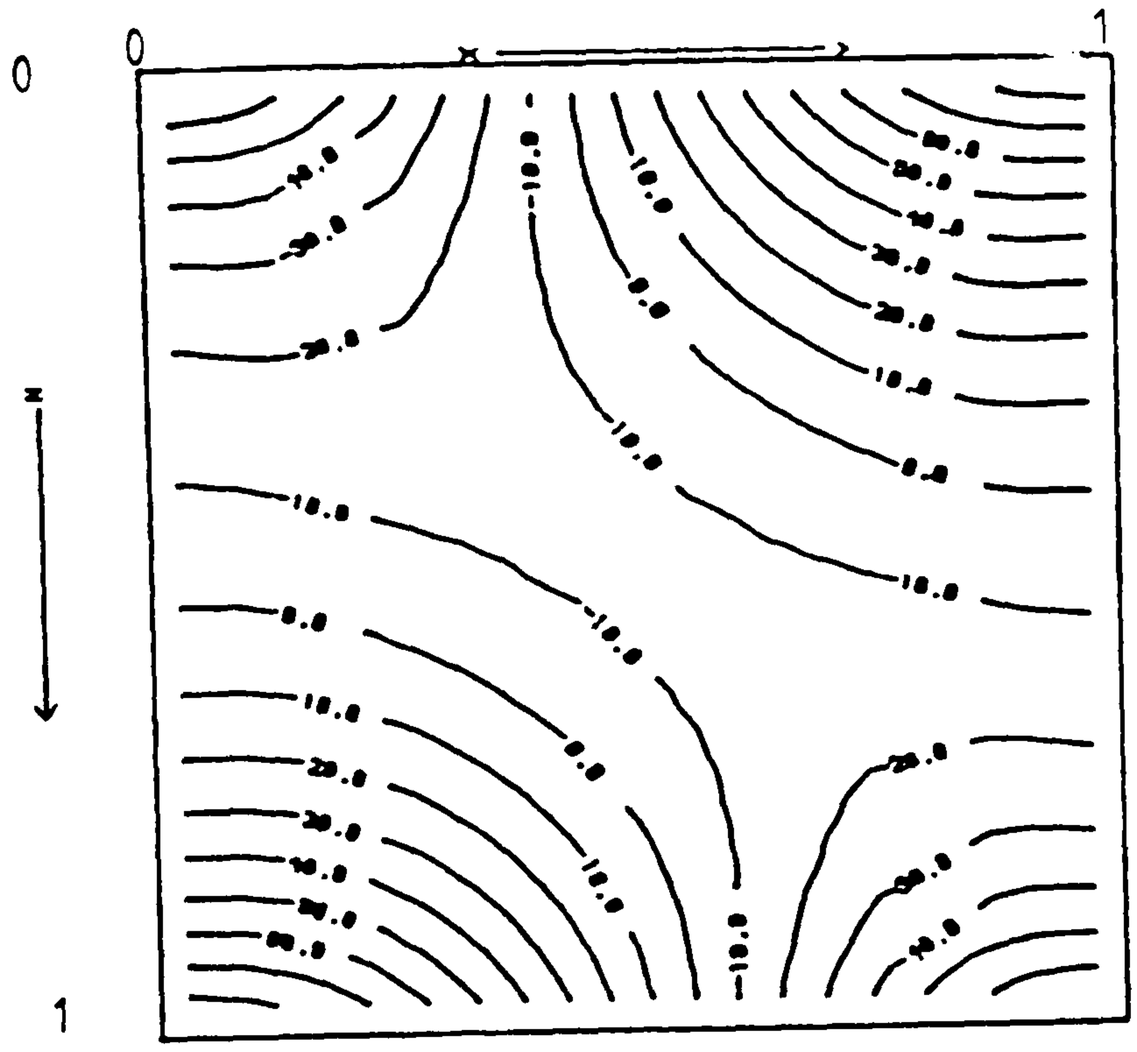

Figure 6.18 Pressure contours at plane A, near the end wall

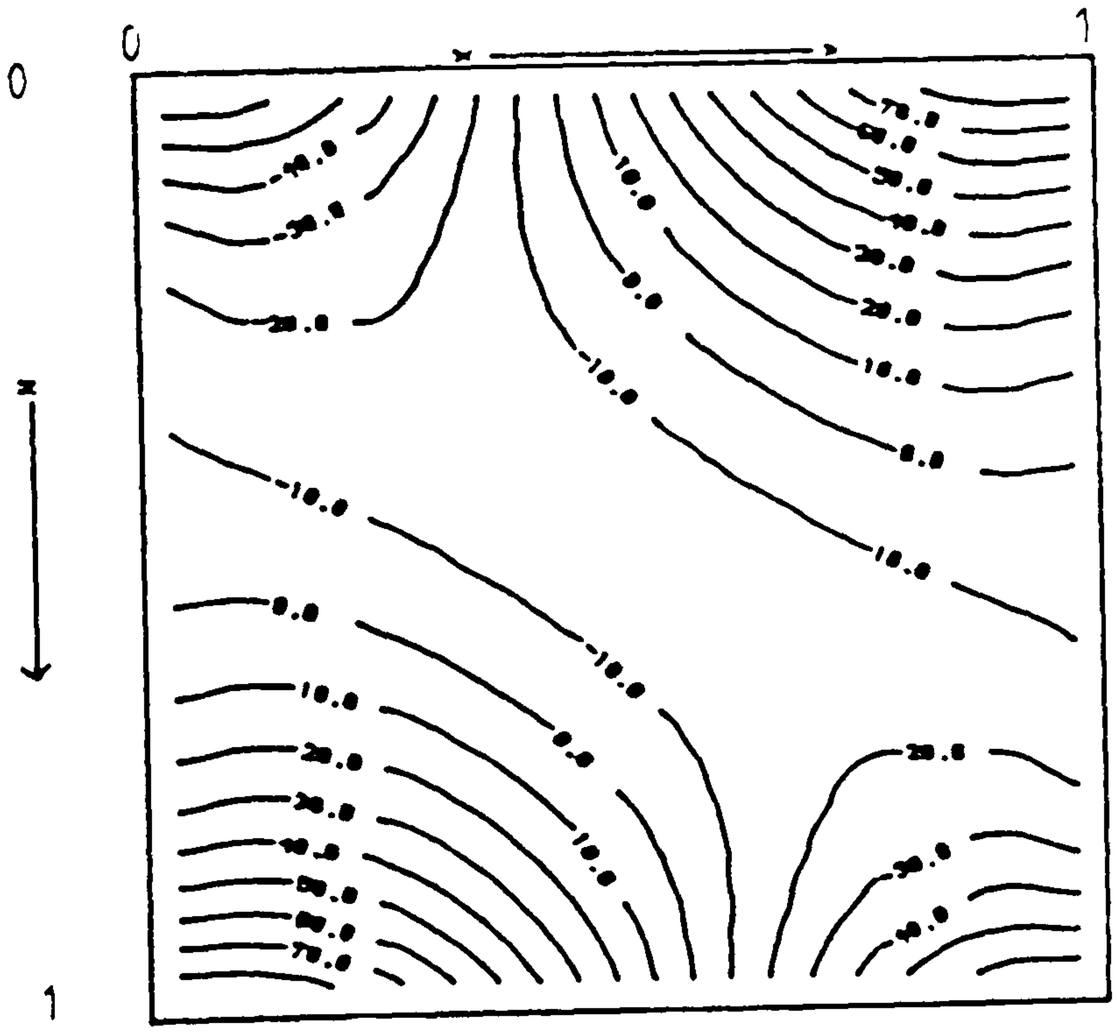

Figure 6.19 Pressure contours at plane B, near the symmetry plane

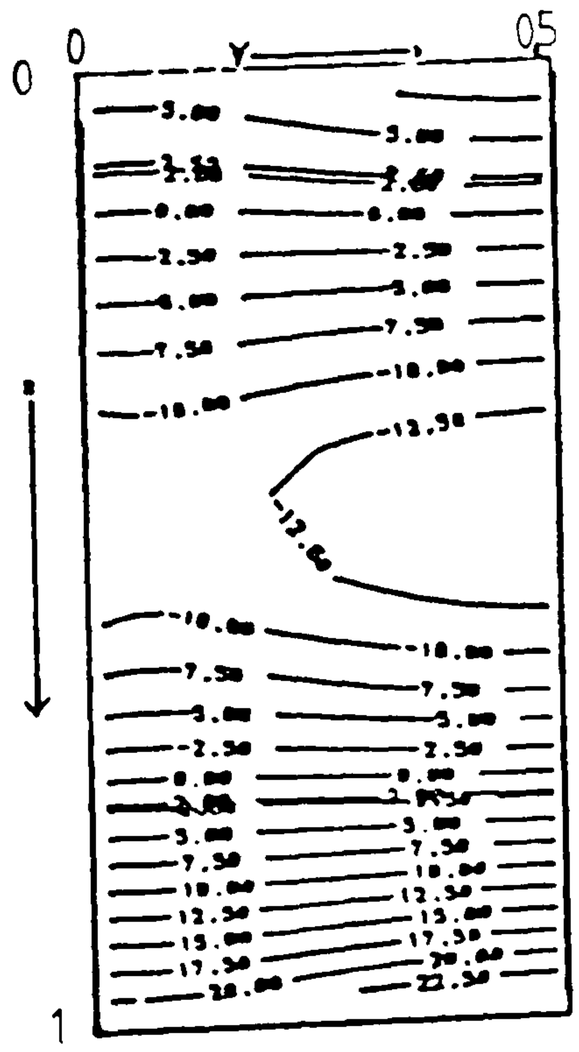

Figure 6.20 Pressure contours at plane C, $(0.5 - hx/2, y, z)$

Window Cavity (1,2,1): length aspect ratio Hy = 2.0

This cavity is exactly the same as that described above, except that the third dimension is twice as long. A single recirculating roll of fluid describes the fluid flow in this cavity. A particle path traced from the point $(.35, 1.0, .35)$ exhibits the roll and the toroidal surface the particle lies on, see Figure 6.21.

Figures 6.22, 6.23 and 6.24 are contour plots of the ratio R at planes A, B and C respectively. The contours exhibit behaviour similar to that in the shorter cavity Hy = 1.0.

Velocity vectors, isotherms and pressure contours exhibit similar behaviour to those in the shorter cavity, Hy = 1. They have been presented here Figures 6.25-6.33 to clarify some of the features described above for the cavity with the length aspect ratio Hy=1. Only distinctive features that arise with this larger length aspect ratio are commented upon.

Near the end wall the thermal solution for Hy=2 is very similar to that obtained for Hy=1. However, near the symmetry plane the thermal solution for Hy=2 is slightly more convective than that obtained for Hy=1. This is expected since with a longer cavity the influence of the end wall at the symmetry plane is smaller compared to that in the shorter cavity purely because of the greater distance between the symmetry plane and the end wall. Thus the reduction of convection at the symmetry plane is smaller with the longer cavity leading to a maximum value of around 0.1 for $\partial\theta/\partial y$.

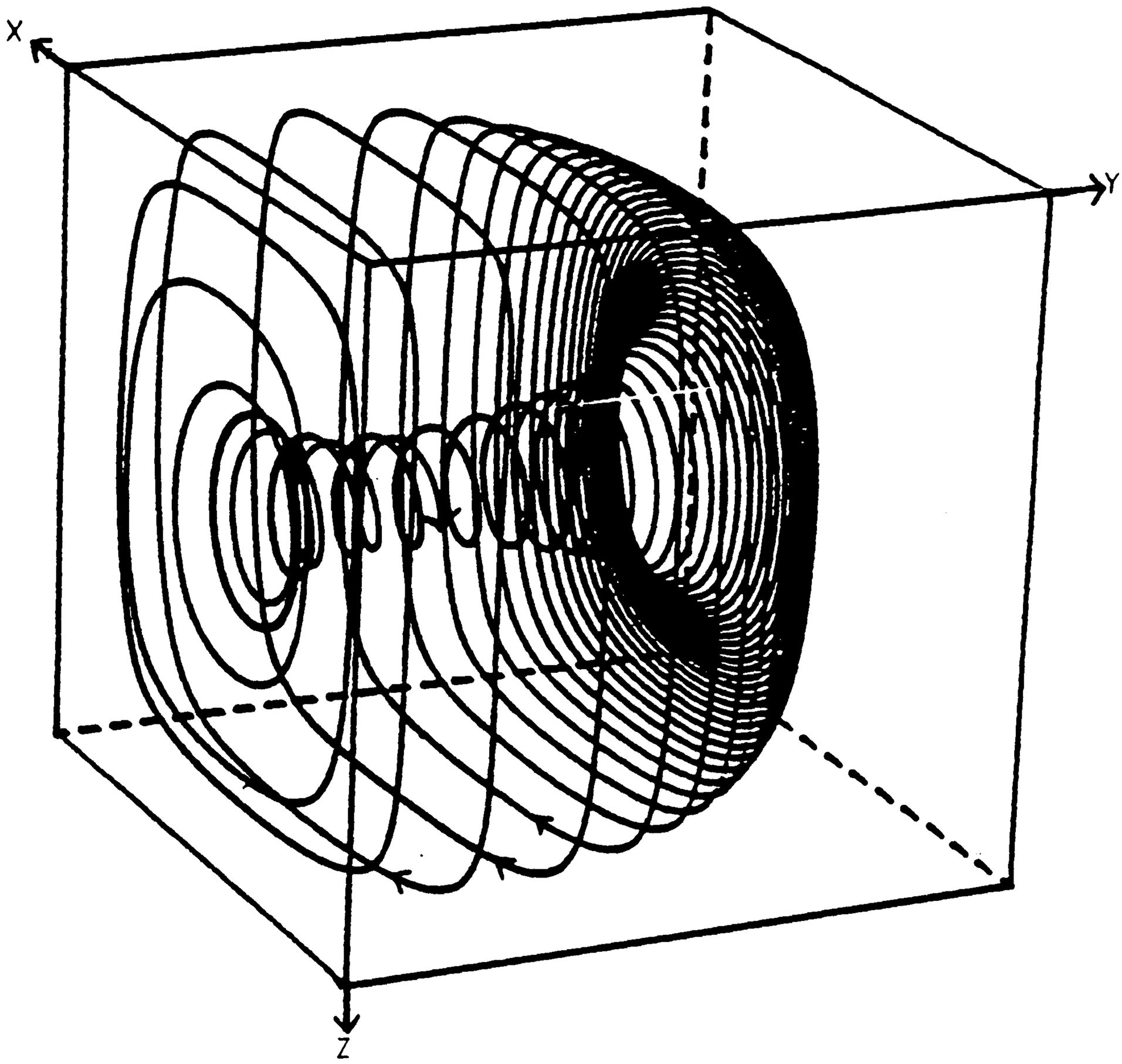

Figure 6.21 Particle track for air at Ra = 10^3, cavity (1,2,1)

Fluid = air, Ra = 10^3, Hy=2, Hz=1, grid=16x16x16

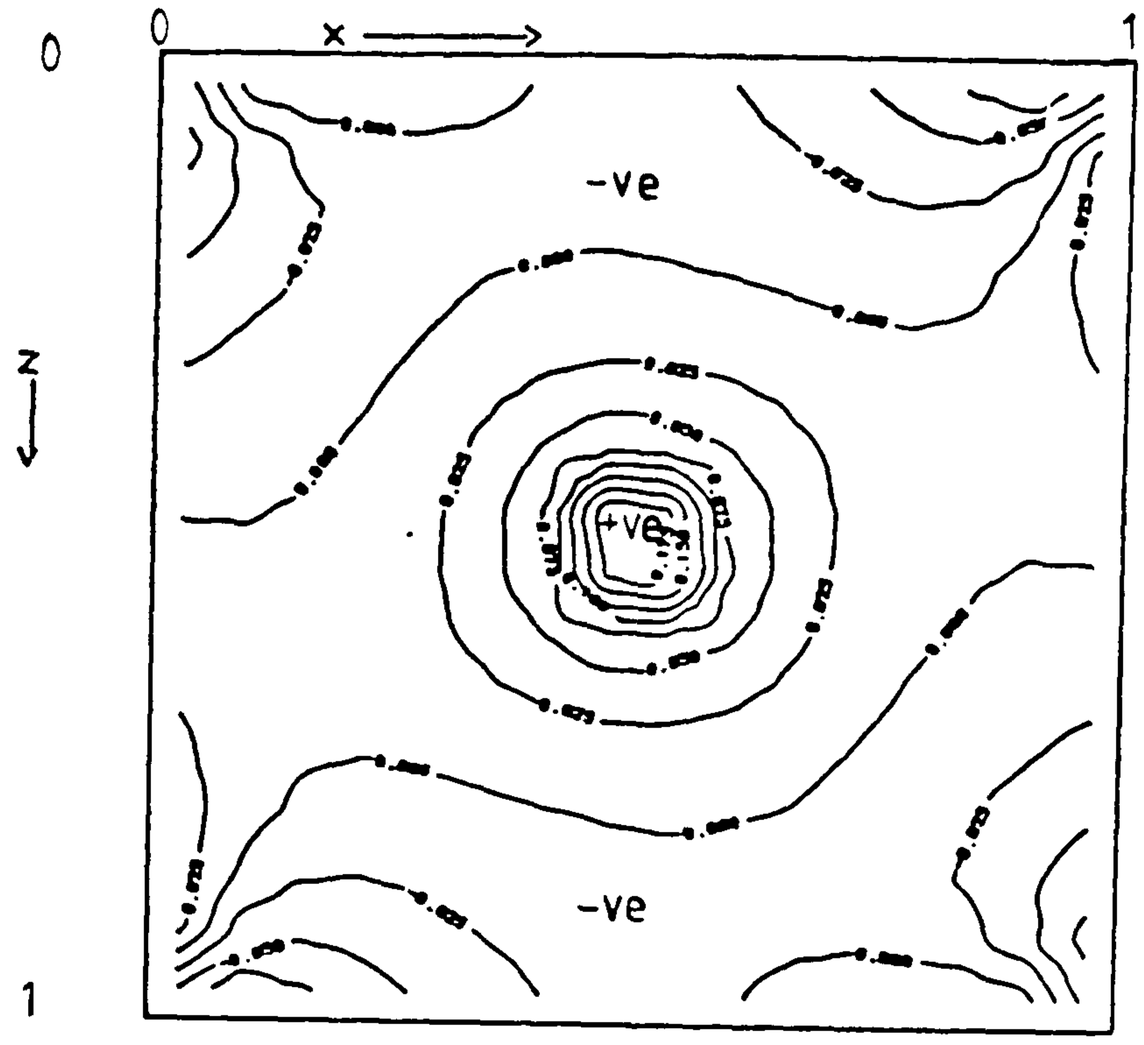

Figure 6.22 Contour plot of ratio R at plane A, near the end wall

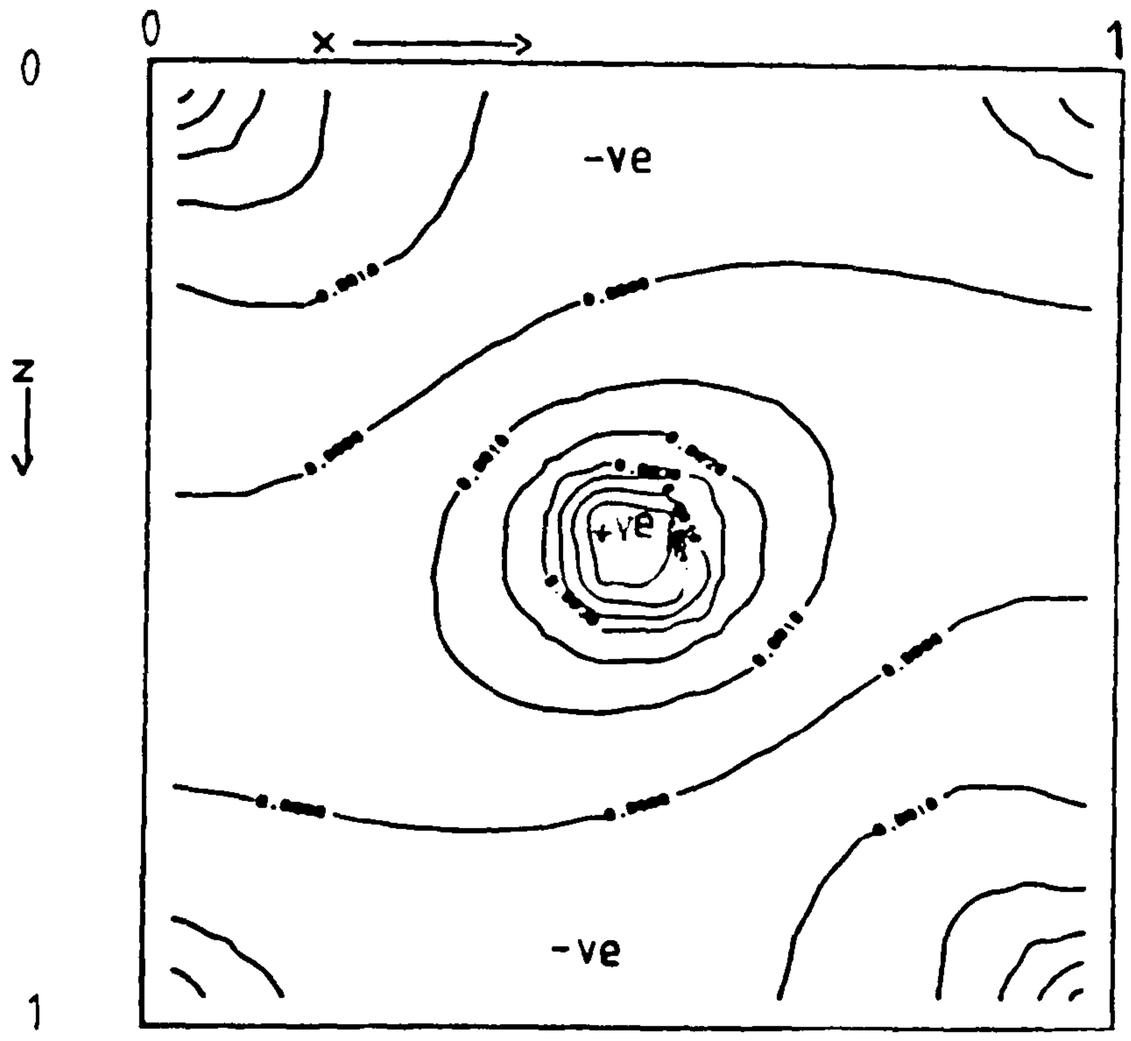

Figure 6.23 Contour plot of ratio R at plane B, near the symmetry plane

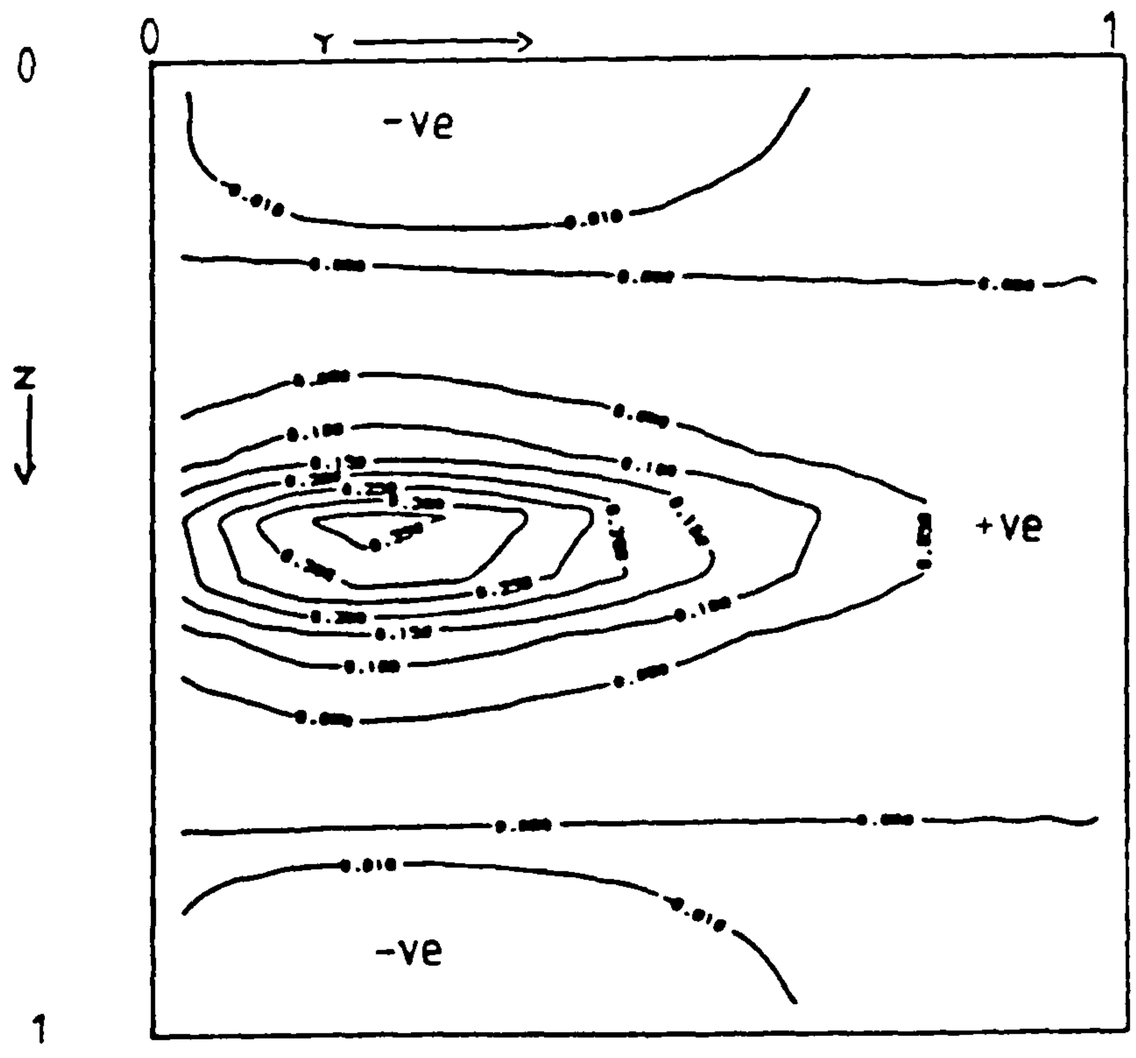

Figure 6.24 Contour plot of ratio R at plane C $(0.5 - hx/2, y, z)$

Fluid = air, Ra = 10^3, Hy=2, Hz=1, grid=16x16x16

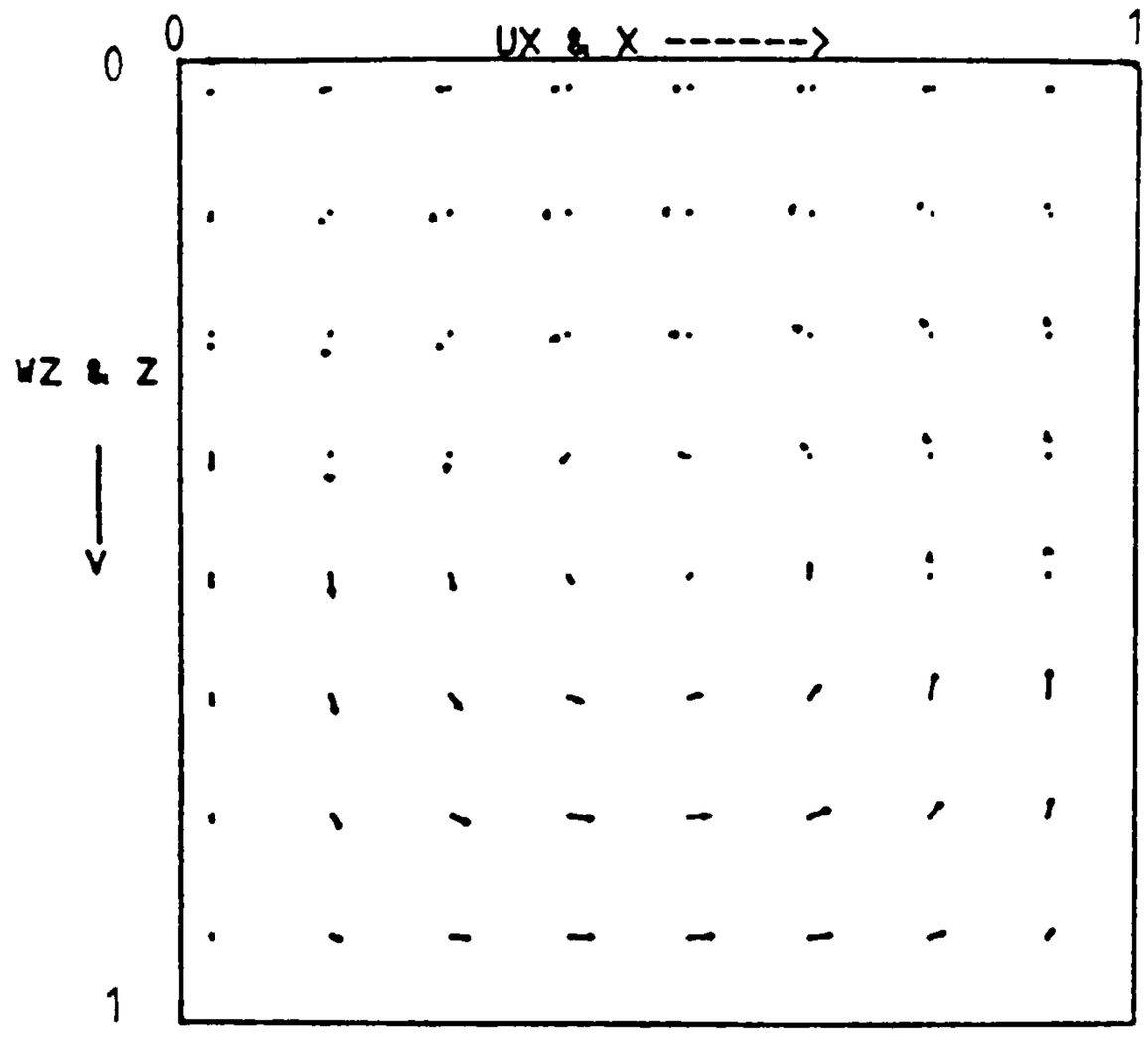

Figure 6.25 Velocity vectors at plane A, near the end wall

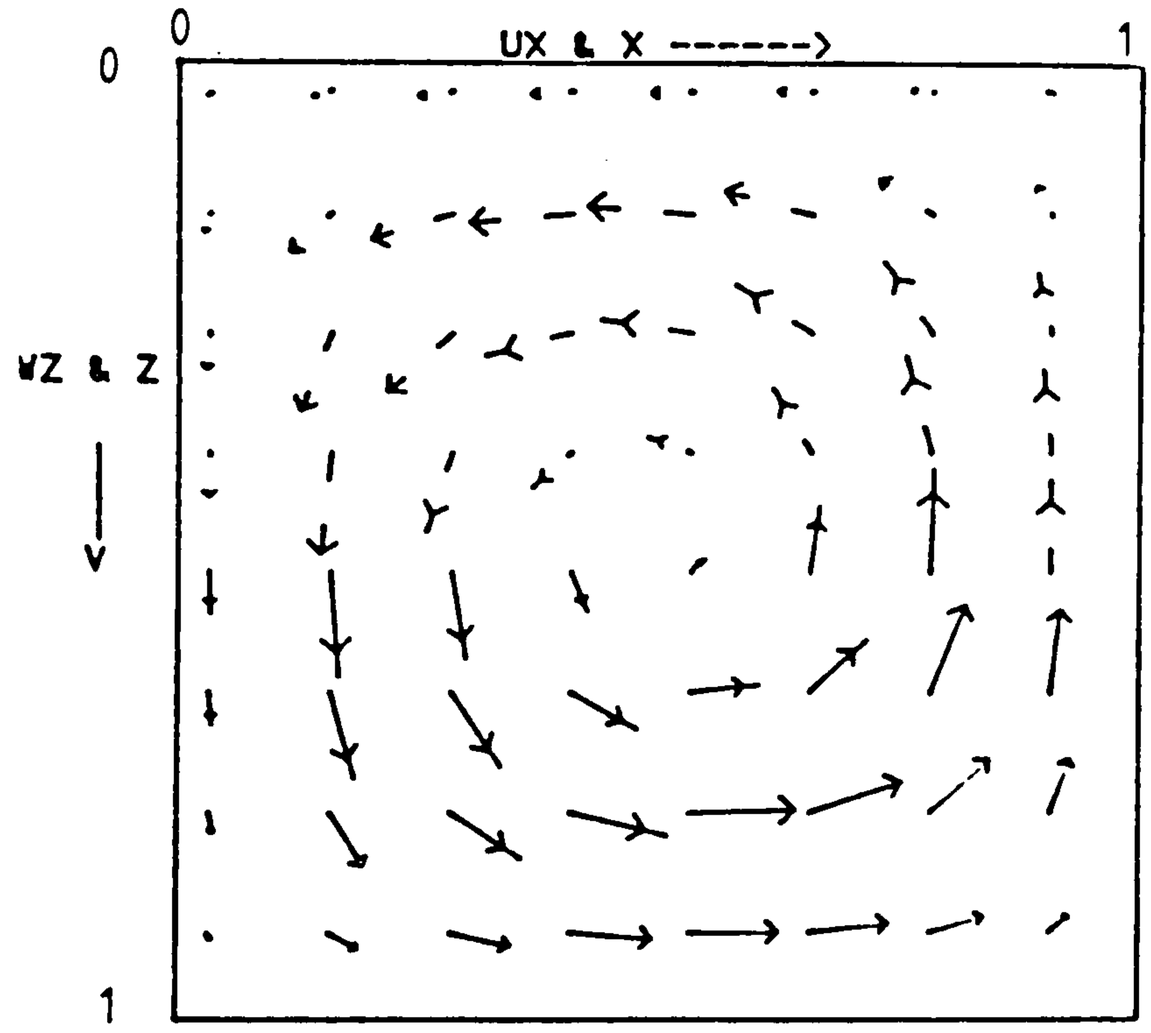

Figure 6.26 Velocity vectors at plane B, near the symmetry wall

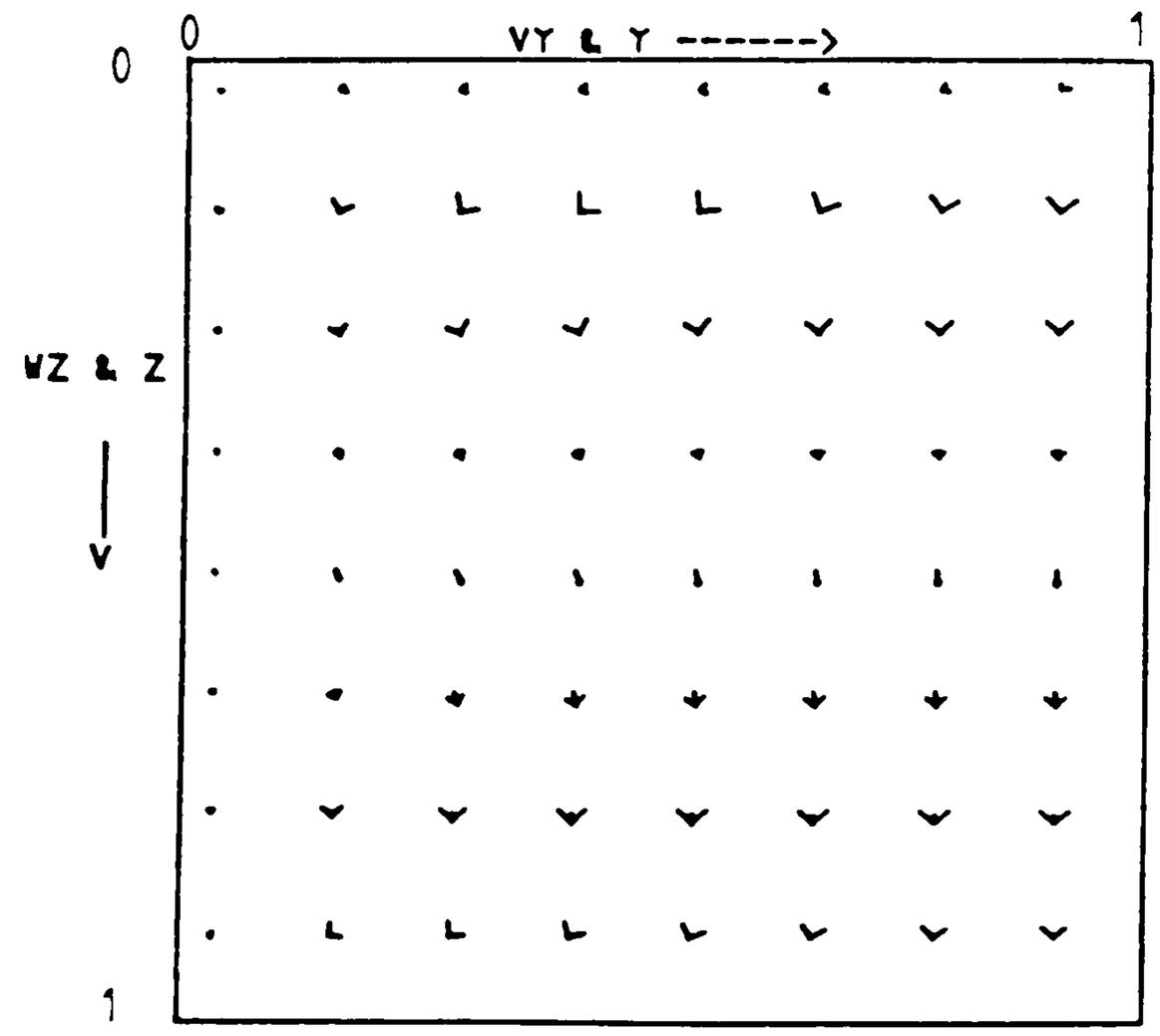

Figure 6.27 Velocity vectors at plane C $(0.5 - hx/2, y, z)$

Fluid = air, Ra = 10^3, Hy=2, Hz=1, grid=16x16x16

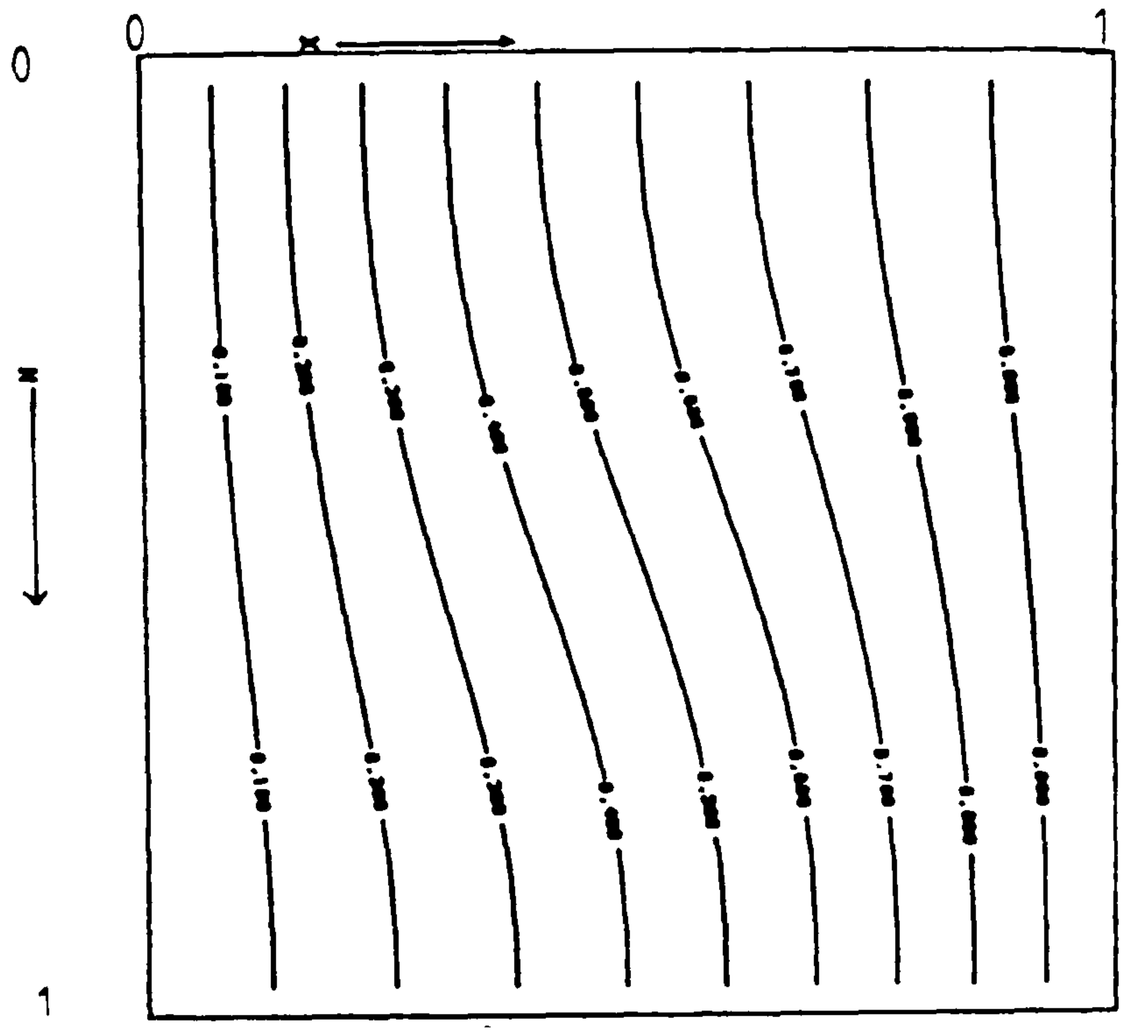

Figure 6.28 Isotherms at plane A, near the end wall

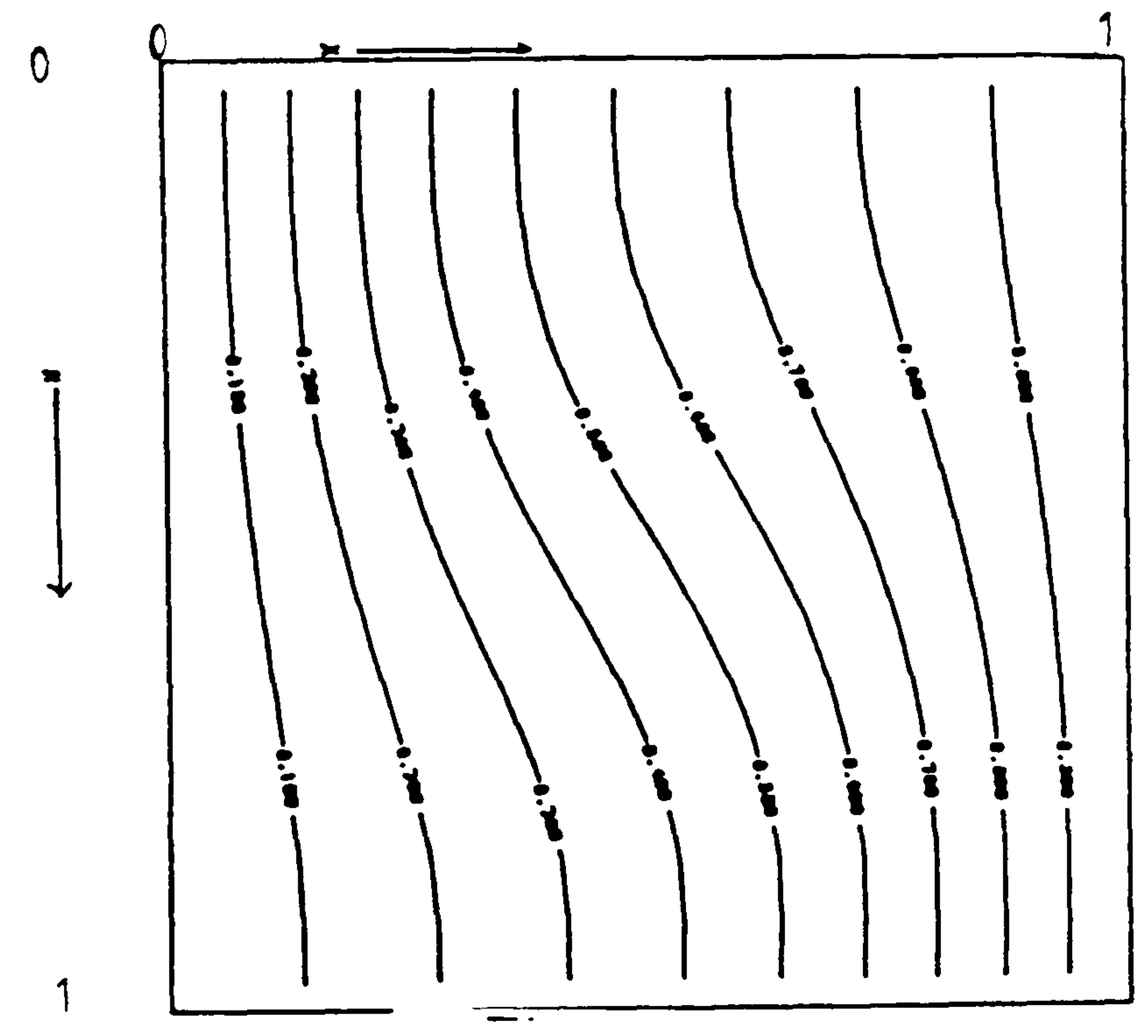

Figure 6.29 Isotherms at plane B, near the symmetry plane

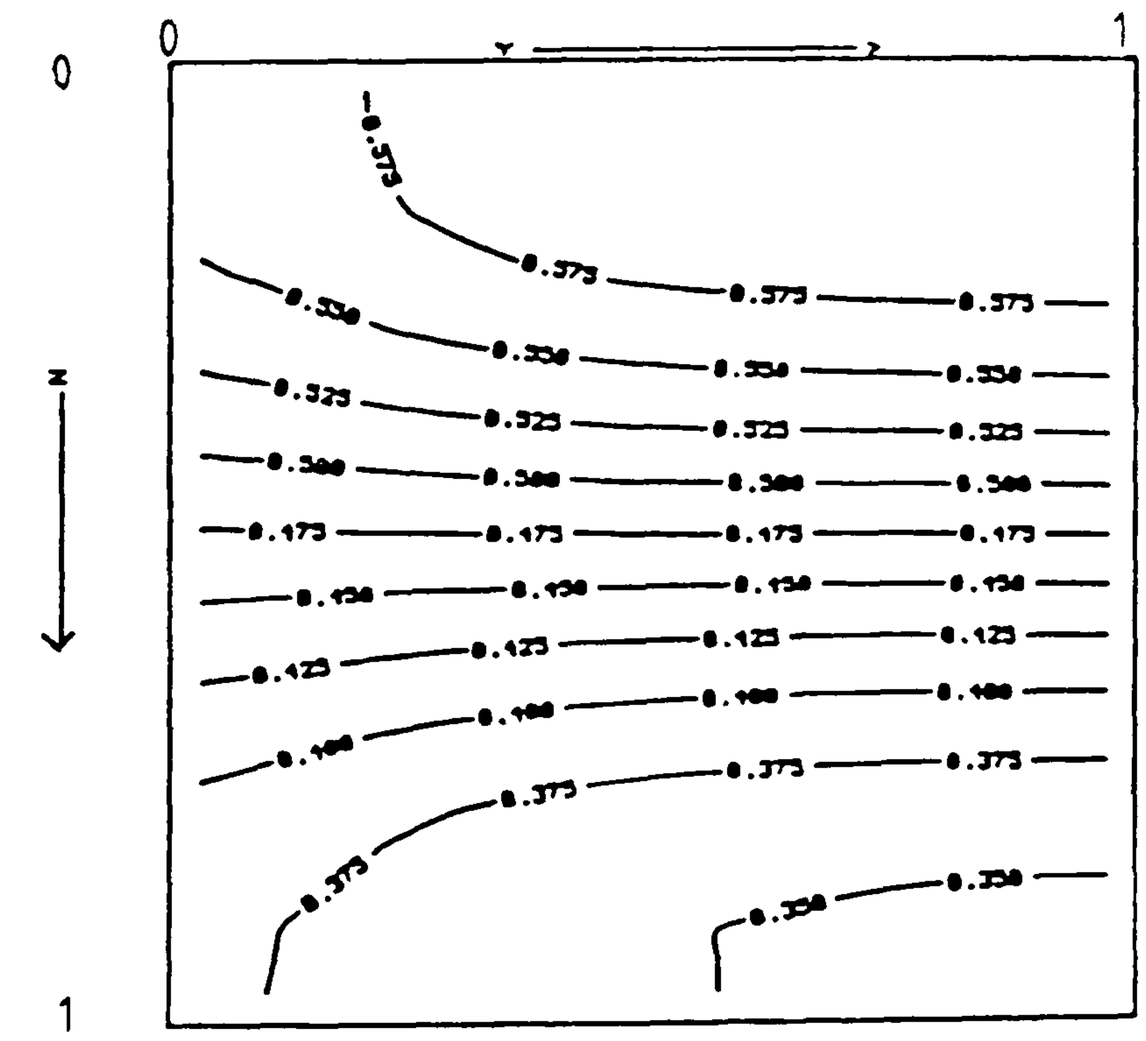

Figure 6.30 Isotherms at plane C, $(0.5 - hx/2, y, z)$

Fluid = air, Ra = 10^3, Hy=2, Hz=1, grid=16x16x16

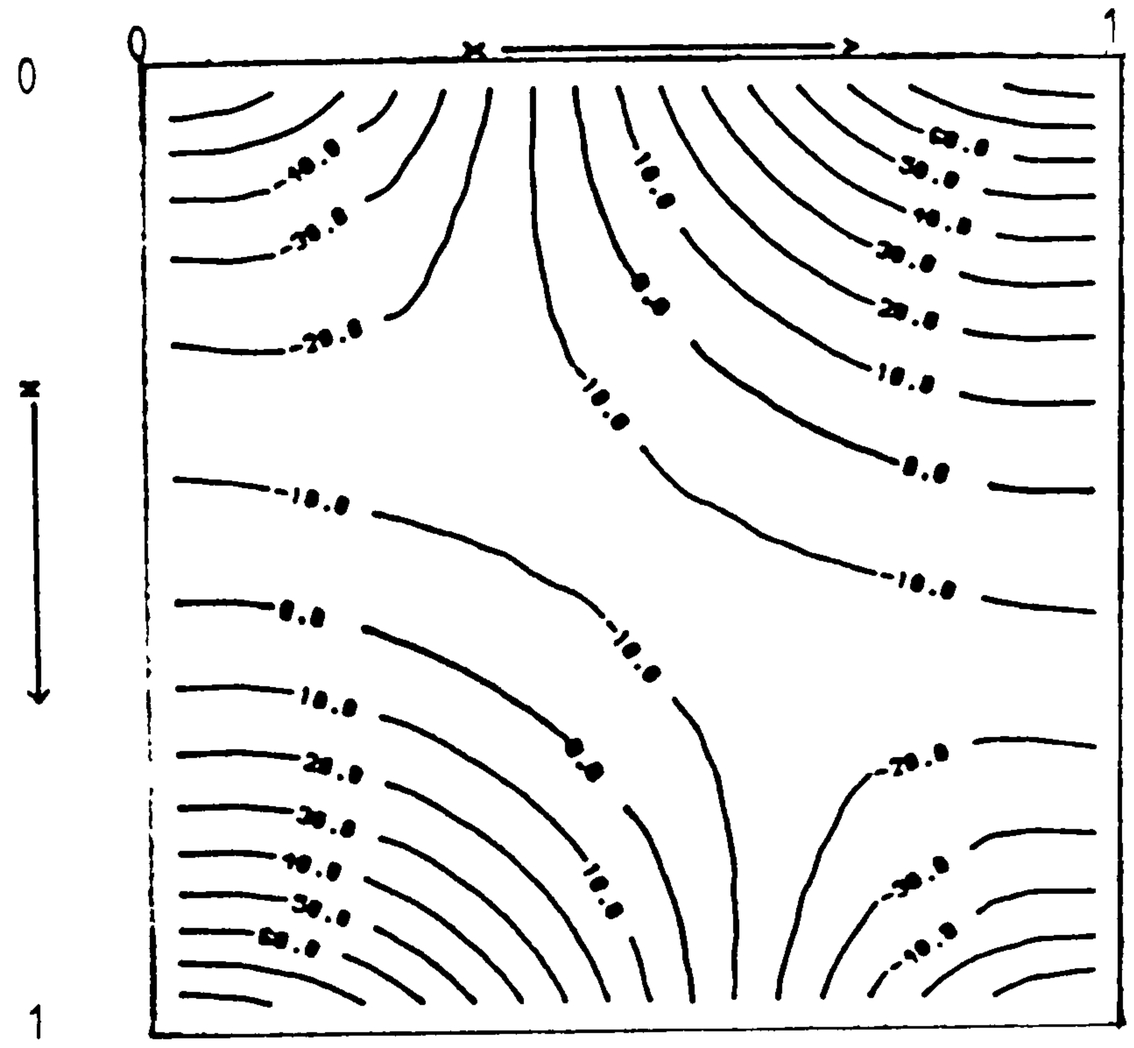

Figure 6.31 Pressure contours at plane A, near the end wall

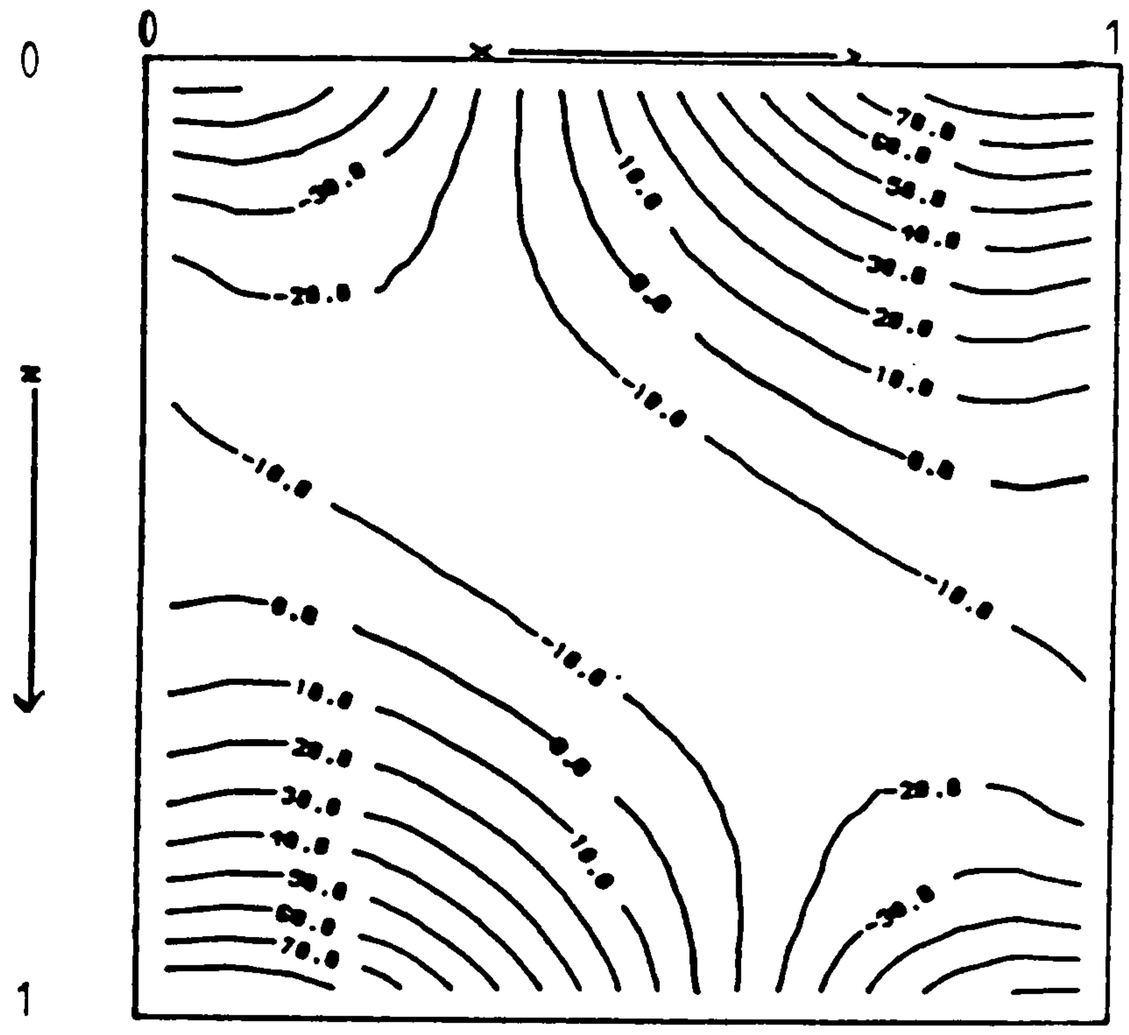

Figure 6.32 Pressure contours at plane B, near the symmetry plane

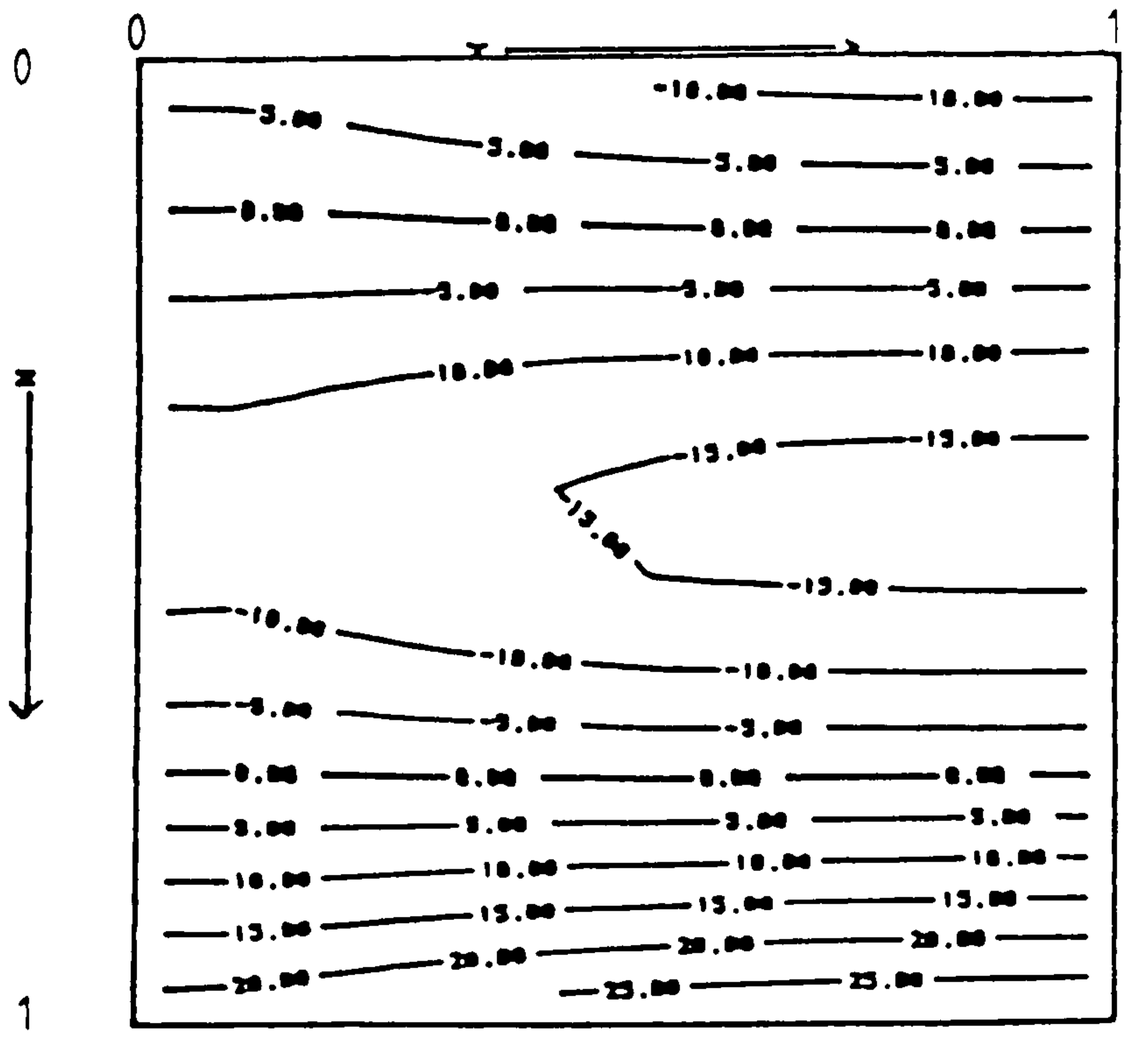

Figure 6.33 Pressure contours at plane C, $(0.5 - hx/2, y, z)$

Window cavity (1,5,1): length aspect ratio Hy=5

Unlike the earlier cases, the recirculating roll with this length aspect ratio, Hy=5, does not occupy the whole solution cavity but only extends to about $y = 1.5$ in the axial direction. The rest of the solution cavity is occupied by a two-dimensional flow. This is illustrated in Figure 6.34. Path1 has been traced from, (.9, .001, .9), very near the end wall. The path starts to coil towards the centre of the end wall. Once the particle reaches the centre of the end wall it moves in the axial direction towards the symmetry plane. The path then starts to uncoil and the motion in the axial direction decays to almost zero giving a tight spiral. At this point the path has been terminated. Path2 has been traced from (.9, .25, .9) and shows the strong axial flow in the boundary layer near the end wall. Path3 has been traced from (.9, 1.0, .9) and shows the particle in the boundary layer returning towards the end wall with weak axial velocity. The other paths traced nearer the symmetry plane show no or very small motion in the axial direction indicating the end wall effect is very small and the flow there is dominated by the buoyancy force thus resulting in two-dimensional flow.

The contour values of R are very small near the symmetry plane and this can be seen from Figure 6.35, which shows the contour values of R near the plane C.

Large axial temperature gradients are to be found near the end wall where the reduction in convection is greatest. This can be seen in Figure 6.36, which shows the axial temperature gradients in the x=0.5 plane and in Figure 6.37, the isotherm plot at plane C. The maximum value of $\partial\theta/\partial y$ is 0.101. The thermal solutions near the end wall and the symmetry plane are very similar to those obtained with Hy = 2.0.

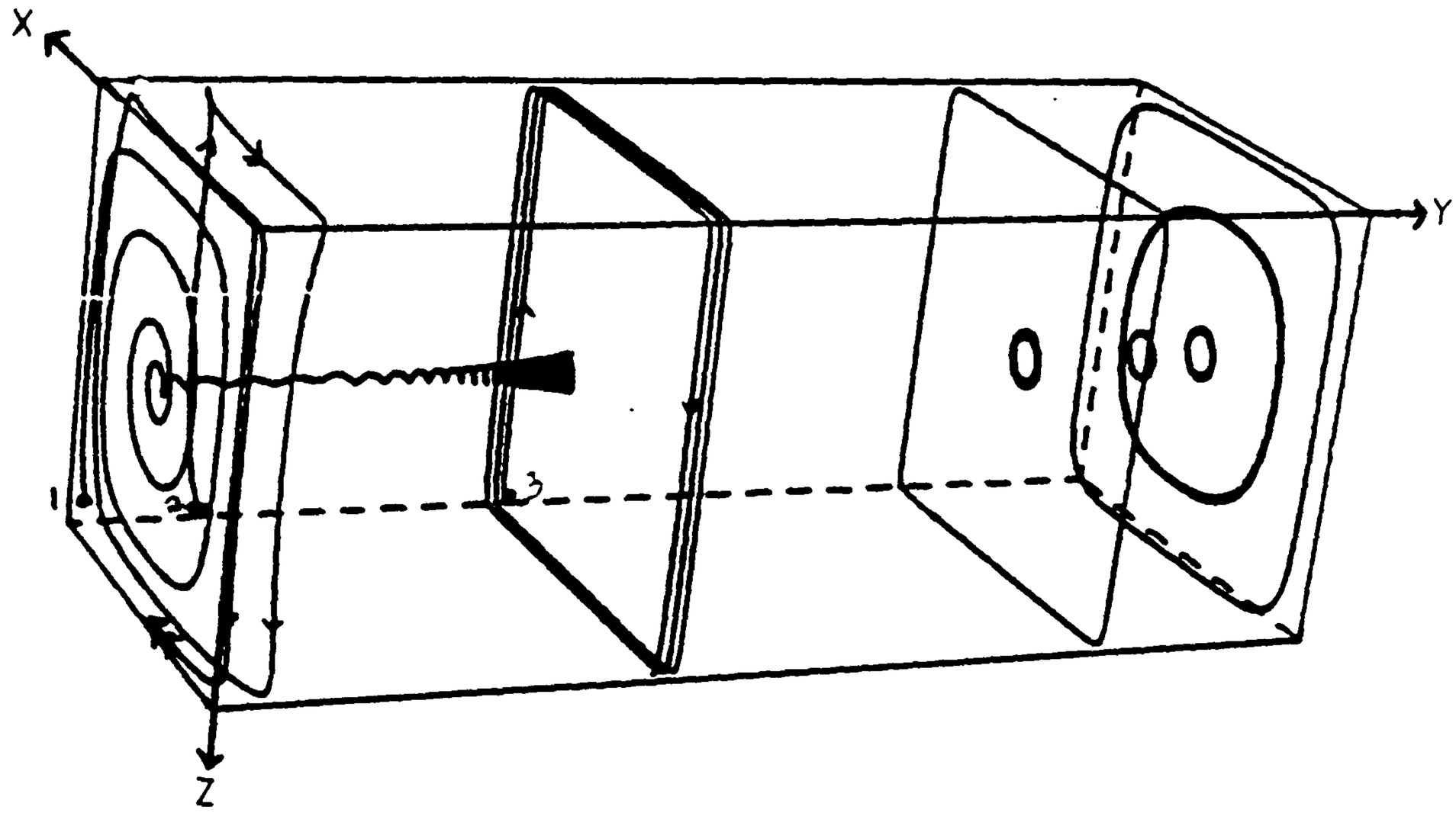

Figure 6.34 Particle track for air at Ra = 10^3, cavity (1,5,1)

Fluid = air, Ra = 10^3, Hy=5, Hz=1, grid=16x40x16

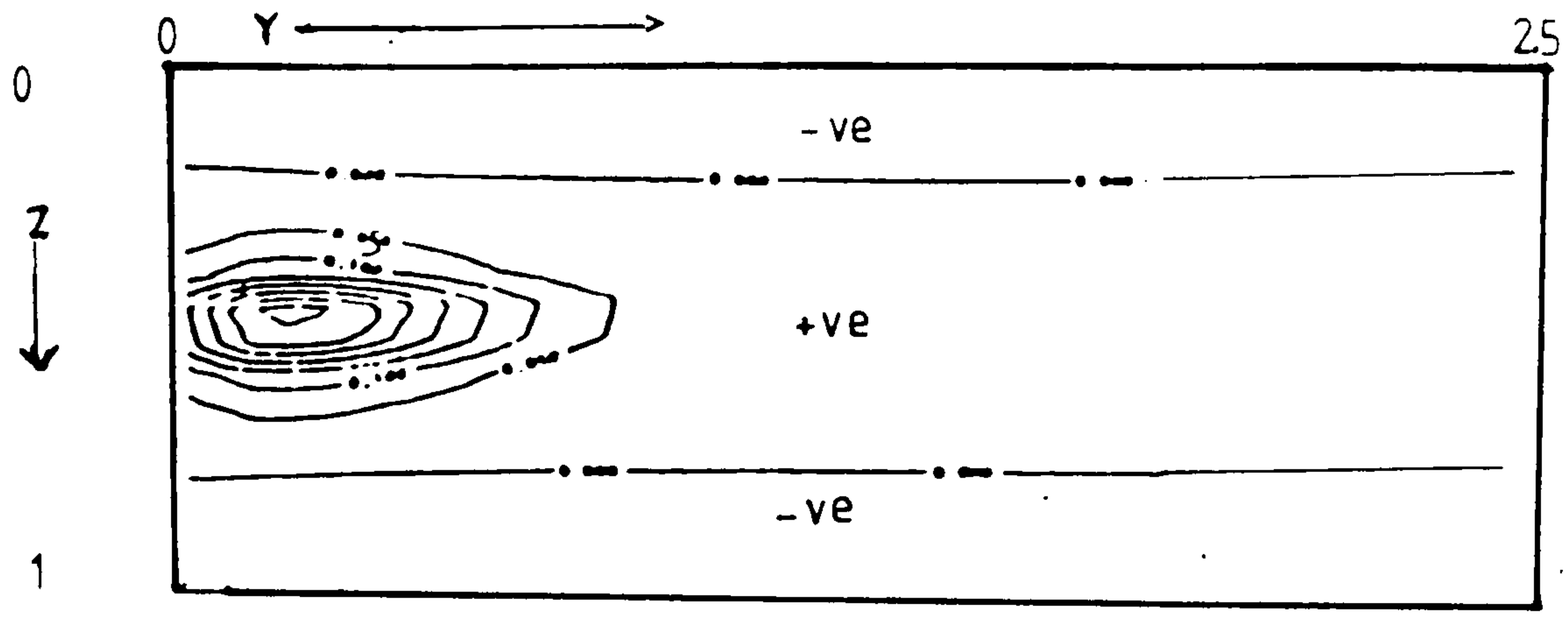

Figure 6.35 Contour plot of the ratio R at plane C, $(0.5 - hx/2, y, z)$

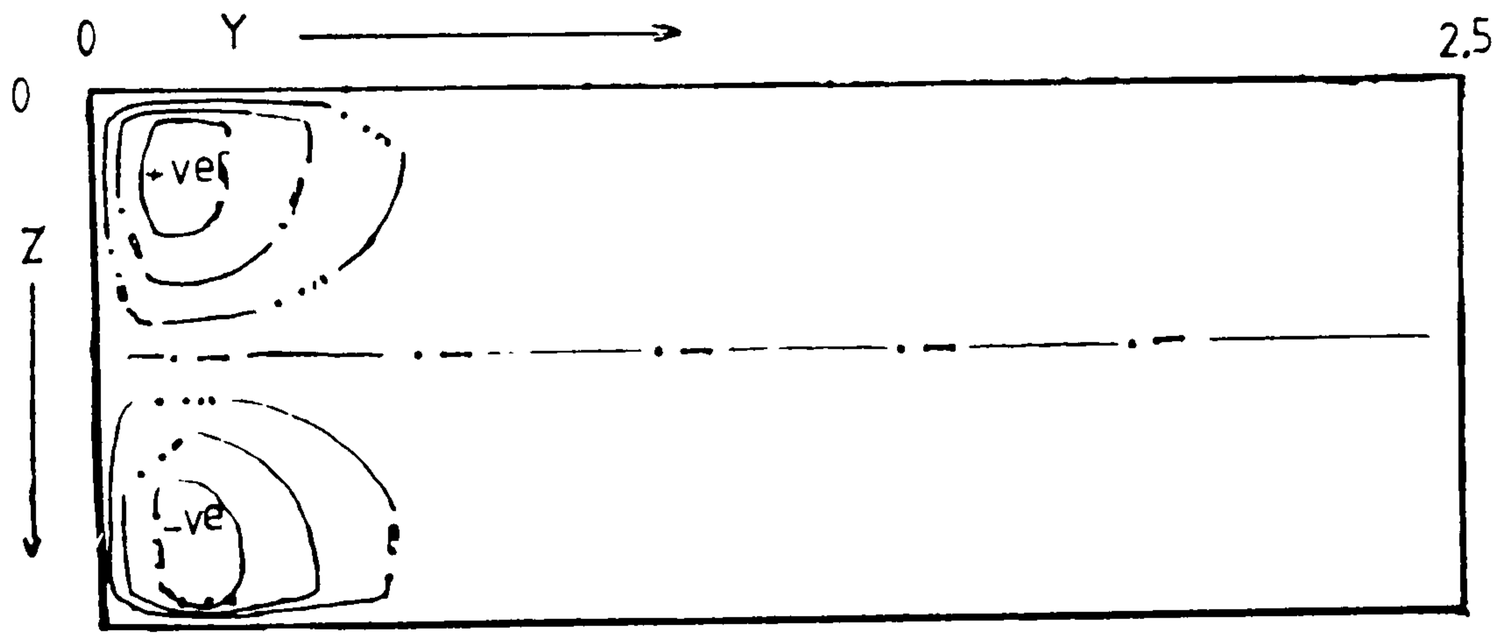

Figure 6.36 Contour plot $\partial\theta/\partial y$ at plane C, $(0.5 - hx/2, y, z)$

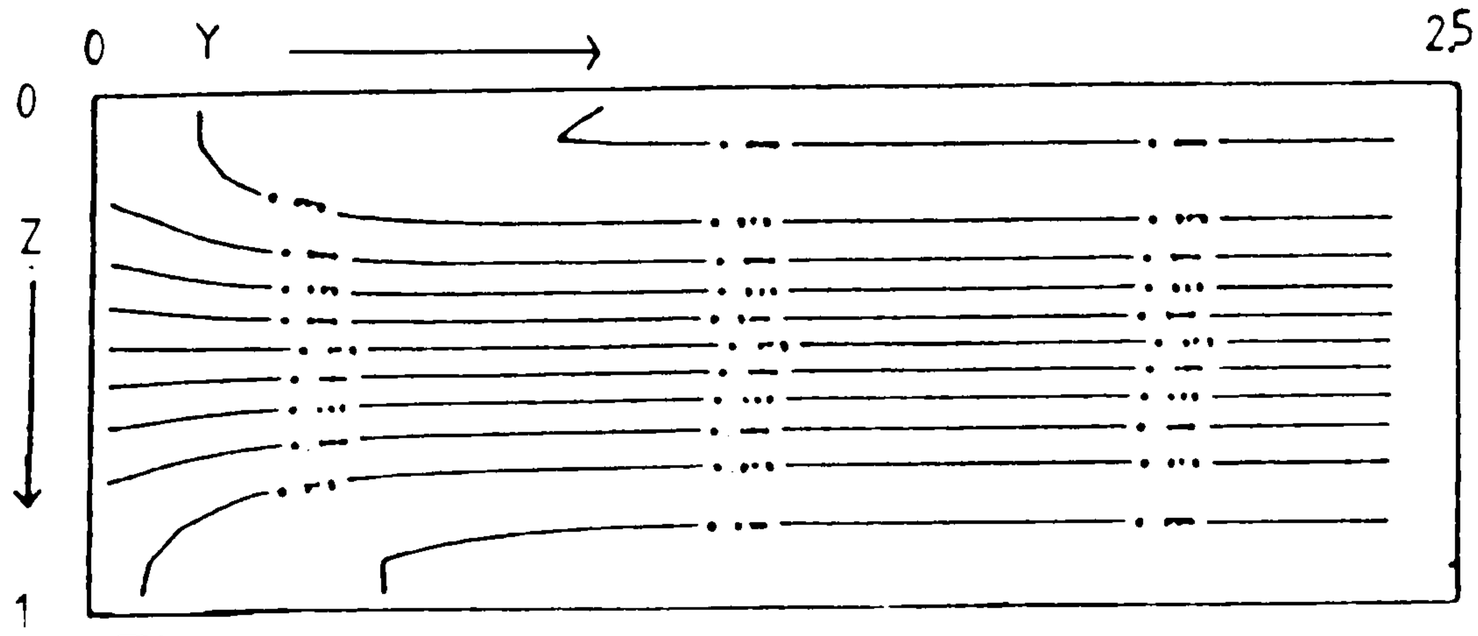

Figure 6.37 Isotherms at plane C, $(0.5 - hx/2, y, z)$

The flow at the symmetry plane is two-dimensional since $v = 0$ and so the streamlines can be plotted there. As a consequence of using staggered grids the cross-sectional velocities u and w are not calculated at the symmetry plane and so have to be interpolated. Figures 6.38-6.40 represent the streamlines at the symmetry plane for Hy=1.2 and 5 respectively. The streamlines are very much like those obtained with the double glazing problem. For the longer cavity, Hy=2, the maximum ψ increases by less than 1% to 1.2. Maximum ψ is of course the strength of the cross-sectional flow at the symmetry plane. The cross-sectional flow strength is dependent on the magnitude of the drag relative to the total buoyancy torque applied along the length of the cavity. The buoyancy torque increases with increasing Hy and thus the cross-sectional flow strength increases with increasing Hy. For Hy=5 the maximum value of ψ is 1.2 which is the same as that obtained with Hy=2.

From the above description of the recirculating roll it is evident that the maximum axial velocity occurs in the centre line. Figure 6.41 is a plot of the axial velocity along the centre line of the cavity. $(.5, y, .5)$. The maximum axial velocity is 0.152 occurring at about y=0.25 for the cavity with length aspect ratio Hy=1.0. For the cavity with length aspect ratio, Hy=2.0 and 5.0 the maximum axial velocity is 0.196 occurring near $y = 0.3$. The reason for the weaker axial flow in the shorter cavity is that in the longer cavities the strength of the cross sectional flow due to the buoyancy force near the symmetry plane is stronger than in the shorter cavity. Hence the difference between the angular velocity at the symmetry plane and the end wall is greater for the longer cavity. Thus there is greater inward radial pressure at the end wall for the larger cavity which is responsible for the stronger axial flow. From the axial velocity graph the end wall effect can be interpreted as follows: it has a strong influence from the end wall to the point at which the maximum axial velocity occurs in the inner core, after which the influence of the end wall decays. From graph C it can be seen that the two-dimensional flow exists for cavities which have length aspect ratio greater than approximately 3.4.

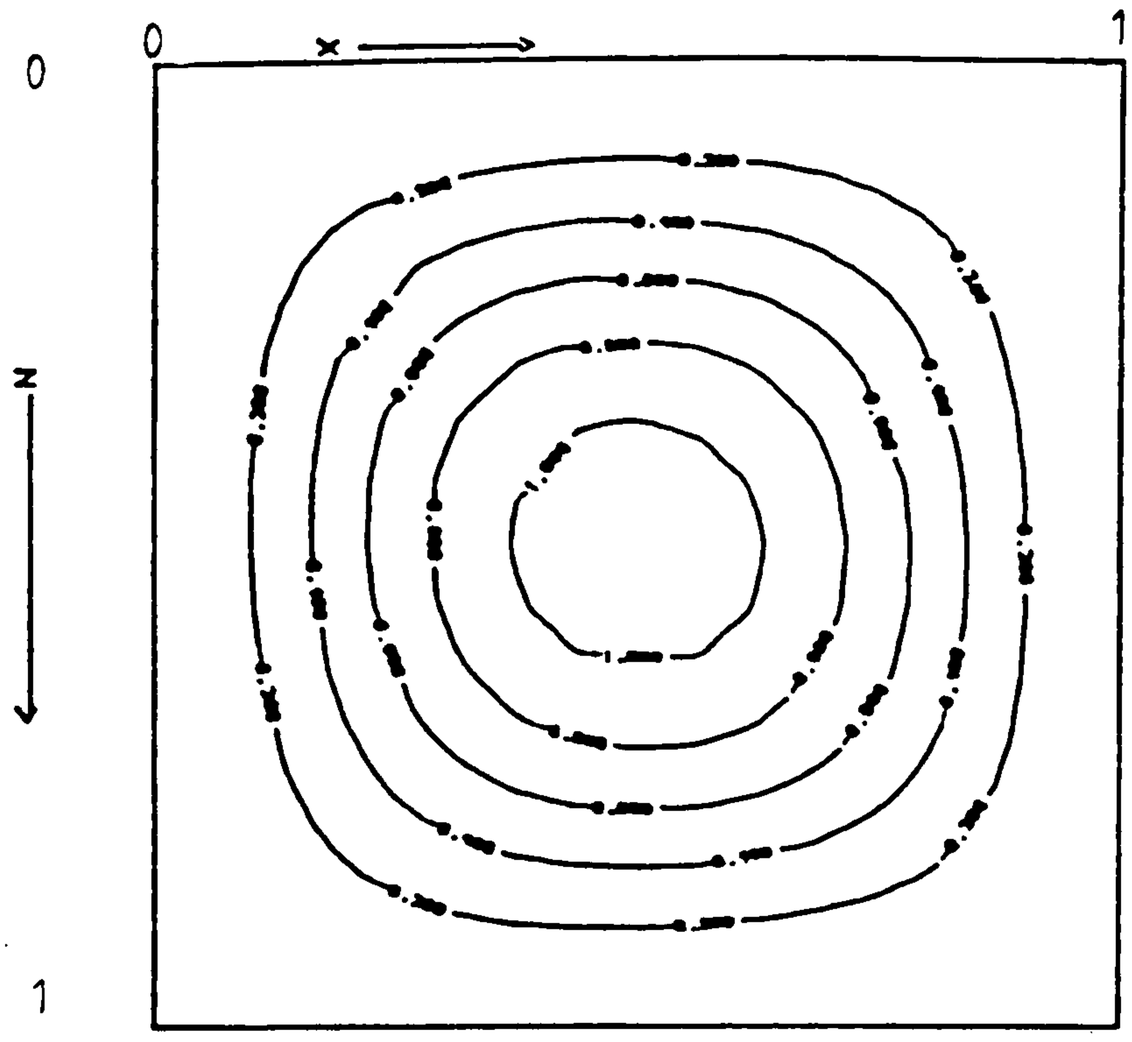

Figure 6.38 Streamline plot at plane B, near the symmetry plane, Hy=1

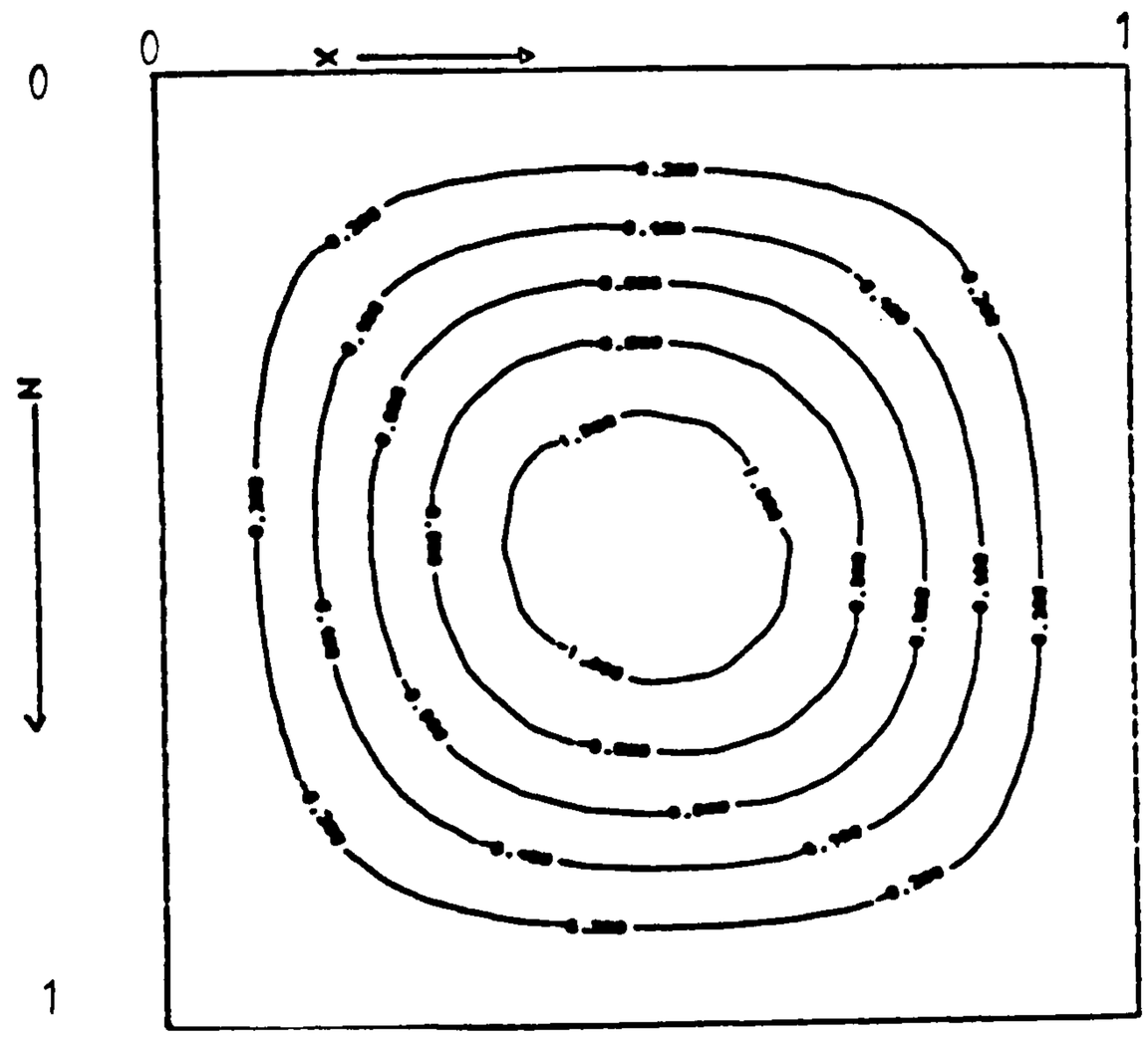

Figure 6.39 Streamline plot at plane B, near the symmetry plane, Hy=2

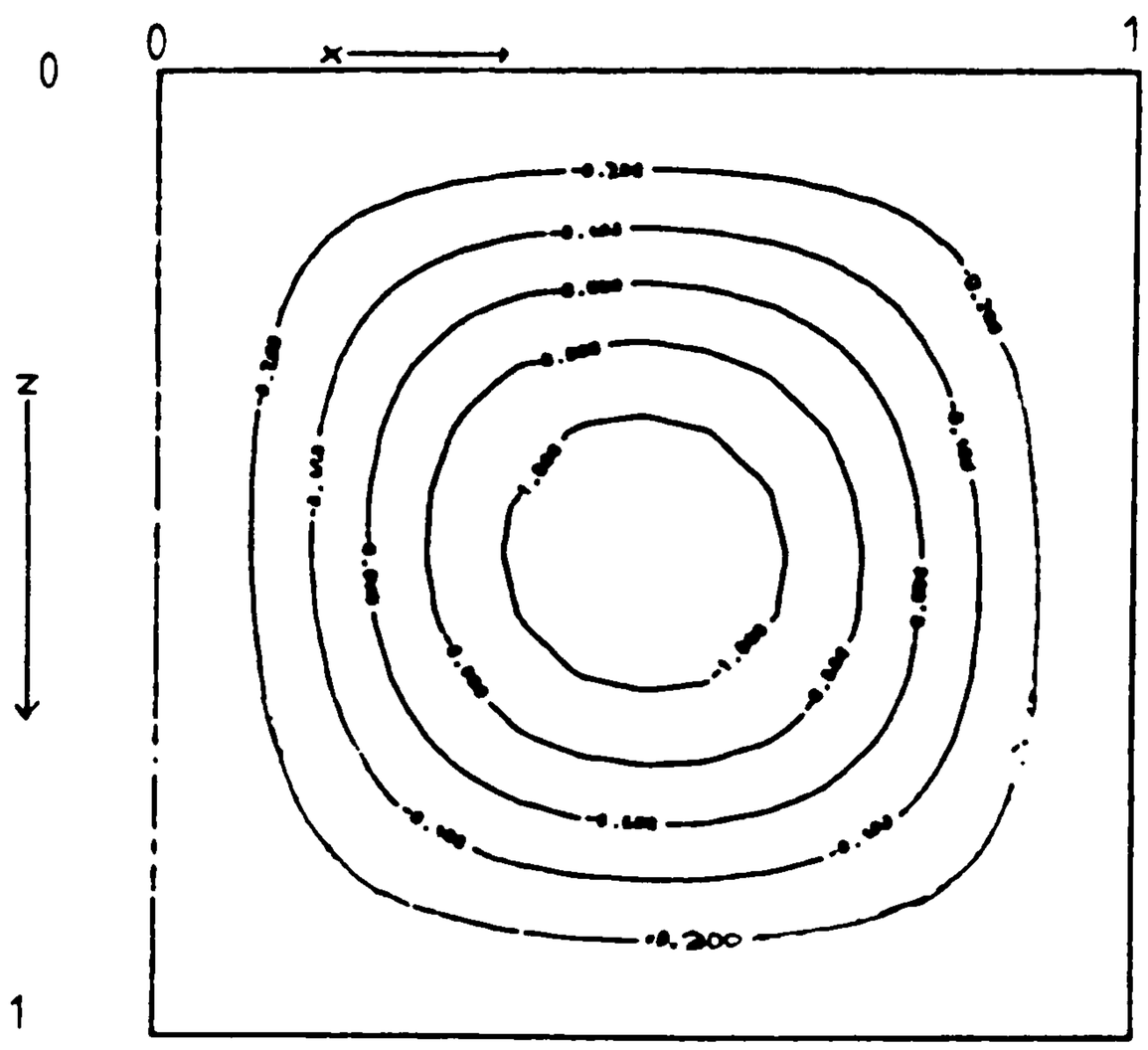

Figure 6.40 Streamline plot at plane B, near the symmetry plane, Hy=5

Graph A: air at Ra = 10^3, Hy=1, Hz=1

Graph B: air at Ra = 10^3, Hy=2, Hz=1

Graph C: air at Ra = 10^3, Hy=5, Hz=1

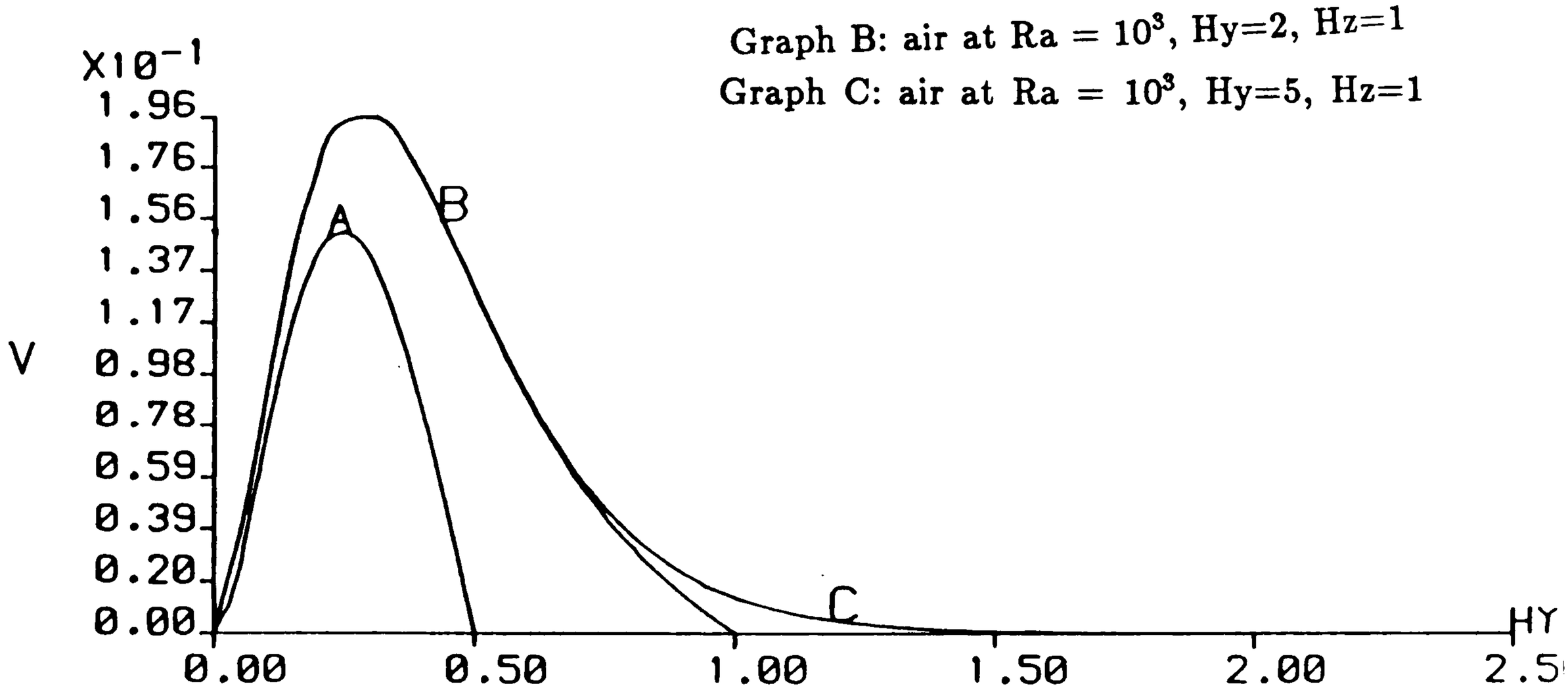

Figure 6.41 Axial-velocity along $(0.5, y, 0.5)$

A fine mesh study with the window cavity (1,1,1)

A fine mesh study for air with Ra = 10^3 in the window cavity (1.1.1), length aspect ratio Hy=1, has been performed in order to assess the effects on truncation errors of further mesh refinement. The mesh lengths in all three directions have been halved to give a finer mesh of 32x32x32 control volumes. No particle paths have been presented since the total number of mesh points exceed the user memory region size that was available on the IBM3084 computer. Since the fluid flow behaviour can be obtained from the velocity vectors, isotherm and contour plots of the ratio R, there is then no need to interpolate the fine mesh variables onto a coarser grid for particle tracking purposes. In fact one can deduce from the graph of the axial velocity along the cavity centre line and the velocity vector plots that the fluid flow is described by a single recirculating roll.

Figures 6.42, 6.43 and 6.44 are contour plots of the ratio R at planes A, B and C respectively. The features of the contours are very similar to those obtained with the coarse grid.

Velocity vectors, isotherms, axial temperature gradients and pressure contours all have the same characteristic behaviour as that obtained with the coarser grid. The maximum value of $\partial\theta/\partial y$ is 0.104 which is about 4% greater than the coarser grid value. The maximum value of ψ is 1.1, the same as that obtained with the coarser grid. The axial velocity along the centre line has been plotted for the two mesh sizes, Figure 6.45, the solid line representing the axial velocity for the fine mesh 32x32x32 and the asterisks representing the axial velocity for the coarse grid 16x16x16. The coarse grid under predicts the maximum axial velocity by about 6%.

The close agreement between the coarse grid and fine grid results gives a certain measure of confidence in the results for these parameter values. However a need to follow up with finer grid studies for a few more cases still exists.

Fluid = air, Ra = 10^3, Hy=1, Hz=1, grid=32x32x32

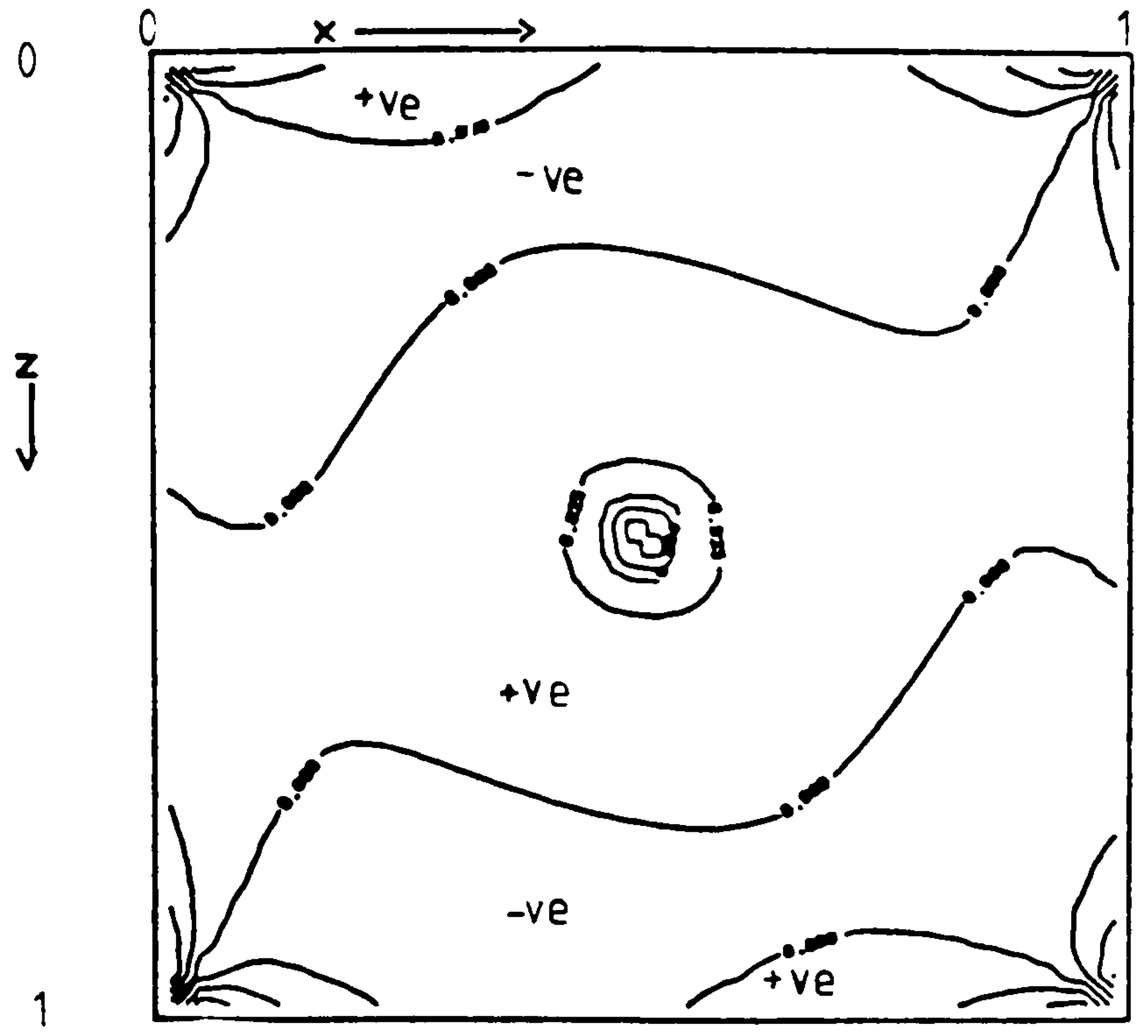

Figure 6.42 Contour plot of ratio R at plane A, near the end wall

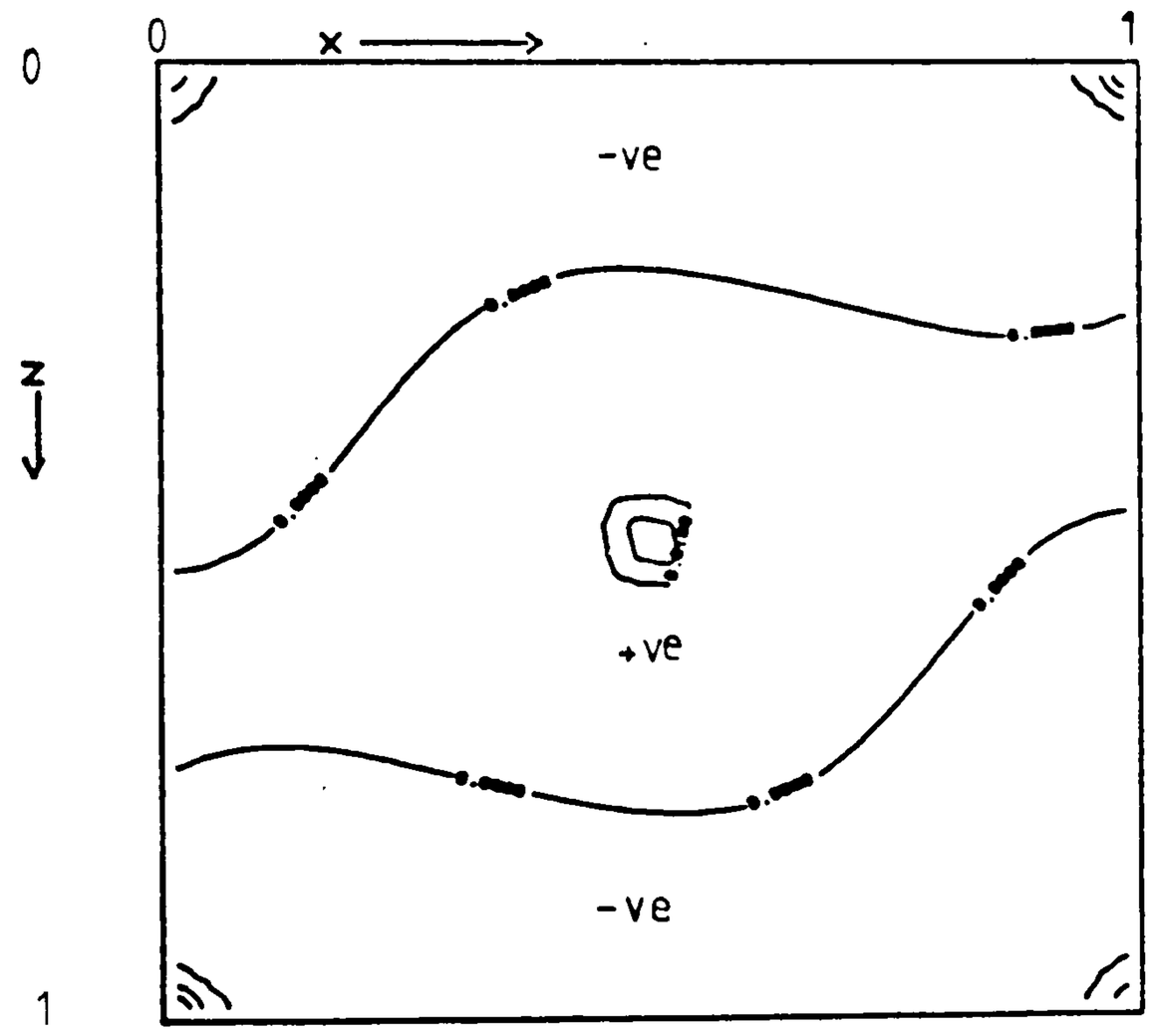

Figure 6.43 Contour plot of ratio R at plane B, near the symmetry plane

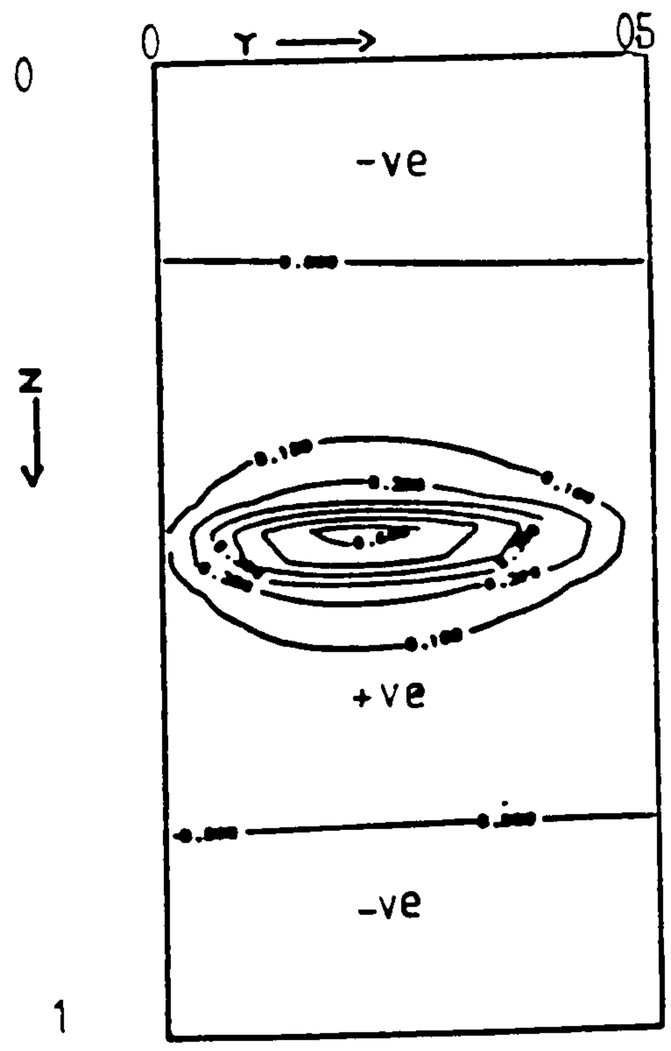

Figure 6.44 Contour plot of ratio R at plane C $(0.5 - hx/2, y, z)$

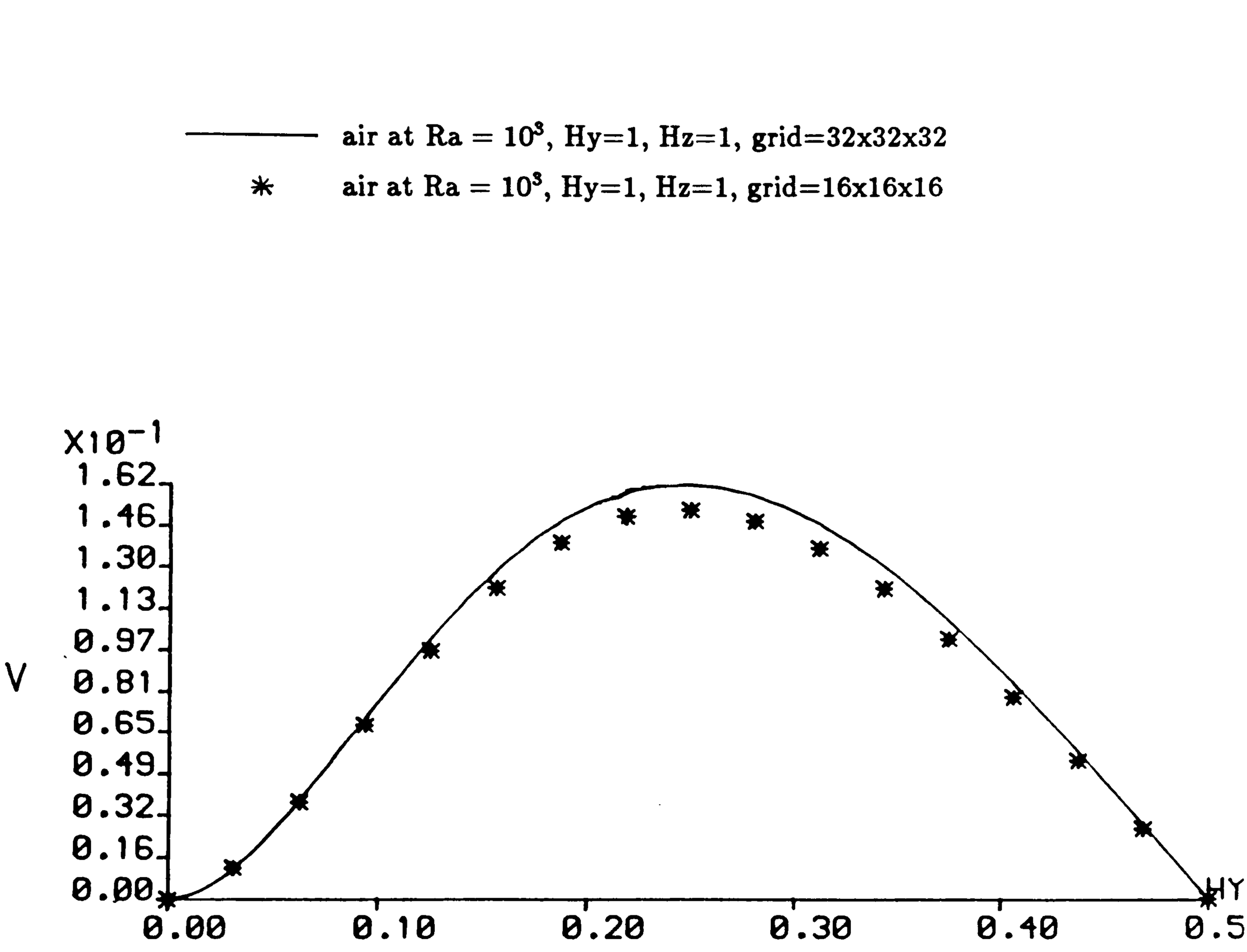

Figure 6.45 Axial-velocity along $(0.5, y, 0.5)$

6.6.2 Results obtained for Air ($\mathbf{Pr} = 0.71$) with $\mathbf{Ra} = 10^5$

The two-dimensional problem at this Rayleigh number produces a secondary flow in the centre of the cavity. This has already been discussed in section 6.3.

Window cavity (1,1,1): length aspect ratio Hy=1.0

For this Rayleigh number, the structure of the three-dimensional flow is complicated by the occurrence of secondary motion. The cross-sectional flow far from the end wall reveals two secondary rotating rolls. Figure 6.46 shows a particle traced from $(.45, .49, .5)$ and is viewed from $(.5, 30, .7)$ which reveals the secondary motion. The flow at this higher Rayleigh number differs from the single roll flow at $\mathrm{Ra} = 10^3$, in that each secondary roll forms a spiral centre for the inward moving flow. Figure 6.47 shows two traced particle paths. One particle is traced from $(.45, .001, 5)$. This particle traverses towards the symmetry plane tracing a spiral around the axes of one of the secondary rolls and then recirculates around both axis of the secondary rolls. It then uncoils near the symmetry plane. The second particle has been traced from $(.95, .4, .5)$. This particle shows the return flow, returning via the boundary layers. In Figure 6.48 a particle has been traced from the point $(.3, .1, .3)$. Here the particle recirculates around the two secondary rolls, uncoiling as it moves towards the symmetry plane, and returns to the end wall via the boundary layers. Figure 6.49 shows a side view of this particle path, viewed from $(.5, .25..5)$.

Figures 6.50, 6.51 and 6.52 are contour plots of the ratio R at planes A, B and C respectively. Figures 6.50 and 6.51 reveal the two inner cores. The maximum R contours in the cross-sectional planes now occur in pairs indicating the existence of the secondary spirals.

Figure 6.53, 6.54 and 6.55 show the isotherms at planes A, B and C respectively. The isotherms near the symmetry plane are much more convective than those near the end wall. The isotherms near the end wall, figure 6.54, clearly show the change in the sign of $\partial\theta/\partial x$ which leads to the generation of the secondary flow. Figure 6.56 is a contour plot of $\partial\theta/\partial y$ in the plane C. In the case of the lower Rayleigh number, $\mathrm{Ra} = 10^3$, only positive $\partial\theta/\partial y$ existed in the upper half and only negative $\partial\theta/\partial y$ existed in the lower half of the cavity. At this higher Rayleigh number weak negative $\partial\theta/\partial y$ exist in the upper half and weak positive $\partial\theta/\partial y$ exist in the lower half of the cavity. These changes in sign of $\partial\theta/\partial y$ along the axial direction are a direct result

of the secondary flow structure. That is, a change in the sign of $\partial\theta/\partial x$ produces a change in sign of $\partial\theta/\partial y$ along y. The maximum $\partial\theta/\partial y$ that occurs in the domain is 0.794.

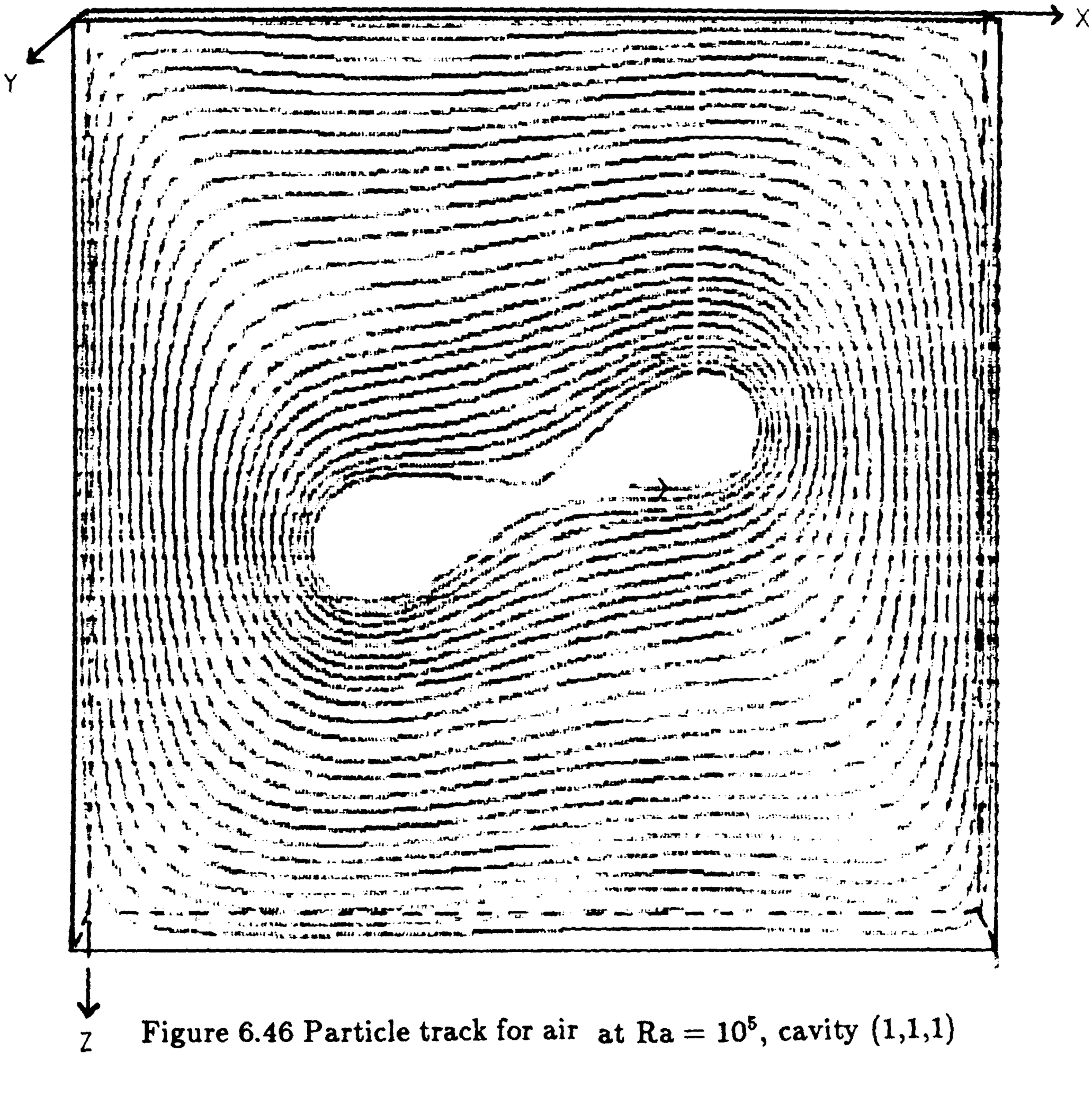

Figure 6.46 Particle track for air at Ra = 10^5, cavity (1,1,1)

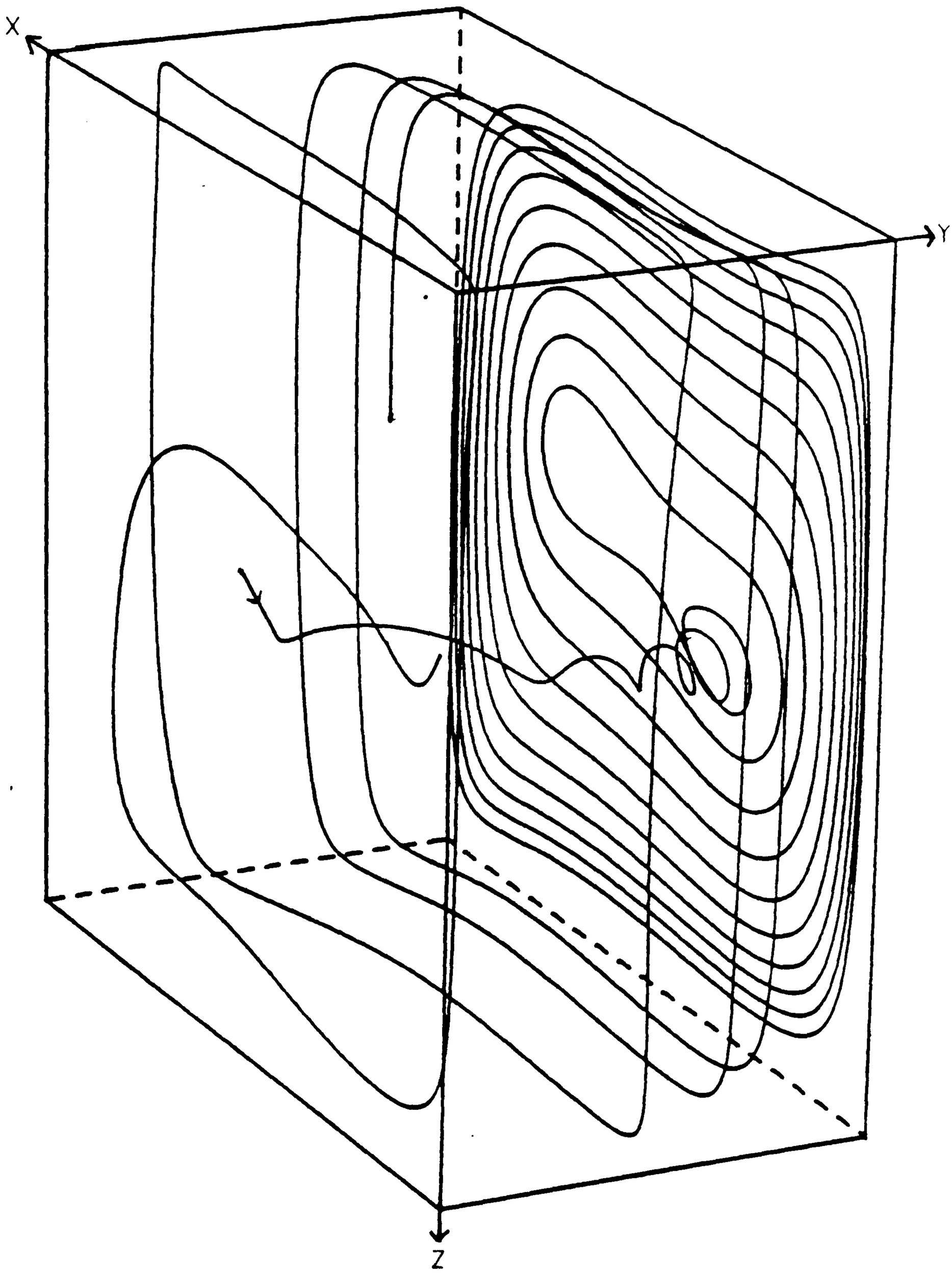

Figure 6.47 Particle track for air at Ra = 10^5, cavity (1,1,1)

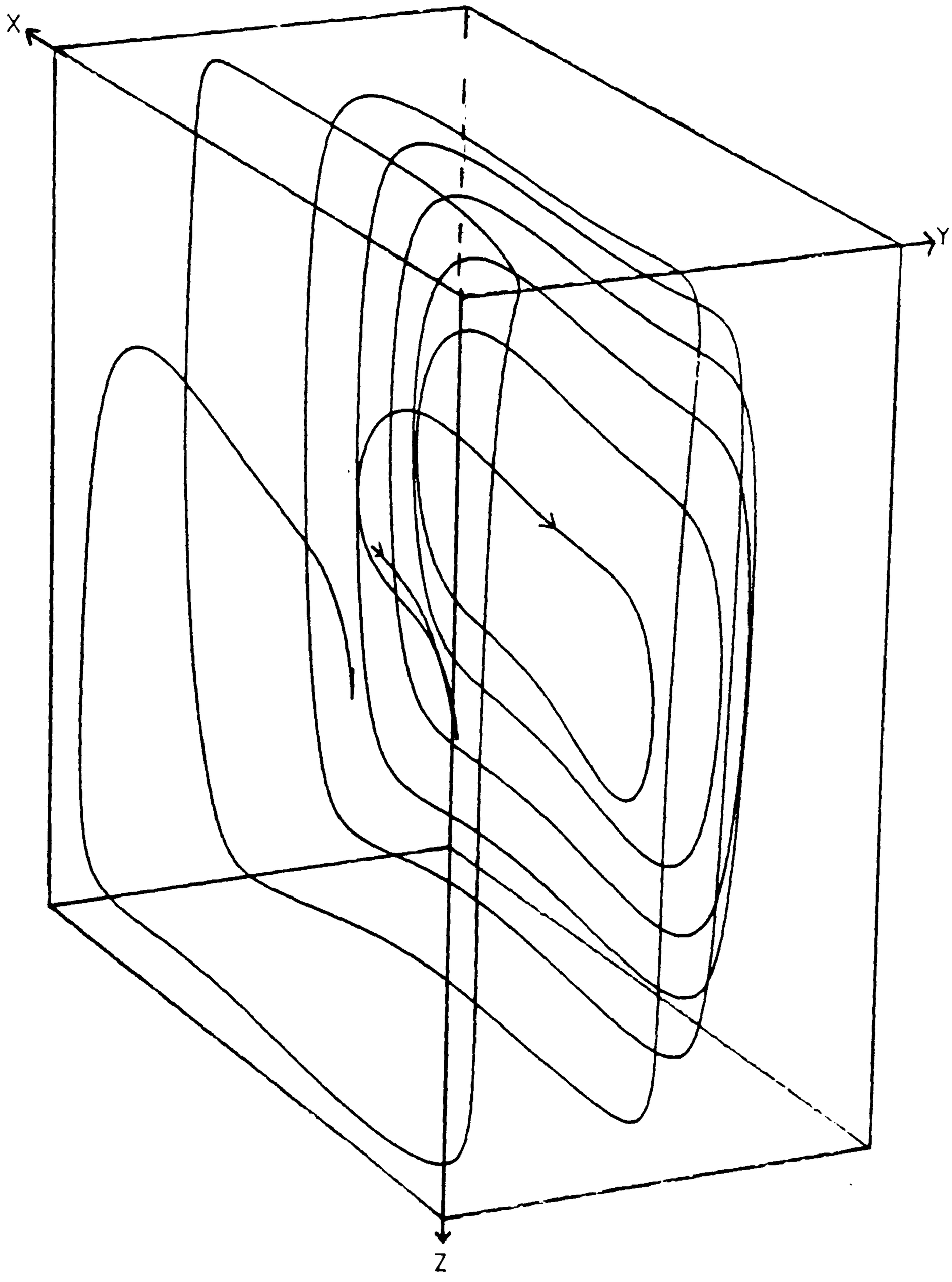

Figure 6.48 Particle track for air at Ra = 10^5, cavity (1,1,1)

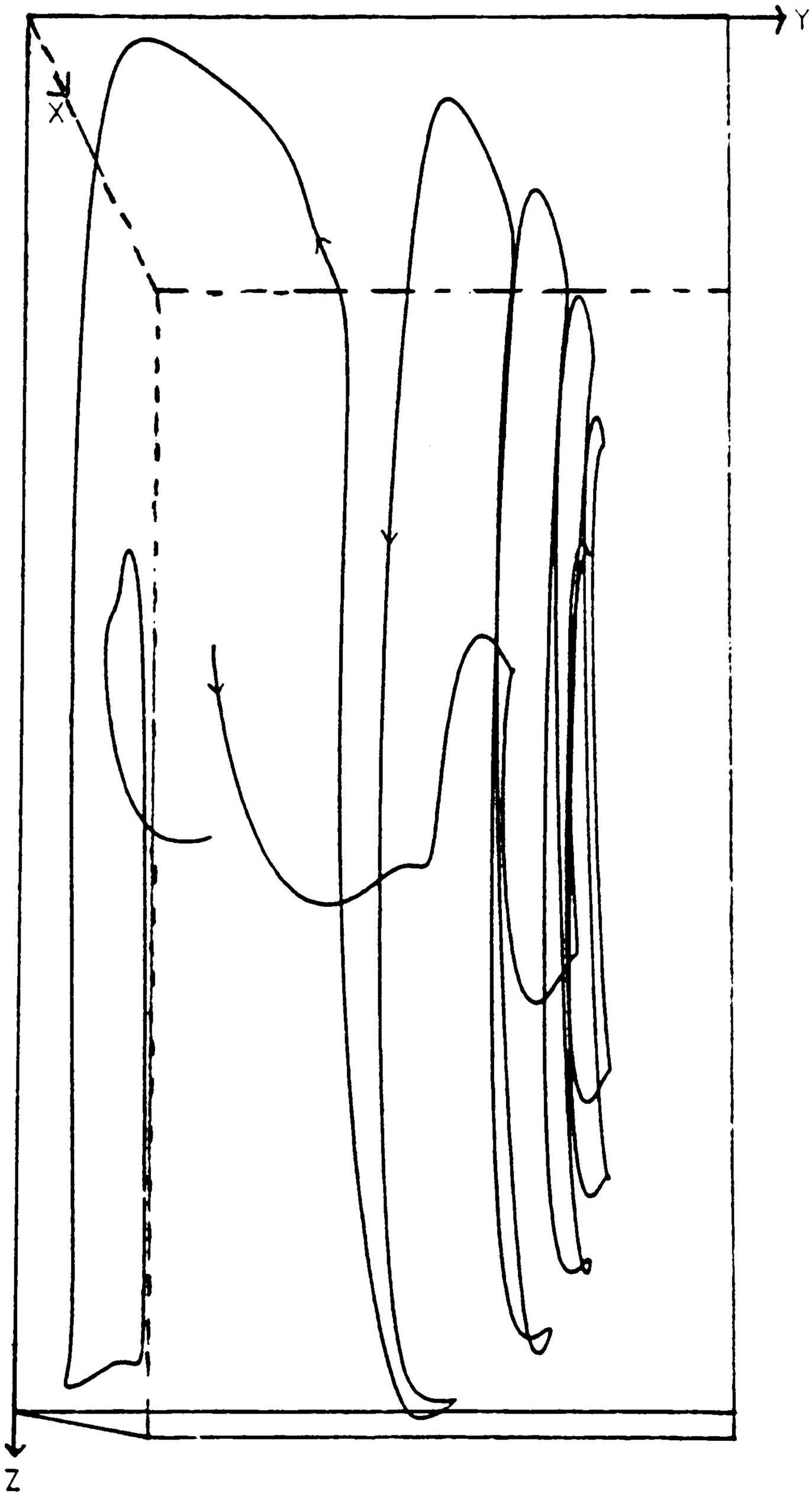

Figure 6.49 Side view of Figure 6.48

Fluid = air, Ra = 10^5, Hy=1, Hz=1, grid=16x16x16

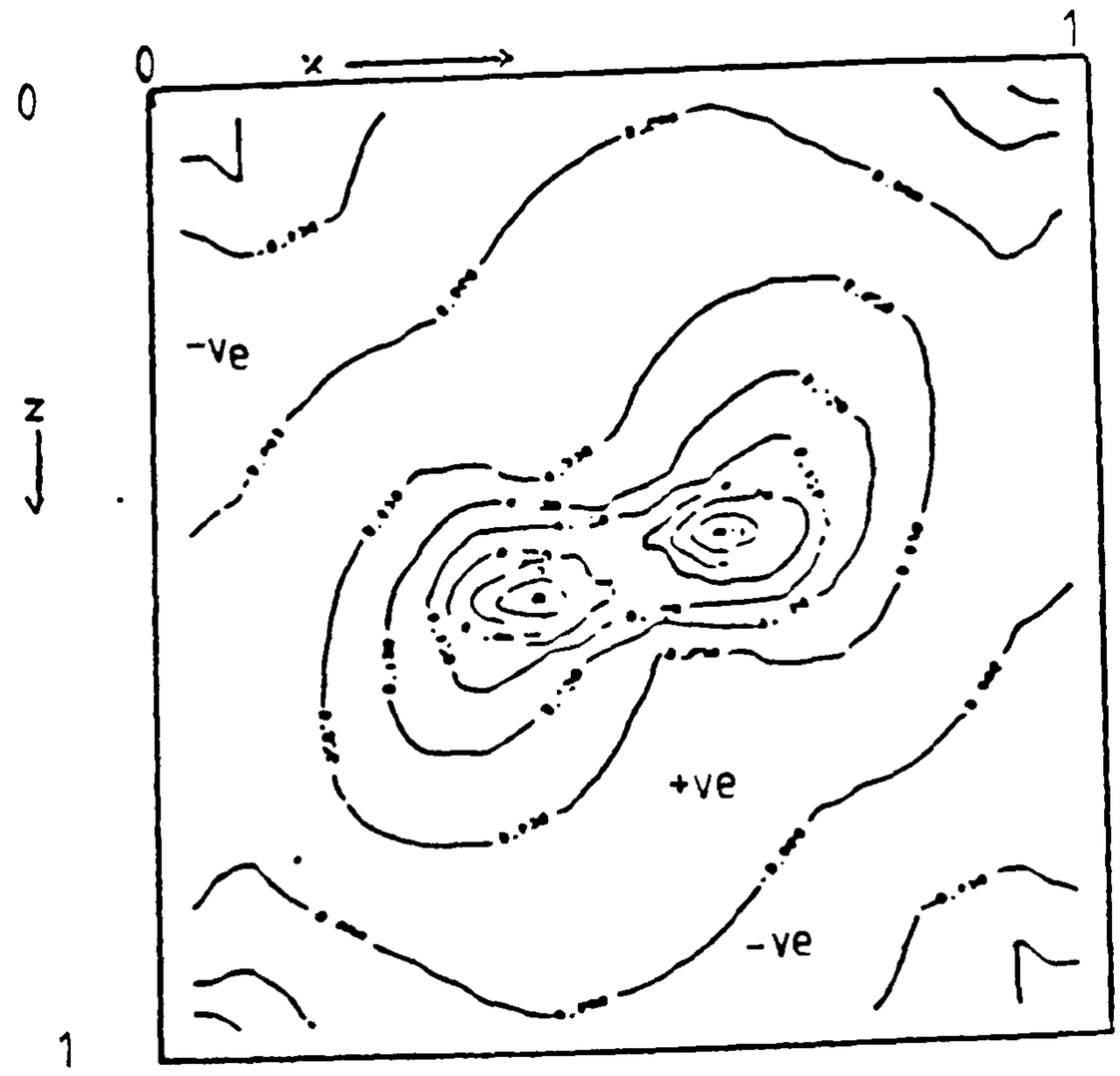

Figure 6.50 Contour plot of ratio R at plane A, near the end wall

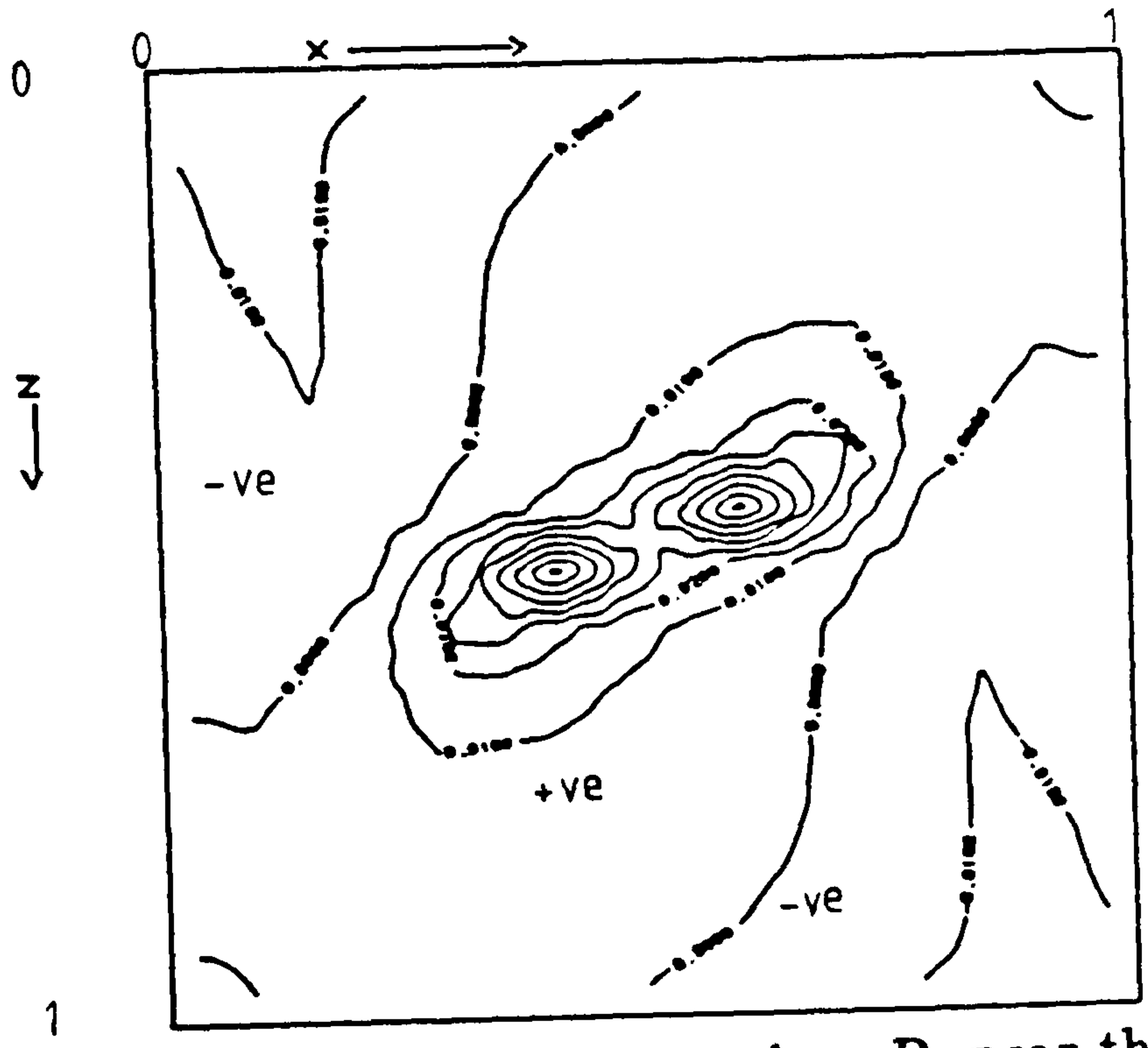

Figure 6.51 Contour plot of ratio R at plane B, near the symmetry plane

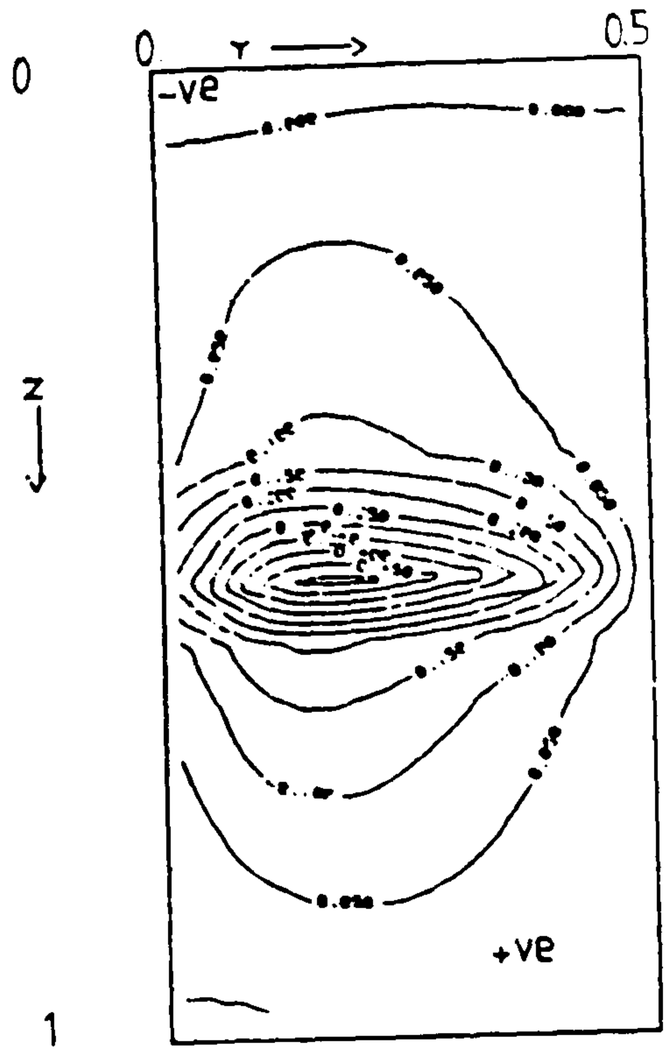

Figure 6.52 Contour plot of ratio R at plane C $(0.5 - hx/2, y, z)$

Fluid = air, Ra = 10^5, Hy=1, Hz=1, grid=16x16x16

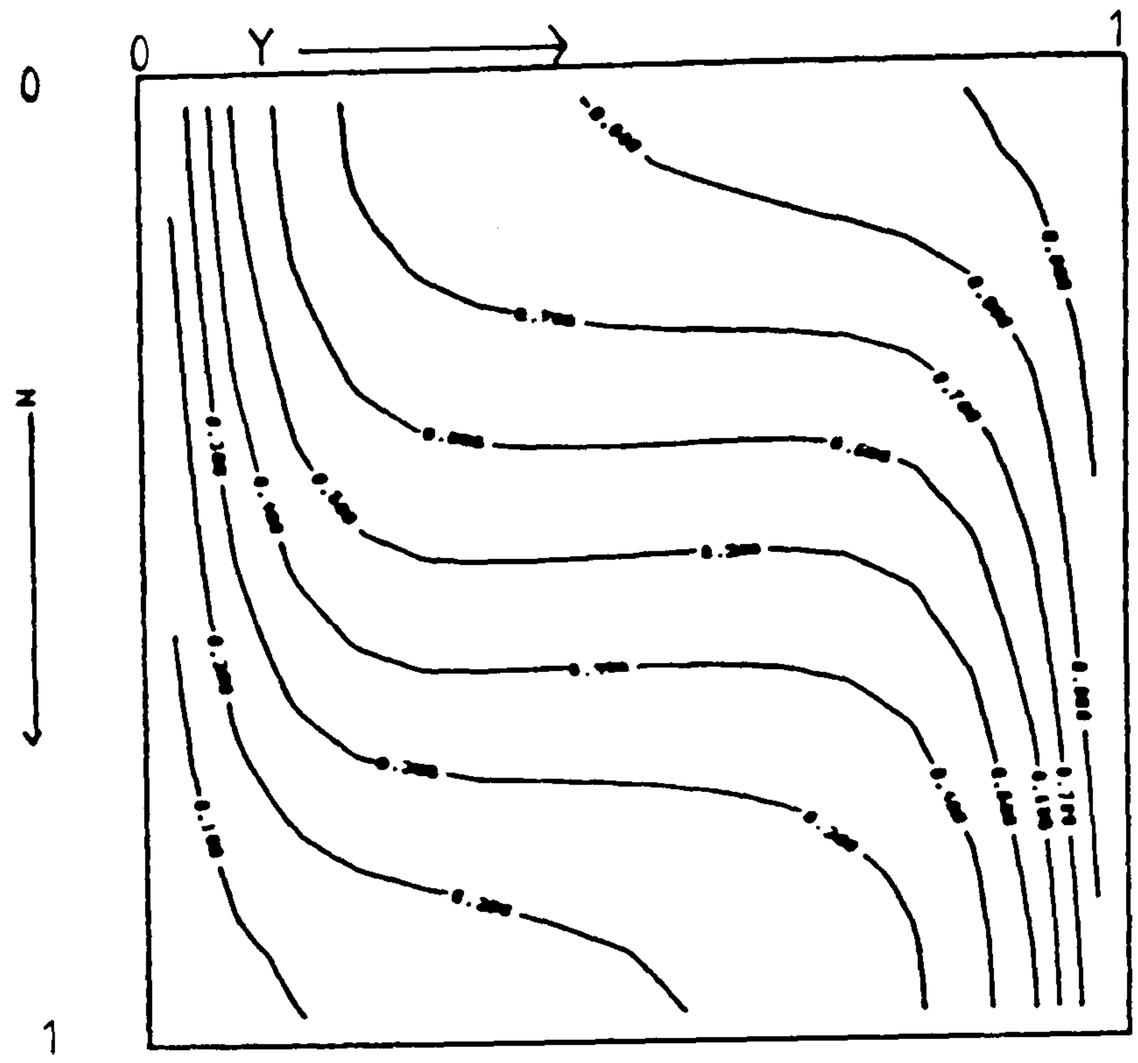

Figure 6.53 Isotherms at plane A, near the end wall

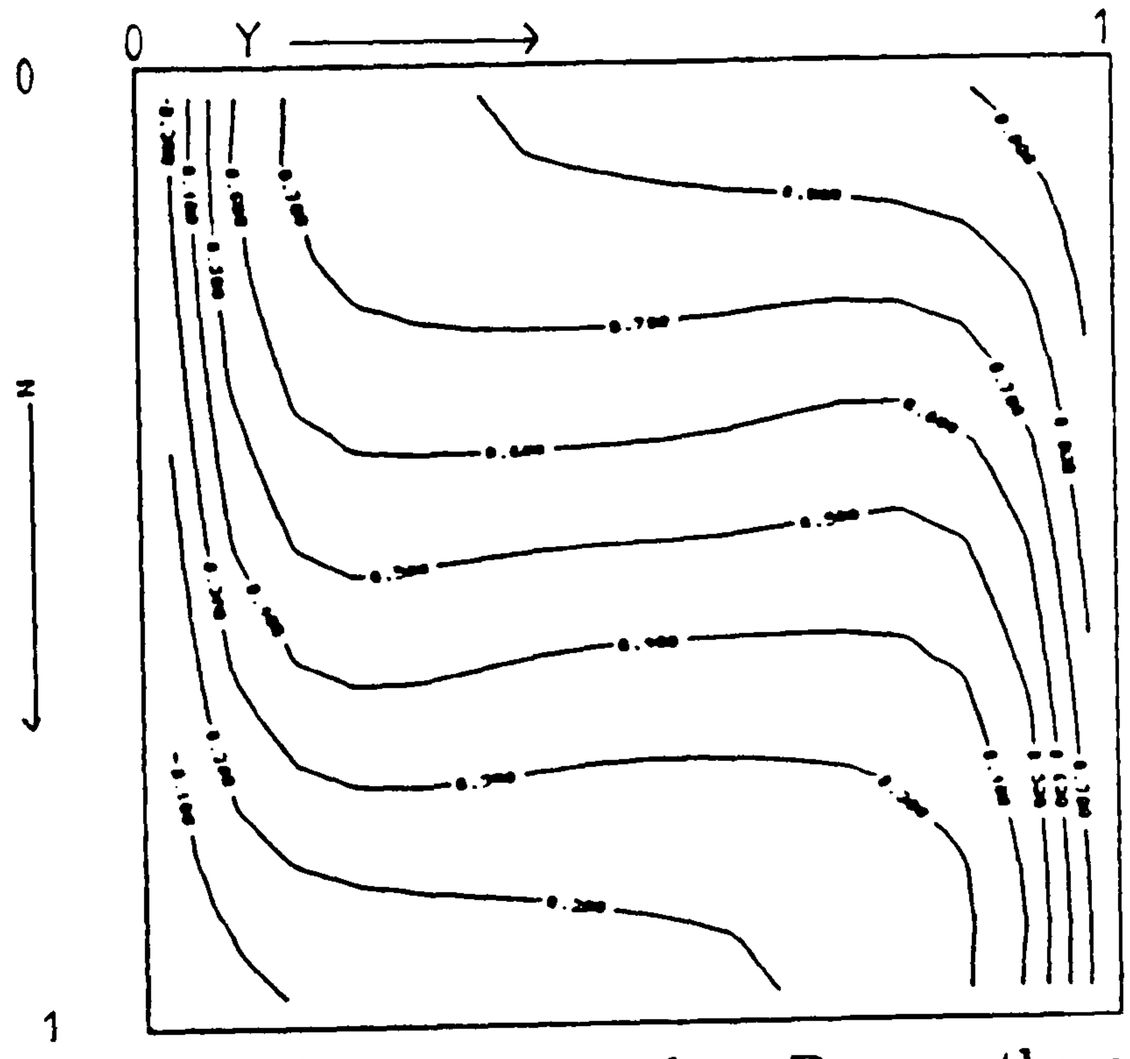

Figure 6.54 Isotherms at plane B, near the symmetry plane

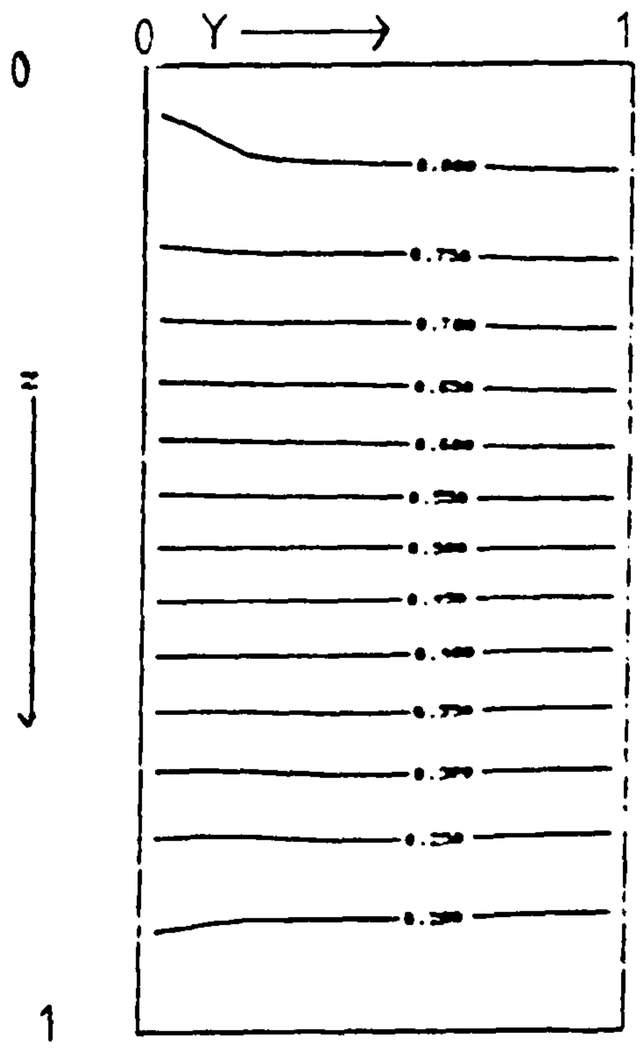

Figure 6.55 Isotherms at plane C, $(0.5 - hx/2, y, z)$

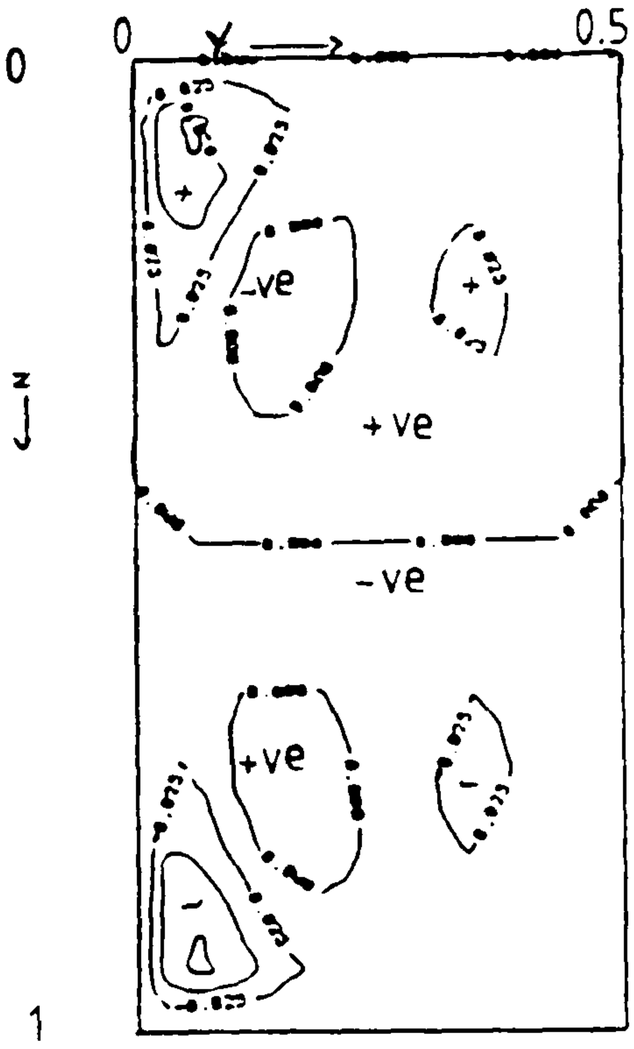

Figure 6.56 $\partial\theta/\partial y$ at plane C, $(0.5 - hx/2, y, z)$

Window cavity (1,2,1): length aspect ratio Hy=2.0

With this length aspect ratio a further complication develops in the flow. The secondary rolls obtained with the length aspect ratio Hy=1.0 are now separated from the symmetry plane by a reverse flow which is illustrated in Figure 6.57. Path1 has been traced from $(.9, .001, .9)$ and represents the forward flow. This particle moves away from the end wall in the inner core, recirculates around the two secondary rolls and returns via the boundary layers towards the end wall. Path2 has been traced from $(.35, .75, .55)$ near the symmetry plane and represents the reverse flow. This particle moves from the symmetry plane towards the end wall in the inner core, recirculates around the two secondary rolls, uncoils and then returns towards the symmetry plane via the boundary layers. Path3 has been started very close to the symmetry plane from $(.35, .95, .55)$. The particle moves slightly towards the end wall, recirculates around the secondary flow, uncoiling and returns towards the symmetry plane. Figure 6.58 is a side view of Figure 6.57 and clearly exhibits the reverse flow.

Figure 6.59, 6.60 and 6.61 are contour plots of the ratio R at the planes A, B and C respectively. Figure 6.59 represents the contour plots of R for the forward flow and shows positive axial velocity in the inner core. Figure 6.60 represents the contour plots of R for the reverse flow and shows negative axial velocity in the inner core. Figure 6.61 exhibits the existence of the forward and reverse flow.

Contour values of R in Figures 6.59 and 6.60 indicate that the reverse axial flow is weaker than the forward axial flow. The forward flow occupies more of the cavity than the reverse flow. The reverse flow penetrates into the region of forward flow, so that the surface separating the two flows is not plane but convex to the end of the cavity.

As before, the forward flow is a result of the inertial end wall effect and the strong $\partial\theta/\partial y$ near the z-boundaries at the end wall. The reverse flow is a result of the convective effects of the secondary flow which generates negative $\partial\theta/\partial y$ in the upper half and positive $\partial\theta/\partial y$ in the lower half of the cavity. That is, it is due to the generation of vorticity by $\partial\theta/\partial y$ near the axis of rotation which acts against the forward flow, see Figure 6.62. The maximum $\partial\theta/\partial y$ over the whole domain is 0.656, smaller than the corresponding value obtained with the shorter cavity, Hy=1.0. The cause of the decrease of $\partial\theta/\partial y$ with this length aspect ratio is discussed in the summary section 6.7.

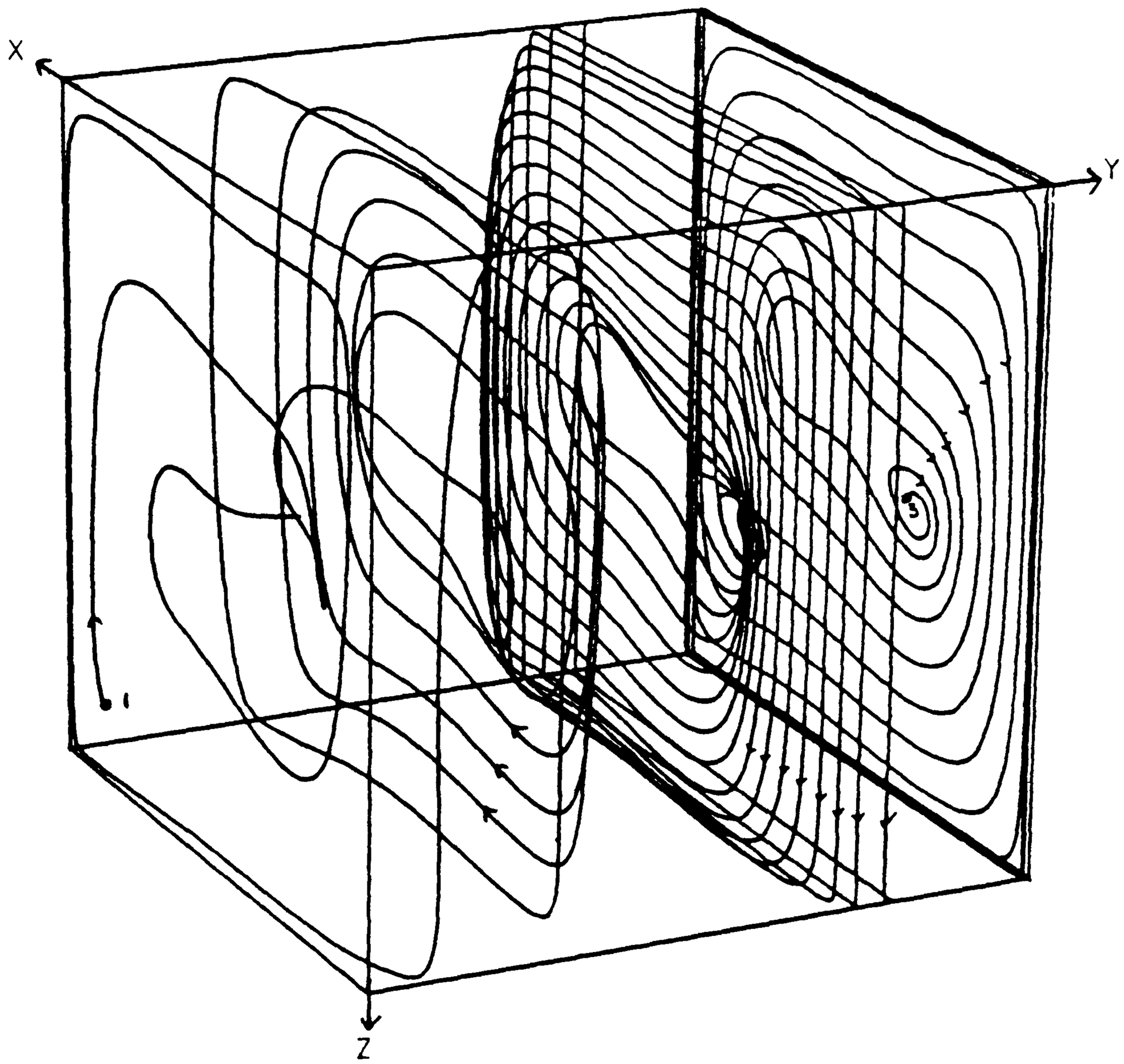

Figure 6.57 Particle tracks for air at Ra = 10^5, cavity (1,2,1)

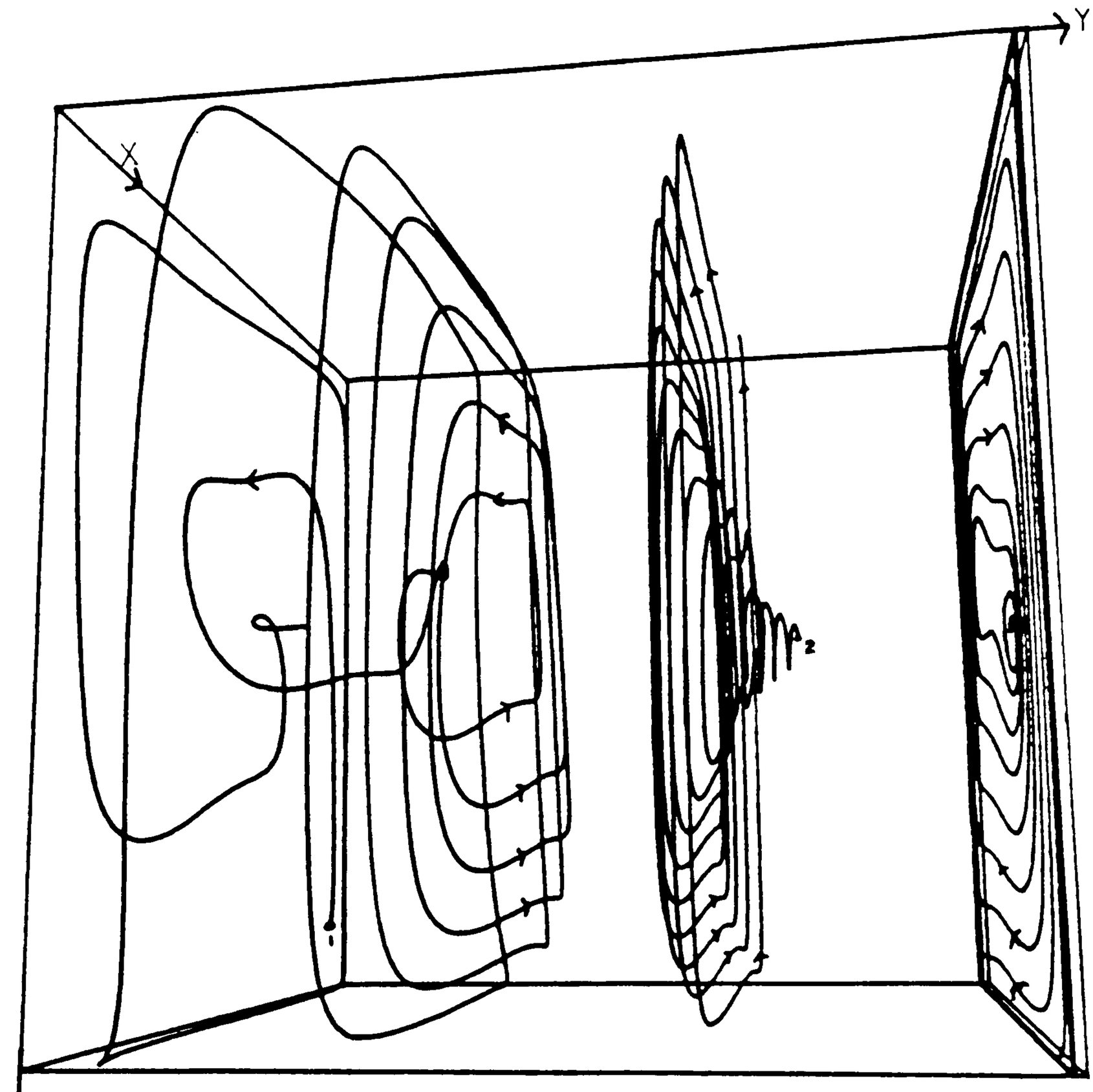

Figure 6.58 Side view of Figure 6.57

Fluid = air, Ra = 10^5, Hy=2, Hz=1, grid=16x16x16

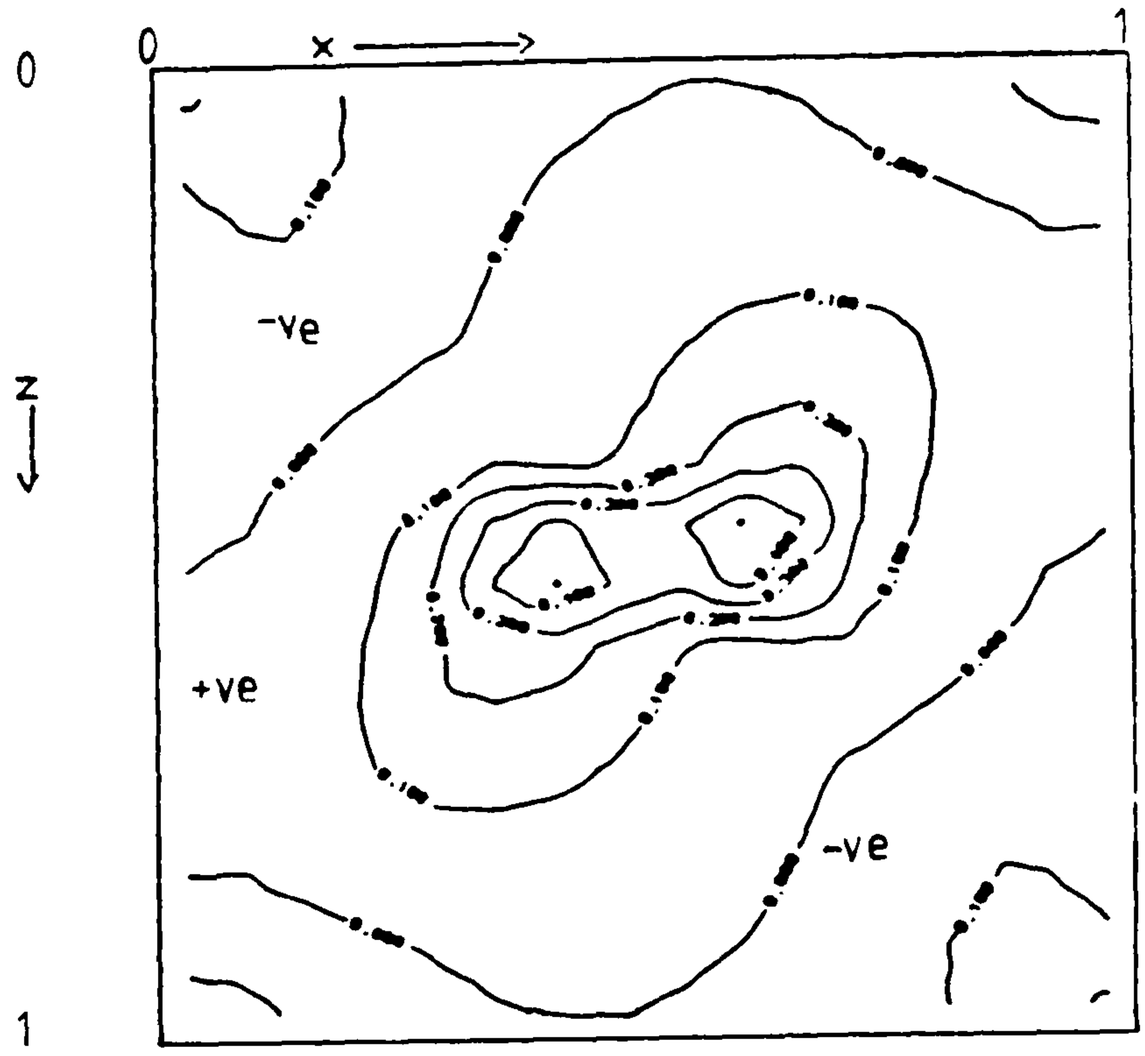

Figure 6.59 Contour plot of ratio R at plane A, near the end wall

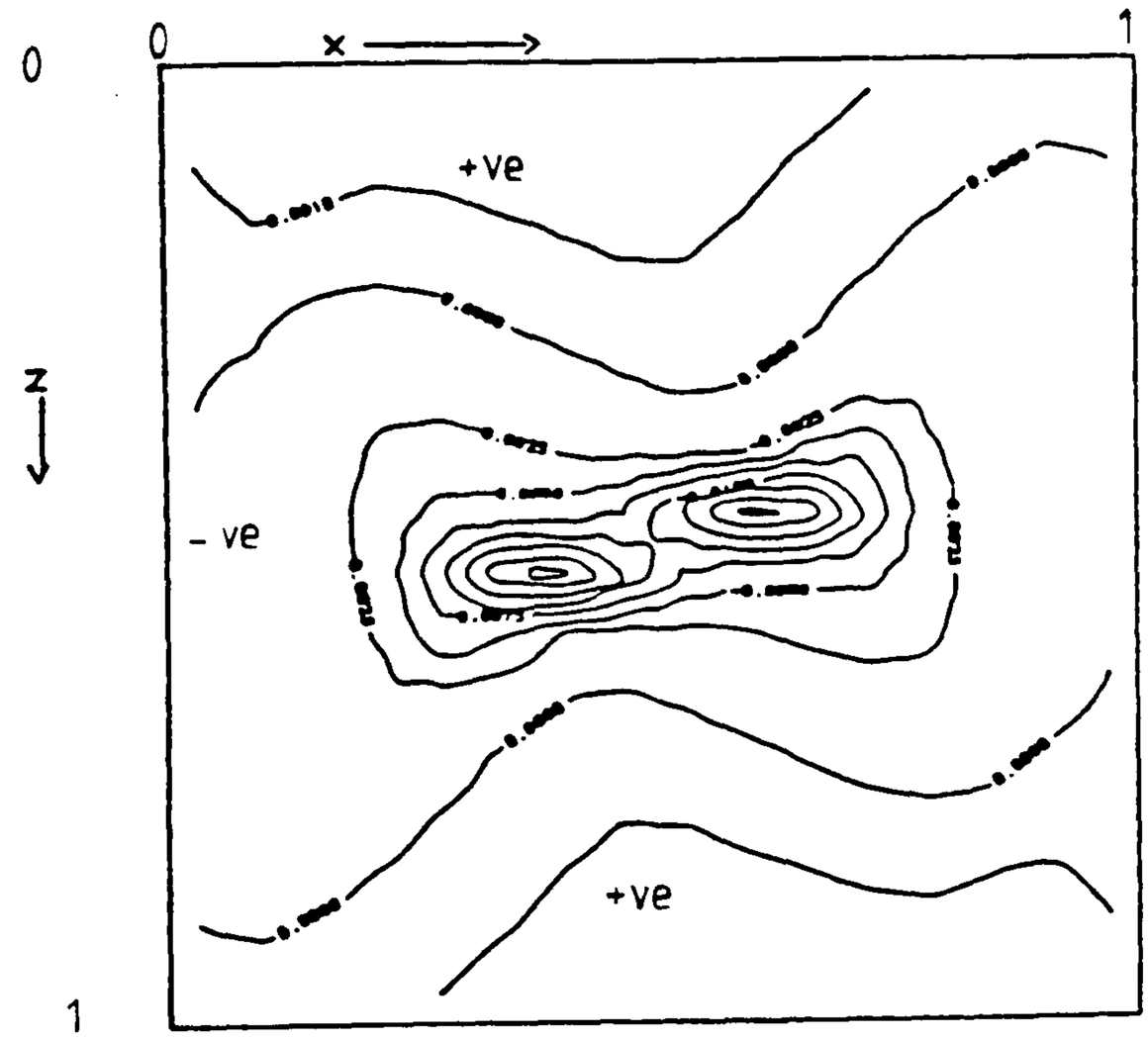

Figure 6.60 Contour plot of ratio R at plane B, near the symmetry plane

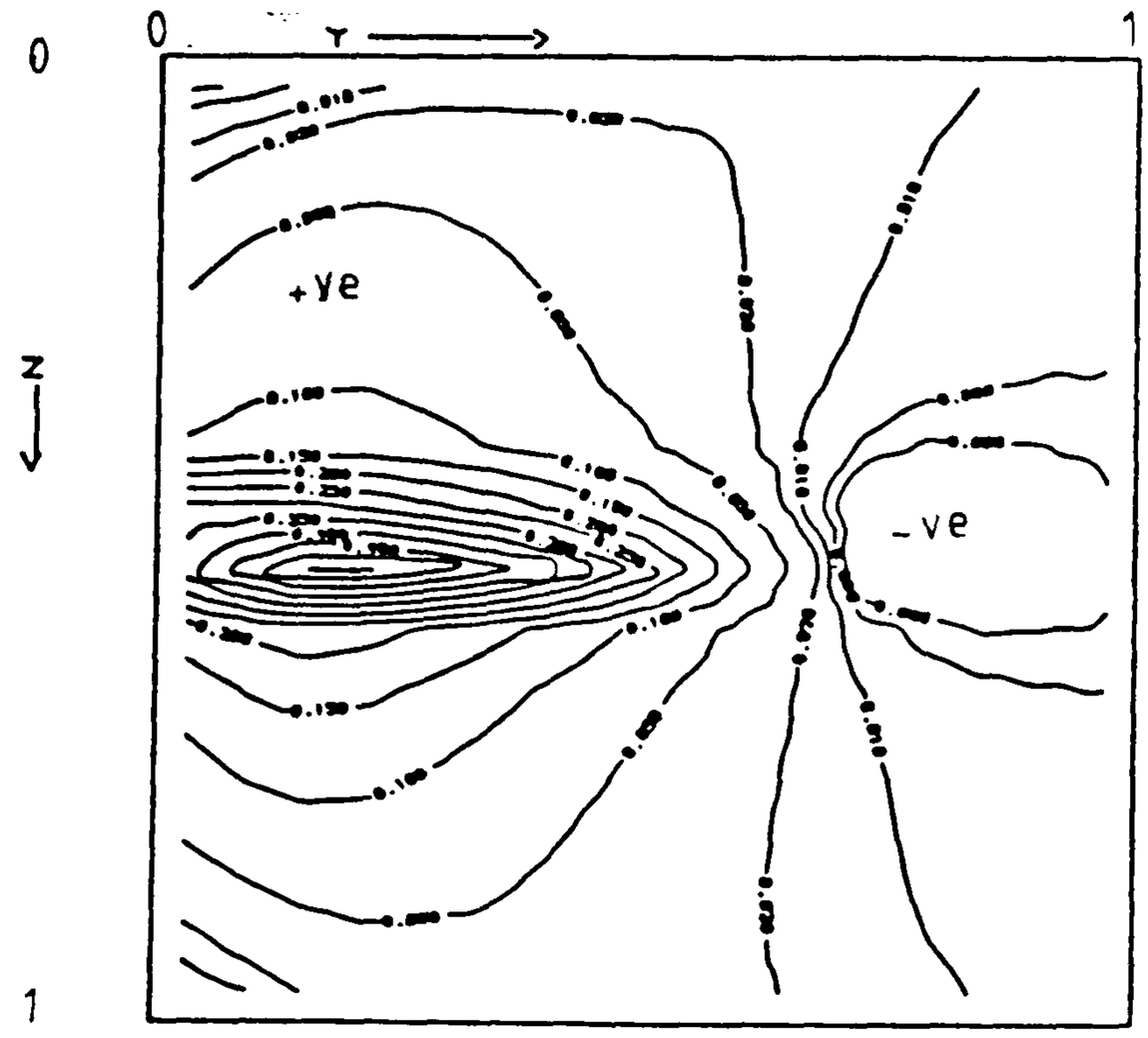

Figure 6.61 Contour plot of ratio R at plane C $(0.5 - hx/2, y, z)$

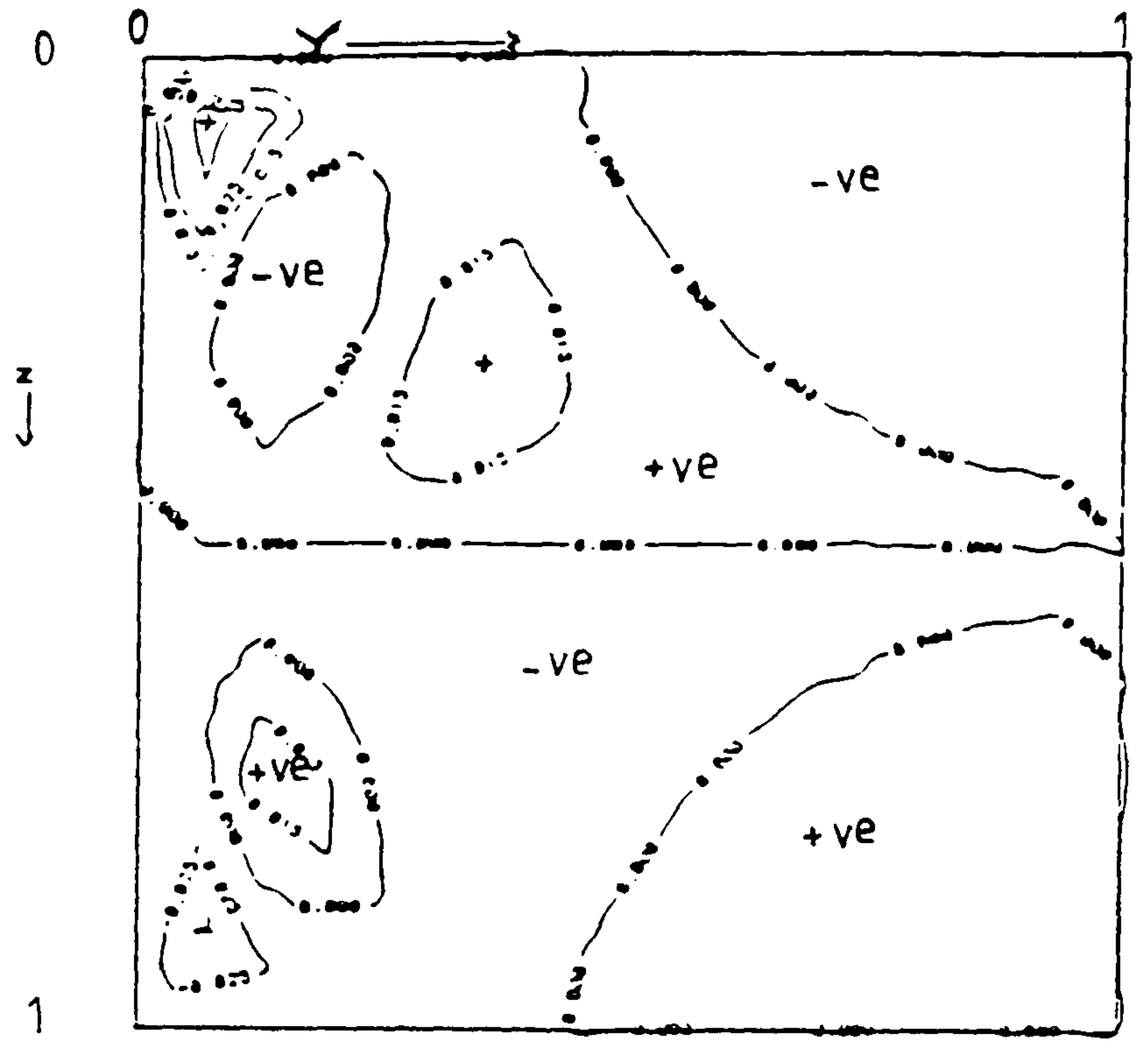

Figure 6.62 $\partial\theta/\partial y$ at plane C, $(0.5 - hx/2, y, z)$

Fluid = air, Ra = 10^5, Hy=1, Hz=1, grid=16x16x16

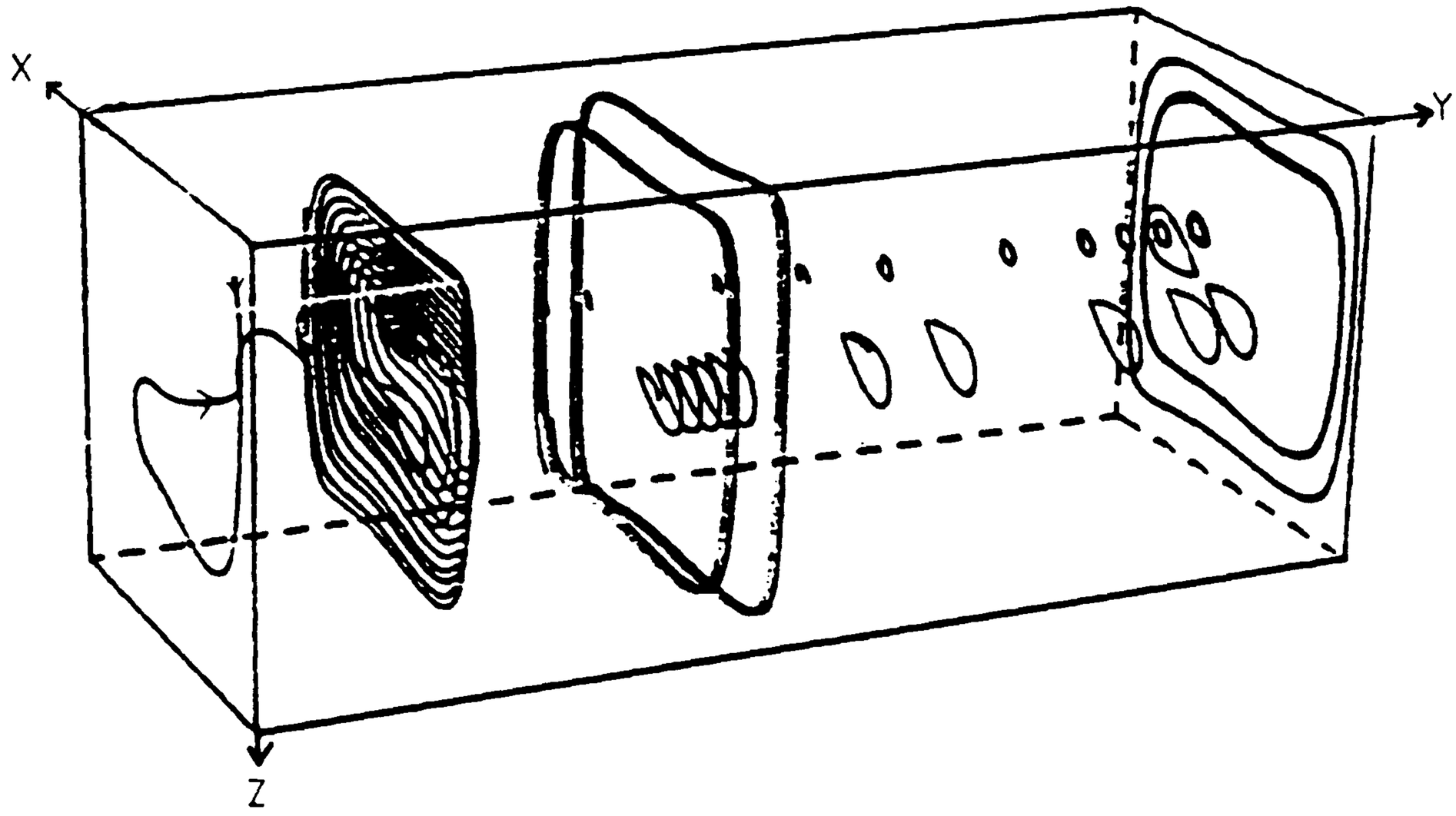

Figure 6.63 Particle tracks for air at Ra = 10^5, cavity (1,5,1), grid = 16x40x16

Window cavity (1,5,1): length aspect ratio Hy=5.0

The fluid flow behaviour in this length aspect ratio cavity is similar to that in the shorter cavity Hy=2.0. A forward recirculating roll occupies the solution cavity near the end wall and a reverse recirculating roll occupies the rest of the solution cavity. Particles path for this cavity have been presented in Figure 6.63. Path1 has been traced from (.1, .001, .1) and shows the extent of the forward flow in the axial direction. The rest of the particle paths describe the reverse flow and show the relative magnitude of the axial motion to the cross-sectional motion.

Figures 6.64, 6.65 and 6.66 are contour plots of the ratio R at planes A, B and C respectively. Figure 6.64 shows the inner core for the forward flow and Figure 6.65 shows the inner core for the reverse flow. Figure 6.66 shows the extent of the regions occupied by the forward and reverse flows. Values of R in the forward flow are in general greater than in the reverse flow, indicating the stronger magnitude of the axial velocity to the cross-sectional velocity in the forward flow compared to that in the reverse flow. The axial flow is weaker in the reverse roll due to the reverse roll being generated only by the thermal effect, which itself is weak. Figure 6.67 is a contour plot of $\partial\theta/\partial y$ at plane C and is very similar to the shorter cavity Hy=2.0. The maximum $\partial\theta/\partial y$ over the whole domain is 0.656.

Fluid = air, Ra = 10^5, Hy=5, Hz=1, grid=16x40x16

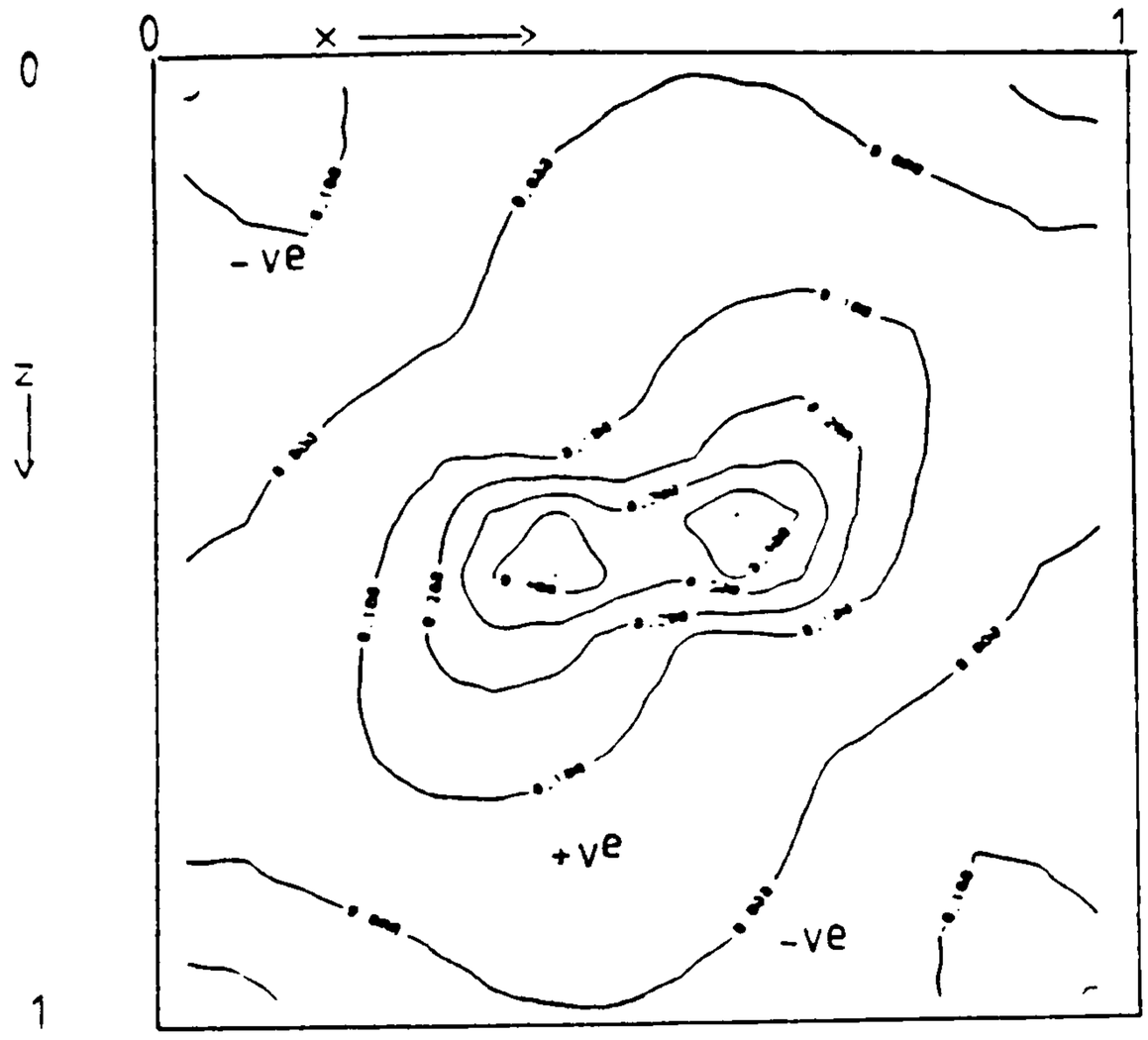

Figure 6.64 Contour plot of ratio R at plane A, near th

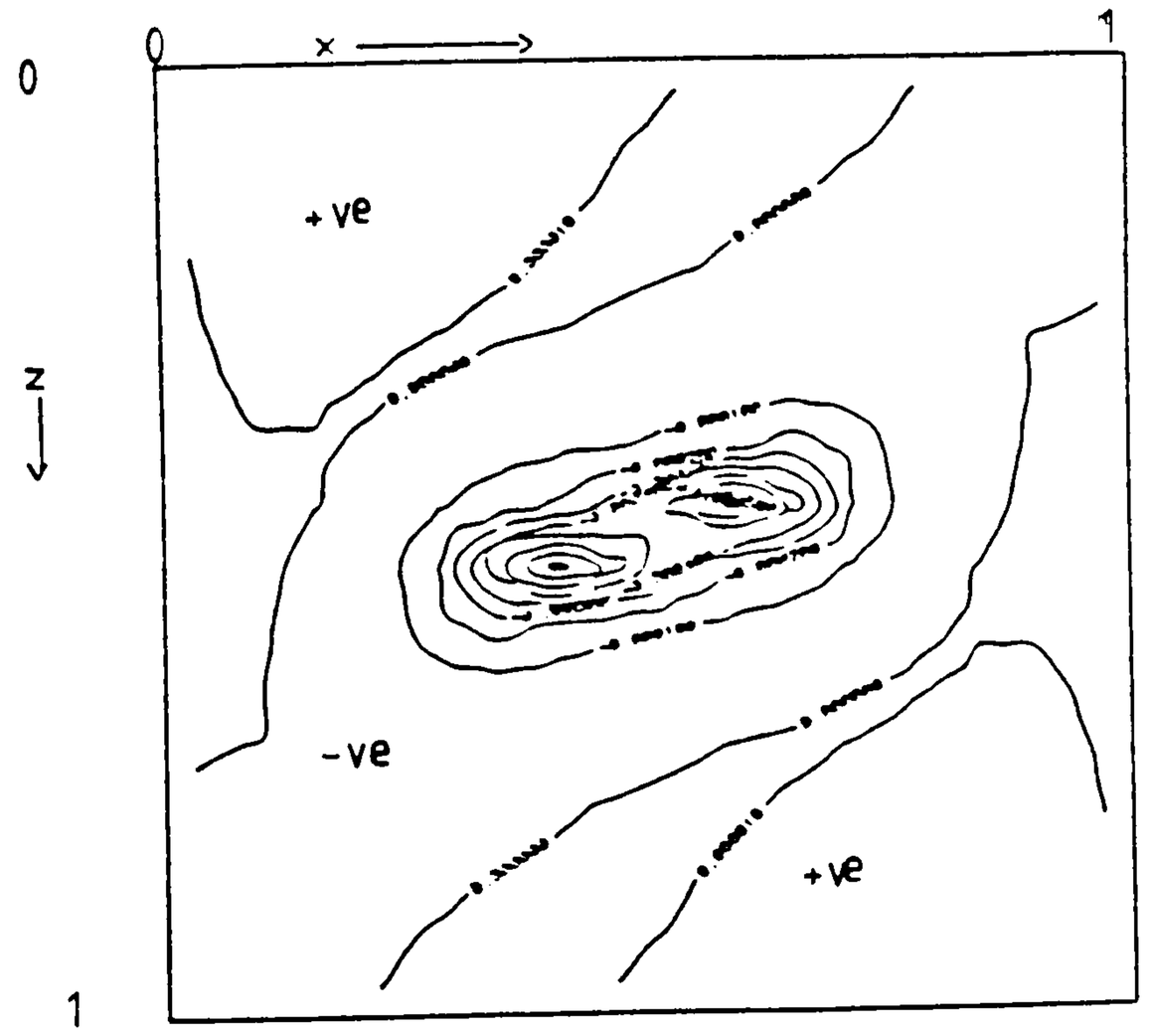

Figure 6.65 Contour plot of ratio R at plane B, near the symmetry plane

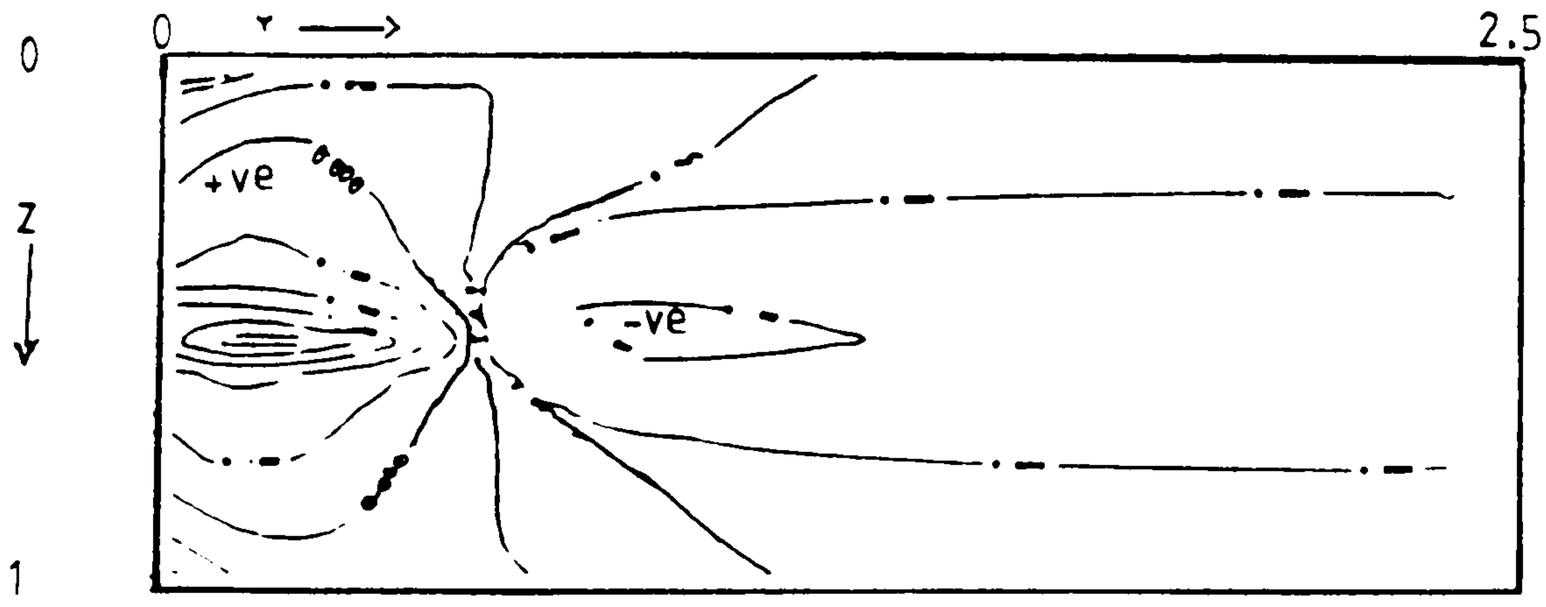

Figure 6.66 Contour plot of ratio R at plane C $(0.5 - hx/2, y, z)$

Figures 6.68, 6.69 and 6.70 are streamlines at the symmetry plane for Hy=1, 2 and 5, they all exhibit the secondary flow clearly. The maximum ψ occurring in Hy=1, 2 and 5 is 12.0, 11.0 and 11.0 respectively. The reason for the longer cavities maximum ψ being smaller than that of the shorter cavity is because the strong forward roll in the longer cavities can no longer contribute to the convection of heat near the symmetry plane as the region near the symmetry plane is now occupied by a weak reverse roll.

The axial velocity along the centre line (.5,y,.5) has been plotted for the cavities with the length aspect ratios Hy=1.0, 2.0 and 5.0, Figure 6.71. The axial velocity has only been plotted in one half of the cavity due to the symmetry of the problem. The graphs show that the reverse flow develops for Hy $>$ 1.0 and the reverse flow in the cavity with Hy=2.0 is weaker than that for Hy=5.0. An interesting feature of the velocity profile is that the peak axial velocity along the centre line in the forward flow is slightly greater for Hy=2.0 than Hy=5.0. This implies that the vorticity opposing the forward flow with Hy=5.0 are greater than those obtained with Hy=2.0. The reduction in the end wall effect as Hy increases from two upwards can also be seen by the fact that the forward flow with Hy=2.0 penetrates the axial direction more than with Hy=5.0. The reverse flow with Hy=2.0 starts at about y=0.7 and with Hy=5.0 at about y=0.6. The axial flow is again restricted in the shorter cavity.

Mallinson and de Vahl Davis [39] for air with Ra $= 5 \times 10^5$ found that when the reverse flow is established the penetration of the forward flow is independent of Hy and that the forward flow penetrates to about y=0.6 for Hy=2 and 5. Mallinson and de Vahl Davis's results are for Ra $= 5 \times 10^5$ when the secondary flow is well established whereas Ra $= 10^5$ appears to be near the critical value of secondary flow development. Note no two-dimensional flow exists for cavities with length aspect ratio Hy $\leq$ 5.0.

Fluid = air, Ra = 10^6, Hy=5, Hz=1

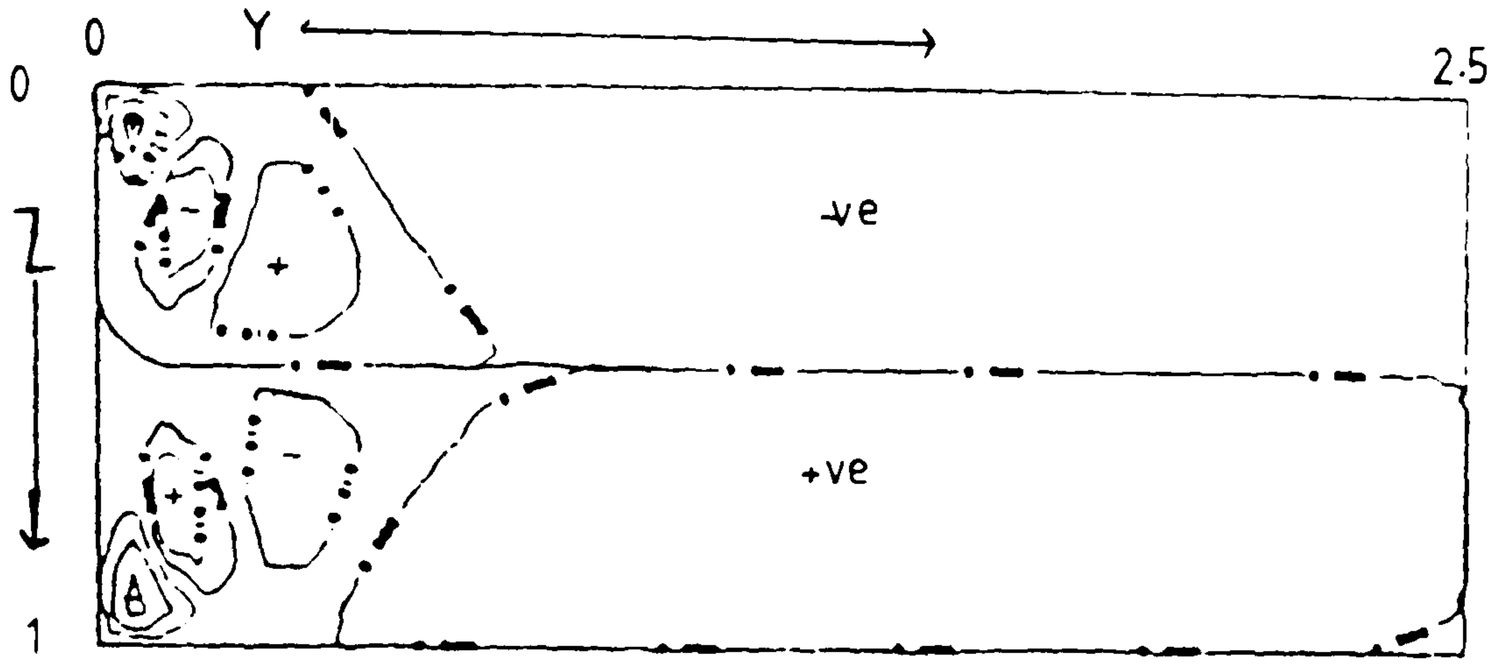

Figure 6.67 $\partial\theta/\partial y$ at plane C, $(0.5 - hx/2, y, z)$

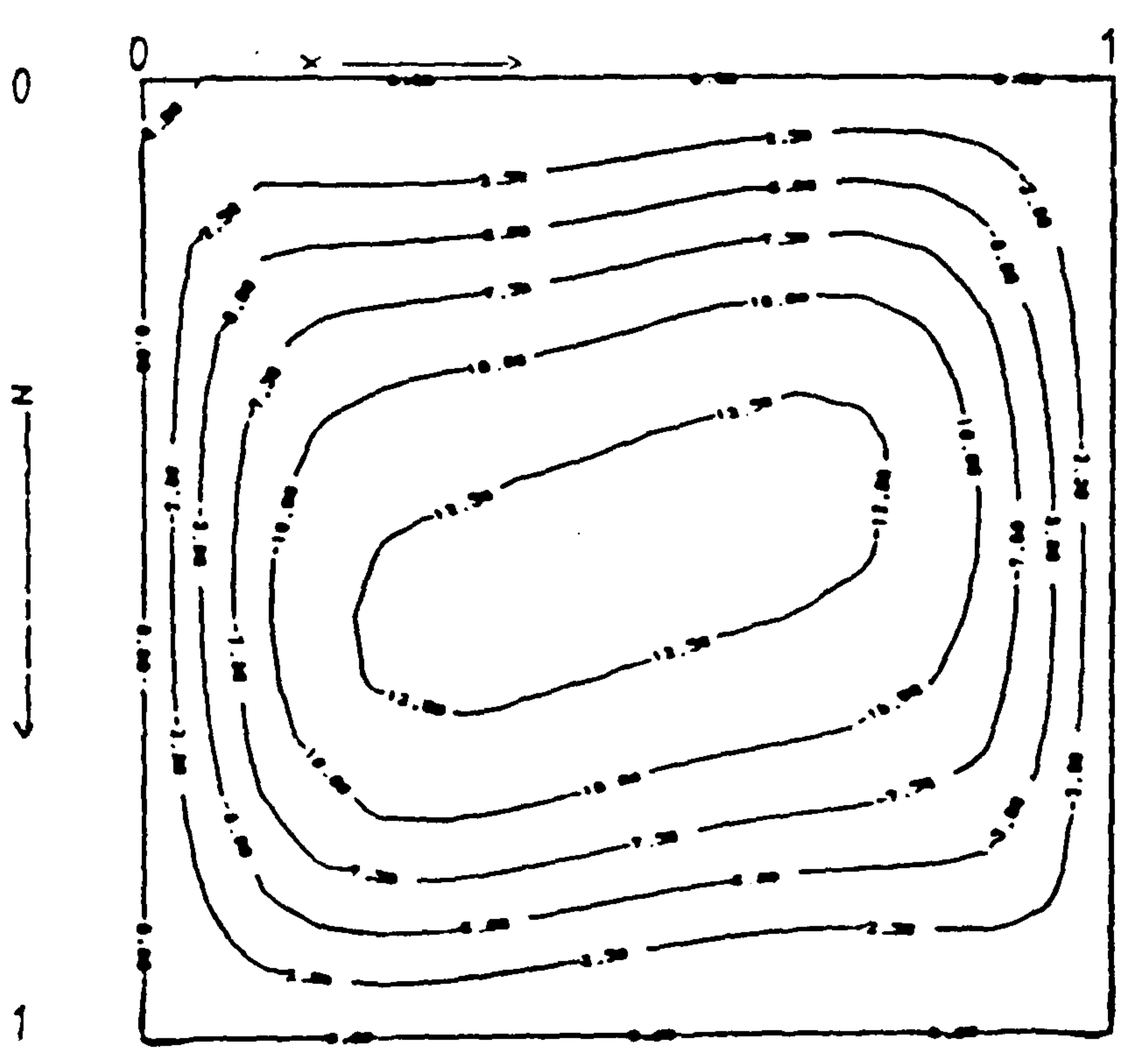

Figure 6.68 Streamlines near the symmetry plane, Hy=1

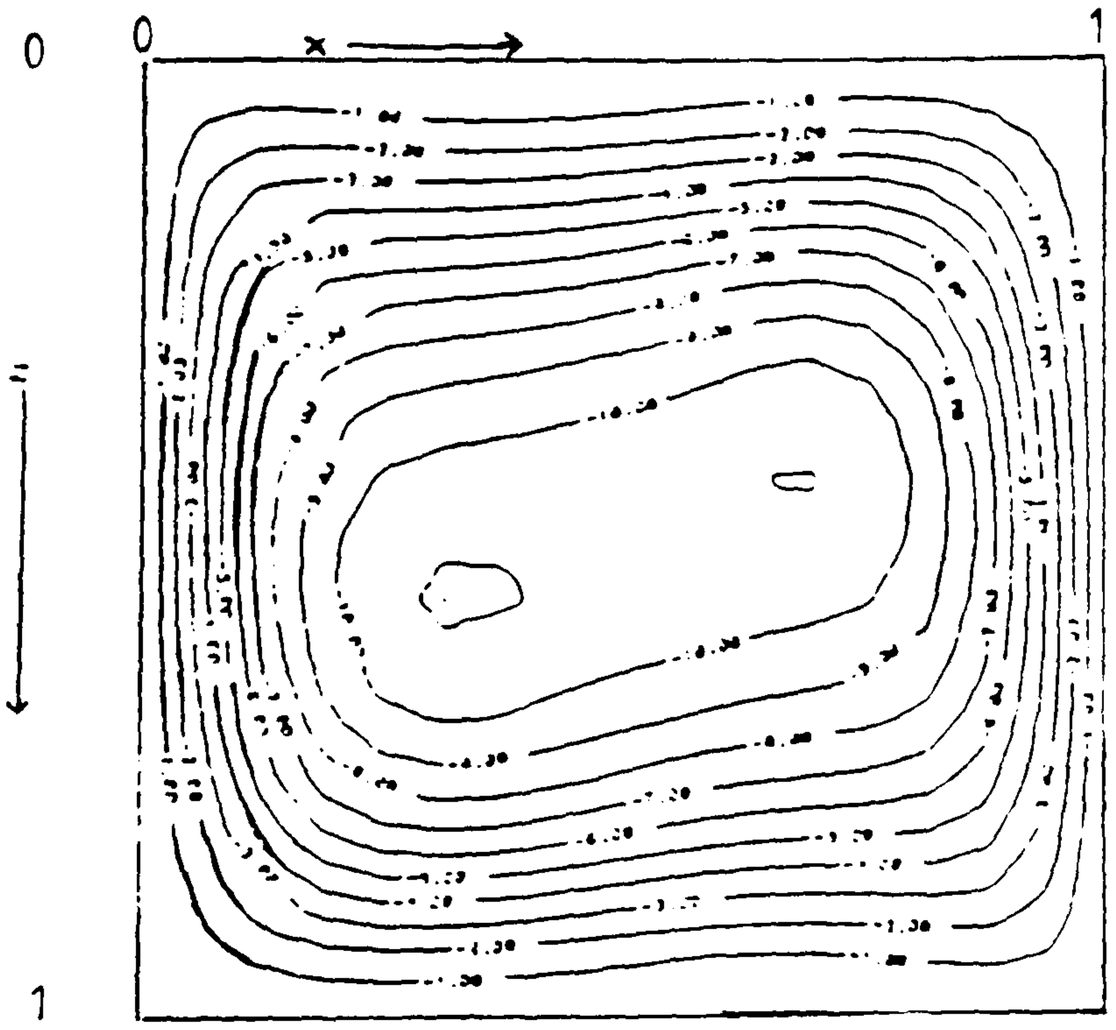

Figure 6.69 Streamlines near the symmetry plane, Hy=2

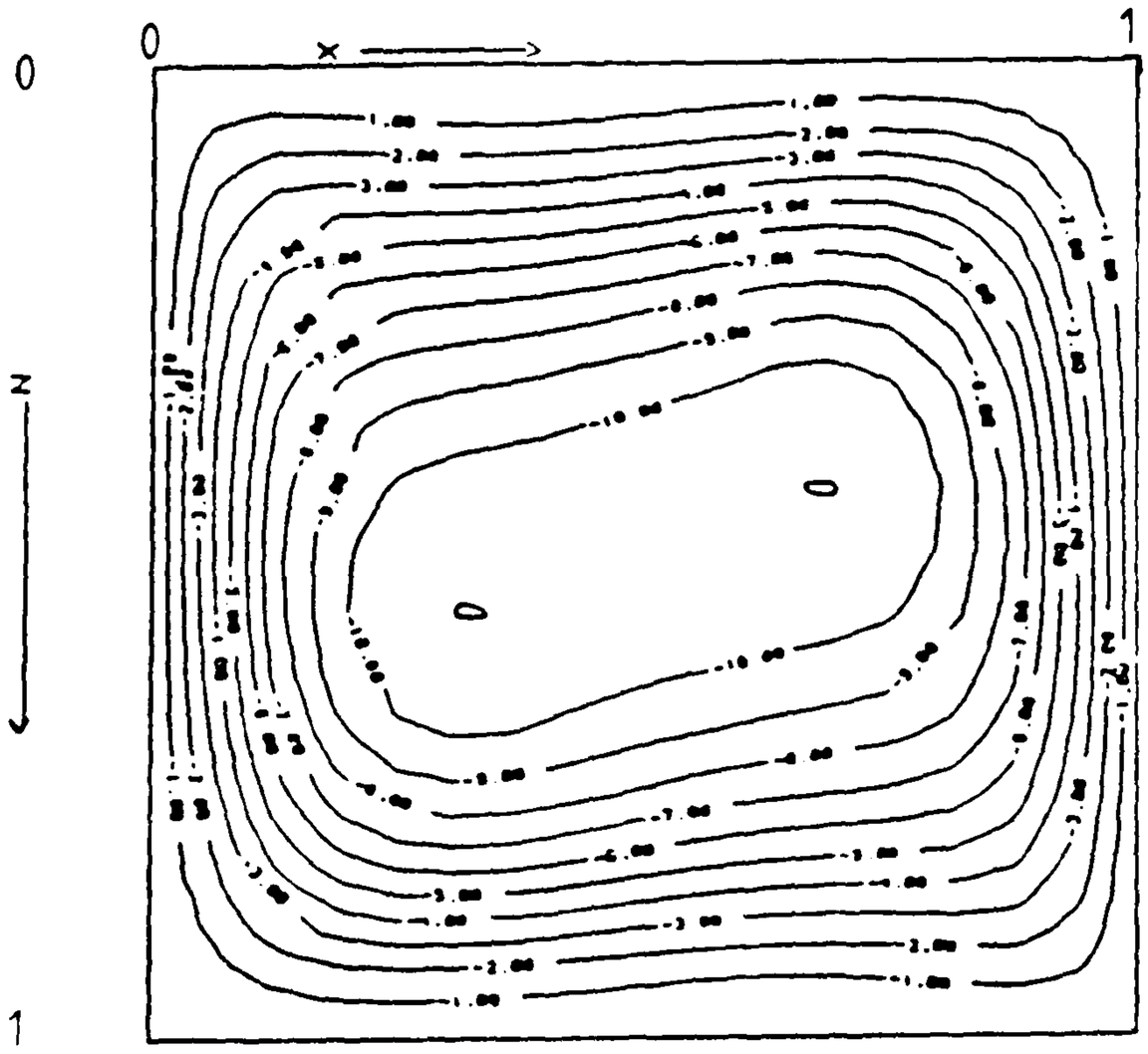

Figure 6.70 Streamlines near the symmetry plane, Hy=5

Graph A: air at Ra = 10^5, Hy=1, Hz=1

Graph B: air at Ra = 10^5, Hy=2, Hz=1

Graph C: air at Ra = 10^5, Hy=5, Hz=1

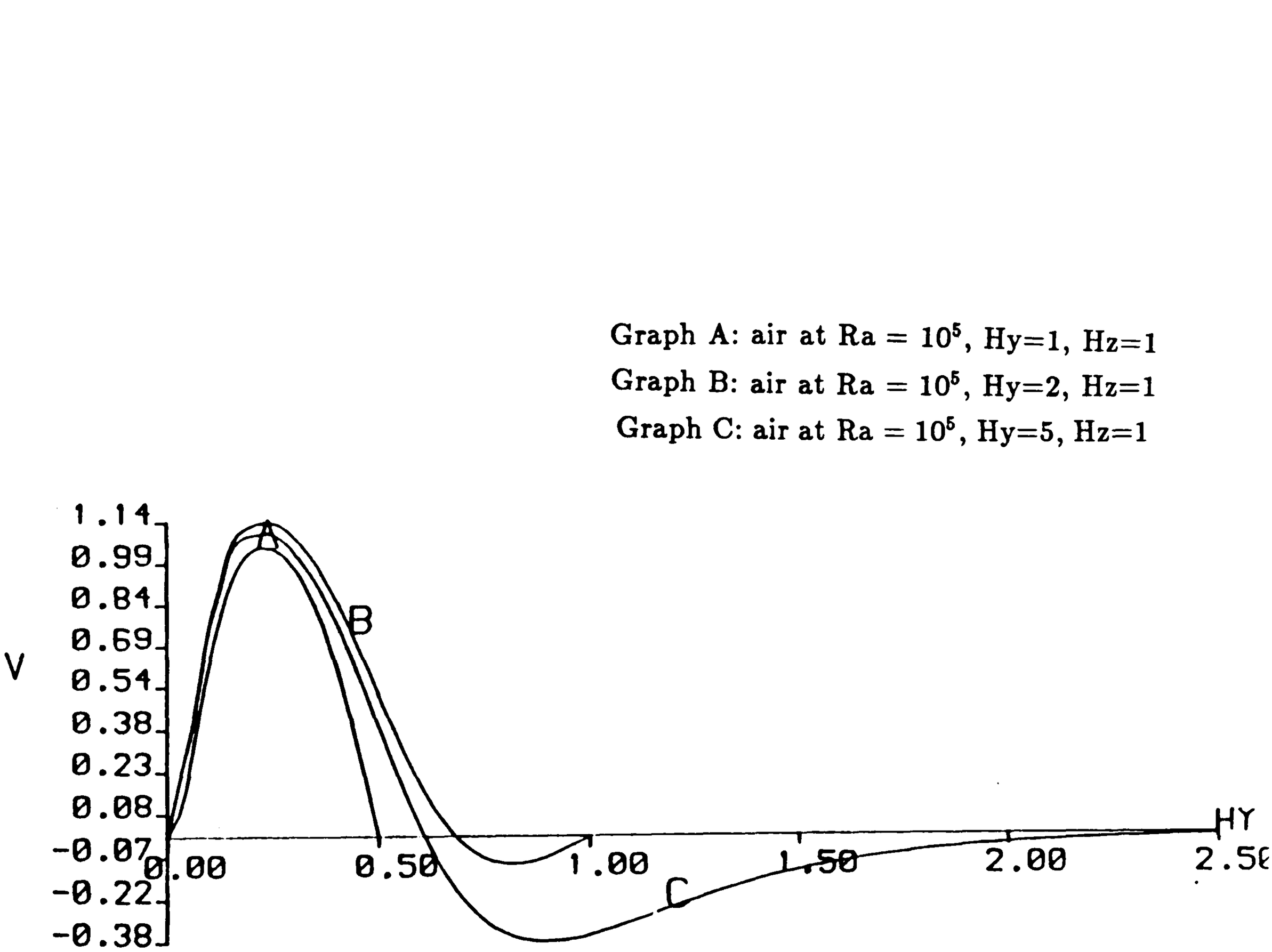

Figure 6.71 Axial-velocity along $(0.5, y, 0.5)$

6.6.3 Cerrobase ($\mathbf{Pr} = 0.035$) with $\mathbf{Ra} = 10^3$

Window cavity (1,1,1): length aspect ratio Hy=1.0

A single forward recirculating roll describes the flow in this cavity with cerrobase. In Figure 6.72 a single particle path has been traced from (.45, .01, .5). The particle takes about two to three revolutions about the centre line to traverse from the end wall to near the symmetry plane and about one to two revolutions to return to the end wall. This indicates the presence of strong axial velocities in the inner and outer cores. The flow pattern obtained with cerrobase is radically different from those obtained with air at the lower Rayleigh number.

Figures 6.73, 6.74 and 6.75 are contour plots of R at planes A, B and C respectively. These figures show that the turning points of the particles with respect to the axial direction lie on a cylindrical surface. Also it should be noted that there are no positive R contours attached to the side walls unlike the case with air. Changes in the sign of $\partial\theta/\partial y$ do exist near the side walls as they did with air but the vorticity generated is not strong enough to overcome the return flow in the boundary layers. This suppresses the undulations in the axial directions as seen with air.

Figures 6.76, 6.77 and 6.78 represent the velocity vectors at planes A, B and C respectively. The cross-sectional velocity with cerrobase near the end wall is directed more towards the centre of the cross-section and near the symmetry plane more towards the side walls than with air at the respective positions. The axial flow compared to the cross-sectional flow is stronger with cerrobase than with air. This can be seen by comparing the velocity vectors near the plane C for air and cerrobase, Figure 6.14 against Figure 6.77, and comparing R contours Figures 6.6 and 6.7 against 6.73 and 6.74 respectively. This behaviour of the fluid is due to the low Prandtl number fluid, cerrobase, having lower effective viscosity (greater inertia) than the moderate Prandtl number fluid, air. Figures 6.79, 6.80 and 6.81 show the isotherms at planes A, B and C respectively. The overall thermal solution for cerrobase is more conductive than that obtained with air. The axial temperature gradients are not as large as those for air, Figure 6.82. The maximum $\partial\theta/\partial y$ is 0.0679 which is about 33% smaller than that obtained with air. This implies the vorticity generated by the axial temperature gradients for cerrobase is not as strong as that generated by air. Thus the thermal end effect with cerrobase is not as large as that with air. Since corresponding values of R indicate that the overall end wall effect is greater with cerrobase than with air,

then the smaller thermal end effect with cerrobase must imply that the inertial end effect dominates with cerrobase and is much greater than that for air.

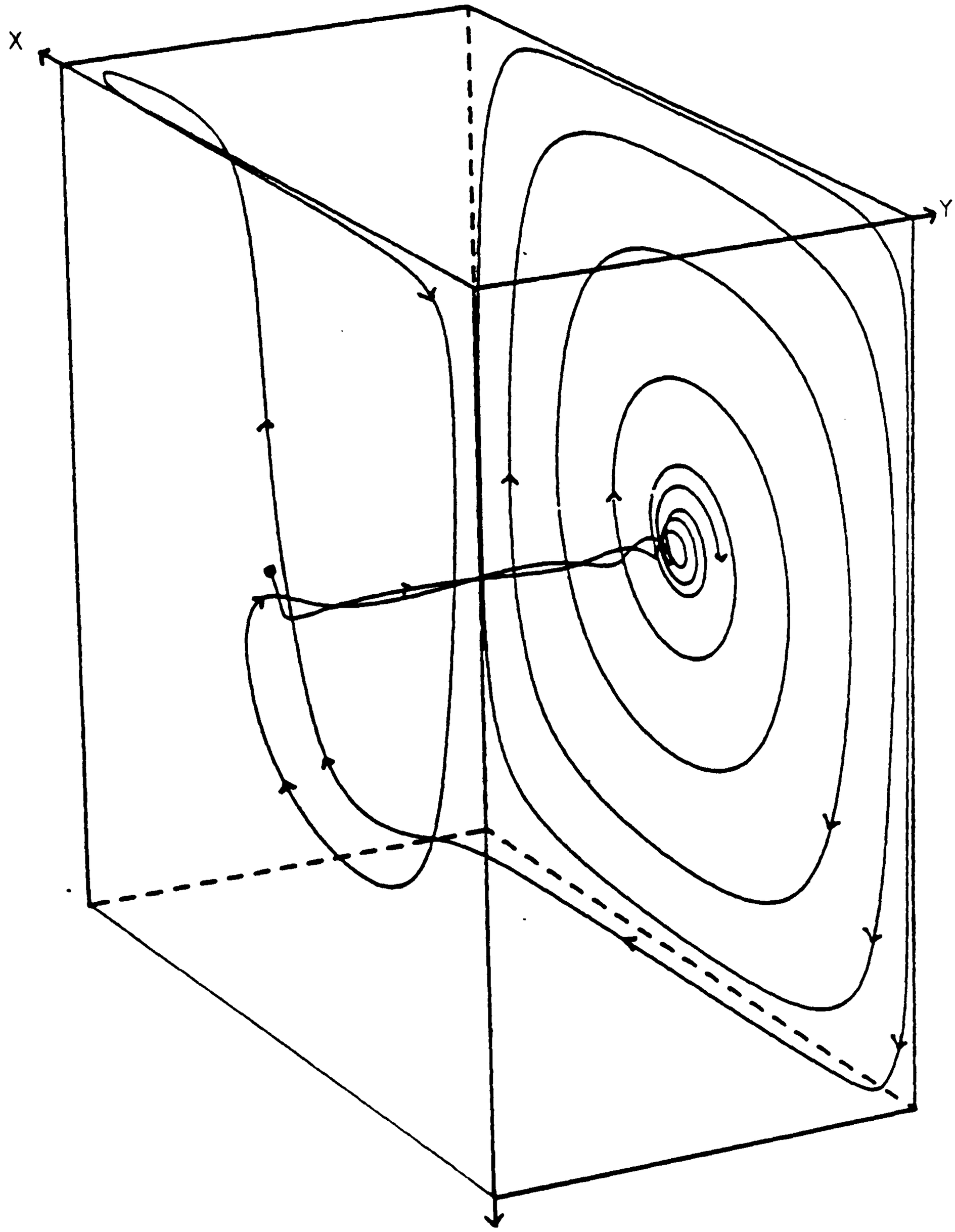

Figure 6.72 Particle track for cerrobase at $Ra = 10^3$, cavity (1,1,1)

Fluid = cerrobase, Ra = 10^3, Hy=1, Hz=1, grid=16x16x16

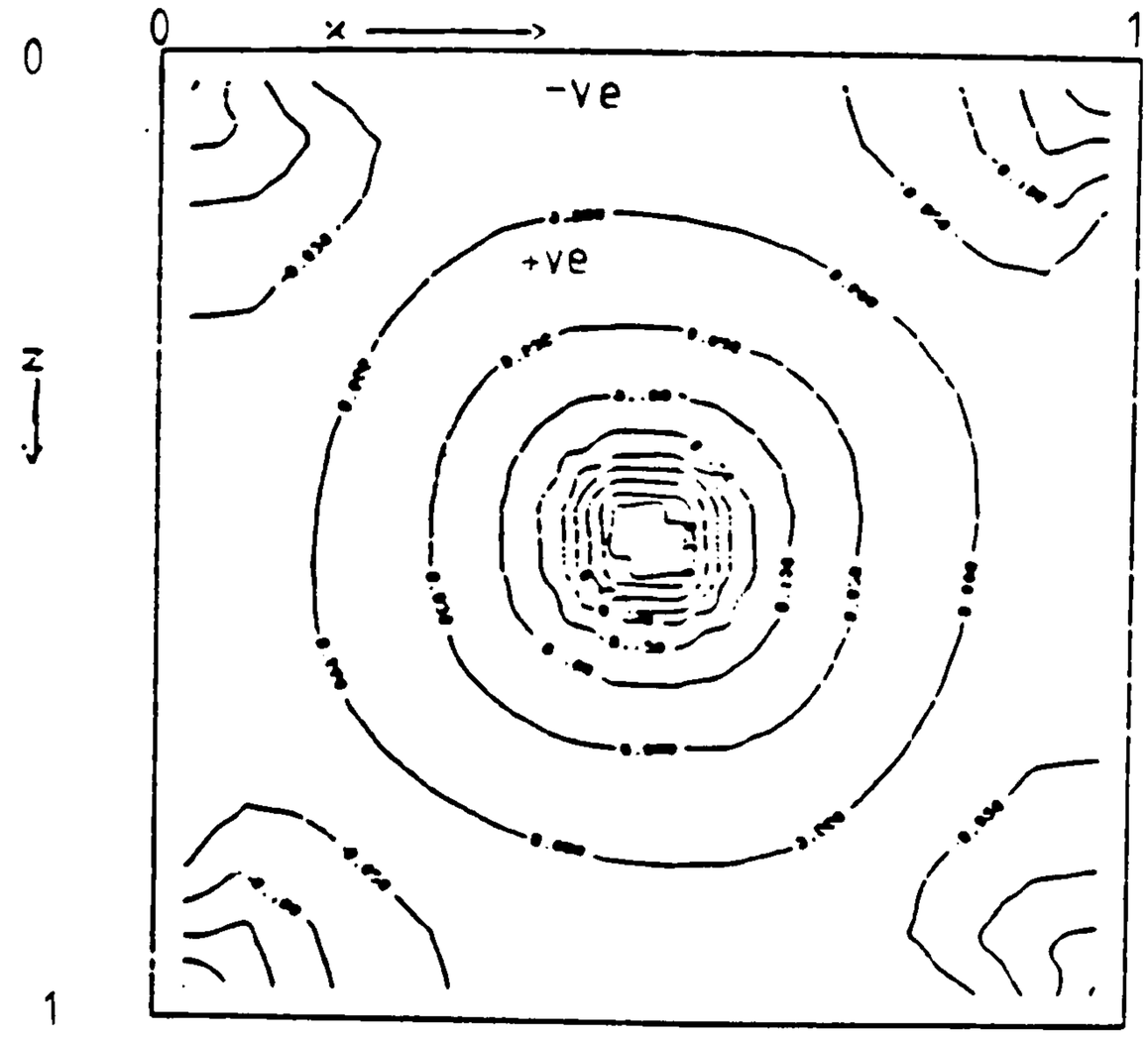

Figure 6.73 Contour plot of ratio R at plane A, near the end wall

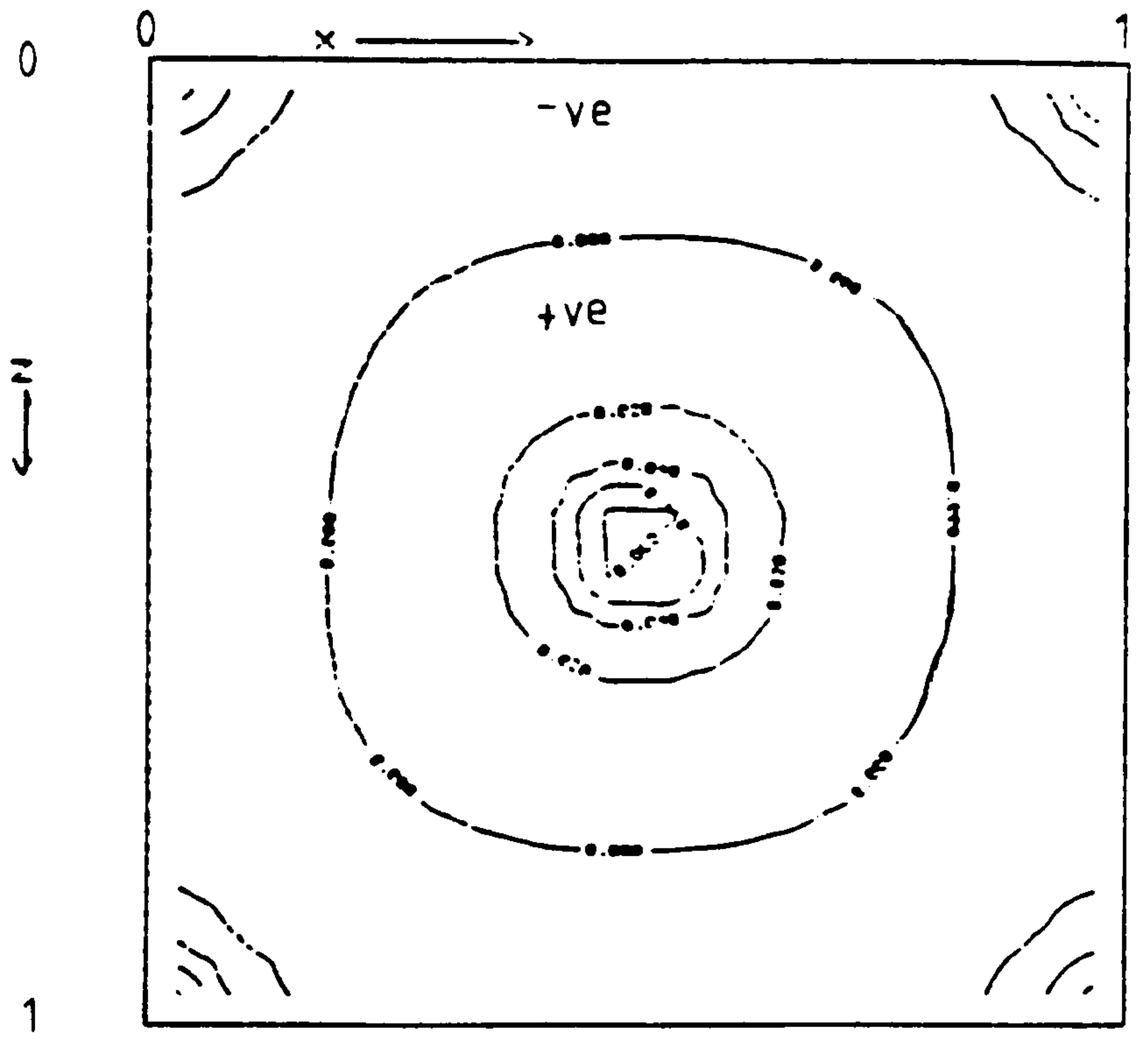

Figure 6.74 Contour plot of ratio R at plane B, near the symmetry plane

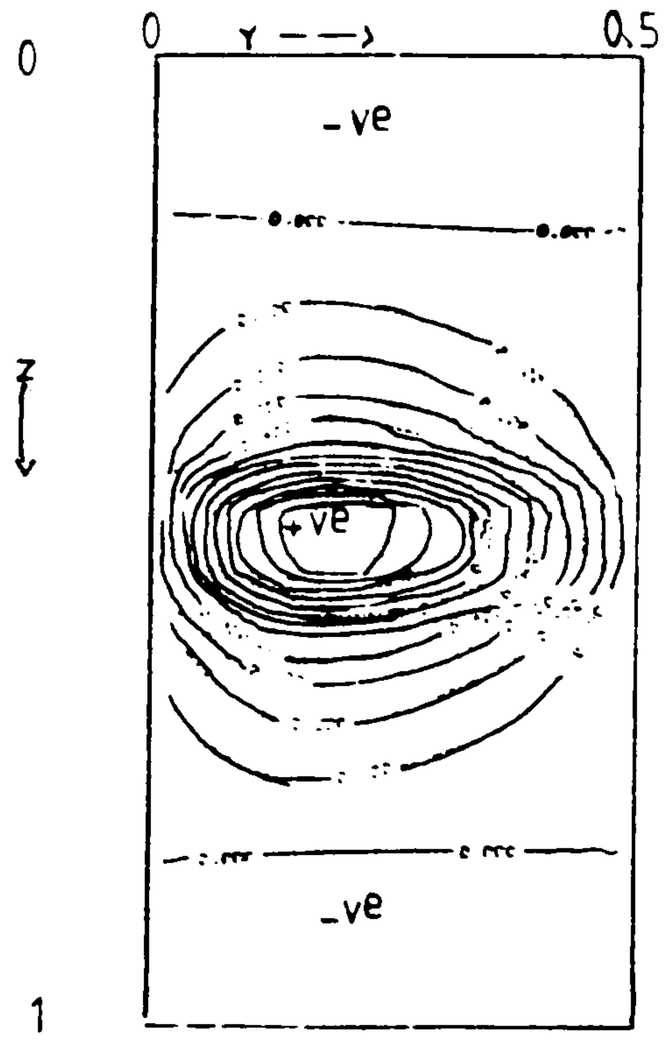

Figure 6.75 Contour plot of ratio R at plane C $(0.5 - hx/2, y, z)$

Fluid = cerrobase, Ra = 10^5, Hy=1, Hz=1, grid=16x16x16

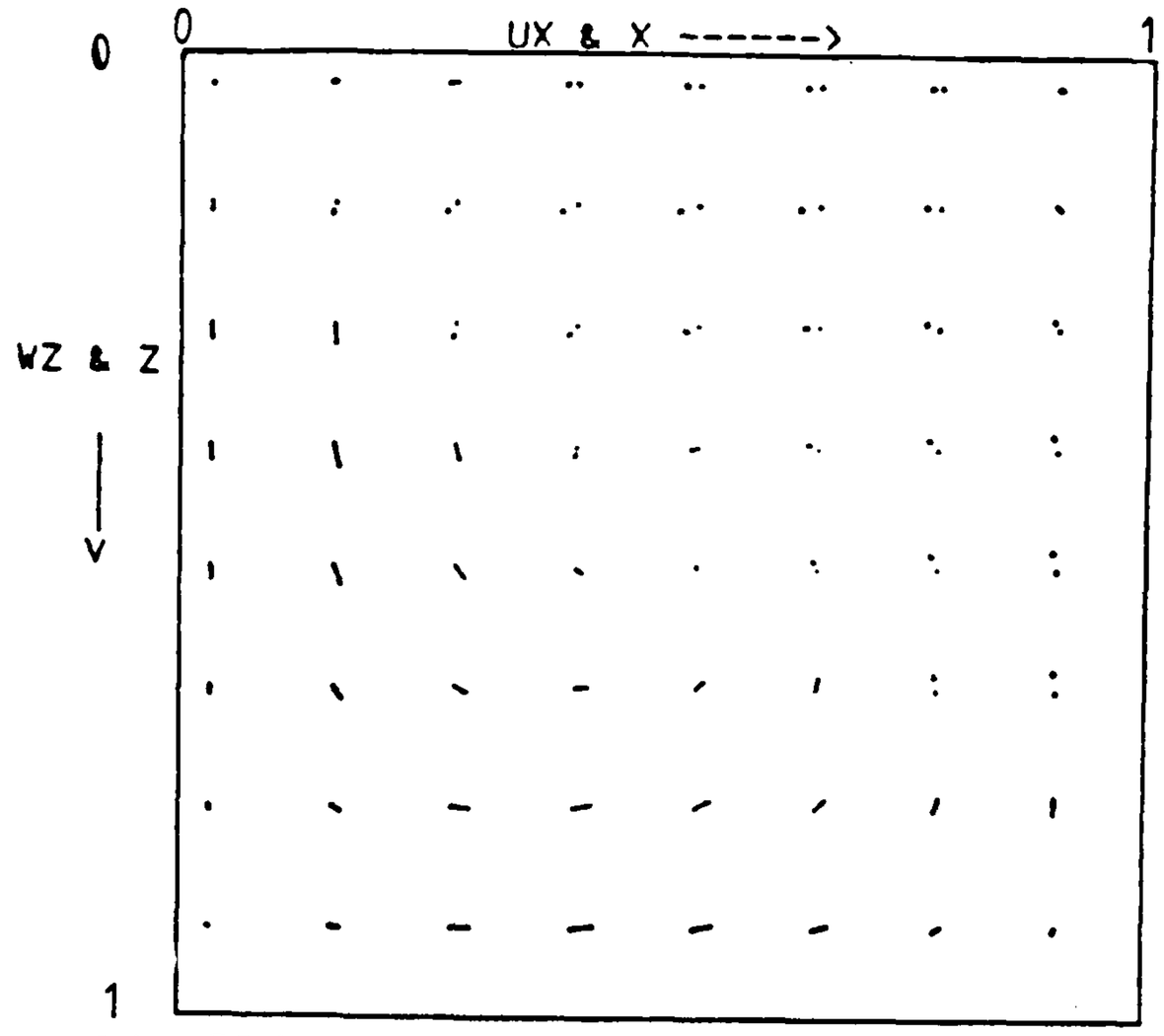

Figure 6.76 Velocity vectors at plane A, near the end wall

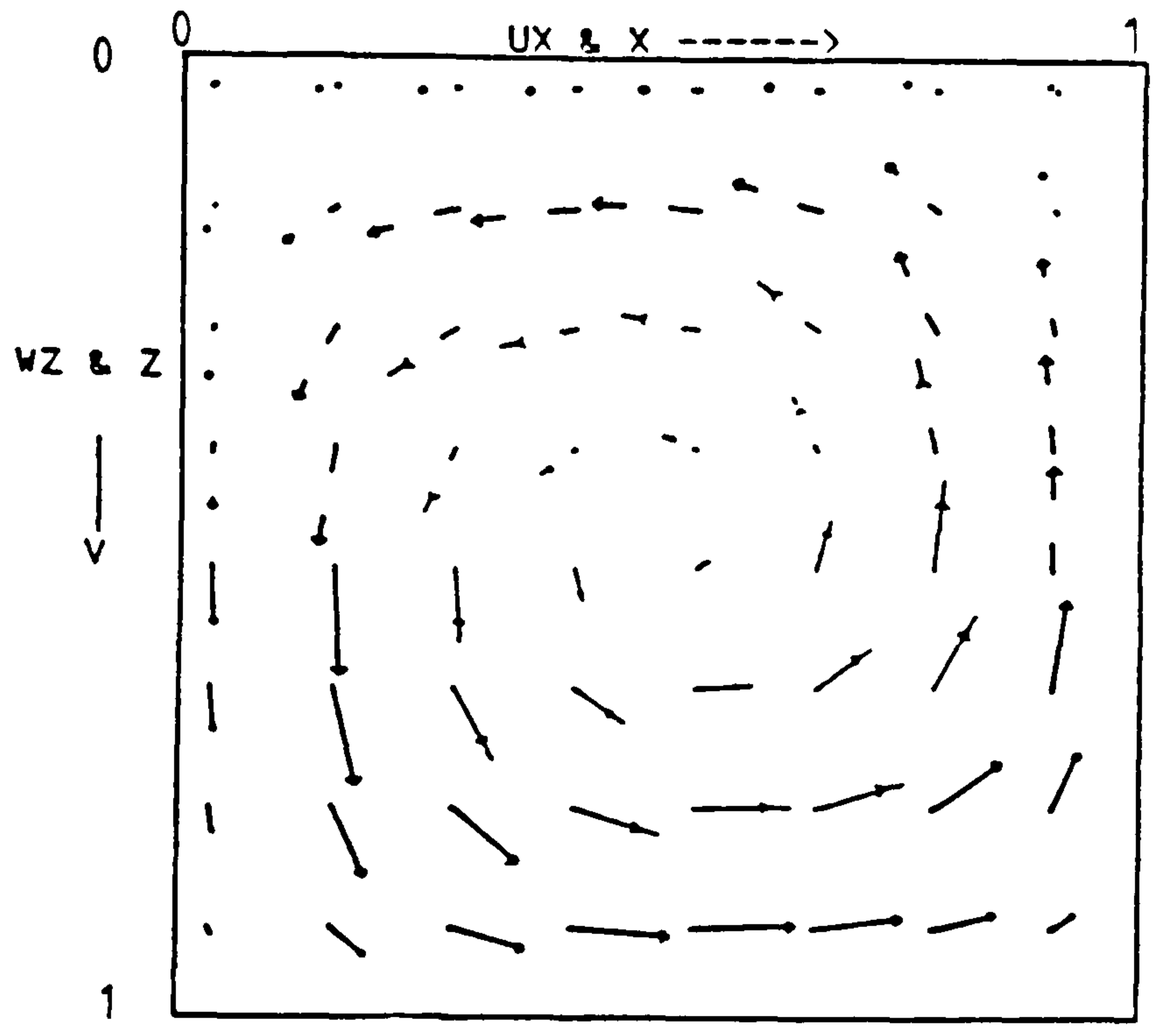

Figure 6.77 Velocity vectors at plane B, near the symmetry plane

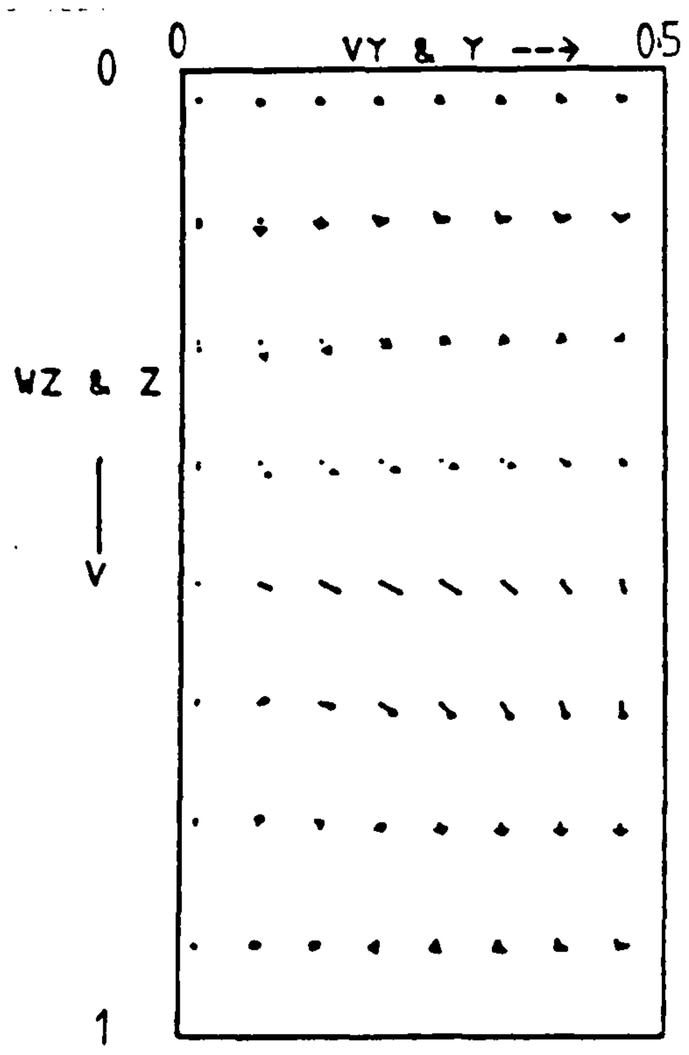

Figure 6.78 Velocity vectors at plane C $(0.5 - hx/2, y, z)$

Fluid = cerrobase, Ra = 10^3, Hy=1, Hz=1, grid=16x16x16

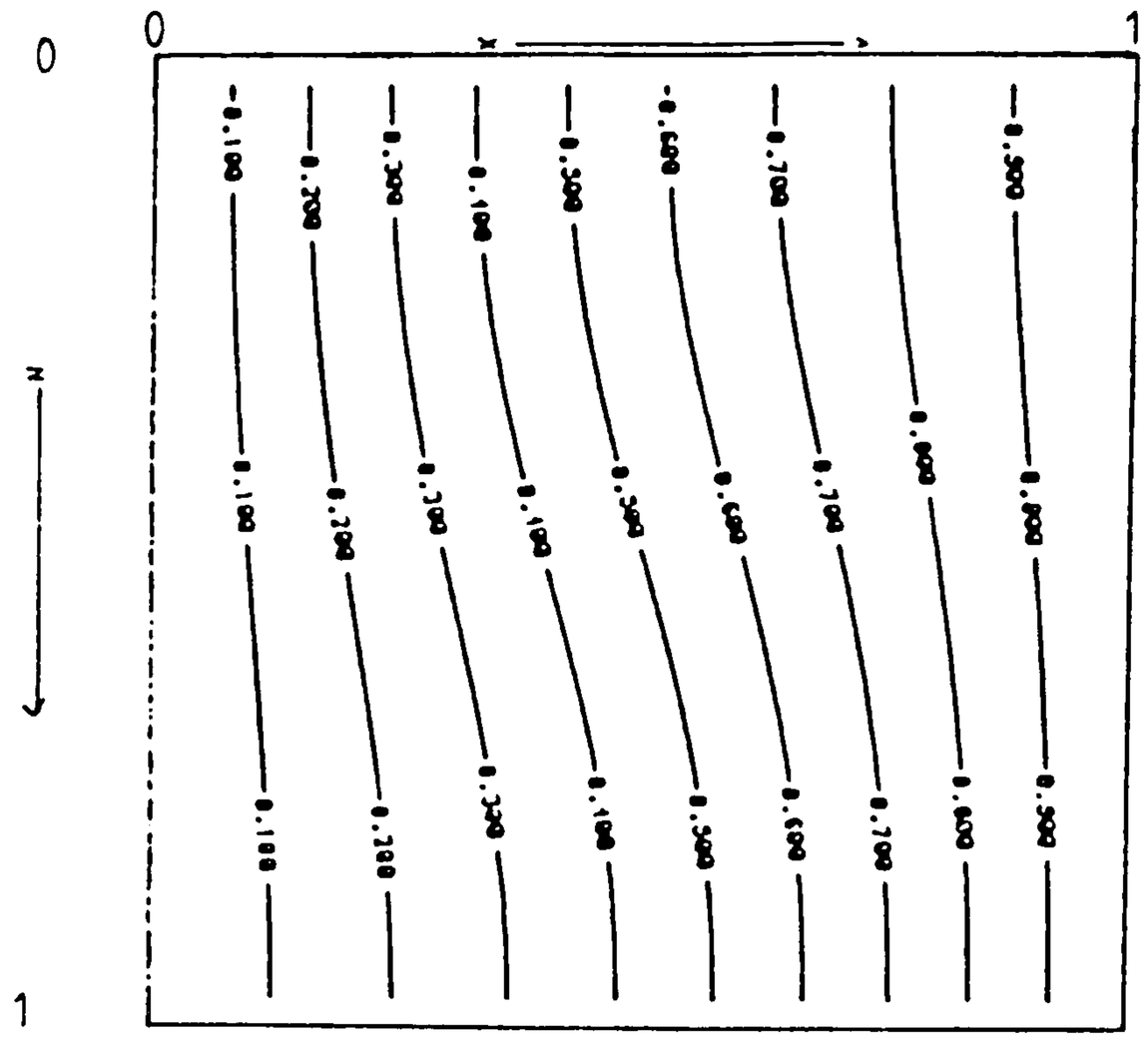

Figure 6.79 Isotherms at plane A, near the end wall

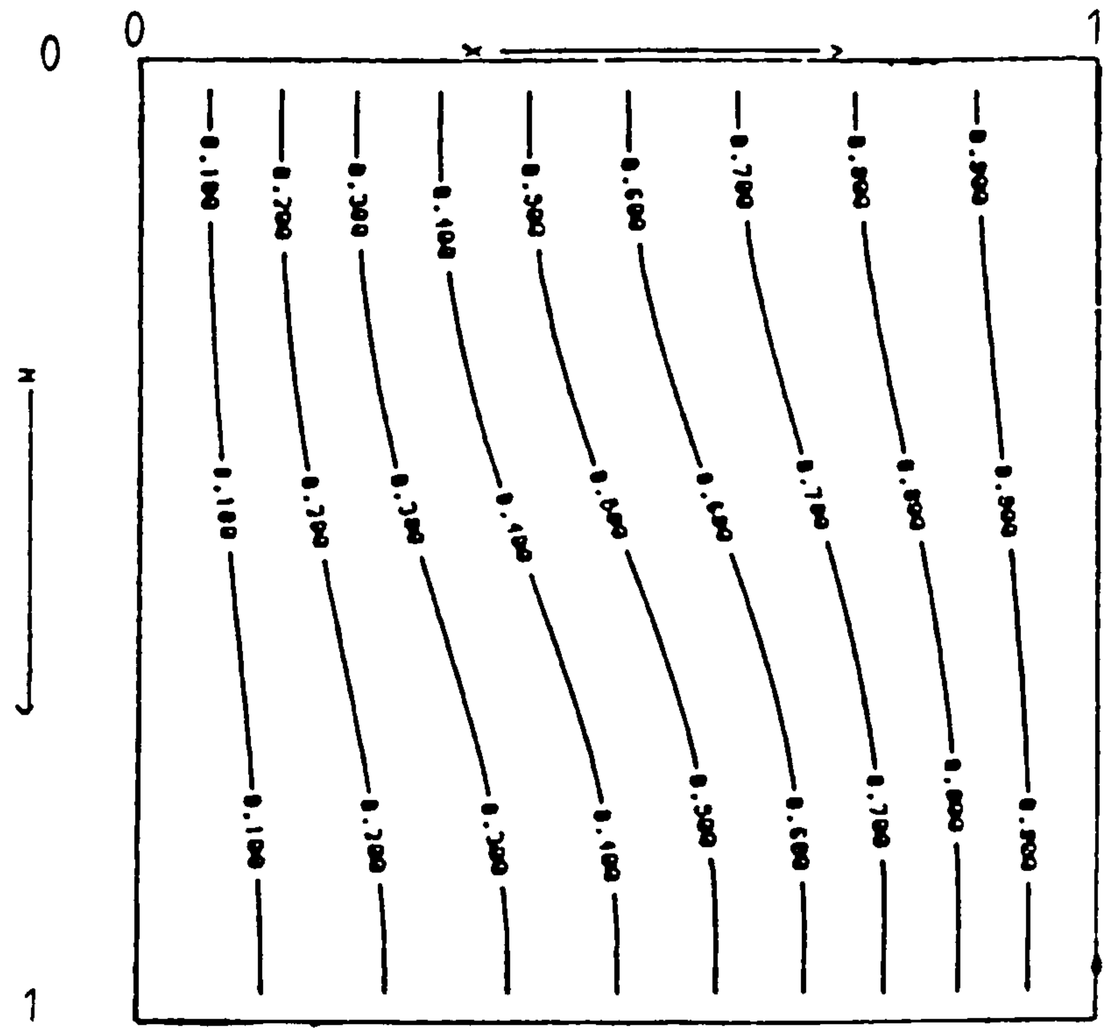

Figure 6.80 Isotherms at plane B, near the symmetry plane

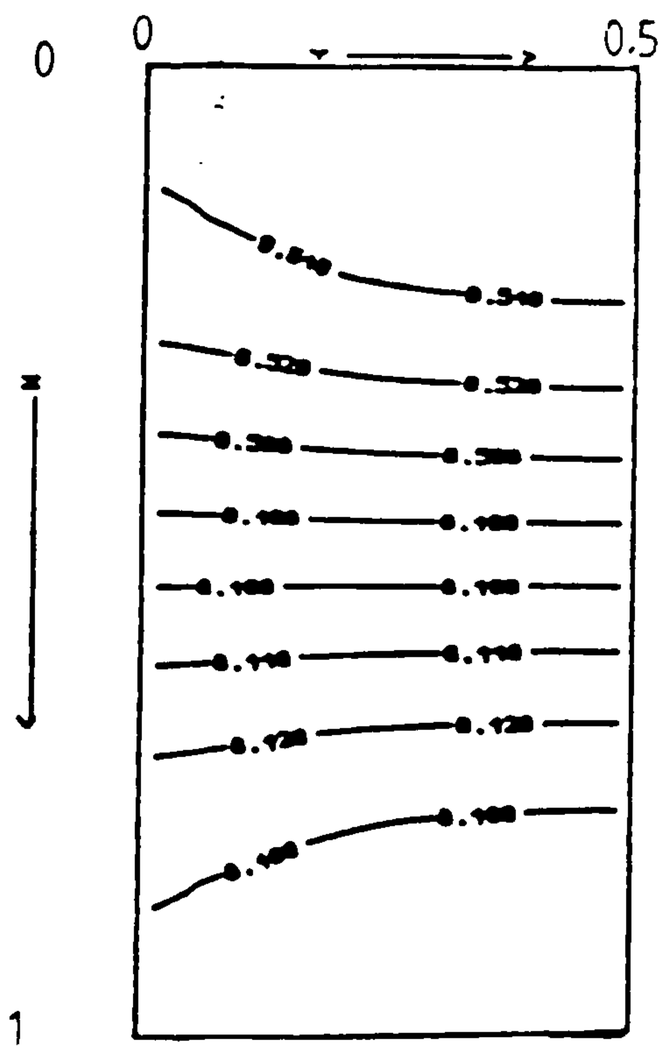

Figure 6.81 Isotherms at plane C, $(0.5 - hx/2, y, z)$

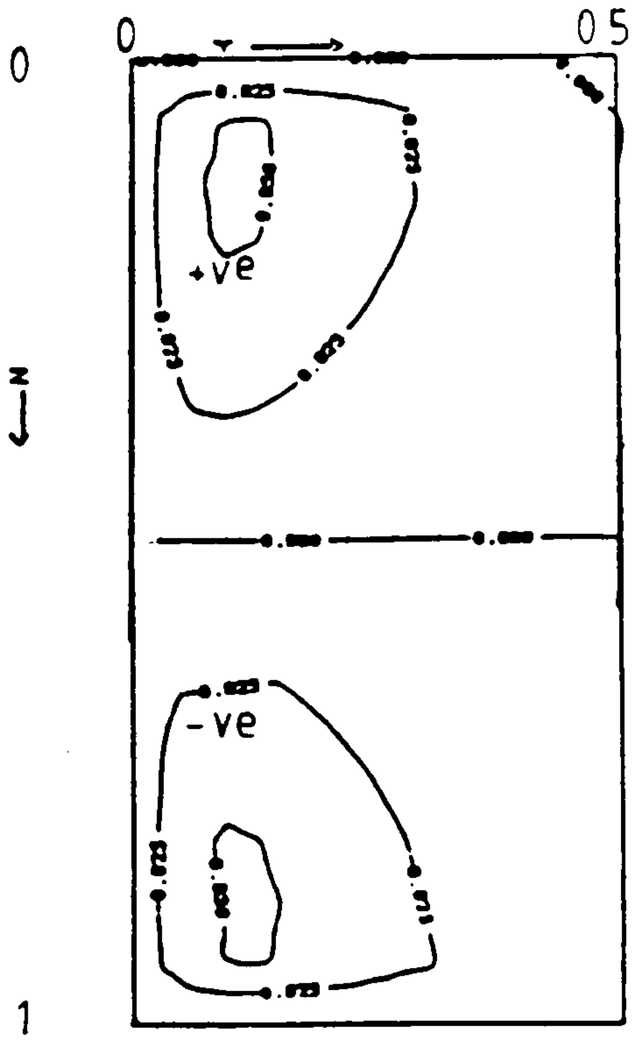

Figure 6.82 $\partial\theta/\partial y$ at plane C, $(0.5 - hx/2, y, z)$

Window cavity (1,2,1): length aspect ratio Hy=2.0

The flow in this cavity is described by a single forward recirculating roll. Particle paths have been traced and are presented in Figure 6.83 and 6.84. In Figure 6.83 a particle has been traced from the point (.9, .001, .9) and in Figure 6.84 a particle has been traced from the point (.3, .1, .3). The flow behaviour is similar to that in the shorter cavity Hy=1.0.

The turning points of the particles lie on a cylindrical surface and no positive R contours exist in the boundary layers. The isotherms near the end wall are similar to those obtained with the shorter cavity Hy=1.0, but the isotherms near the symmetry plane are more convective for this case. The maximum $\partial\theta/\partial y$ over the domain is 0.0683 which is the same as that obtained with Hy=1.0. The contour plots of R, velocity vectors and isotherms are not presented since they depict similar features to those obtained with the shorter cavity Hy=1.0.

Window cavity (1,5,1): length aspect ratio Hy=5.0

The flow here is again described by a single forward recirculating roll which fills the half cavity, see Figure 6.85. The contour plots of the ratio R, velocity vectors and isotherms exhibit similar behaviour to that obtained with the shorter cavity. The thermal solution near the end wall is similar to that obtained with Hy=1.0 and the solution near the symmetry is more convective than that obtained with Hy=2.0. The maximum $\partial\theta/\partial y$ over the domain is 0.0689 which is the same as those obtained in the shorter cavities.

Figure 6.86 represents the streamlines near the symmetry plane for the length aspect ratio, Hy=5. The streamlines for the shorter cavities are similar to Figure 6.86 and are not presented. The maximum value of ψ for Hy=1, 2 and 5 is 0.72, 0.78 and 0.82 respectively.

The axial velocity profile along the centre line for these three length aspect ratio cavities Hy=1.0, 2.0 and 5.0 are presented in Figure 6.87. It can be seen that as Hy increases the peak axial velocity tends to near 0.622 and the position along the y-axis at which this peak occurs is at about y=1/4. After the axial velocities reach their peaks they decay linearly with Hy=1.0 and 2.0, and exponentially with Hy=5.0. Note no two-dimensional flow develops for cavities of length aspect ratios $\leq$ 5.0. The axial flow in the shorter cavity is again restricted.

Figure 6.83 Particle track for cerrobase at Ra = 10^3,
cavity (1,2,1) grid = 16x16x16

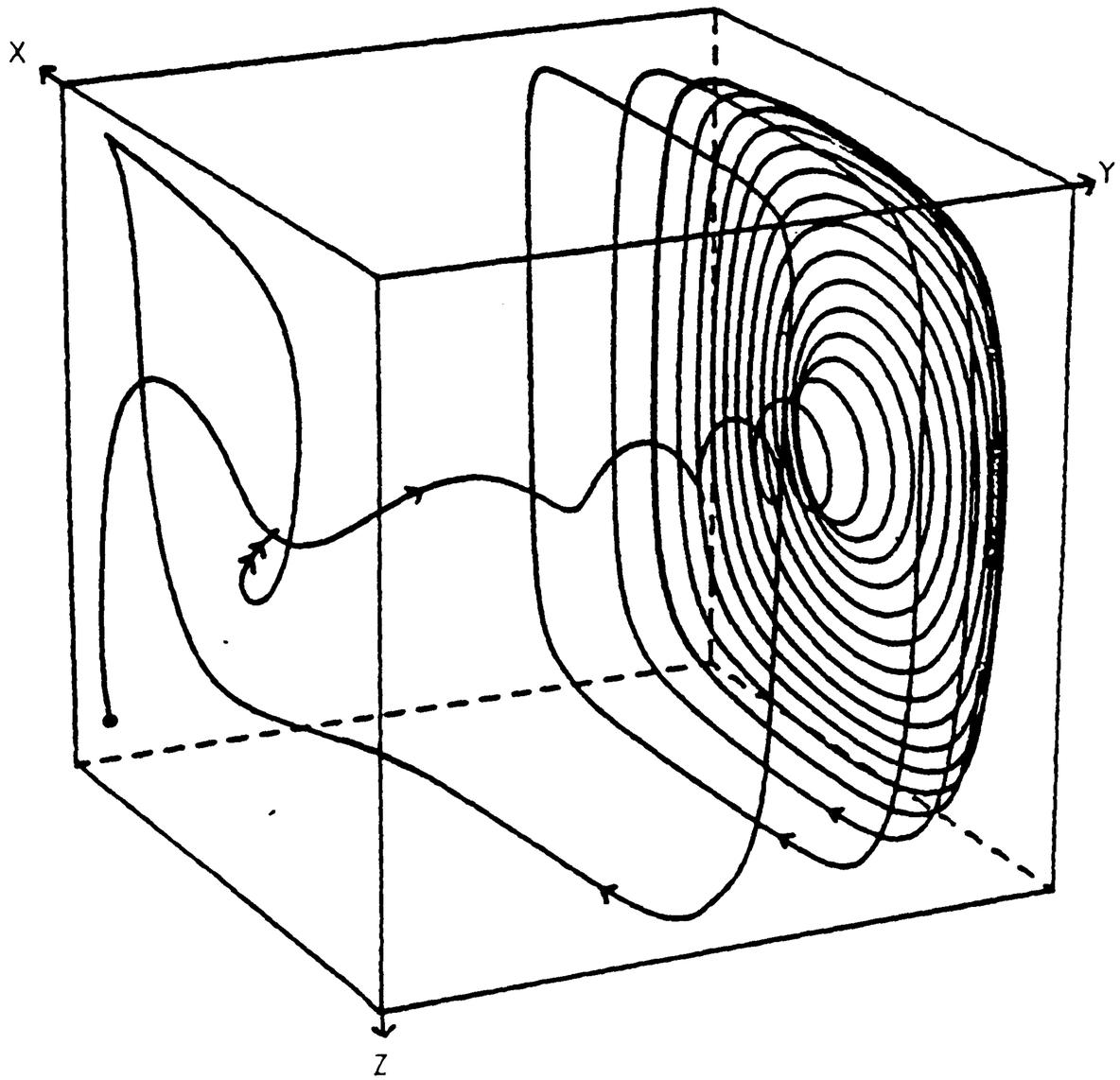

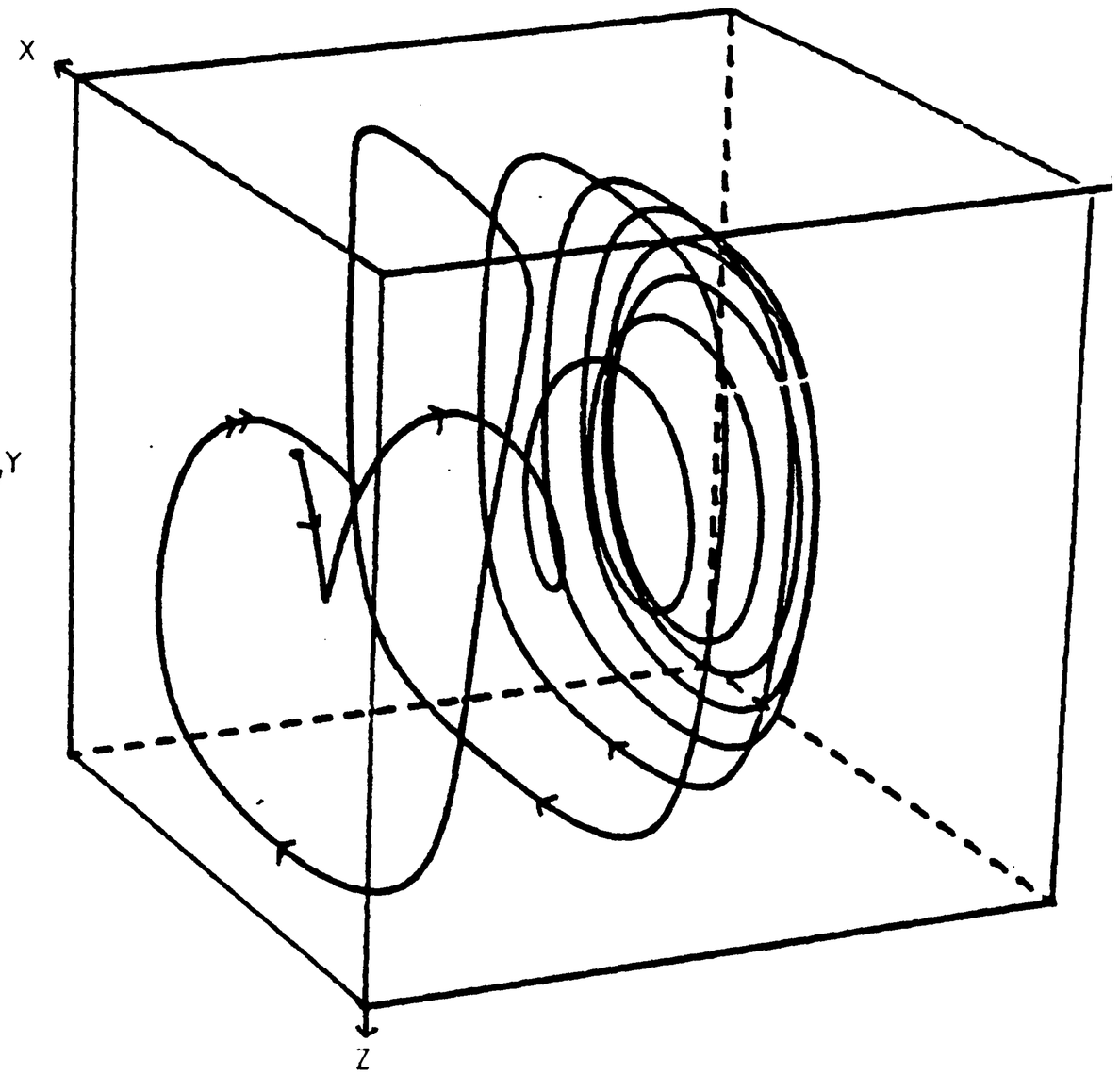

Figure 6.84 Particle track for cerrobase at Ra = 10^3,
cavity (1,2,1) grid = 16x16x16

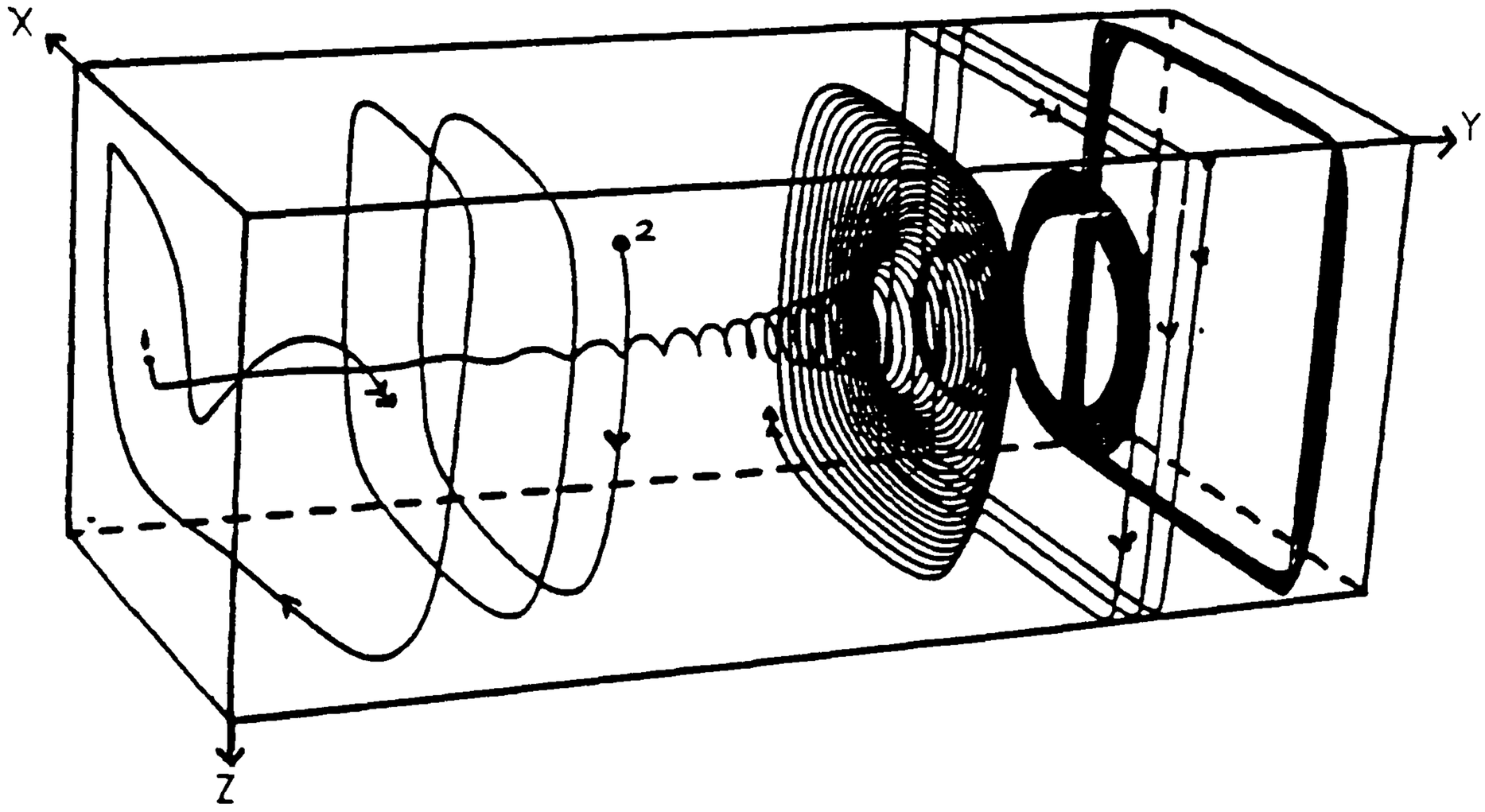

Figure 6.85 Particle track for cerrobase at Ra = 10^3, cavity (1,5,1) grid = 16x40x16

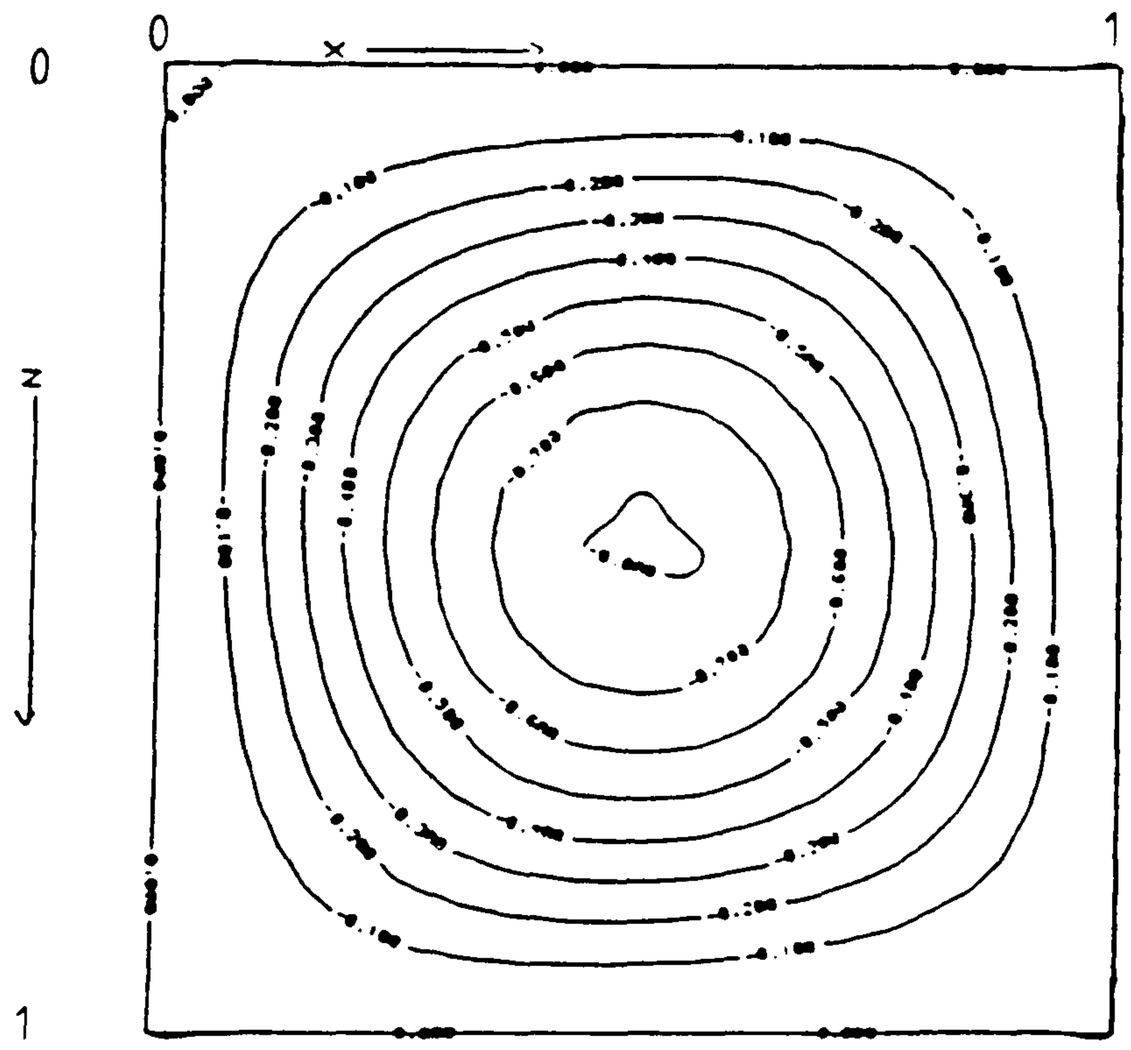

Figure 6.86 Streamlines near the symmetry plane, Hy=5

Graph A: cerrobase at Ra = 10^3, Hy=1, Hz=1

Graph B: cerrobase at Ra = 10^3, Hy=2, Hz=1

Graph C: cerrobase at Ra = 10^3, Hy=5, Hz=1

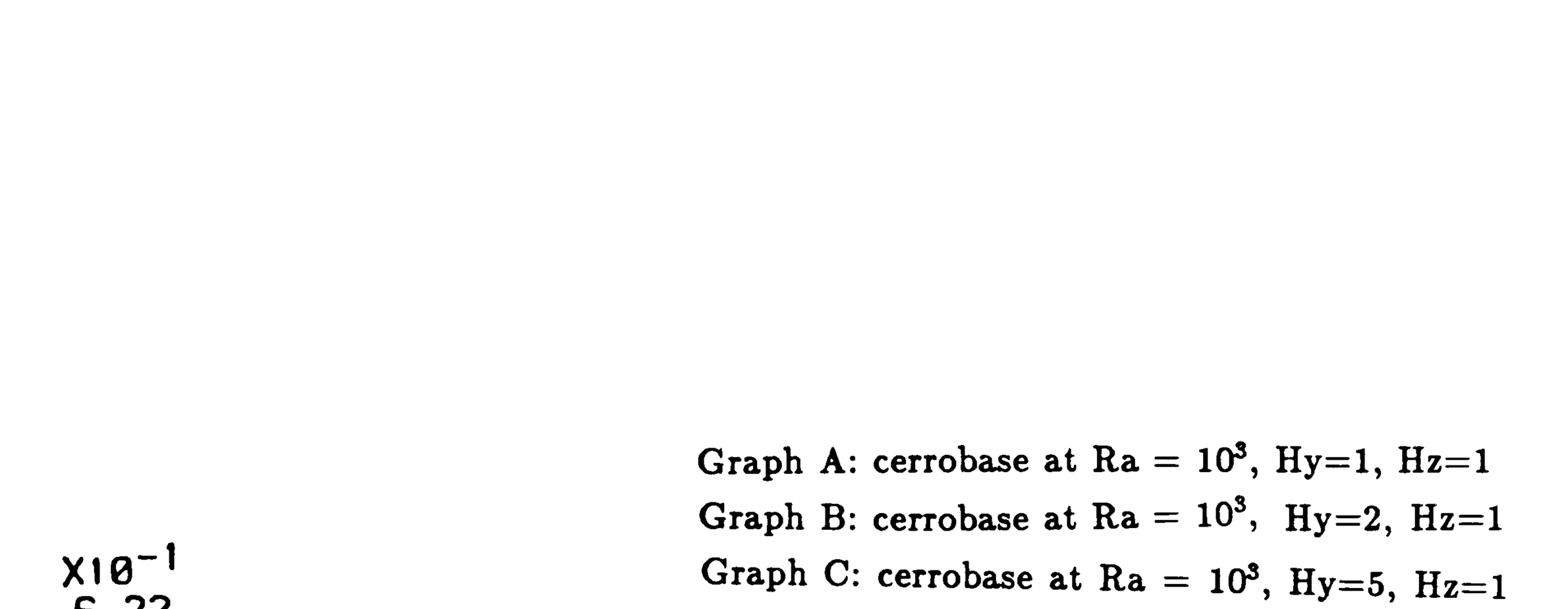

Figure 6.87 Axial-velocity along $(0.5, y, 0.5)$

A fine mesh study with the window cavity (1,1,1)

The mesh lengths in all three directions have been halved giving a finer mesh of 32x32x32 control volumes. The contour plots of the ratio R, velocity vectors and the isotherms display similar flow features to those obtained with the coarser grid. The maximum $\partial\theta/\partial y$ is 0.076 which is about 11% greater than that obtained with the coarse grid. The maximum ψ obtained is 0.76 which is about 5% greater than the coarser grid value. Axial velocity profiles along the centre line have been plotted for both the fine and coarse mesh, see Figure 6.88. Graph A, the solid line, is the axial velocity profile obtained with the fine mesh and graph B, the asterisks, is the axial velocity profile obtained with the coarse mesh. The maximum difference between the profiles occur where the velocities peak. At this point the coarse grid velocity is 16% smaller than the fine grid velocity.

The coarse grid accuracy for results obtained with cerrobase is worse than that obtained with air. This is due to the much higher Grashof number, giving effectively a higher Reynolds number type of flow.

cerrobase at Ra = 10^3, Hy=1, Hz=1, grid=32x32x32

cerrobase at Ra = 10^3, Hy=1, Hz=1, grid=16x16x16

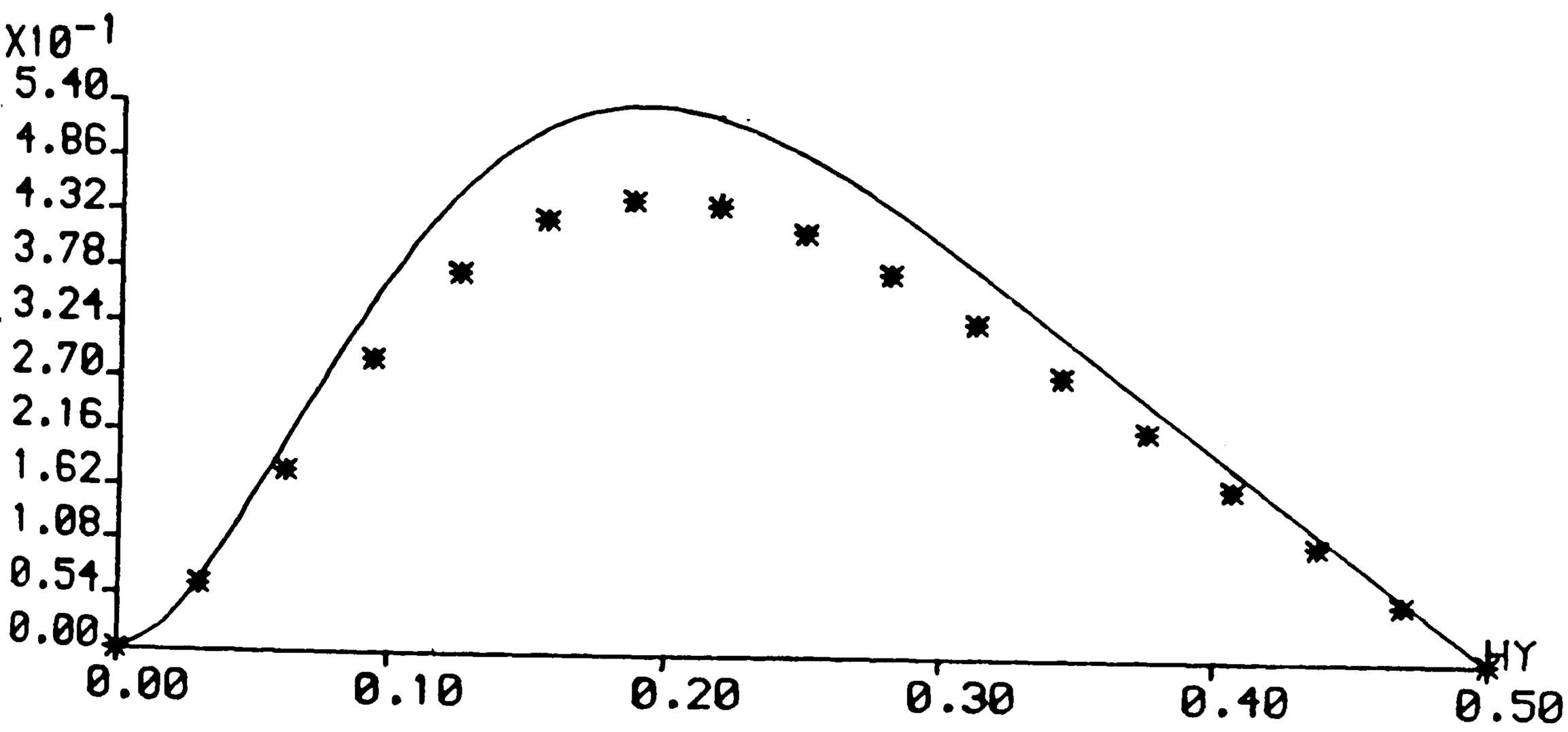

Figure 6.88 Axial- velocity along $(0.5, y, 0.5)$

6.6.4 Cerrobase (Pr=0.035) with Ra=5×10^3

Window cavity (1,1,1): length aspect ratio Hy=1.0

A single forward recirculating roll describes the flow in this cavity with cerrobase. Figure 6.89 shows a particle path traced from the point (.45,.01,.5). Figure 6.90, 6.91 and 6.92 are contours of the ratio R in the planes A, B and C respectively. These figures show the turning points of the particles with respect to the axial direction lie on a cylindrical surface. Also there are no positive R contours attached to the side walls hence undulations do not appear in the particle tracks. The velocity vectors and isotherms exhibit similar flow features to those obtained with the lower Rayleigh number, Ra = 10^3, and are not presented. The overall thermal solution is much more convective than that obtained for air at the lower Ra = 10^3, as expected. Figure 6.93 is a plot of $\partial\theta/\partial y$ contours at the plane C. The figure exhibits a change in the sign of $\partial\theta/\partial y$ in the upper and lower halves of the cavity in the inner core. This change in $\partial\theta/\partial y$, as exhibited in Figure 6.93 has not been noticed in previous studies of the window cavity problem with moderate and large Prandtl number fluids. An explanation of this phenomenon is given at the end of this section.

The vorticity generated by these changes in the sign of $\partial\theta/\partial y$ in the centre of the cavity is much weaker than the inertial end effect and thus no undulations in the axial direction or change in the general flow behaviour are produced.

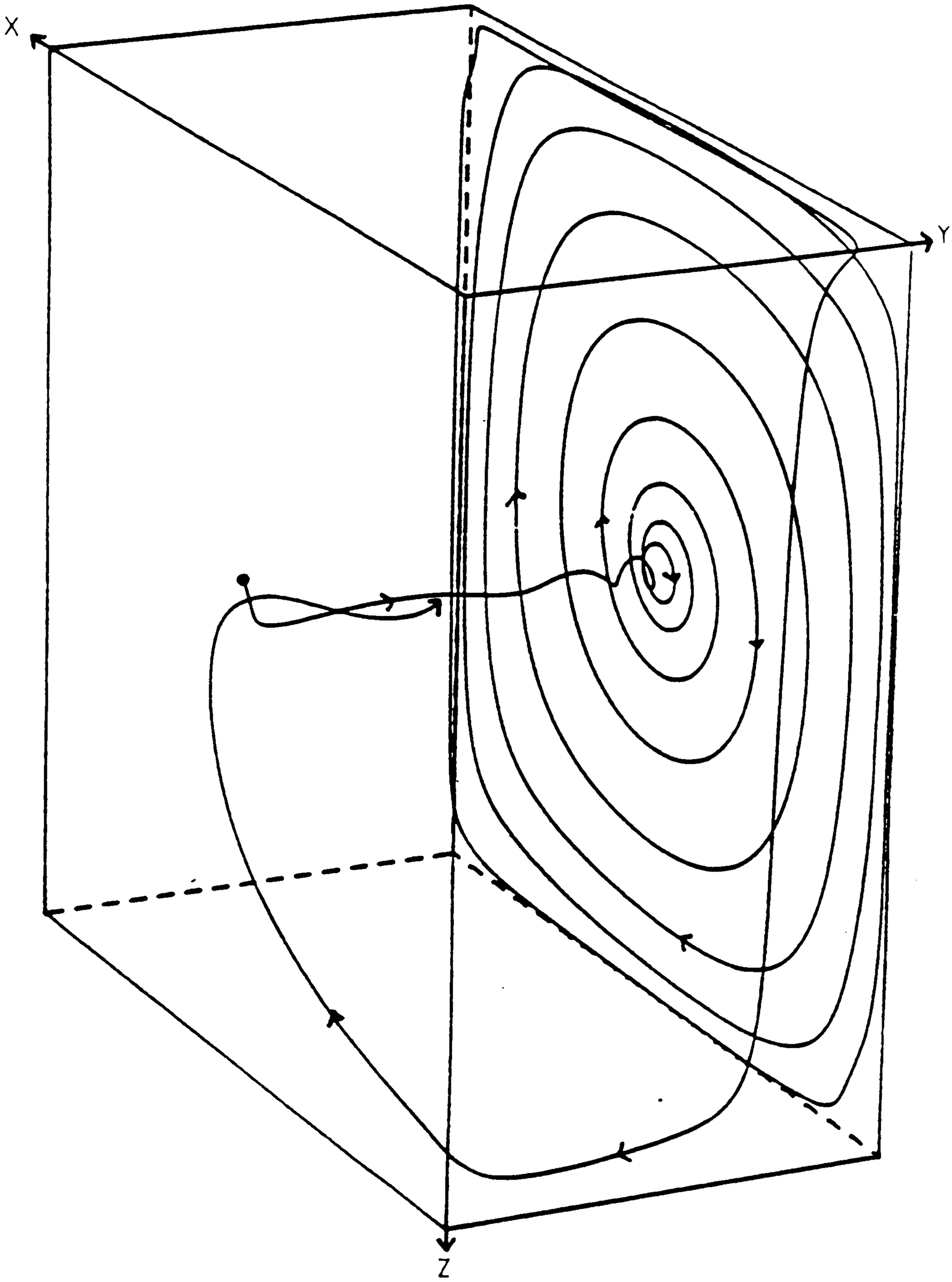

Figure 6.89 Particle track for cerrobase at $Ra = 5 \times 10^3$,
cavity (1,1,1) grid = 16x16x16

Fluid = cerrobase, Ra = 5×10^3, Hy=1, Hz=1, grid=16x16x16

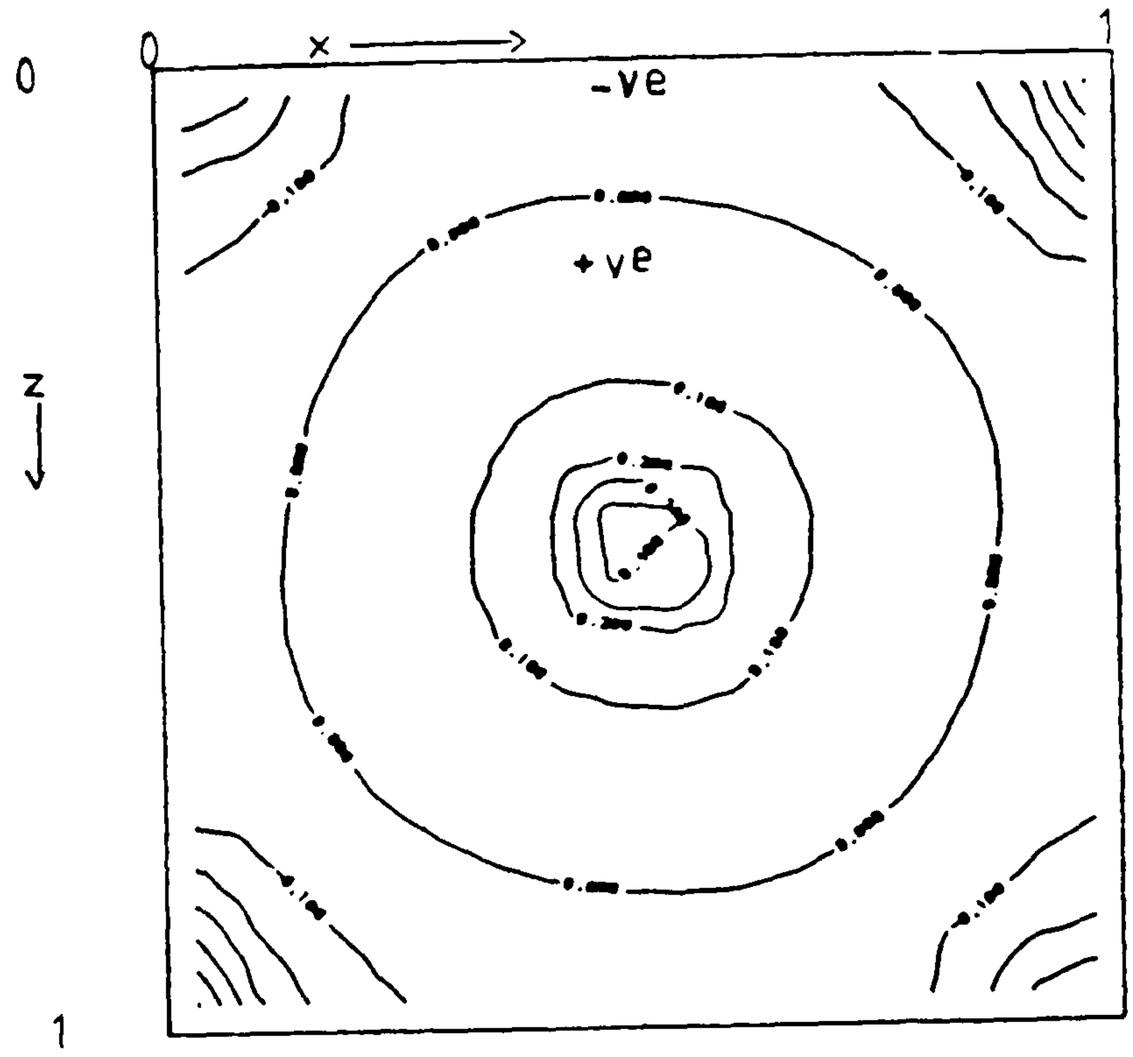

Figure 6.90 Contour plot of ratio R at plane A, near the end wall

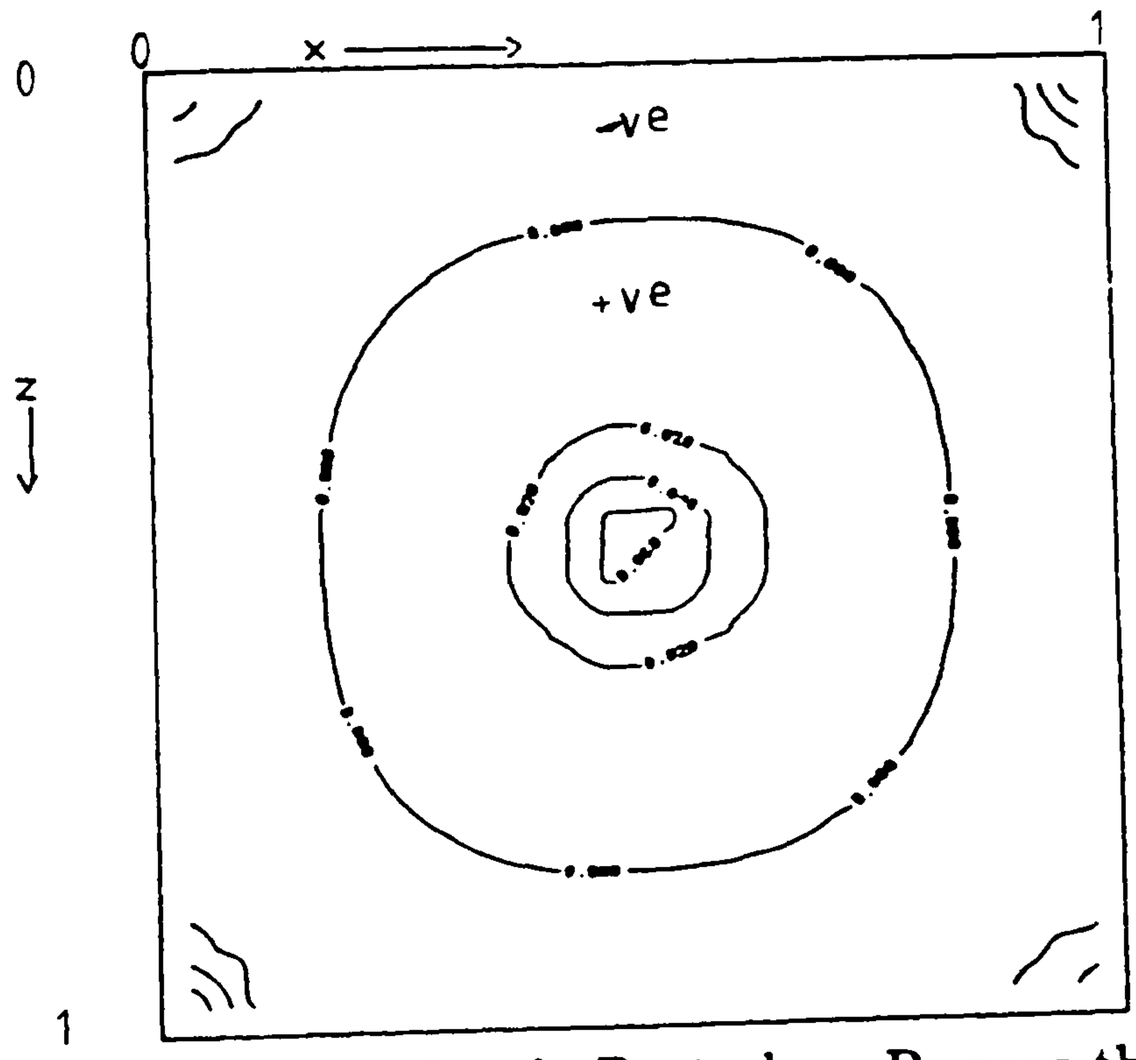

Figure 6.91 Contour plot of ratio R at plane B, near the symmetry plane

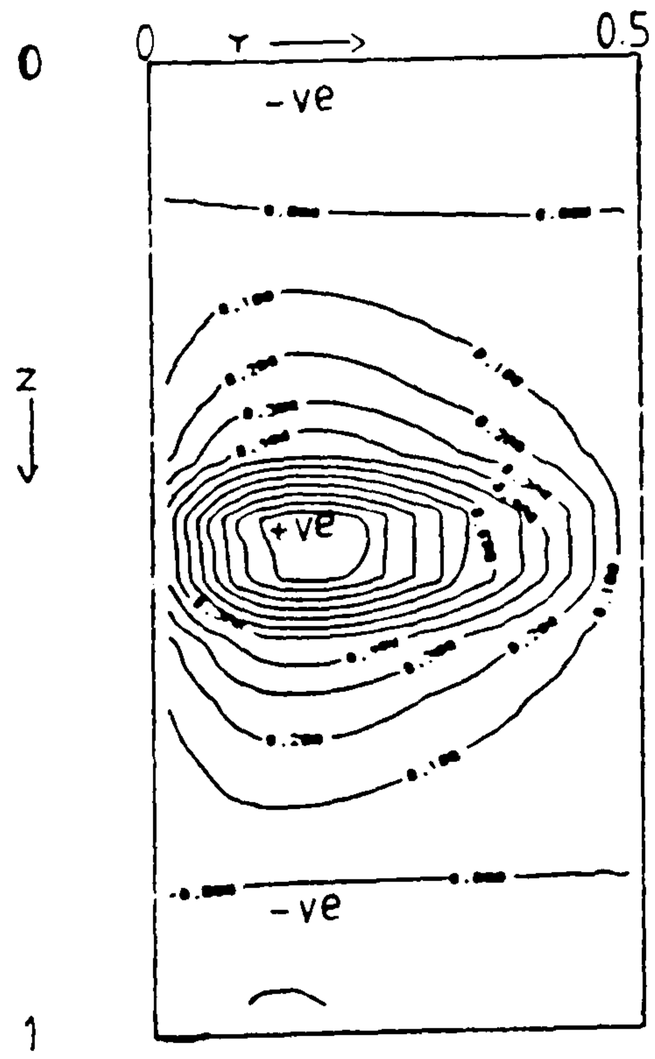

Figure 6.92 Contour plot of ratio R at plane C $(0.5 - hx/2, y, z)$

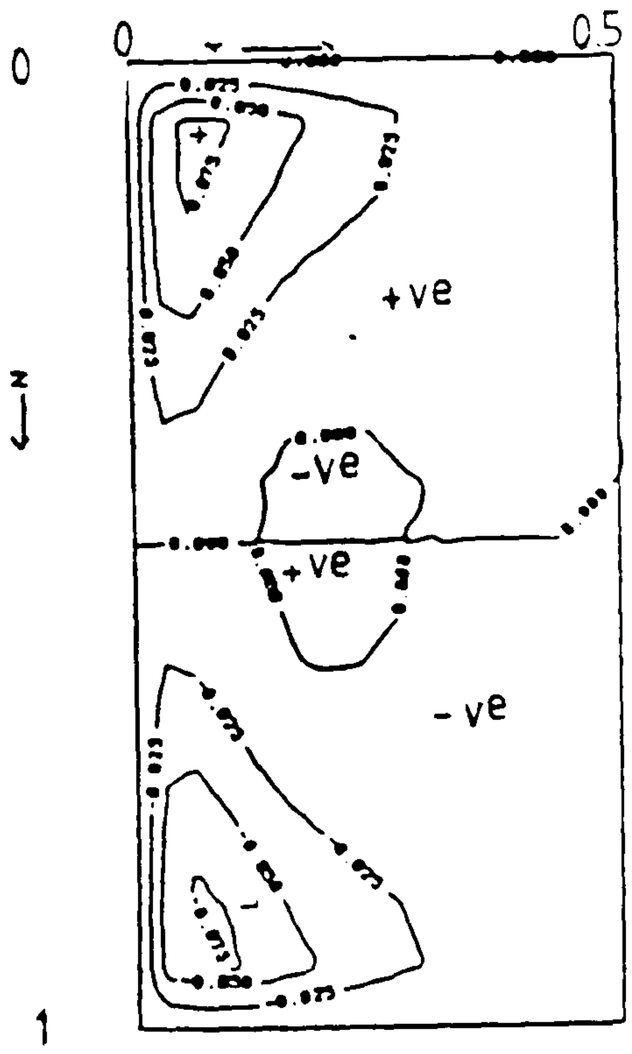

Figure 6.93 $\partial\theta/\partial y$ at plane C, $(0.5 - hx/2, y, z)$

Window cavity (1,2,1): length aspect ratio Hy=2.0

A single forward recirculating roll describes the fluid flow behaviour in this cavity. Figure 6.94 and 6.95 describe particle paths traced from $(.9, .01, .9)$ and $(.3, .1, .3)$ respectively. The contour plots of the ratio R, the velocity vectors and the isotherms exhibit similar features to that obtained in the shorter cavity Hy=1.0. The maximum value of $\partial\theta/\partial y$ is 0.173 which is slightly smaller than that obtained with the shorter cavity Hy=1.0. Figure 6.96 is a contour plot of $\partial\theta/\partial y$ and exhibits the change of sign of $\partial\theta/\partial y$ in the upper and lower halfs of the cavity.

Window cavity (1,5,1): length aspect ratio Hy=5.0.

The fluid flow behaviour in this cavity is described by a single forward recirculating roll. Figure 6.97 shows two particle paths, one demonstrating the forward flow and the other demonstrating the return flow.

Plots of the ratio R, velocity vectors and isotherms reveal similar features to those obtained in the shorter cavities and are thus not presented. The maximum value of $\partial\theta/\partial y$, 0.174 is slightly larger than that obtained with the shorter cavity Hy=2.0. Figure 6.98 is a contour plot of $\partial\theta/\partial y$ at the plane C and exhibits a change in the sign of $\partial\theta/\partial y$ in the upper and lower halves of the cavity.

Figure 6.99 is a streamline plot near the symmetry plane for Hy=5, the plots for Hy=1 and 2 are similar to this and are not presented. The maximum value of ψ for Hy=1, 2 and 5 are 2.0, 2.1 and 2.2 respectively.

Axial velocity profiles along the centre line for the three aspect ratio cavities Hy=1.0, 2.0 and 5.0 are presented in Figure 6.100. No two-dimensional flow exists for cavities with length aspect ratio, $Hy \leq 5.0$. The axial flow in the shorter cavity is again restricted.

The change in sign of $\partial\theta/\partial y$ in the inner core occurs near the region of peak axial velocity. It thus appears that the change of sign of $\partial\theta/\partial y$ is associated with the region of strong axial flow. The contribution to the convection of heat by the axial flow seems to be concentrated near the region of peak axial velocity, acting like a heat source there. The fact that the change in sign of $\partial\theta/\partial y$ is associated with the region of strong axial flow can be supported by observing that the change in sign of $\partial\theta/\partial y$ in the longer cavities also occur in the region of the strong axial flow and $\partial\theta/\partial y$ does not change sign elsewhere.

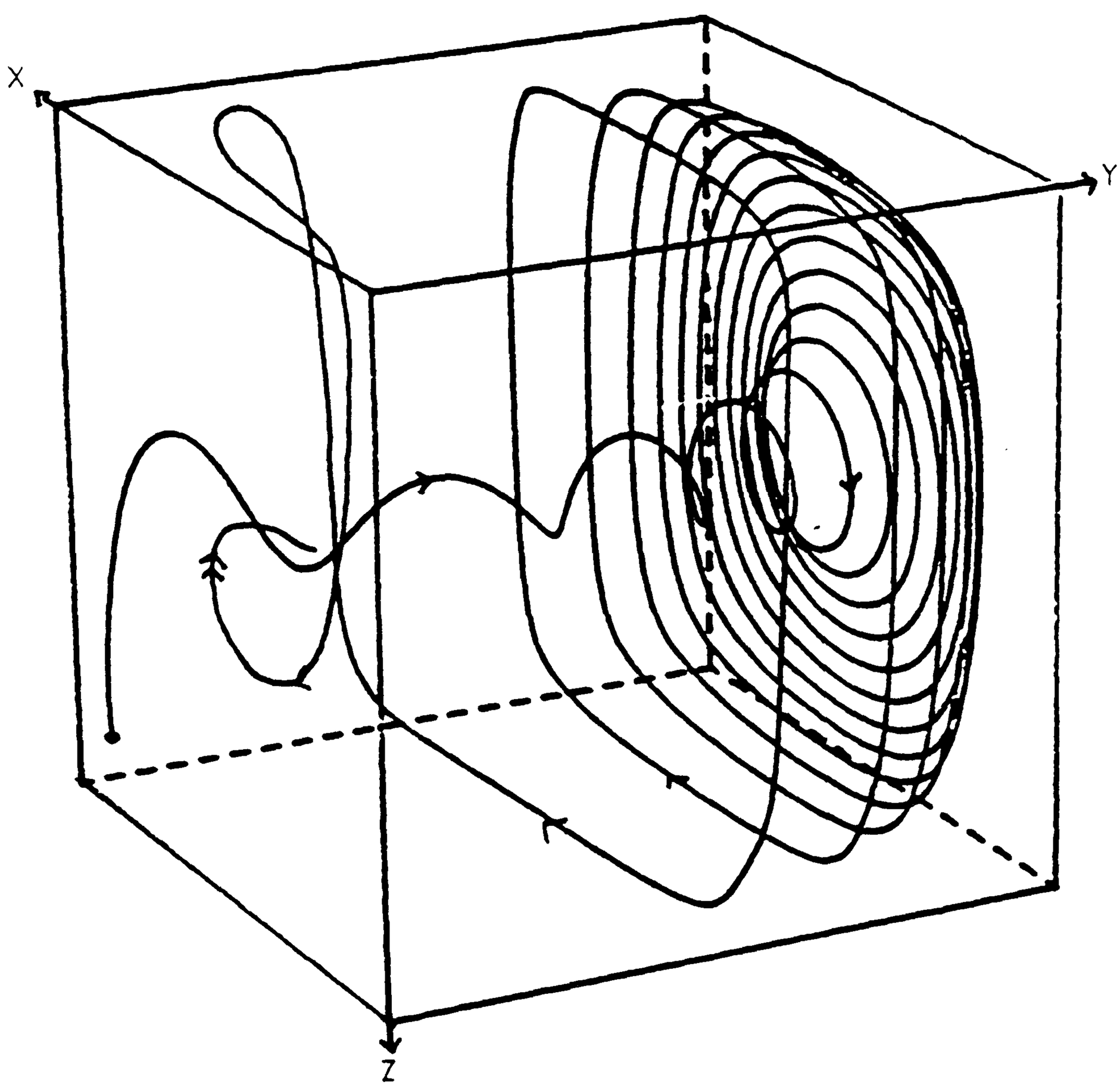

Figure 6.94 Particle track for cerrobase at Ra = 5×10^3,
cavity (1,2,1) grid = 16x16x16

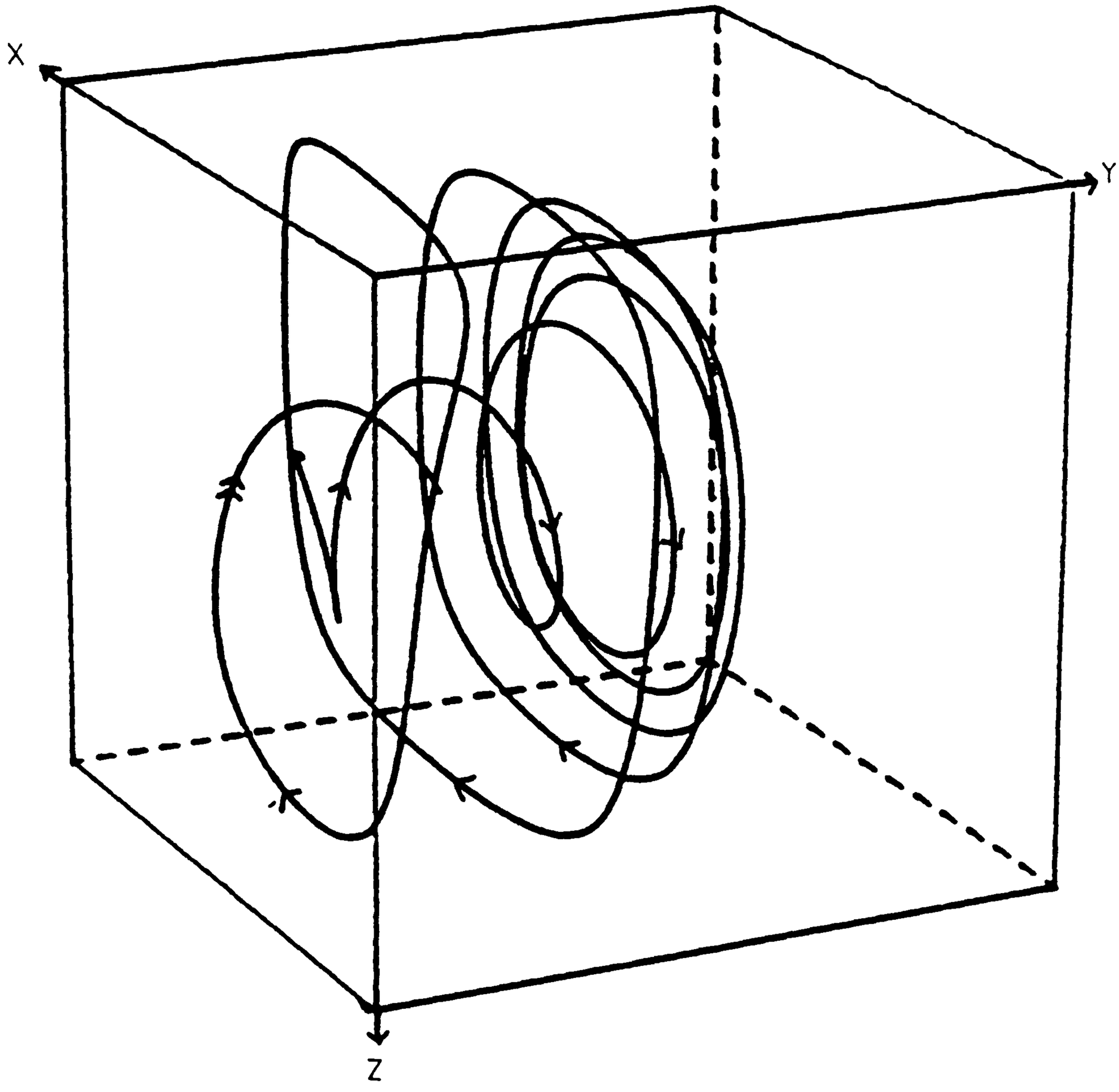

Figure 6.95 Particle track for cerrobase at Ra = 5×10^3,
cavity (1,2,1) grid = 16x16x16

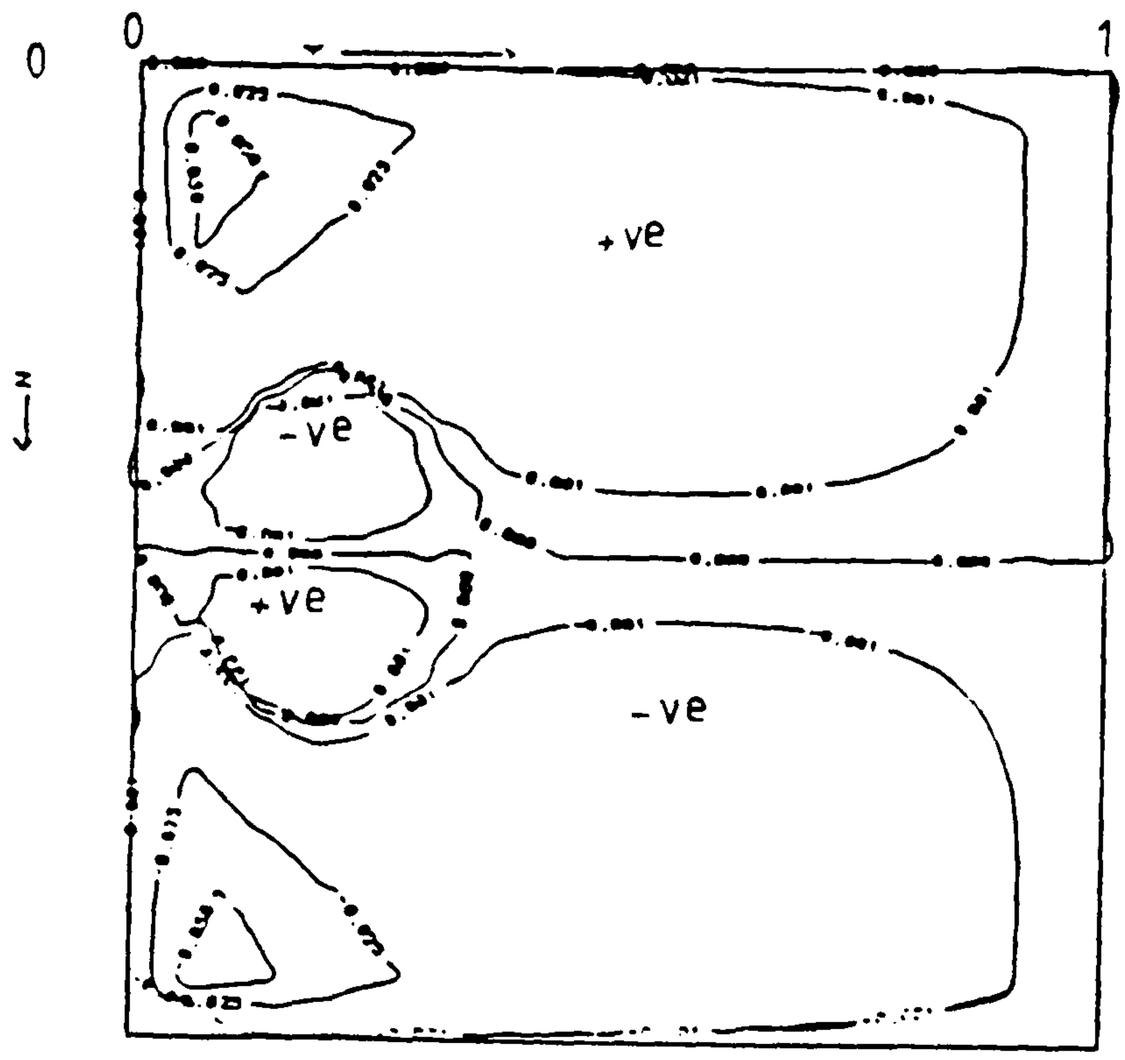

Figure 6.96 $\partial\theta/\partial y$ at plane C, $(0.5 - hx/2, y, z)$, Hy=2

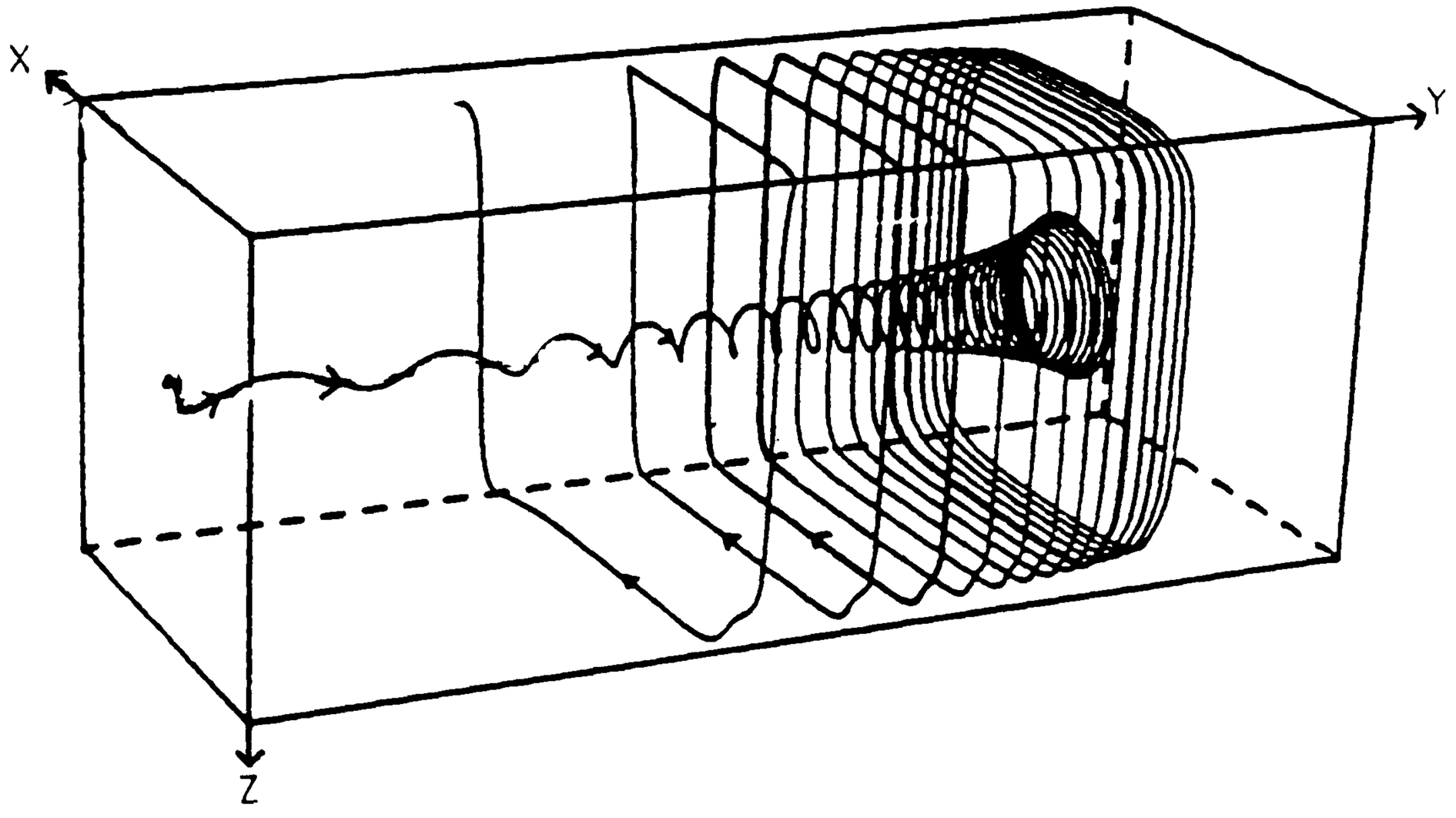

Figure 6.97 Particle track for cerrobase at Ra $= 5 \times 10^3$, cavity (1,2,1) grid = 16x40x16

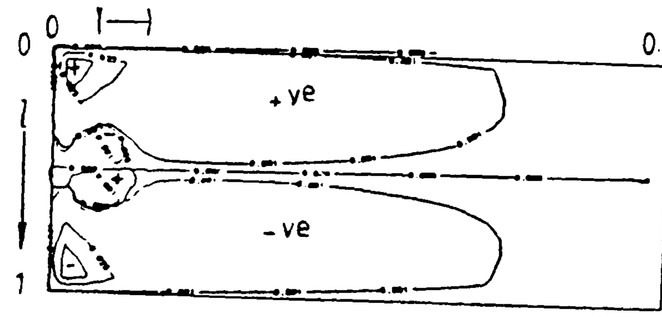

Figure 6.98 $\partial\theta/\partial y$ at plane C, $(0.5 - hx/2, y, z)$, Hy=5

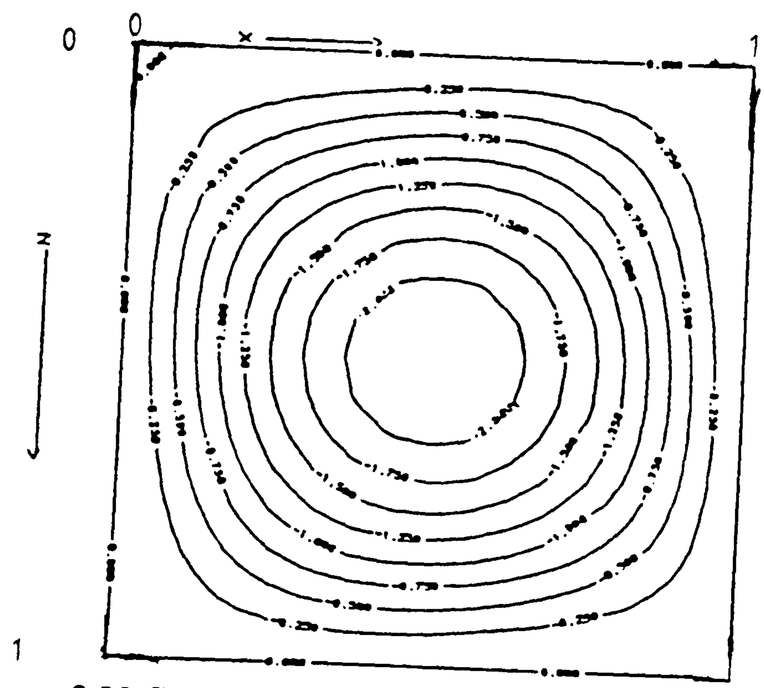

Figure 6.99 Streamlines near the symmetry plane, Hy=5

Graph A: cerrobase at Ra = 5×10^3, Hy=1, Hz=1

Graph B: cerrobase at Ra = 5×10^3, Hy=2, Hz=1

Graph C: cerrobase at Ra = 5×10^3, Hy=5, Hz=1

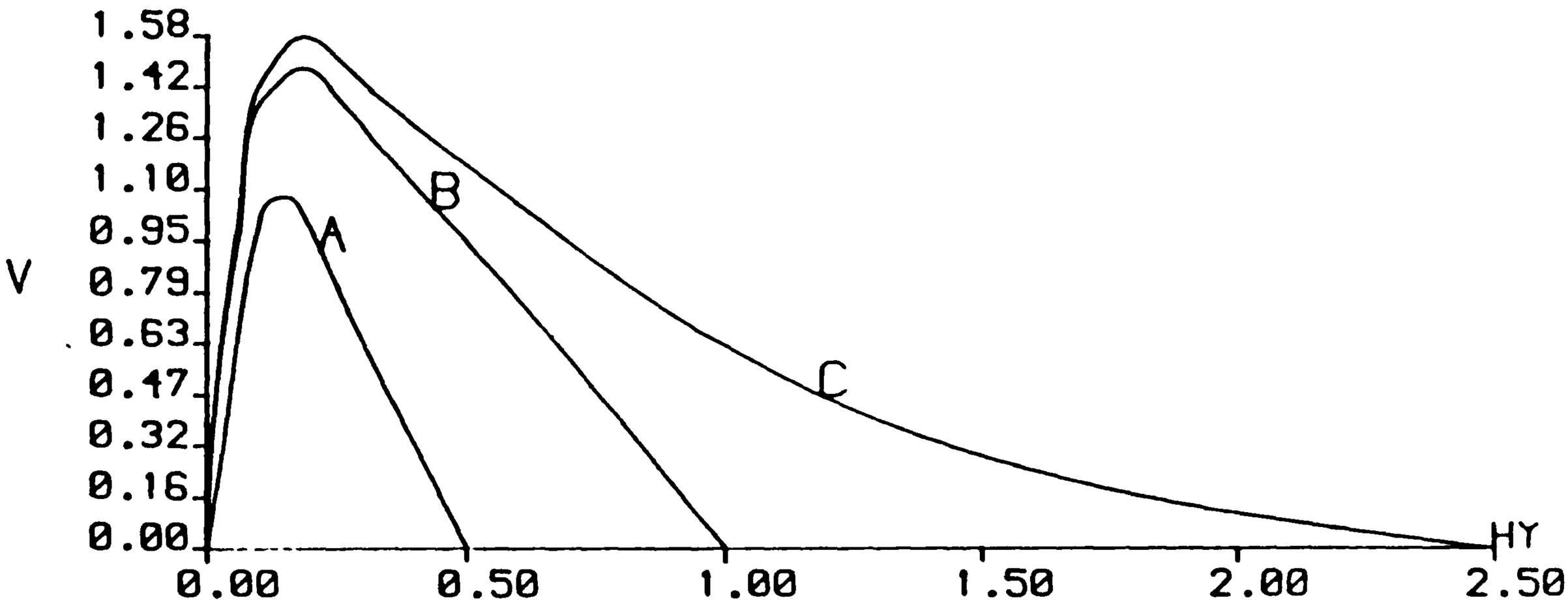

Figure 6.100 Axial-velocity along $(0.5, y, 0.5)$

6.6.5 The effect of three-dimensional motion on the heat transfer with Hz=1

The total non-dimensional heat flux at the isothermal wall x=0 is given by

$$\mathrm{HyHzNu}_{av} = \int_0^{\mathrm{Hz}} \int_0^{\mathrm{Hy}} \mathrm{Nu}(y,z)dydz \tag{6.8}$$

where Nu_{av} is the average Nusselt number for the wall and $\mathrm{Nu}(y,z)$ is as defined in (6.6). In the two-dimensional model the heat flux is a function of z alone and the average flux, denoted by Nu_{2d}, is given by

$$\mathrm{HzNu}_{2d} = \int_0^{\mathrm{Hz}} \mathrm{Nu}(z)dz. \tag{6.9}$$

In a three-dimensional model it is informative to compute, Nu_v, the vertical average of the Nusselt number at any value of y, viz. The variation of this quantity gives some indication of the three dimensional motion of the flow.

Nu_{vm} denotes the value of $\mathrm{Nu}(y)$ at y=Hy/2, the symmetry plane.

$$\mathrm{HzNu}_v(y) = \int_0^{\mathrm{Hz}} \mathrm{Nu}(y,z)dz \tag{6.10}$$

For comparison with two-dimensional problem the values of Nu_{2d} used are those obtained from the two-dimensional study described in chapter 2.

Figures 6.101, 6.102 and 6.103 are plots of Nu_v along the isothermal wall, x=0, for the solutions in a cavity with length aspect ratios Hy=1.0, 2.0 and 5.0 respectively. Figure 6.104 is a plot of Nu_v along the isothermal wall, x=0 for air with $\mathrm{Ra} = 10^5$ and length aspect ratios Hy=1.0, 2.0 and 5.0.

Note the values of Nu_v obtained for the shorter cavity coincide at most points with those obtained for the longer cavity. $\mathrm{Nu}_v(y)$ decreases as the end wall is approached and indicates the extent of the thermal boundary layer in which the convection of heat is reduced. As Ra increases the thickness of this layer decreases. For air at $\mathrm{Ra} = 10^3$, $\mathrm{Nu}_v(y)$ increases slightly as $y \rightarrow 0$ until the end boundary layer is reached, see Figures 6.103 and 6.104. The gradual increase results from the increasing magnitude of the axial velocity in the boundary as the end wall is approached.

The average Nusselt number, Nu_{av}, is less than Nu_{2d} for air and cerrobase. As Hy increases $\mathrm{Nu}_{av} \rightarrow \mathrm{Nu}_{2d}$. The vertical average Nusselt number, Nu_{vm}, for air is always greater than Nu_{2d} except for $\mathrm{Ra} = 10^3$ in the shorter cavity Hy=1.0. This contrasts with the fact that ψ_{max} at the symmetry plane is always less than two-dimensional ψ_{2-d}^{max}, see Table 6.2.

FLUID	CAVITY	Nu_{2d}	Nu_{av}	Nu_{vm}	ψ_{2-d}^{max}	ψ_{max}	max $\partial x/\partial z$
air Ra $= 10^3$	1x1x1	1.142	1.099	1.122	1.25	1.10	.1008
	1x2x1		1.126	1.149		1.20	.1014
	1x5x1		1.141	1.151		1.20	.1014
air Ra $= 10^5$	1x1x1	5.229	5.013	5.358	11.9	12.00	.7940
	1x2x1		5.144	5.251		11.00	.6560
	1x5x1		5.202	5.241		11.00	.6560
cerrobase Ra $= 10^3$	1x1x1	1.107	1.064	1.081	0.85	0.72	.0679
	1x2x1		1.077	1.090		0.78	.0683
	1x5x1		1.086	1.092		0.82	.0689
cerrobase Ra $= 5 \times 10^3$	1x1x1	1.532	1.378	1.435	2.50	2.00	.1900
	1x2x1		1.432	1.468		2.10	.1730
	1x5x1		1.466	1.486		2.20	.1740

Table 6.2: Comparison of two-and three-dimension results for Hz=1.0.

This illustrates that outside the thermal boundary layer at the ends of the cavity the contribution to the convection of heat by the axial flow is more than sufficient to offset the influence of the reduction of the cross sectional flow due to the drag induced by the end wall. Note that for air with Ra $= 10^3$ in the shorter cavity Nu_{vm} is less than Nu_{2d}. This is due to the cross-sectional flow at the symmetry plane being weaker than the two-dimensional flow (i.e. no 2-d flow exits for hy=1.) As a result the convection of heat at the symmetry plane is less than with the two-dimensional flow hence Nu_{vm} is expected to be smaller than Nu_{2d}. For air with Ra $= 10^5$ the Nu_{vm} obtained with Hy=2.0 and 5.0 is smaller than that obtained with Hy=1.0. This is due to the existence of the weak reverse flow in the former cavities. Whose contribution to the convection of heat is smaller than that of the strong forward flow existing in the shorter cavity. Nu_{vm} obtained with Hy=2.0 is greater than that obtained with Hy=5.0. This is due to the forward flow with the cavity Hy=2.0 being stronger and longer than that with Hy=5.0. Thus it contributes more to the convection of heat than the forward flow in Hy=5.0.

For low Rayleigh number flow the increase in heat transfer over the two-dimensional flow for air at Ra $= 10^3$ in Hy=5 is less than 1% and for the higher Rayleigh number for air at Ra $= 10^5$ in Hy=5 is also less than 0.3%.

For cerrobase the Nu_{vm} is less than Nu_{2d}. This is expected as the two-dimensional

flow does not result for Hy$\leq$5 as the flow at the symmetry plane is still under the influence of the end wall. Hence the convection of heat at the symmetry plane is weaker than that in the two-dimensional problem.

Figure 6.105 represents $Nu_v(y)$ along the isothermal wall, x=0, for the coarse and the fine mesh sizes for air with Ra = 10^3 in the cavity (1.2.1) and Figure 6.106 is that of cerrobase with Ra = 10^3 in the cavity (1.2.1). Solid line graphs represent the fine grid results and the asterisks the coarse grid results. With air the coarse grid results are 2% greater than the fine grid results and with cerrobase 1%. The coarse grid heat transfer results can be considered to be good initial bench mark results to compare against.

In order to compare results with Mallinson and de Vahl Davies [39], solutions for air with other Rayleigh numbers have been computed at Hy=1.0.. Results obtained

Ra	Nu^*_{av}	Nu^*_{vm}	Nu_{av}	Nu_{vm}	ψ^*_{max}	ψ_{max}
10^4	2.20	2.32	2.23	2.35	—	—
1.5×10^5	5.14	5.30	5.40	5.65	—	—
5×10^5	7.43	7.62	7.88	8.18	18.4	17.9

Table 6.3: Comparing Nusselt numbers and stream function values with those obtained by Mallinson and de Vahl Davis.

by Mallinson and de Vahl Davis are denoted by *.

At large Ra the average and vertical Nusselt number over-predicted those obtained by Mallinson and de Vahl Davis [39], whereas the maximum stream function obtained under predicts that obtained by Mallinson and de Vahl Davis [39]. The principle reason for the discrepancies with the results obtained for the high Rayleigh numbers in this study and those obtained by Mallinson and de Vahl Davies is primarily due to numerical errors as both sets of results have been obtained on coarse grids. However, both sets of results show the same trends. The discrepancies in the Nusselt numbers could arise as a result of Mallinson and de Vahl Davis using the 3-point forward difference to calculate the Nusselt number and then using the composite trapezoidal rule to calculate the averages. The slight discrepancy with the stream function values arise due to using staggered grids which require the stream function at the symmetry plane to be calculated by interpolating velocities from a distance a half y-meshlength away from the symmetry plane.

Graph A: cerrobase at Ra = 10^3, Hy=1, Hz=1

Graph B: cerrobase at Ra = 5×10^3, Hy=1, Hz=1

Graph C: air at Ra = 10^3, Hy=1, Hz=1

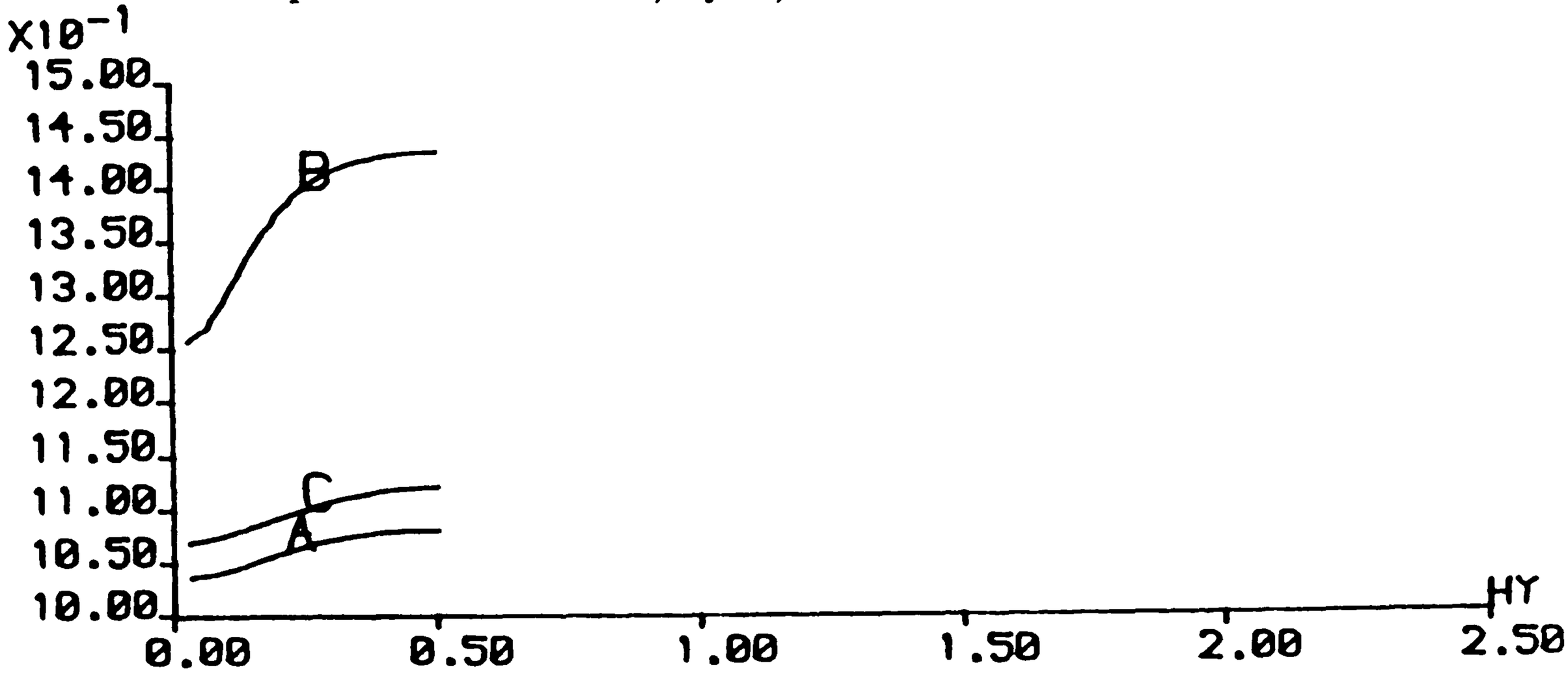

Figure 6.101 Nusselt number along the hot wall

Graph A: cerrobase at Ra = 10^3, Hy=1, Hz=1

Graph B: cerrobase at Ra = 5×10^3, Hy=1, Hz=1

Graph C: air at Ra = 10^3, Hy=1, Hz=1

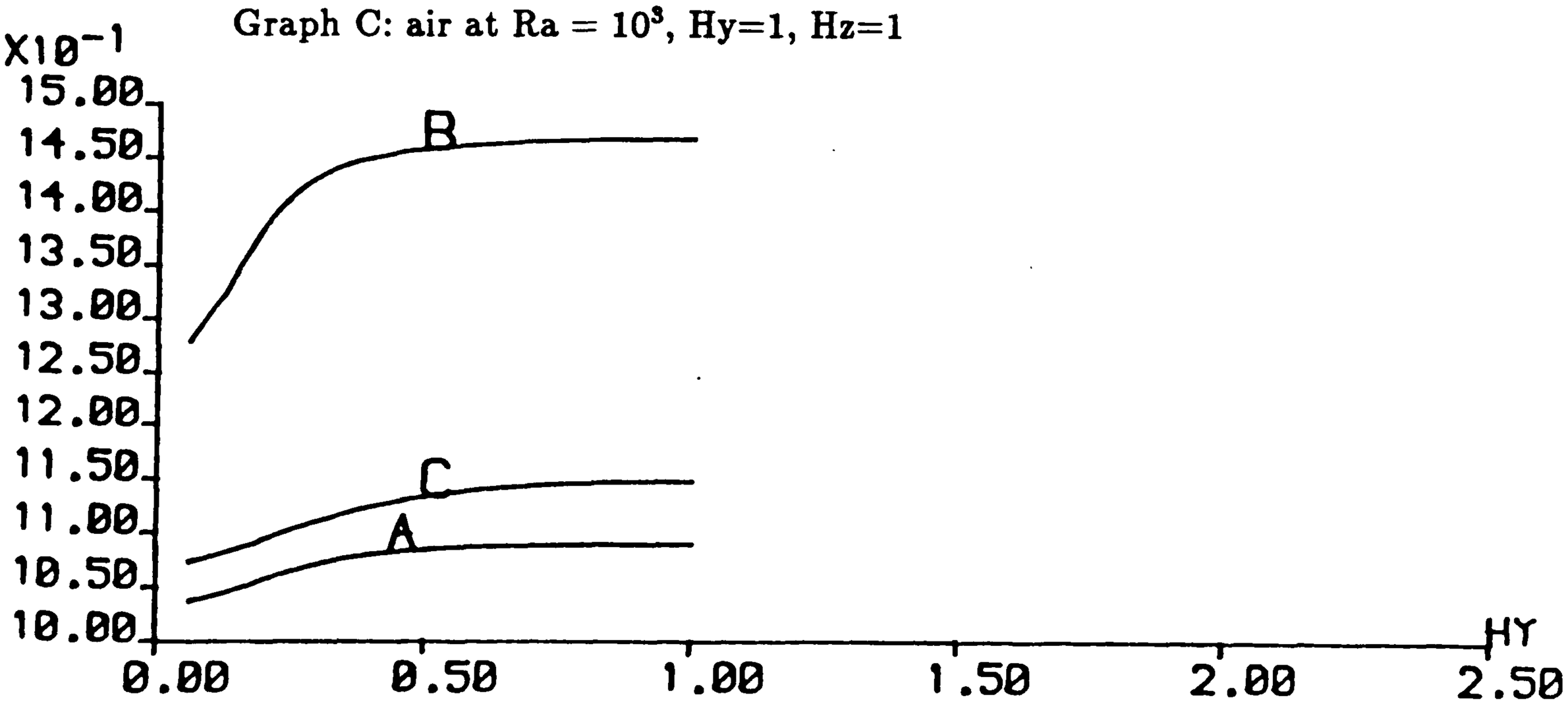

Figure 6.102 Nusselt number along the hot wall

Graph A: cerrobase at Ra = 10^3, Hy=1, Hz=1

Graph B: cerrobase at Ra = 5×10^3, Hy=1, Hz=1

Graph C: air at Ra = 10^3, Hy=1, Hz=1

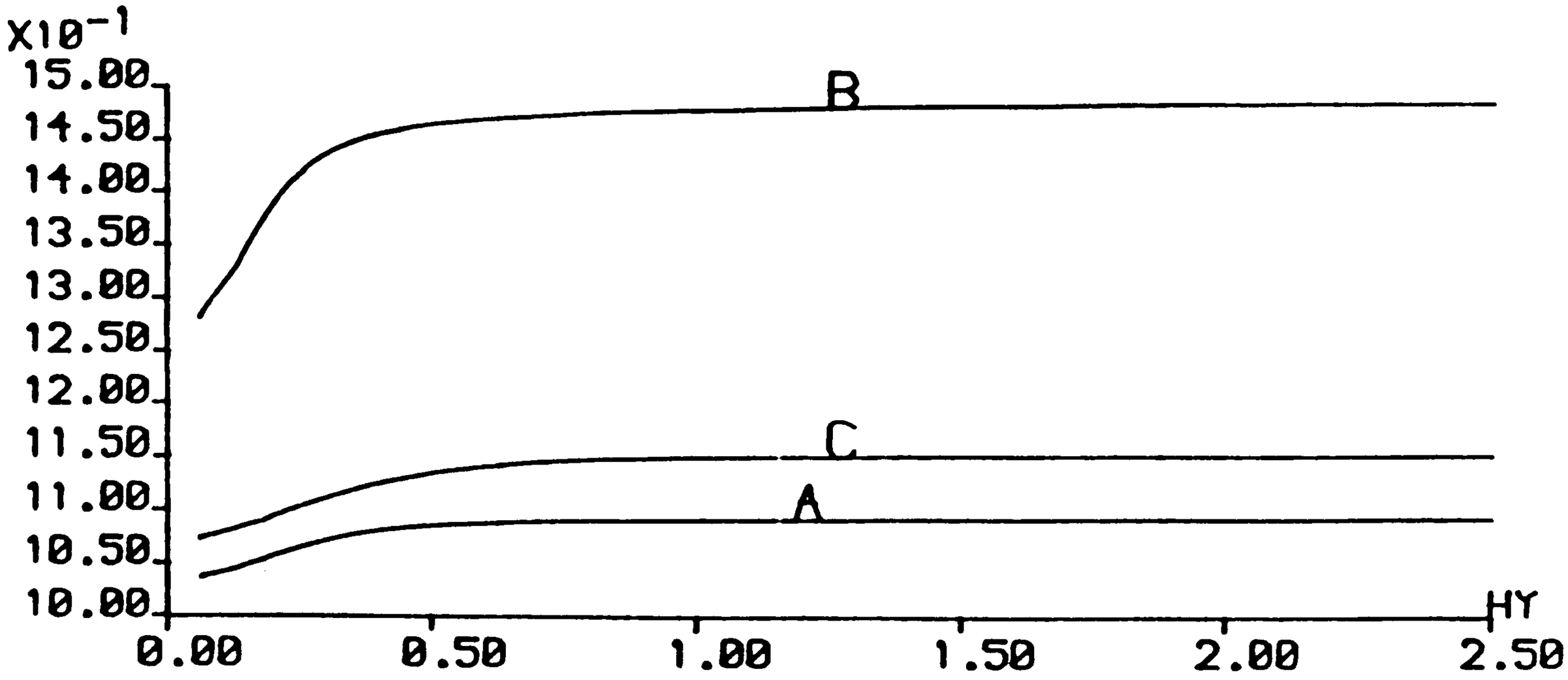

Figure 6.103 Nusselt number along the hot wall

Graph A: air at Ra = 10^5, Hy=1, Hz=1

Graph B: air at Ra = 10^5, Hy=2, Hz=1

Graph C: air at Ra = 10^5, Hy=5, Hz=1

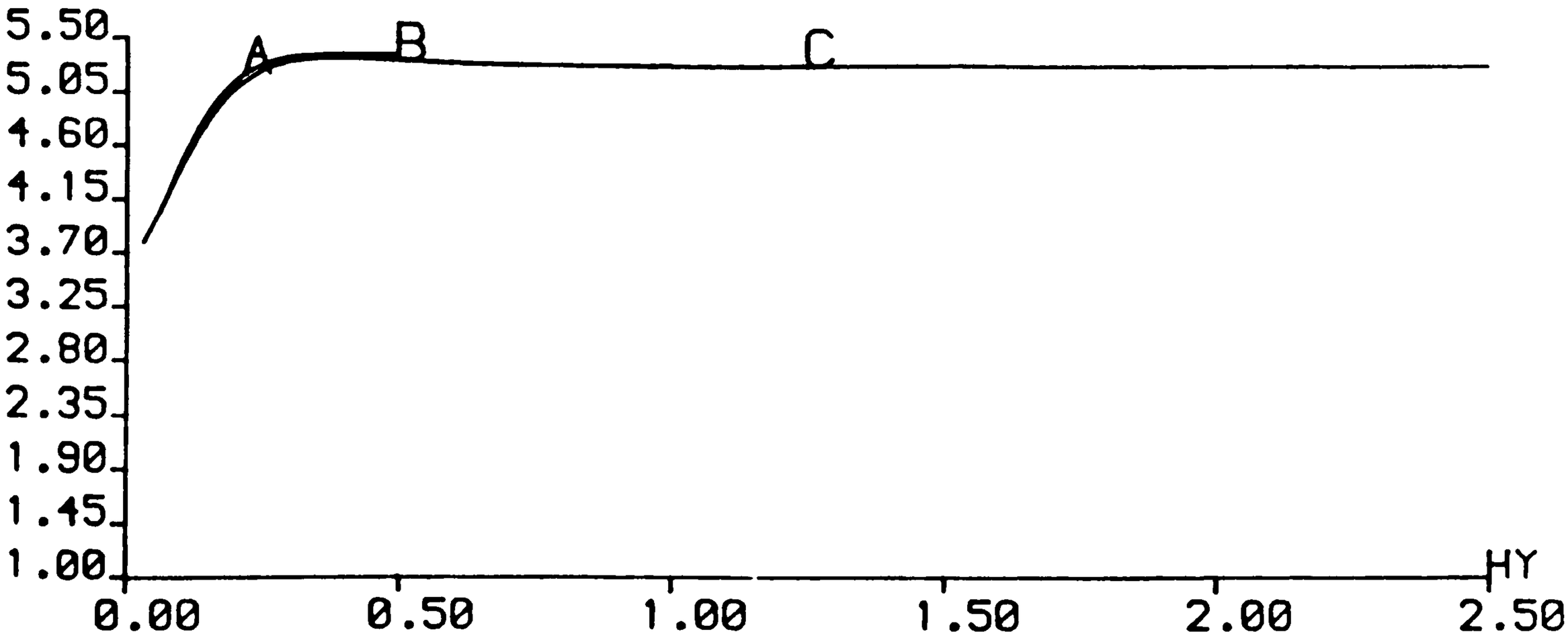

Figure 6.104 Nusselt number along the hot wall

air at Ra = 10^3, Hy=1, Hz=1, grid = 16x16x16

air at Ra = 10^3, Hy=1, Hz=1, grid = 32x32x32

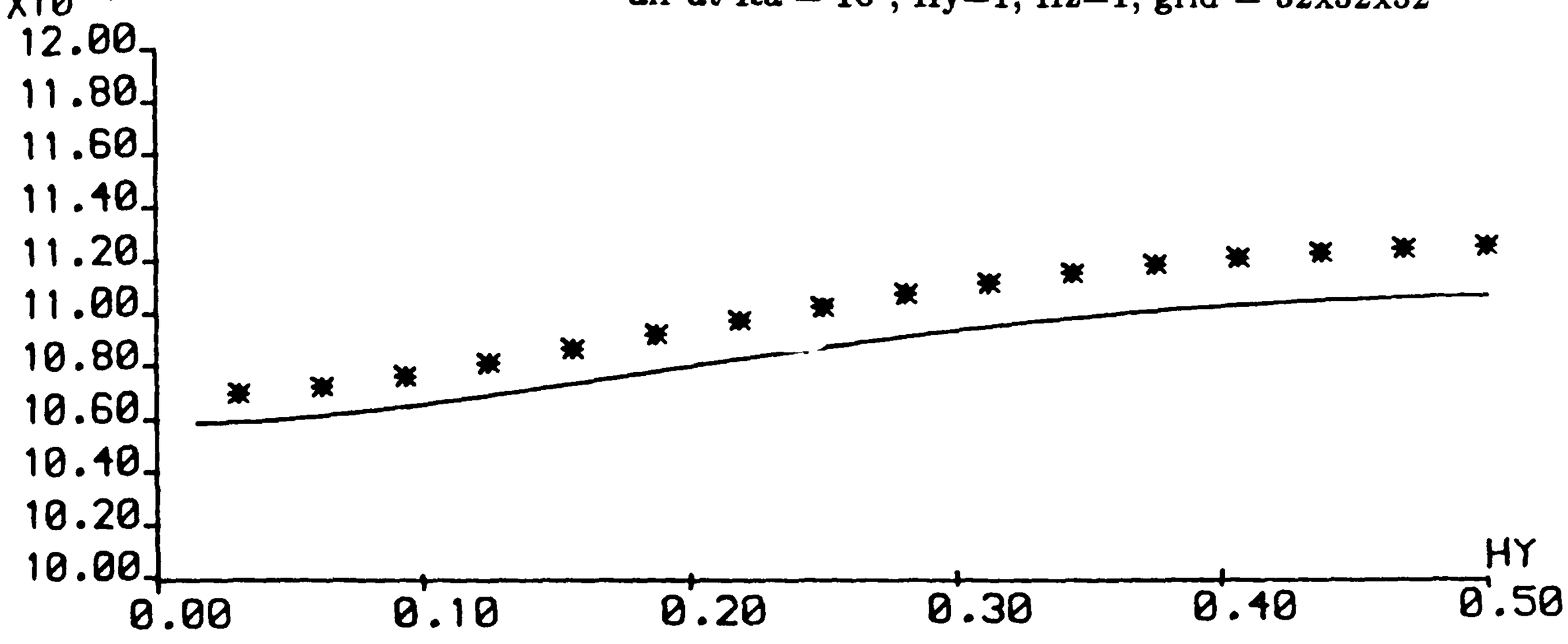

Figure 6.105 Nusselt number along the hot wall

cerrobase at Ra = 10^3, Hy=1, Hz=1, grid = 16x16x16

cerrobase at Ra = 10^3, Hy=1, Hz=1, grid = 32x32x32

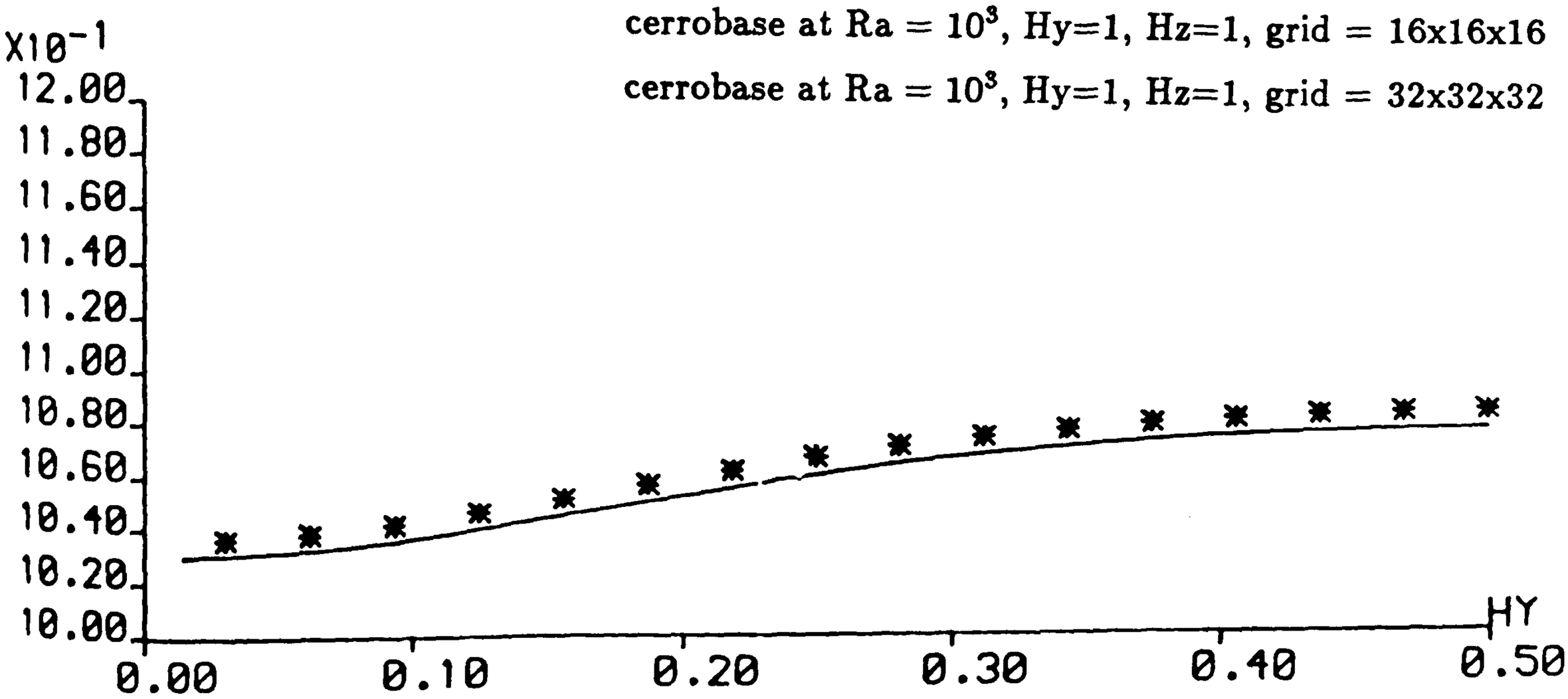

Figure 6.106 Nusselt number along the hot wall

6.6.6 Summary for the square cross section window cavity, Hz=1.0

The fluid flow structure for the low Rayleigh number with air and cerrobase in the square cross-section window cavity results in a single forward recirculating roll. The roll has been illustrated by tracing particle paths which lie on a torus like surface. The fluid roll is a result of the end wall influence and consists of two distinct mechanisms which generate the three dimensional fluid flow. The first mechanism, termed the inertial end effect, is a result of the kinematic interaction of a rotating fluid next to a flat plate and the second mechanism, termed the thermal end effect is a result of the axial temperature gradients.

The result of the no-slip boundary condition at the end wall is to reduce the magnitude of the cross-sectional velocity of the fluid in the vicinity of the end wall. This leads to the introduction of the inertial end effect. The decrease in the magnitude of the cross-sectional velocity of the fluid near the end wall also leads to the reduction in the convection of heat there. Thus the thermal solution is more conductive near the end wall than near the symmetry plane. This results in the non-zero axial temperature gradients which lead to the generation of vorticity sources near the end wall, thus the thermal end effect is introduced.

The axial flow is generated as a result of the end wall. Hence it is always greatest in the vicinity of the end wall and weakest near the symmetry plane. The cross-sectional flow generated by the buoyancy force is always greatest furthest from the end wall, (that is, near the symmetry plane), where there is minimum viscous drag to oppose the buoyancy force. It is weakest near the end wall where there is maximum viscous drag to oppose the buoyancy force.

Strong axial temperature gradients in window cavities filled with air generate vorticity source that augment the axial flow creating *undulations* in the particle paths. The axial temperature gradients in window cavities filled with cerrobase are small and thus generate weak vorticity sources resulting in very weak undulations in the particle paths. The turning points of the cerrobase particles with respect to the axial direction lie on an almost perfect cylindrical surface. The undulation in particle paths reported here have not been commented upon in other investigations of this problem, although undulations can be seen in the particle tracks presented by Mallinson and de Vahl Davis [39].

From Table 6.2 it can be seen that the thermal end effect, dependent on the axial temperature gradients, is much weaker for cerrobase than air. The overall end wall effect, represented by the ratio R, for cerrobase is generally greater than air thus indicating that the inertial end effect is greater for cerrobase than air. This is expected due to the lower effective viscosity (greater inertia) of cerrobase. As a result of the strong end wall effect, cerrobase particle paths wind a looser toroidal path near the end wall. This makes the flow with cerrobase radically different to the flow with air, whose particles wind a tighter spiral.

The end wall effect is very dependent on the length/depth of the cavity. For very short cavities the cross-sectional flow at the end wall is under the influence of the viscous drag due to the end wall. As a result the cross-sectional velocities at the end wall and the symmetry plane are going to be of similar magnitude, hence the axial temperature gradients are going to be small. This will result in a small inertial and thermal end effects compared to when the difference between the cross-sectional velocities at the symmetry plane and the end wall is large, which is the case of the longer/deeper cavities. In the longer cavities the viscous drag due to the end wall does not effect the flow at the symmetry plane leading to two-dimensional flow near the symmetry plane. The difference between the cross-sectional flow at the symmetry plane and the end wall in the longer cavity is greater than the short cavities leading to larger inertial and thermal end effects. Hence the end wall effect in the longer cavities is stronger than in the shorter cavities. This can be seen in figures 6.41, 6.87 and 6.100 where the maximum axial velocity in the shorter cavity is always less than that in the longer cavities. The limiting value of the maximum axial velocity can be obtained from the longer cavities.

For cerrobase with $\mathrm{Ra} = 5 \times 10^3$ a change in the sign of $\partial\theta/\partial y$ results in the inner core near the vicinity of where the peak axial velocity occurs. This is due to the strong axial flow contributing to the convection of heat. As a result of larger opposing axial temperature gradients in the longer cavities than in the shorter cavities, the maximum $\partial\theta/\partial y$ for the longer cavities is smaller than that of the shorter cavity Hy=1.0. For larger Rayleigh numbers, $\mathrm{Ra} \geq 5 \times 10^3$, with cerrobase it appears that secondary flow may develop if the contribution to convection of heat near the peak axial velocity were to increase.

The fluid flow structure for the higher Rayleigh number with air in the square cross-section window cavity, consists of a reverse flow accompanying the forward flow. The

forward roll occurs as described for the lower Rayleigh number. The appearance of the reverse roll is due to the convective effects of the secondary flow with respect to the cross section, viz the change in sign of $\partial\theta/\partial x$ in the cross section. This results in a sign change of $\partial\theta/\partial y$ which in turn generates vorticity that opposes the forward flow. When this vorticity is sufficiently strong enough it overcomes the forward flow, producing a reverse flow. The opposing vorticity generated in the shorter cavity, Hy=1, is not sufficiently strong enough to overcome the forward flow. Hence reverse flow is not produced with this shorter length aspect ratio. As a result of a reverse flow occurring in the longer cavities, Hy=2 and 5, the maximum $\partial\theta/\partial y$ in these cavities are smaller than in the shorter cavity.

The Nusselt number along the isothermal wall, $Nu_v(y)$, decreases as the end wall is approached. This indicates the extent of the thermal boundary layer in which the convection of heat is reduced. As the Rayleigh number increases the thickness of this layer decreases. The average Nusselt number, Nu_{av}, is less than the Nusselt number obtained with two-dimensional problem, Nu_{2d}. This is expected due to the thermal boundary layer and of course as Hy increases $Nu_{av} \longrightarrow Nu_{2d}$. The Nusselt number at the symmetry plane, Nu_{vm}, for air is always greater than Nu_{2d} for the lower and higher Rayleigh number flows investigated. This is expected for the lower Rayleigh number flow as two-dimensional flow exists in the longer cavities so Nu_{vm} is expect to be at least equal to Nu_{2d}, but as a result of the axial flow contributing to convection of heat, Nu_{vm} becomes greater than Nu_{2d}. Although for higher Rayleigh number flow two-dimensional flow does not exist, the contribution to the convection of heat by the axial flow is sufficient for $Nu_{vm} \geq Nu_{2d}$.

When two-dimensional flow does not exist in the cavity and the contribution to the convection of heat by the axial flow is small then Nu_{vm} is expected to be less than Nu_{2d}, as is the case with air with $Ra = 10^3$ in the shorter cavity Hy=1.0 and with cerrobase with $Ra = 10^3$ and 5×10^3 in the cavity with length aspect ratios Hy=1, 2 and 5. The effect of the three dimensional motion on the heat transfer is relatively small. For low Rayleigh number flow the increase in heat transfer over the two-dimensional flow for air at $Ra = 10^3$ in Hy=5 is less than 1% and for the higher Rayleigh number for air at $Ra = 10^5$ in Hy=5 is also less than .3%.

For the low Rayleigh number flow for air, two-dimensional flow exists for cavities $Hy \geq 3.4$. Which is a larger range than that predicted by Linthorst et al. [34], they predict $Hy \geq 4$ for two-dimensional flow to exist with air at $10^3 \leq Ra \leq 5 \times 10^4$.

Mallinson and de Vahl Davis [39] regard the reverse flow as two-dimensional and hence predict for two-dimensional flow to exist Hy ≥ 1.2. Regarding the reverse flow as two dimensional is clearly incorrect.

Two-dimensional flow does not exist for air at the higher Rayleigh number, Ra $= 10^5$, for Hy $\leq 10^5$. Two-dimensional flow also does not exist for cerrobase at Ra $= 10^3$ and 5×10^3 with Hy ≤ 5. This is a further indication of the total end wall effect being stronger with cerrobase than air.

Comparison of results with those obtained by Mallinson and de Vahl Davis for air are good for the low Rayleigh number flow. Slight discrepancies arise with the higher Rayleigh number flow probably due to both set of results being obtained on coarse grids. Mallinson and de Vahl Davis using 11x11x11 mesh and results obtained with this study being calculated on a 16x16x16 mesh.

To investigate the effect of truncation errors for the coarse grid a fine mesh study, 32x32x32, for air and cerrobase at Ra $= 10^3$ in the shorter cavity have been performed. For air the coarse mesh results under-predict maximum $\partial\theta/\partial y$ by about 3%, under-predict the peak axial velocity by about 16%, over-predict the average Nusselt number by 2%, over-predict the Nusselt number at the symmetry plane by 2% compared with those obtained with the fine mesh. The results for the maximum stream function are same on both meshes. Overall the coarse grid results for air at low Rayleigh number can be considered quite good.

For cerrobase, the results obtained with the coarse mesh under-predict the maximum $\partial\theta/\partial y$ by about 8%, under-predict the peak axial velocity by about 16%, over predict the average Nusselt number by 1%, over-predict the Nusselt number at the symmetry plane by 1% and under-predict the maximum value of the stream function by 5%. Clearly the results obtained for cerrobase using the coarse grid should not be digested quantitatively but rather qualitatively.

The position of the peak axial velocity with respect to the y-direction appears to be independent of the Rayleigh number, the Prandtl number and the length aspect ratio, Hy, for the parameters investigated. The peak axial velocity seems to occur at .25Hy from the end wall.

Due to the nature of the flow for the liquid metal considered being different from that of air, care needs to taken when using simulant fluids such as air and water to experimentally model liquid metal flows. The three-dimensional effects are considerably stronger with liquid metals, even for Hy=5. Hence the length of the cavity needs

to be considered with great care when investigating the two-dimensional problem with liquid metal flows. However, the axial variation in the heat transfer is not as great as flow variation with the three dimensional results.

6.7 Window cavities with a shallow cross section, Hz=0.5

As far as the author is aware the three-dimensional fluid flow behaviour in the the shallow window cavity has not appeared elsewhere in the literature. For that reason comparisons with other three-dimensional studies is not possible.

6.7.1 Results obtained for Air (Pr=0.71) with Ra = 10^3

Results and flow features that occur in cavities with length aspect ratio Hy=1, 2 and 5 are presented in this section. The fluid flow behaviour in these cavities is described by a single forward recirculating roll as obtained with the square cross sectional cavity. The fluid roll in the shallow cavity is more elliptical than circular due to the nature of the cavity. Figure 6.107, 6.108 and 6.109 show particle paths to illustrate the flow in the cavities with length aspect ratio Hy=1, 2 and 5 respectively. In cavities with Hy=1 and 2 the forward roll fills the cavity completely whereas with Hy=5 the roll only partly fills the cavity with the rest of the cavity occupied with two-dimensional motion.

Figure 6.110, 6.111 and 6.112 show the contour plots of the ratio R for the length aspect ratio Hy=1.0 at planes A, B and C respectively. The plots reveal positive R contours attached to the side walls indicating undulations in the particle paths in the boundary layer with respect to the axial direction. Positive R contours are also attached to the side walls with the cavities whose length aspect ratio is Hy=2.0 and 5.0.

Figures 6.113 - 6.119 are plots of velocity vectors, isotherms and contours of $\partial\theta/\partial y$ for Hy=1.0 and exhibit similar features to those described in the square cavity. Figure 6.120 is a contour plot of $\partial\theta/\partial y$ for Hy=5. For all three values of Hy, isotherms at the symmetry plane are only slightly more convective than those at the end wall. The isotherms at the symmetry plane are very similar for all three values of Hy, unlike the square cavity where the isotherms at the symmetry plane with Hy=5.0 are much more convective than those obtained with Hy=1.0.

Figure 6.121 shows the streamlines at the symmetry plane for Hy=5 which exhibits primary flow. The streamlines for Hy=1 and 2 are not presented as they exhibit similar behaviour. Maximum values of the stream function obtained near the symmetry plane

with Hy=1, 2 and 5 is 0.16 for the three length aspect ratios.

Figure 6.122 shows the axial-velocity along the centre line. The end wall effect in the shorter cavity Hy=1.0 is only slightly restricted. This implies the difference between the strength of the cross-sectional flow at the symmetry plane and the end wall for the shorter cavity is similar to that for the longer cavities. This is unlike the square cross section window cavity. Also the strong axial temperature gradients in the shorter cavity have increased slightly the magnitude of the axial flow. Two-dimensional flow exists for Hy $\geq$ 2.5 compared to Hy $\geq$ 3.5 for the square cross sectional cavity, this is an indication of the end wall effect in the square cross-section window cavity being greater than that in the shallow cavity.

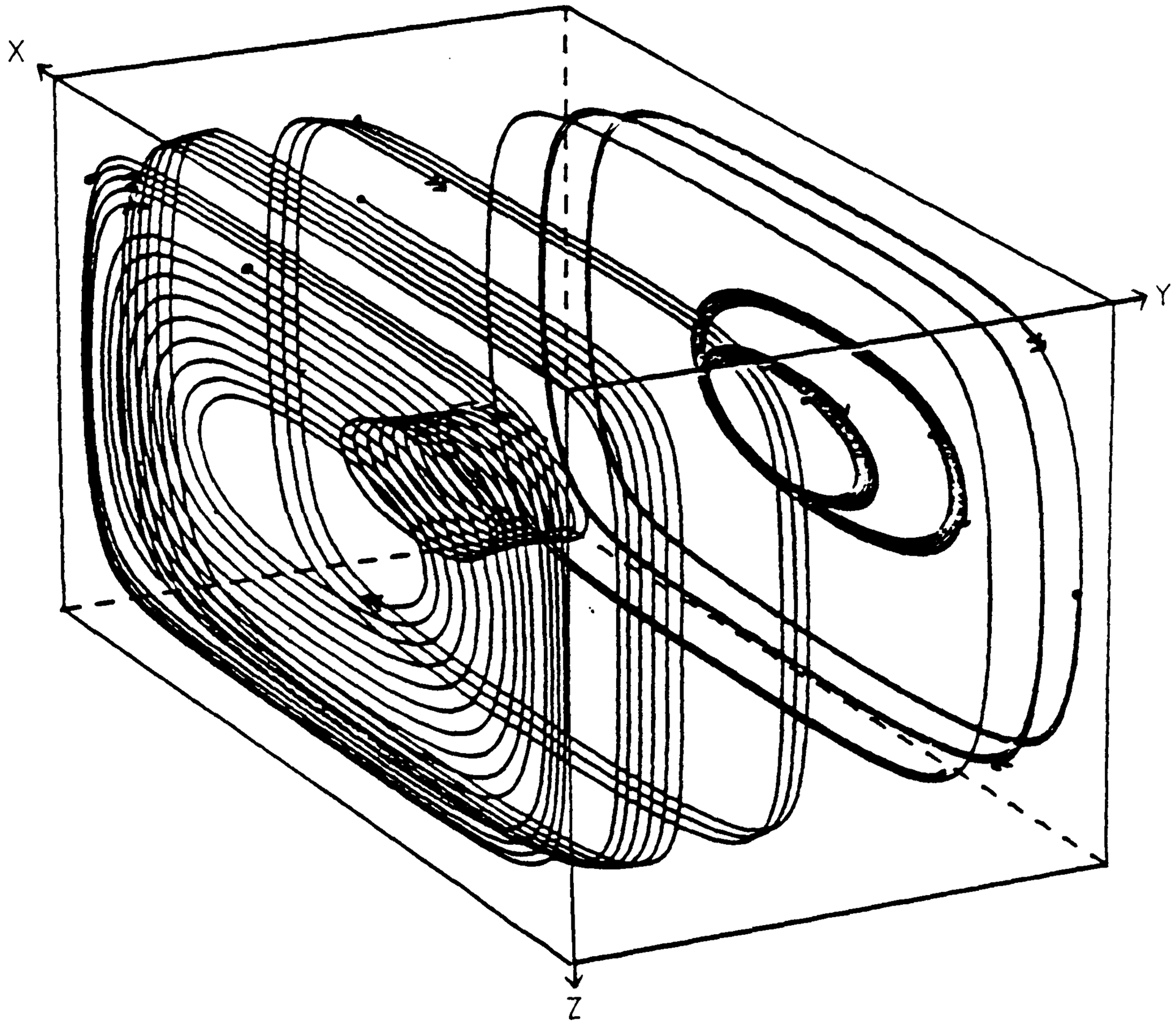

Figure 6.107 Particle track for air at Ra = 10^3, cavity (1,1,0.5) grid = 16x16x16

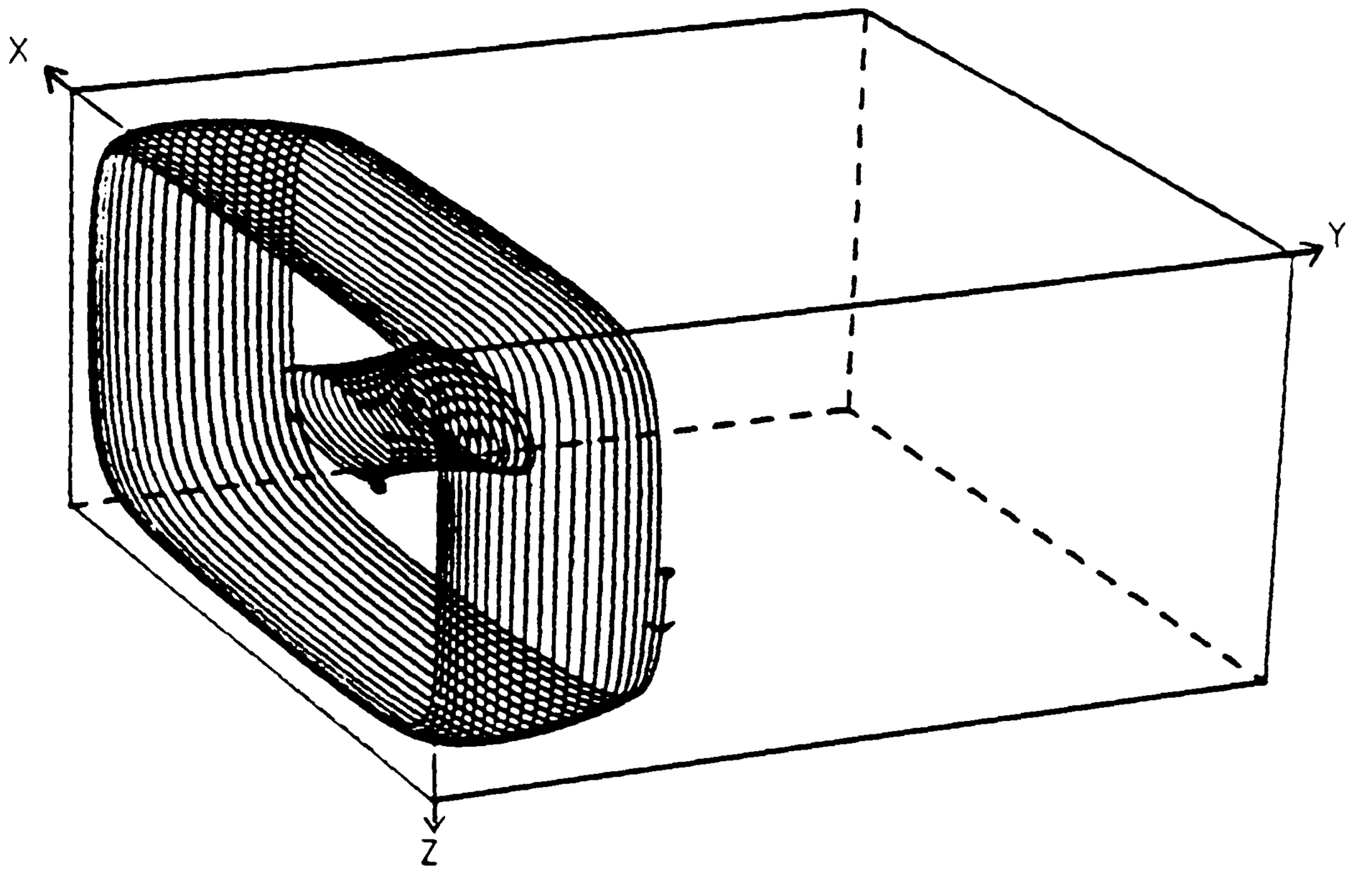

Figure 6.108 Particle track for air at Ra = 10^3, cavity (1,2,0.5) grid = 16x16x16

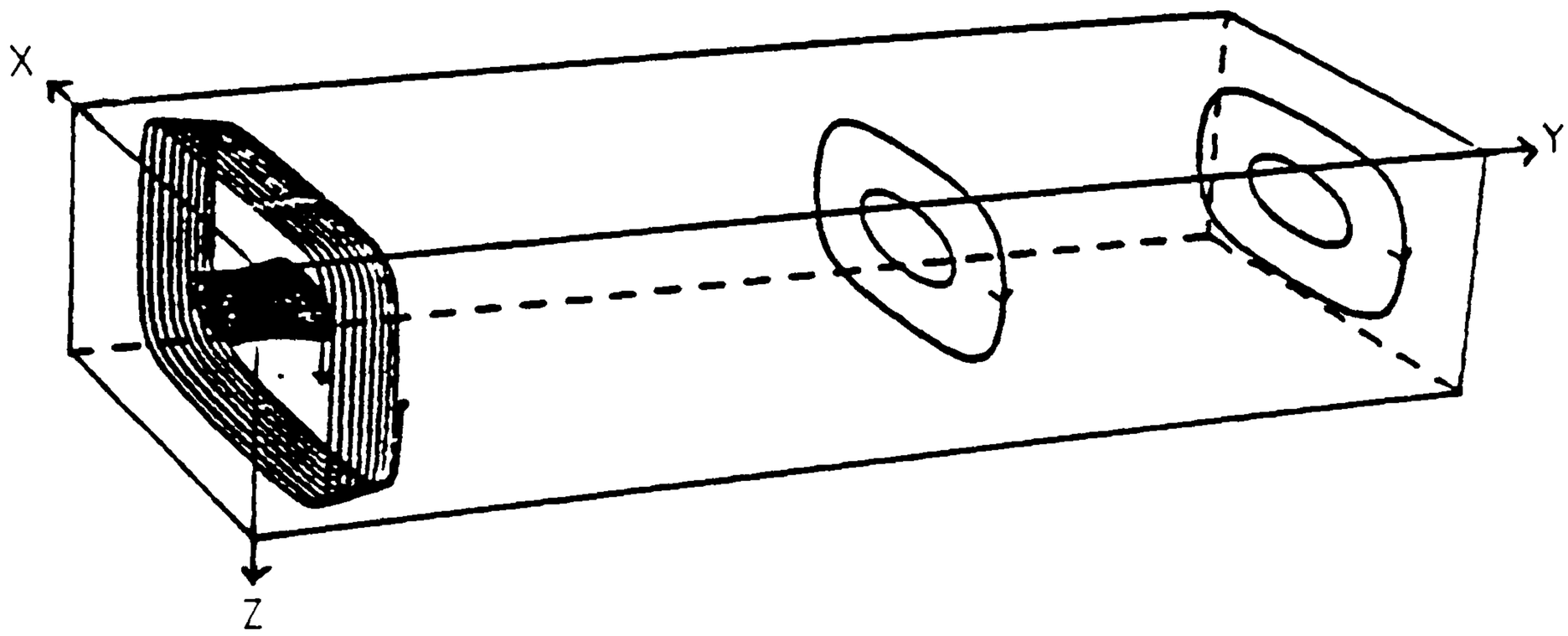

Figure 6.109 Particle track for air at Ra = 10^3, cavity (1,5,0.5) grid = 16x40x16

Fluid = air, Ra = 10^3, Hy=1, Hz=0.5, grid=16x16x16

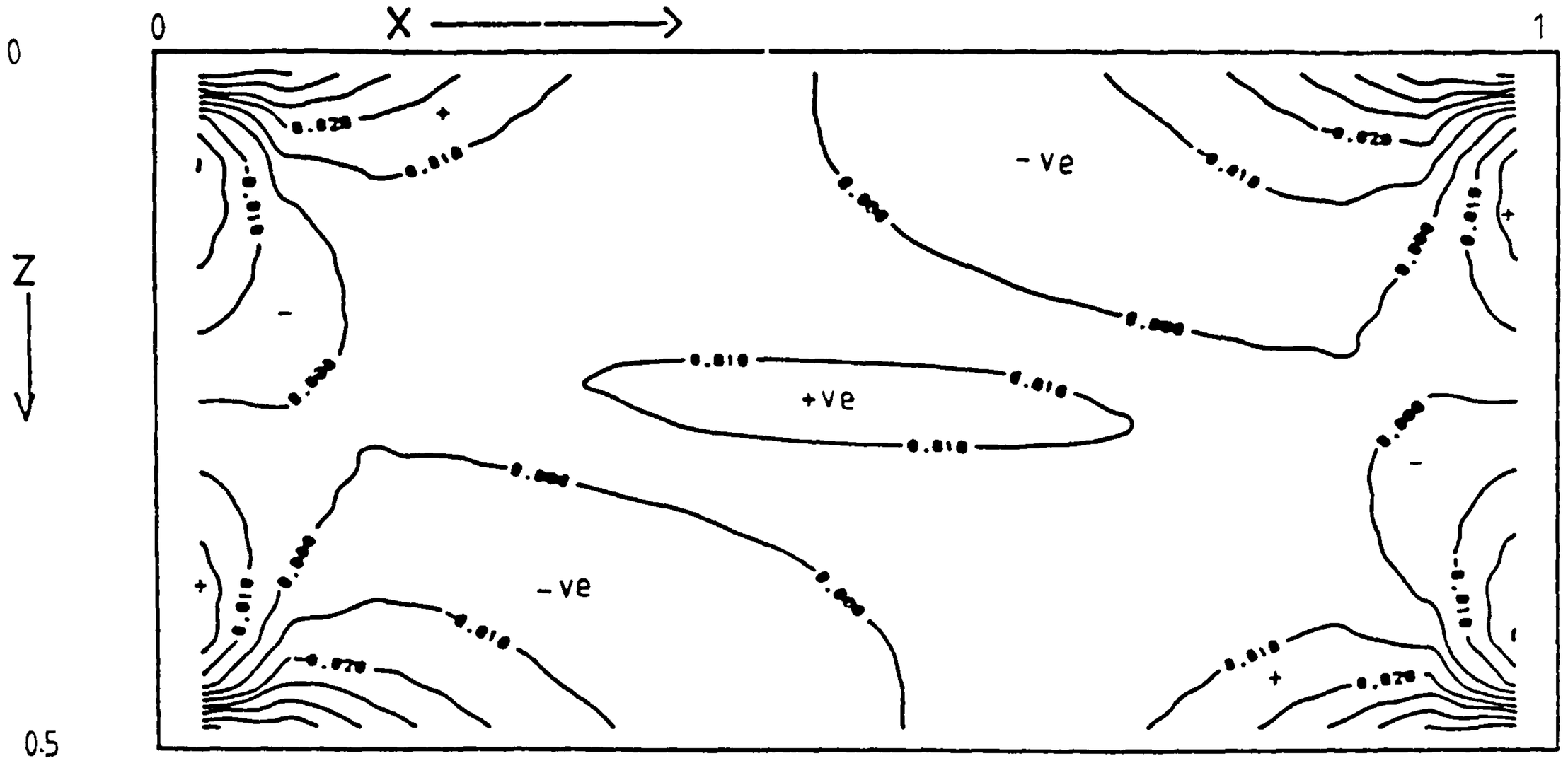

Figure 6.110 Contour plot of ratio R at plane A, near the end wall

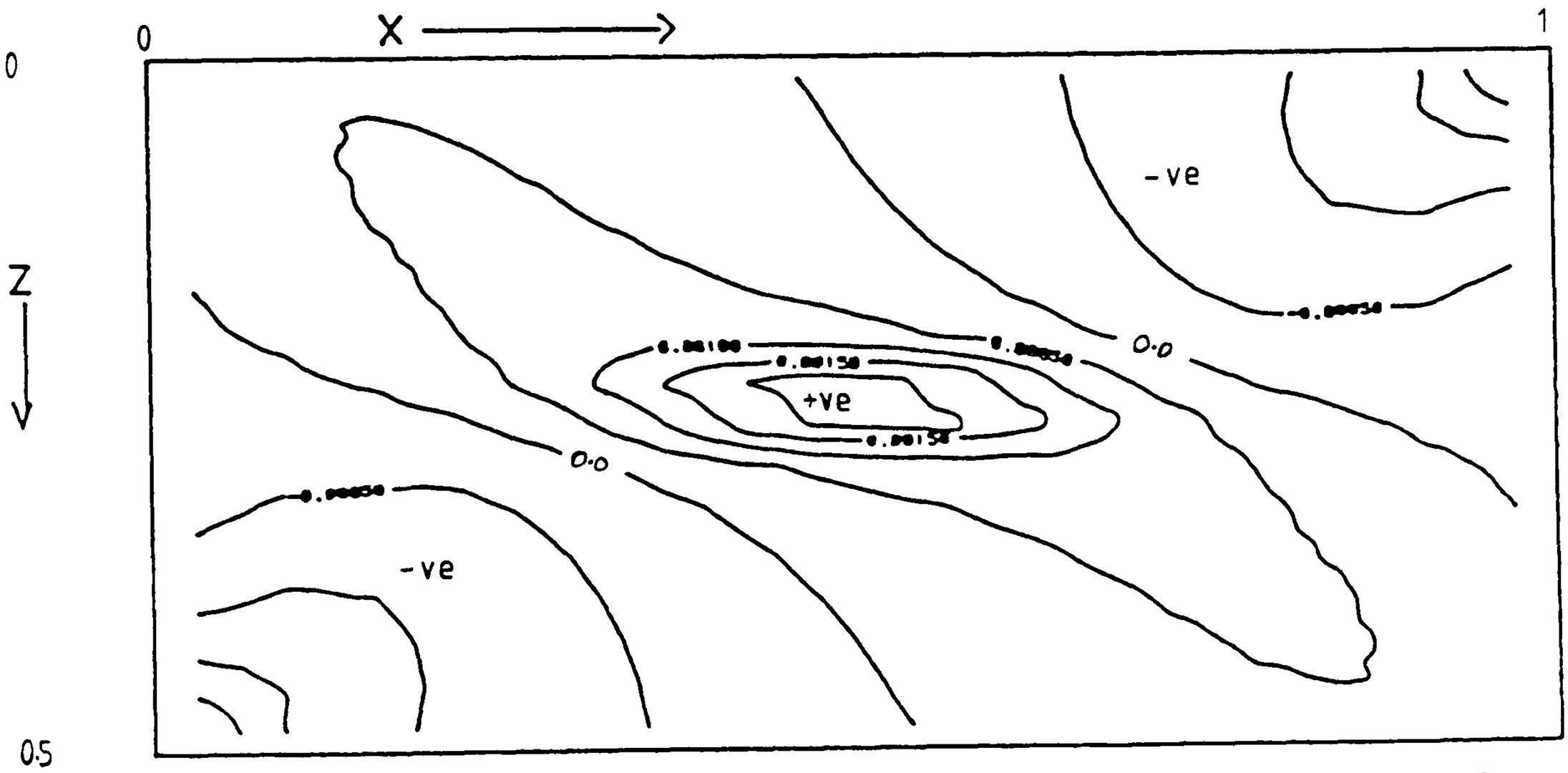

Figure 6.111 Contour plot of ratio R at plane B, near the symmetry plane

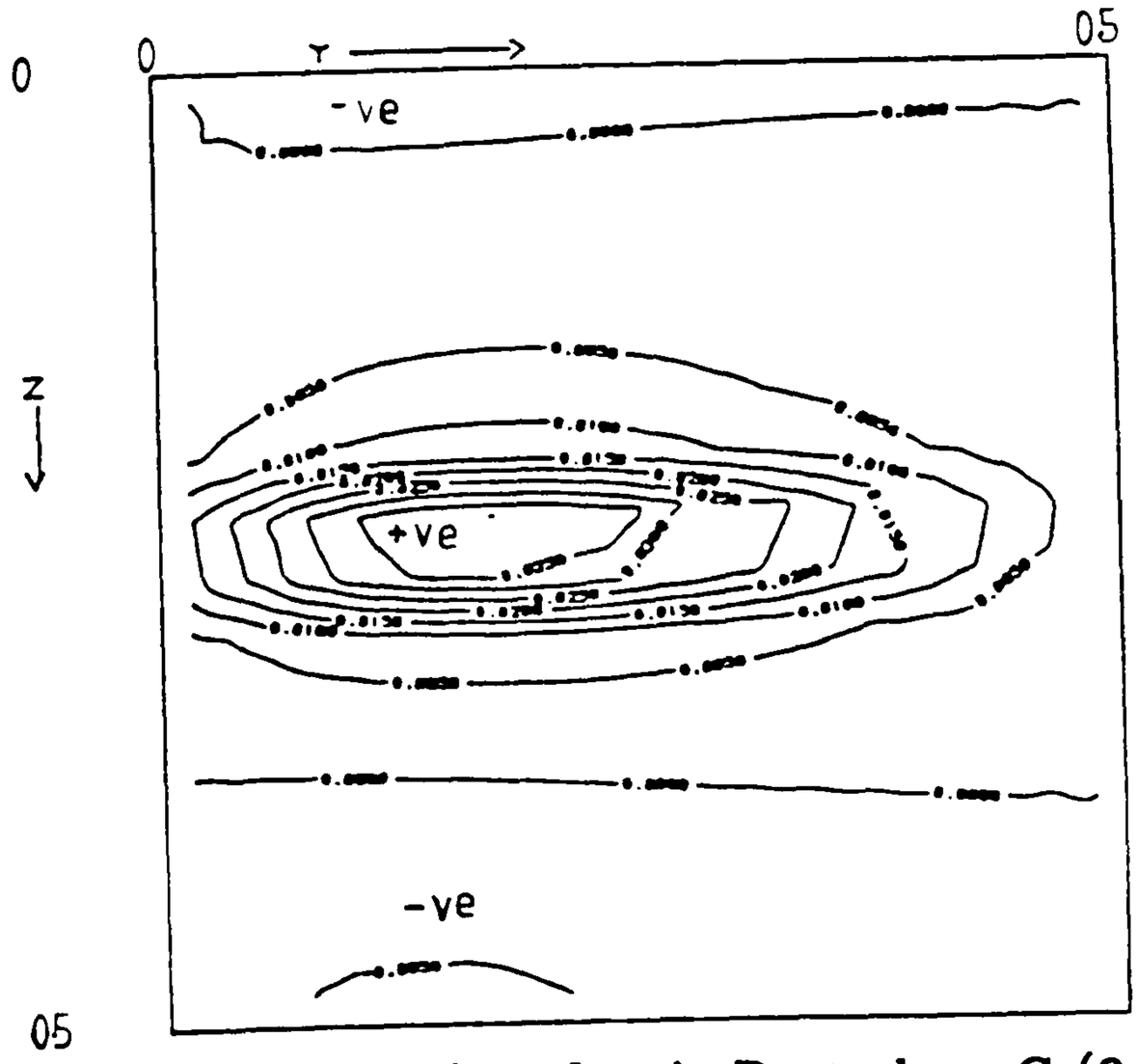

Figure 6.112 Contour plot of ratio R at plane C $(0.5 - hx/2, y, z)$

Fluid = air, Ra = 10^3, Hy=1, Hz=0.5, grid=16x16x16

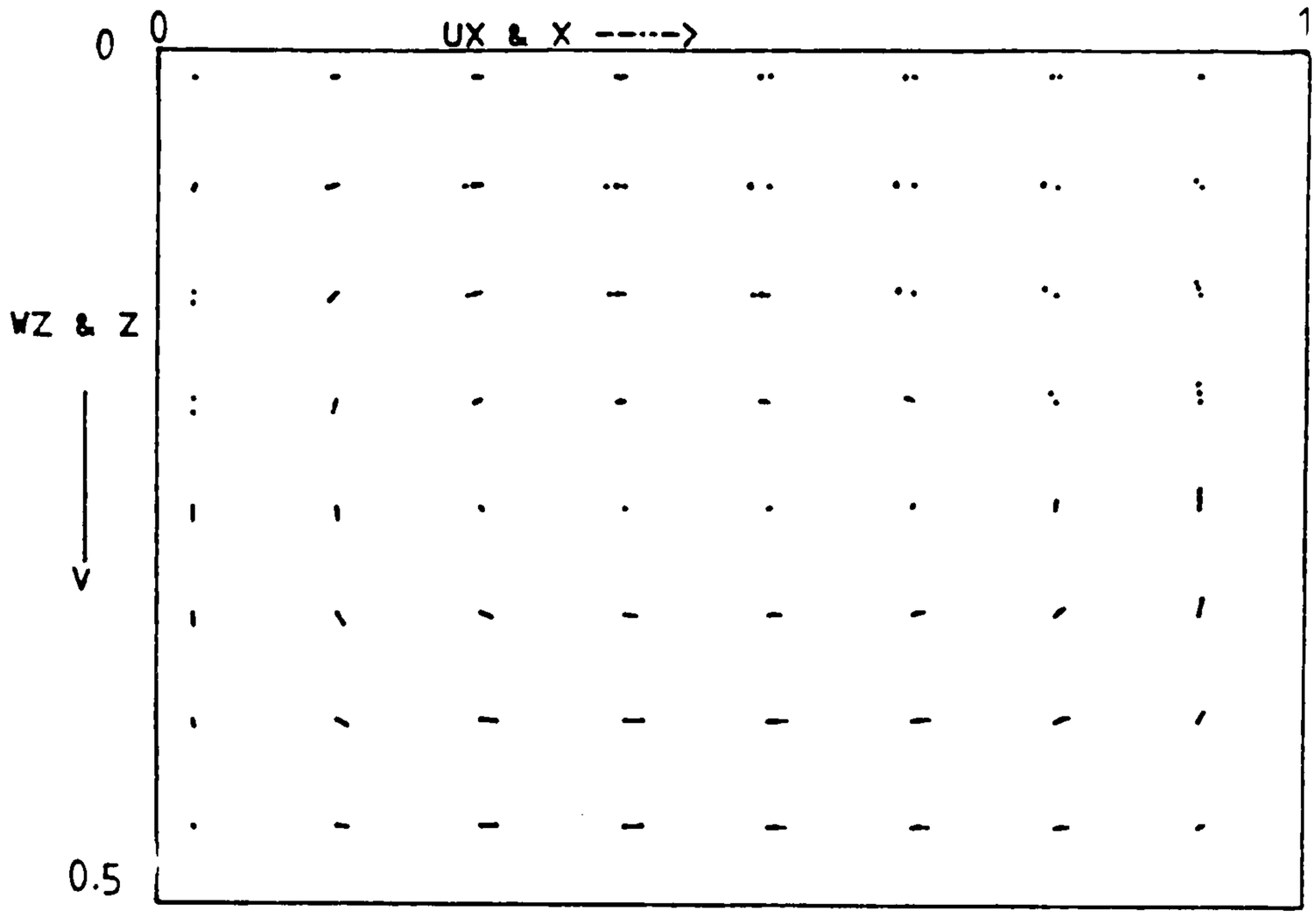

Figure 6.113 Velocity vectors at plane A, near the end wall

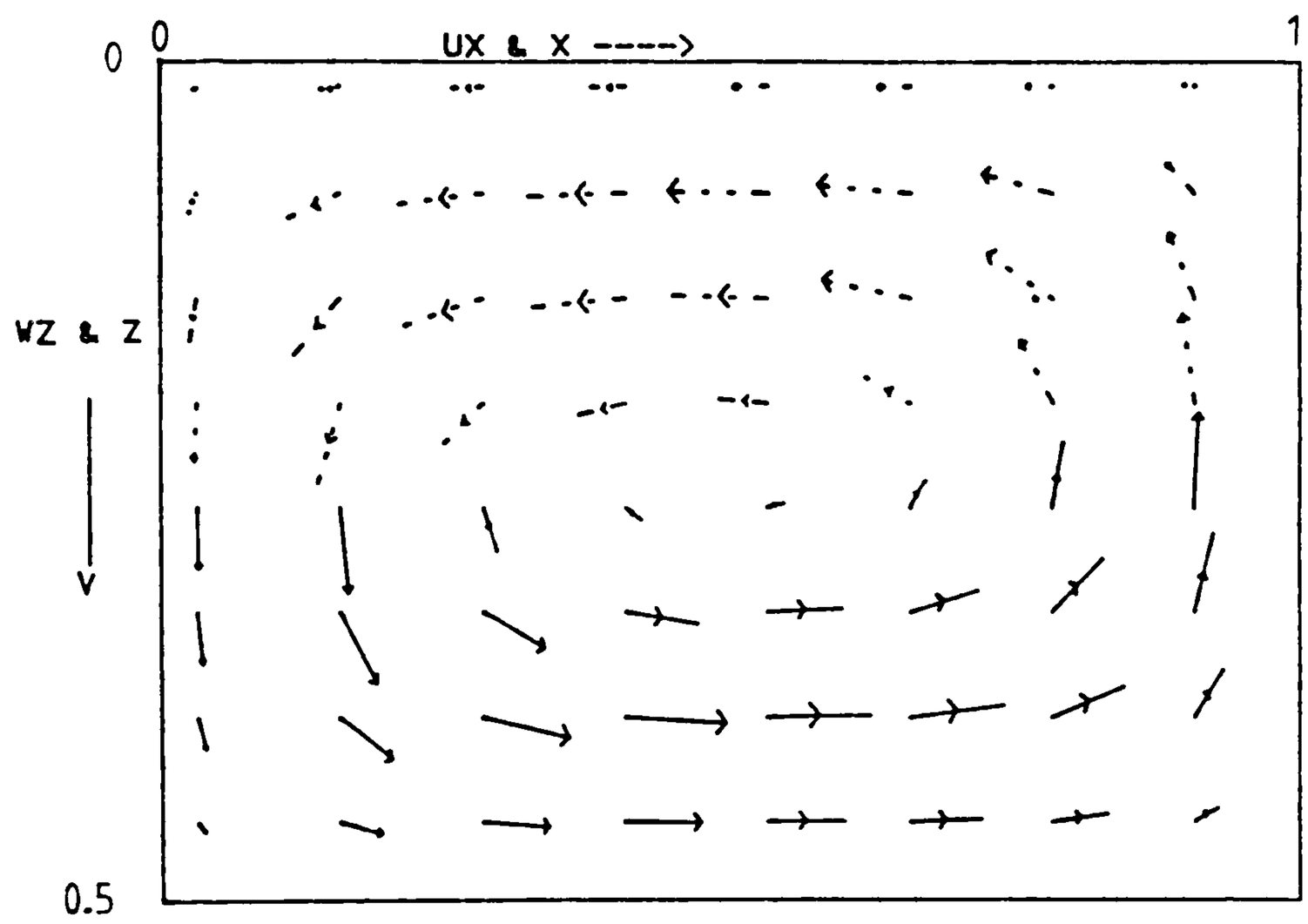

Figure 6.114 Velocity vectors at plane B, near the symmetry plane

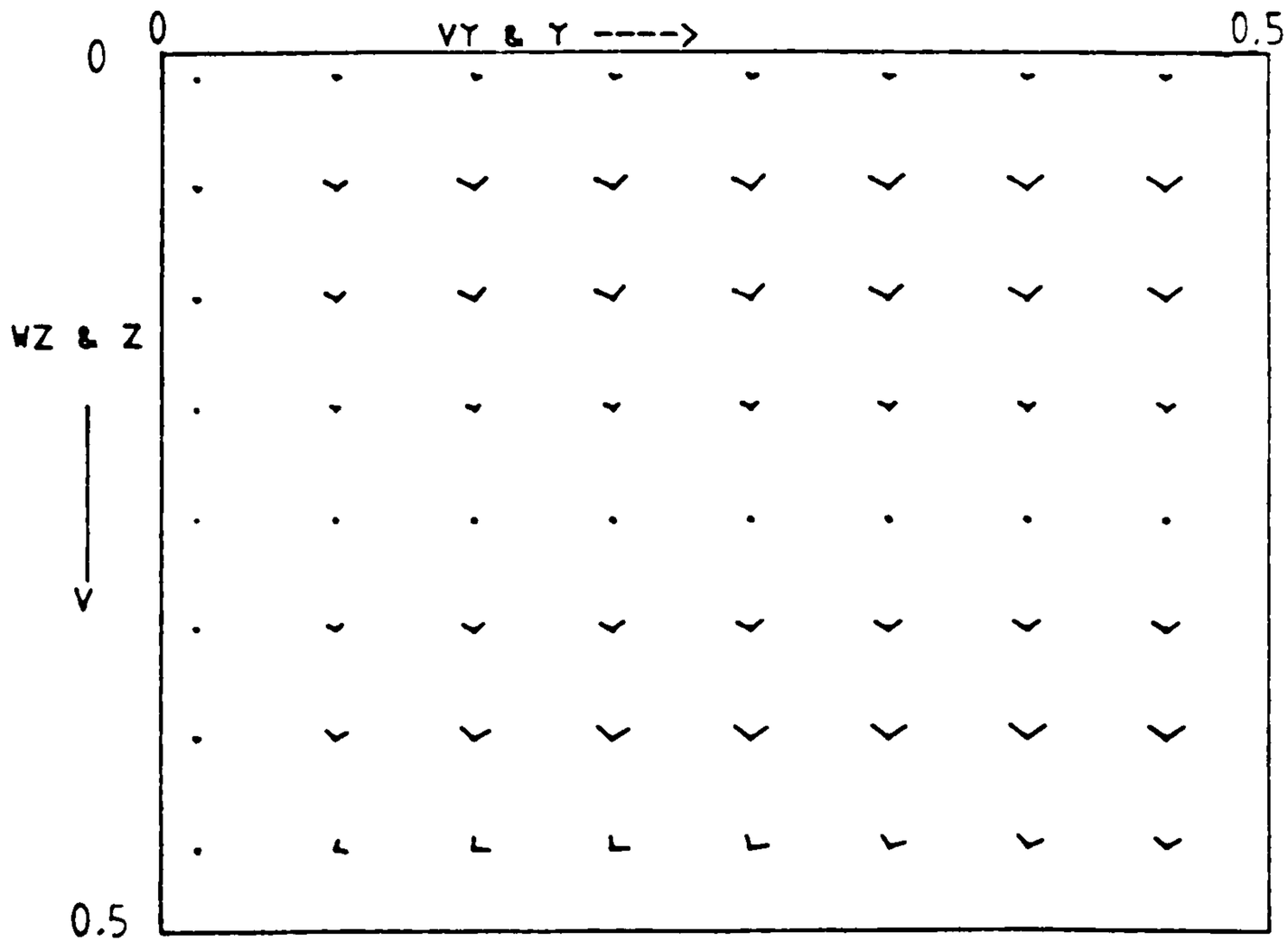

Figure 6.115 Velocity vectors at plane C $(0.5 - hx/2, y, z)$

Fluid = air, Ra = 10^3, Hy=1, Hz=0.5, grid=16x16x16

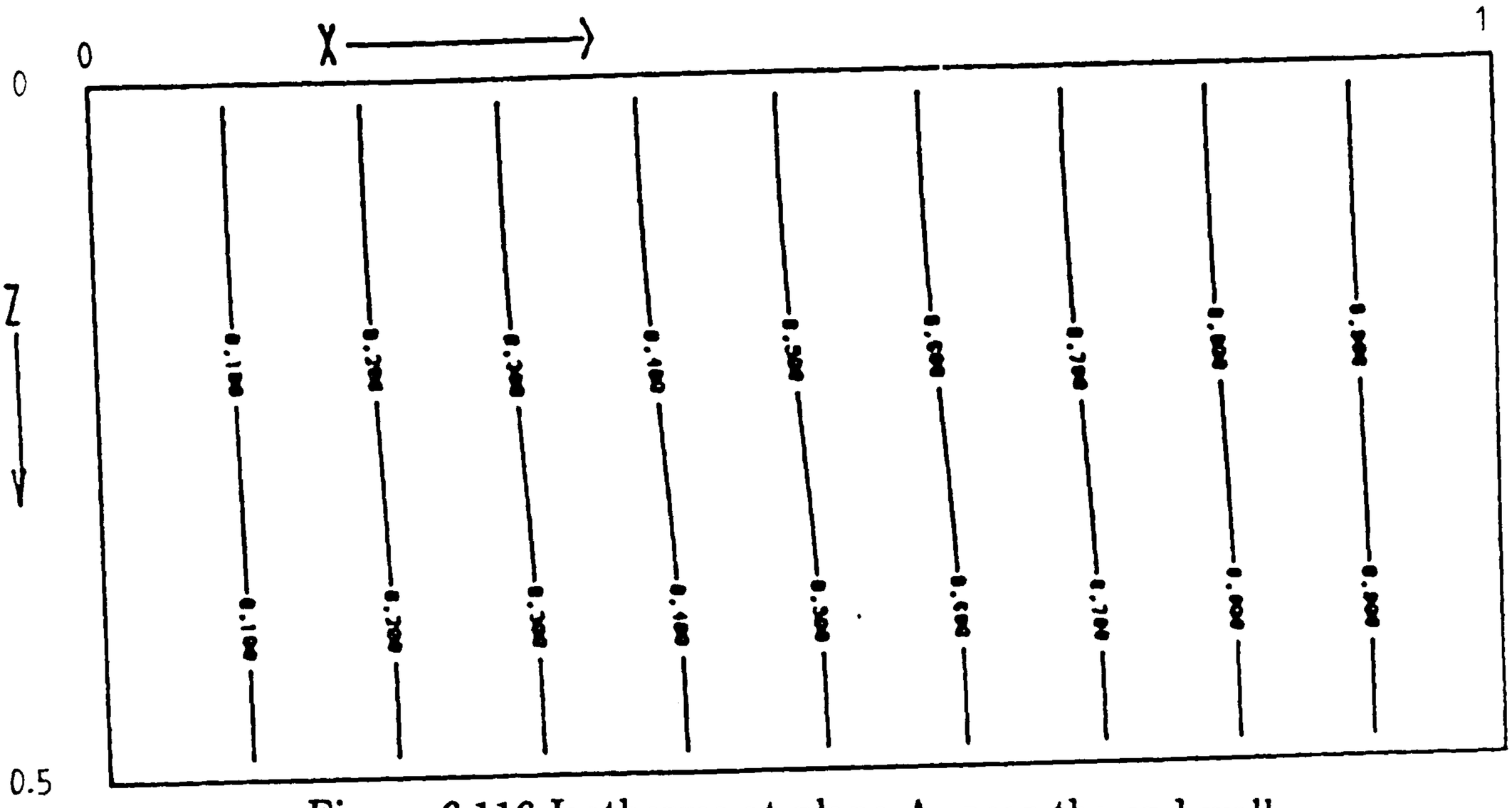

Figure 6.116 Isotherms at plane A, near the end wall

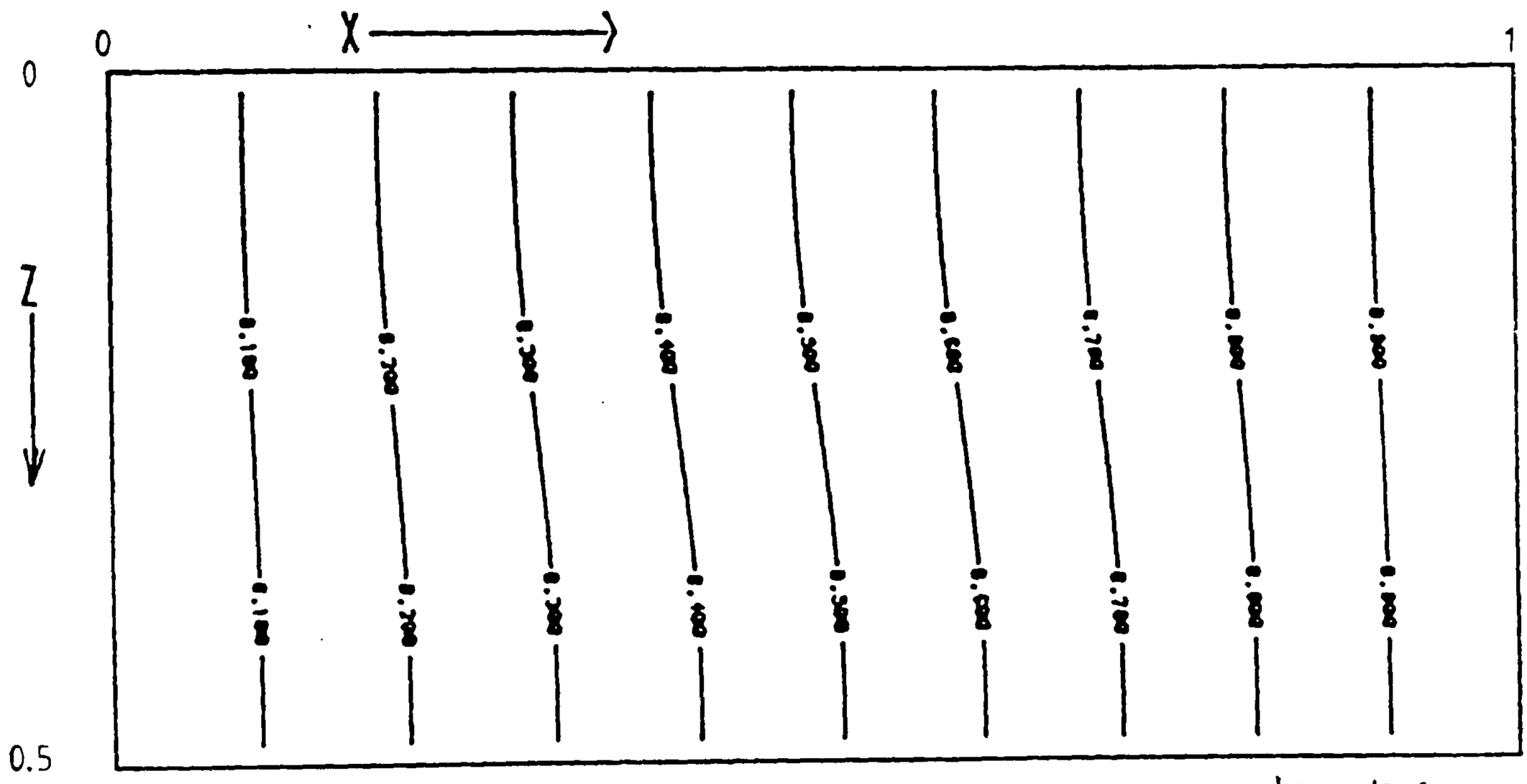

Figure 6.117 Isotherms at plane B, near the symmetry plane

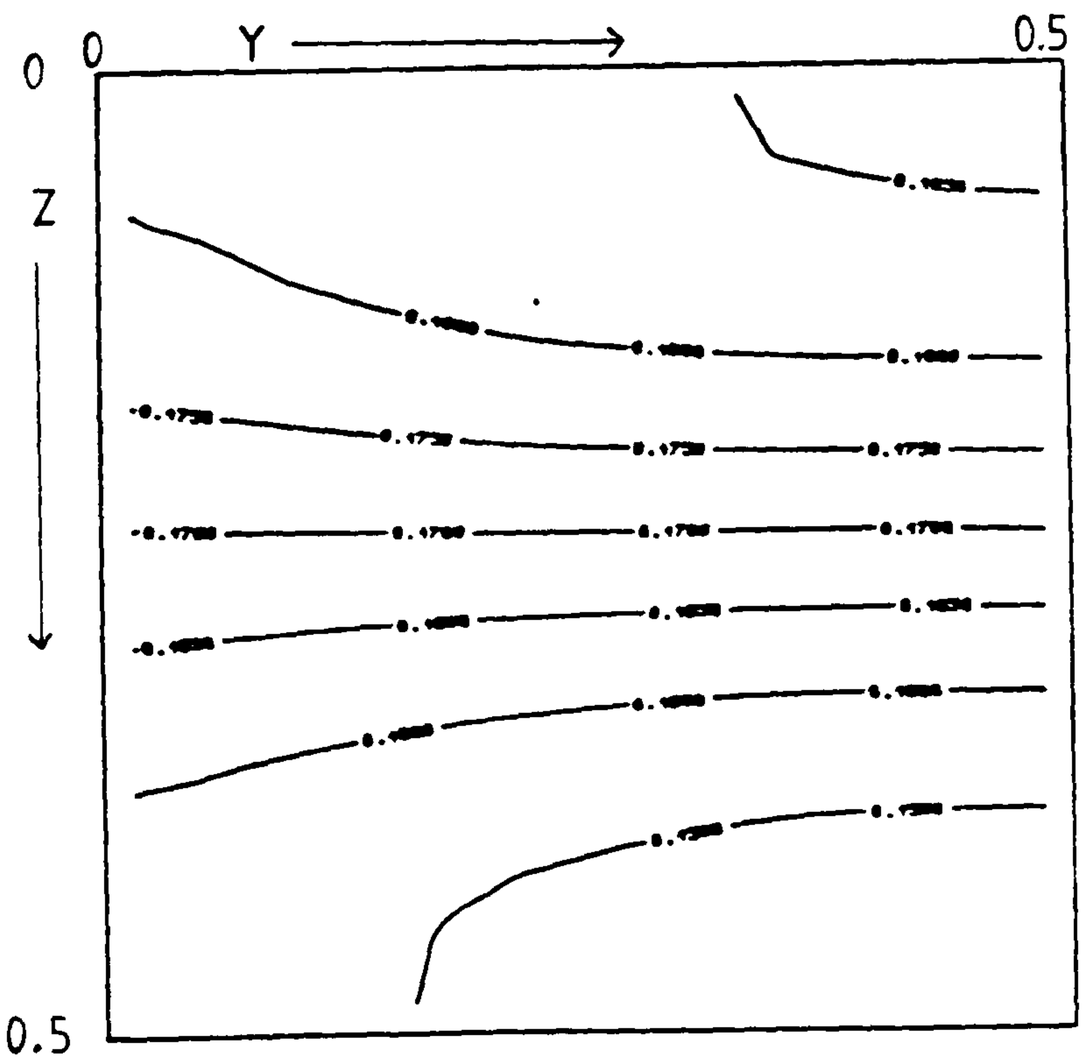

Figure 6.118 Isotherms at plane C, $(0.5 - hx/2, y, z)$

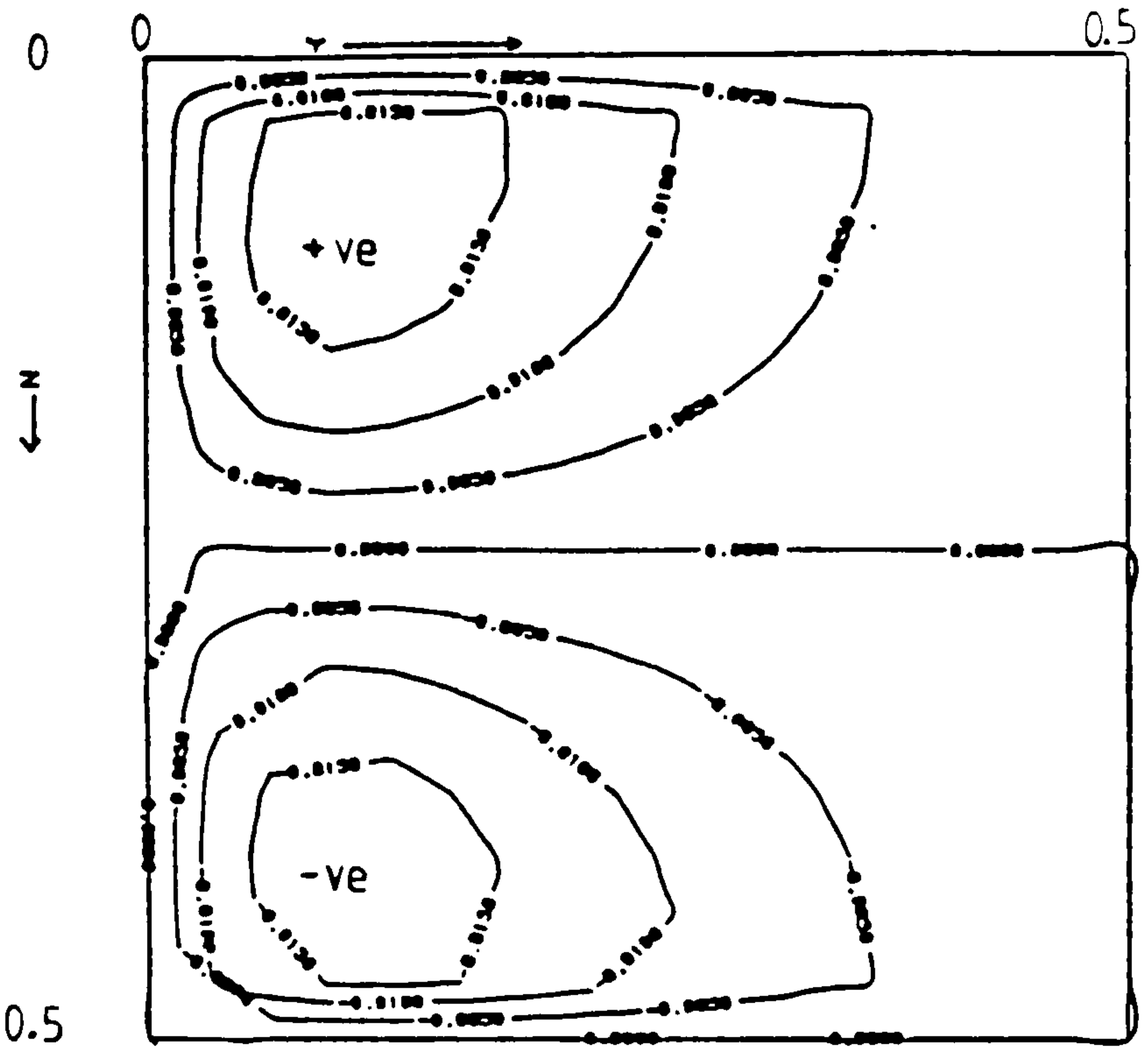

Figure 6.119 $\partial\theta/\partial y$ **at plane C,** $(0.5 - hx/2, y, z)$**, Hy=1**

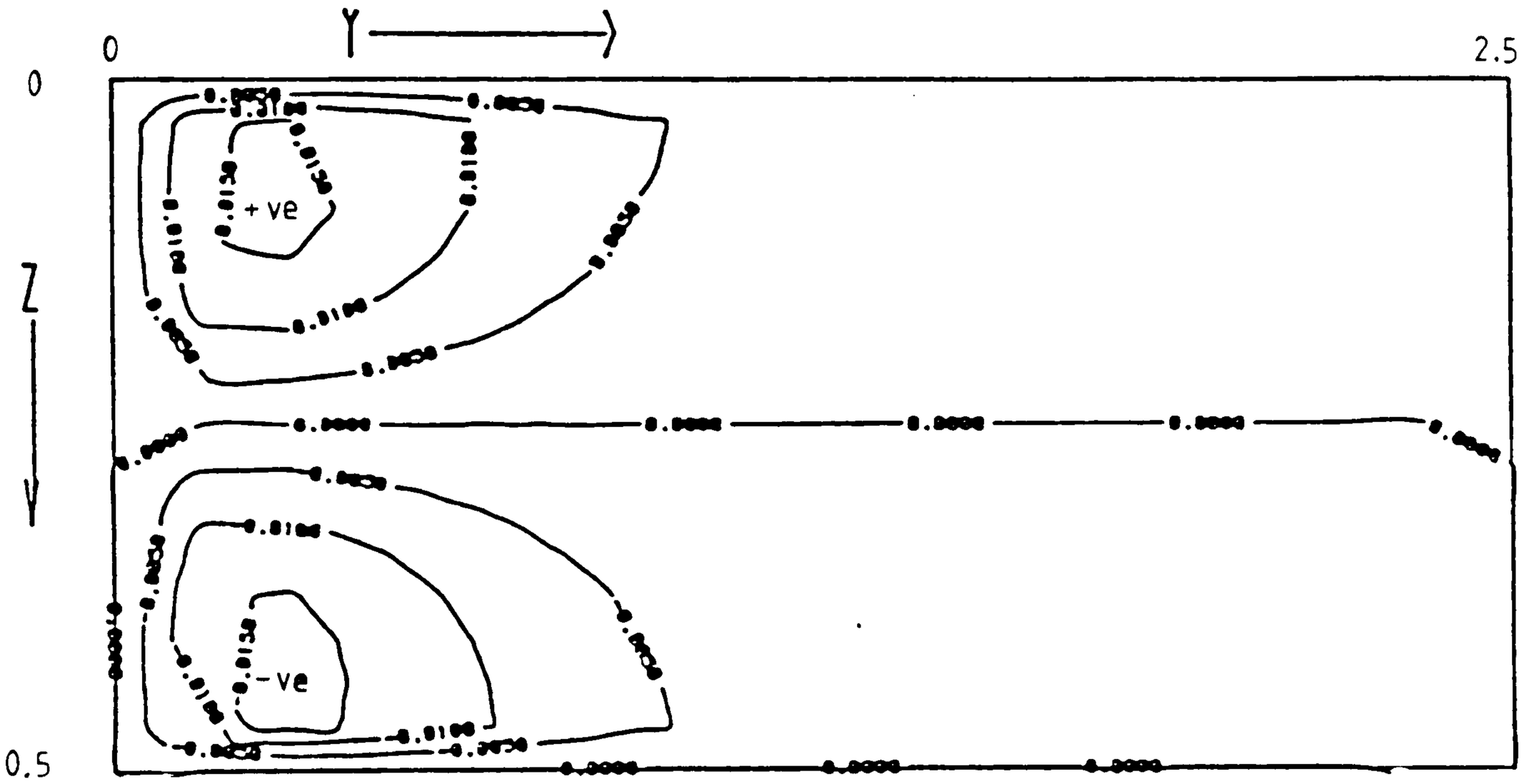

Figure 6.120 $\partial\theta/\partial y$ **at plane C,** $(0.5 - hx/2, y, z)$**, Hy=5**

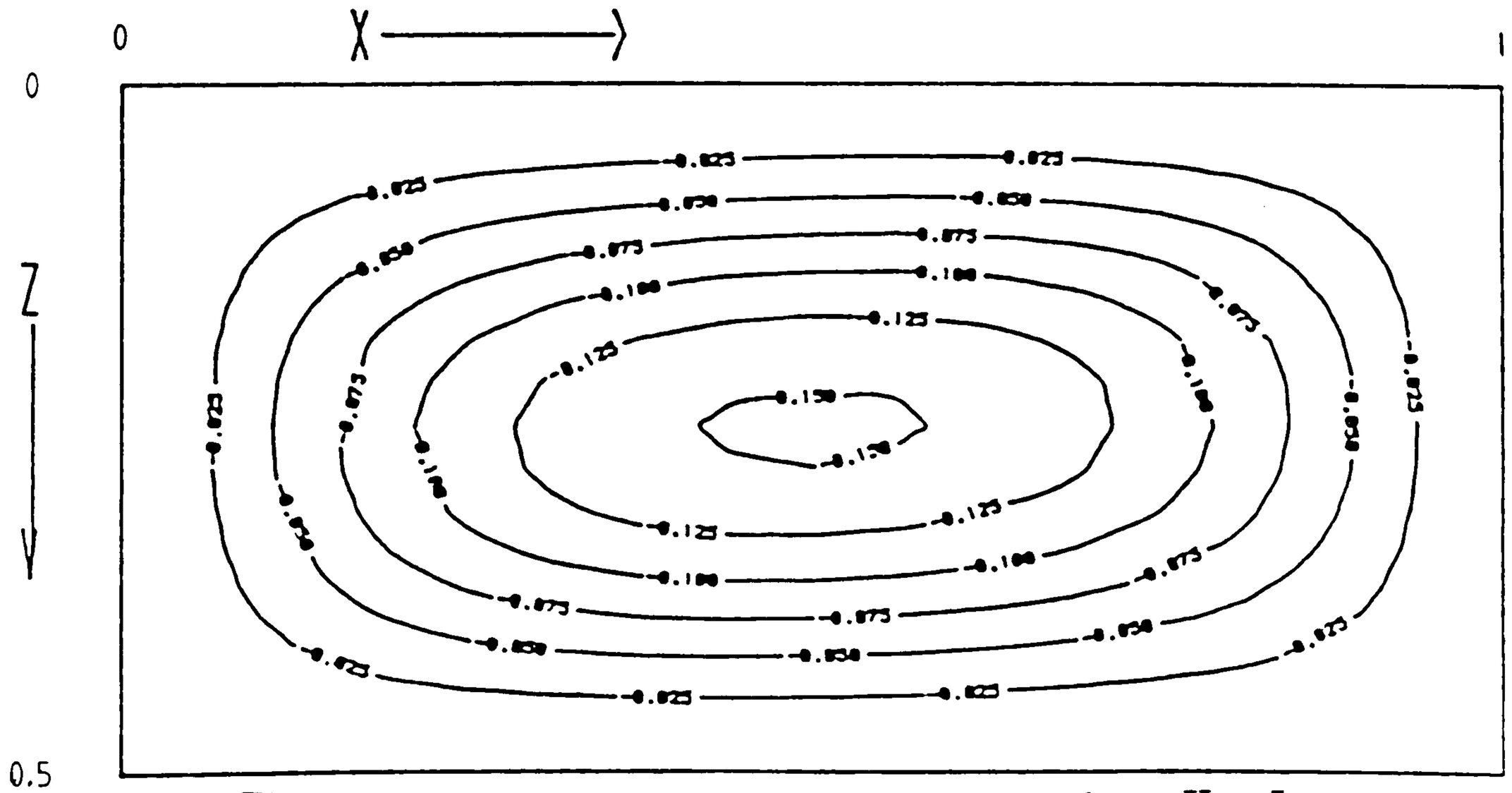

Figure 6.121 Streamlines near the symmetry plane, Hy=5

Graph A: air at Ra = 10^3, Hy=1, Hz=0.5

Graph B: air at Ra = 10^3, Hy=2, Hz=0.5

Graph C: air at Ra = 10^3, Hy=5, Hz=0.5

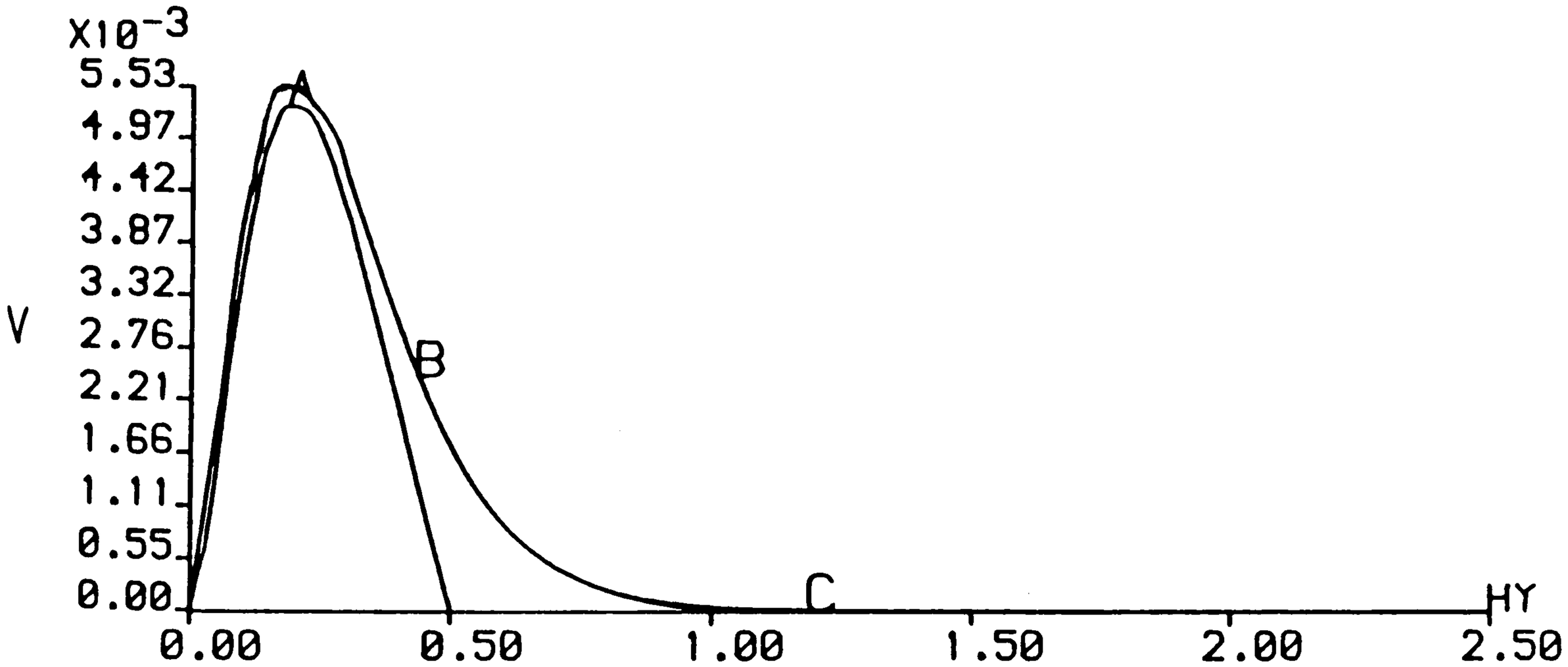

Figure 6.122 Axial-velocity along $(0.5, y, 0.25)$

6.7.2 Air (Pr=0.71) with Ra=10^5

Results and flow features that occur with length aspect ratio Hy=1, 2 and 5 are described in this section. The fluid flow in these cavities is described by two weak secondary rolls embedded in a forward roll. Figures 6.123, 6.124 and 6.125 show particle paths in cavities with length aspect ratio Hy=1, 2 and 5 respectively to illustrate the fluid flow behaviour. With the length aspect ratios Hy=1 and 2 the forward roll fills the solution cavity. With Hy=5 the forward roll only occupies part of the cavity with the rest of the cavity occupied with two-dimensional flow. For this Rayleigh number with the longer cavities, Hy=2 and 5, reverse roll does not exist as it did with the square cross-sectional cavities.

Figures 6.126, 6.127 and 6.128 are contour plots of the ratio R at planes A, B and C respectively for the shorter cavity Hy=1. Figures 6.126 and 6.127 show the location of the secondary roll centres quite clearly. They also show positive contours attached to the side walls. Figure 6.128 shows the inner core region increasing in height with increase in y and negative R contours do not appear in the inner core. These features also occur with the longer cavities, Hy=2 and 5.

Figures 6.129-6.134 are plots of the velocity vectors and isotherms for Hy=1.0. In the cross-section $\partial\theta/\partial x$ does not change sign, see Figures 6.132 and 6.133 but is very close to changing sign. Thus only a weak secondary flow is generated. The isotherms for Hy=2 and 5 are similar to those obtained for Hy=1 near the end wall and the symmetry plane respectively.

Figures 6.135-6.137 are contour plots of $\partial\theta/\partial y$ at the plane x=0.5 for the length aspect ratios Hy=1, 2 and 5 respectively. With the length aspect ratio Hy=1, positive axial temperature gradients dominate the upper half of the cavity and negative axial temperature gradients dominate the lower half. With the length aspect ratio Hy=2 there is one sign change of $\partial\theta/\partial y$ along the length of the cavity which is associated with the secondary flow convective effects. With Hy=5 there are two sign changes of $\partial\theta/\partial y$. The first is associated with the convective effects of the secondary flow and the second appears to be associated with the two-dimensional flow that occupies the cavity from where the forward roll ends to the symmetry plane. Note that the vorticity generated by the first sign change acts against the forward roll. It appears not to be sufficiently strong enough to create a reverse roll but does prevent the penetration of the forward roll resulting in a two-dimensional flow in the vicinity of the symmetry plane. The second change of $\partial\theta/\partial y$ could thus be a result of further contribution of

heat at the interface of the forward roll and the two-dimensional flow.

Figure 6.138 is a streamline plot near the symmetry plane for Hy=5. The flow is bordering between primary and a weak secondary flow. The streamlines for Hy=1 and 2 are very similar to that of Hy=5 and have not been presented.

Figure 6.139 is a plot of the axial-velocity along the centre line. Note that the axial flow is not restricted in the shorter cavity, that is the peak axial velocity in the shorter cavity Hy=1.0 is of similar magnitude to that occurring with Hy=2 and 5. This is due to the stronger axial gradients in the shorter cavity that augment the axial flow. Also the two-dimensional flow exists for cavities with length aspect ratio Hy$\geq$3.0 implying the axial flow is not as strong as with the square cross section window cavity. A reverse roll does not exist for cavities with length aspect ratio, Hy$\leq$5.

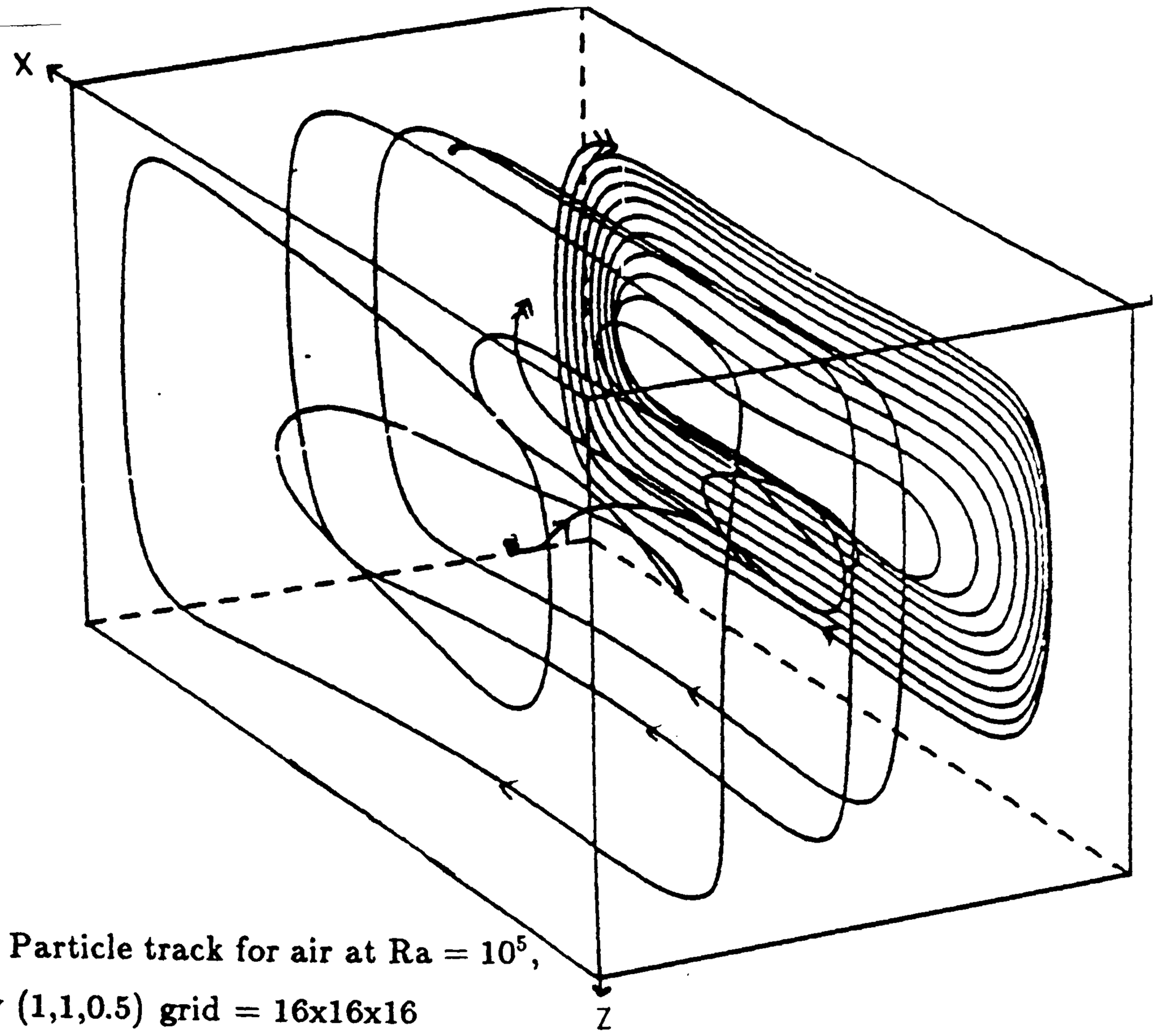

Figure 6.123 Particle track for air at Ra = 10^5, cavity (1,1,0.5) grid = 16x16x16

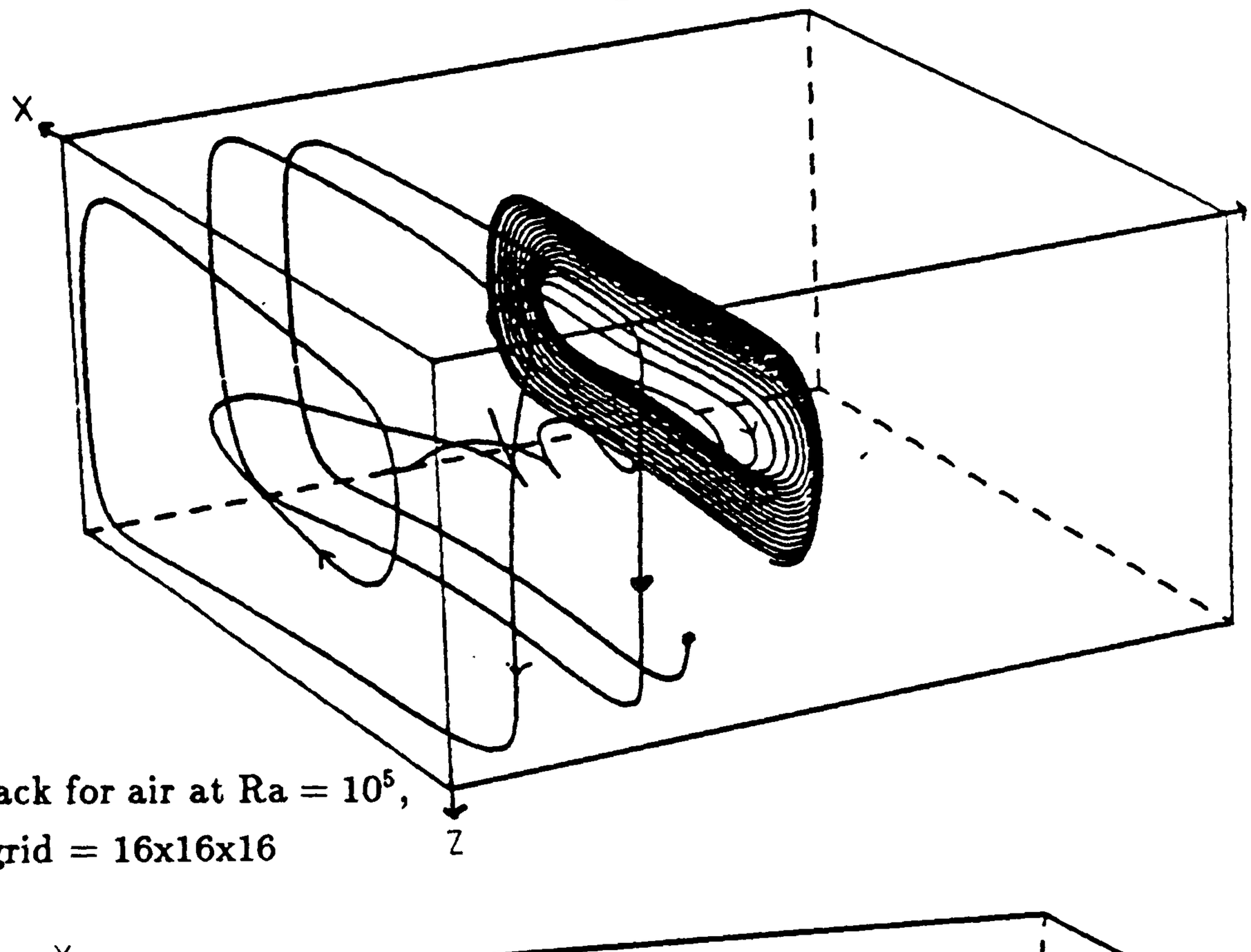

Figure 6.124 Particle track for air at Ra = 10^5, cavity (1,2,0.5) grid = 16x16x16

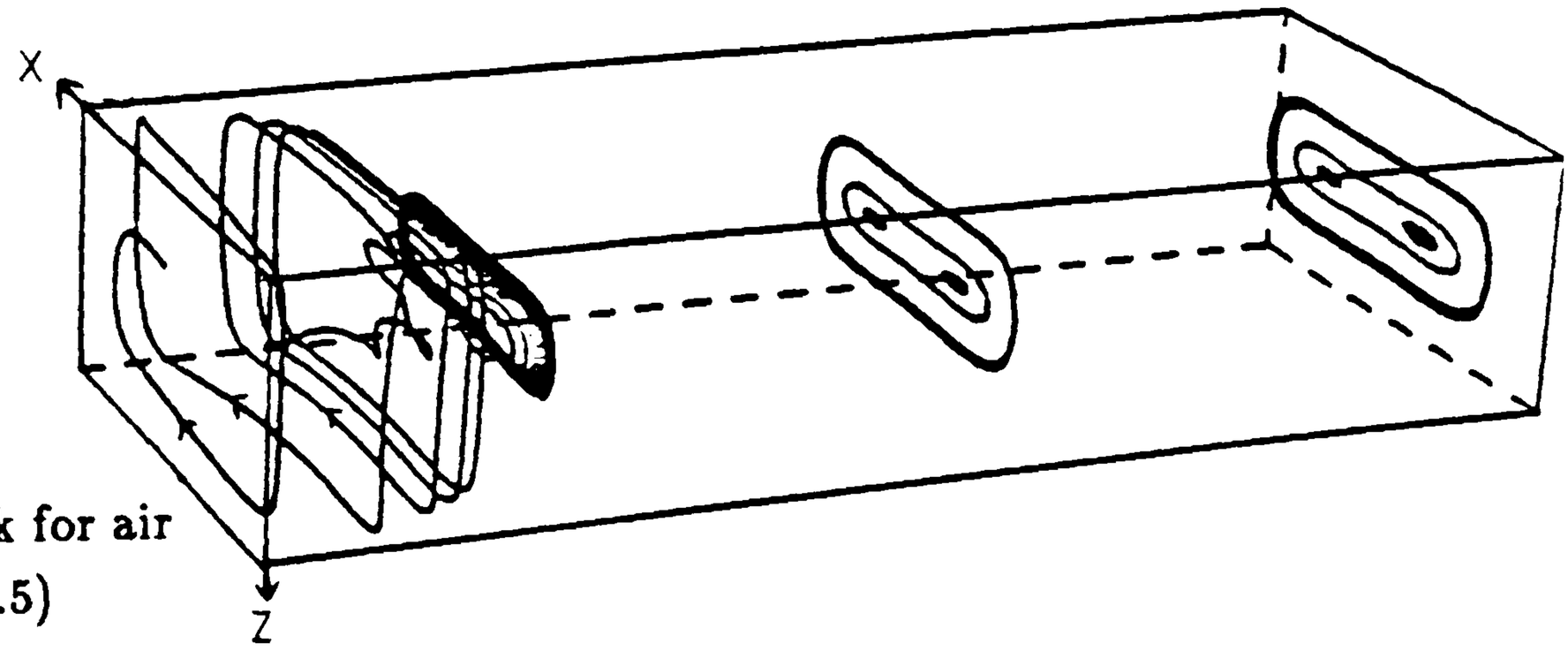

Figure 6.125 Particle track for air at Ra = 10^5, cavity (1,5,0.5) grid = 16x40x16

Fluid = air, Ra = 10^5, Hy=1, Hz=0.5, grid=16x16x16

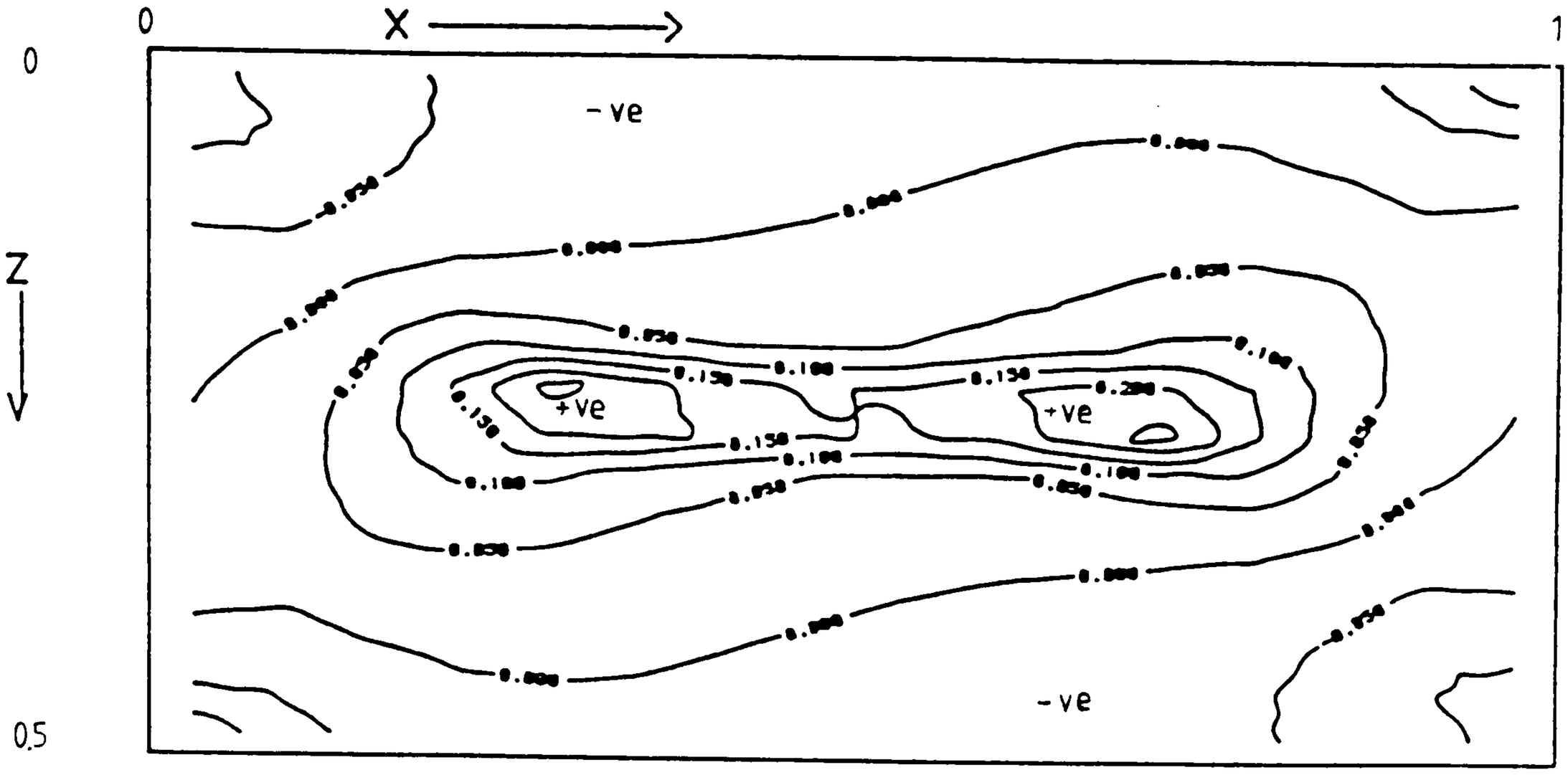

Figure 6.126 Contour plot of ratio R at plane A, near the end wall

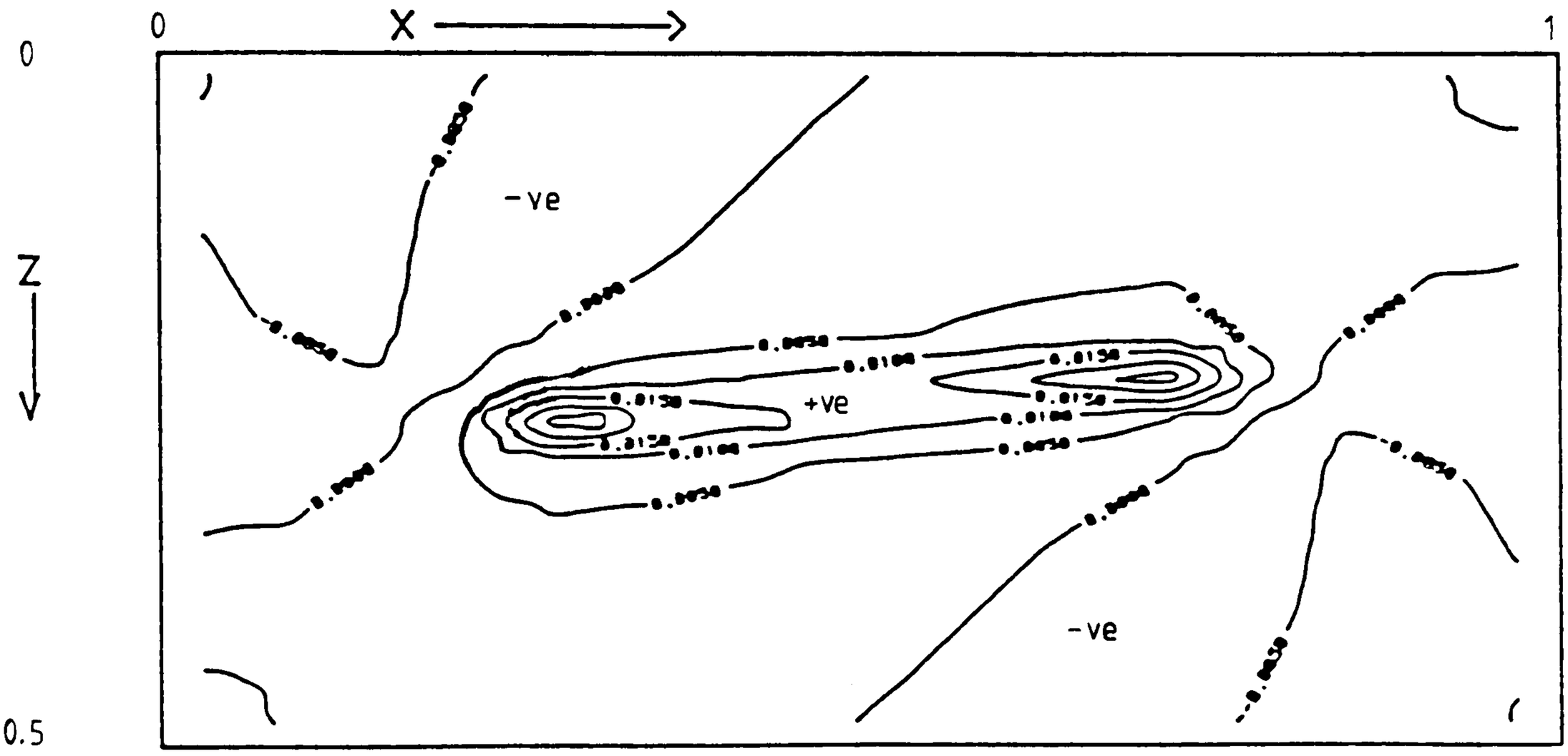

Figure 6.127 Contour plot of ratio R at plane B, near the symmetry plane

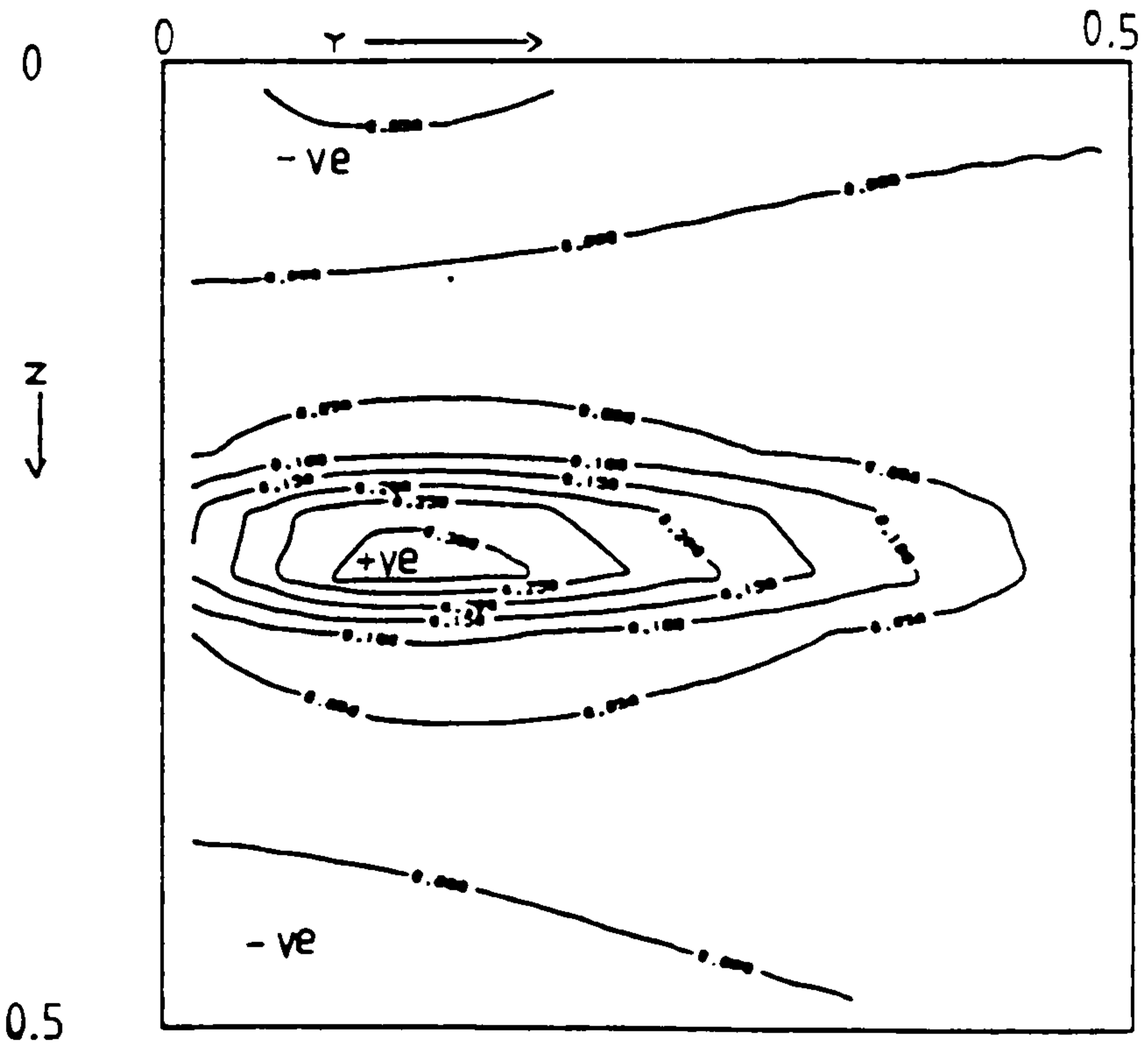

Figure 6.128 Contour plot of ratio R at plane C $(0.5 - hx/2, y, z)$

Fluid = air, Ra = 10^5, Hy=1, Hz=0.5, grid=16x16x16

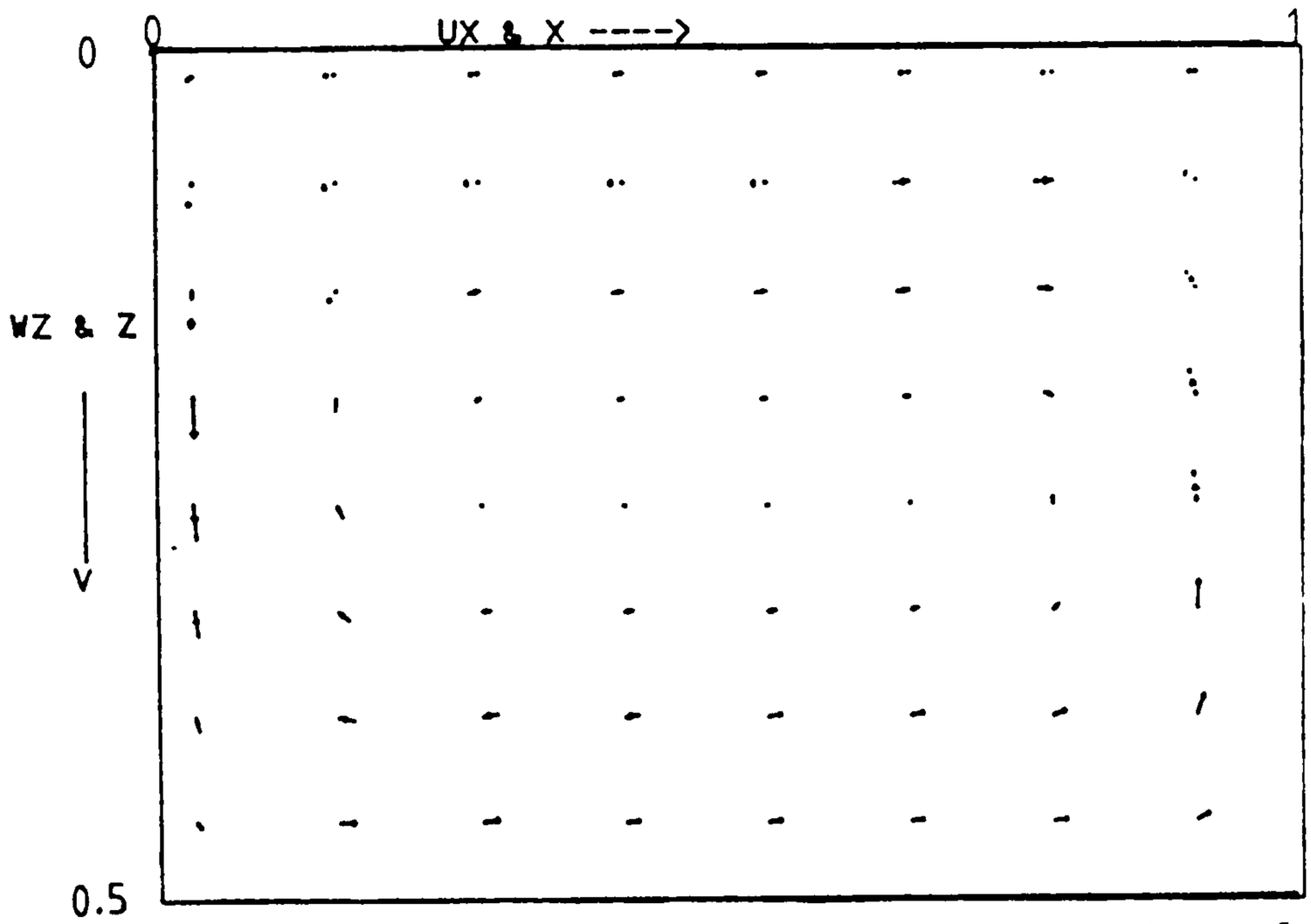

Figure 6.129 Velocity vectors at plane A, near the end wall

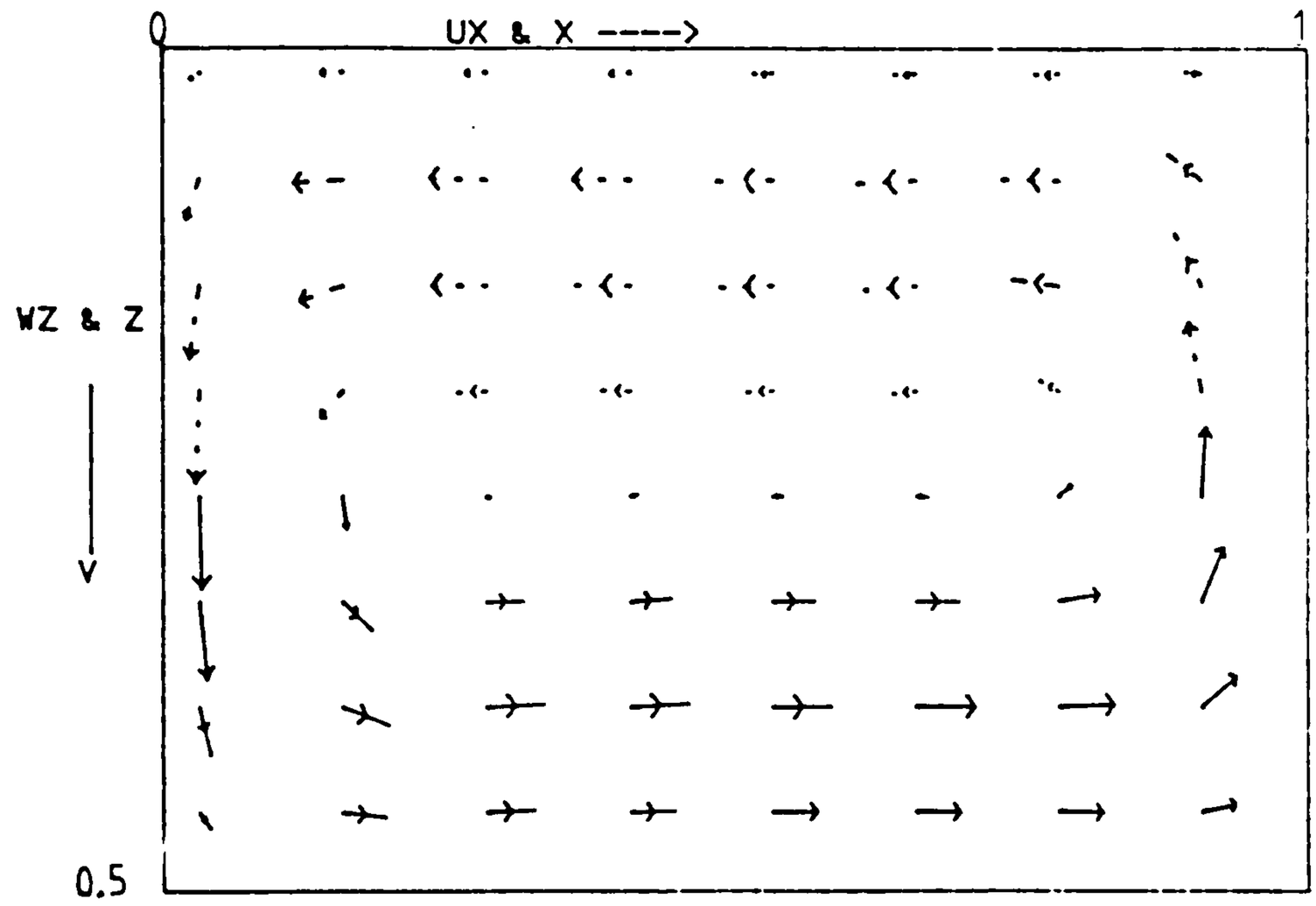

Figure 6.130 Velocity vectors at plane B, near the symmetry plane

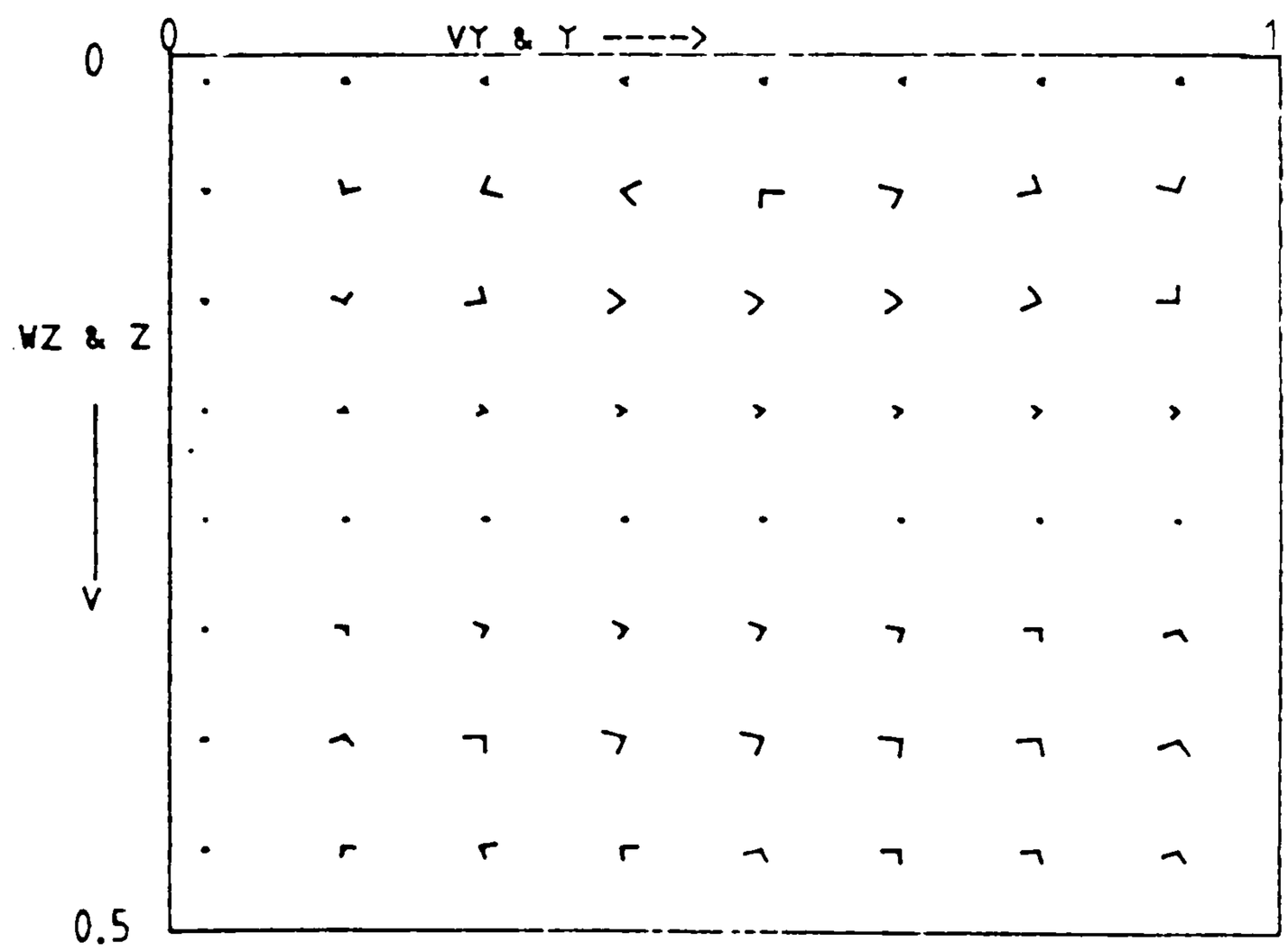

Figure 6.131 Velocity vectors at plane C (0.5 −

Fluid = air, Ra = 10^5, Hy=1, Hz=0.5, grid=16x16x16

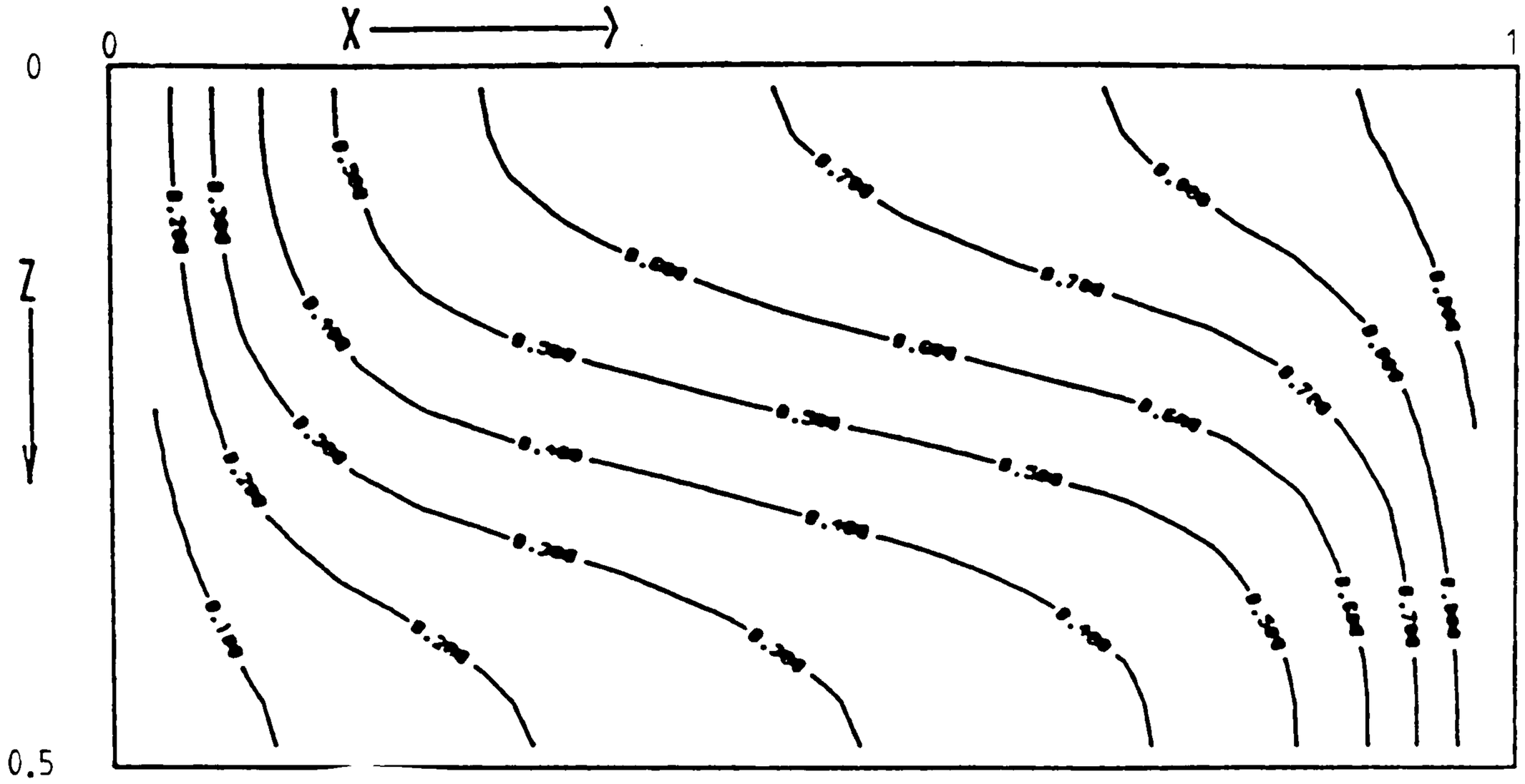

Figure 6.132 Isotherms at plane A, near the end wall

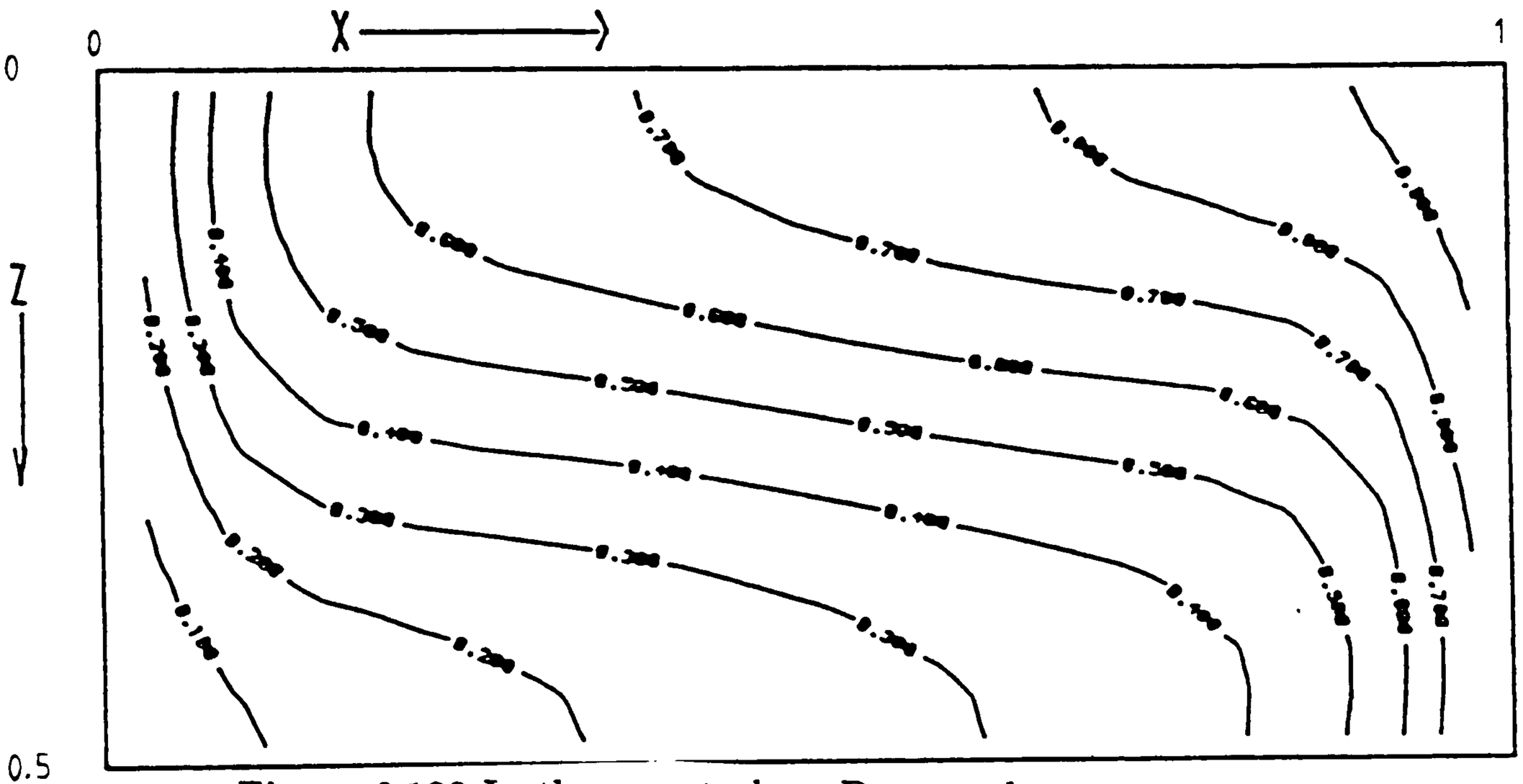

Figure 6.133 Isotherms at plane B, near the symmetry plane

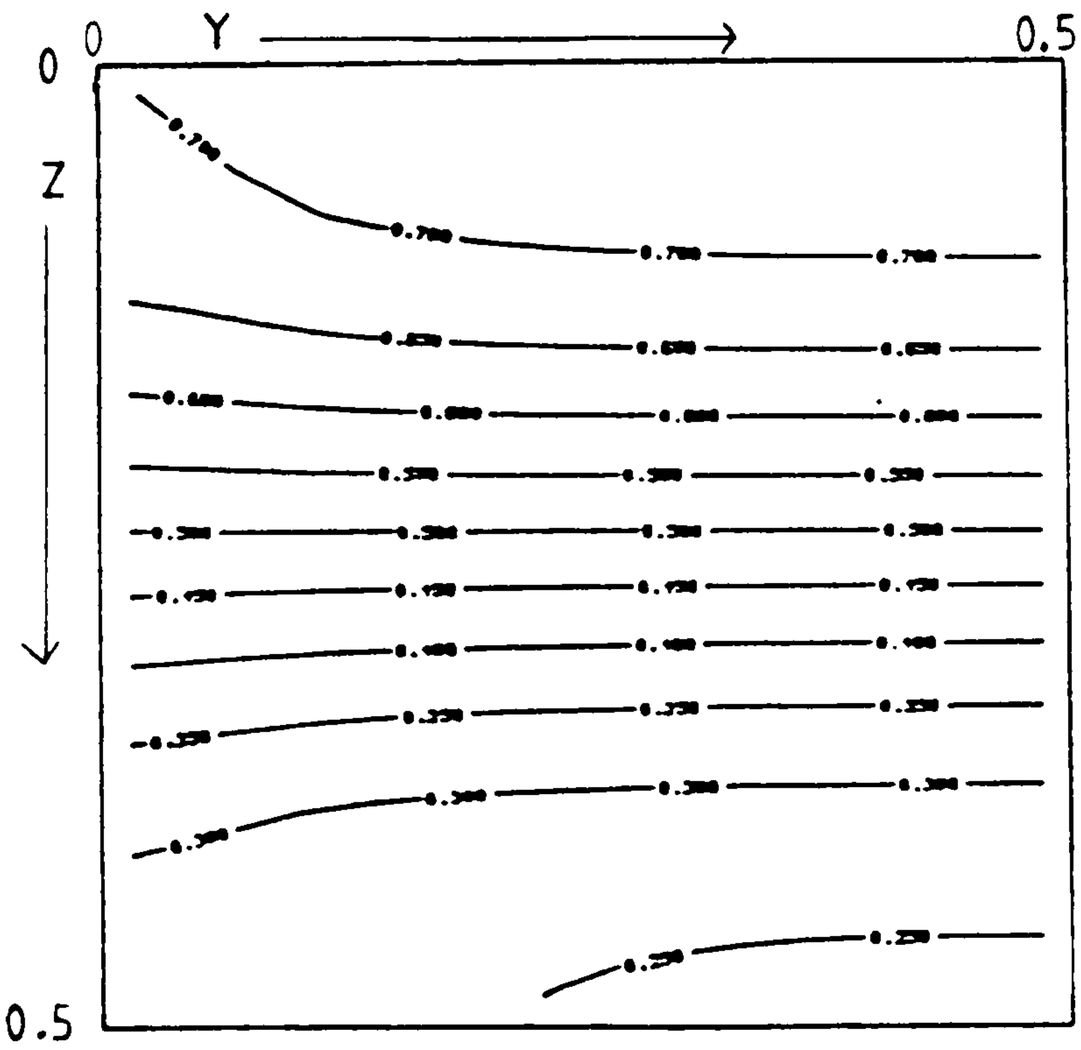

Figure 6.134 Isotherms at plane C, $(0.5 - hx/2, y, z)$

Fluid = air, Ra = 10^5, Hy=1, Hz=0.5, grid=16x16x16

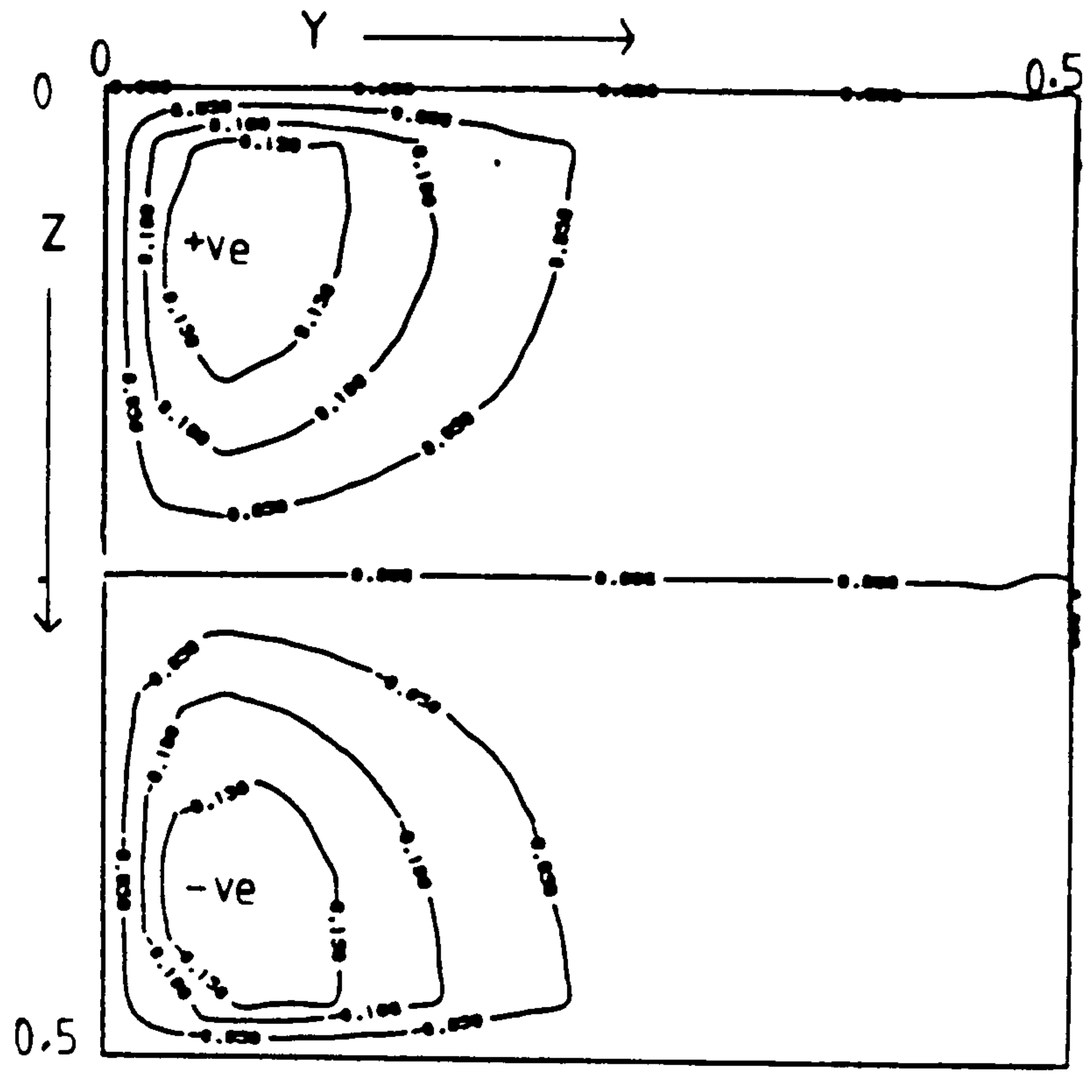

Figure 6.135 $\partial\theta/\partial y$ at plane C, $(0.5 - hx/2, y, z)$, Hy=1

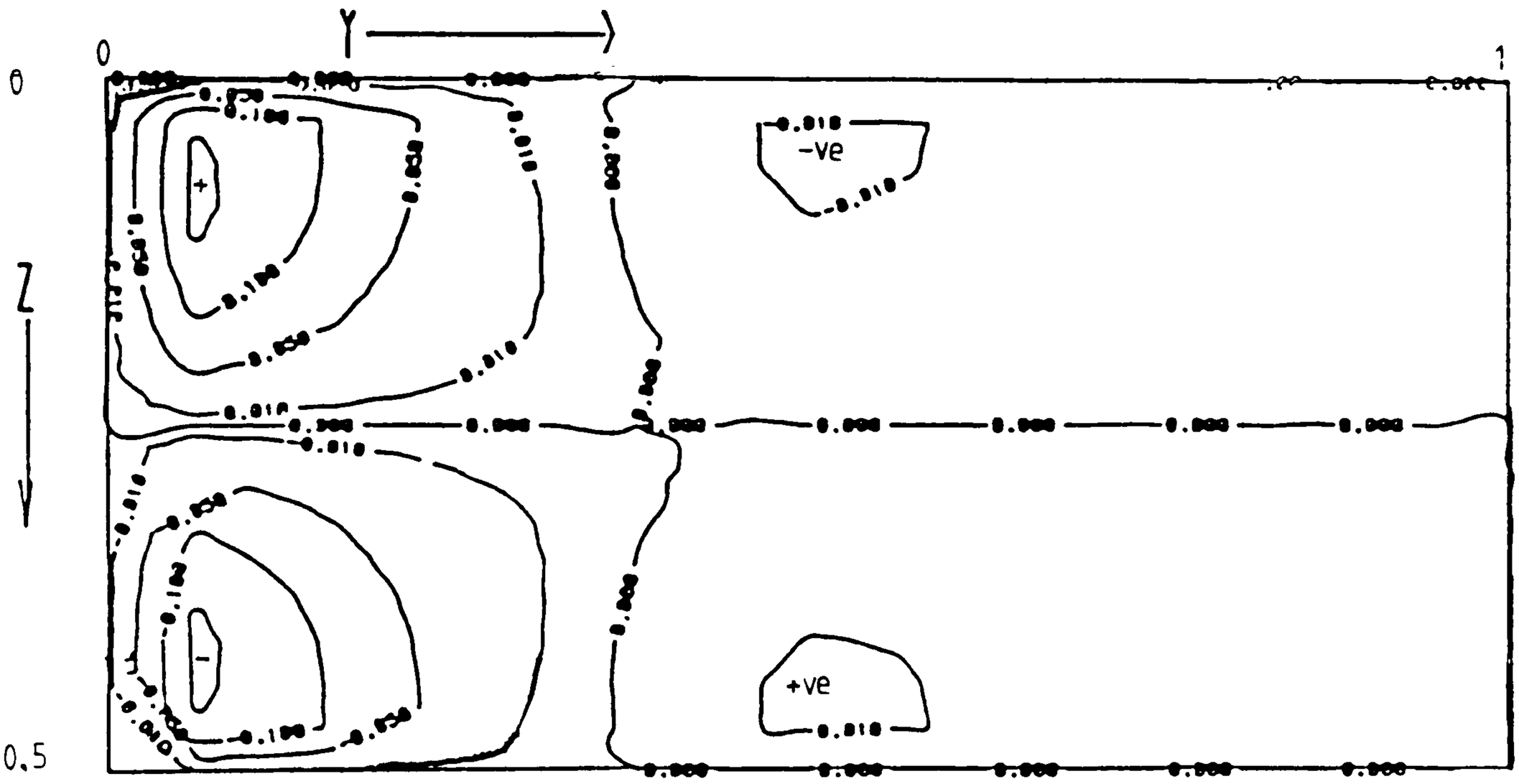

Figure 6.136 $\partial\theta/\partial y$ at plane C, $(0.5 - hx/2, y, z)$, Hy=2

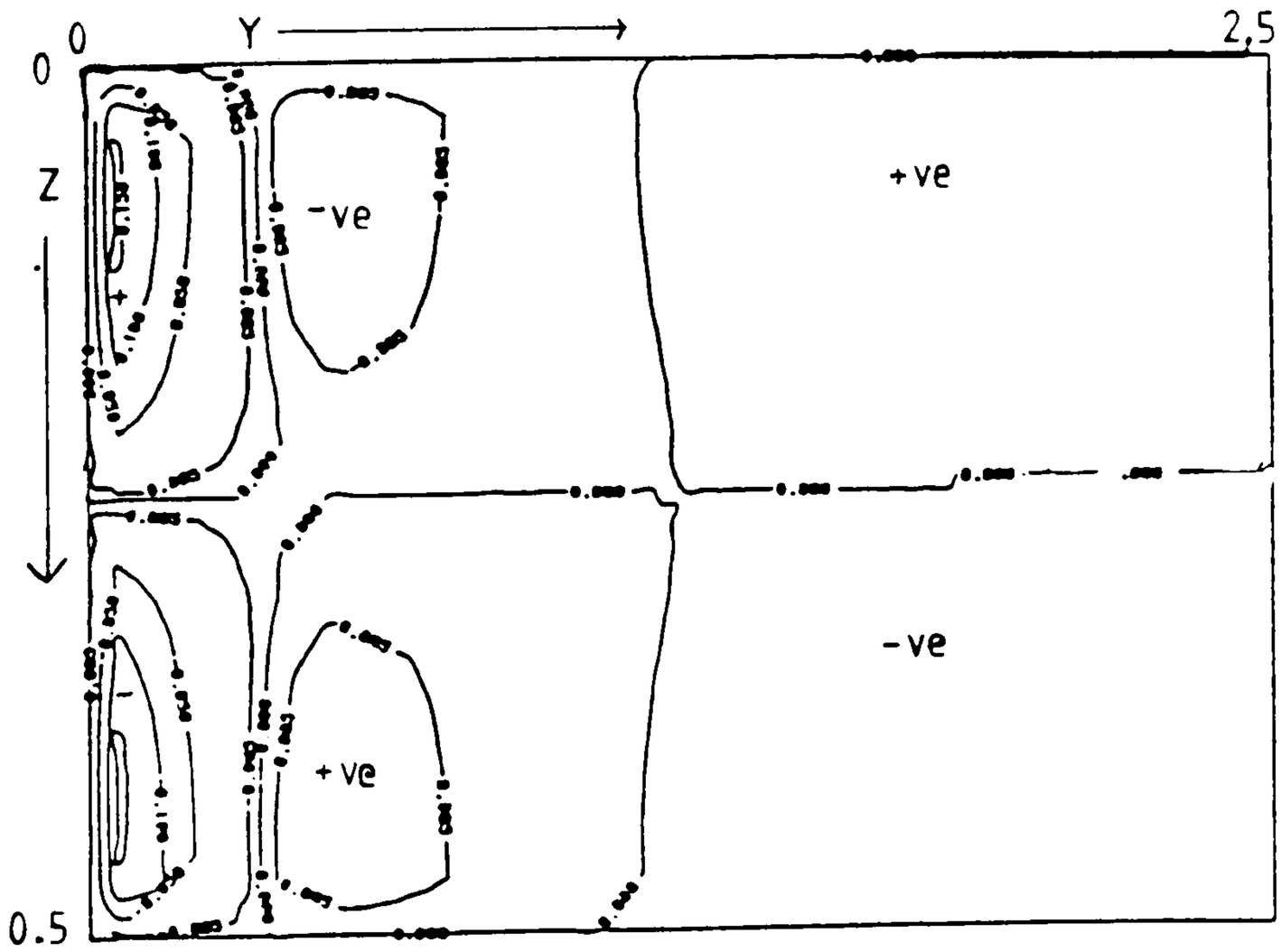

Figure 6.137 $\partial\theta/\partial y$ at plane C, $(0.5 - hx/2, y, z)$, Hy=5

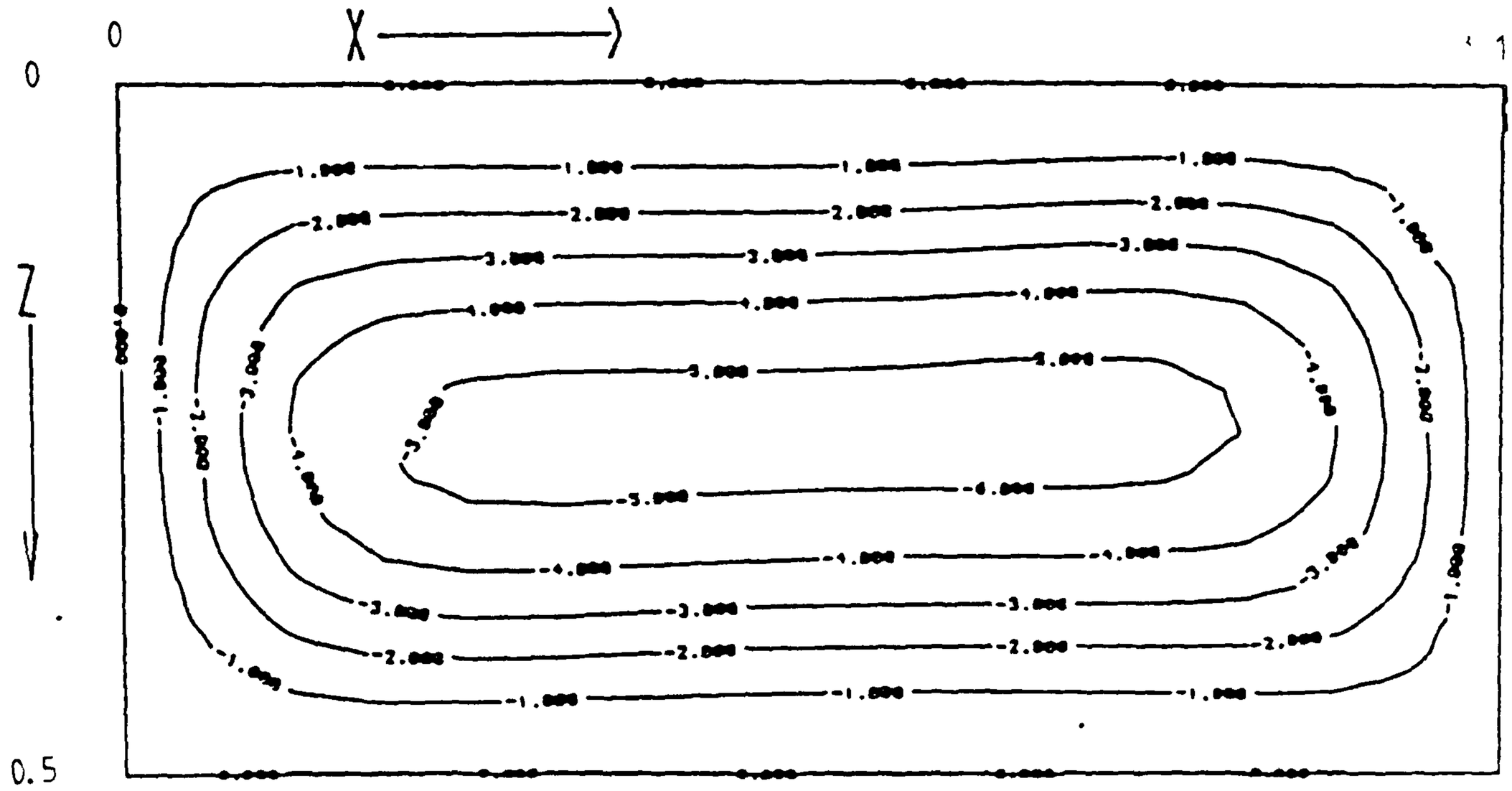

Figure 6.138 Streamlines near the symmetry plane, Hy=5

Graph A: air at Ra = 10^5, Hy=1, Hz=0.5

Graph B: air at Ra = 10^5, Hy=2, Hz=0.5

Graph C: air at Ra = 10^5, Hy=5, Hz=0.5

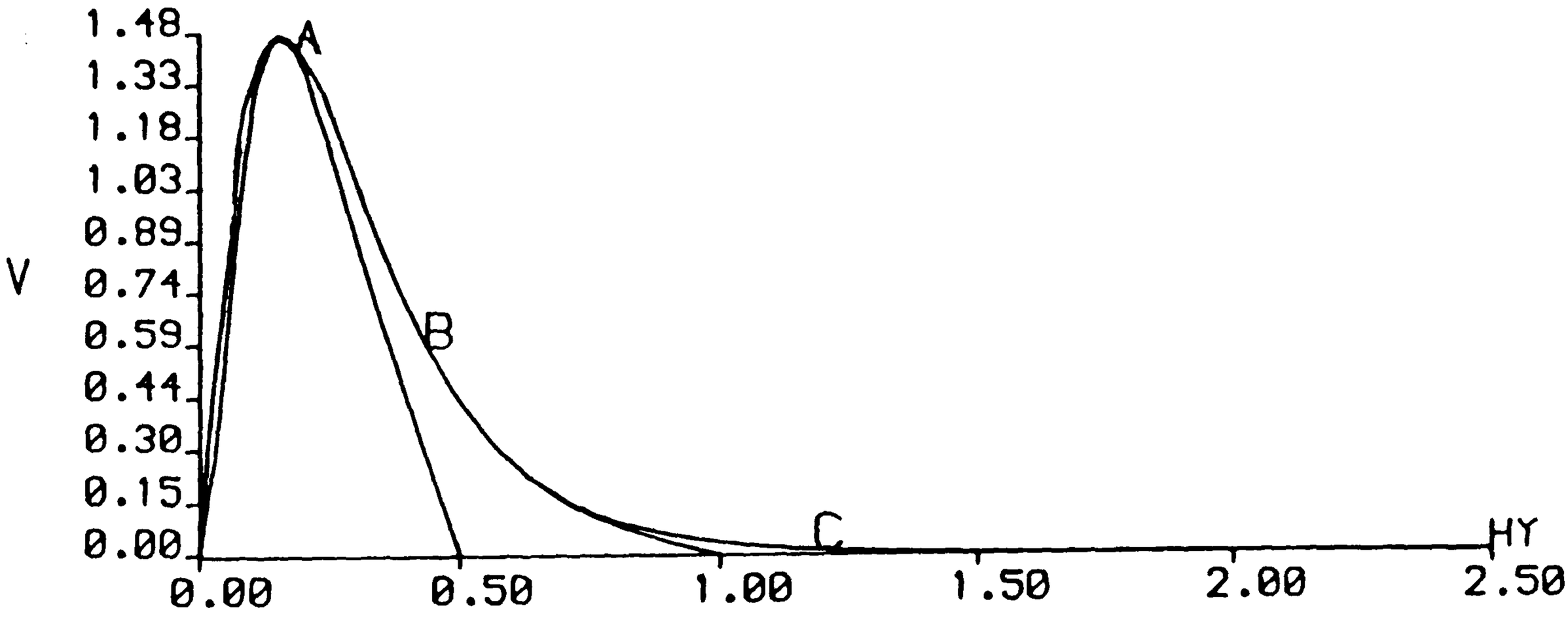

Figure 6.139 Axial-velocity along $(0.5, y, 0.25)$

6.7.3 Cerrobase $\mathbf{Ra = 10^3}$

The fluid flow behaviour in this shallow cavity with length aspect ratios Hy=1, 2 and 5 for cerrobase with $Ra = 10^3$ is described by a single forward recirculating roll. For Hy=5.0 the fluid roll only occupies a part of the cavity with the rest of the cavity being occupied with two-dimensional flow. Figures 6.140-6.142 illustrate the flow in the cavities with length aspect ratios Hy=1, 2 and 5 respectively.

Figures 6.143-6.145 are the contour plots of the ratio R at planes A, B and C respectively for the cavity with length aspect ratio Hy=1.0. Positive R contours are attached to the top and bottom walls of the cavity and so the turning points of the particles no longer lie on a cylindrical surface as they did in the cavities with square cross sections. From figures 6.143 and 6.144 it can be seen that undulations in the flow with respect to the axial direction exist in the top and bottom boundary layers but not in the side boundary layers.

Figures 6.146-6.151 are plots of the velocity vectors and isotherms at planes A, B and C respectively for the length aspect ratio Hy=1.0. Isotherms obtained with Hy=1.0, 2.0 and 5.0 are similar.

Figures 6.152 - 6.154 are contour plots of $\partial\theta/\partial y$ at the plane x=0.5 for the length aspect ratio Hy=1.0, 2.0 and 5.0 respectively. Note that $\partial\theta/\partial y$ does not change sign in the axial direction.

Figure 6.155 is a streamline plot near the symmetry plane for Hy=5. The plot shows a primary flow. The streamline plots for Hy=1 and 2 exhibit similar behaviour and have not been presented.

Figure 6.156 is a plot of the axial-velocity along the centre line. The three-dimensional flow is slightly restricted in the cavity Hy=1.0. Note the strong axial gradients in the shorter cavity cannot bridge the difference between the axial flow created by the inertial end effect in the shorter cavity and that created in the longer cavity. Two-dimensional flow exists for cavities with length aspect ratio,Hy, ≥ 2.5. In the square cross-section window cavity two-dimensional flow did not result for cavity length aspect ratios shorter than Hy$\leq$ 5.0. Indicating that the end wall effect with the square cross-section window cavity is much greater than that obtained with the shallow cross-section window cavity.

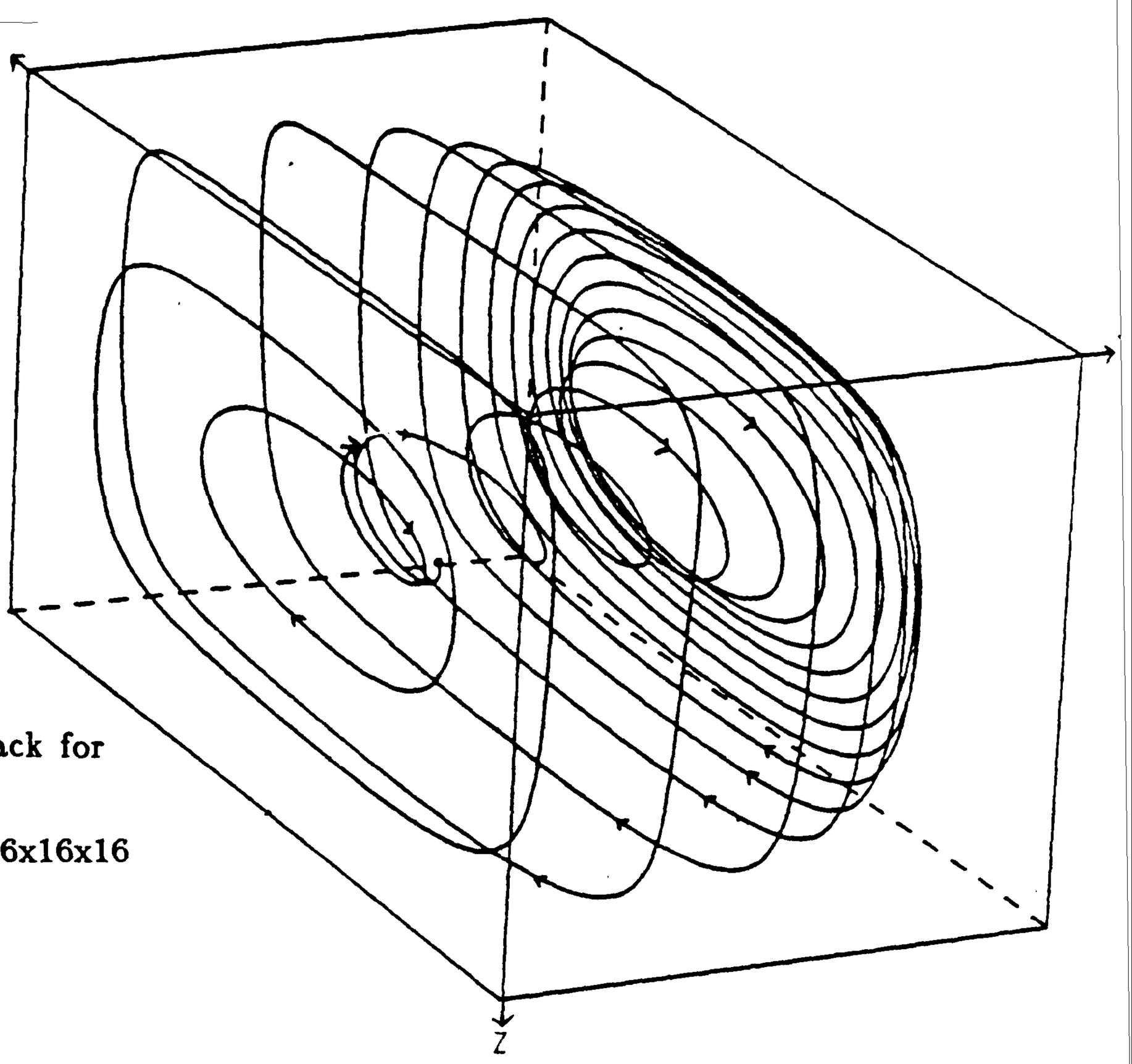

Figure 6.140 Particle track for cerrobase at Ra = 10^3, cavity (1,1,0.5) grid = 16x16x16

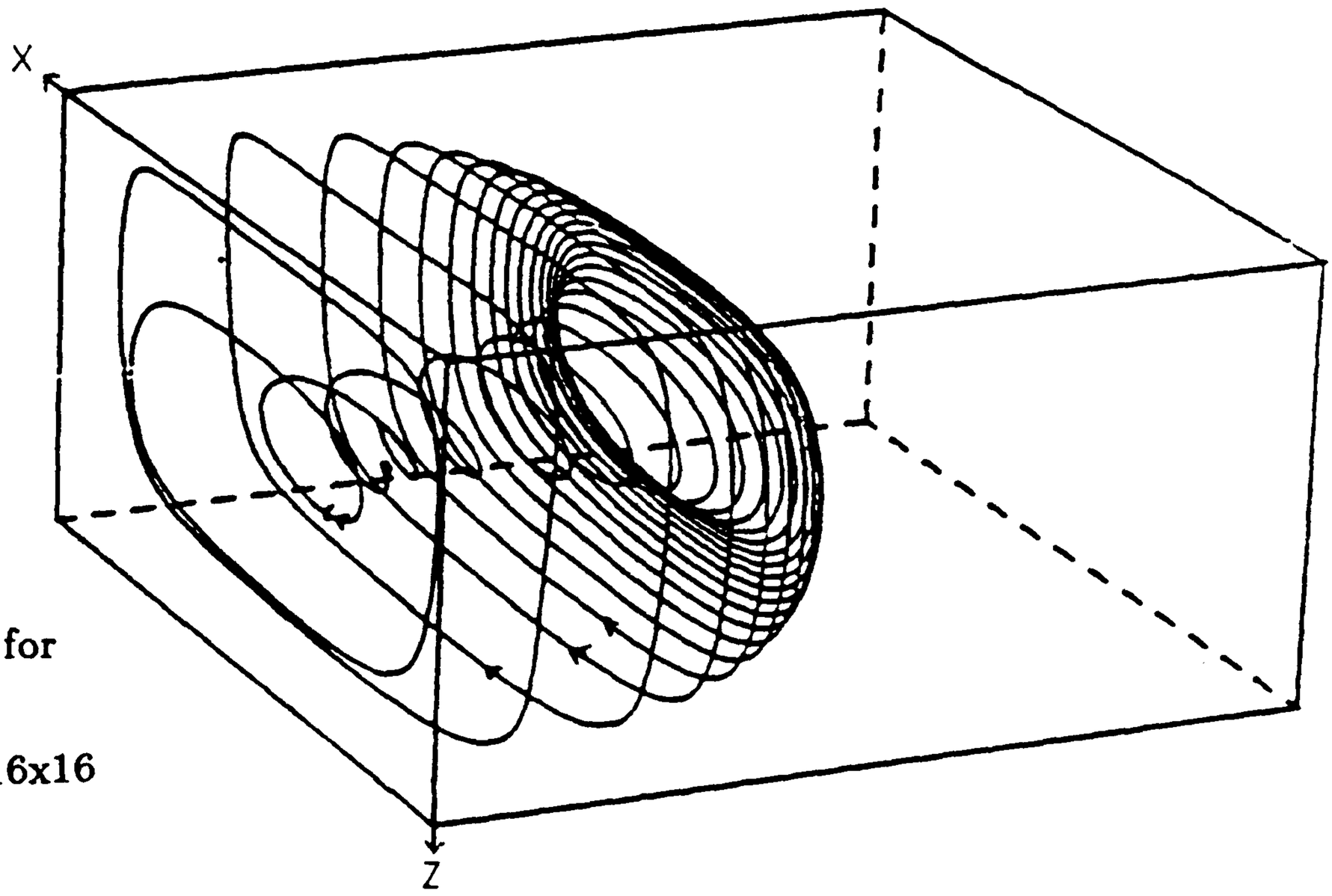

Figure 6.141 Particle track for cerrobase at Ra = 10^3, cavity (1,2,0.5) grid = 16x16x16

Figure 6.142 Particle track for cerrobase at Ra = 10^3, cavity (1,5,0.5) grid = 16x40x16

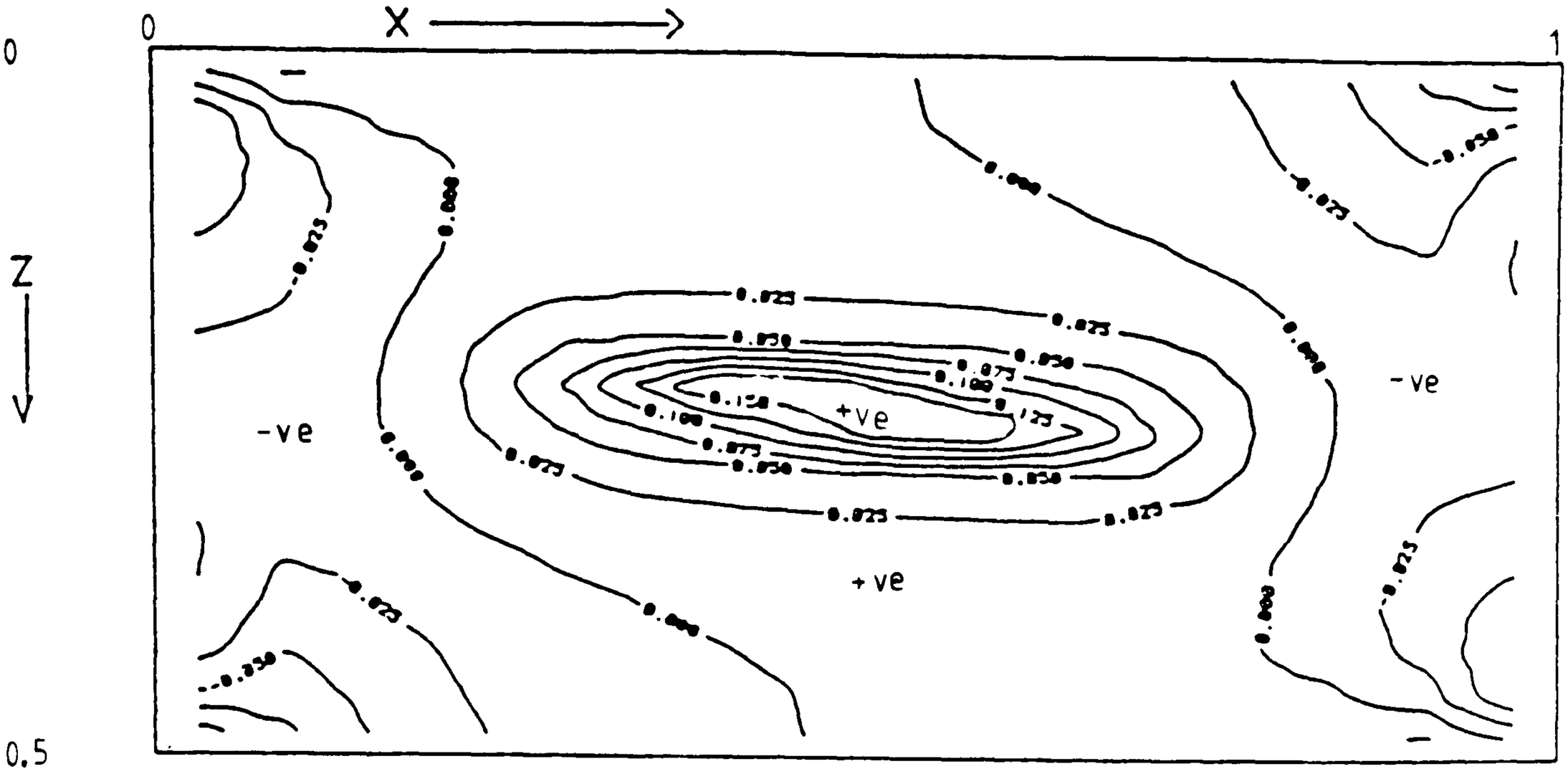

Figure 6.143 Contour plot of ratio R at plane A, near the end wall

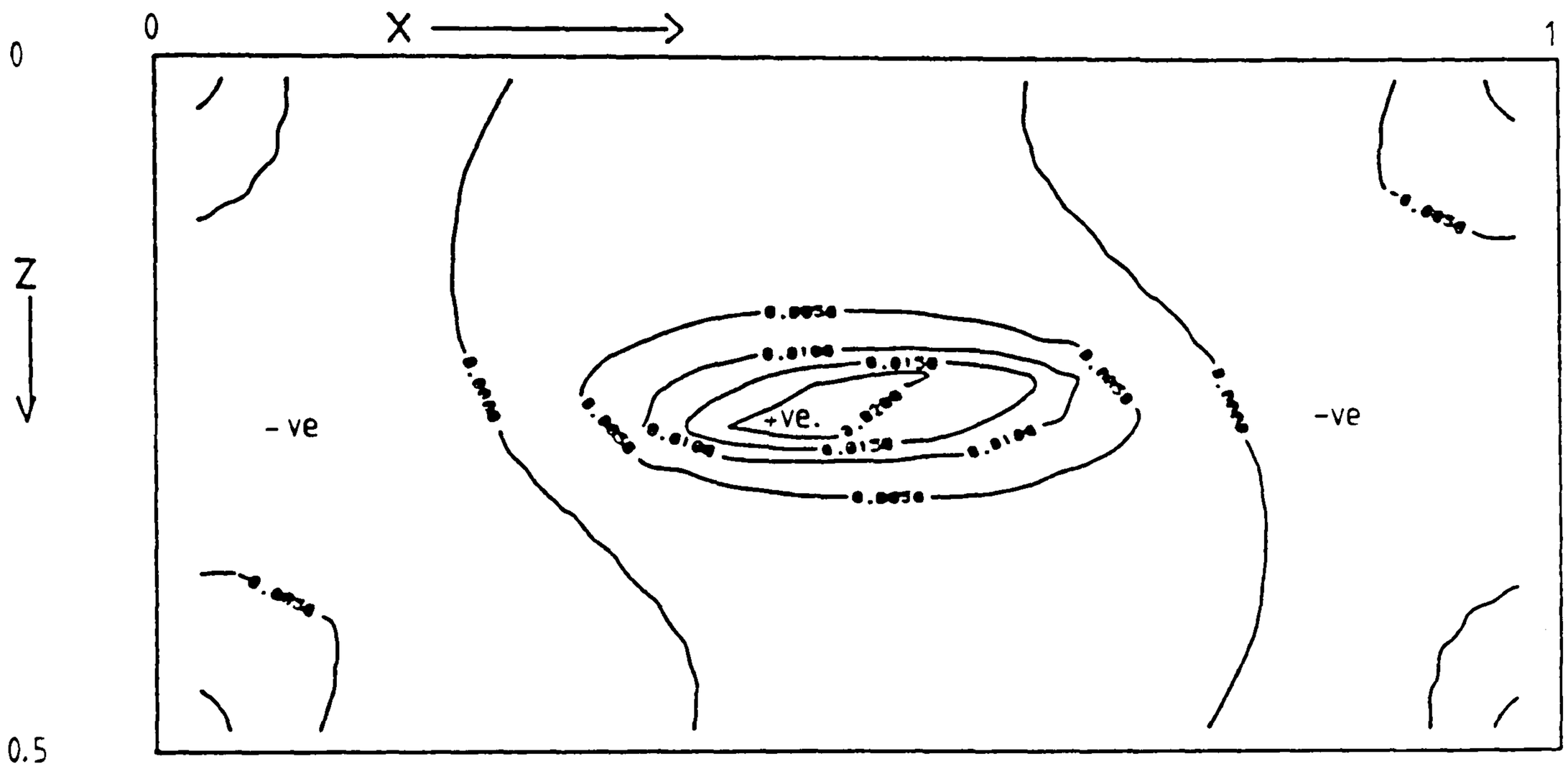

Figure 6.144 Contour plot of ratio R at plane B, near the symmetry plane

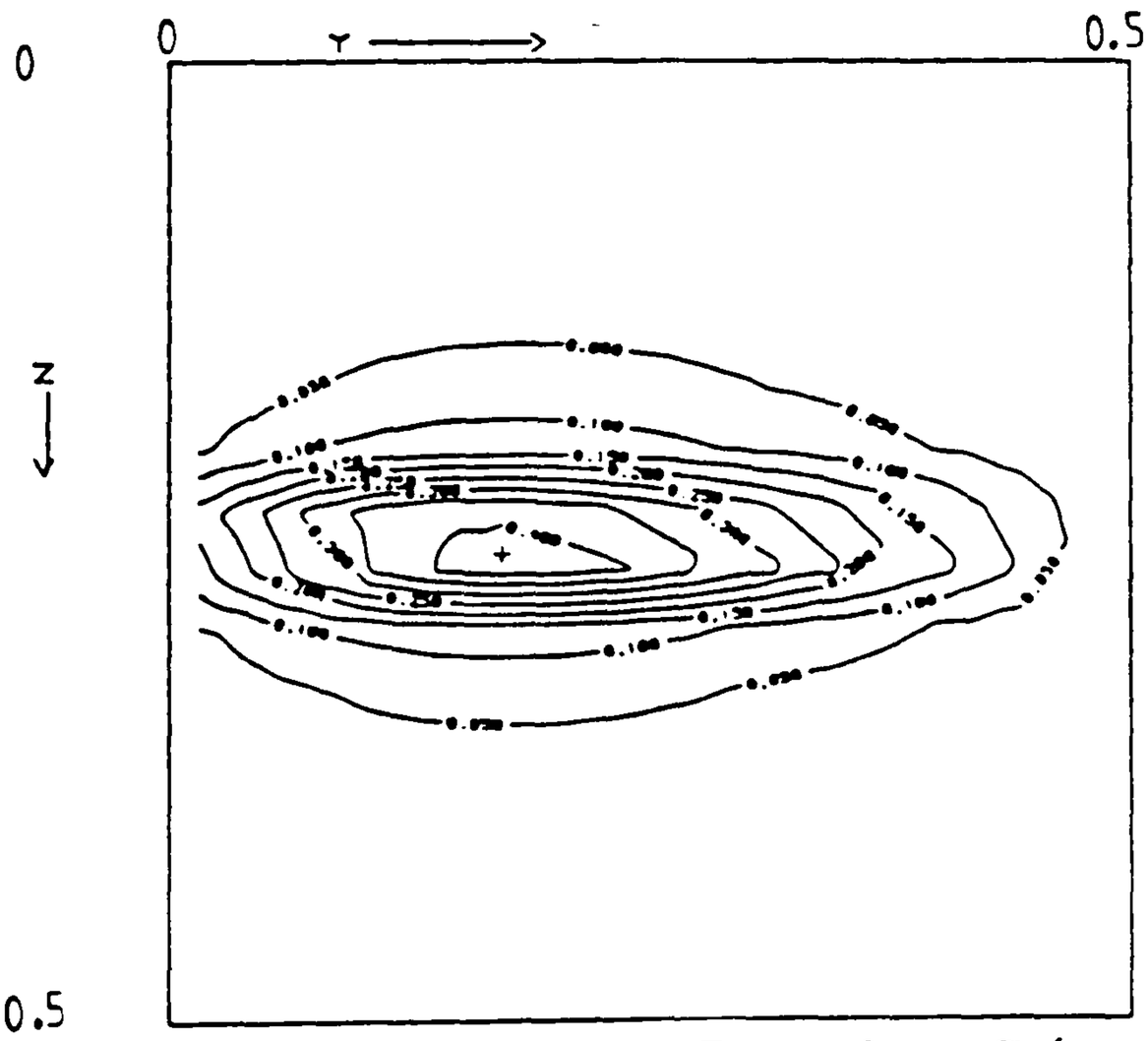

Figure 6.145 Contour plot of ratio R at plane C $(0.5 - hx/2, y, z)$

Fluid = cerrobase, Ra = 10^3, Hy=1, Hz=0.5, grid=16x16x16

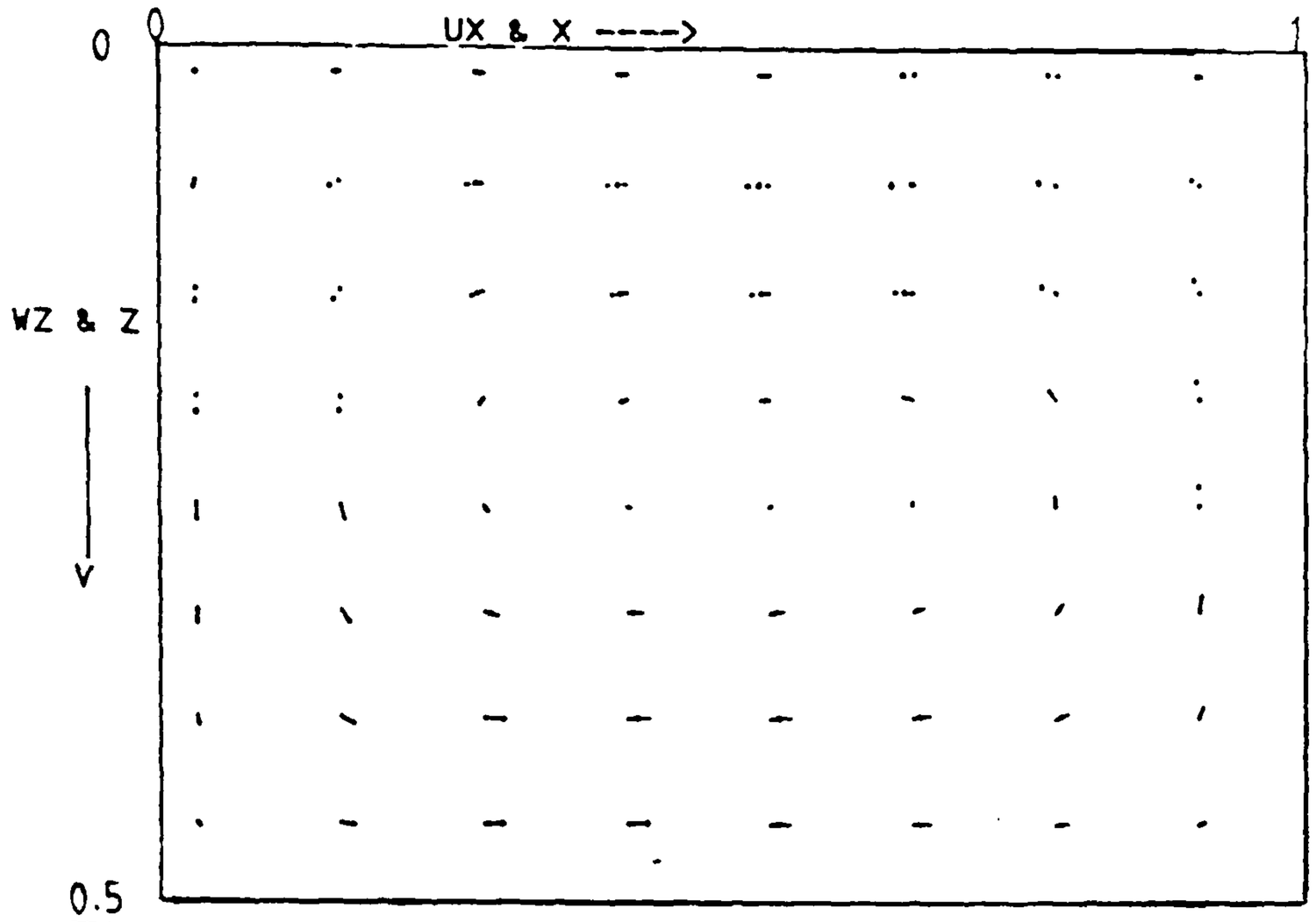

Figure 6.146 Velocity vectors at plane A, near the end wall

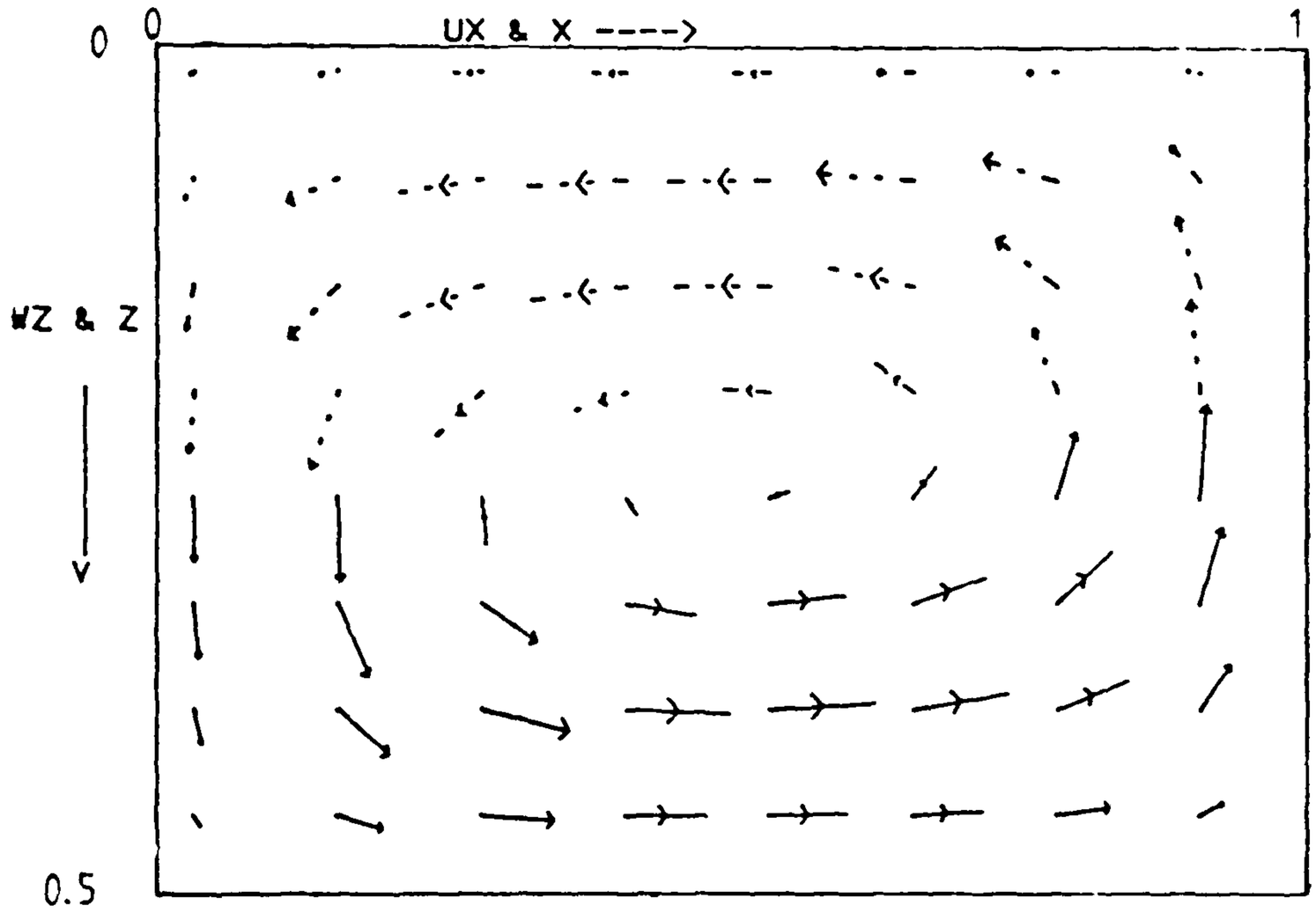

Figure 6.147 Velocity vectors at plane B, near the symmetry plane

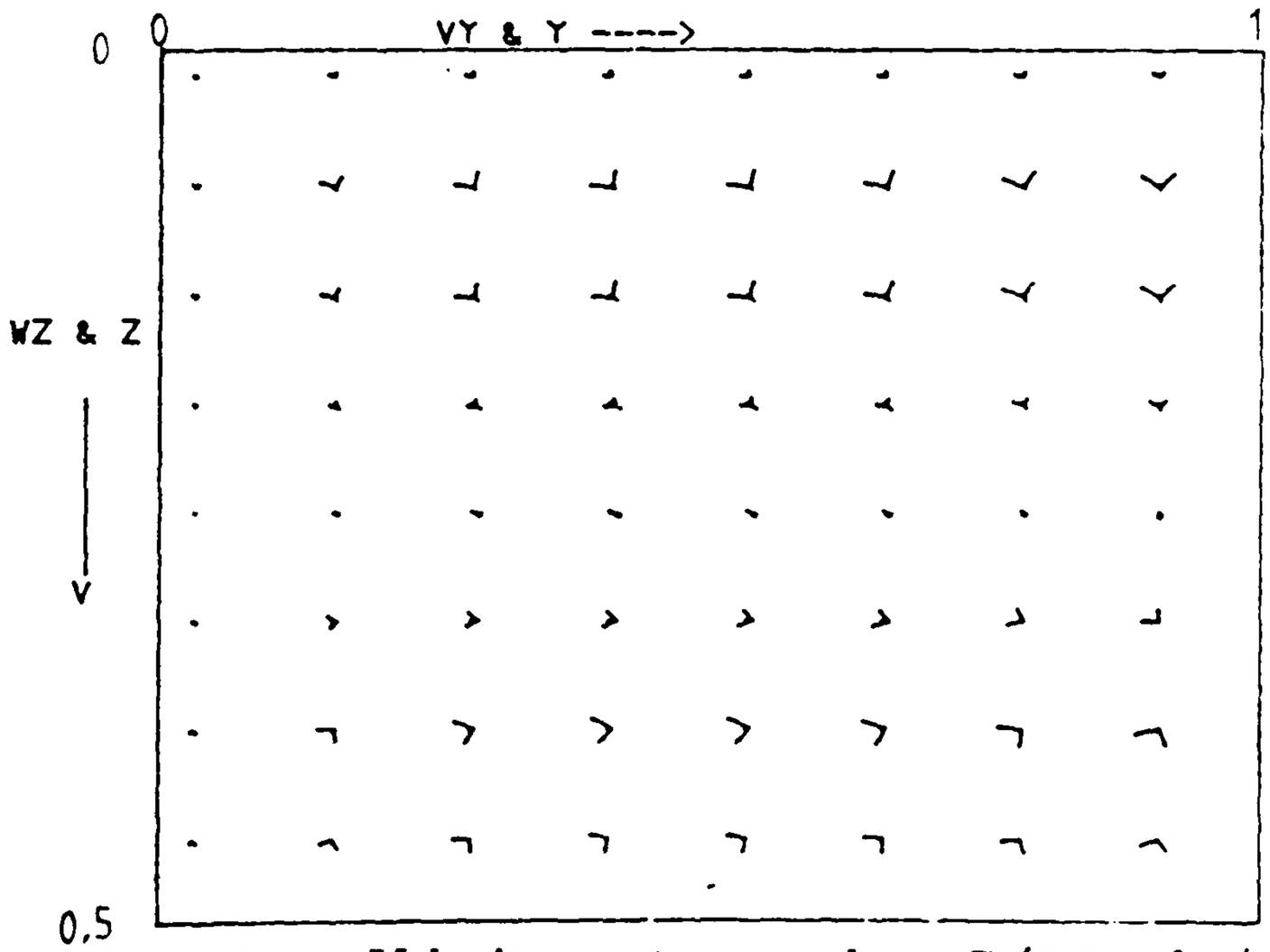

Figure 6.148 Velocity vectors at plane C $(0.5 - hx/2, y, z)$

Fluid = cerrobase, Ra = 10^3, Hy=1, Hz=0.5, grid=16x16x16

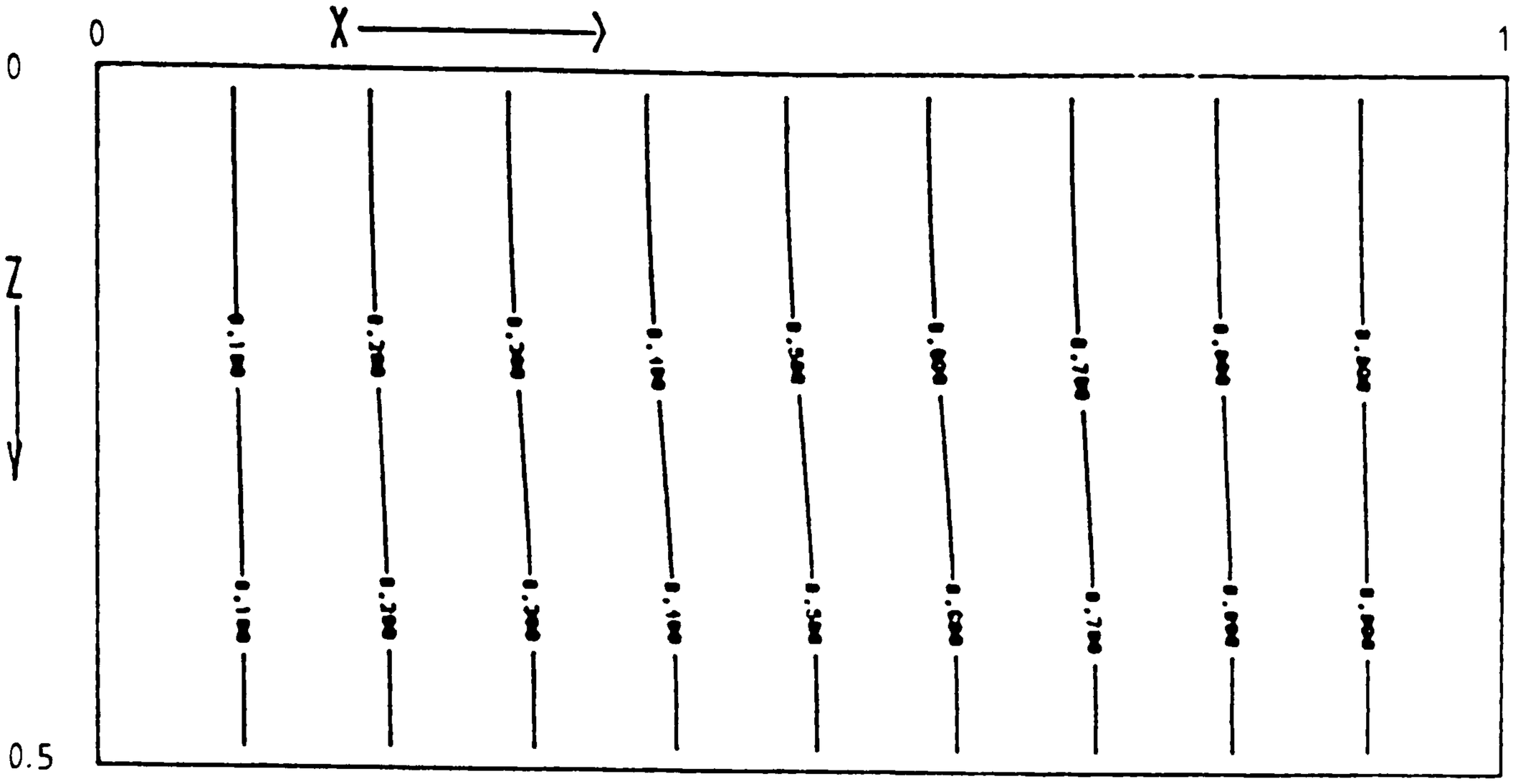

Figure 6.149 Isotherms at plane A, near the end wall

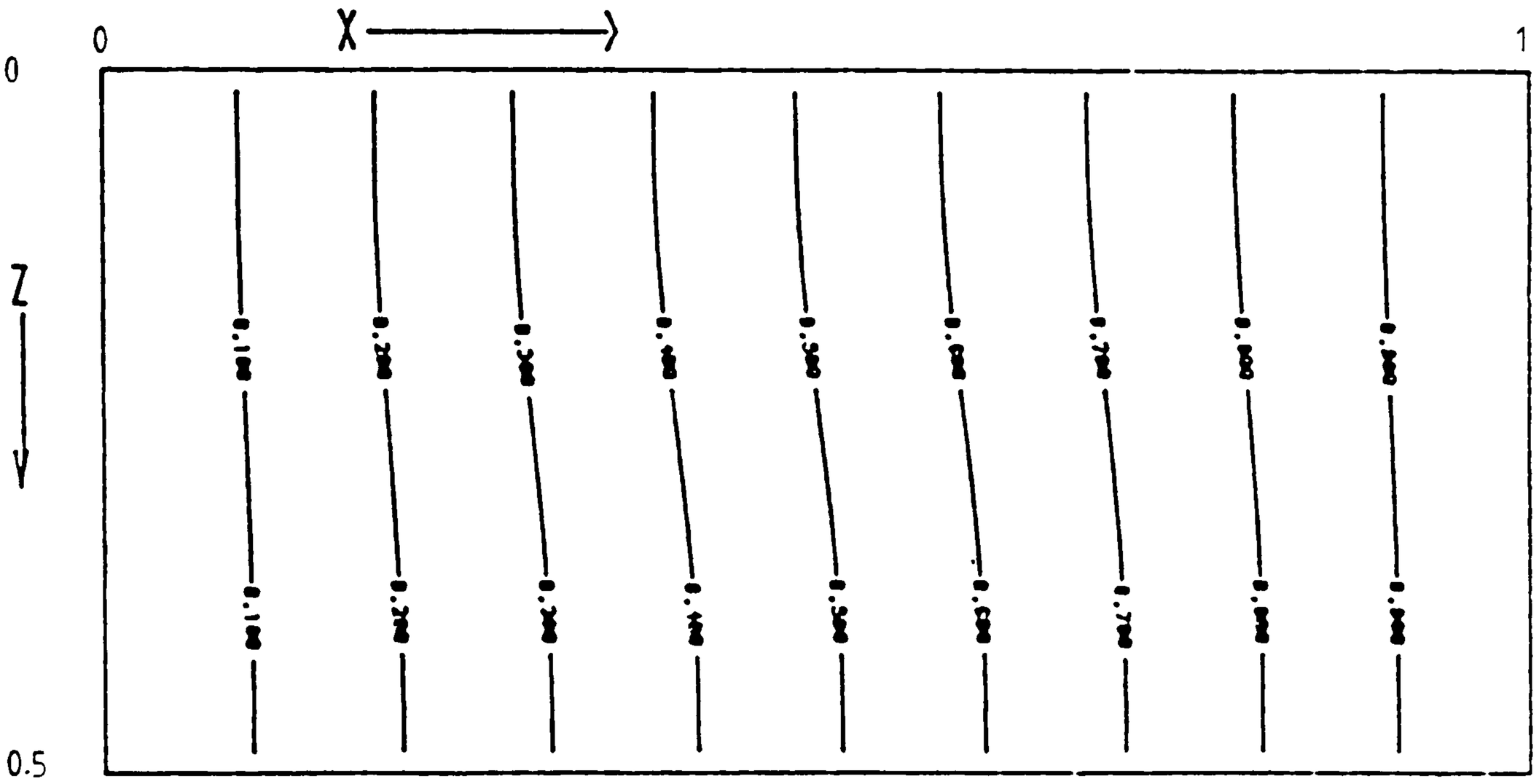

Figure 6.150 Isotherms at plane B, near the symmetry plane

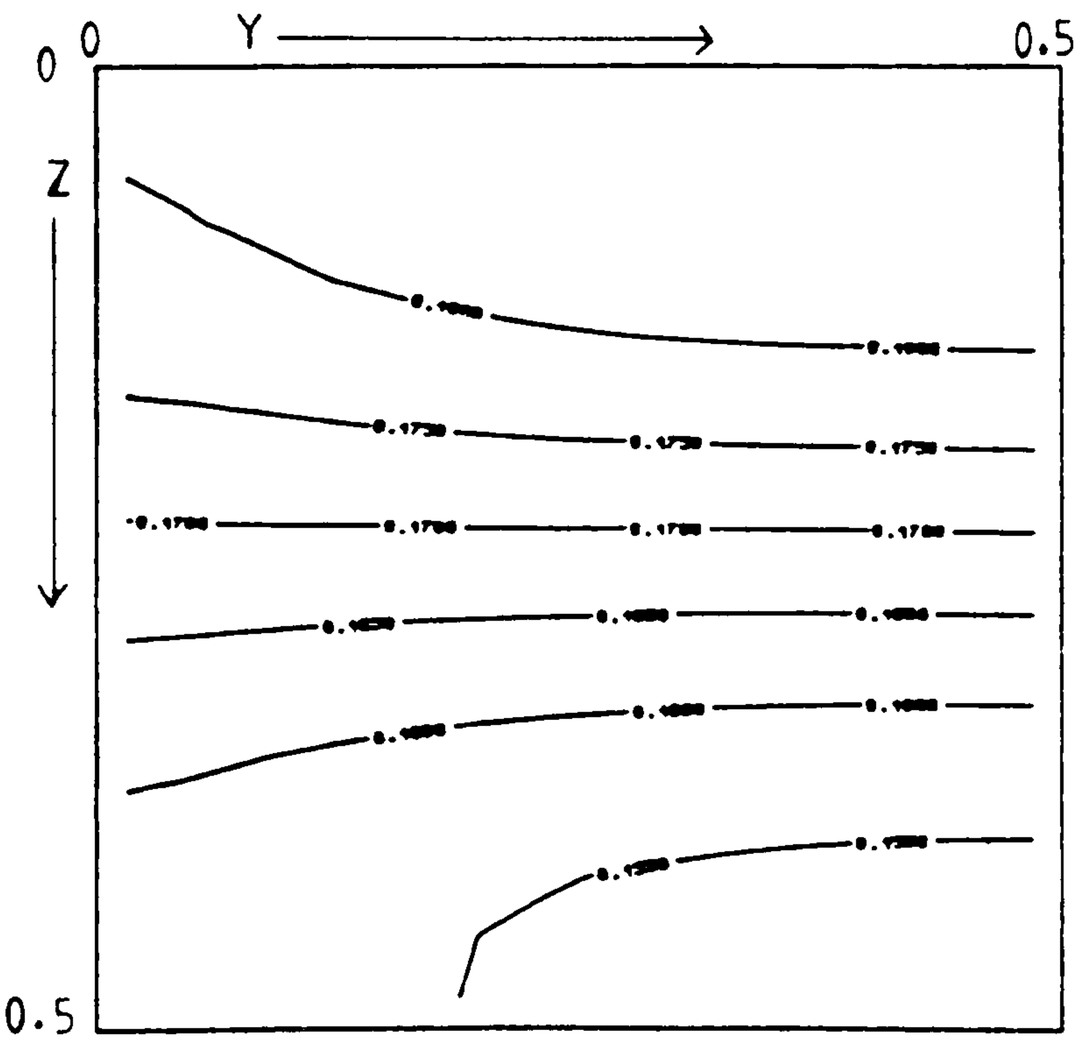

Figure 6.151 Isotherms at plane C, $(0.5 - hx/2, y, z)$

Fluid = cerrobase, Ra = 10^3, Hy=1, Hz=0.5

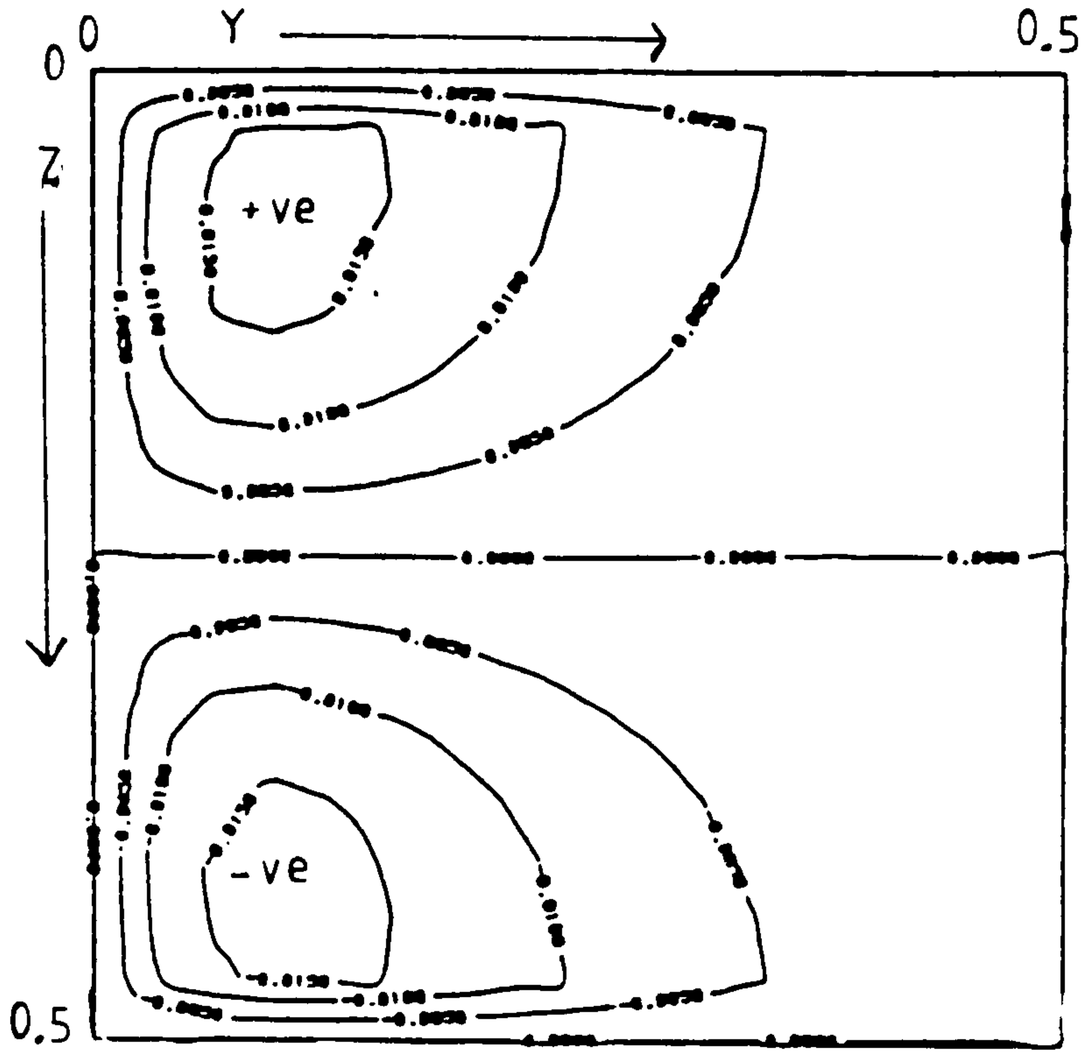

Figure 6.152 $\partial\theta/\partial y$ at plane C, $(0.5 - hx/2, y, z)$, Hy=1

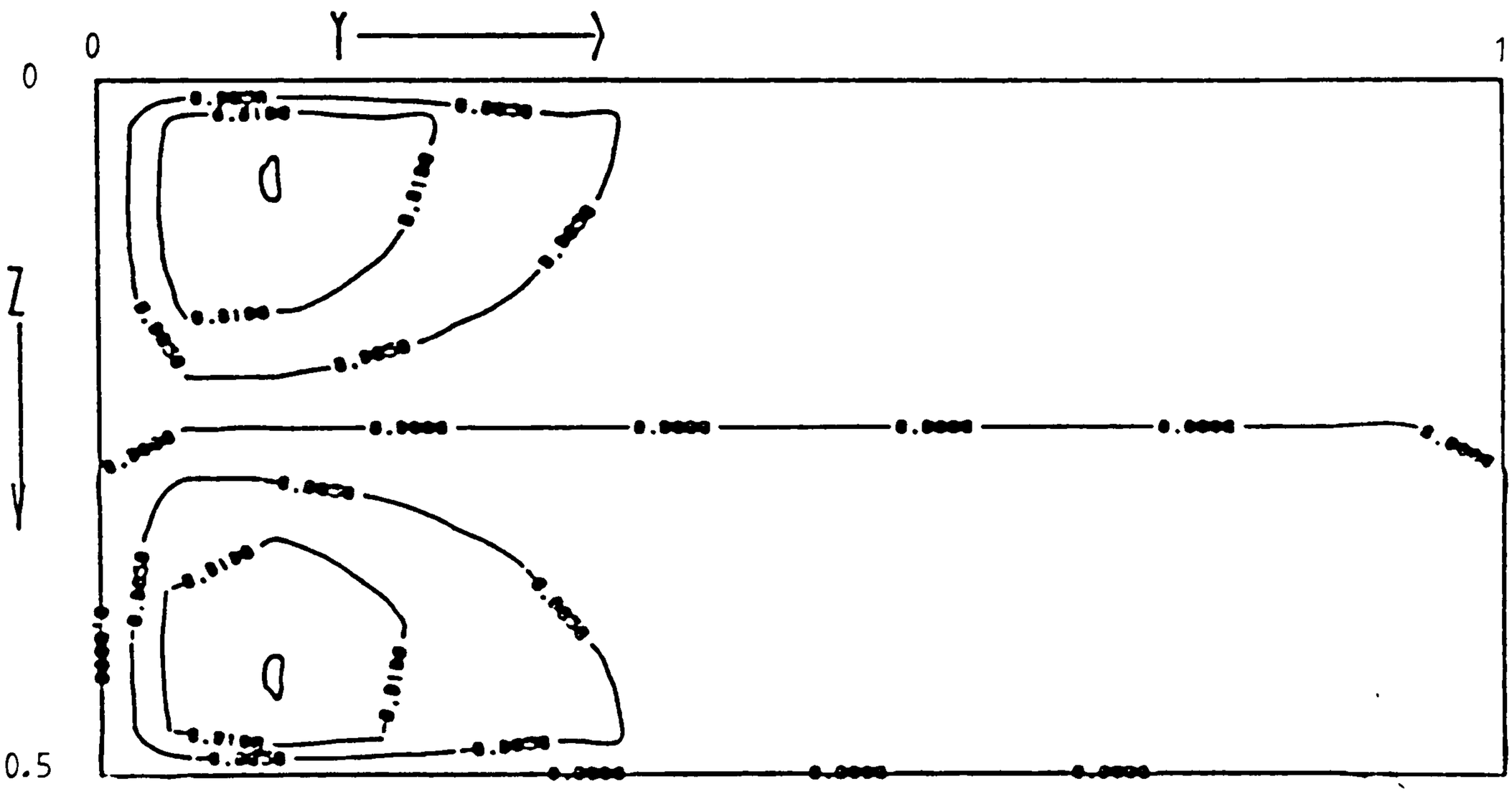

Figure 6.153 $\partial\theta/\partial y$ at plane C, $(0.5 - hx/2, y, z)$, Hy=2

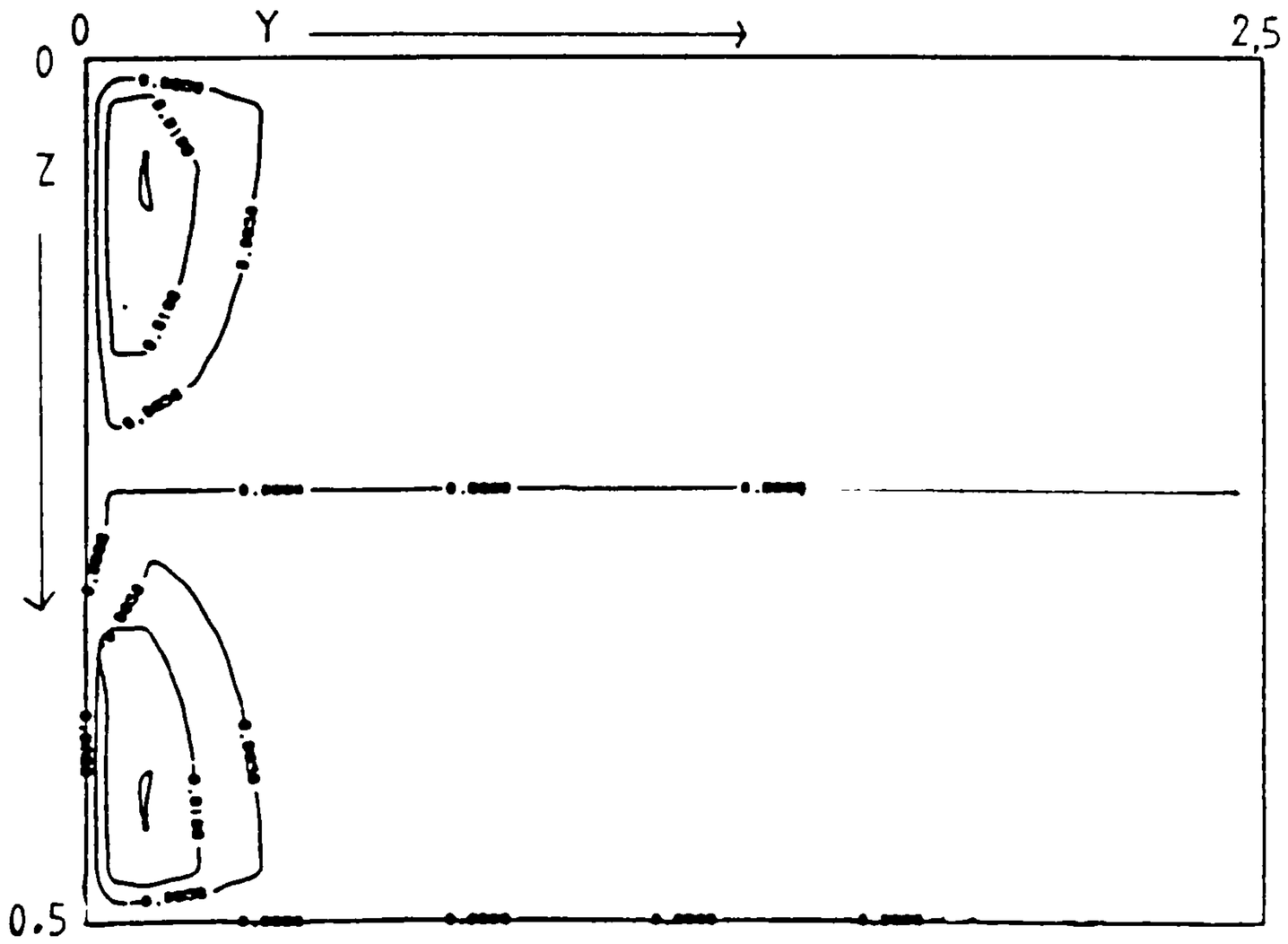

Figure 6.154 $\partial\theta/\partial y$ at plane C, $(0.5 - hx/2, y, z)$, Hy=5

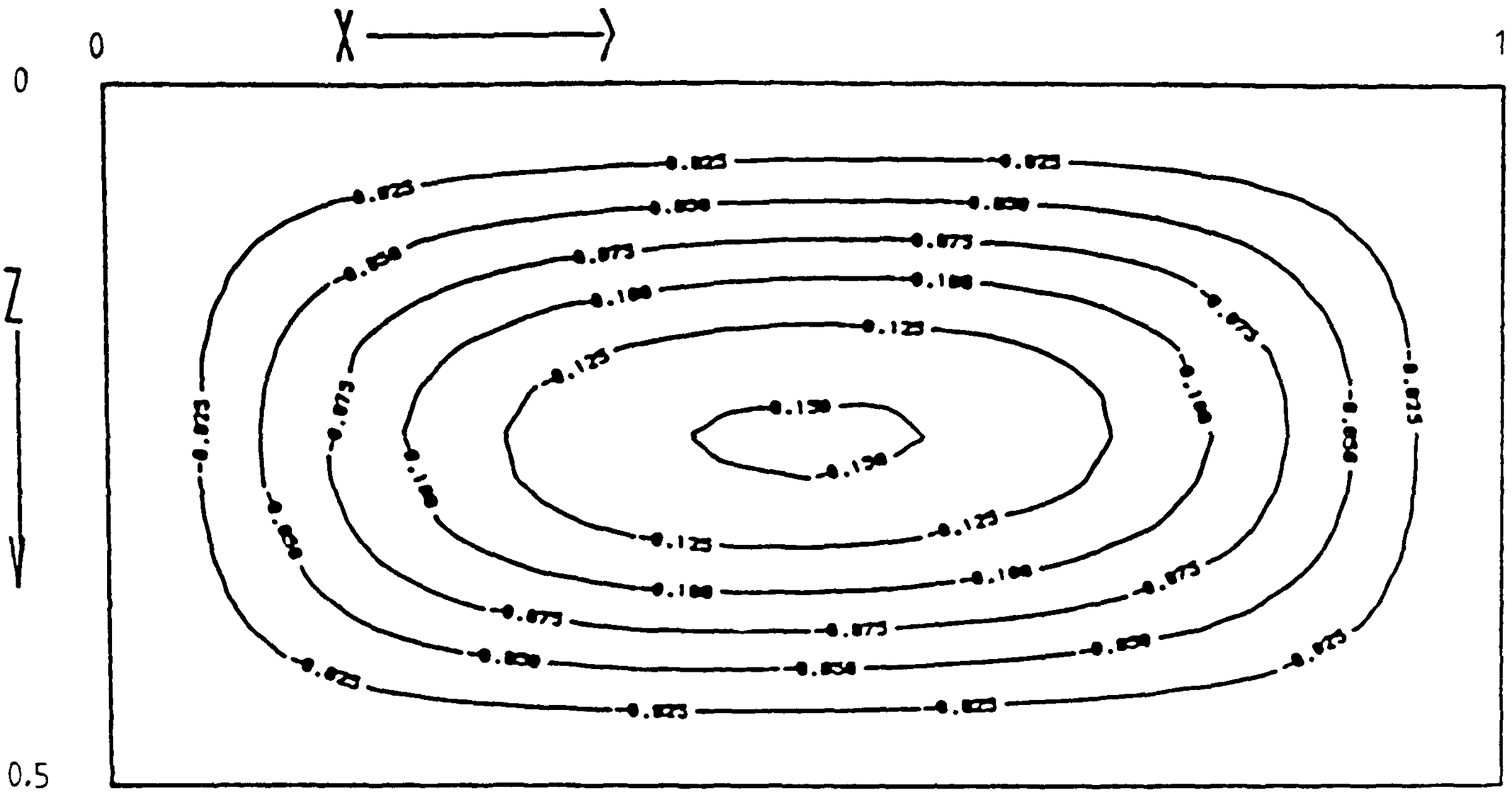

Figure 6.155 Streamlines near the symmetry plane, Hy=5

Graph A: cerrobase at Ra = 10^3, Hy=1, Hz=0.5

Graph B: cerrobase at Ra = 10^3, Hy=2, Hz=0.5

Graph C: cerrobase at Ra = 10^3, Hy=5, Hz=0.5

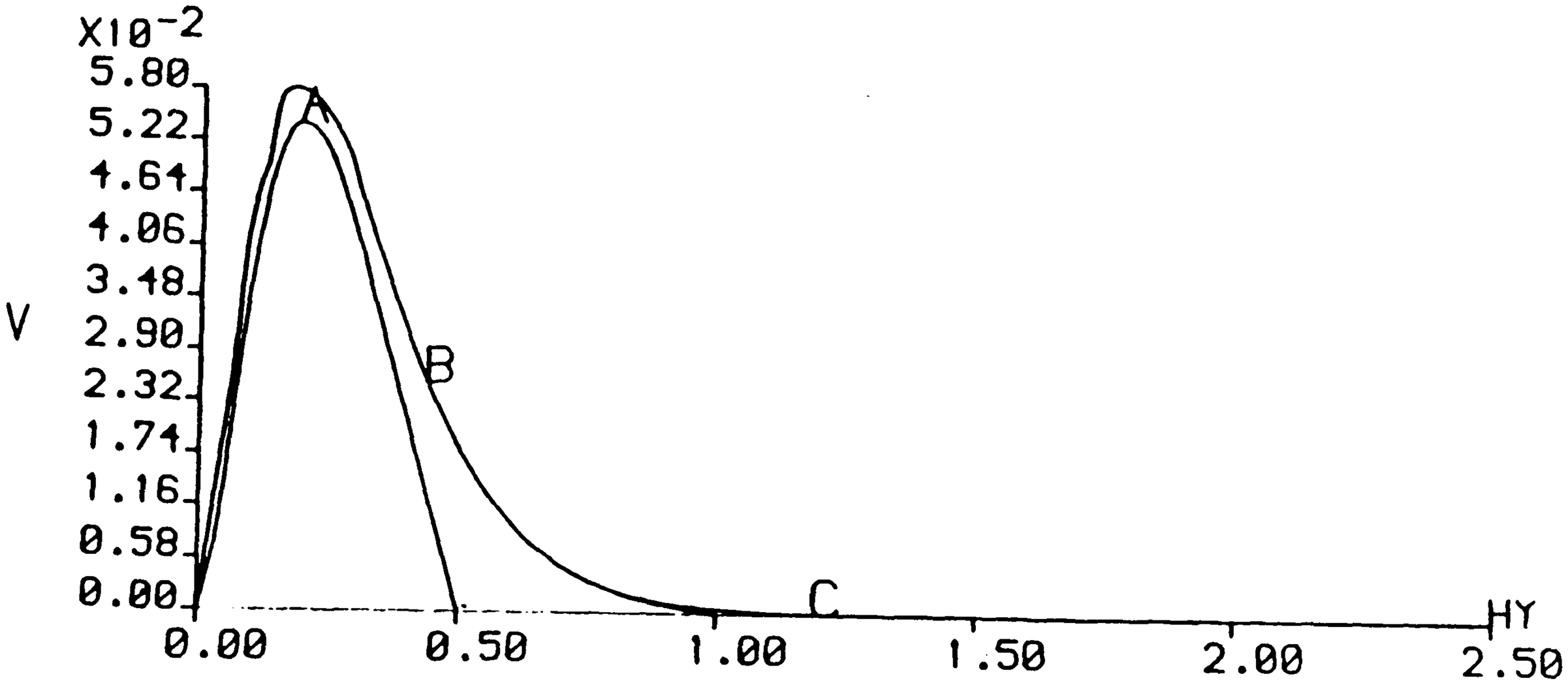

Figure 6.156 Axial-velocity along $(0.5, y, 0.25)$

6.7.4 Cerrobase $\mathbf{Ra} = 5 \times 10^3$

The fluid flow behaviour in this shallow cavity with length aspect ratio Hy=1.0, 2.0 and 5.0 for cerrobase with $Ra = 5 \times 10^3$ is described by a single forward recirculating roll. With length aspect ratios Hy=1.0 and 2.0 the forward roll occupies the whole solution cavity whereas with Hy=5.0 the forward roll only occupies part of the cavity with rest of the cavity solution being occupied with two-dimensional flow. Figures 6.157-159 illustrate the flow in a cavity with length aspect ratios Hy=1, 2 and 5 respectively.

Figures 6.160-6.162 are contour plots of R at planes A, B and C respectively for Hy=1.0. The positive R contours are attached to the top and bottom of the cavity walls. The positive R contours at the top and bottom walls occupy a smaller area than those obtained with $Ra = 10^3$. This is due to the strong end wall effect overcoming the opposing vorticity created by the axial temperature gradients.

Figures 6.163-168 are plots of the velocity vectors and isotherms at planes A, B and C respectively for Hy=1.0. The isotherms obtained with Hy=2 and 5 are similar to those obtained with Hy=1 and are not presented. Figures 6.169 and 170 are contour plots of $\partial\theta/\partial y$ at the plane x=0.5 for Hy=1.0 and 5.0 respectively. Note that there is no change in the sign $\partial\theta/\partial y$ along the axial direction as obtained with the square cross-section window cavity. Figure 6.171 is a plot of the streamlines near the symmetry plane with length aspect ratio Hy=5.0 and exhibits primary flow.

Figure 6.172 is a plot of the axial-velocity along the centre line. The axial flow in the shorter cavity is restricted. Two-dimensional flow exists for cavities with length aspect ratio, Hy, ≥ 2.5. In the square cross-section window cavity two-dimensional flow did not exist for cavities with length aspect ratios Hy ≤ 5.0. Indicating that the end wall effect with the square cross-section window cavity is much greater than that with the shallow cross-section window cavity.

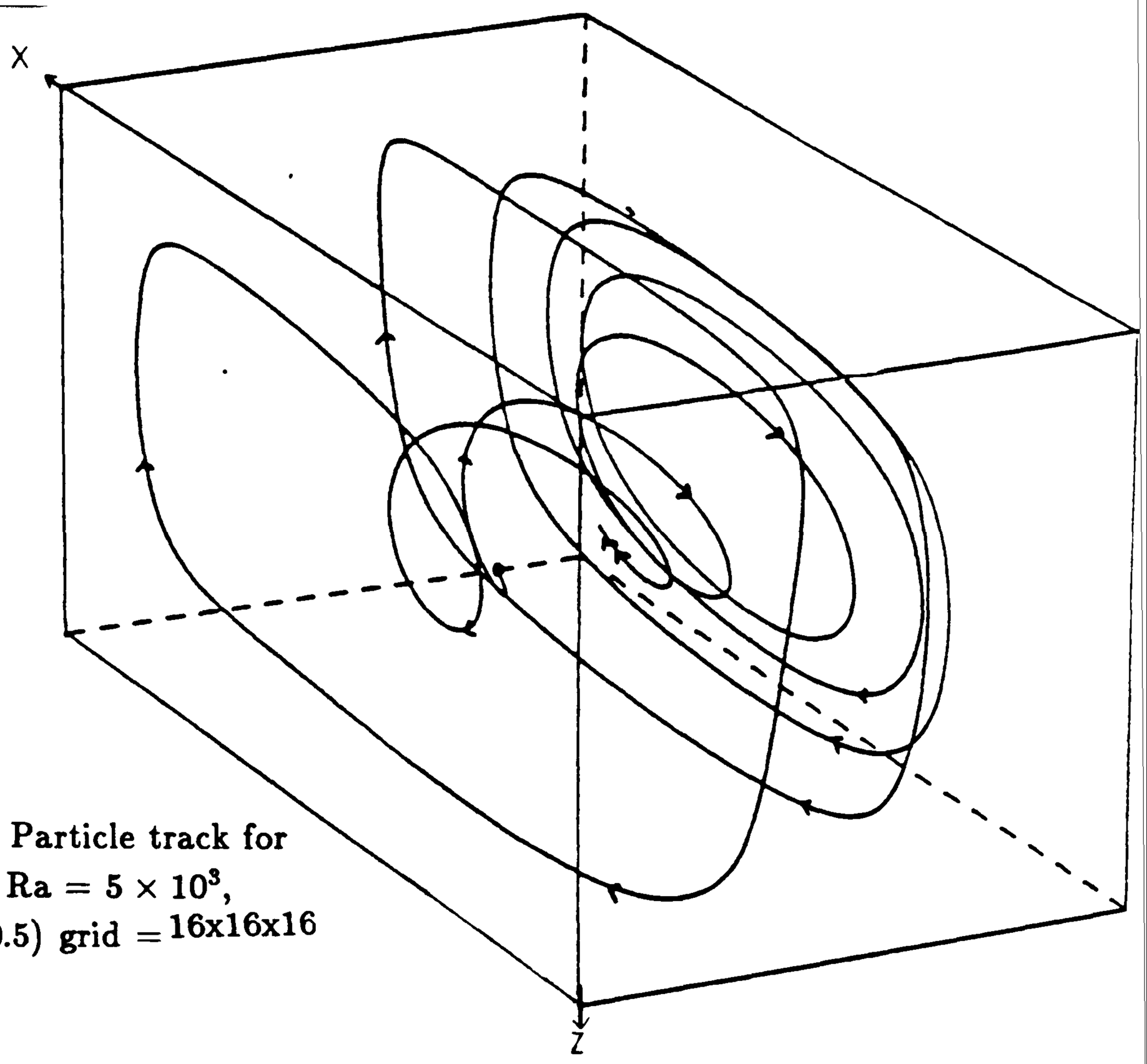

Figure 6.157 Particle track for cerrobase at Ra = 5×10^3, cavity (1,1,0.5) grid = 16x16x16

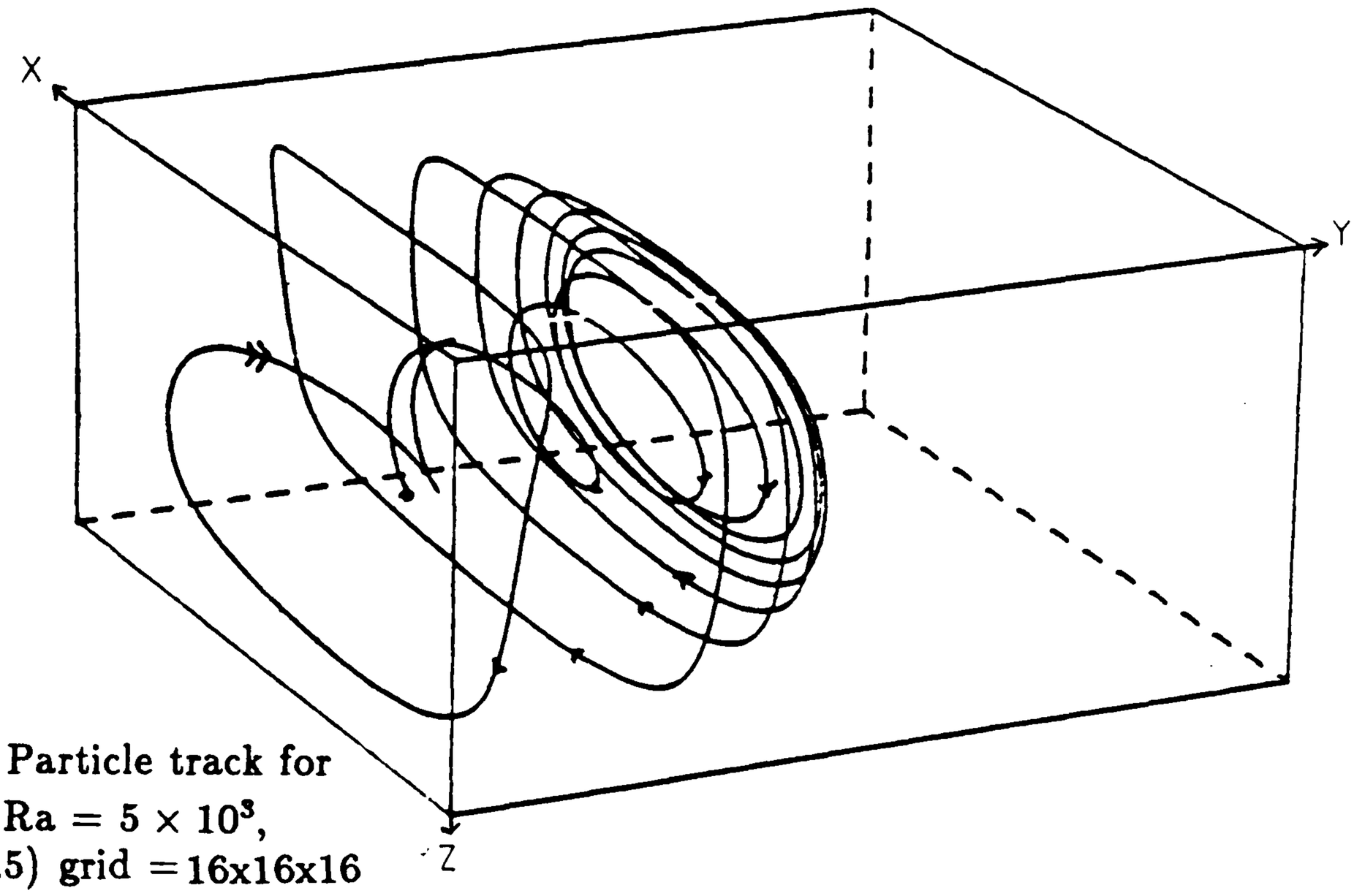

Figure 6.158 Particle track for cerrobase at Ra = 5×10^3, cavity (1,2,0.5) grid = 16x16x16

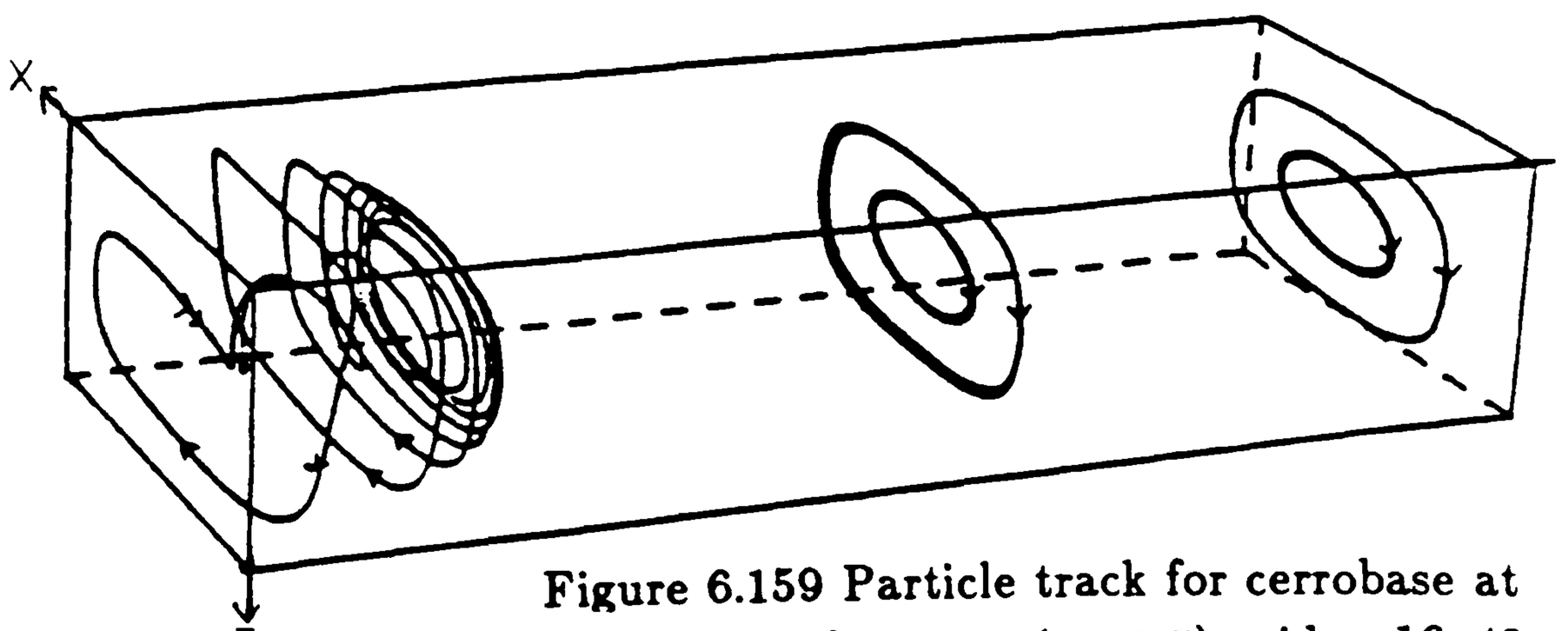

Figure 6.159 Particle track for cerrobase at Ra = 5×10^3, cavity (1,5,0.5) grid = 16x40x

Fluid = cerrobase, Ra = 5×10^3, Hy=1, Hz=0.5, grid=16x16x16

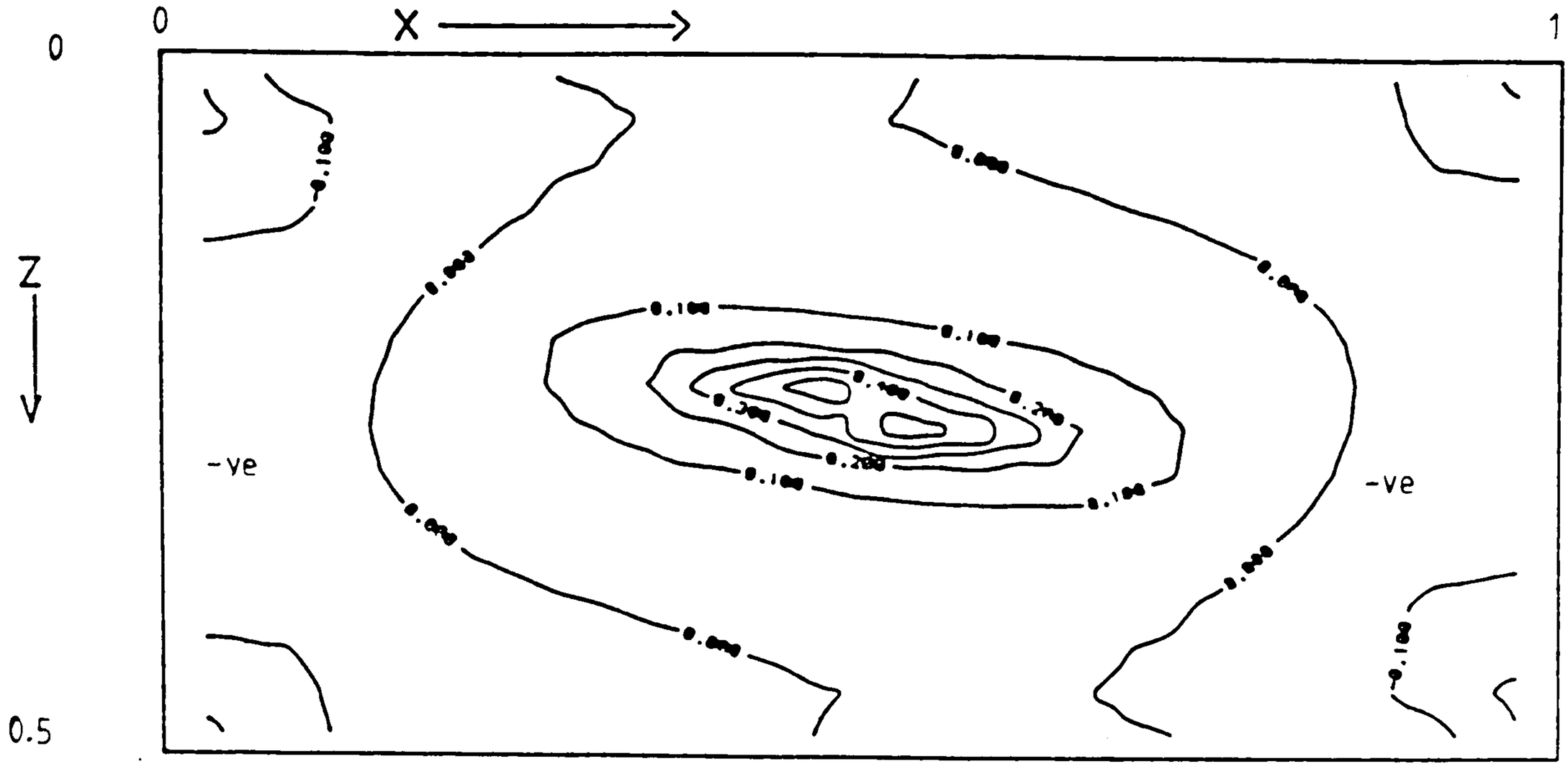

Figure 6.160 Contour plot of ratio R at plane A, near the end wall

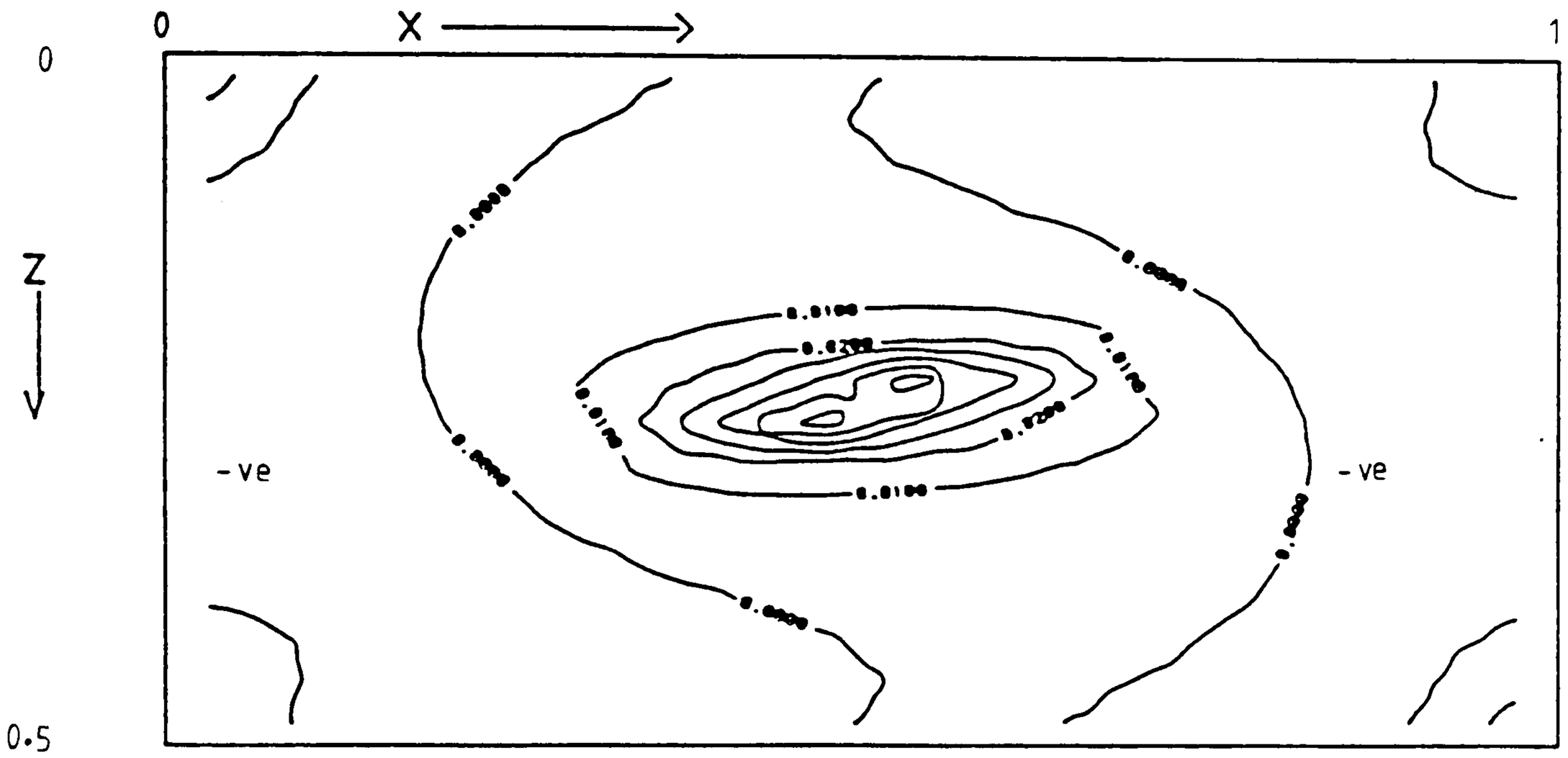

Figure 6.161 Contour plot of ratio R at plane B, near the symmetry plane

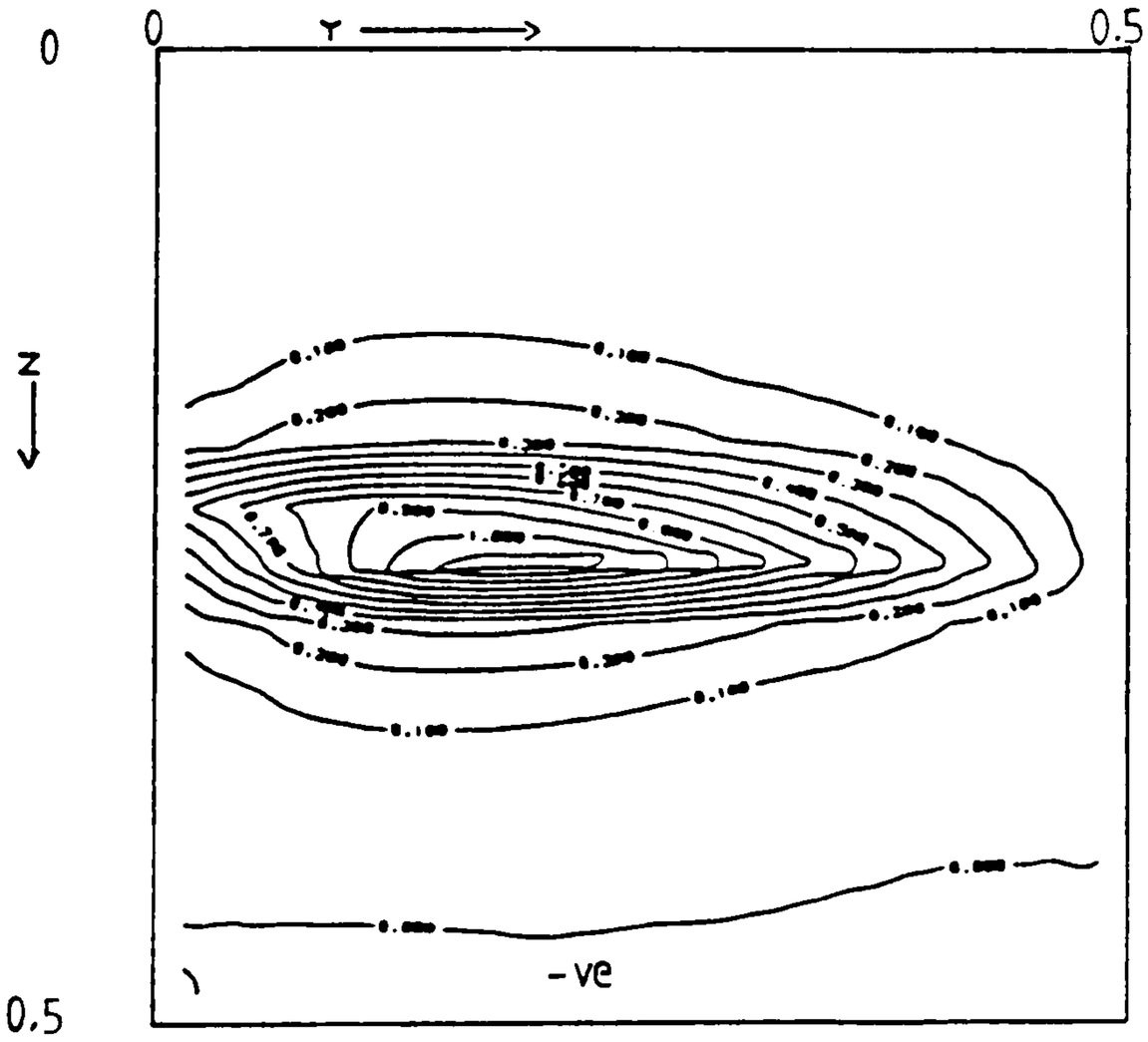

Figure 6.162 Contour plot of ratio R at plane C $(0.5 - hx/2, y, z)$

Fluid = cerrobase, Ra = 5×10^3, Hy=1, Hz=0.5, grid=16x16x16

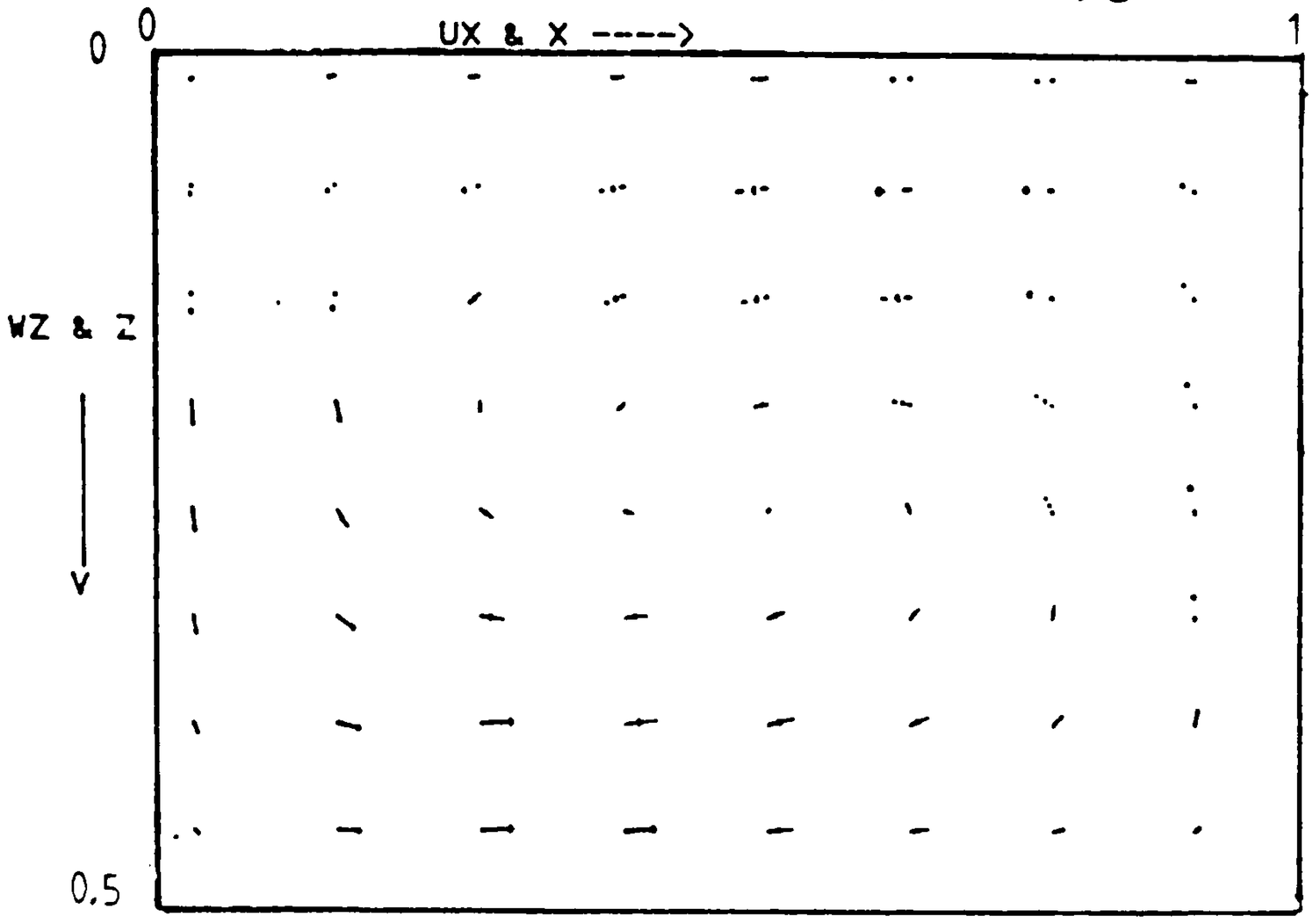

Figure 6.163 Velocity vectors at plane A, near the end wall

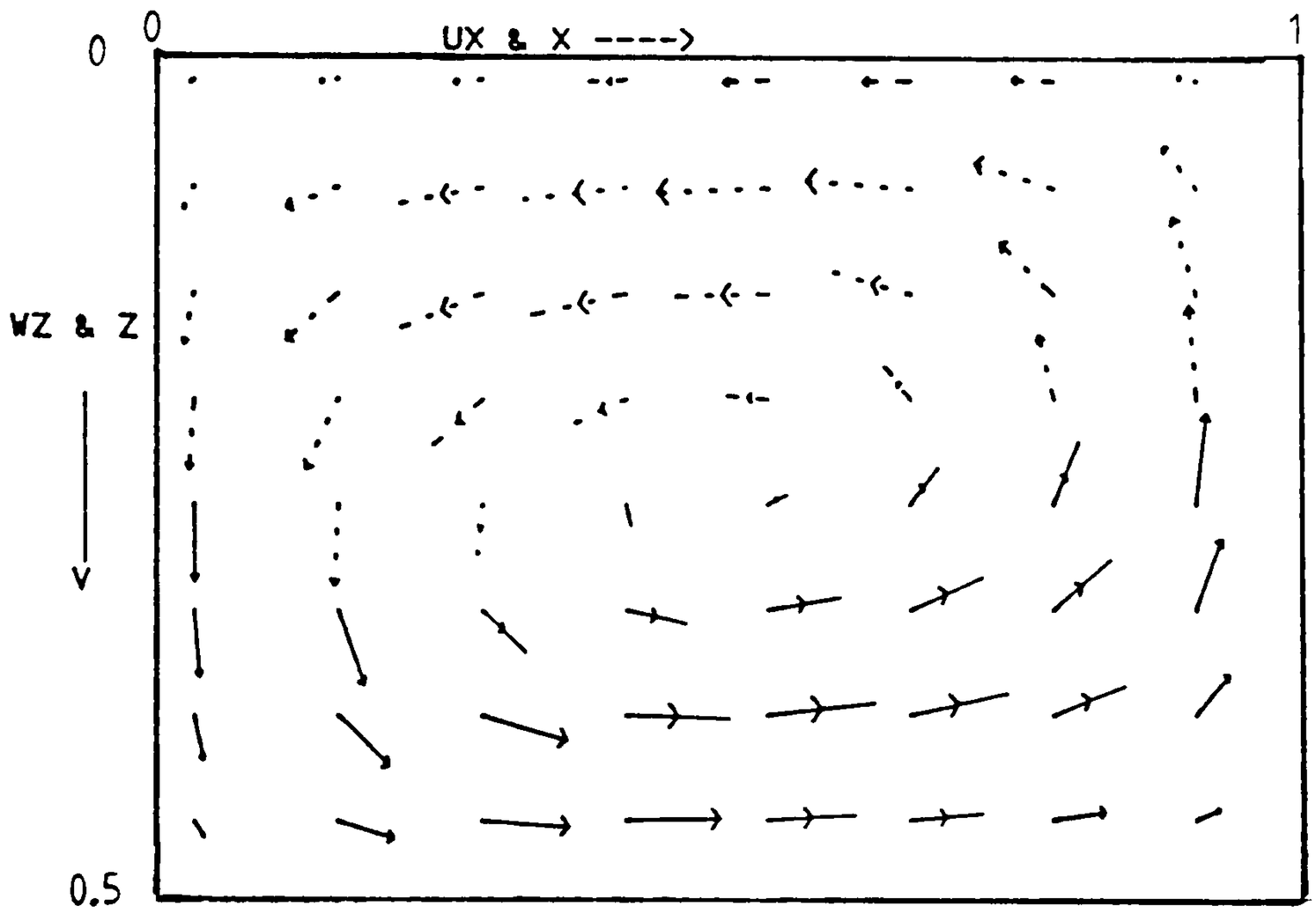

Figure 6.164 Velocity vectors at plane B, near the symmetry plane

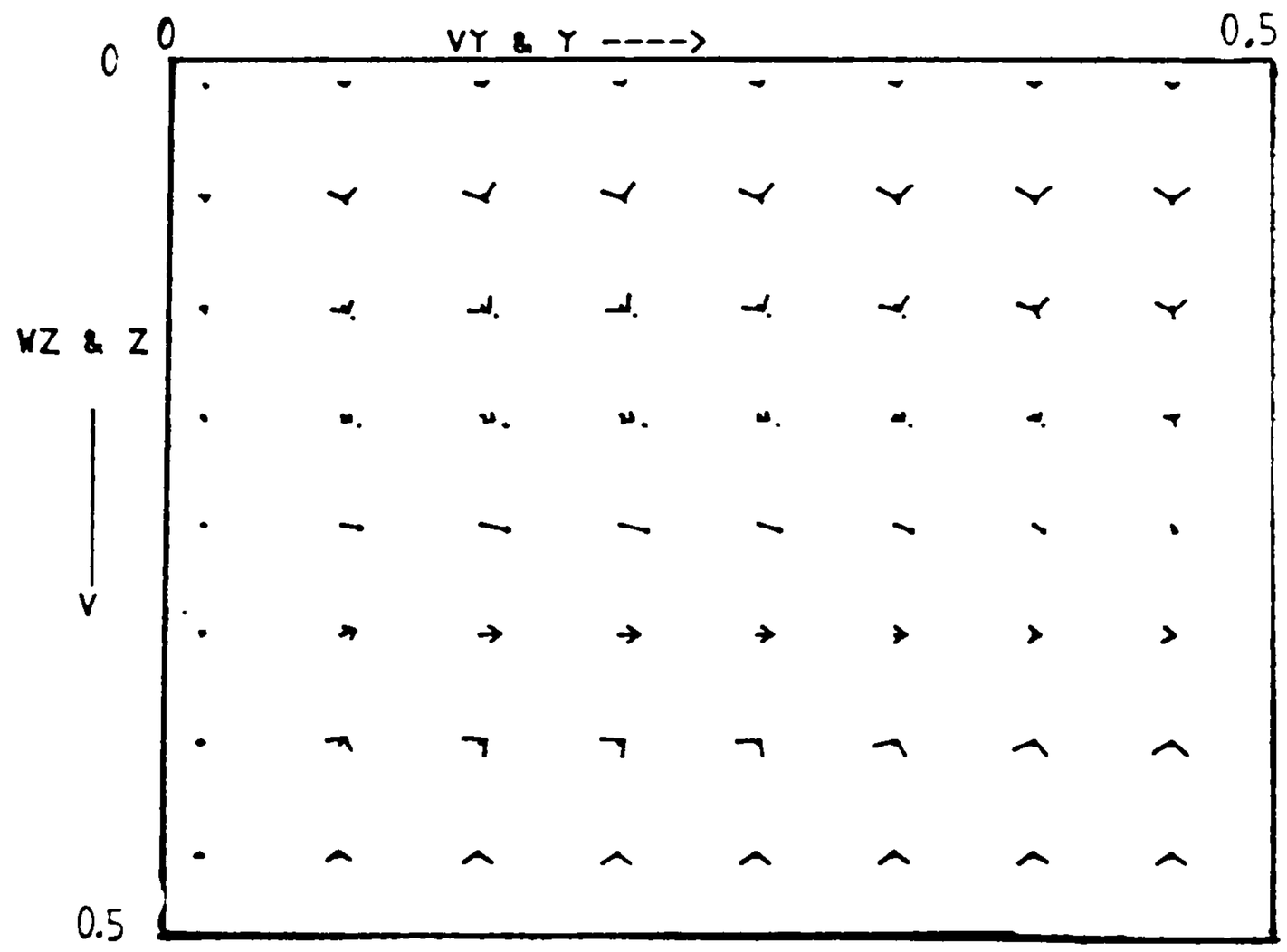

Figure 6.165 Velocity vectors at plane C $(0.5 - hx/2, y, z)$

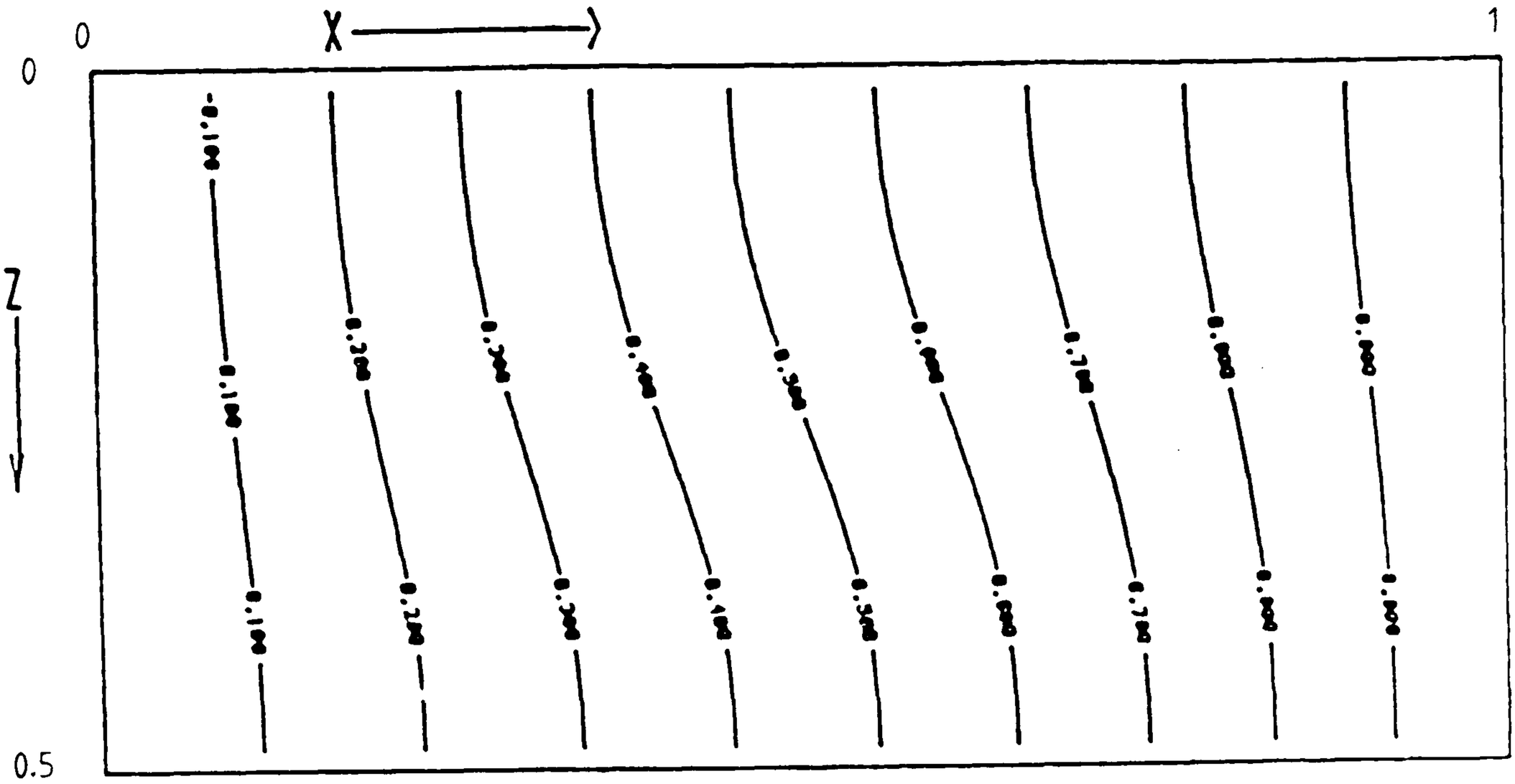

Figure 6.166 Isotherms at plane A, near the end wall

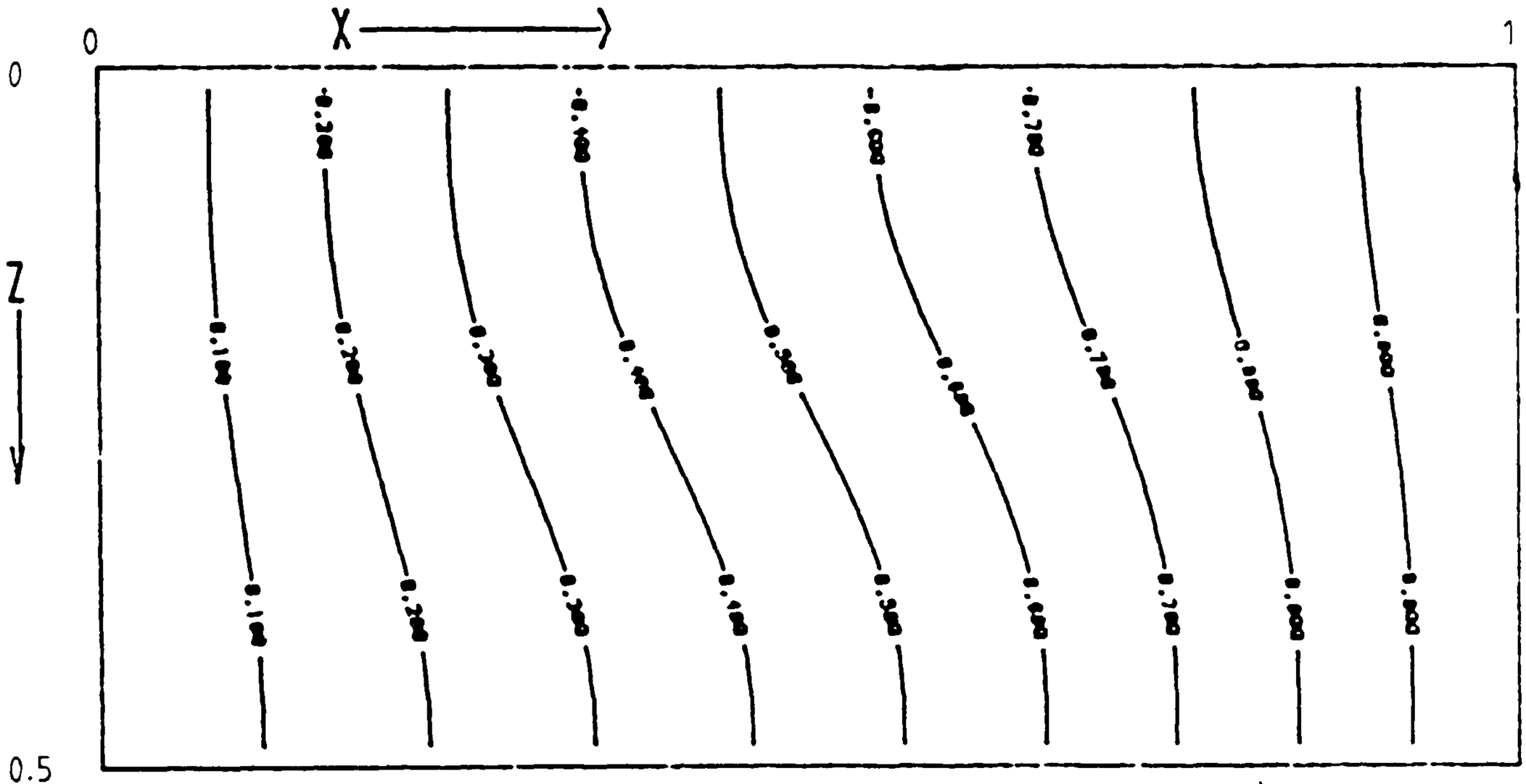

Figure 6.167 Isotherms at plane B, near the symmetry plane

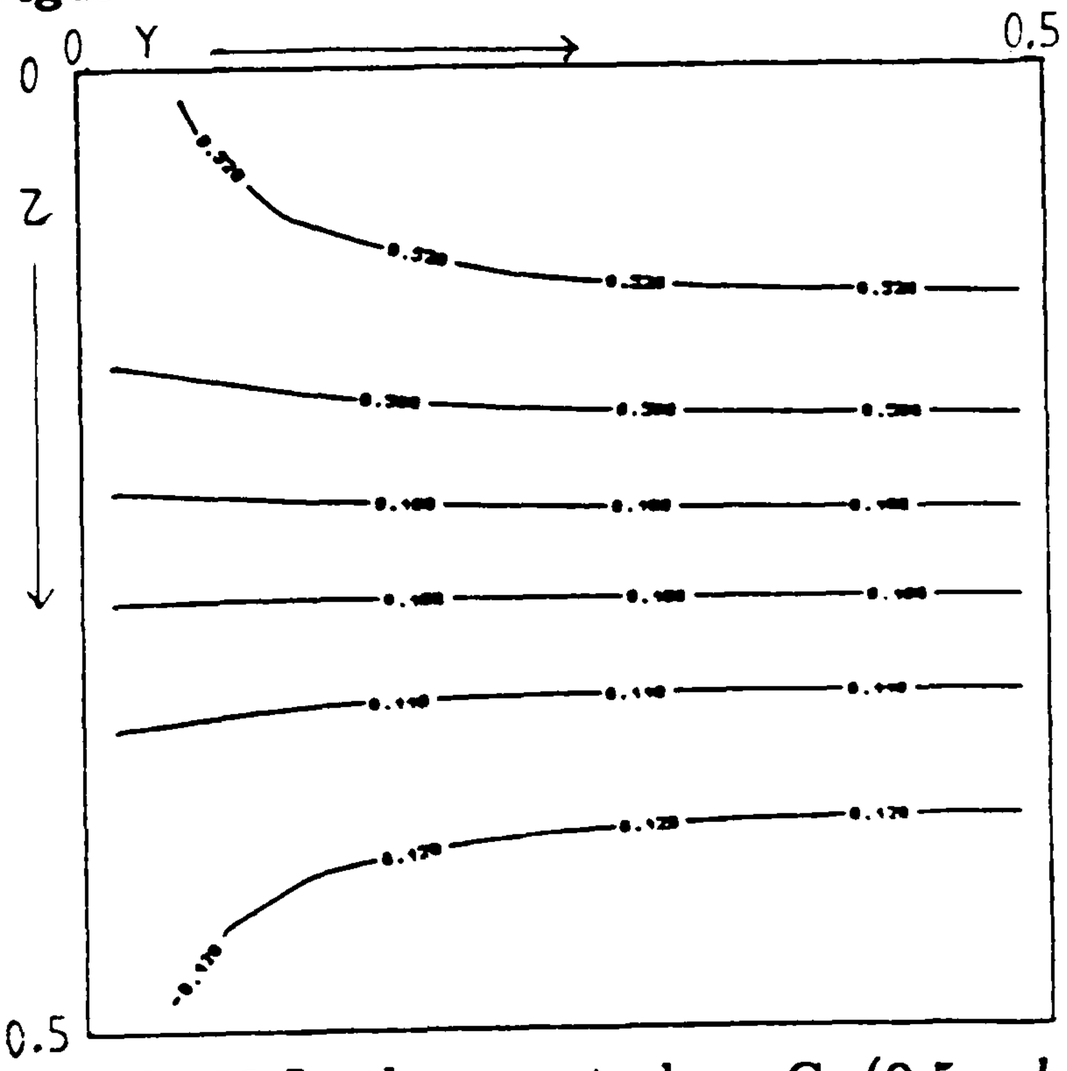

Figure 6.168 Isotherms at plane C, $(0.5 - hx/2, y, z)$

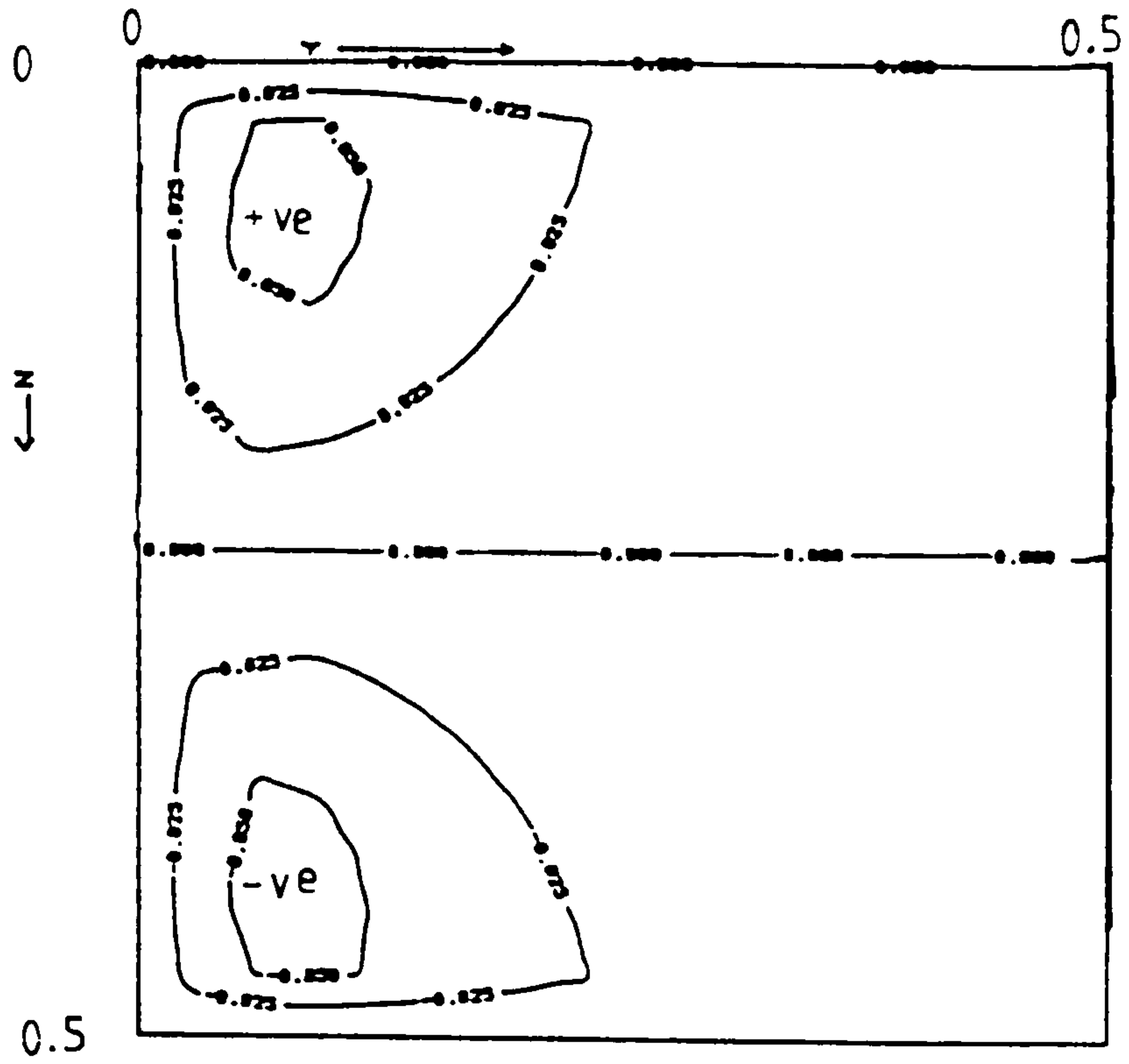

Figure 6.169 $\partial\theta/\partial y$ at plane C, $(0.5 - hx/2, y, z)$, Hy=1

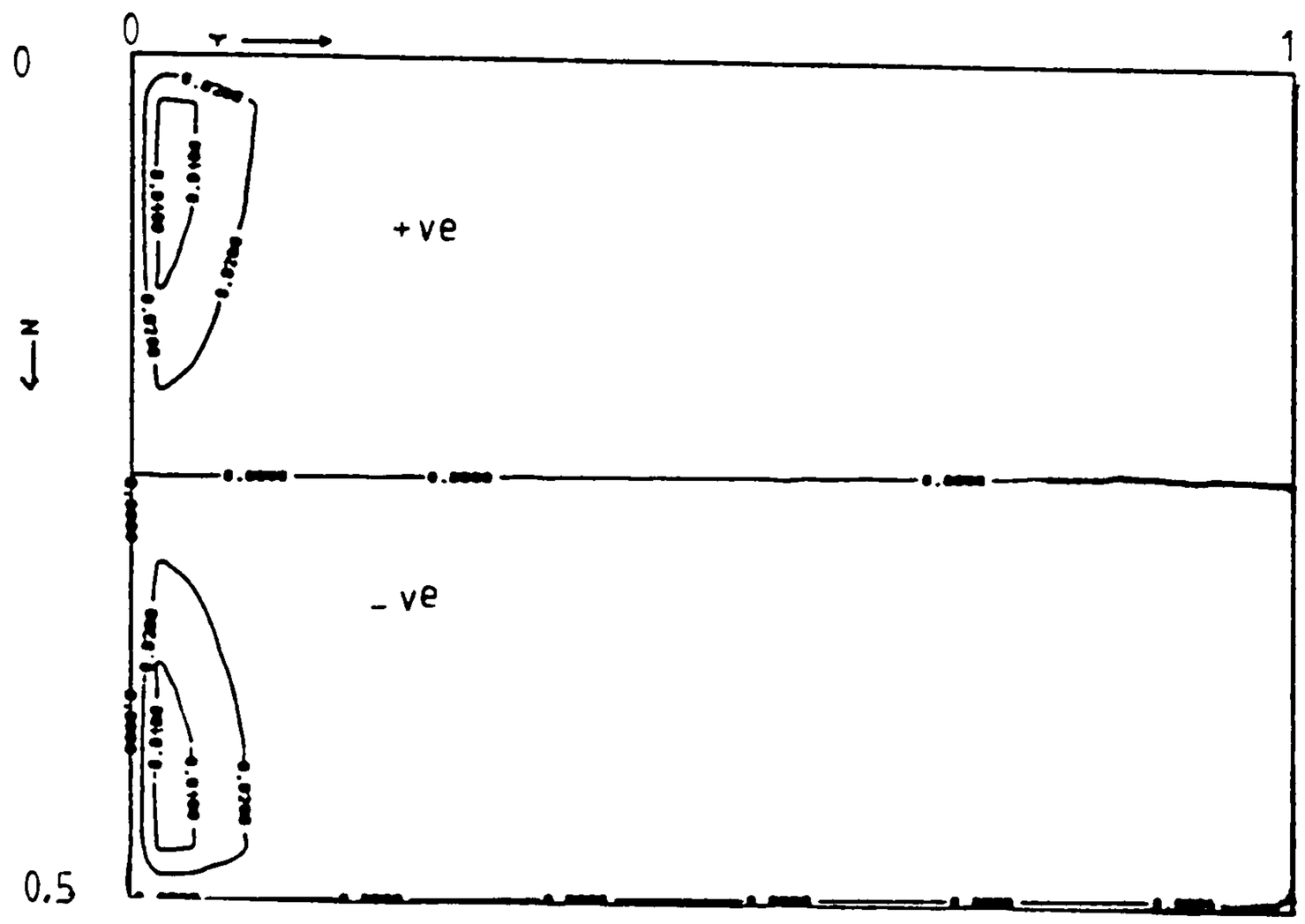

Figure 6.170 $\partial\theta/\partial y$ at plane C, $(0.5 - hx/2, y, z)$, Hy=5

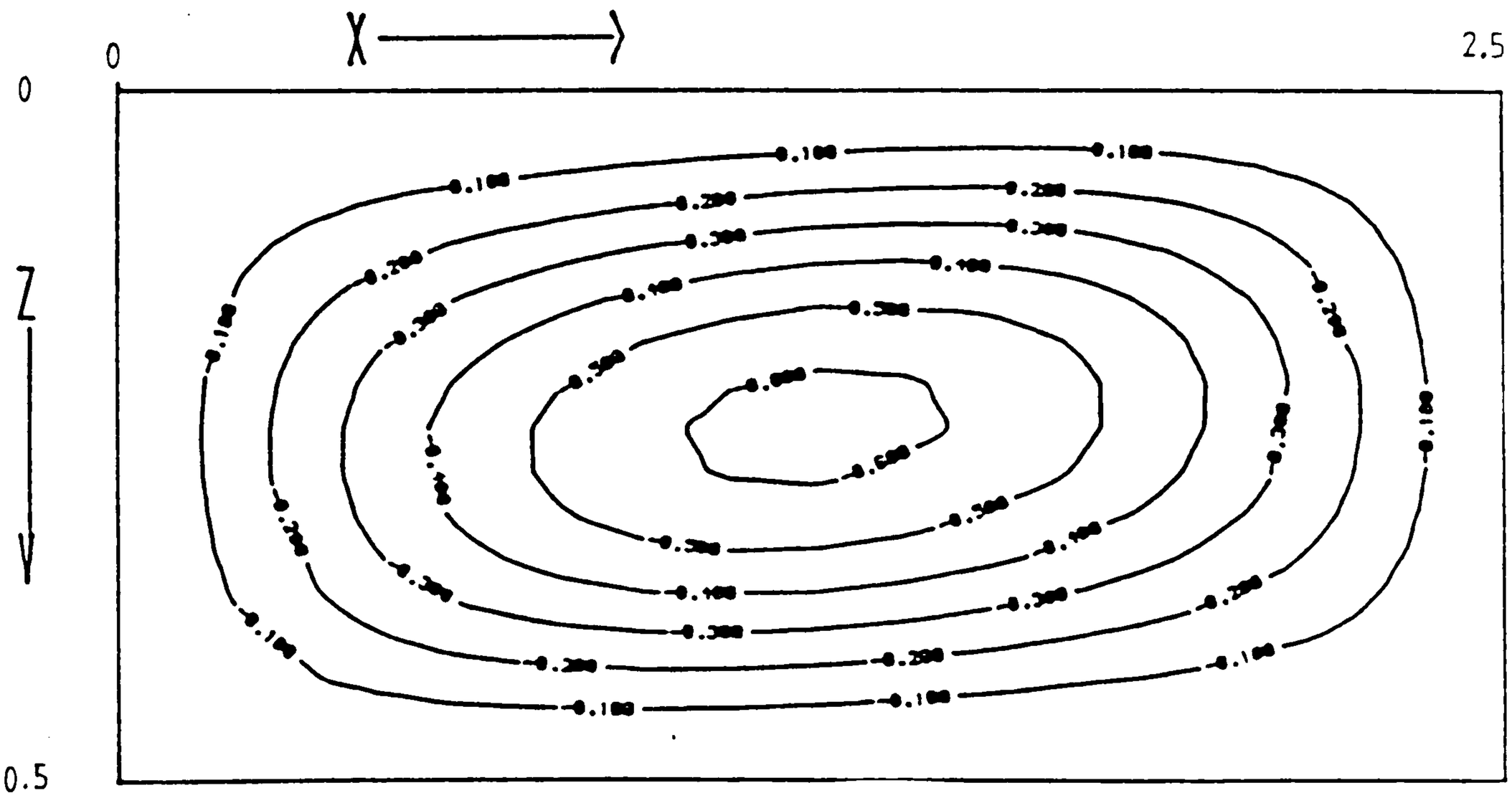

Figure 6.171 Streamlines near the symmetry plane, Hy=5

Graph A: cerrobase at Ra = 5×10^3, Hy=1, Hz=0.5

Graph B: cerrobase at Ra = 5×10^3, Hy=2, Hz=0.5

Graph C: cerrobase at Ra = 5×10^3, Hy=5, Hz=0.5

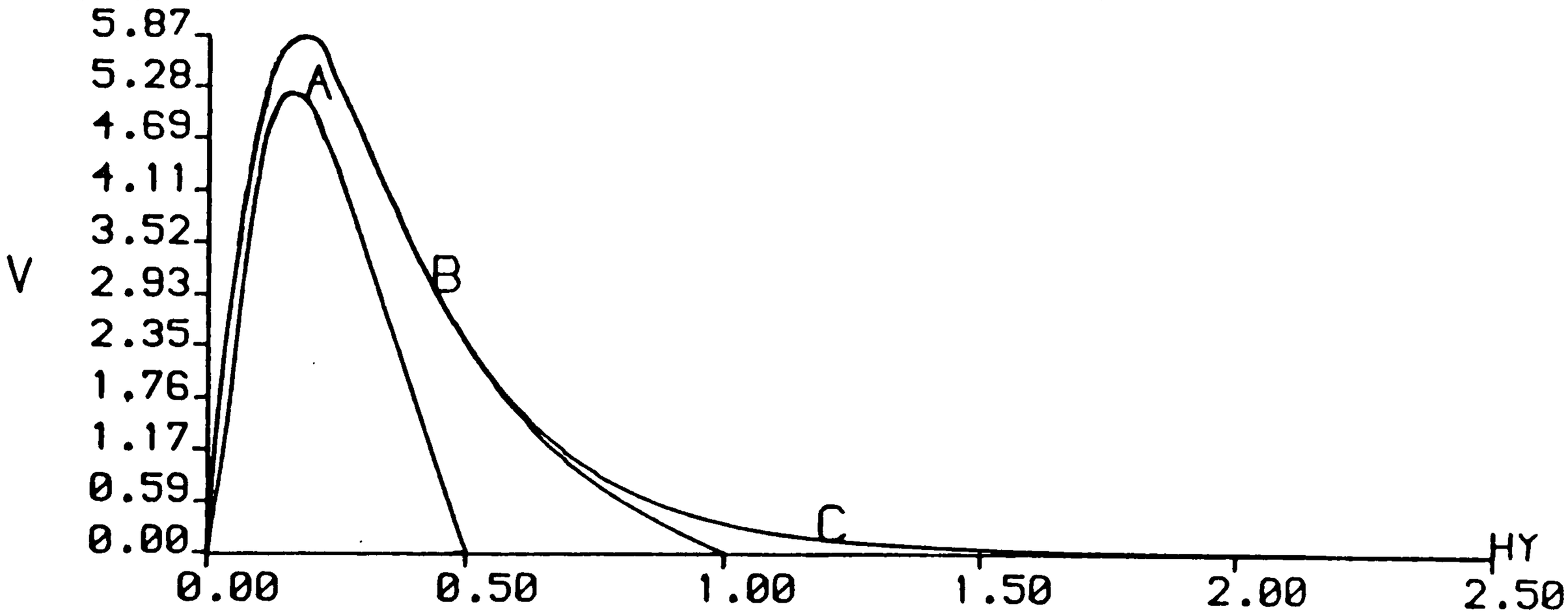

Figure 6.172 Axial-velocity along $(0.5, y, 0.25)$

6.7.5 Heat transfer results for the shallow cross section window cavity

Figures 6.173 - 6.175 are plots of Nu_v along the isothermal wall, x=0, for cavities with length aspect ratio Hy=1, 2 and 5 respectively. Each plot has the Nu_v along the hot wall for air at $Ra = 10^3$ and cerrobase at $Ra = 10^3$ and 5×10^3. Figure 6.176 is a plot of Nu_v along the isothermal wall, x=0, for air with $Ra = 10^5$ in cavities with length aspect ratio Hy=1, 2 and 5. The values of Nu_v obtained for the shorter cavity coincide at most points with those obtained for the larger cavity. $Nu_v(y)$ decreases as the end wall is approached and indicates the extent of the thermal boundary layer in which the convection of heat is reduced. As the Rayleigh number increases the thickness of this layer decreases. With the longer cavity, Hy=5.0, $Nu_v(y)$ increases slightly as $y \rightarrow 0$ until the end boundary layer is reached. The gradual increase results from the increasing magnitude of the axial velocity in the boundary layer as the end wall is approached.

Heat transfer at the wall with the low and moderate Prandtl number fluids with $Ra = 10^3$ are very similar. They only differ near the end wall in the thermal boundary layer where the heat flow with air is greater than with cerrobase.

FLUID	CAVITY	Nu_{av}	Nu_{vm}	ψ_{max}	$(\partial\theta/\partial y)_{max}$
air $Ra = 10^3$	1x1x1	1.015	1.016	0.16	0.019
	1x2x1	1.016	1.017	0.16	0.017
	1x5x1	1.017	1.017	0.16	0.017
air $Ra = 10^5$	1x1x1	4.09	4.385	5.36	0.616
	1x2x1	4.24	4.362	5.40	0.511
	1x5x1	4.31	4.359	5.40	0.511
cerrobase $Ra = 10^3$	1x1x1	1.014	1.017	0.15	0.018
	1x2x1	1.015	1.016	0.15	0.016
	1x5x1	1.016	1.016	0.15	0.016
cerrobase $Ra = 5 \times 10^3$	1x1x	1.092	1.114	0.59	0.0675
	1x2x1	1.102	1.112	0.63	0.0674
	1x5x1	1.107	1.111	0.63	0.0674

Table 6.5: Nu_{av}, Nu_{vm}, ψ_{max} and $(\partial\theta/\partial y)_{max}$ for Hz=0.5

Nu_{vm} for air at $Ra = 10^5$ is greater with the shorter cavity (Hy=1.0) than the

longer cavities (Hy=2.0,and 5.0). This is due to the contribution to the convection of heat from the developed axial flow with Hy=1.0. For the longer cavity the axial flow does not increase the convection of heat since the flow is mostly two-dimensional.

For the same reason Nu_{vm} for cerrobase with $Ra = 10^3$ and 5×10^3 is greater for the shorter cavity Hy=1.0 than for the longer cavities Hy=2.0 and 5.0.

Bejan and Tien published the following correlation from their study of the two-dimensional problem for air in the shallow cavity, see [34].

$$Nu_{BT} = 1 + \left[\left(\frac{Ra^2 Hz^8}{362880}\right)^n + \left(\frac{0.625 Ra^{0.2}}{Hz^{0.4}}\right)^n\right]^{1/n} \tag{6.12}$$

where $n = -0.386$ for $0.01 \leq Hz \leq 1.0$, $10^2 \leq Ra.Hz \leq 10^6$. The Nusselt number for air at $Ra = 10^3$ with Hz=0.5 using the above correlation is 1.008. The respective Nu_{vm} obtained is approximately 1% larger than the correlation value. The Nusselt number for air at $Ra = 10^5$ with Hz=0.5 using the above correlation is 4.633. The respective Nu_{vm} obtained is approximately 6% smaller than the correlation value. The Nu_{vm} obtained compare well with those obtained from Bejan and Tiens correlation. Unfortunately such correlation for the low Prandtl number investigated in this study appear not to have been published.

Graph A: cerrobase at Ra = 10^3, Hy=1, Hz=0.5

Graph B: cerrobase at Ra = 5×10^3, Hy=1, Hz=0.5

Graph C: air at Ra = 10^3, Hy=1, Hz=0.5

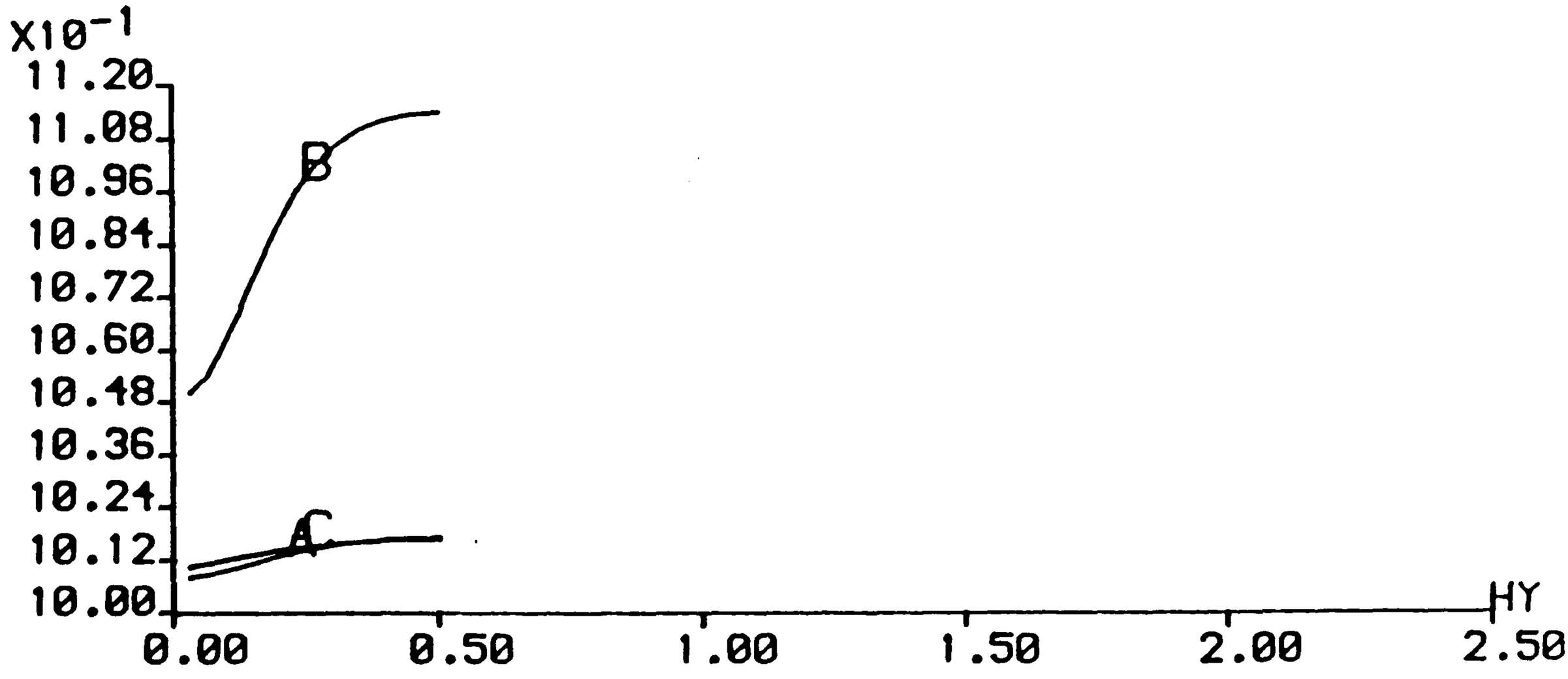

Figure 6.173 Nusselt number along the hot wall

Graph A: cerrobase at Ra = 10^3, Hy=1, Hz=0.5

Graph B: cerrobase at Ra = 5×10^3, Hy=1, Hz=0.5

Graph C: air at Ra = 10^3, Hy=1, Hz=0.5

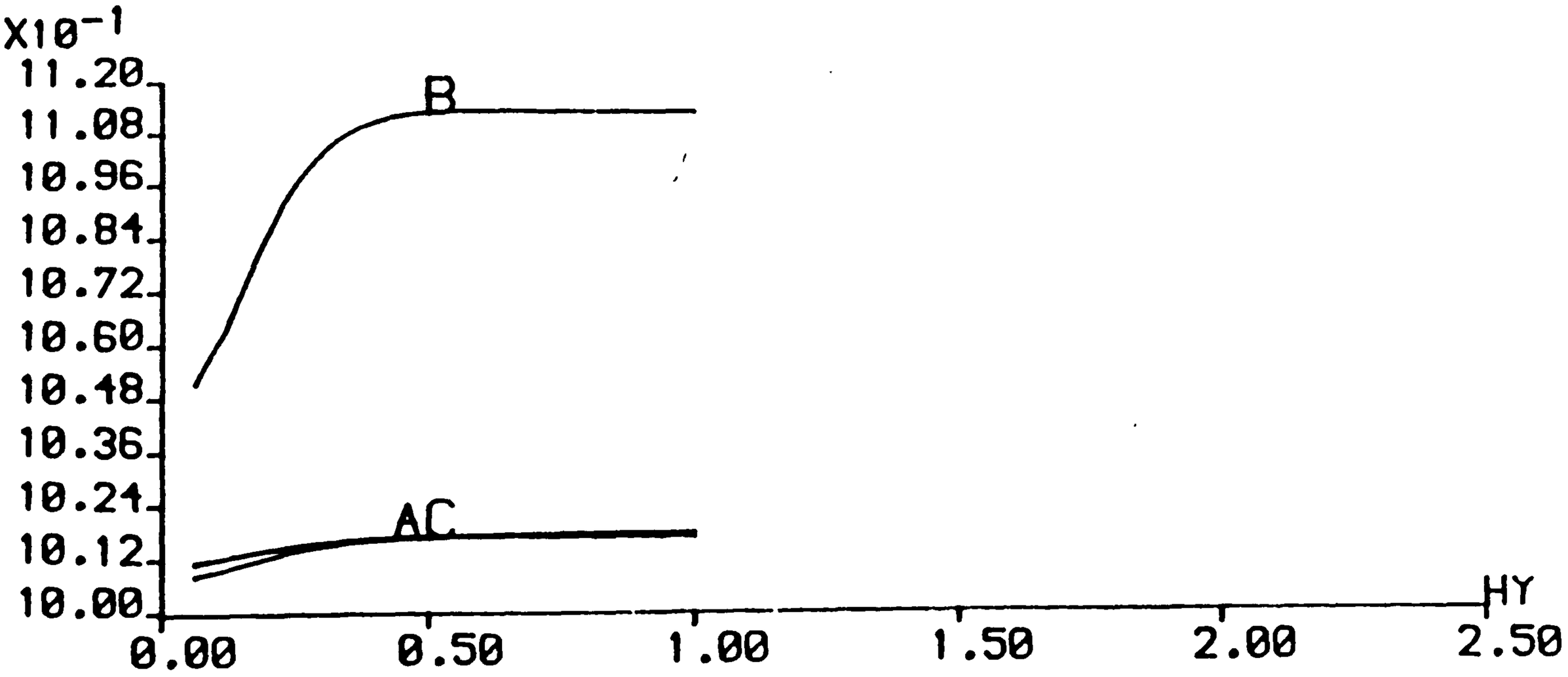

Figure 6.174 Nusselt number along the hot wall

Graph A: cerrobase at Ra = 10^3, Hy=1, Hz=0.5

Graph B: cerrobase at Ra = 5×10^3, Hy=1, Hz=0.5

Graph C: air at Ra = 10^3, Hy=1, Hz=0.5

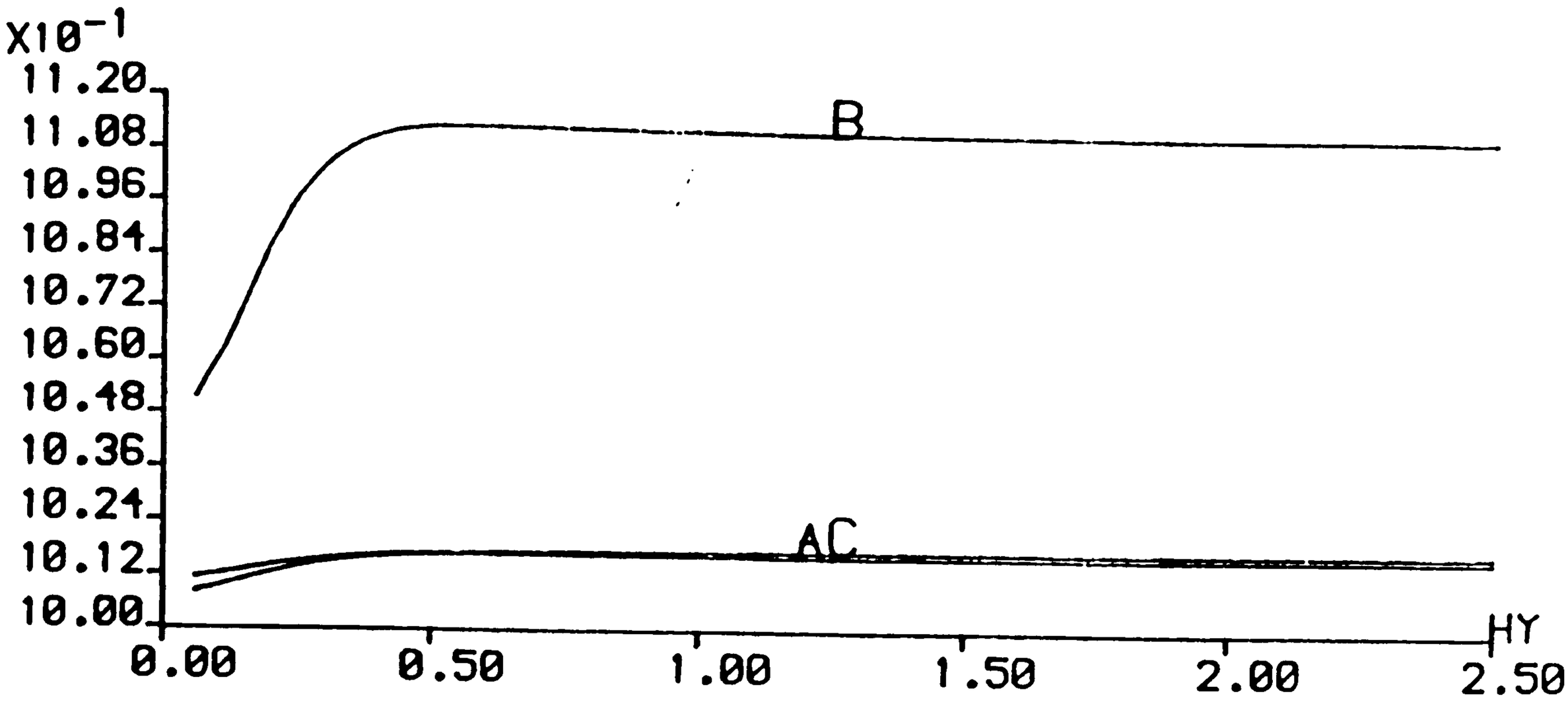

Figure 6.175 Nusselt number along the hot wall

Graph A: air at Ra = 10^5, Hy=1, Hz=0.5

Graph B: air at Ra = 10^5, Hy=2, Hz=0.5

Graph C: air at Ra = 10^5, Hy=5, Hz=0.5

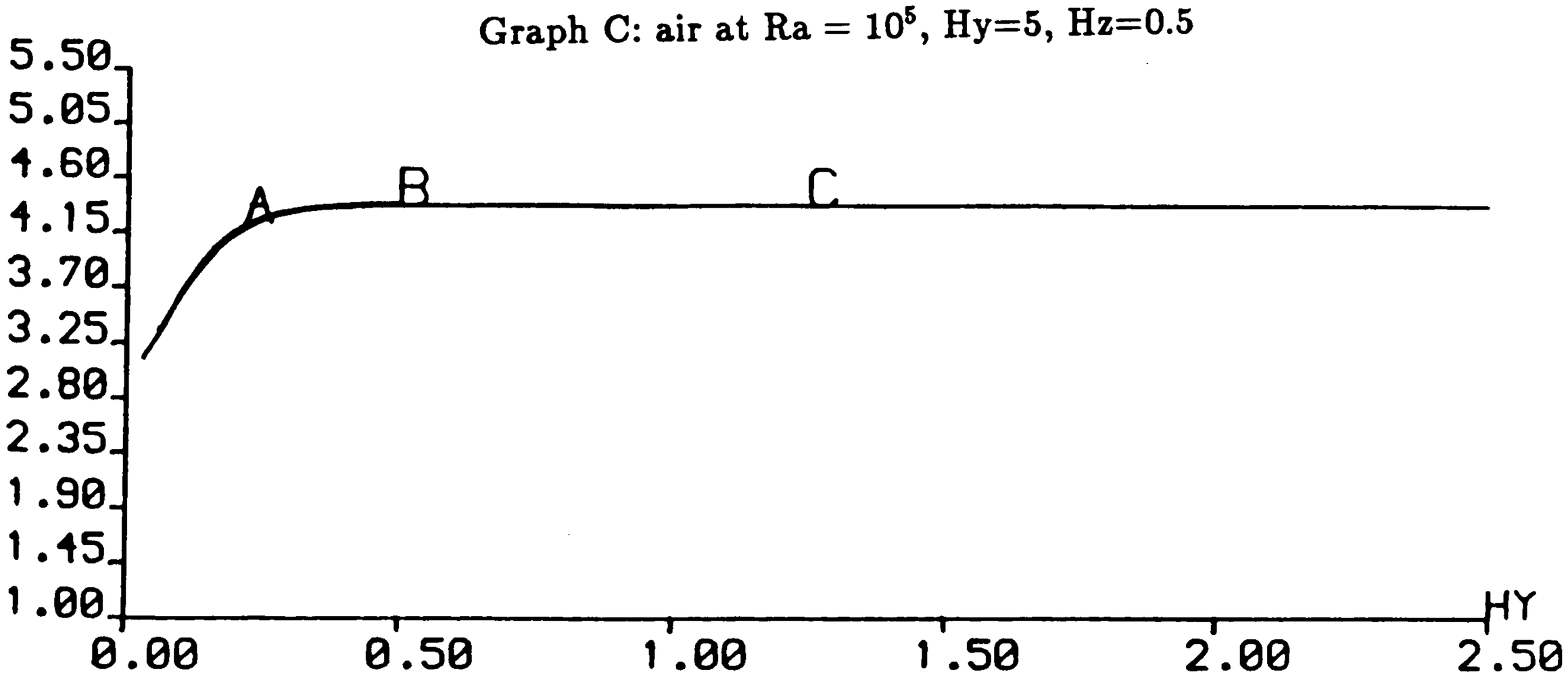

Figure 6.176 Nusselt number along the hot wall

6.7.6 Summary for the shallow cavity, Hz=0.5

The results obtained with this study for the shallow cross-section window cavity cannot be compared against other work as these appear to be the first to emerge.

The fluid flow structure for the low Rayleigh number with air and cerrobase in this window cavity result in a single forward recirculating roll. The particle paths traced lie on an elliptic toroidal shaped surface. The elliptic nature of the roll is due to the shape of the cavity. The forward roll is generated in the same manner as described for the square cross-section window cavity. The characteristics of the square cross-section window cavity flow also exist here. These being: the magnitude of the cross-sectional velocity being greater near the symmetry plane than near the end wall; the thermal solution being more convective near the symmetry plane than near the end wall; the axial flow being strongest in the vicinity of the end wall and weakest near the symmetry plane, and the strong axial temperature gradients generating vorticity sources that augment the inertial end effect creating undulations in the particle paths.

The thermal end effect for air and cerrobase appears to be of equal magnitude, for air maximum $\partial\theta/\partial y$ is 0.019, 0.017 and 0.017 for Hy=1, 2 and 5 respectively, and for cerrobase maximum $\partial\theta/\partial y$ is 0.018, 0.016 and 0.016 for Hy=1, 2 and 5 respectively. Values of the ratio R, which is the ratio of the axial flow to the cross-sectional flow are generally larger for cerrobase than air. Hence the overall end effect is greater for cerrobase than air as the thermal end effects are similar for air and cerrobase. This implies that the inertial end effect is greater for cerrobase than air.

Two-dimensional flow exists with air at $Ra = 10^3$ for $Hy \geq 2.5$, with cerrobase at $Ra = 10^3$ for $Hy \geq 2.5$ and with cerrobase at $Ra = 5 \times 10^3$ for $Hy \geq 3.5$. As the two-dimensional flow does not exist with cerrobase for $Hy \leq 5.0$ in the square cross-section window cavity it can be concluded that the end wall effect and hence the axial flow, is comparatively weaker in the shallow cavity. This is also the case with air.

The three-dimensional flow has less influence on the low Rayleigh number flow than the higher number flow. This is supported by the fact that a shorter window cavity is required for two-dimensional flow to exist at the lower Rayleigh number flow, such as cerrobase at $Ra = 10^3$, than at the higher Rayleigh number flow, such as cerrobase at $Ra = 5 \times 10^3$. The ratio R contour plots indicate undulations in the boundary layer near the top and bottom boundaries but not at the side boundaries x=0 and x=1. As a result turning points of the particles do not lie on a cylindrical surface as they did

with the square cross-section window cavity. For the particle tracks presented in this section undulations in the tracks do not exist as these tracks lie inbetween the inner core and the boundary layer flow.

FLUID	CAVITY	max $\partial\theta/\partial y$	max ψ_{max}
Air Ra $= 10^3$	1x1x0.5	0.019	0.16
	1x2x0.5	0.017	0.16
	1x5x0.5	0.017	0.16
Air Ra $= 10^5$	1x1x0.5	0.616	5.37
	1x2x0.5	0.511	5.40
	1x5x0.5	0.511	5.40
Cerrobase Ra $= 10^3$	1x1x0.5	0.018	0.15
	1x2x0.5	0.016	0.15
	1x5x0.5	0.016	0.15
Cerrobase Ra $= 5 \times 10^3$	1x1x0.5	0.067	0.59
	1x2x0.5	0.067	0.63
	1x5x0.5	0.067	0.63

Table 6.6: Maximum $\partial\theta/\partial y$ and ψ_{max} for the shallow cavity

The thermal end effect for air at Ra $= 10^3$ in the cavities Hy=1, 2 and 5 are of similar magnitude and similarly for cerrobase at Ra $= 10^3$ and 5×10^3, as can be seen from the above table.

The value of $\partial\theta/\partial y$ does not change sign in the inner core for cerrobase at Ra $= 5 \times 10^3$ which is unlike the situation in the square window cavity. This is due to the weaker axial flow in the shallow window cavity compared to that in the square window cavity. Hence the contribution to the convection of heat by the axial flow in the shallow cavity is less than that by the axial flow in the square window cavity.

The fluid flow structure for the higher Rayleigh number, Ra $= 10^5$, with air in the shallow cavity consists of a single forward roll with two weak secondary rolls embedded within it. The single forward roll completely fills the cavity with length aspect ratio Hy=1 and 2, and is accompanied by a two dimensional flow in the larger cavity Hy=5. Reverse rolls do not exist for the length aspect ratios investigated, which is unlike the case in the square cross-section window cavity. The reason for the secondary flow being weak is because $\partial\theta/\partial x$ has not changed sign in the window cross-section. In the shorter cavity $\partial\theta/\partial y$ does not change sign but it changes sign once in Hy=2 and

twice in Hy=5. The first sign change appears to be associated with the secondary convective effects as in the square window cavity. The second sign change with Hy=5, which occurs where the two-dimensional flow starts, appears to be associated with the two-dimensional flow near the symmetry plane.

For this higher Rayleigh number flow, two-dimensional flow exists for Hy $\geq$ 3. The existence of the axial flow in the shallow cavity is weaker than in the square cross-section window cavity where no two-dimensional flow exists for Hy $\leq$ 5.

The thermal solution for air at Ra = 10^3 and cerrobase Ra = 10^3 and 5×10^3 are very much conduction dominated.

An interesting phenomenon that occurs is that $\partial\theta/\partial y$ for Hy=1 is slightly greater than that for Hy=2 and 5 for all fluids.

The fluid flow characteristics for cerrobase are very different to those of air, as was the case in the square cross-section window cavity. The end wall effect with this shallow cross-section window cavity for the fluids investigated is smaller than that obtained for the same fluids in the square cross-section window cavity.

6.8 Window cavities with a tall cross section, Hz=5.0

For this problem particle paths in the longer length aspect ratio, Hy=5, are not presented due to the user computer memory limit. The contour plots for this height aspect ratio have been scaled down in the z-direction by a fifth.

6.8.1 Results obtained for air with $Ra = 10^3$

The fluid flow behaviour in this tall cavity is described by a single forward recirculating roll which fills the cavity with the length aspect ratios Hy=1, 2 and 5. The flow is illustrated in Figure 6.177 and 6.178 where particle paths are traced in cavities with Hy=1 and 2 respectively and from points A, B and C respectively. Mallinson and de Vahl Davis for air with $Ra = 10^4$ in the cavity Hz=Hy=5.0 found a single forward recirculating roll which filled the half cavity.

Figures 6.179-6.181 are contour plots of the ratio R at planes A, B and C respectively for Hy=1.0. The plots at planes A and B reveal strong axial flow in the upper and lower boundaries of the cavity. They lead one to believe that two inner cores exist representing two cells one on top of another in a column. This is not the case as can be seen from the particle paths presented. The strong axial flow near the top and bottom of the cavity is a result of greater viscous drag at the top and bottom walls producing comparatively greater reduction of convection at the top and bottom of the cavity than in the centre. Thus the vorticity generated by the axial temperature gradients is stronger at the top and bottom walls than in the centre.

Figures 6.182-6.184 are contour plots of the ratio R at planes A, B and C for Hy=2. The characteristics of the plots are very similar to those described above for Hy=1.

Figures 6.185-6.187 are isotherms at planes A, B and C respectively for Hy=1.0. Plots at planes A, B and C show convection of heat taking place near the cavity boundaries whilst the flow in the centre of the cavity is relatively conductive.

The features of the thermal flow for Hy=2 are similar to those obtained with Hy=1.0 and have not been presented.

Figures 6.188-6.190 are the contour plots of R for Hy=5.0 at planes A, B and C respectively. They show the strong axial flow at the top and bottom of the cavity

amalgamating as Hy increases. This is because there is no reduction of convection far from the end wall and thus strong vorticities are not generated near the the top and bottom walls. Figure 6.191-192 are isotherms at planes A, B and C respectively and show the region of conduction of heat in the centre of the cavity.

Figures 6.194-6.196 are a contour plot of $\partial\theta/\partial y$ at the plane x=0.5 for Hy=1, 2 and 5 respectively. Positive $\partial\theta/\partial y$ dominate the upper half and negative $\partial\theta/\partial y$ dominate the lower half of the cavity, generating vorticity sources that augment the inertial end effect. Values of $\partial\theta/\partial y$ in the centre are much smaller than near the top and bottom walls.

Figure 6.197 is a plot of the streamlines near the symmetry plane for Hy=5.0 and exhibits primary flow.

Figure 6.198 is the axial-velocity profile along the centre line of the cavity for Hy=1, 2 and 5 and shows the axial flow being restricted in the shorter cavities. Two dimensional flow does not exist for Hy $\leq$ 5.0. This indicates that the strength of the end wall effect with the tall cross-section window cavity for this fluid is greater than that obtained with the square or the shallow cross-section window cavities for the same fluid.

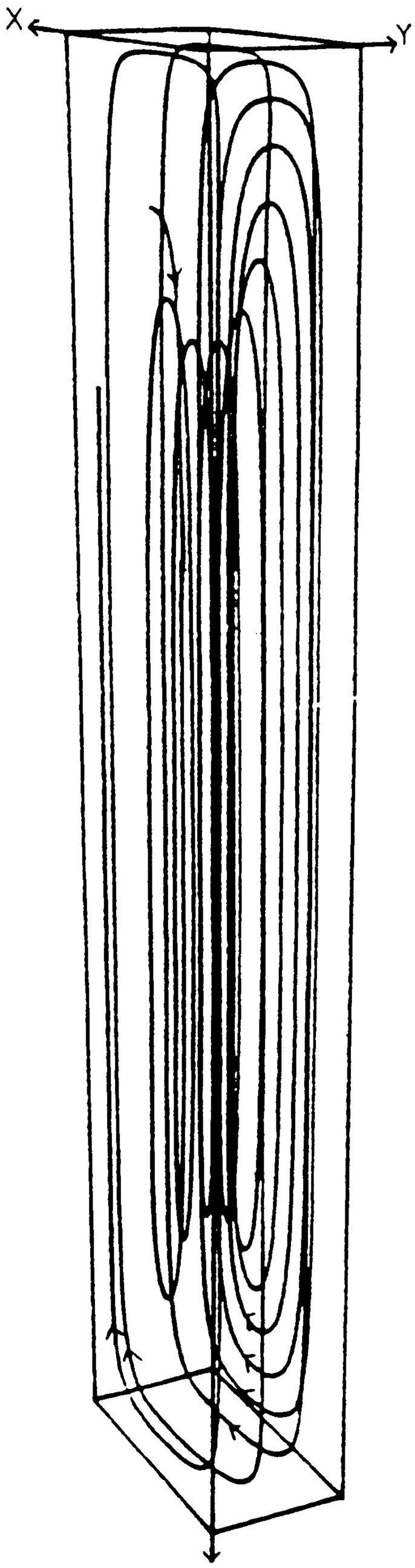

Figure 6.177 Particle track for air at
$Ra = 10^3$, cavity (1,1,5) grid = 16x16x40

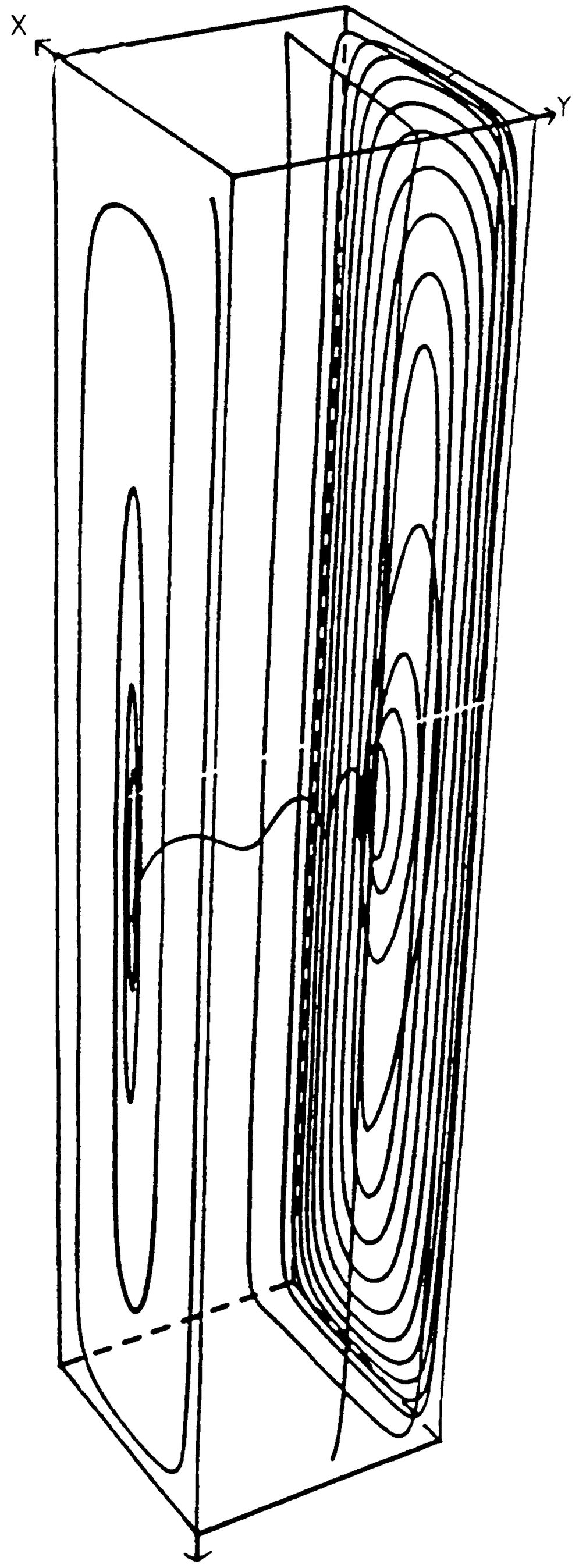

Figure 6.178 Particle track for air at
$Ra = 10^3$, cavity (1,2,5) grid = 16x16x40

Fluid = air, Ra = 10^3, Hy=1, Hz=5, grid=16x16x40

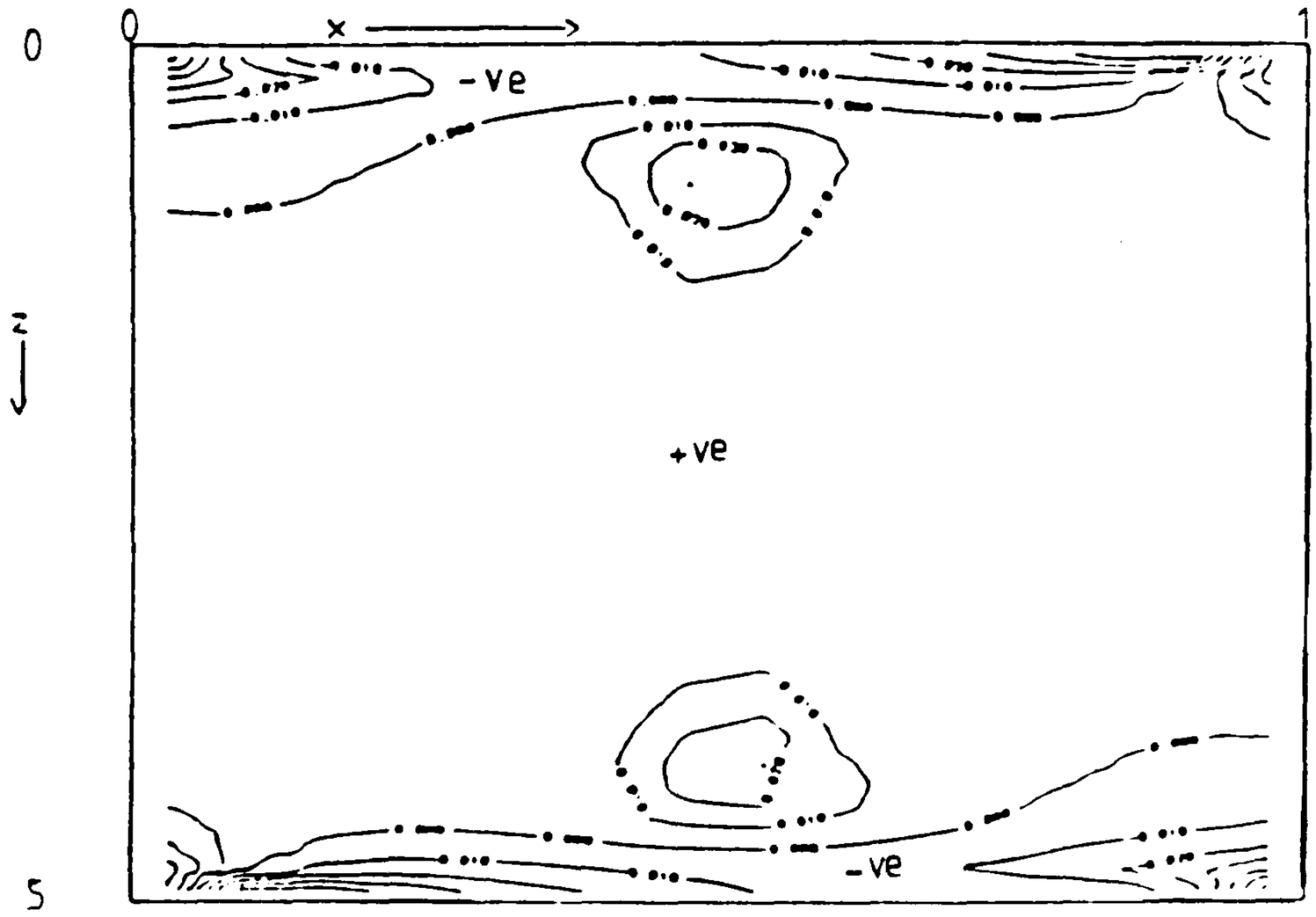

Figure 6.179 Contour plot of ratio R at plane A, near the end wall

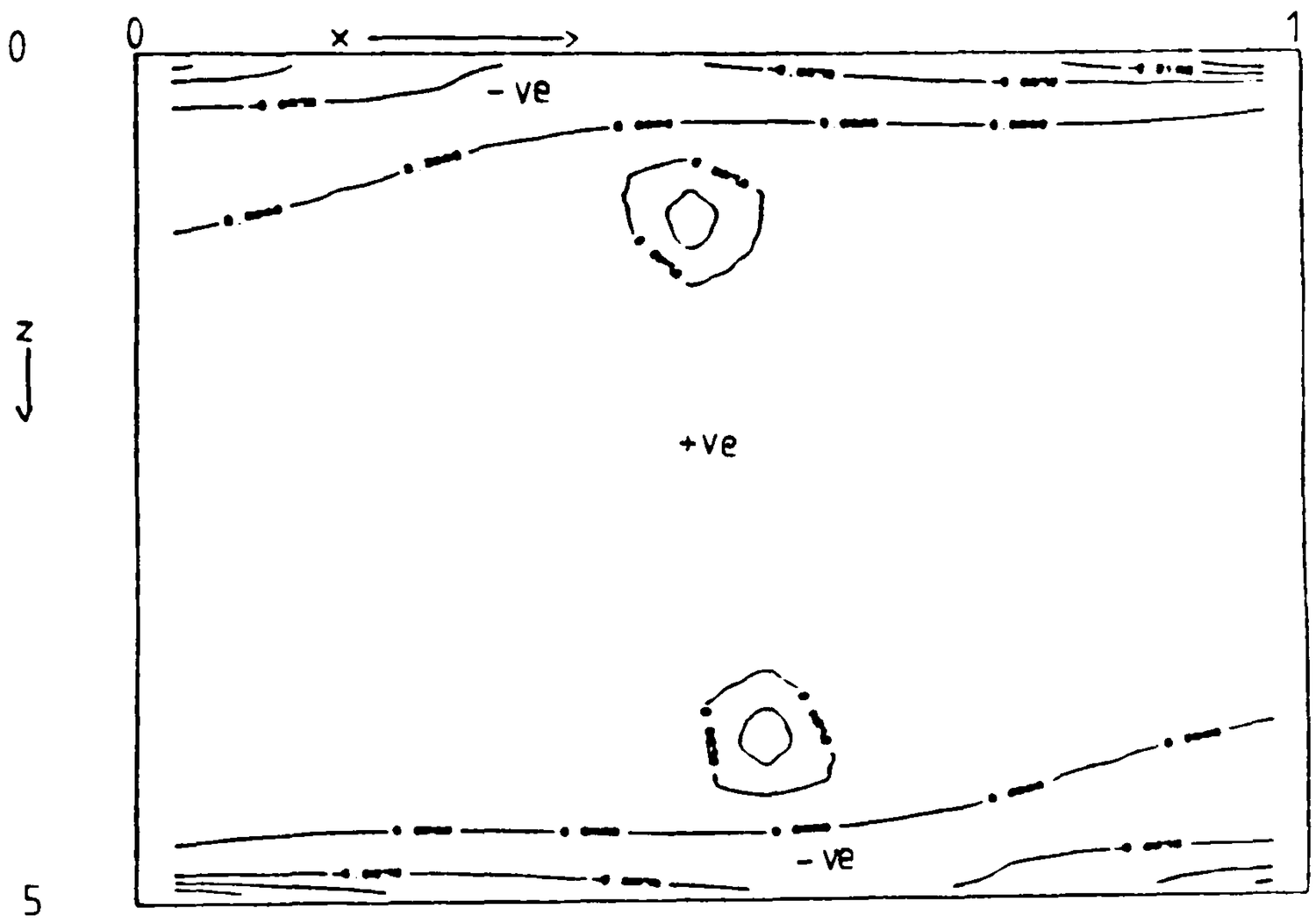

Figure 6.180 Contour plot of ratio R at plane B, near the symmetry plane

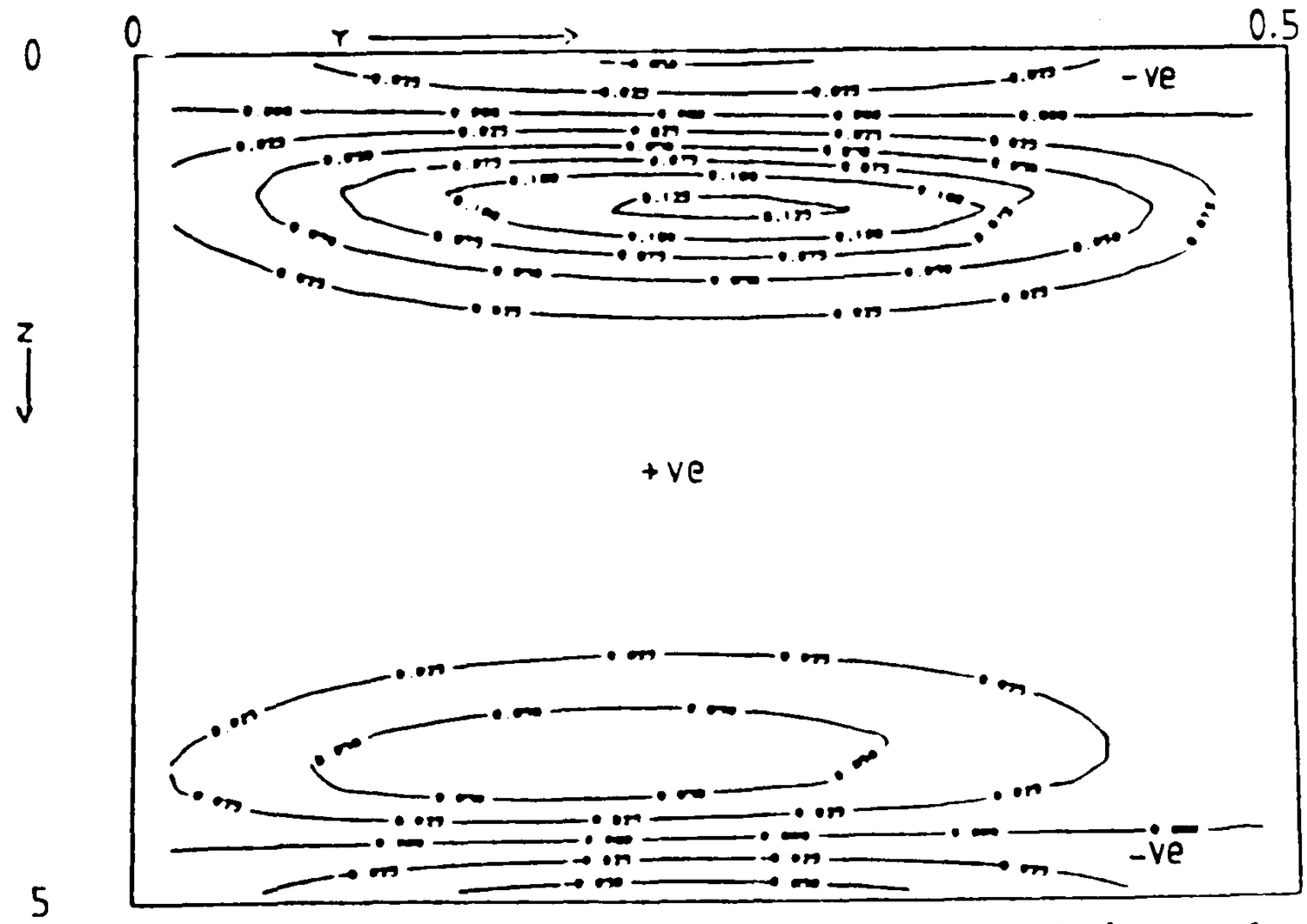

Figure 6.181 Contour plot of ratio R at plane C $(0.5 - hx/2, y, z)$

Fluid = air, Ra = 10^3, Hy=2, Hz=5, grid=16x16x40

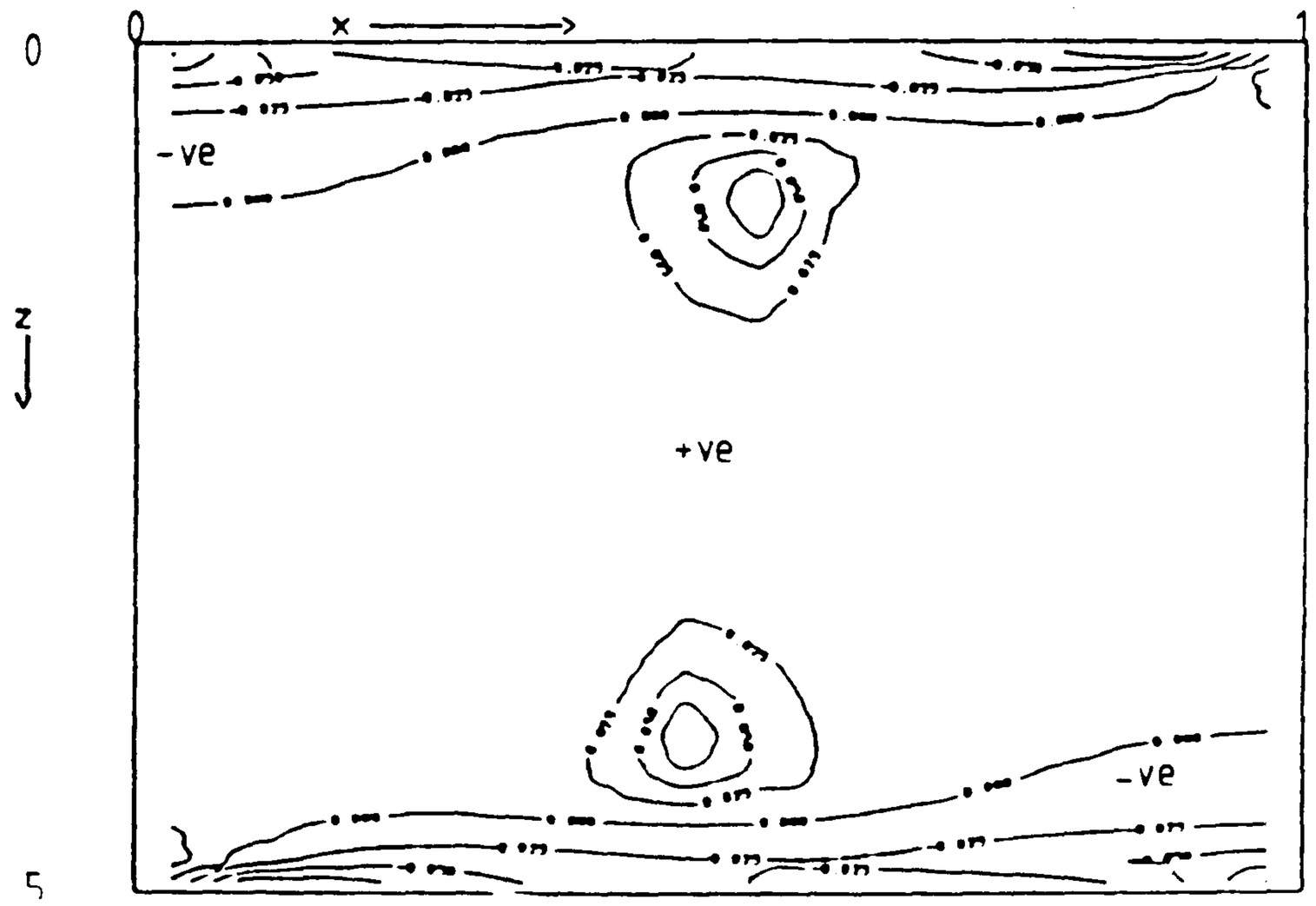

Figure 6.182 Contour plot of ratio R at plane A, near the end wall

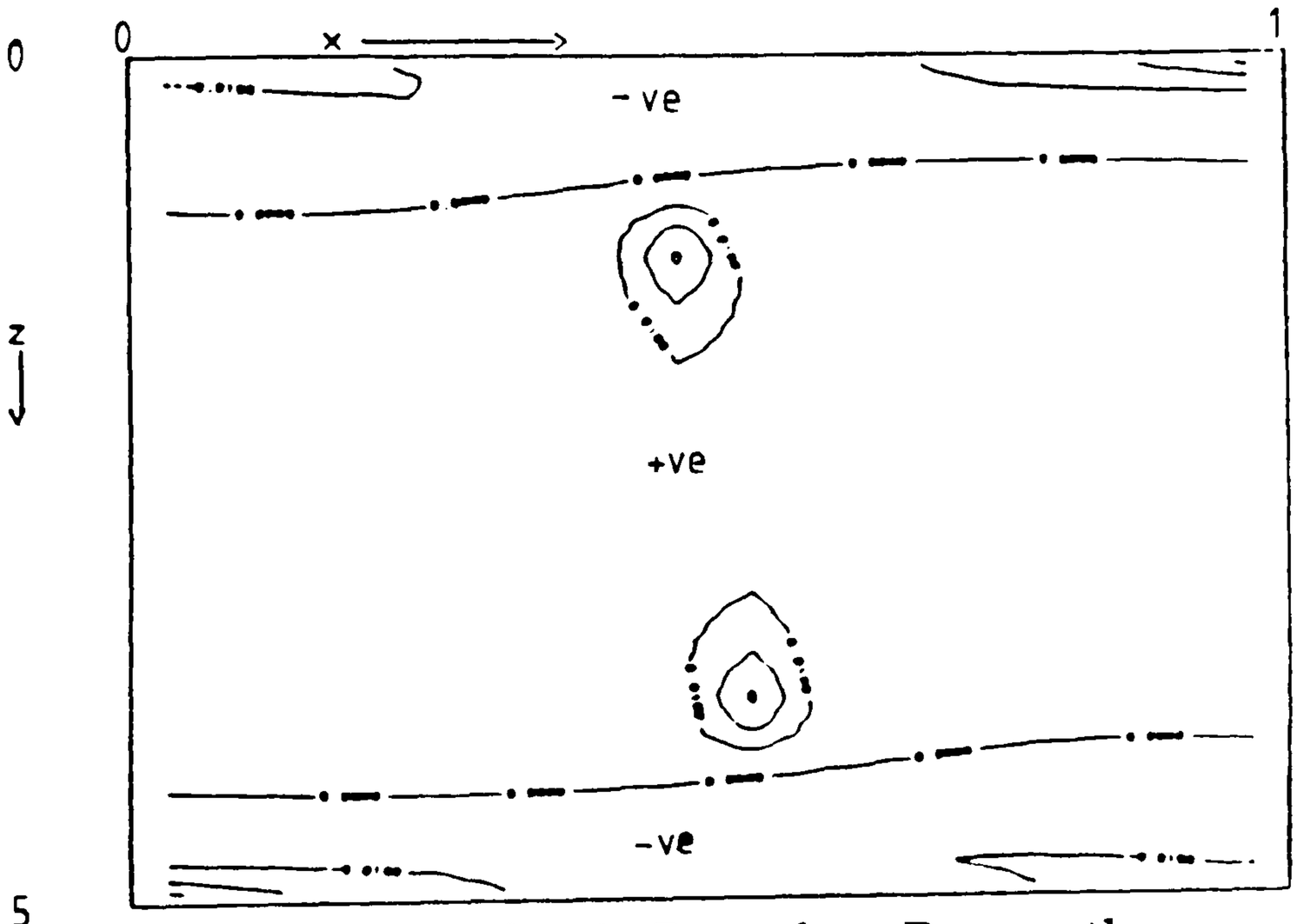

Figure 6.183 Contour plot of ratio R at plane B, near the symmetry plane

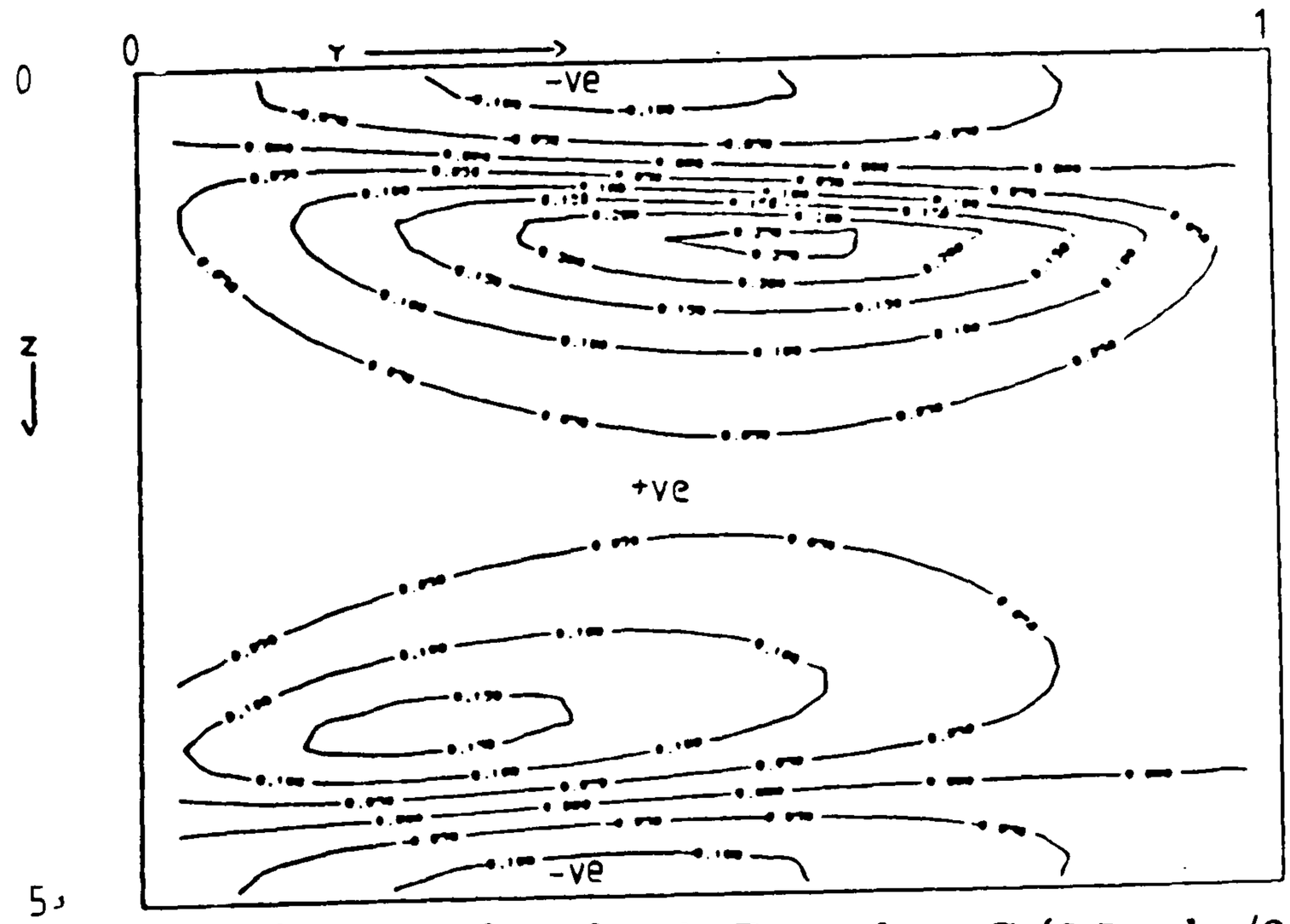

Figure 6.184 Contour plot of ratio R at plane C $(0.5 - hx/2, y, z)$

Fluid = air, Ra = 10^3, Hy=1, Hz=5, grid=16x16x40

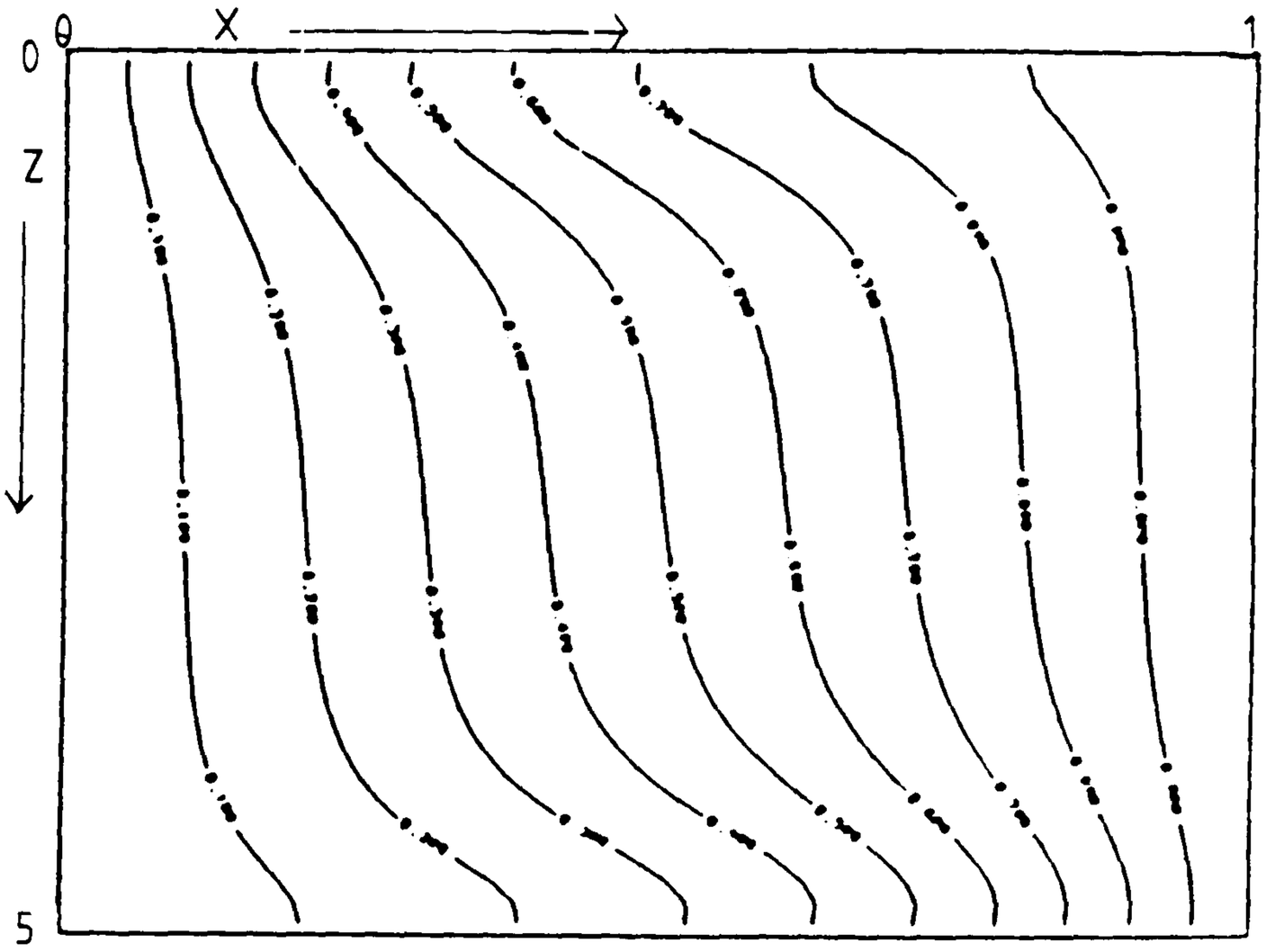

Figure 6.185 Isotherms at plane A, near the end wall

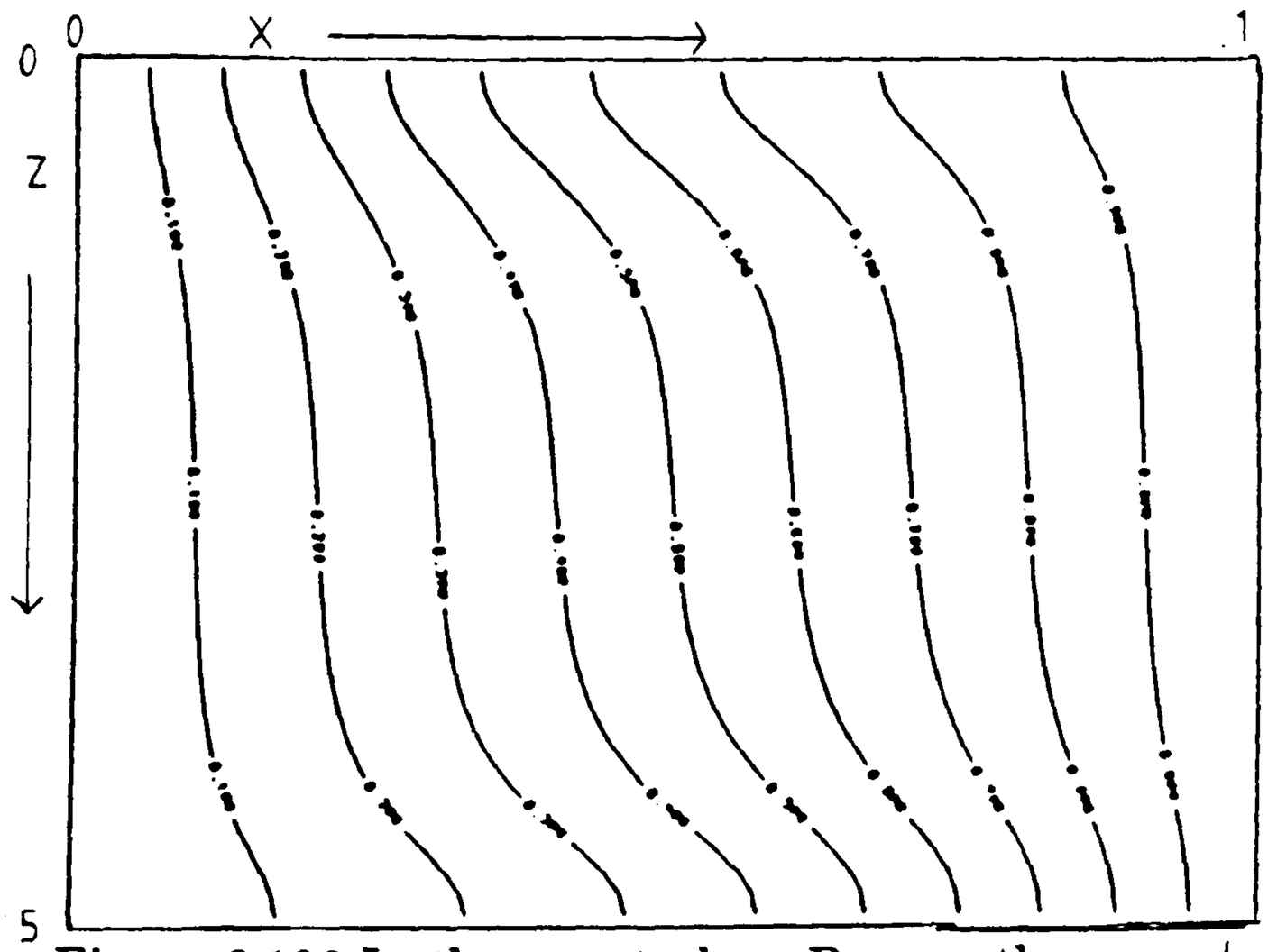

Figure 6.186 Isotherms at plane B, near the symmetry plane

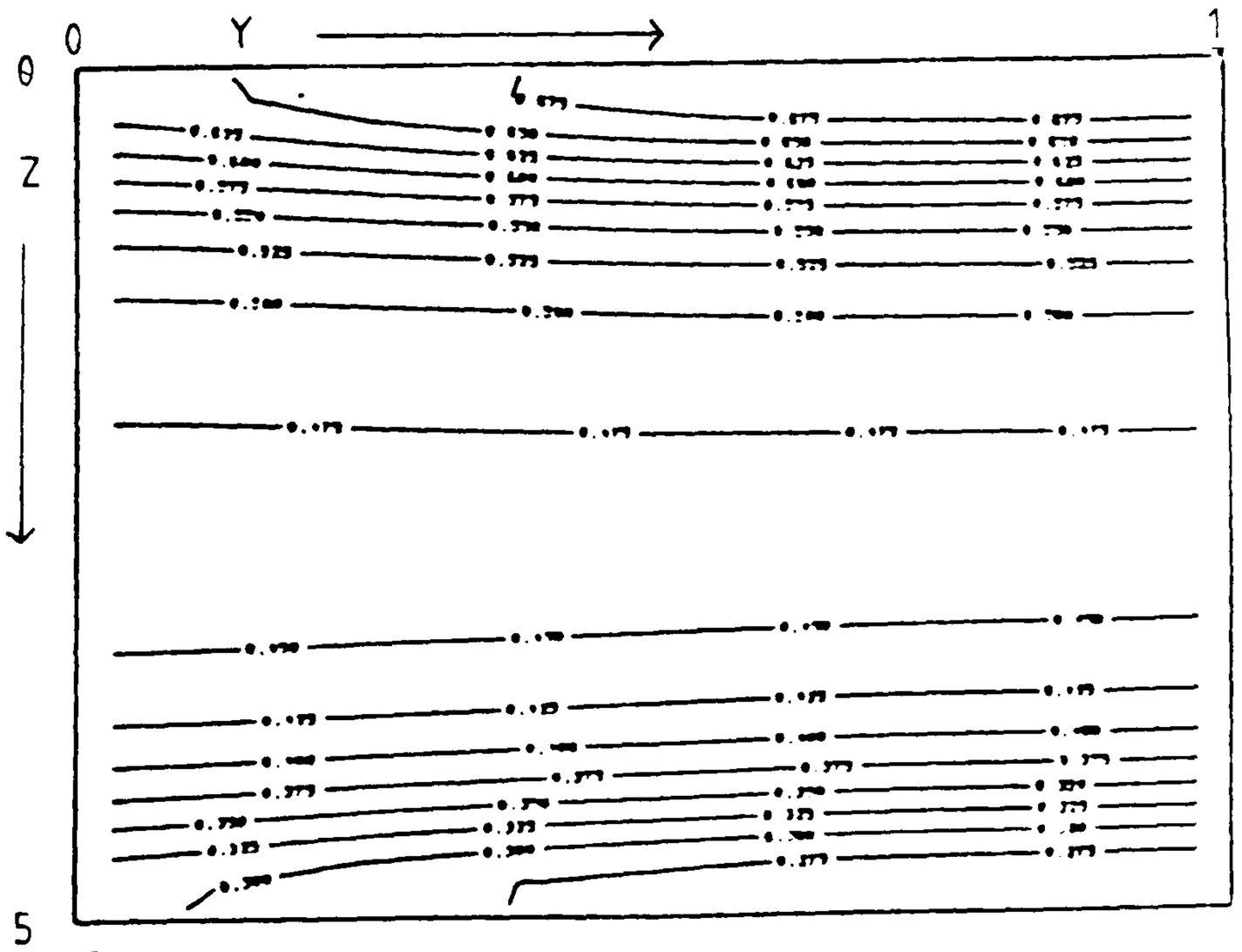

Figure 6.187 Isotherms at plane C, $(0.5 - hx/2, y, z)$

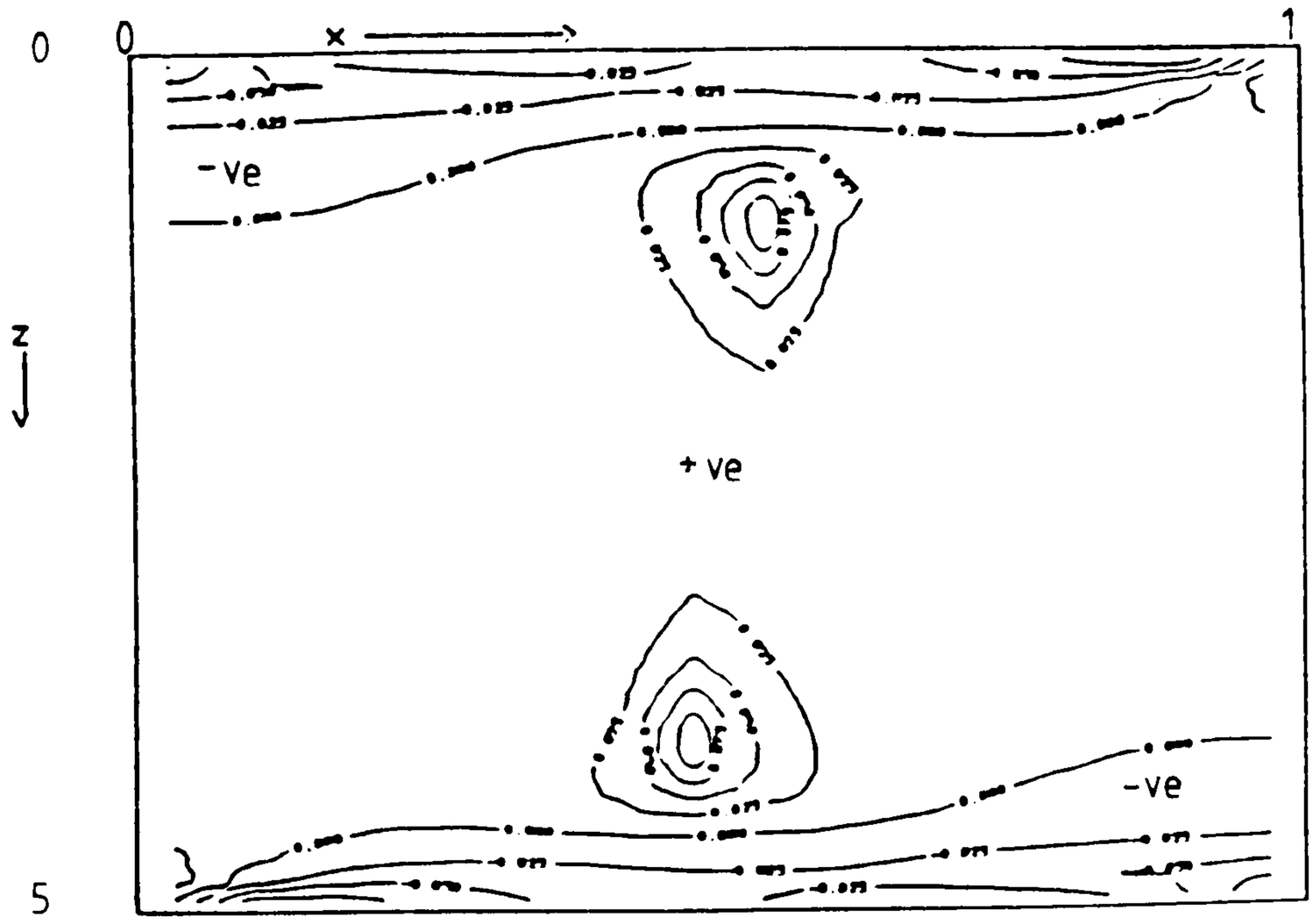

Figure 6.188 Contour plot of ratio R at plane A, near the end wall

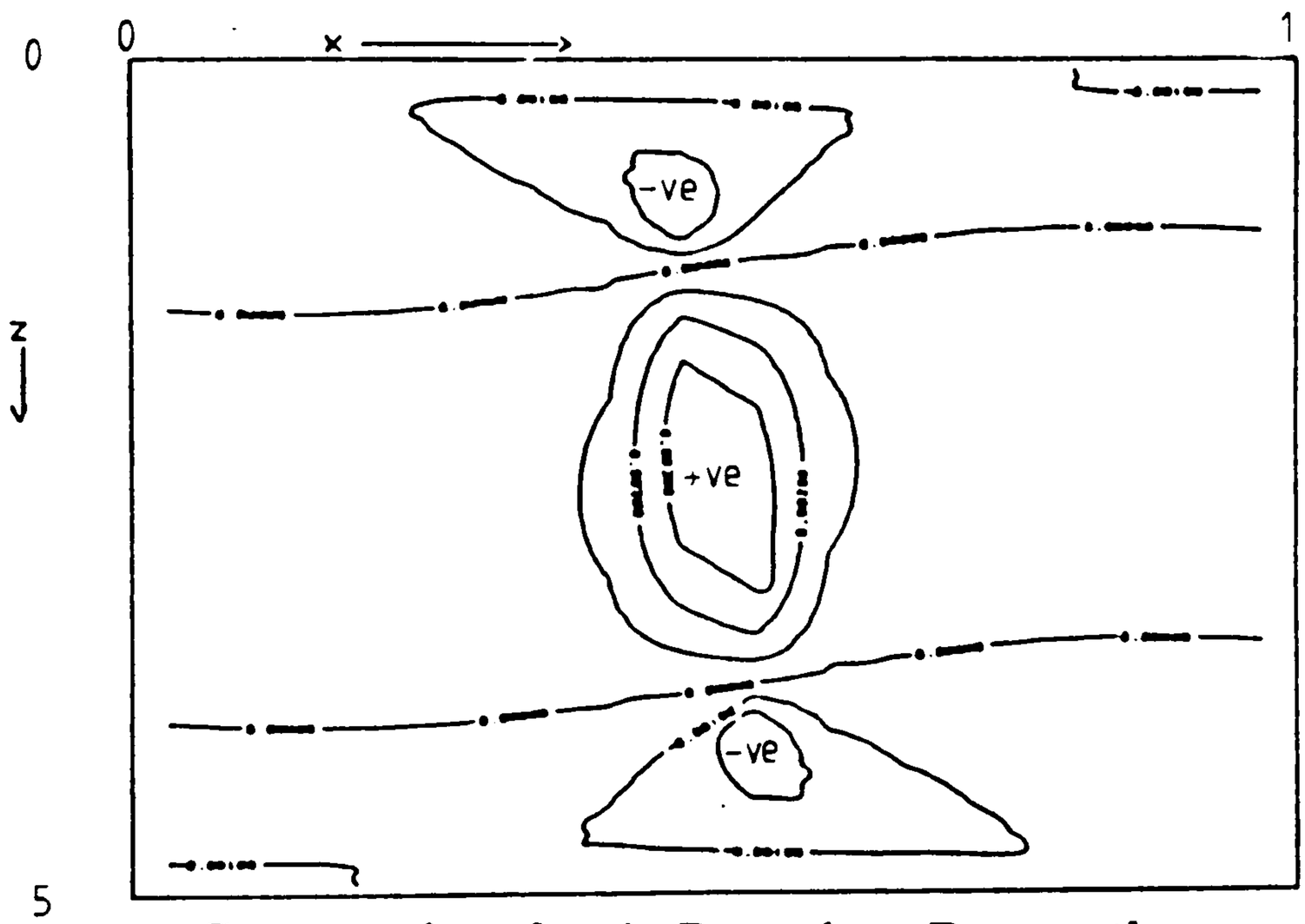

Figure 6.189 Contour plot of ratio R at plane B, near the symmetry plane

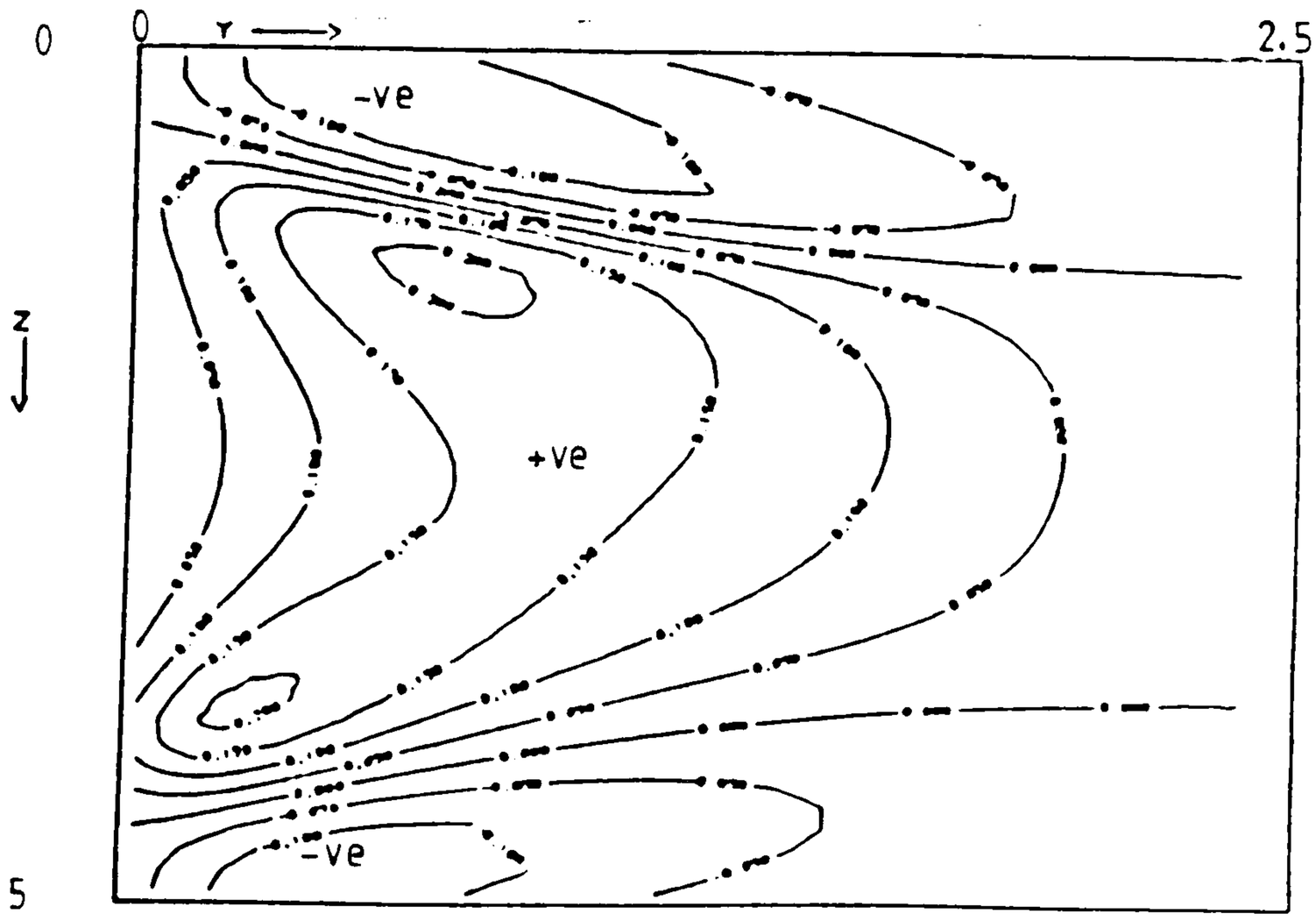

Figure 6.190 Contour plot of ratio R at plane C $(0.5 - hx/2, y, z)$

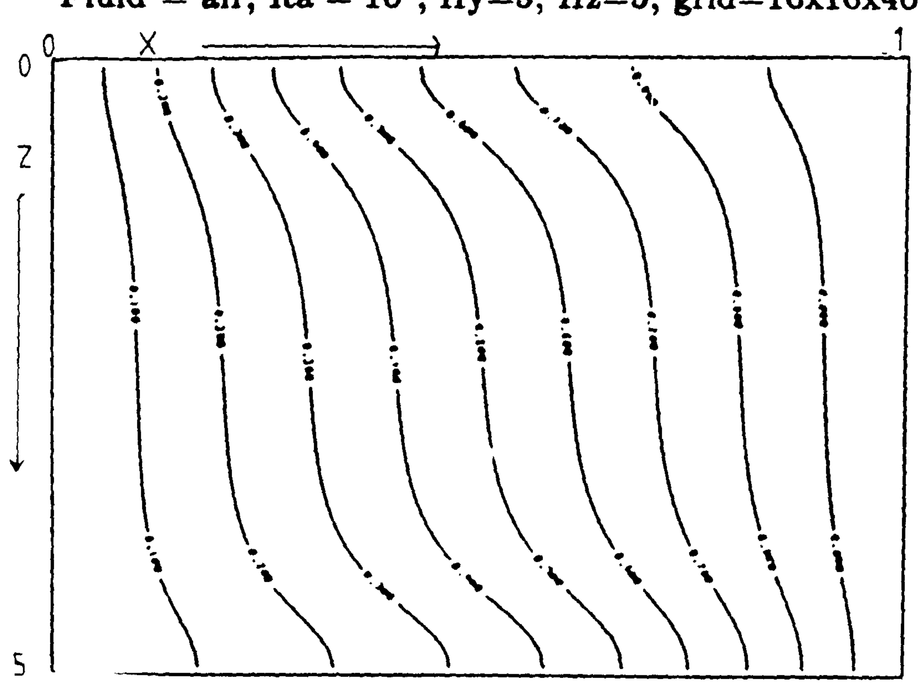

Figure 6.191 Isotherms at plane A, near the end wall

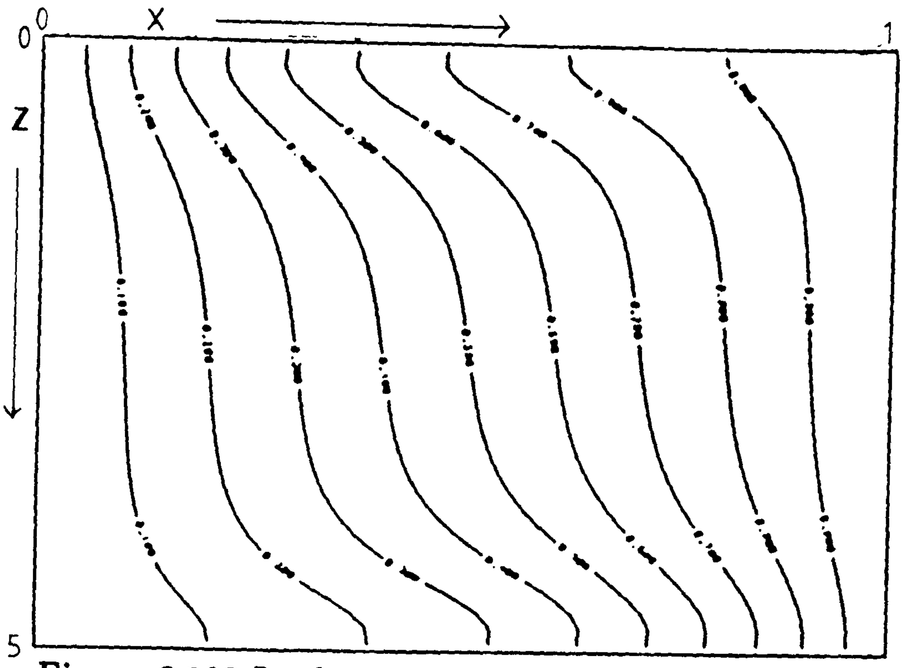

Figure 6.192 Isotherms at plane B, near the symmetry plane

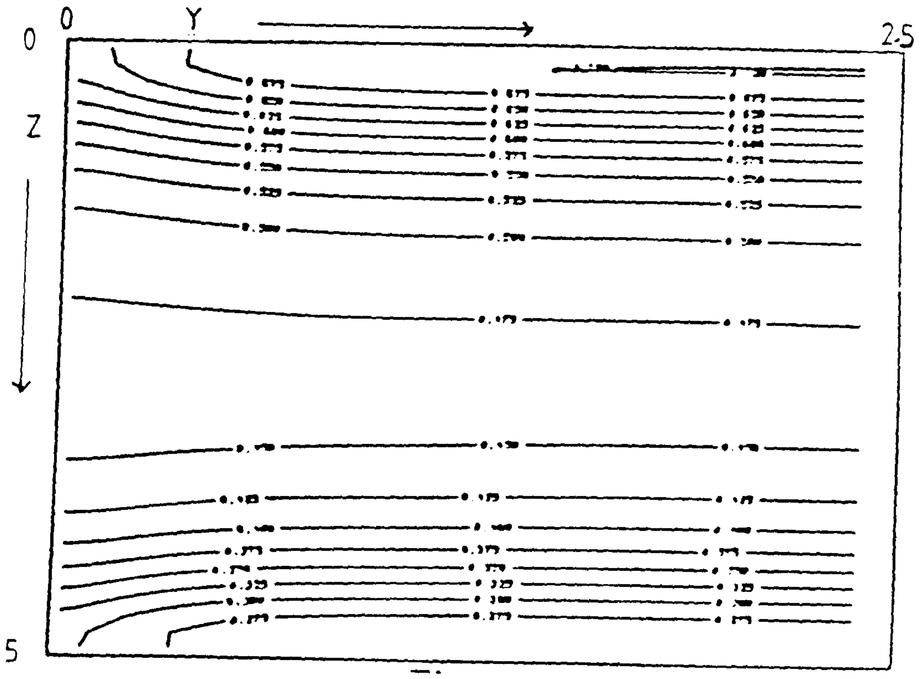

Figure 6.193 Isotherms at plane C, $(0.5 - hx/2, y, z)$

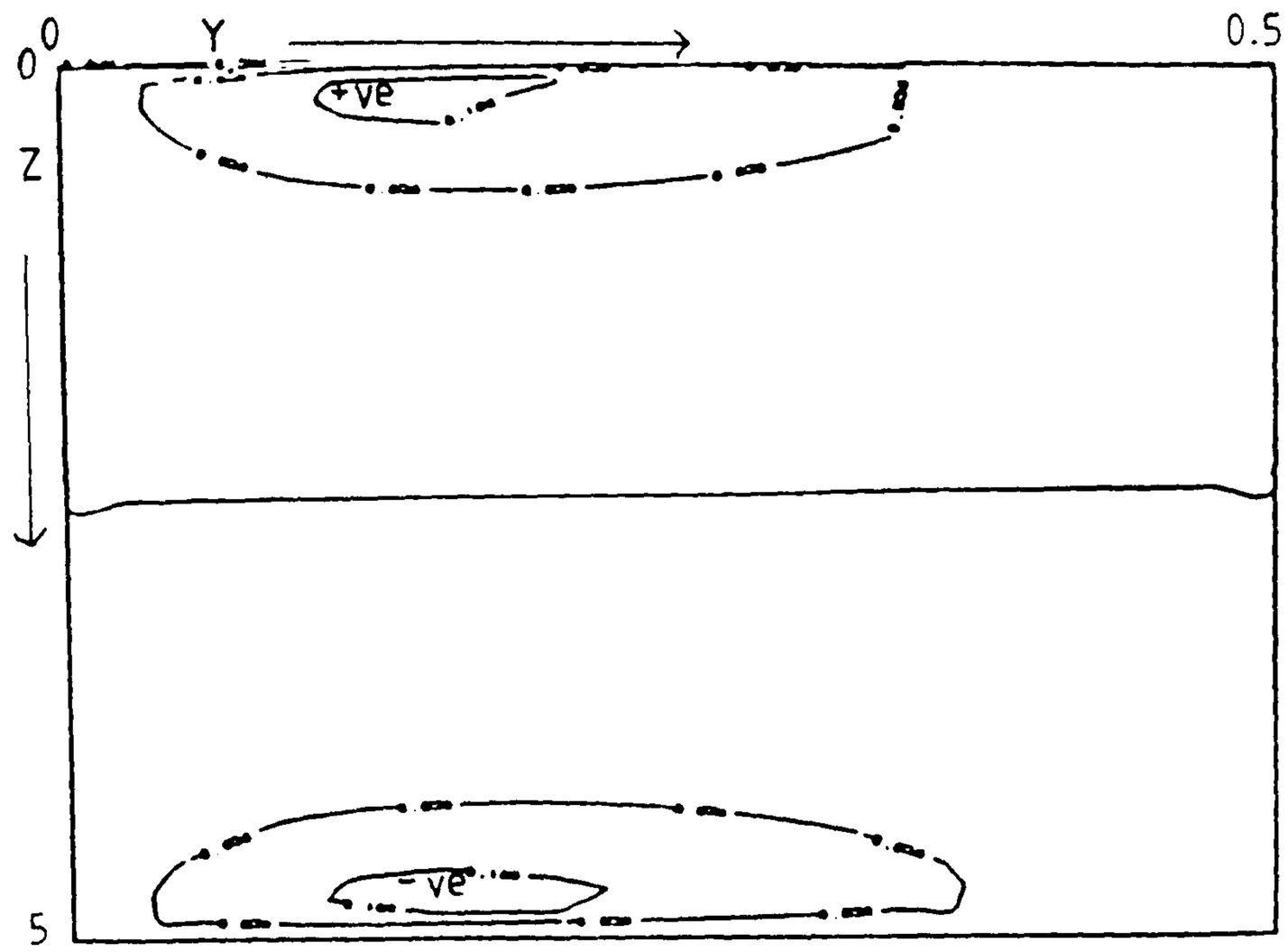

Figure 6.194 $\partial\theta/\partial y$ at plane C, $(0.5 - hx/2, y, z)$, Hy=1

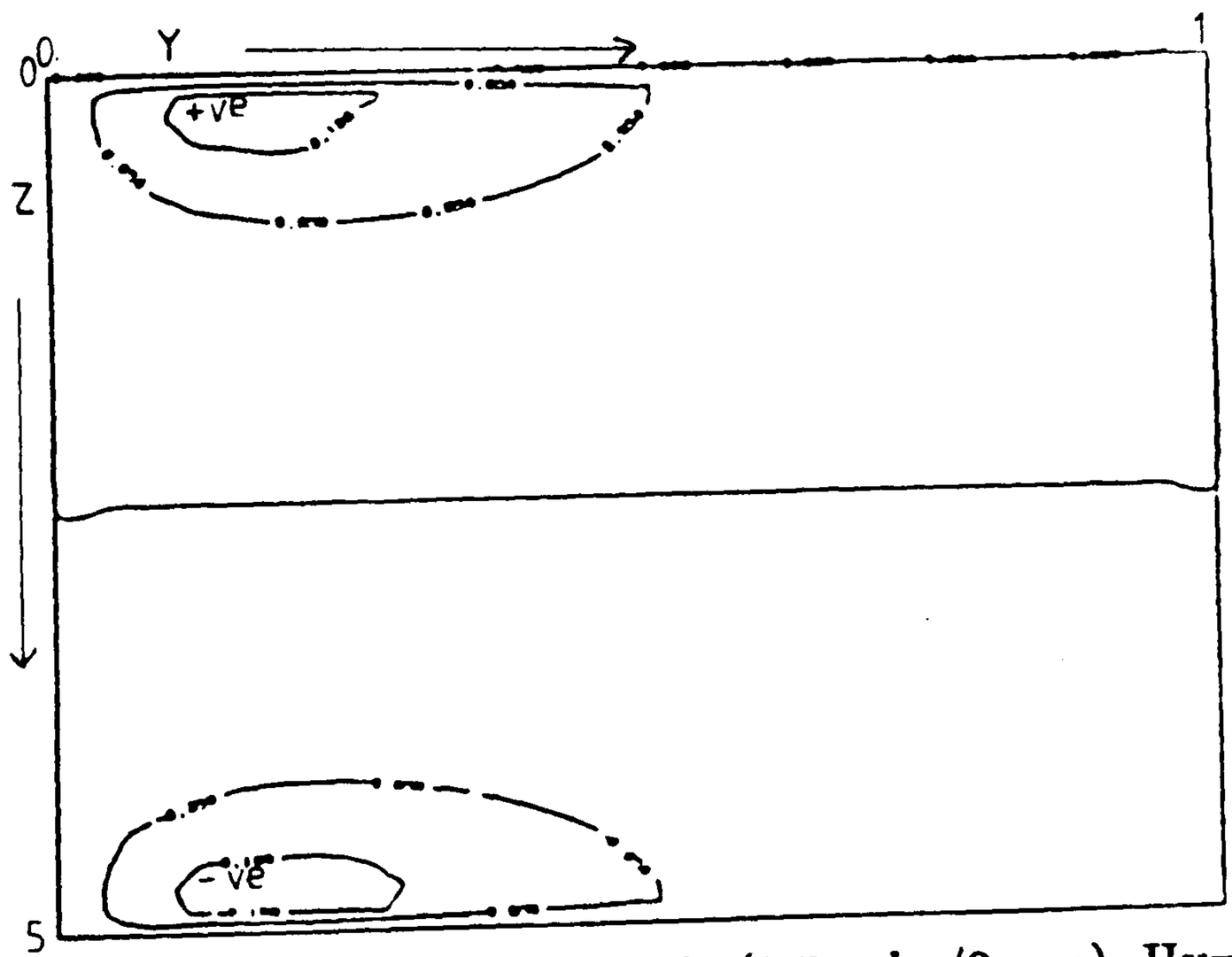

Figure 6.195 $\partial\theta/\partial y$ at plane C, $(0.5 - hx/2, y, z)$, Hy=2

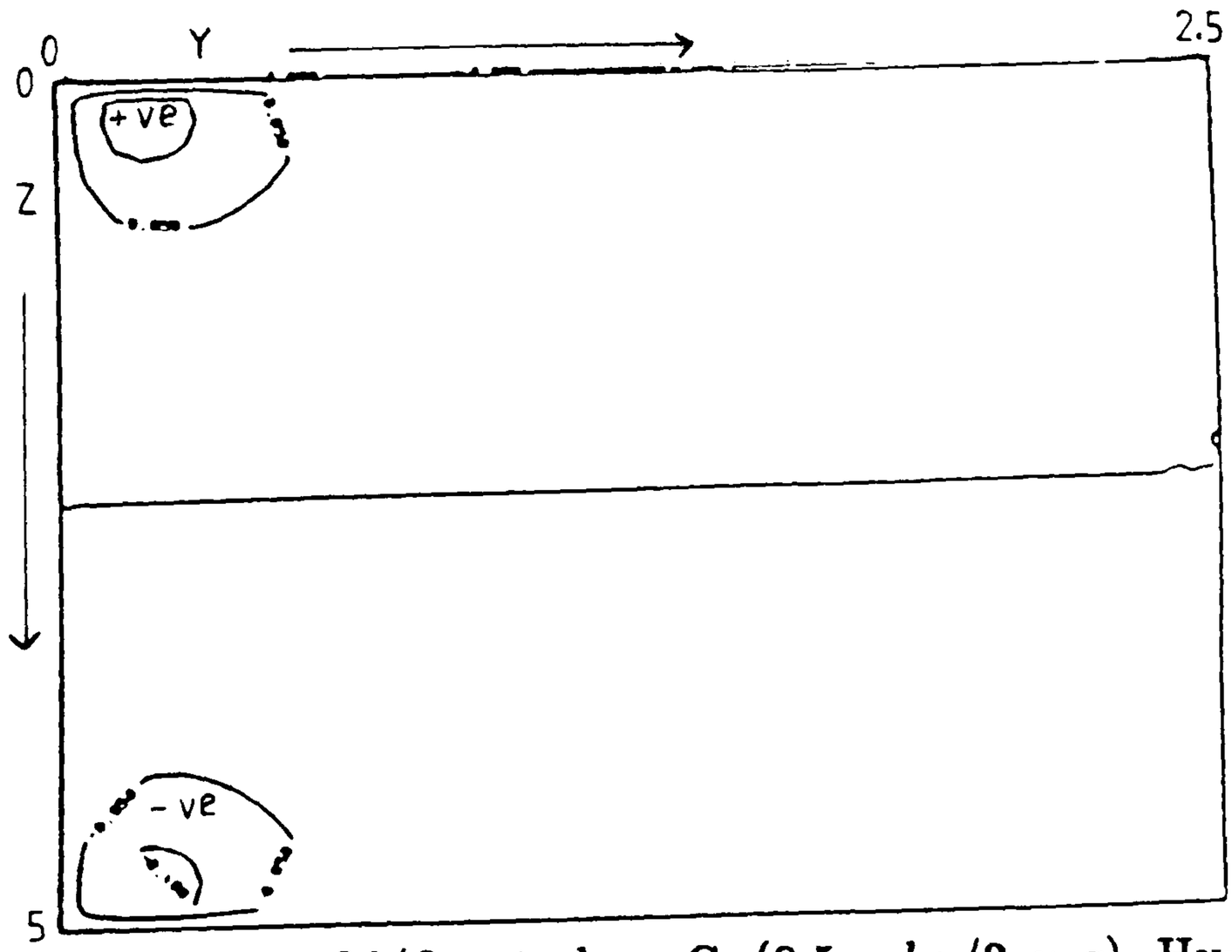

Figure 6.196 $\partial\theta/\partial y$ at plane C, $(0.5 - hx/2, y, z)$, Hy=5

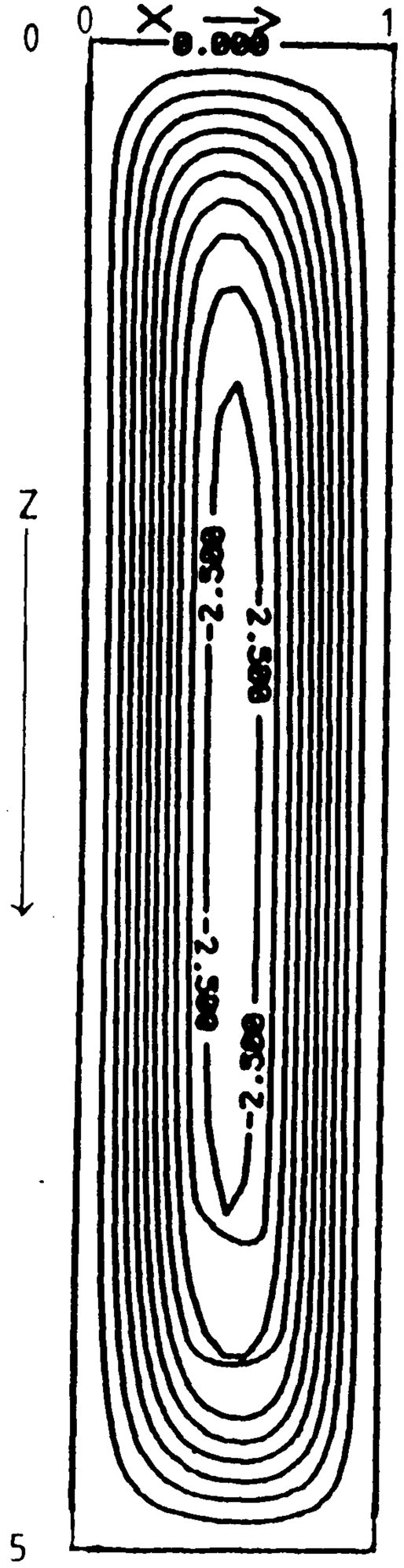

Figure 6.197 Streamlines, Hy=5

Graph A: air at Ra = 10^3, Hy=1, Hz=5

Graph B: air at Ra = 10^3, Hy=2, Hz=5

Graph C: air at Ra = 10^3, Hy=5, Hz=5

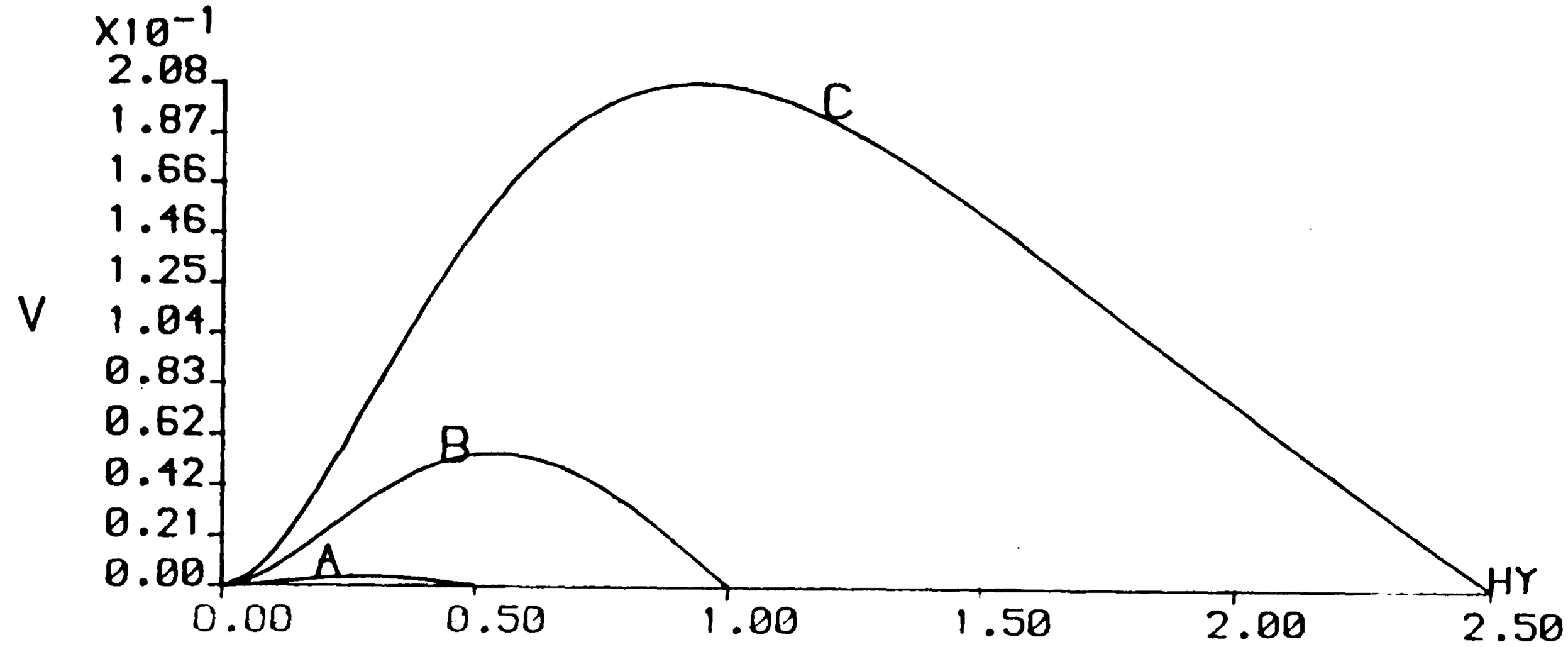

Figure 6.198 Axial-velocity along $(0.5, y, 2.5)$

6.8.2 Results obtained for air with Ra = 10^5

The flow in the two-dimensional problem for this higher height aspect ratio (Hz=5) at this high Rayleigh number results in a multiple cellular fluid flow structure.

The results for this case indicate that for cavities with length aspect ratio Hy=1.0 and 2.0 a single forward recirculating roll fills the cavity. Secondary flow in the cross-section does not occur for this taller height aspect ratio cavity. Figure 6.199 is that of a particle path traced from $(0.5, 0.01, 2.5)$ with Hy=1.0. The path exhibits a single forward roll which occupies the half cavity. Figure 6.200 is that of a particle path traced from $(0.1, 0.01, 0.1)$ with Hy=2.0. The behaviour of the particle is of a very different nature to those encountered in the shallow or the square cross sectional cavities. The path uncoils near the symmetry plane, but, unlike the shallow and square cross-section window cavity where the particle returns via the boundary layer flow, here it returns in the central region traversing towards the end wall before reaching the boundary layer. The particle path having travelled some distance towards the end wall then changes its axial direction and starts to traverse towards the symmetry plane still uncoiling. Near the symmetry plane the particle finally reaches the boundaries and returns to the end wall via the boundary layer. The return flow has not been shown in the particle track figures in order not to obscure the above described phenomenon.

Figure 6.201 and 6.202 are contour plots of the ratio R at planes A and B respectively for Hy=1, while Figures 6.203 and 6.204 are contour plots of R on either side of the plane x=0.5 for Hy=1. In Figure 6.201 four regions of strong axial flow can be seen. The outermost two regions, near the the upper and lower boundaries, are a result of strong vorticity generated by strong $\partial\theta/\partial y$ as in the case Ra = 10^3. The innermost two regions of axial flow are a result of a change in sign of $\partial\theta/\partial y$, see Figure 6.220. Contour plots of R near the the symmetry plane only show the two inner regions of strong axial flow due to $\partial\theta/\partial x$. The two outer regions have diminished due to there being no or very little reduction in convection near the upper and lower boundaries far from the end wall. Figures 6.205 - 6.207 are isotherm plots at planes A, B and C respectively for Hy=1.

Figures 6.208-6.210 are contour plots of R at planes A, B and C respectively for Hy=2.0. The plots show the four regions of strong axial flow near the end wall. Figure 6.210 confirms the behaviour of the particle as described above for Figure 6.200. Figures 6.211-213 are isotherms at planes A, B and C respectively for Hy=2.

For the cavity length aspect ratio Hy=5.0, reverse roll does exist. Figures 6.214-

6.216 are contour plots of R at planes A, B and C respectively for Hy=5. Figure 6.214 shows four regions of strong axial flow which are part of the forward roll. The inner regions are due to changes in the sign of $\partial\theta/\partial x$ and the outer due to vorticity generated as a result of reduction in convection at the upper and lower walls of the cavity. Figure 6.215 shows the two strong axial regions which are a part of the reverse roll resulting from the change in sign of $\partial\theta/\partial x$. Figure 6.216 shows clearly the forward and reverse roll that occupy the cavity. Figure 6.217-6.219 are isotherms at planes A, B and C respectively for Hy=5.

Figure 6.220 is a contour plot of $\partial\theta/\partial y$ at the plane x=0.5 for Hy=1. Note that with this higher Rayleigh number $\partial\theta/\partial y$ the upper half of the cavity is dominated by negative values and the lower half by positive values. This change in the behaviour of $\partial\theta/\partial y$ appears to be the result of the change in sign of $\partial\theta/\partial x$. Figure 6.221 is a contour plot of $\partial\theta/\partial y$ at the plane x=0.5 for Hy=2. The plot shows two sign changes of $\partial\theta/\partial y$ in the upper and lower halves of the cavity with negative $\partial\theta/\partial y$ dominating the upper half and positive $\partial\theta/\partial y$ dominating the lower half. The first sign change of $\partial\theta/\partial y$ near the upper and lower boundaries at the end wall appears to be associated with the convection of heat from the strong return flow. The second sign change occurs along the centre line near the symmetry plane and appears to be associated with the change in sign of $\partial\theta/\partial x$. Figure 6.222 is a contour plot of $\partial\theta/\partial y$ at the plane x=0.5 for Hy=5. Three sign changes of $\partial\theta/\partial y$ occur. The first two sign changes are as described above, while the third sign change appears to be related to the reverse flow.

Figure 6.223 is a plot of the streamlines near the symmetry plane which exhibits primary flow recirculation and not multicellular flow for Hy=5.

Figure 6.224 is the axial-velocity profile along the centre line for Hy=1, 2 and 5. The plot shows that the flow is restricted in the shorter cavity, Hy=1.0. The forward roll obtained with Hy=5.0 does not extend, along the axial direction, as far as that obtained with Hy=2.0. Reverse roll exists with Hy=5.0.

Figure 6.225 is the axial-velocity profile along the centre line for Hy=2.0, 5.0 and 10.0. Note the extra results for Hy=10.0 have been calculated to further confirm and check the behaviour of the forward roll in coexistence with a reverse roll. The output shows that reverse roll exists for Hy $\geq$ 5.0. The forward roll obtained with Hy=10.0 does not extend as far as that obtained with Hy=5.0. This appears to be a result of the strong axial temperature gradients which generate vorticity that acts against the

forward roll, thus restricting it.

Mallinson and de Vahl Davis for Pr=1 with Ra=3x10^4 found the axial flow to decompose into two forward and one reverse rolls in the half cavity of Hy=Hz=5. The reverse roll separating the two forward rolls and the forward roll next to the end wall being by far the strongest. They explain that the confinement of the forward roll near the end wall is due to negative $\partial\theta/\partial x$ in the centre of cavity resulting in positive $\partial\theta/\partial y$ dominating the lower half and negative $\partial\theta/\partial y$ dominating the upper half which generate vorticity that opposes the inertial end effect.

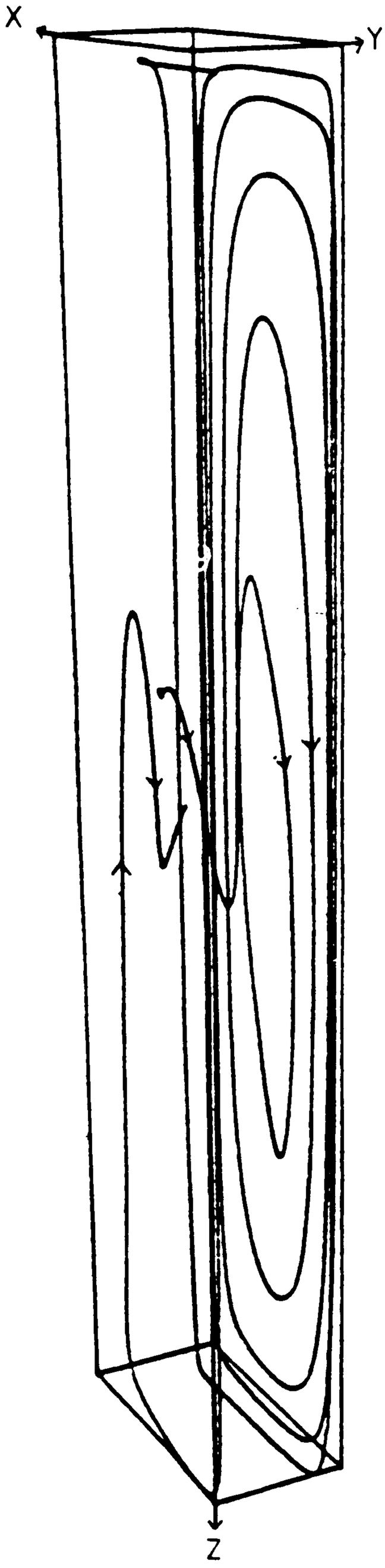

Figure 6.199 Particle track
for air at Ra = 10^5, cavity (1,1,5)
grid = 16x1

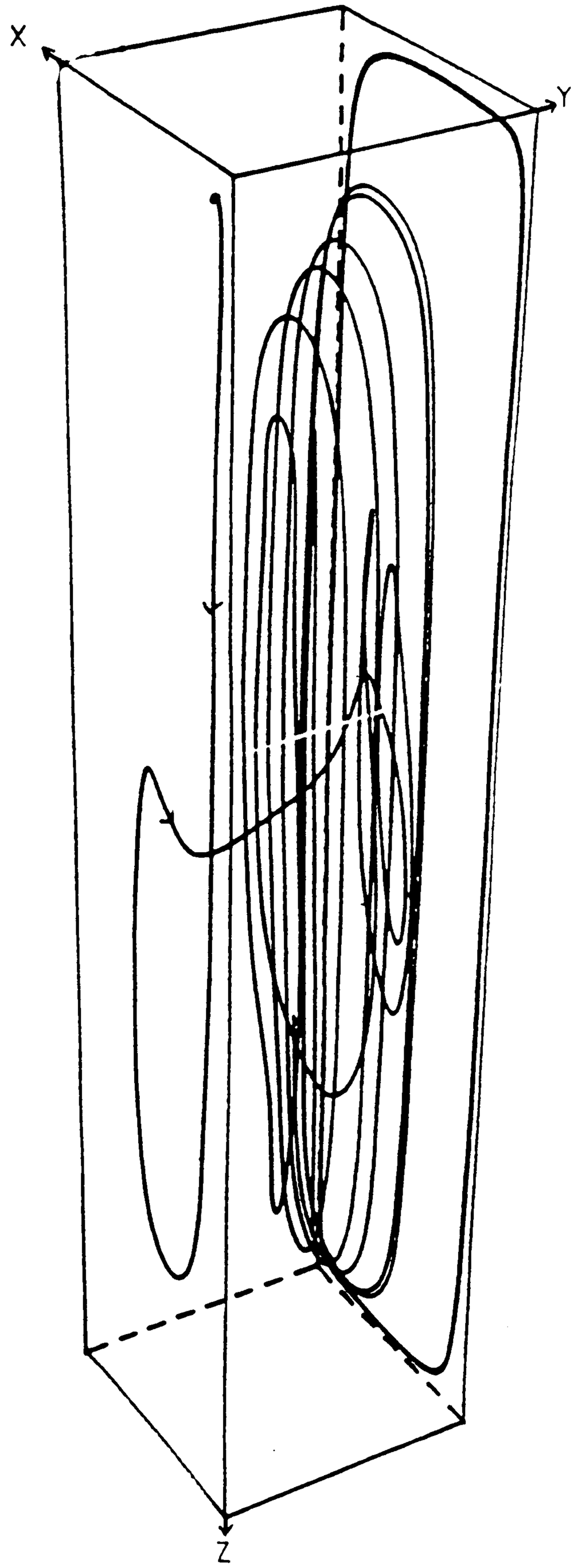

Figure 6.200 Particle track
for air at Ra = 10^5, cavity (1,2,5)
grid = 16x16x40

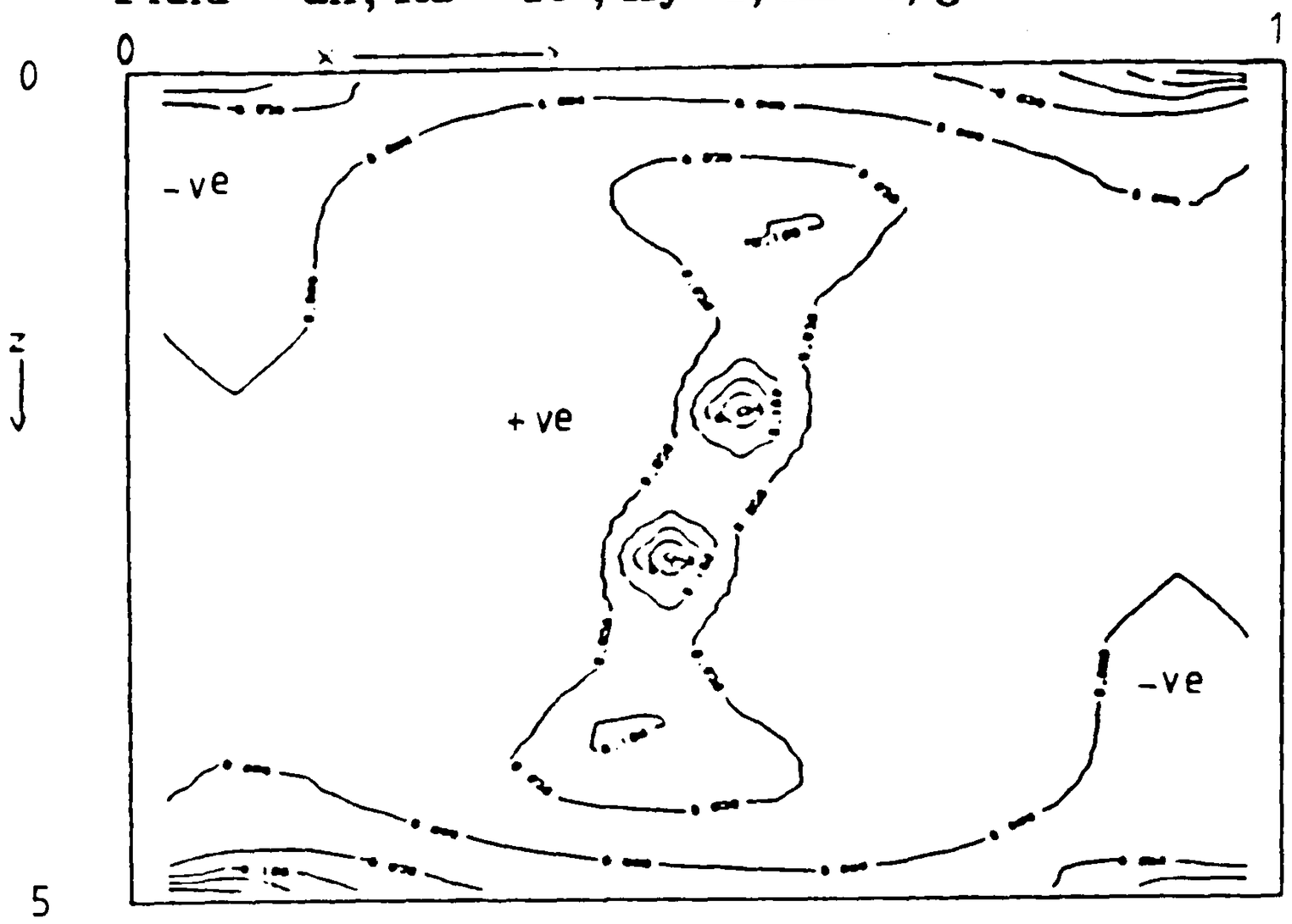

Figure 6.201 Contour plot of ratio R at plane A, near the end wall

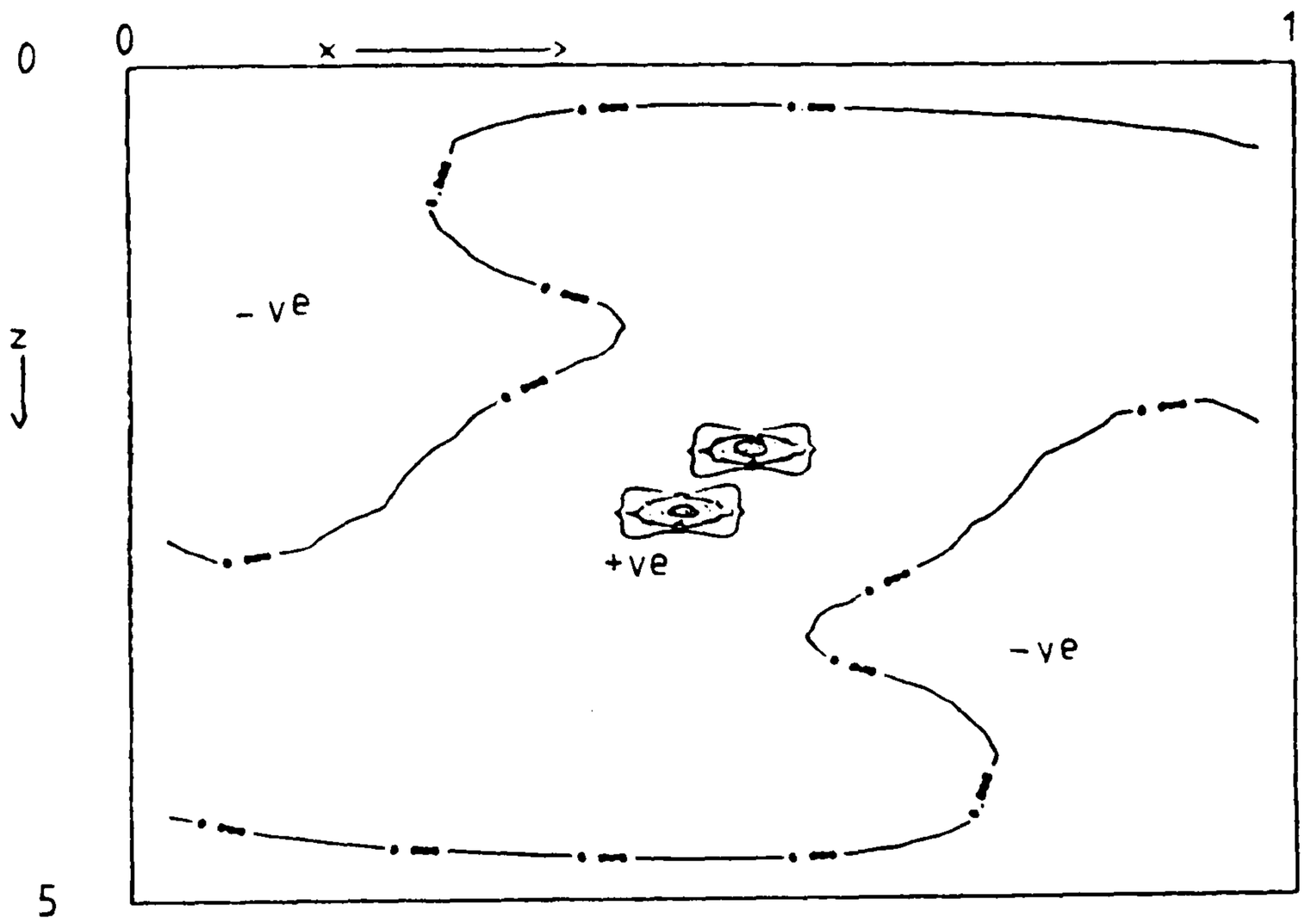

Figure 6.202 Contour plot of ratio R at plane B, near the symmetry plane

Fluid = air, Ra = 10^5, Hy=1, Hz=5, grid=16x16x40

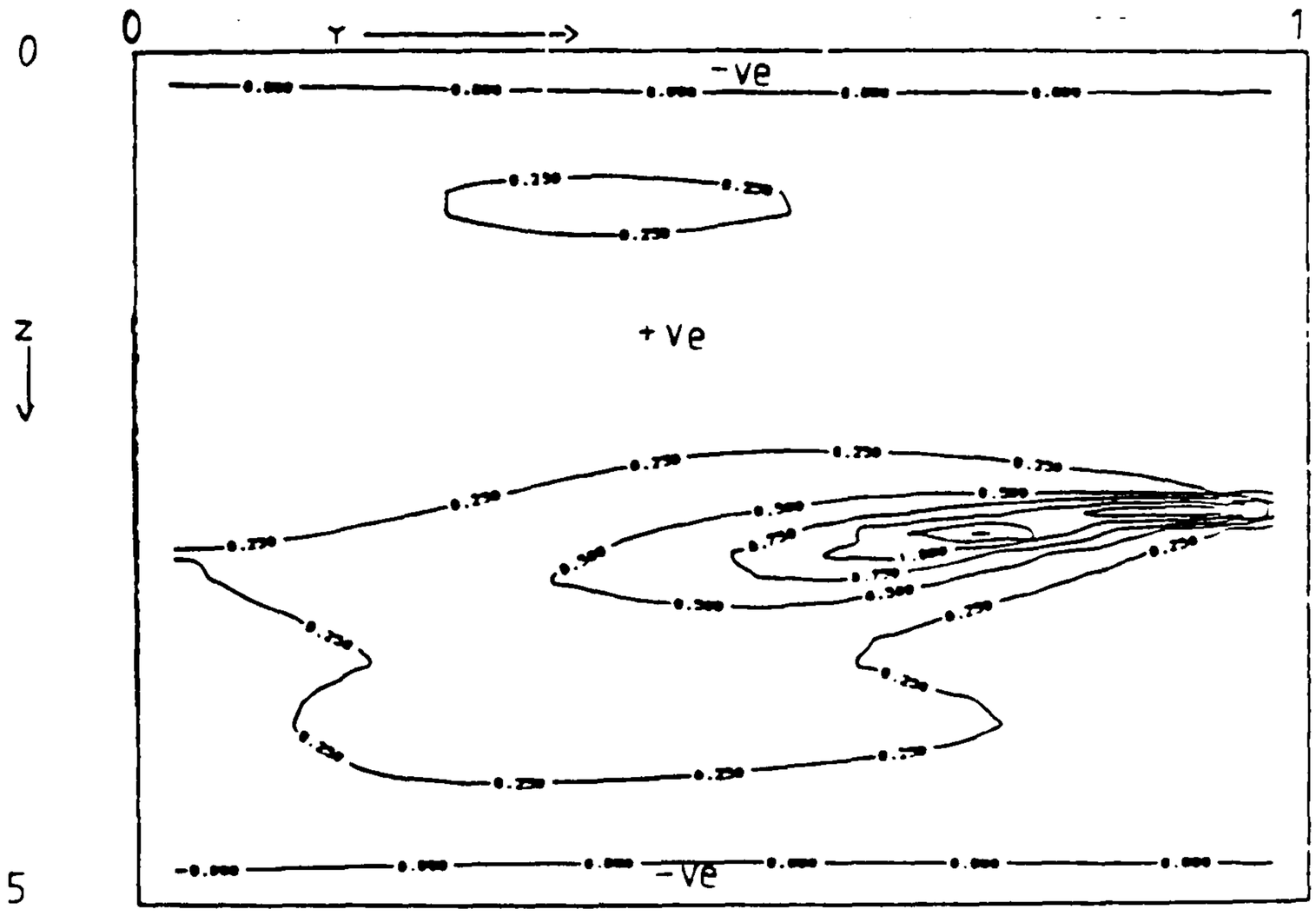

Figure 6.203 Contour plot of ratio R at plane C $(0.5 - hx/2, y, z)$

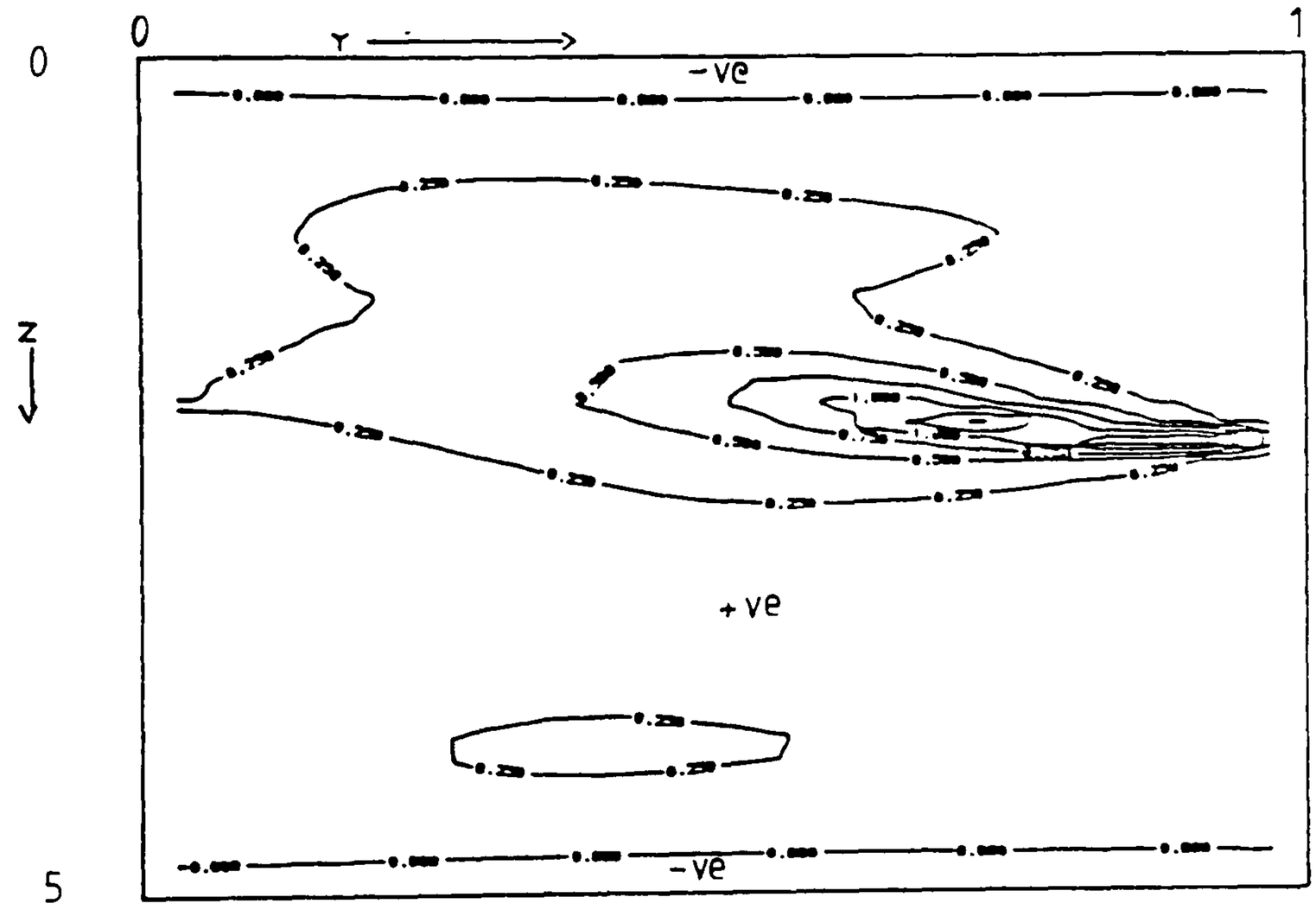

Figure 6.204 Contour plot of ratio R at plane C $(0.5 + hx/2, y, z)$

Fluid = air, Ra = 10^5, Hy=1, Hz=5,

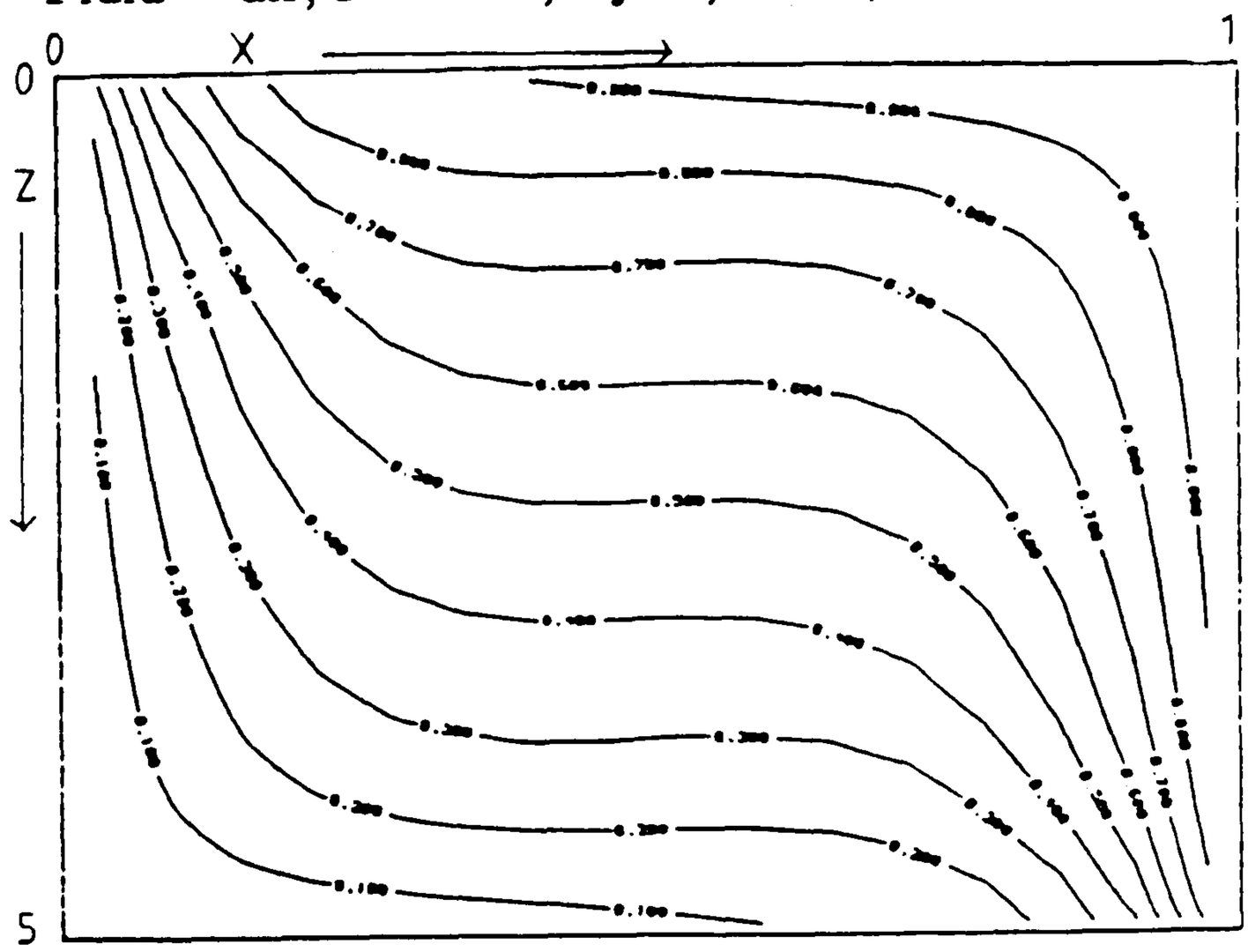

Figure 6.205 Isotherms at plane A, near the end wall

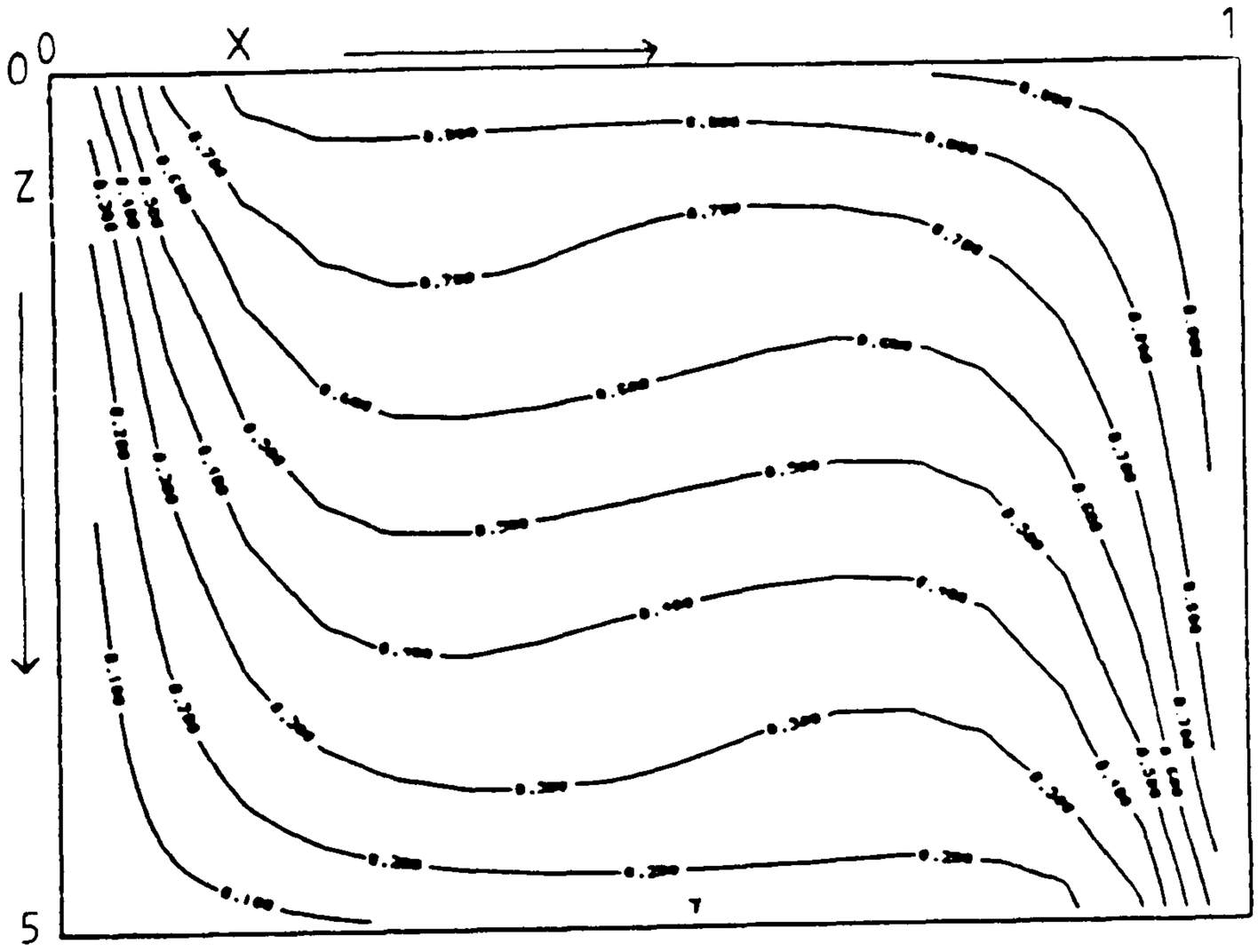

Figure 6.206 Isotherms at plane B, near the symmetry plane

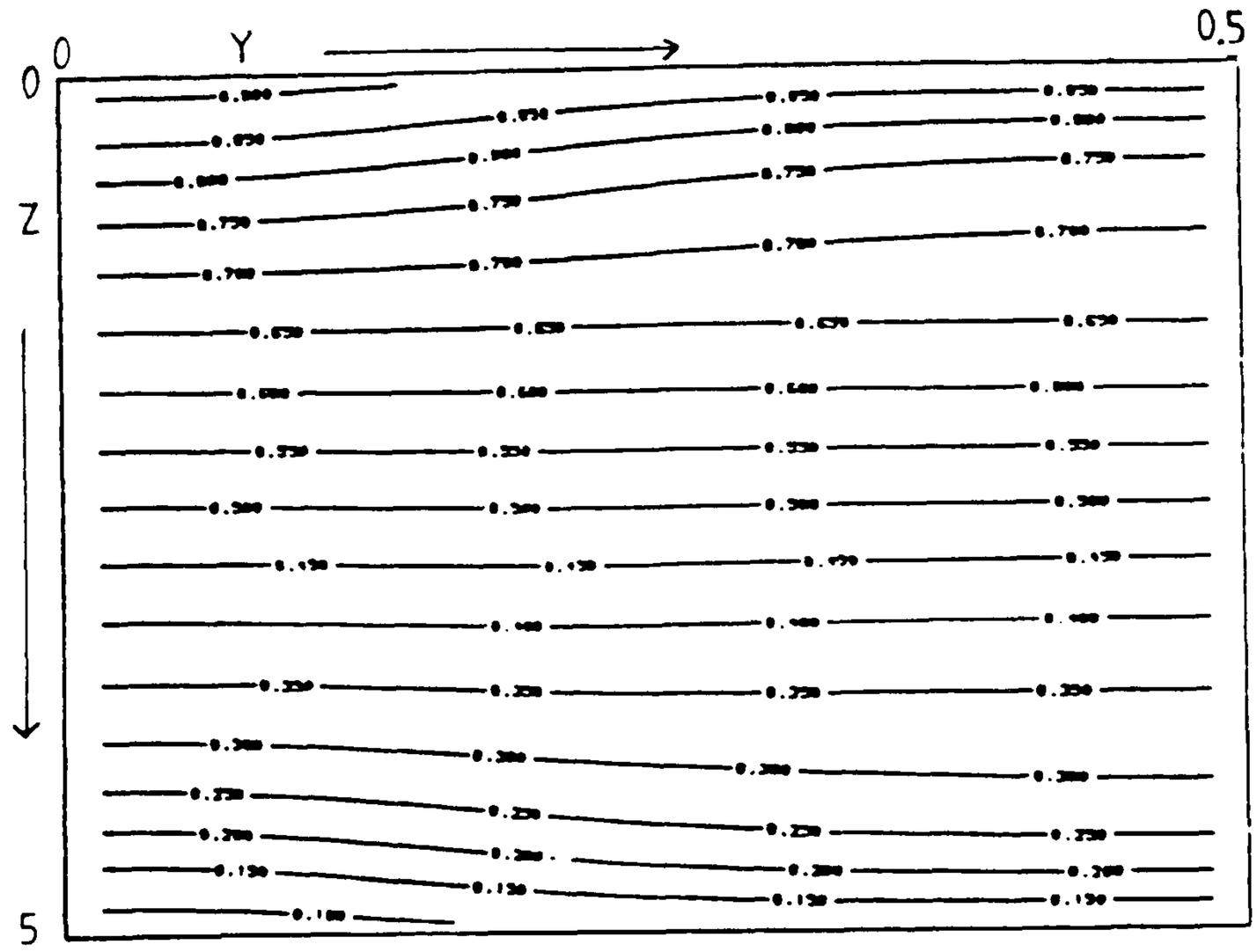

Figure 6.207 Isotherms at plane C, $(0.5 - hx/2, y, z)$

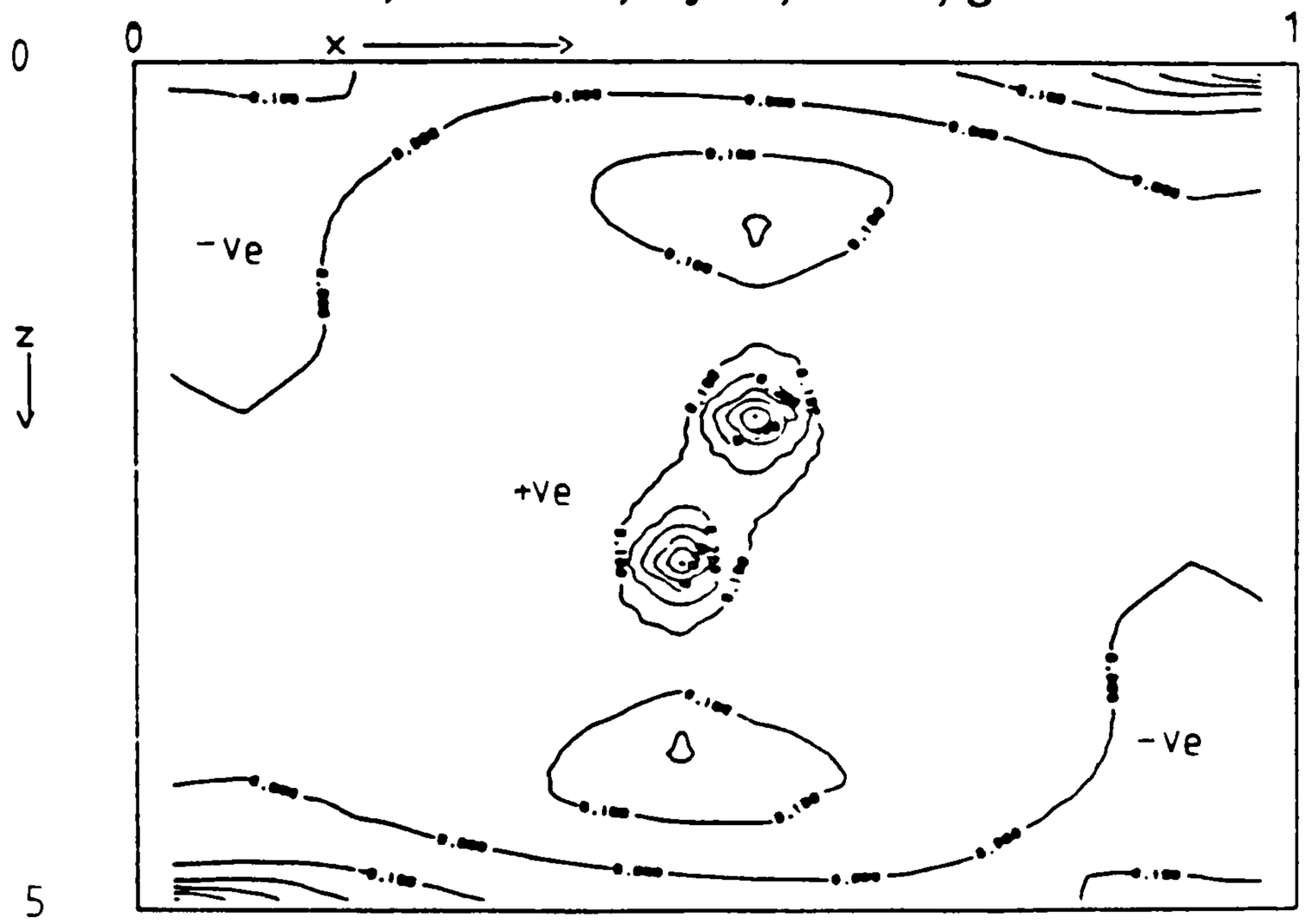

Figure 6.208 Contour plot of ratio R at plane A, near the end wall

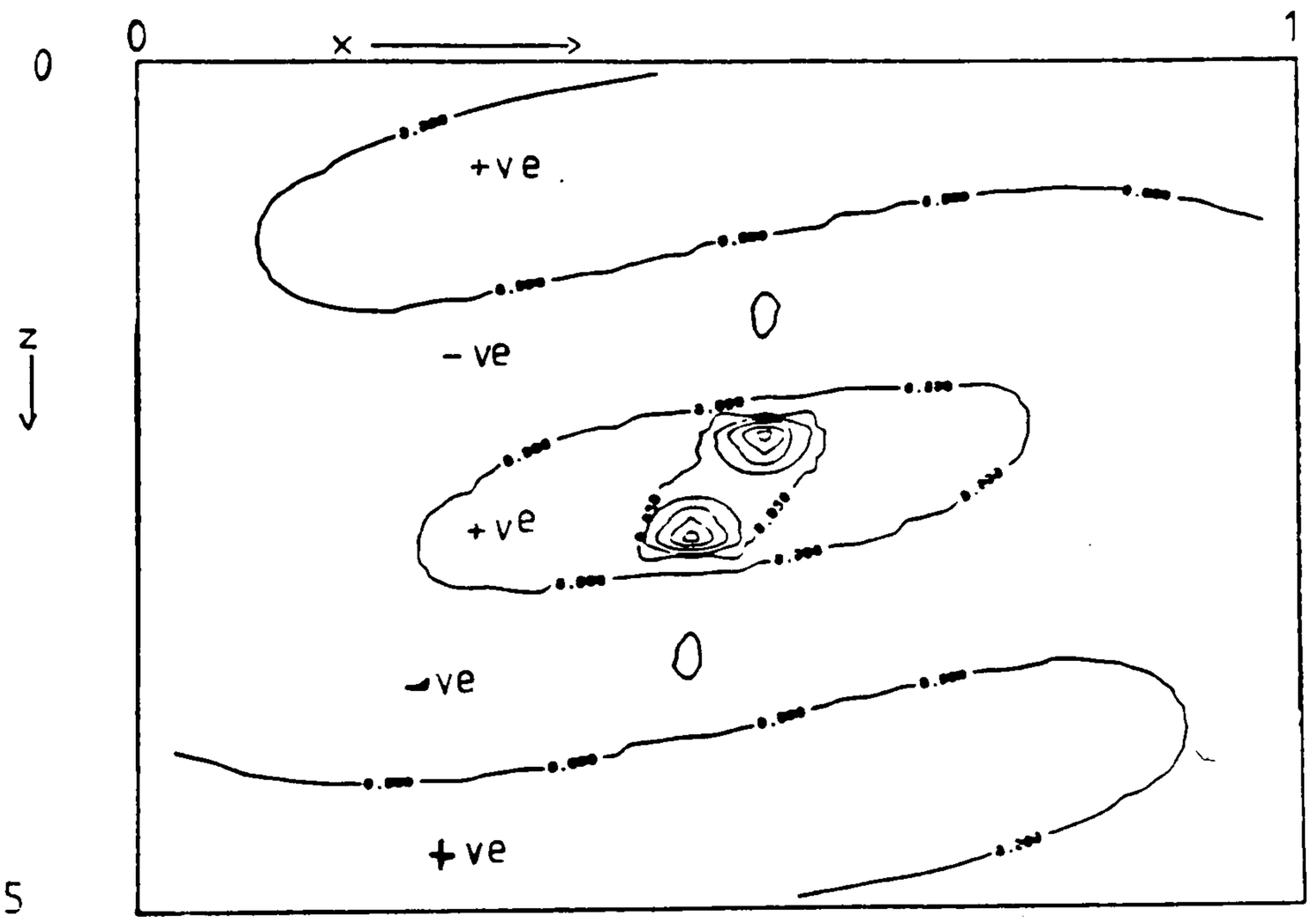

Figure 6.209 Contour plot of ratio R at plane B, near the symmetry plane

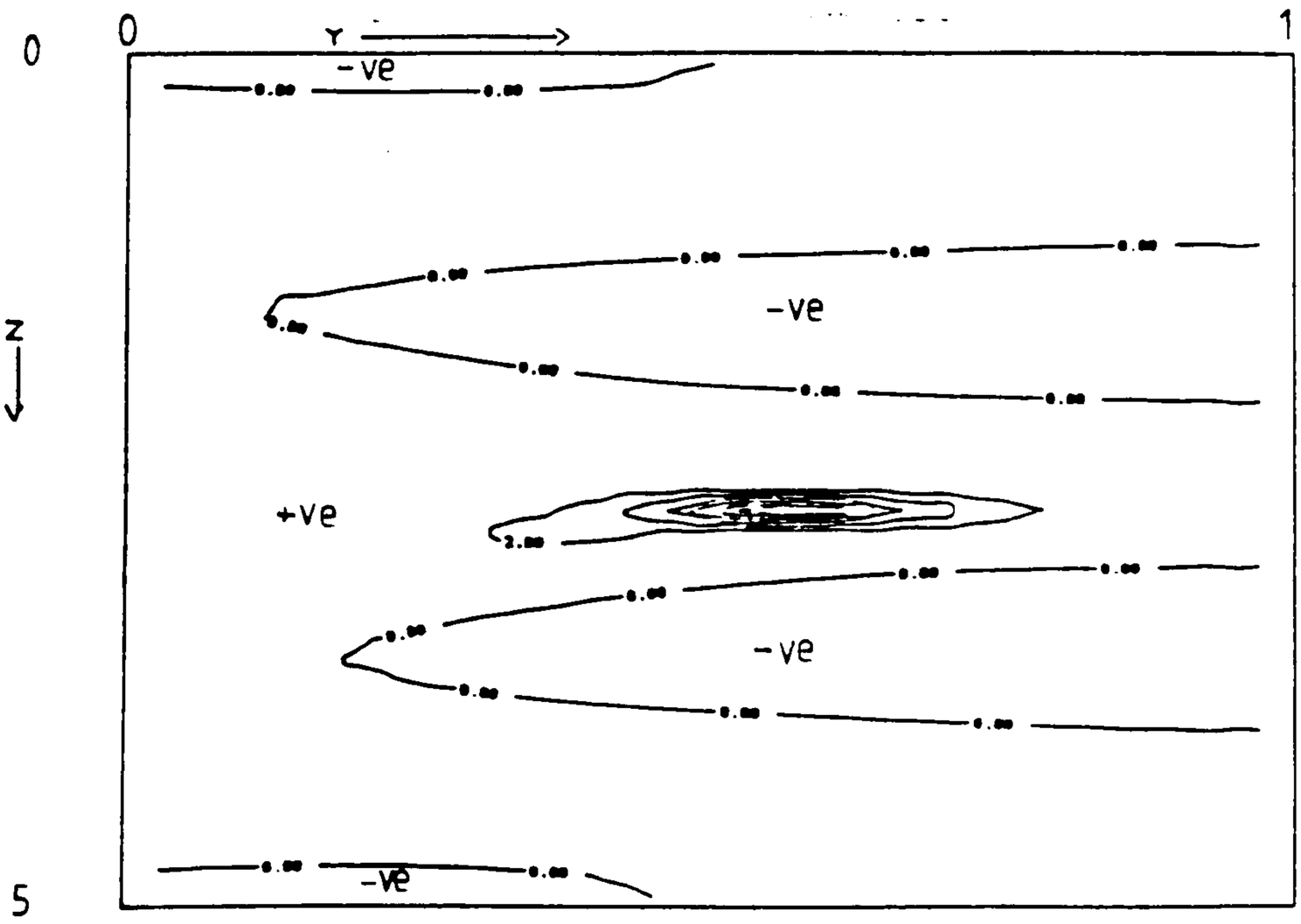

Figure 6.210 Contour plot of ratio R at plane C $(0.5 - hx/2, y, z)$

Fluid = air, Ra = 10^5, Hy=2, Hz=5, grid=16x16x40

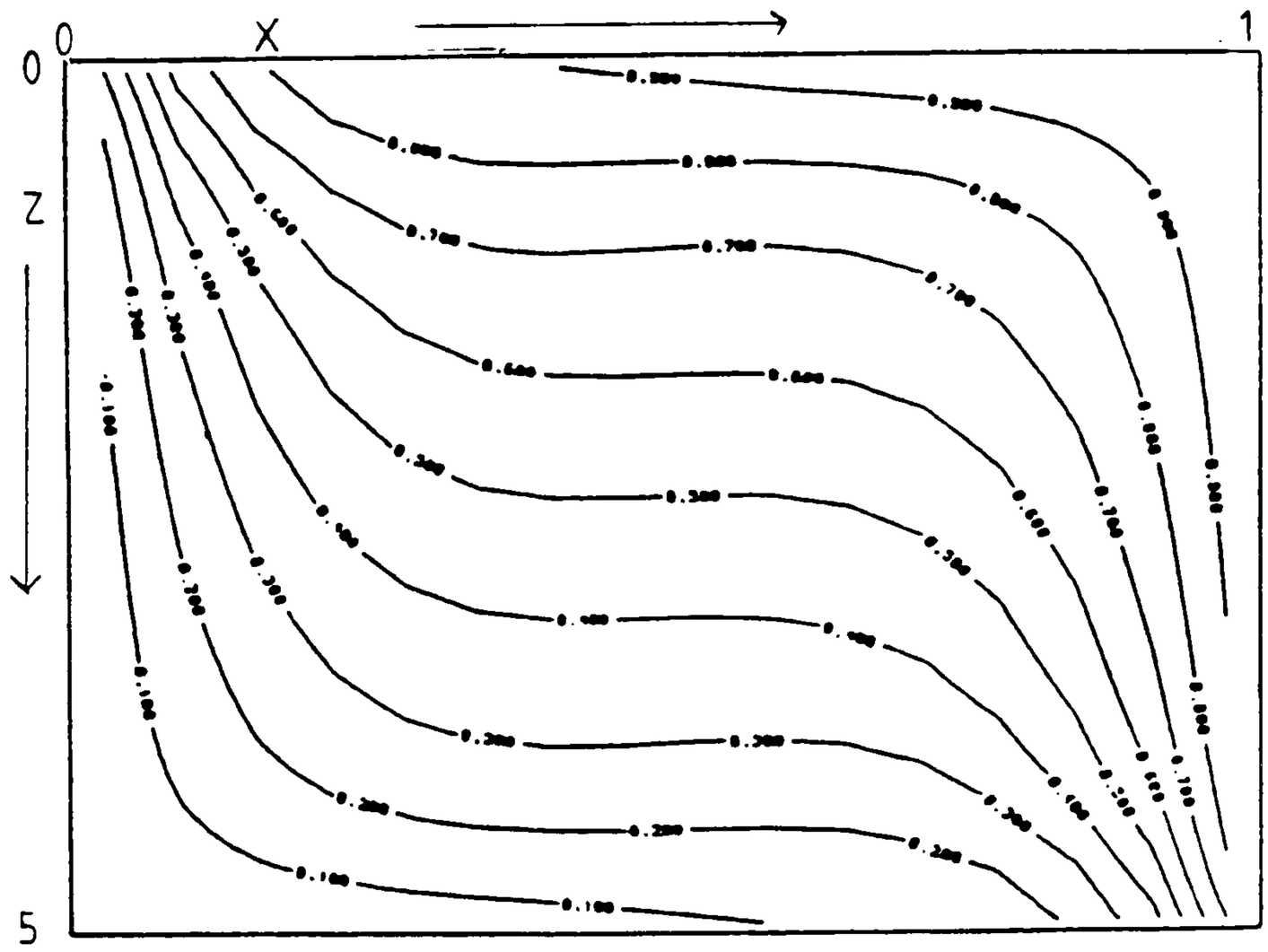

Figure 6.211 Isotherms at plane A, near the end wall

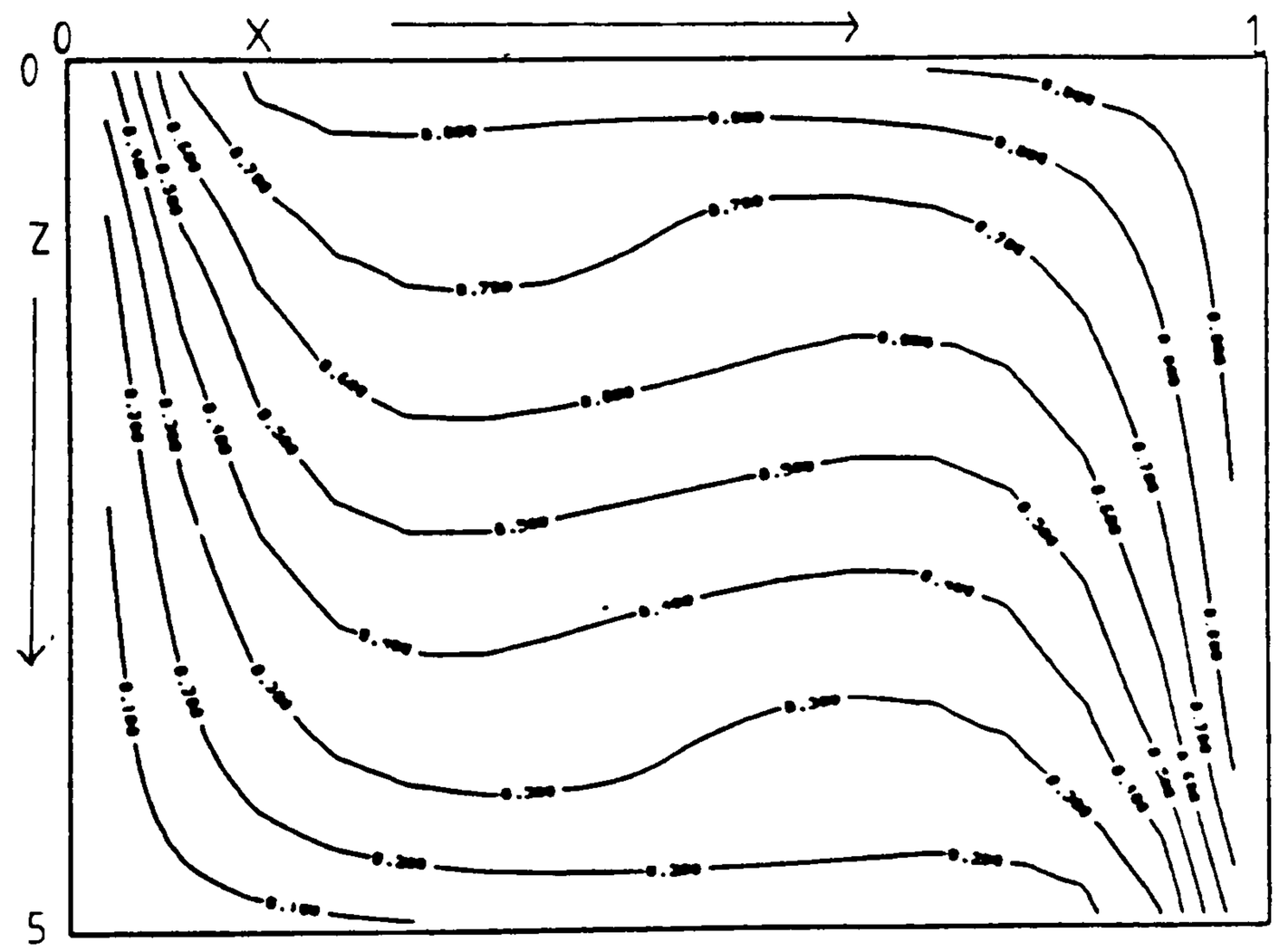

Figure 6.212 Isotherms at plane B, near the symmetry plane

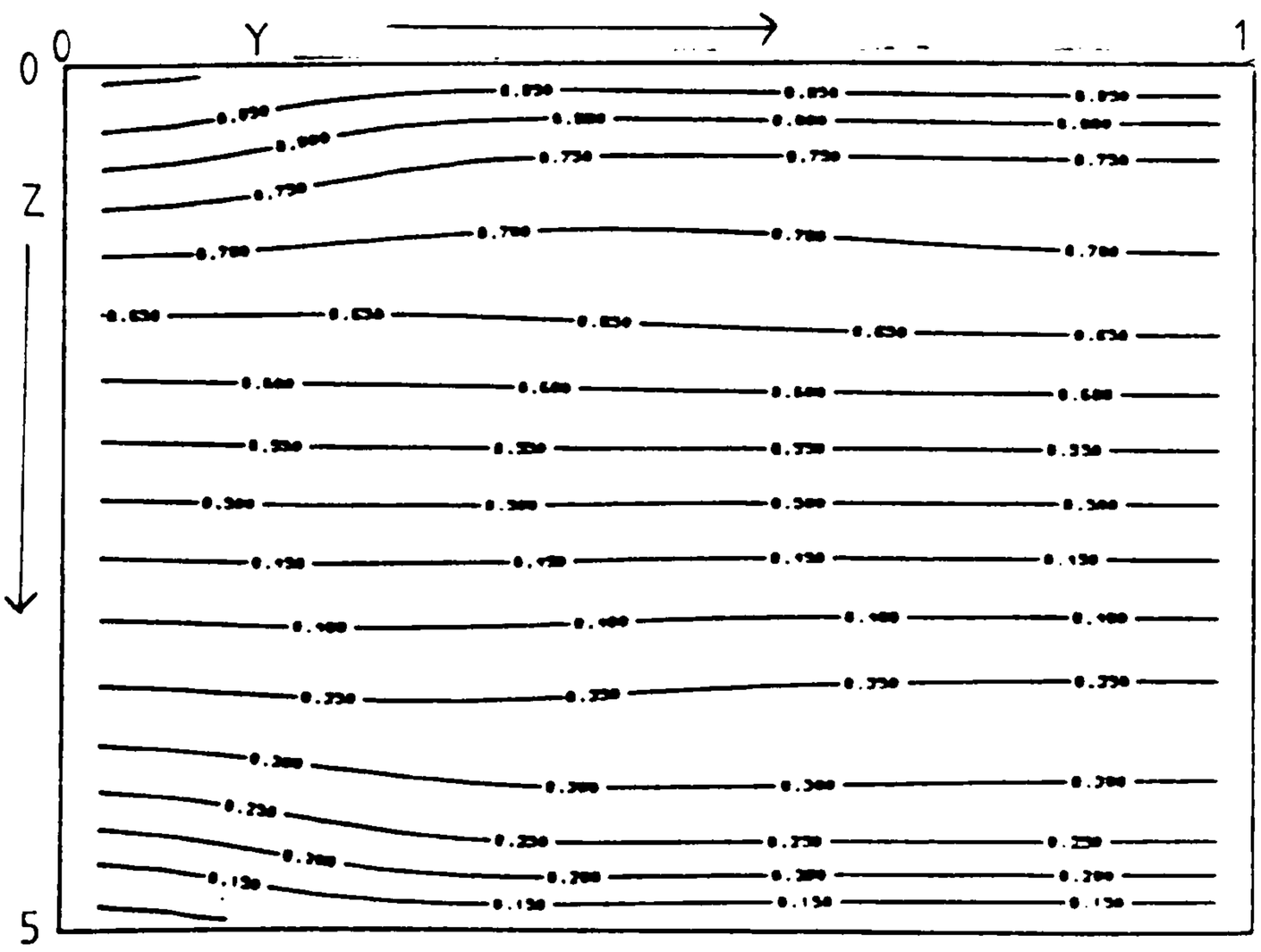

Figure 6.213 Isotherms at plane C, $(0.5 - hx/2, y, z)$

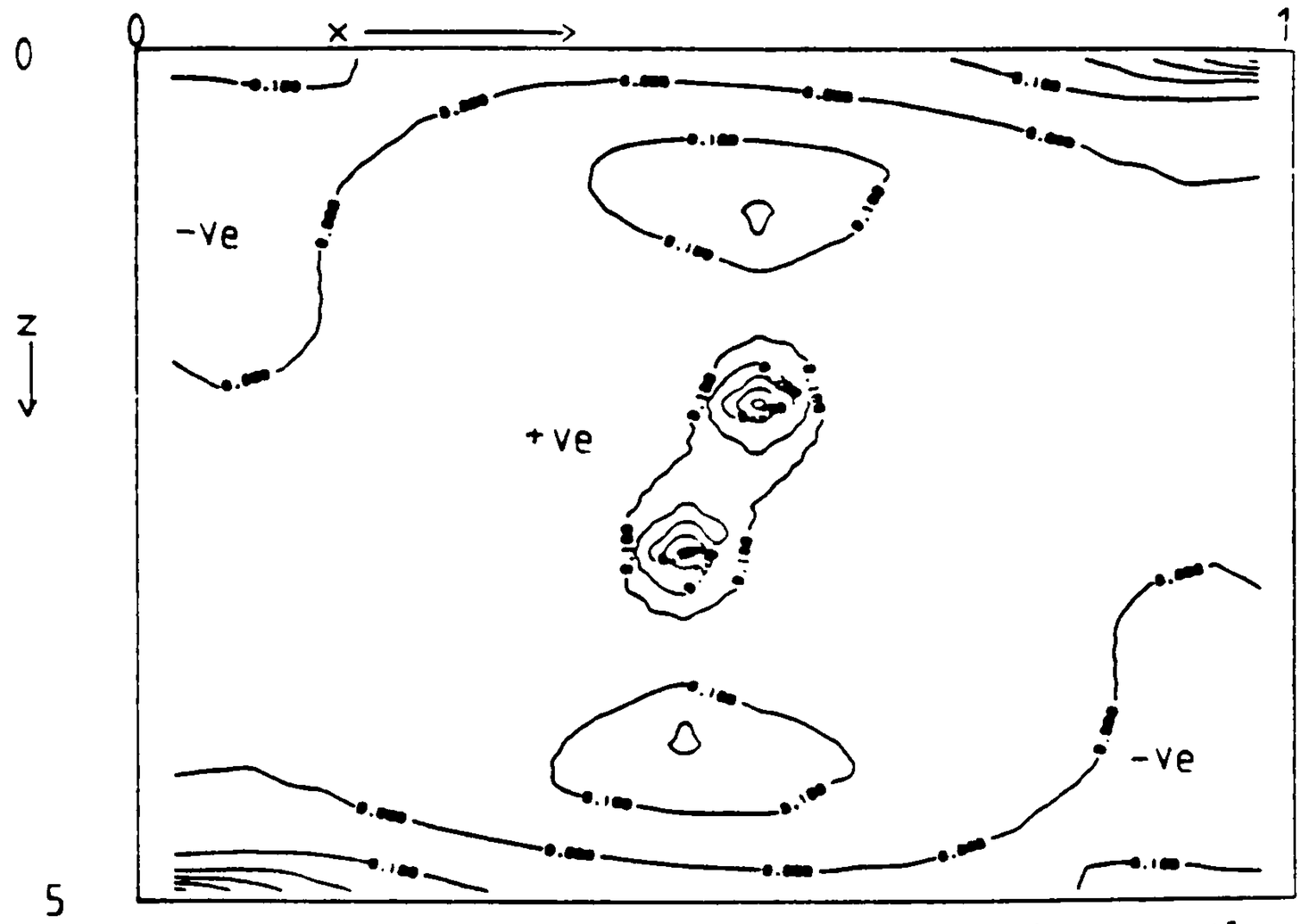

Figure 6.214 Contour plot of ratio R at plane A, near the end wall

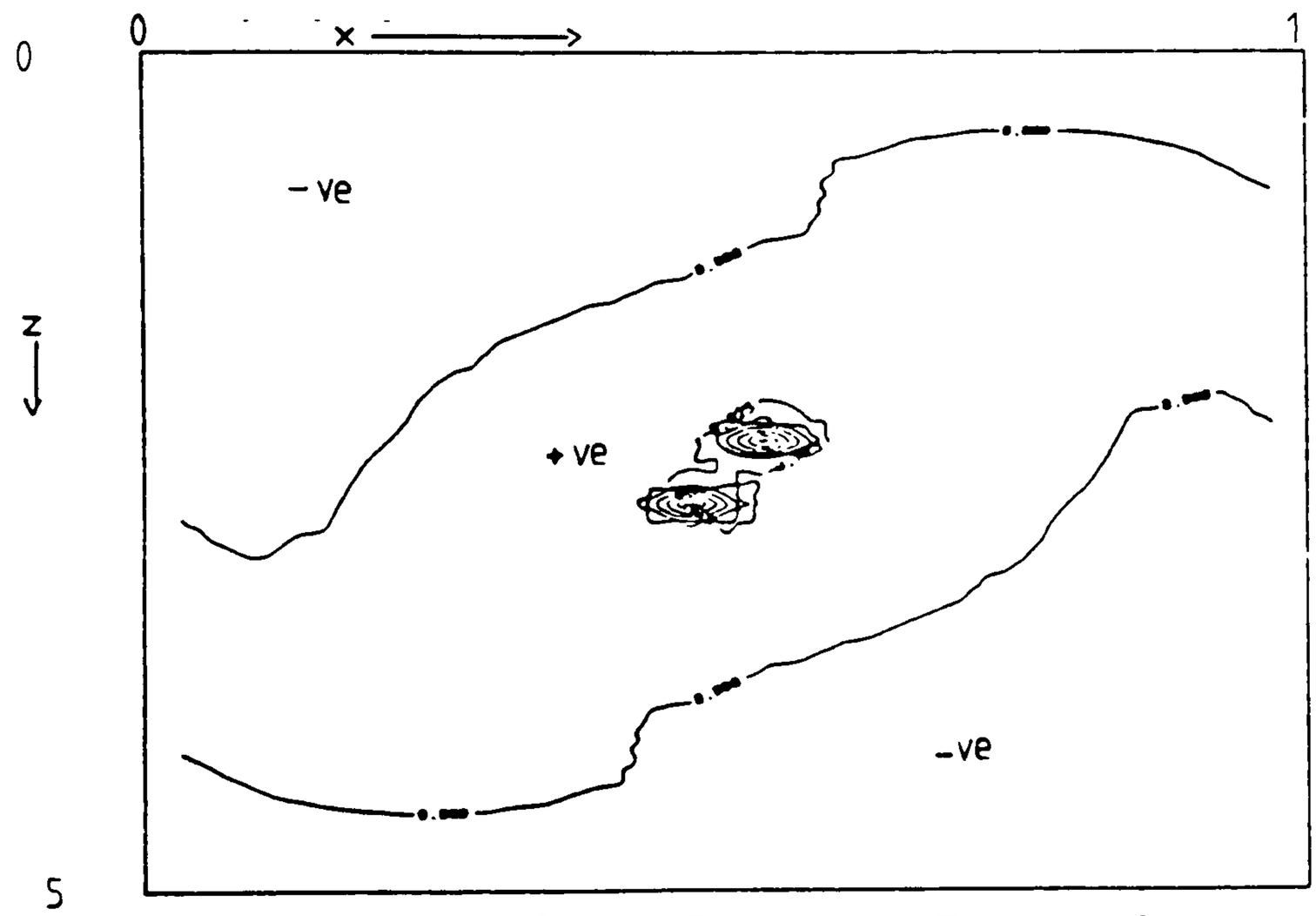

Figure 6.215 Contour plot of ratio R at plane B, near the symmetry plane

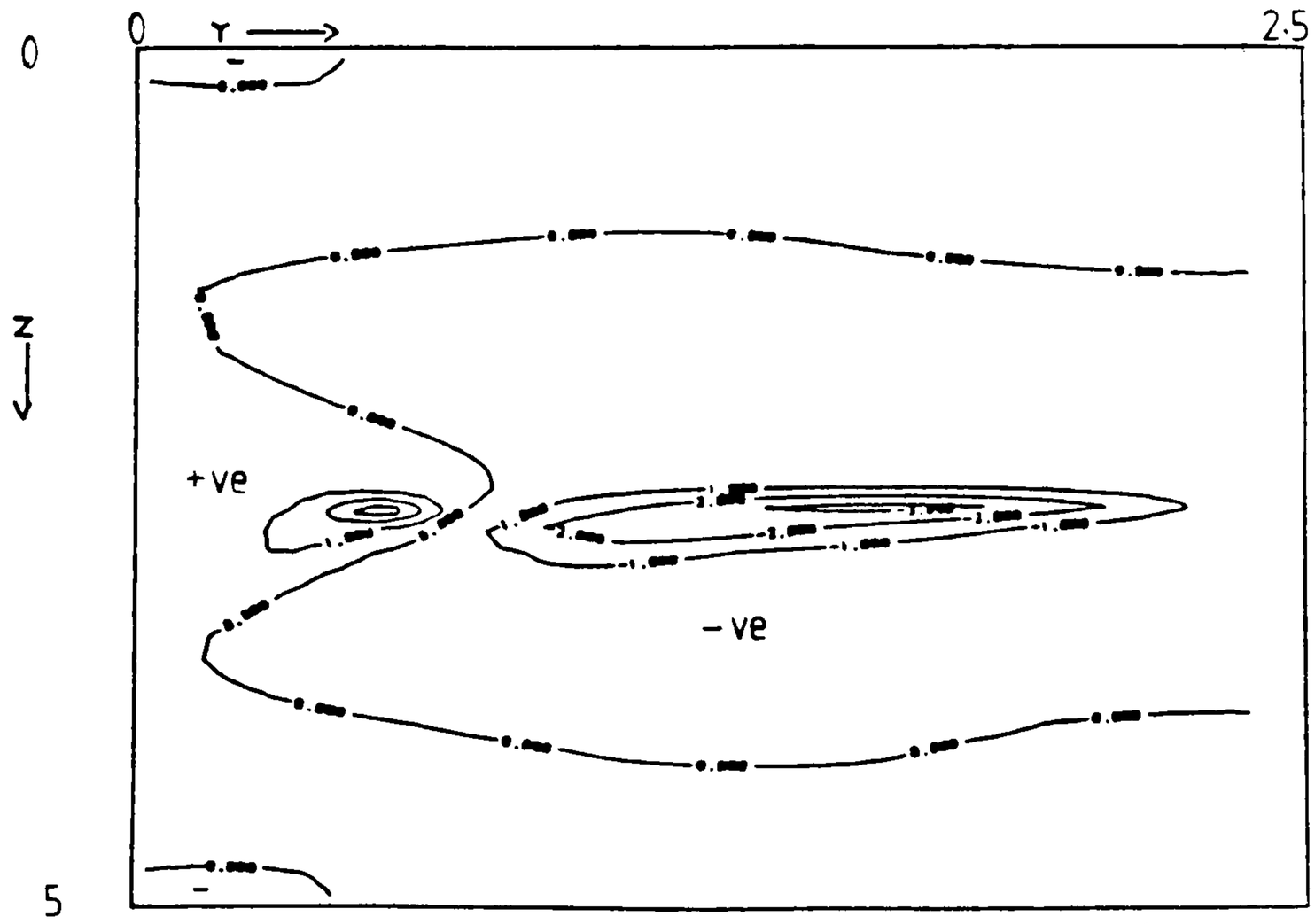

Figure 6.216 Contour plot of ratio R at plane C $(0.5 - hx/2, y, z)$

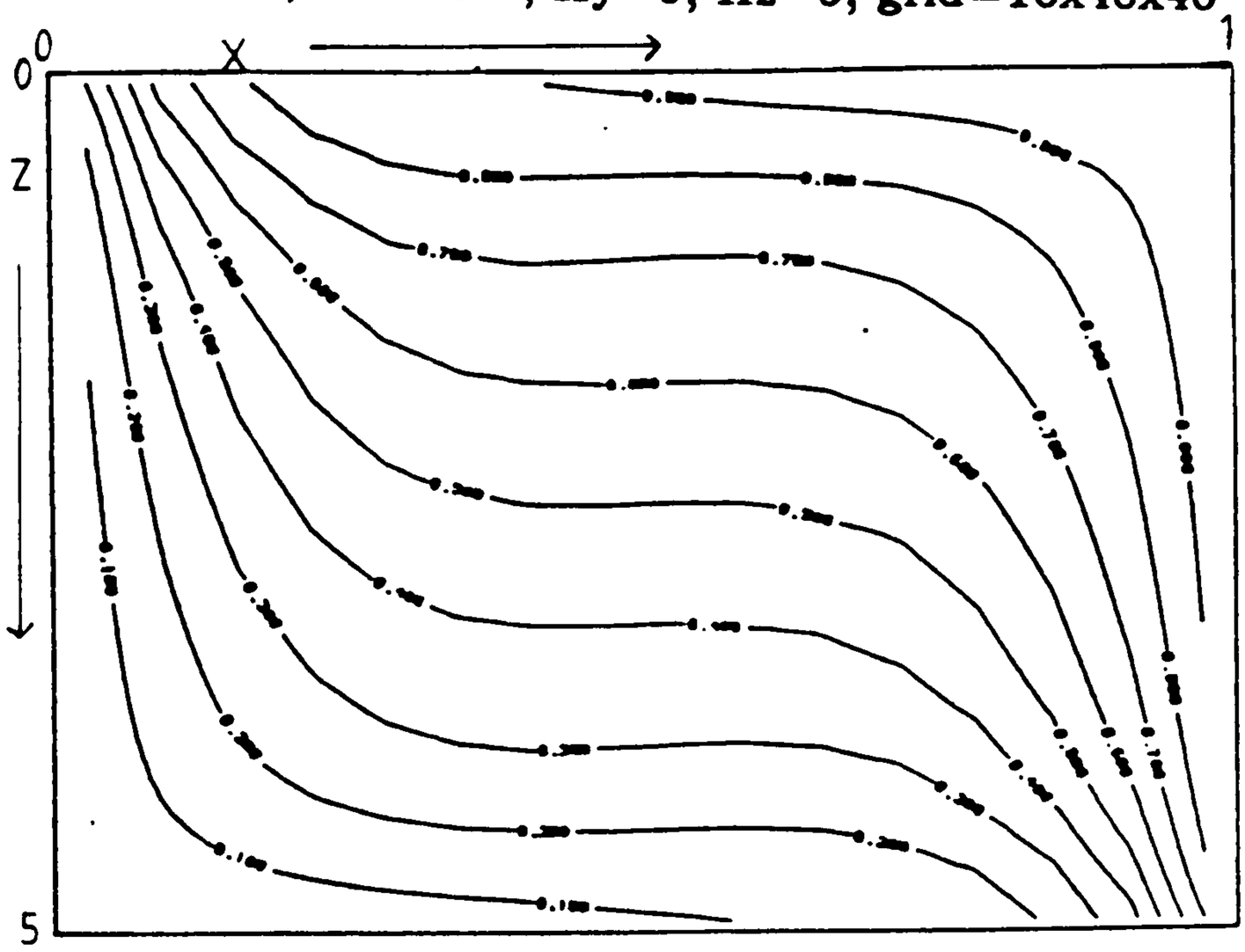

Figure 6.217 Isotherms at plane A, near the end wall

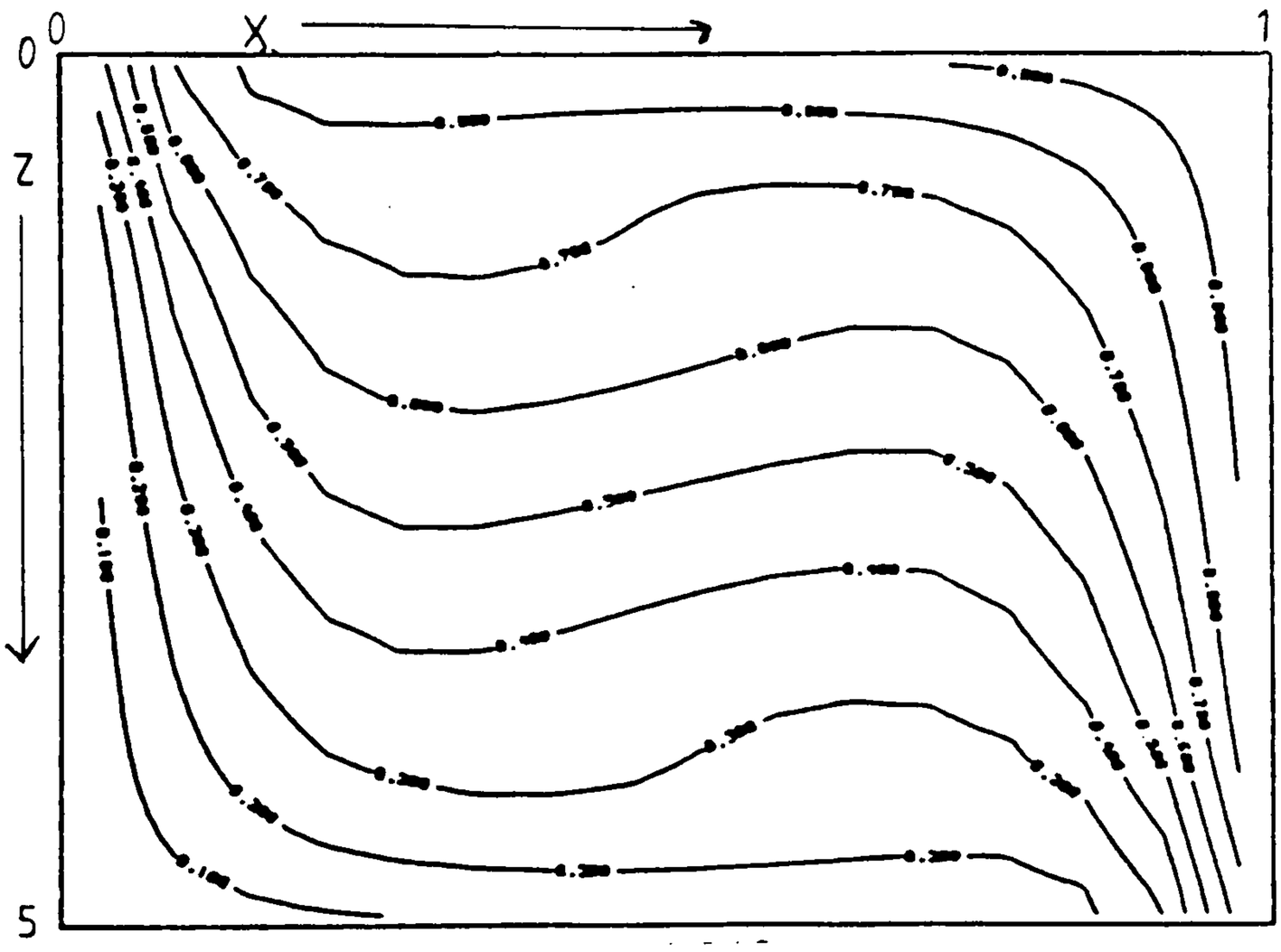

Figure 6.218 Isotherms at plane B, near the symmetry plane

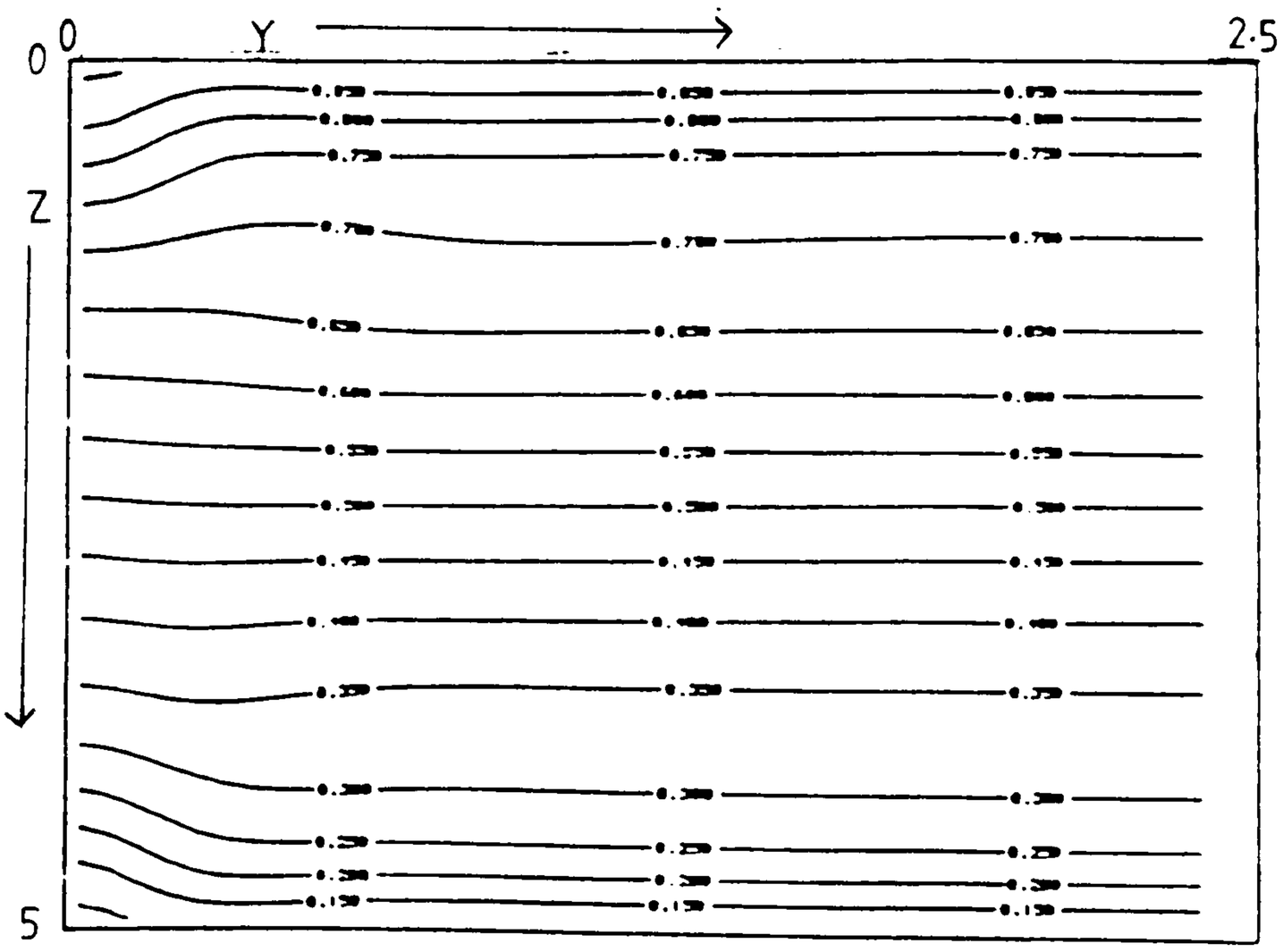

Figure 6.219 Isotherms at plane C, $(0.5 - hx/2, y, z)$

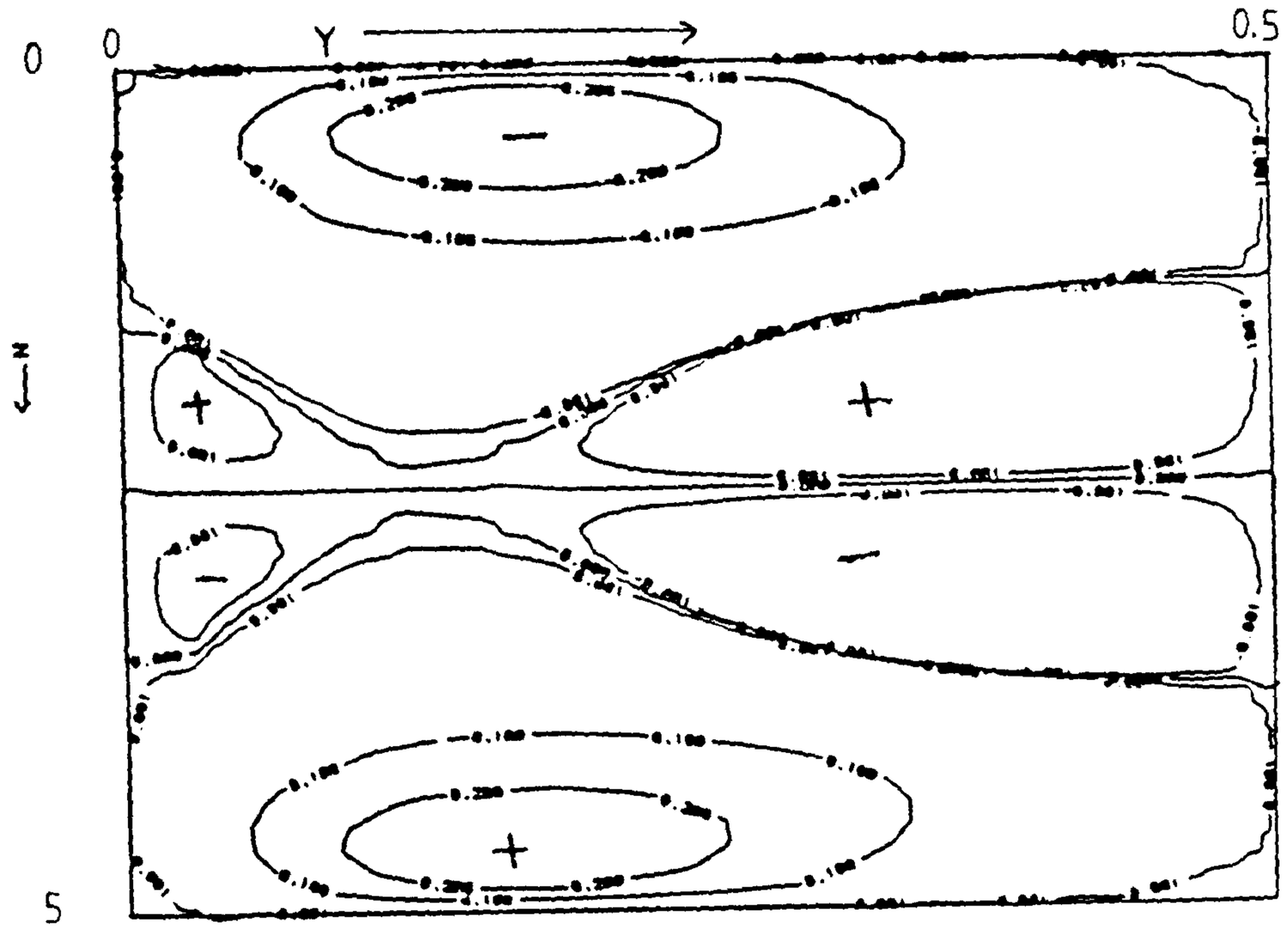

Figure 6.220 $\partial\theta/\partial y$ at plane C, $(0.5 - hx/2, y, z)$, Hy=1

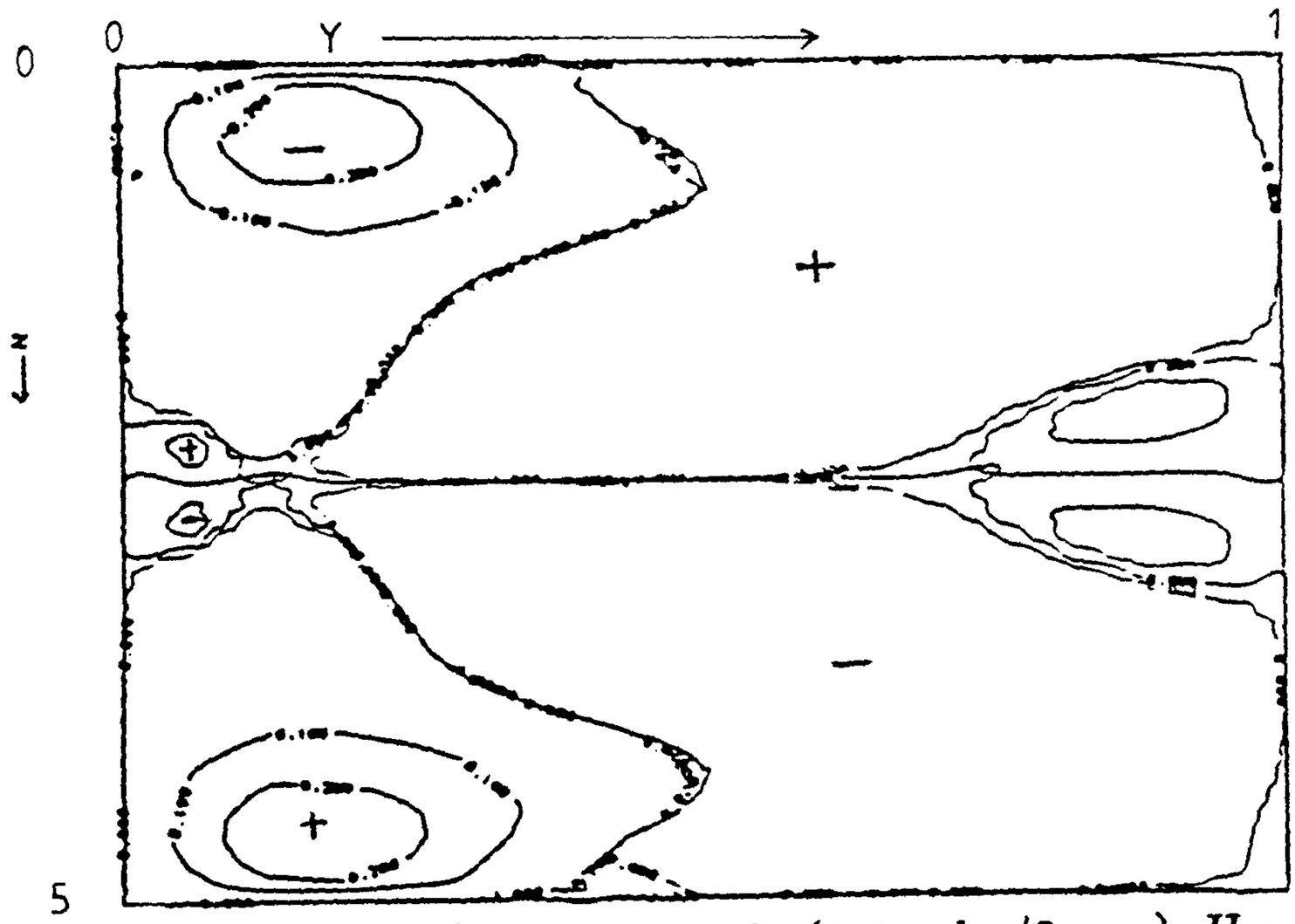

Figure 6.221 $\partial\theta/\partial y$ at plane C, $(0.5 - hx/2, y, z)$, Hy=2

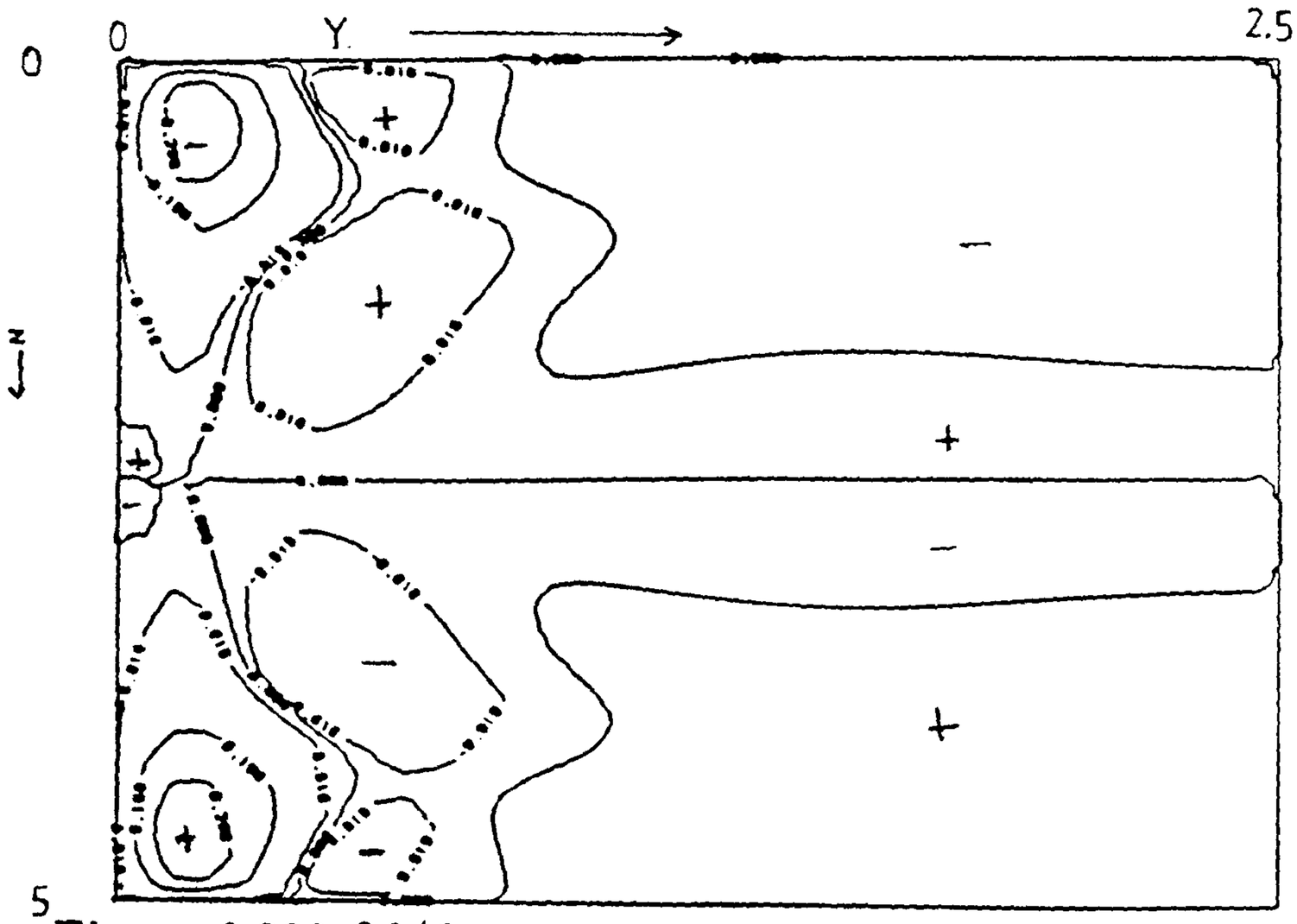

Figure 6.222 $\partial\theta/\partial y$ at plane C, $(0.5 - hx/2, y, z)$, Hy=5

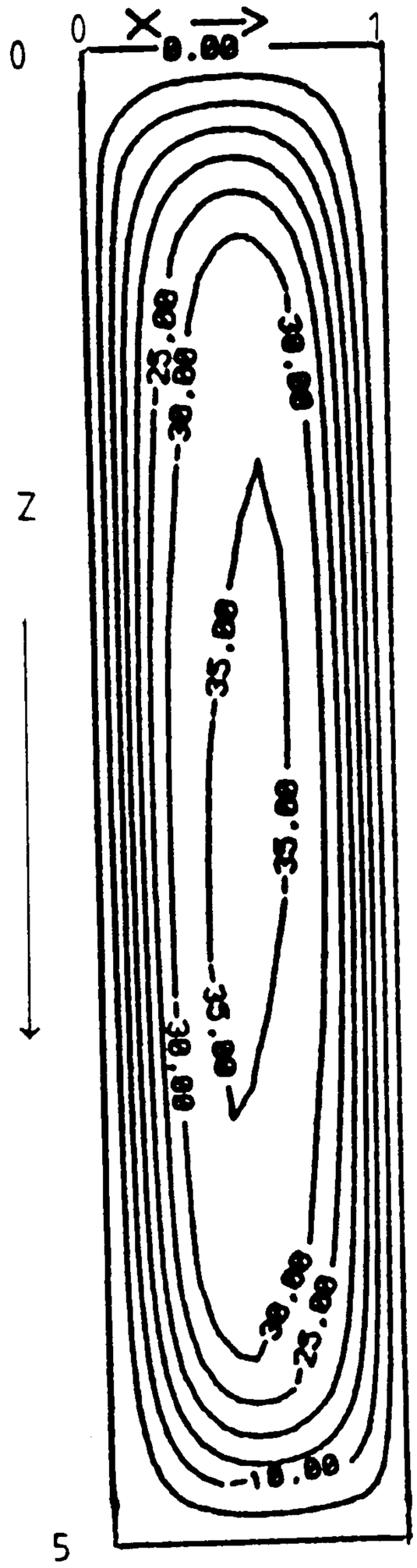

Figure 6.223 Streamlines near the symmetry plane, Hy=5

Graph A: air at Ra = 10^5, Hy=1, Hz=5

Graph B: air at Ra = 10^5, Hy=2, Hz=5

Graph C: air at Ra = 10^5, Hy=5, Hz=5

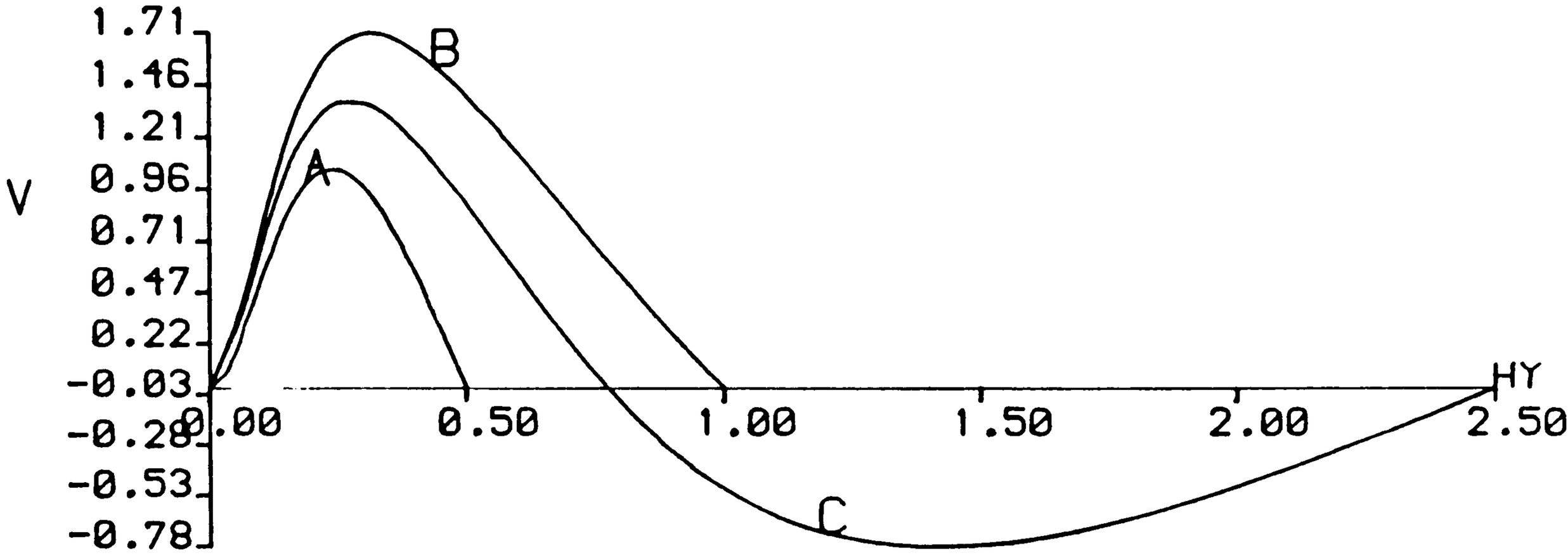

Figure 6.224 Axial-velocity along $(0.5, y, 2.5)$

Graph A: air at Ra = 10^5, Hy=2, Hz=5

Graph B: air at Ra = 10^5, Hy=3, Hz=5

Graph C: air at Ra = 10^5, Hy=10, Hz=5

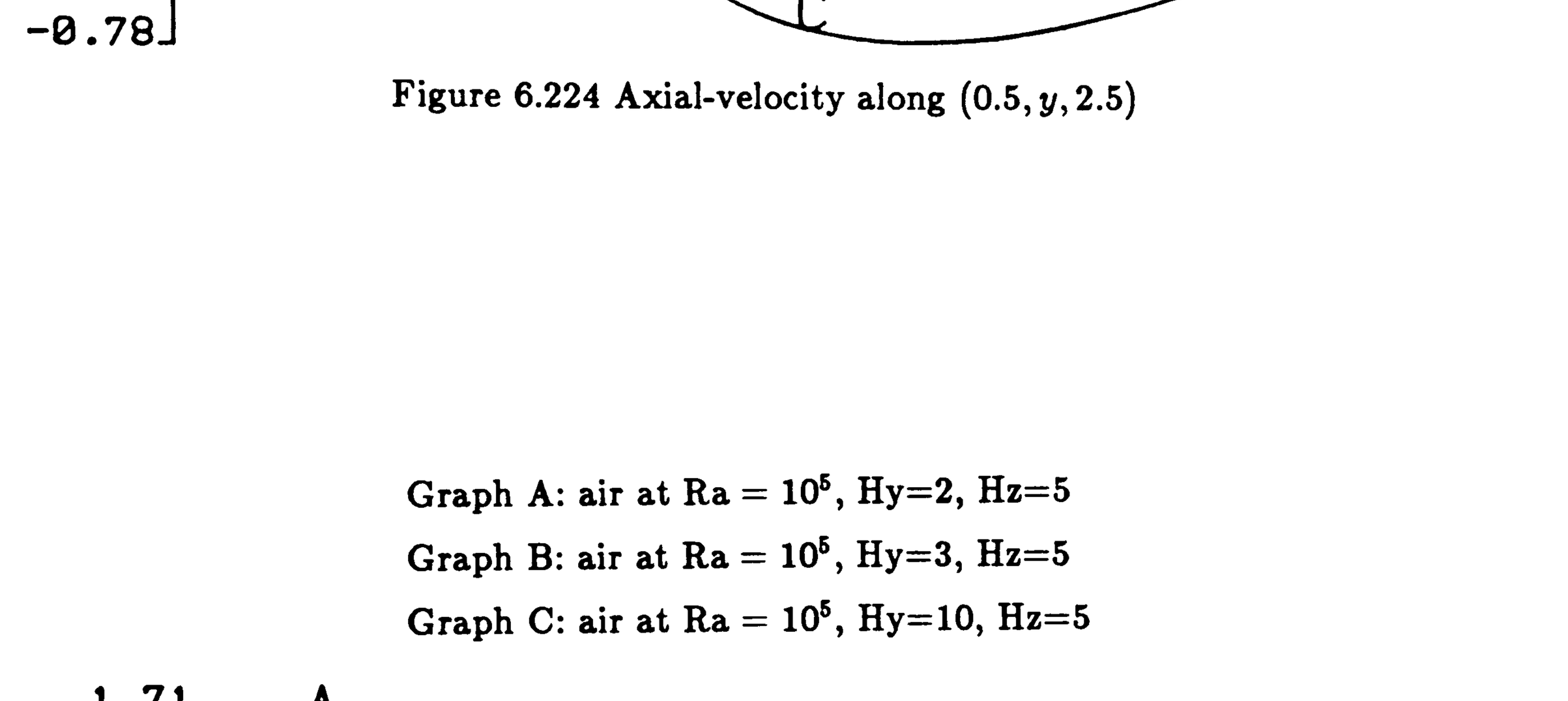

Figure 6.225 Axial-velocity along $(0.5, y, 2.5)$

6.8.3 Results obtained for cerrobase, Ra=10^3

The fluid flow behaviour for this case is described by a single forward recirculating roll which fills the solution cavity for length aspect ratios Hy=1, 2, and 5. Figures 6.226 and 6.227 are particle paths in cavities with aspect ratios Hy=1 and 2 respectively traced from the point (.1, .01, .1) near the end wall.

Figures 6.228-6.230 are contour plots of R at planes A, B and C respectively for the length aspect ratio Hy=1.0. The plots show two strong axial flow regions close together. Near the symmetry plane these have rotated anti-clockwise. Note the positive R contours attached to the side walls.

Figures 6.231-6.233 are isotherm plots at planes A, B and C respectively for the length aspect ratio Hy=1.0. The convection of heat along the upper and lower boundaries is not as great as for air.

Figures 6.234-6.239 are contour plots of R and isotherms at planes A, B and C respectively for Hy=2. The features of these plots are very similar to those obtained with Hy=1.0.

Figures 6.240-6.242 are contour plots of R at planes A, B and C respectively for Hy=5.0. The plots indicate two strong regions of axial flow in the centre of the cross-section near the end wall which have rotated anti-clockwise about the centre line, cf., Figure 6.240 and 6.242. Figure 6.240 also shows two weaker regions of axial flow near the upper and lower boundaries which diminish as y increases. These weaker regions are a result of the reduction in convection near the upper and lower boundaries and the stronger regions appear to be a result of the inner core convection. Figure 6.240 also exhibits a strong return flow in the hot upper right hand corner and the cold lower left hand corner.

Figure 6.243-6.245 are isotherm plots at planes A, B and C respectively. The central region does not depict a conductive thermal solution but rather a convective one due to the inner core.

Figure 6.246 is a contour plot of $\partial\theta/\partial y$ at the plane x=0.5 for Hy=1.0. positive values of $\partial\theta/\partial y$ dominate the upper half and negative $\partial\theta/\partial y$ dominate the lower half and the vorticity generated by the axial temperature augments the inertial end effect. Figure 6.247 is a contour plot $\partial\theta/\partial y$ near the plane x=0.5 for Hy=2. With this length aspect ratio $\partial\theta/\partial y$ changes sign along the centre line near the symmetry plane. The change in sign of $\partial\theta/\partial y$ along the centre line appears to be associated with convection of heat in the inner core. Figure 6.248 is a contour plot of $\partial\theta/\partial y$ near the plane x=0.5

for Hy=5. Two sign changes of $\partial\theta/\partial y$ occur, one along the centre line and two near the symmetry plane in the upper and lower halves of the cavity.

Figure 6.249 is a plot of the streamline near the symmetry plane for Hy=5.0 and exhibits the primary recirculating flow.

Figure 6.250 is the axial-velocity profile along the centre-line for Hy=1, 2 and 5. The forward roll in the shorter cavities is restricted. The inflexion in the velocity profile for Hy=5.0 appears to be associated with the change in sign of $\partial\theta/\partial y$ as it occurs in the same region as the sign change.

In a two-dimensional study performed by Jones [27] for this fluid at $Ra = 10^3$, he obtained two cat's eye cells, one on top of another. These cells do not appear in the three-dimensional problem as can be see in the streamline plot.

Particle track for cerrobase at Ra = 10^3

grid = 16x16x40

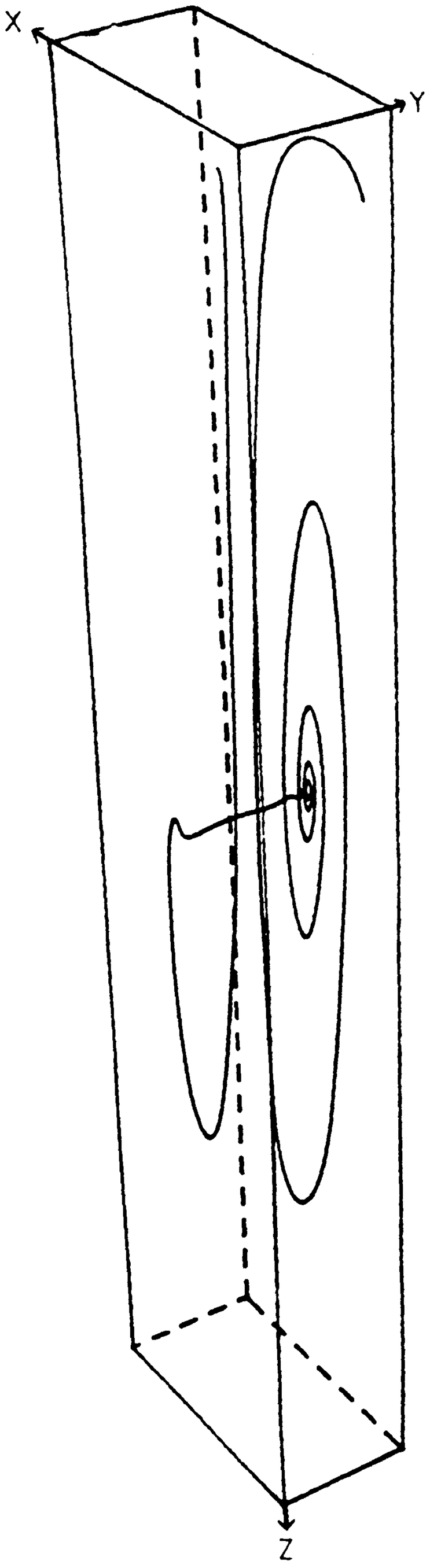

Figure 6.226

cavity (1,1,5)

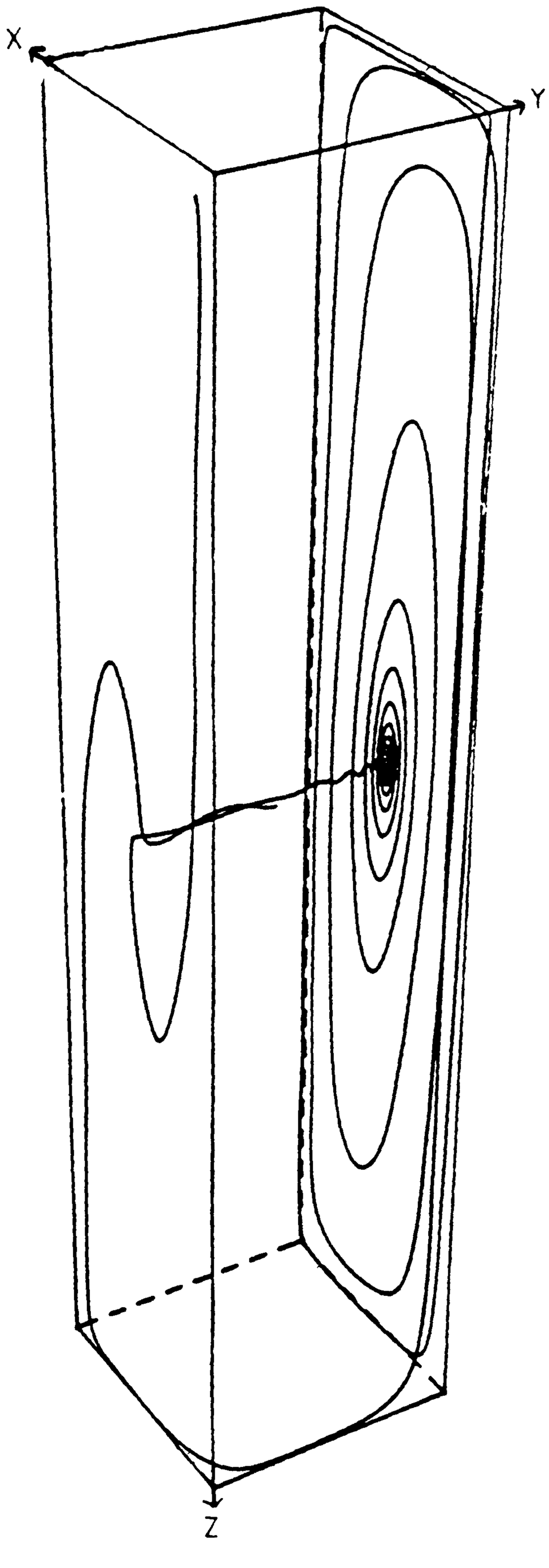

Figure 6.227

cavity (1,2,5)

Fluid = cerrobase, Ra = 10^3, Hy=1, Hz=5, grid=16x16x40

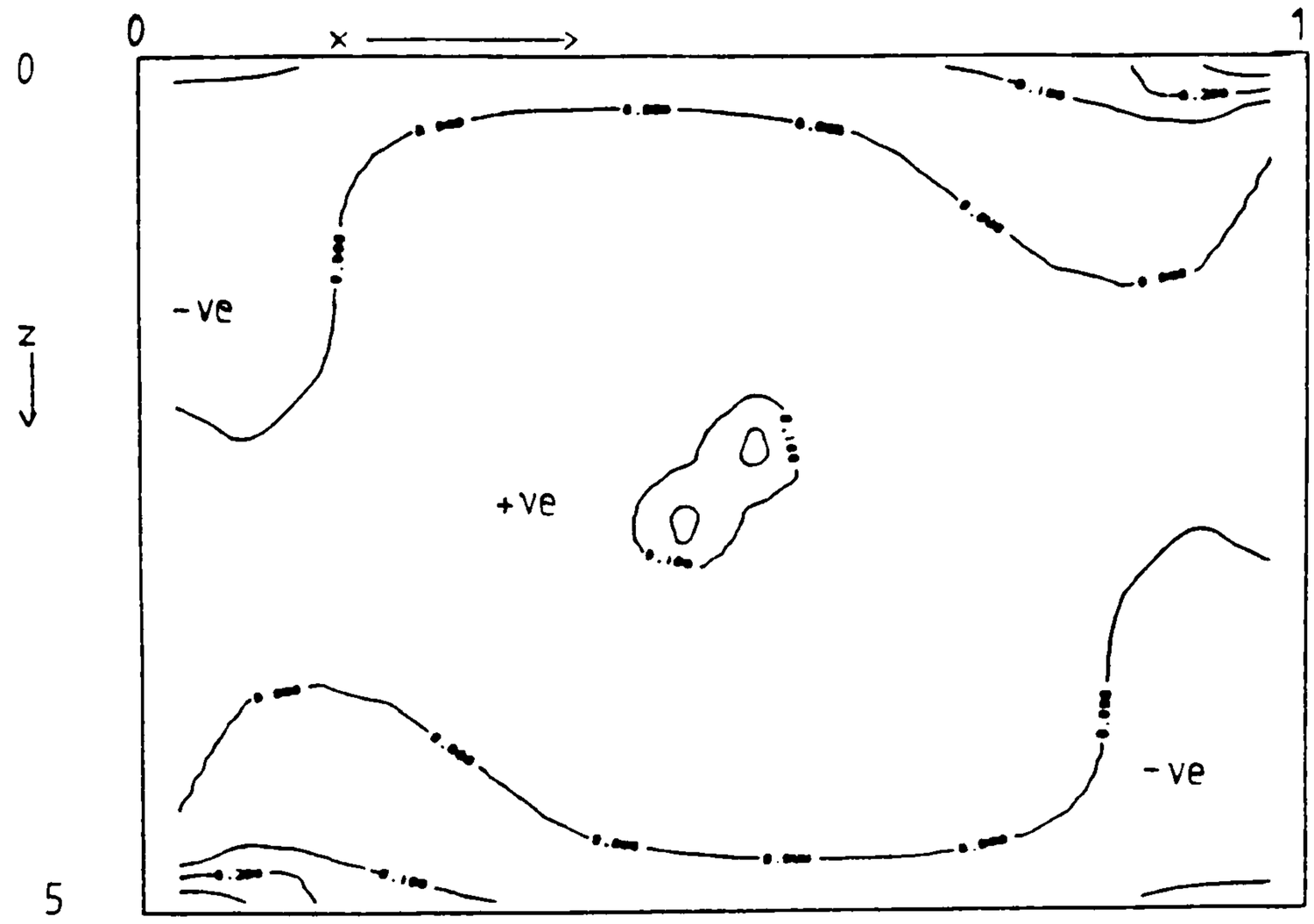

Figure 6.228 Contour plot of ratio R at plane A, near t.

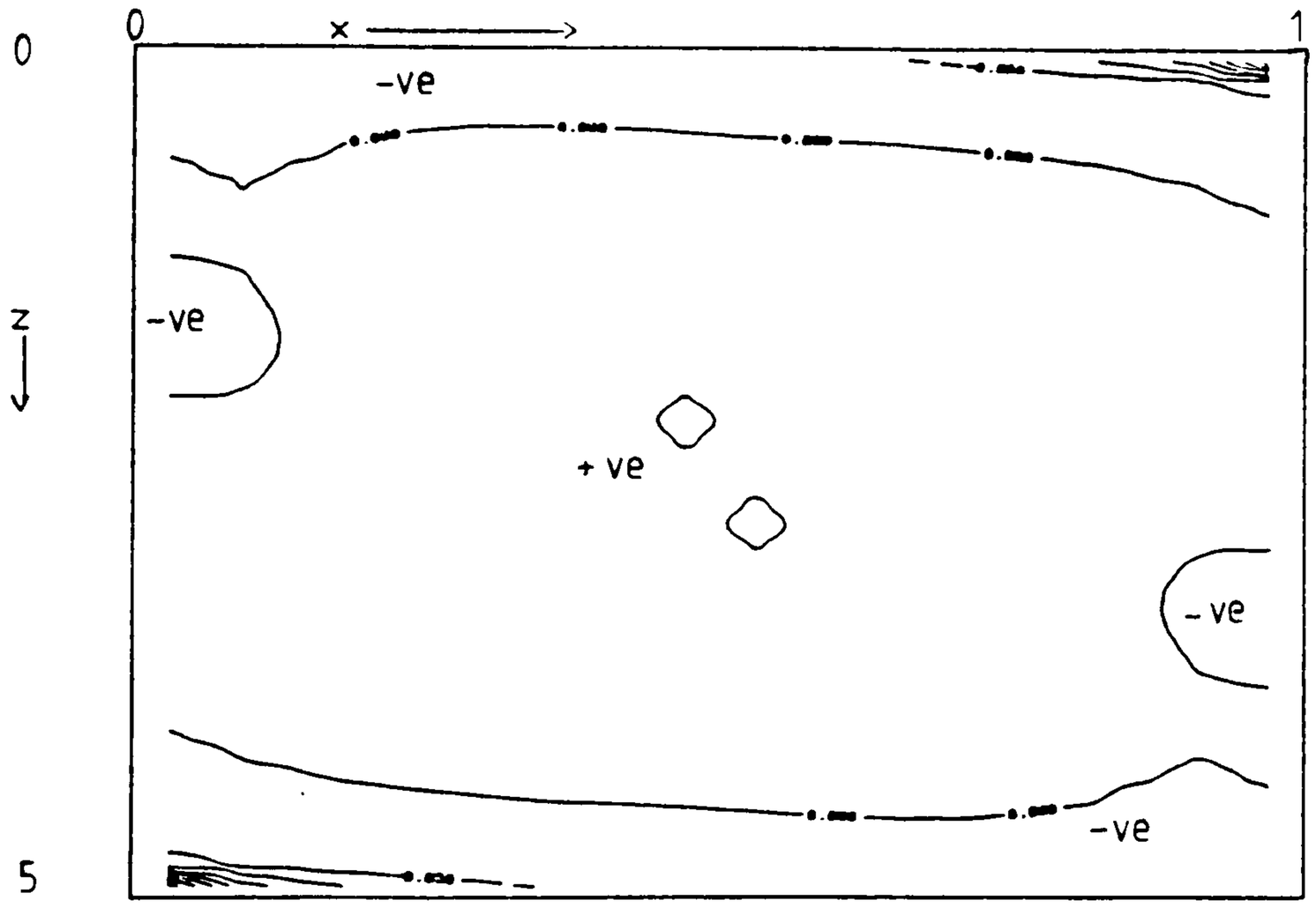

Figure 6.229 Contour plot of ratio R at plane B, near the symmetry plane

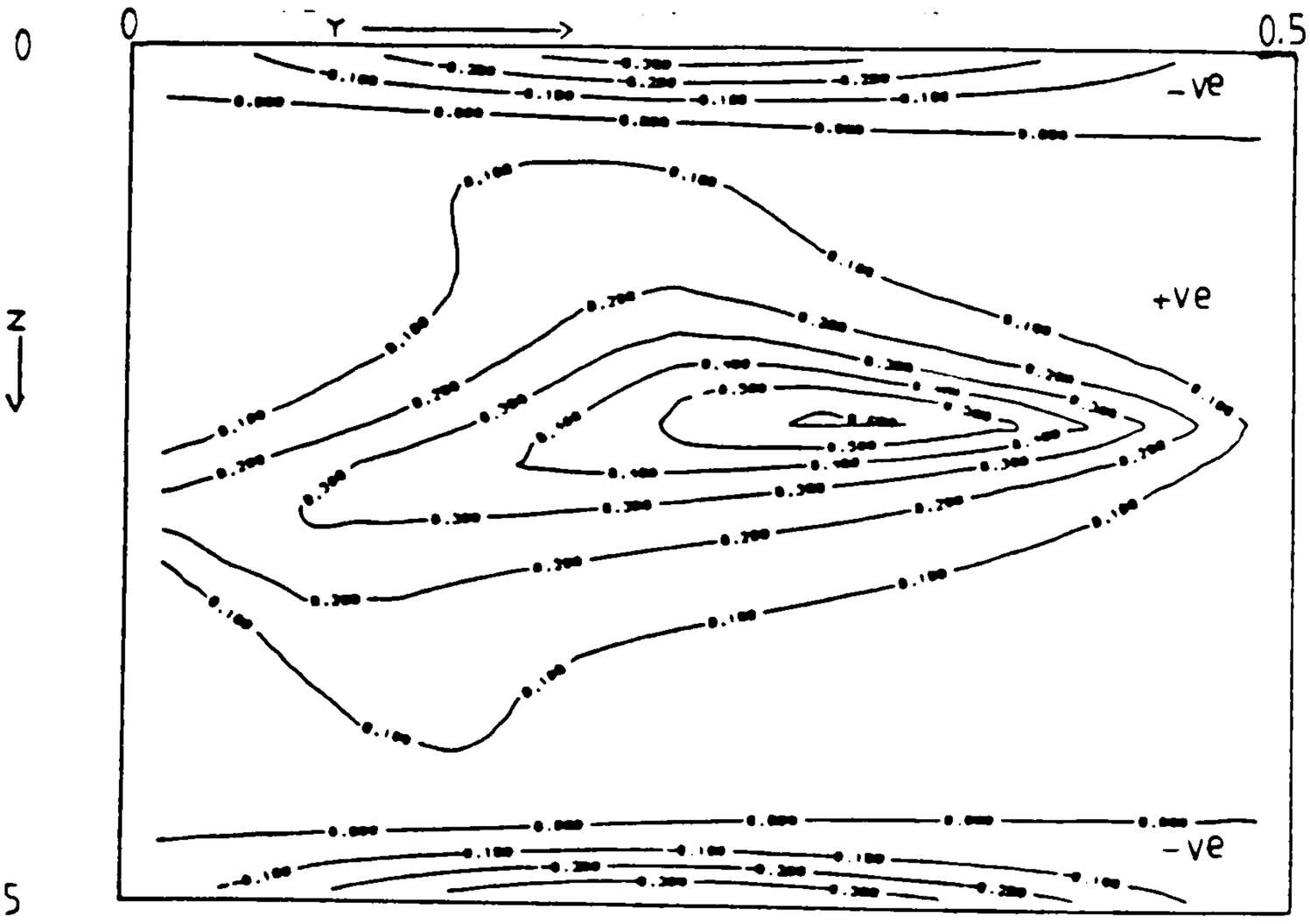

Figure 6.230 Contour plot of ratio R at plane C $(0.5 - hx/2, y, z)$

Fluid = cerrobase, Ra = 10^3, Hy=1, Hz=5, grid=16x16x40

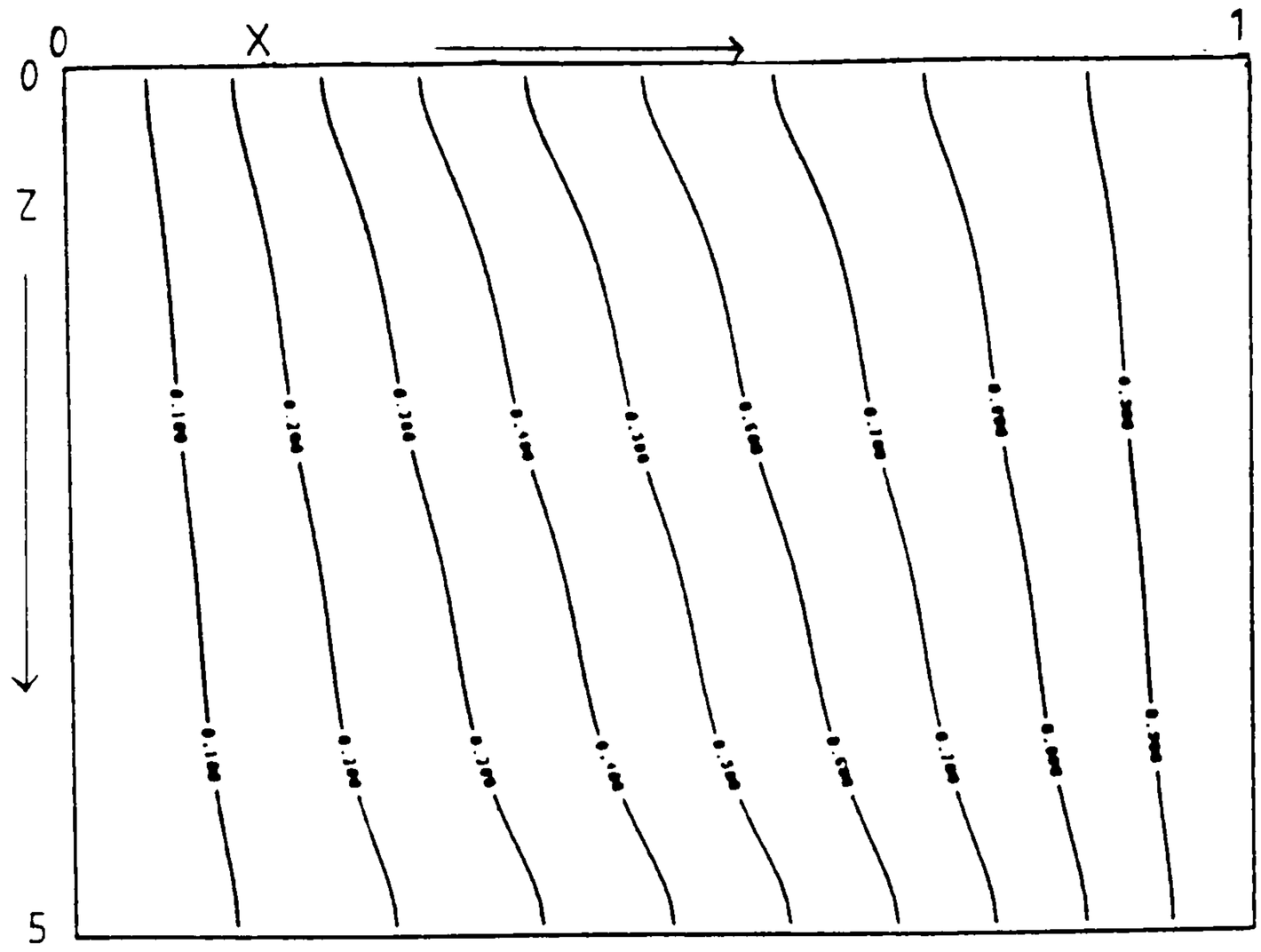

Figure 6.231 Isotherms at plane A, near the end wall

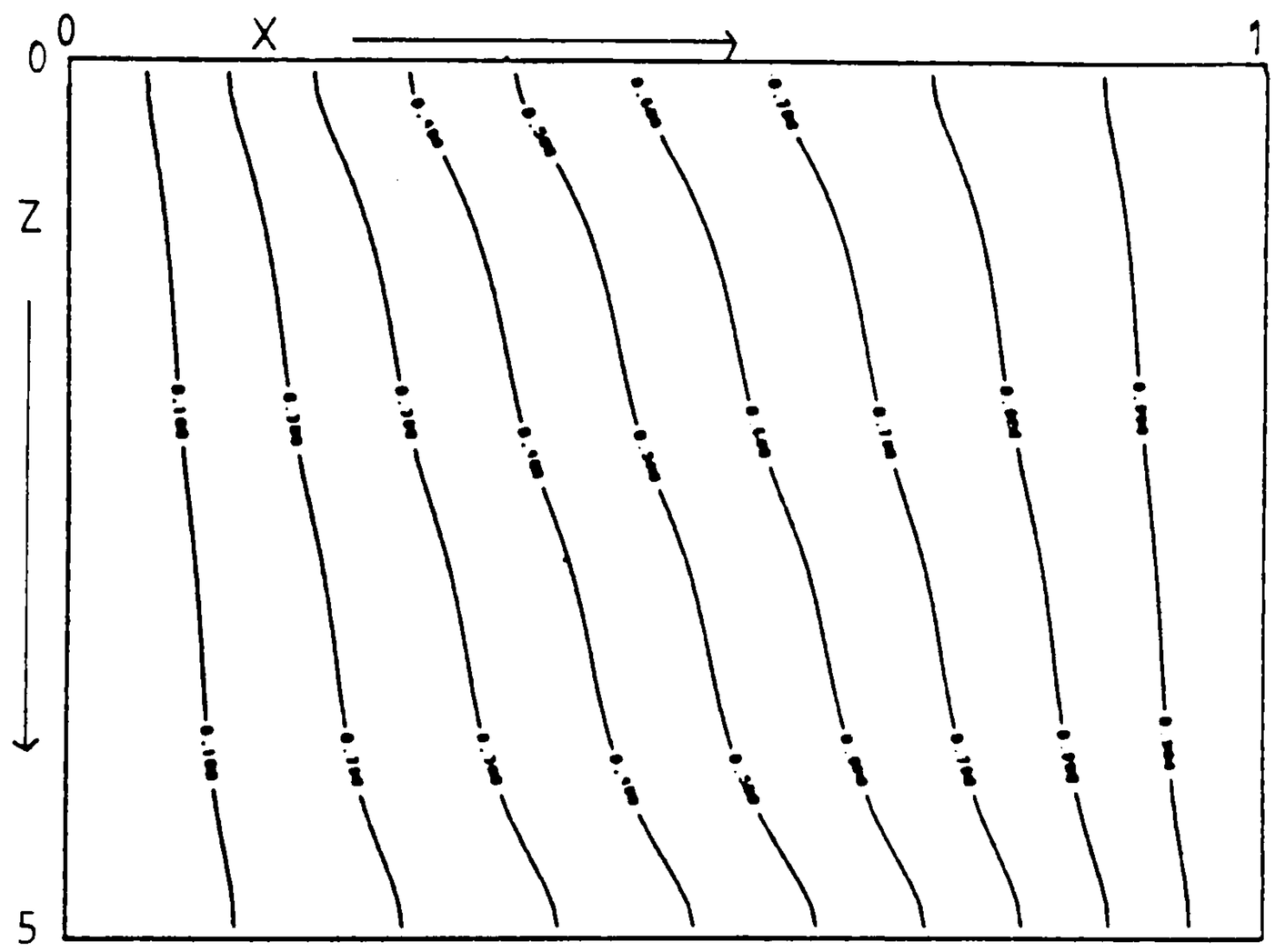

Figure 6.232 Isotherms at plane B, near the symmetry plane

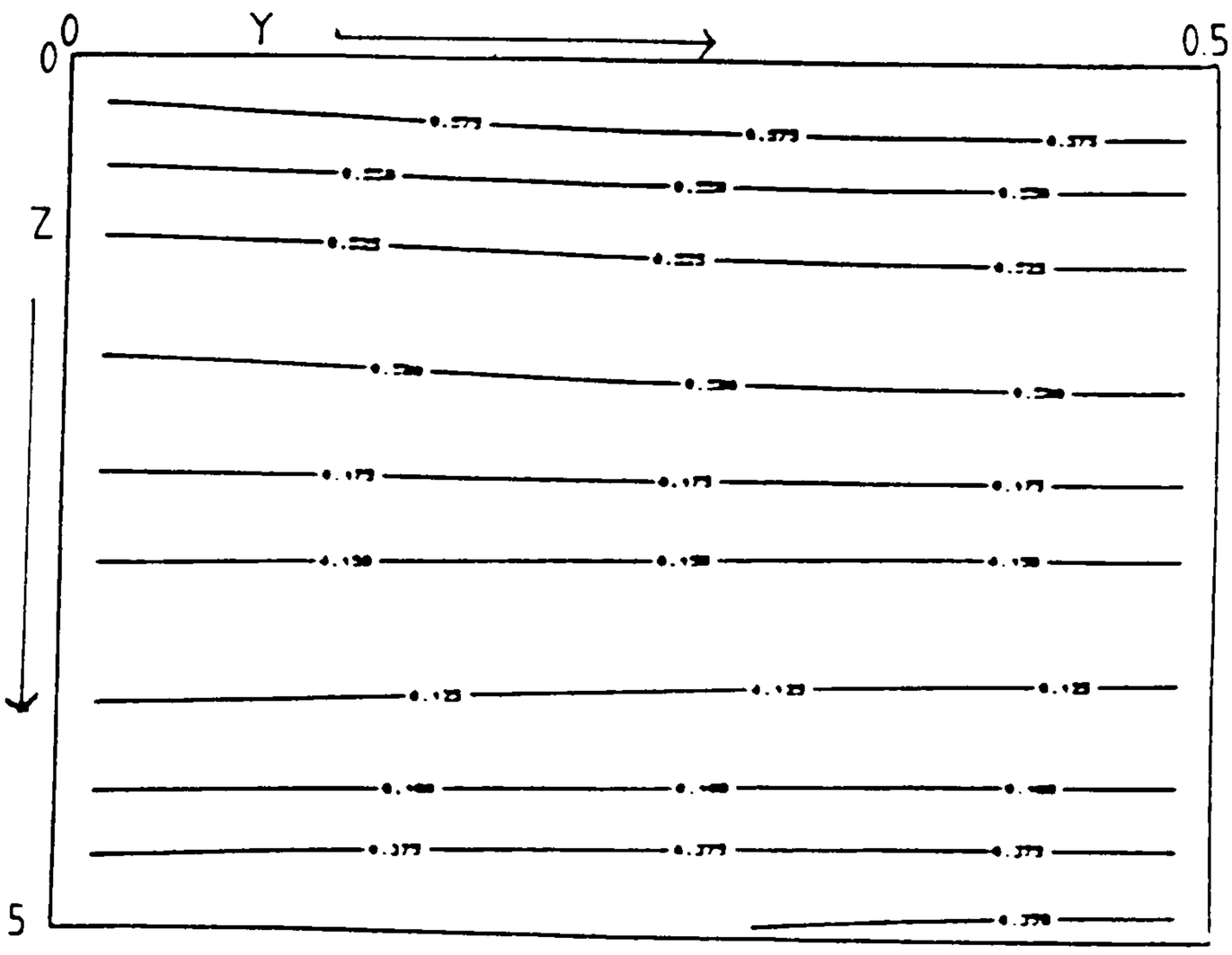

Figure 6.233 Isotherms at plane C, $(0.5 - hx/2, y, z)$

Fluid = cerrobase, Ra = 10^3, Hy=2, Hz=5, grid=16x16x40

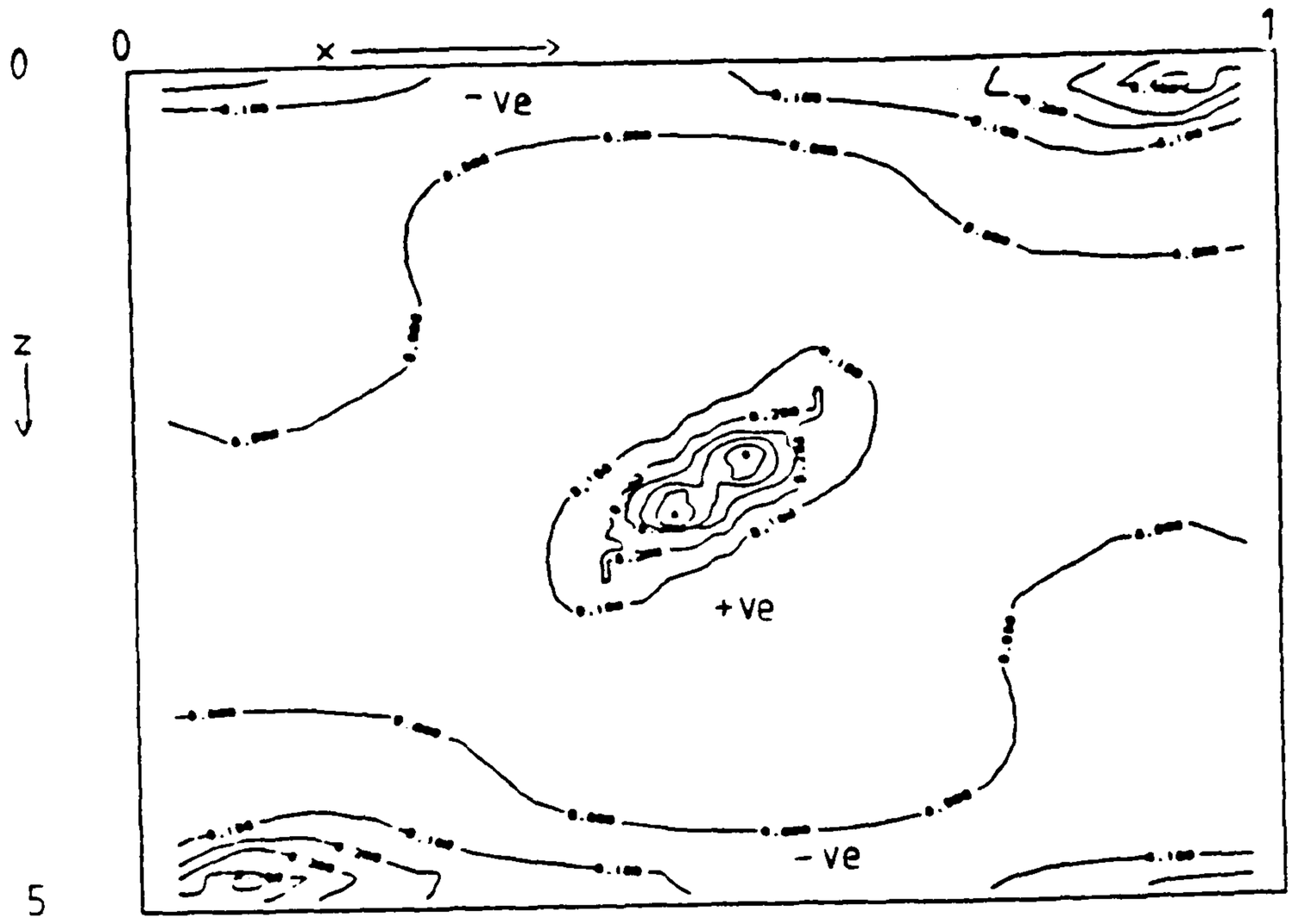

Figure 6.234 Contour plot of ratio R at plane A, near the end wall

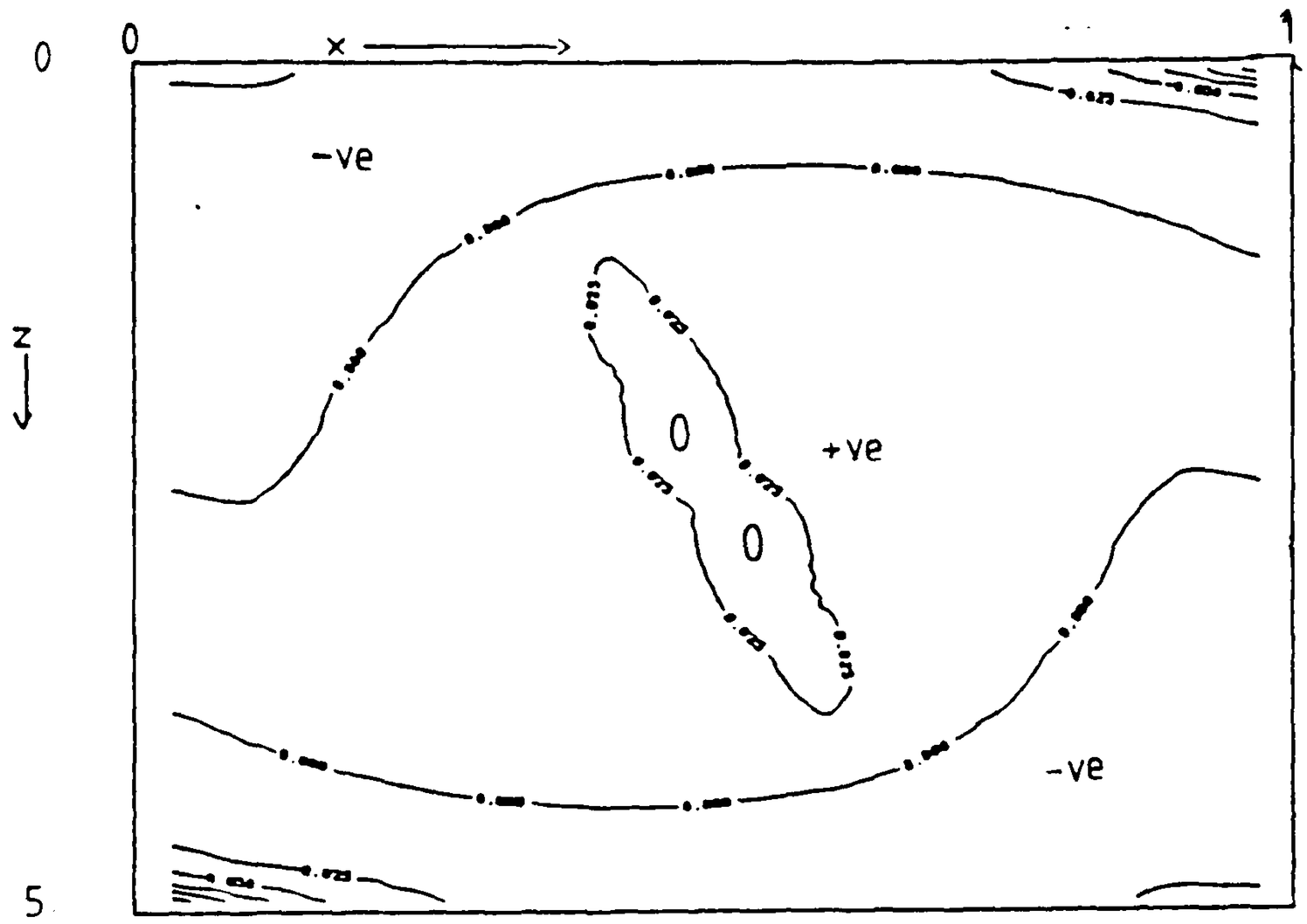

Figure 6.235 Contour plot of ratio R at plane B, near the symmetry plane

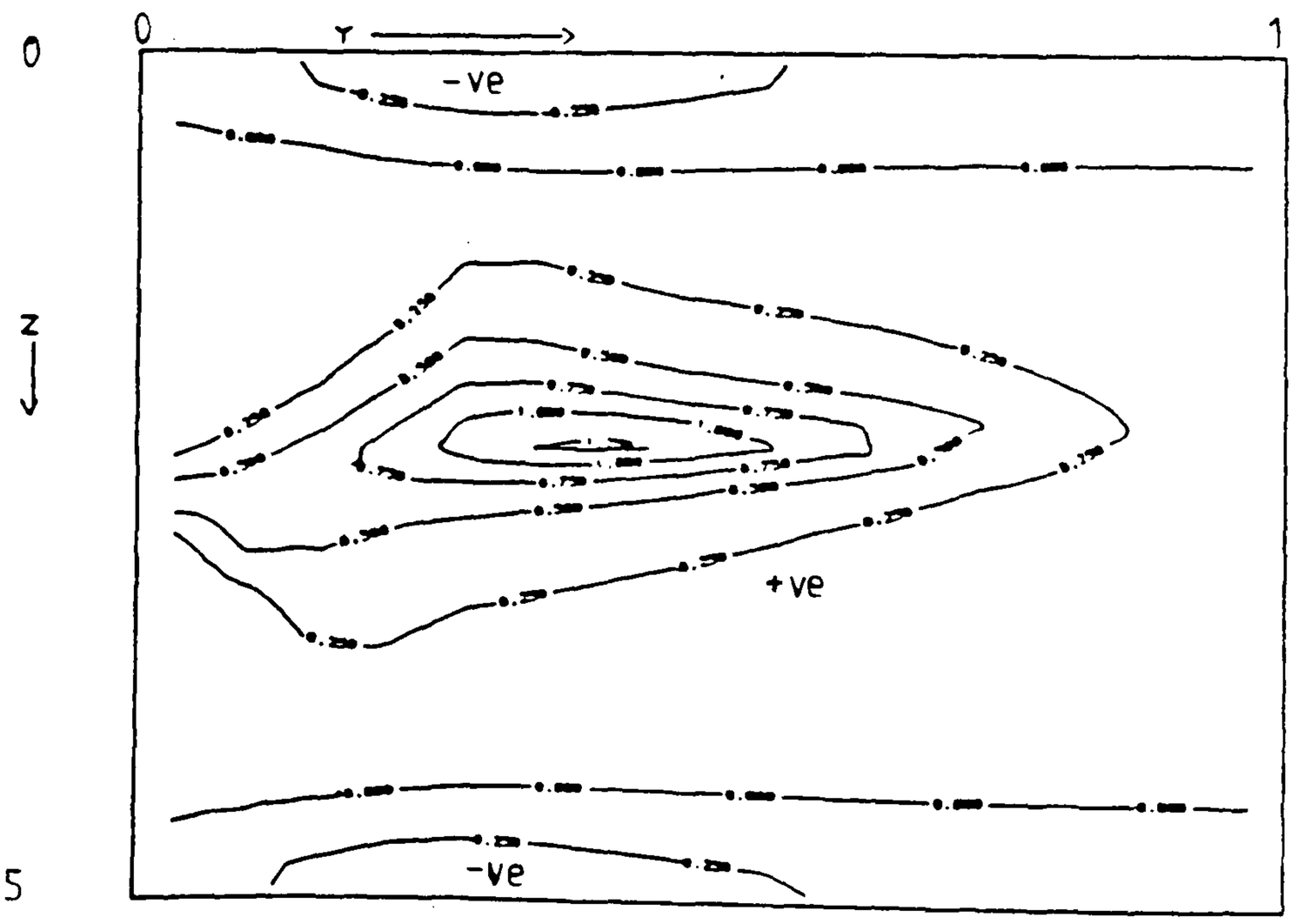

Figure 6.236 Contour plot of ratio R at plane C $(0.5 - hx/2, y, z)$

Fluid = cerrobase, Ra = 10^3, Hy=2, Hz=5, grid=16x16x40

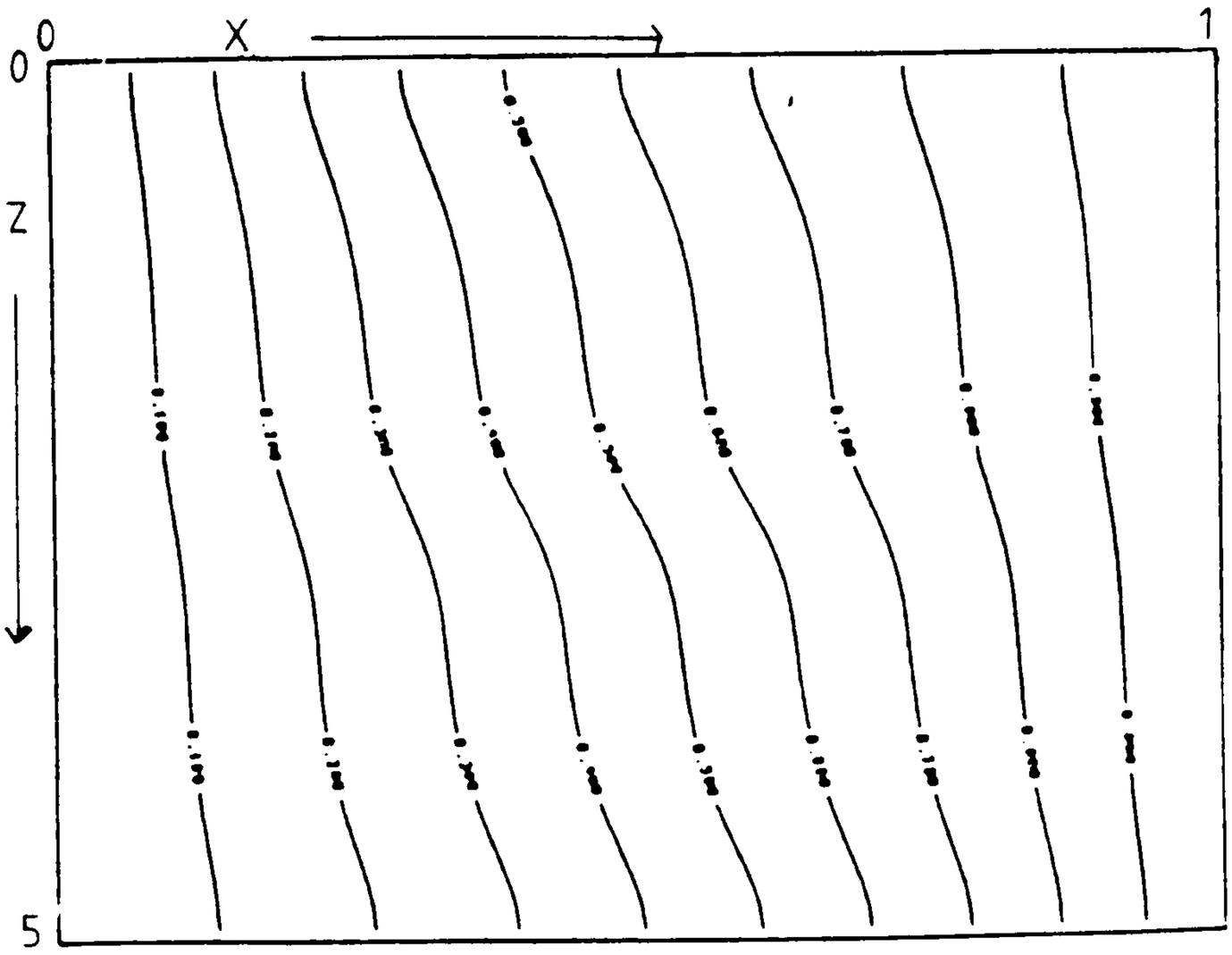

Figure 6.237 Isotherms at plane A, near the end wall

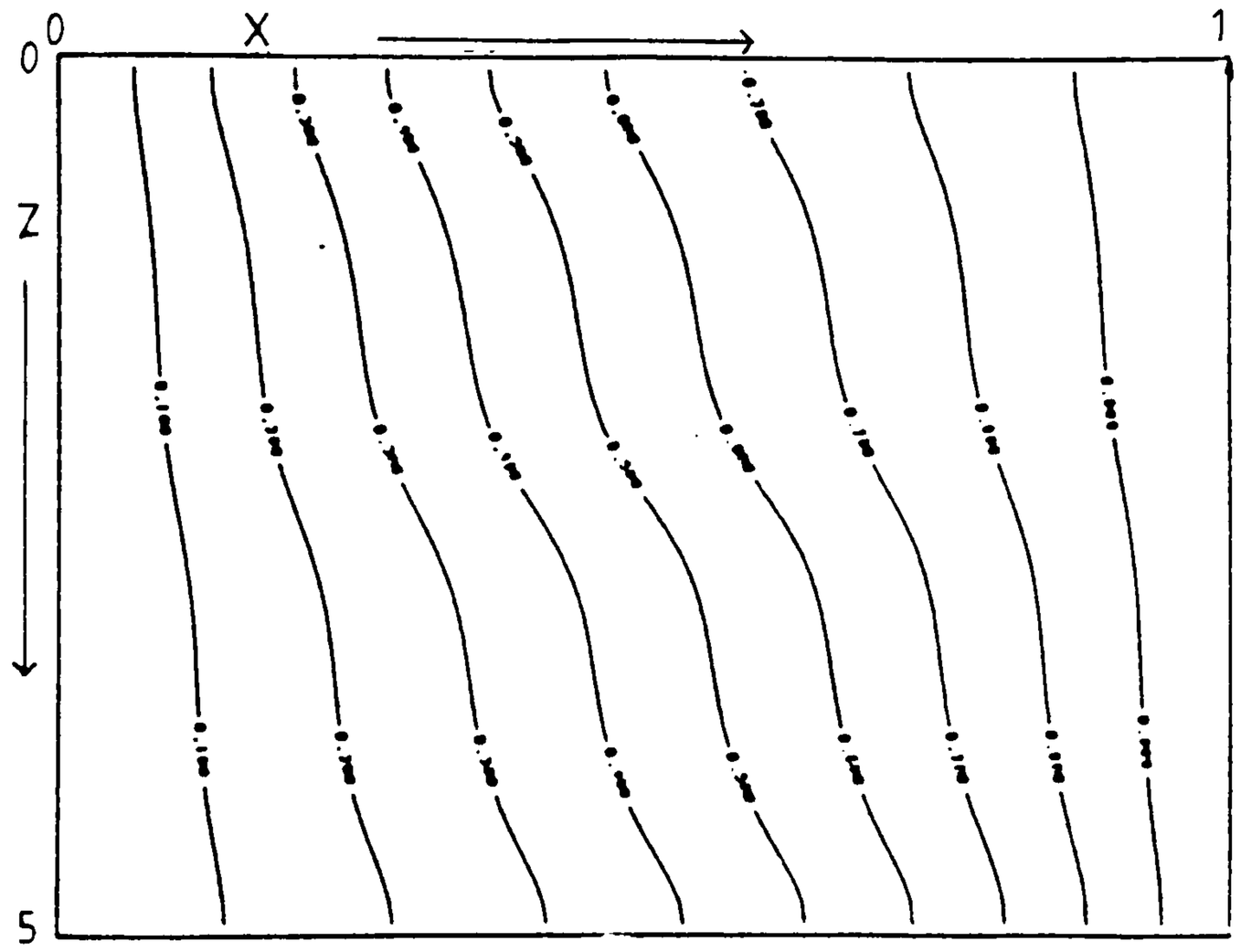

Figure 6.238 Isotherms at plane B, near the symmetry plane

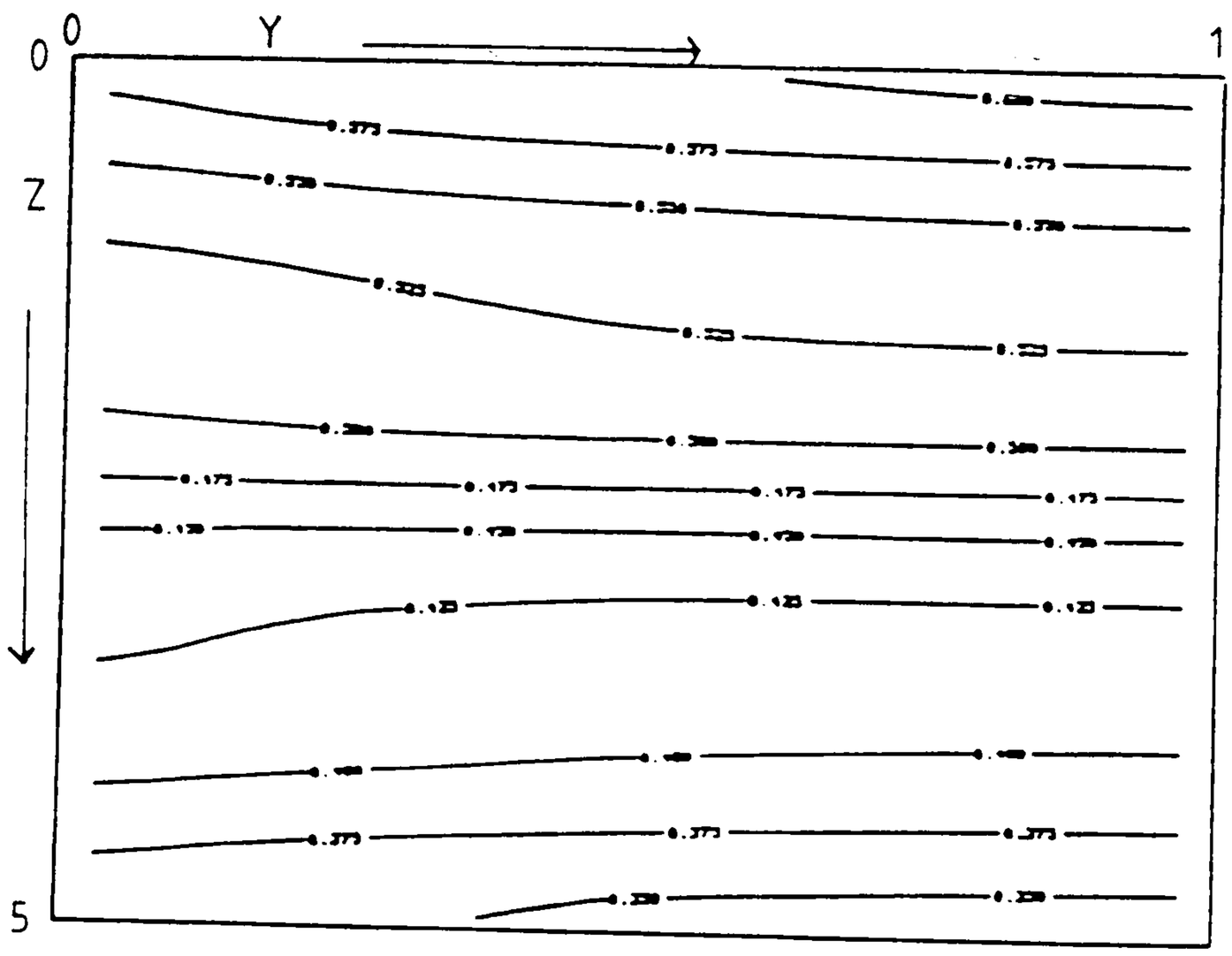

Figure 6.239 Isotherms at plane C, $(0.5 - hx/2, y, z)$

Fluid = cerrobase, Ra = 10^3, Hy=5, Hz=5, grid=16x40x40

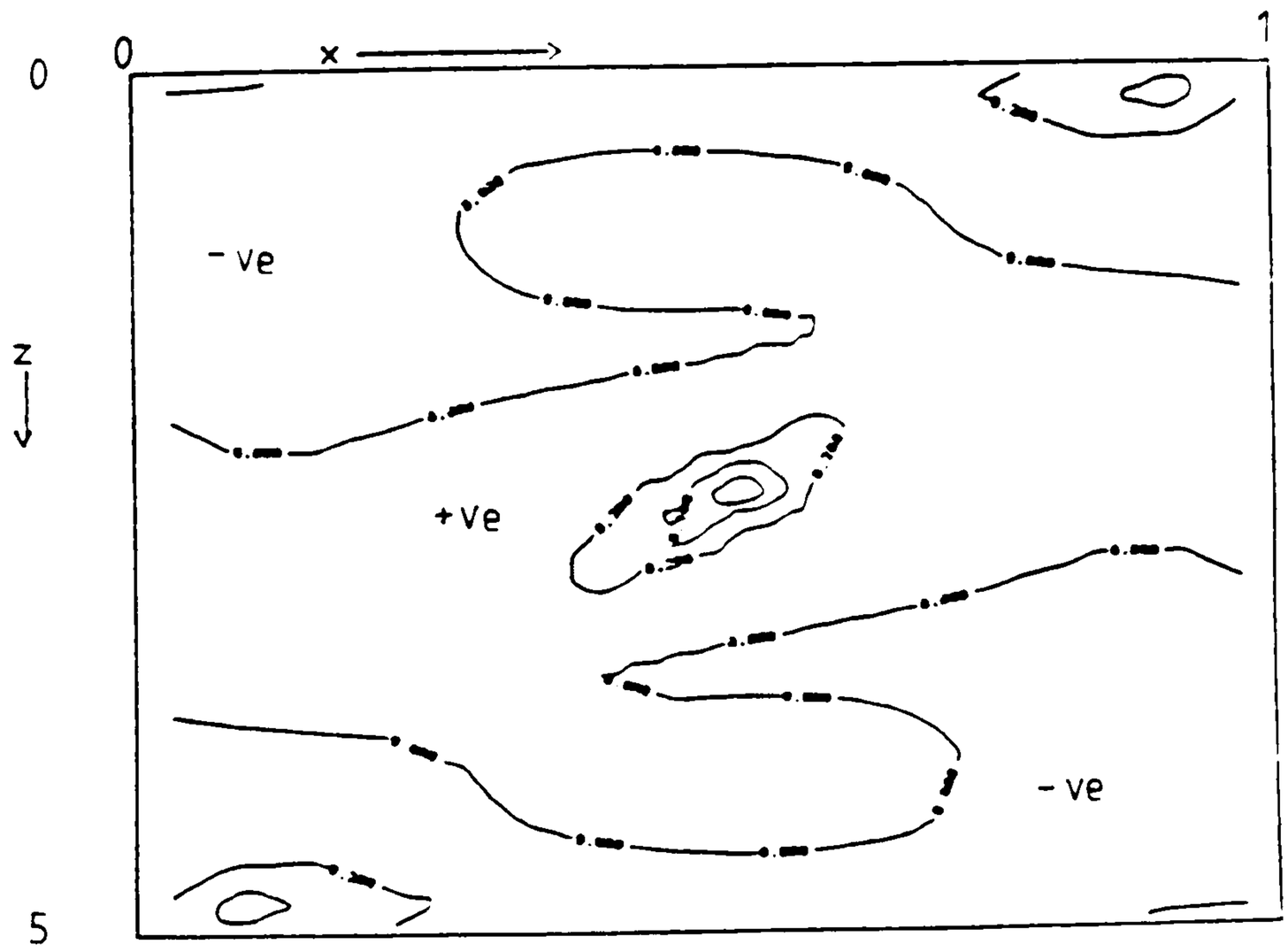

Figure 6.240 Contour plot of ratio R at plane A, near the end wall

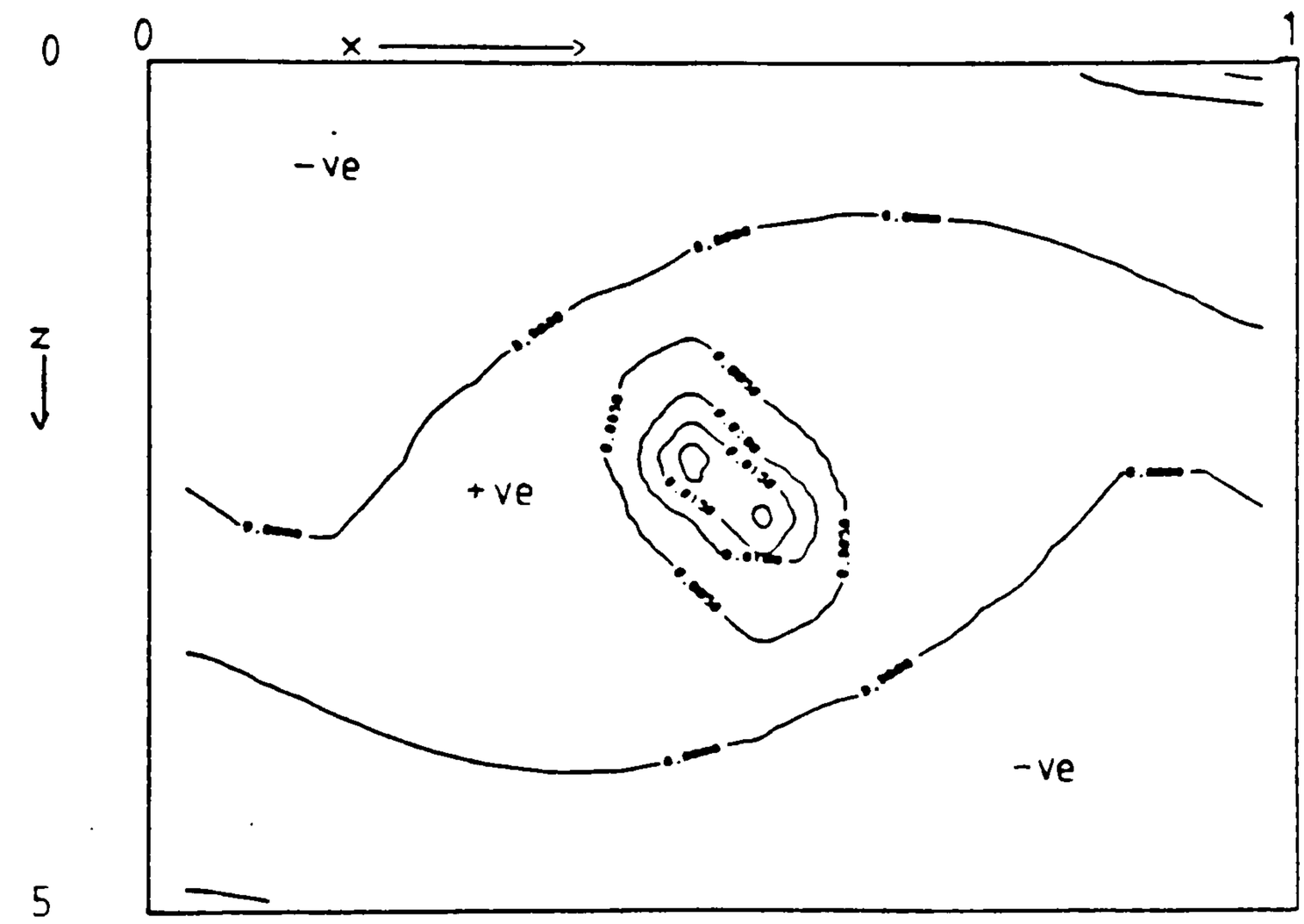

Figure 6.241 Contour plot of ratio R at plane B, near the symmetry plane

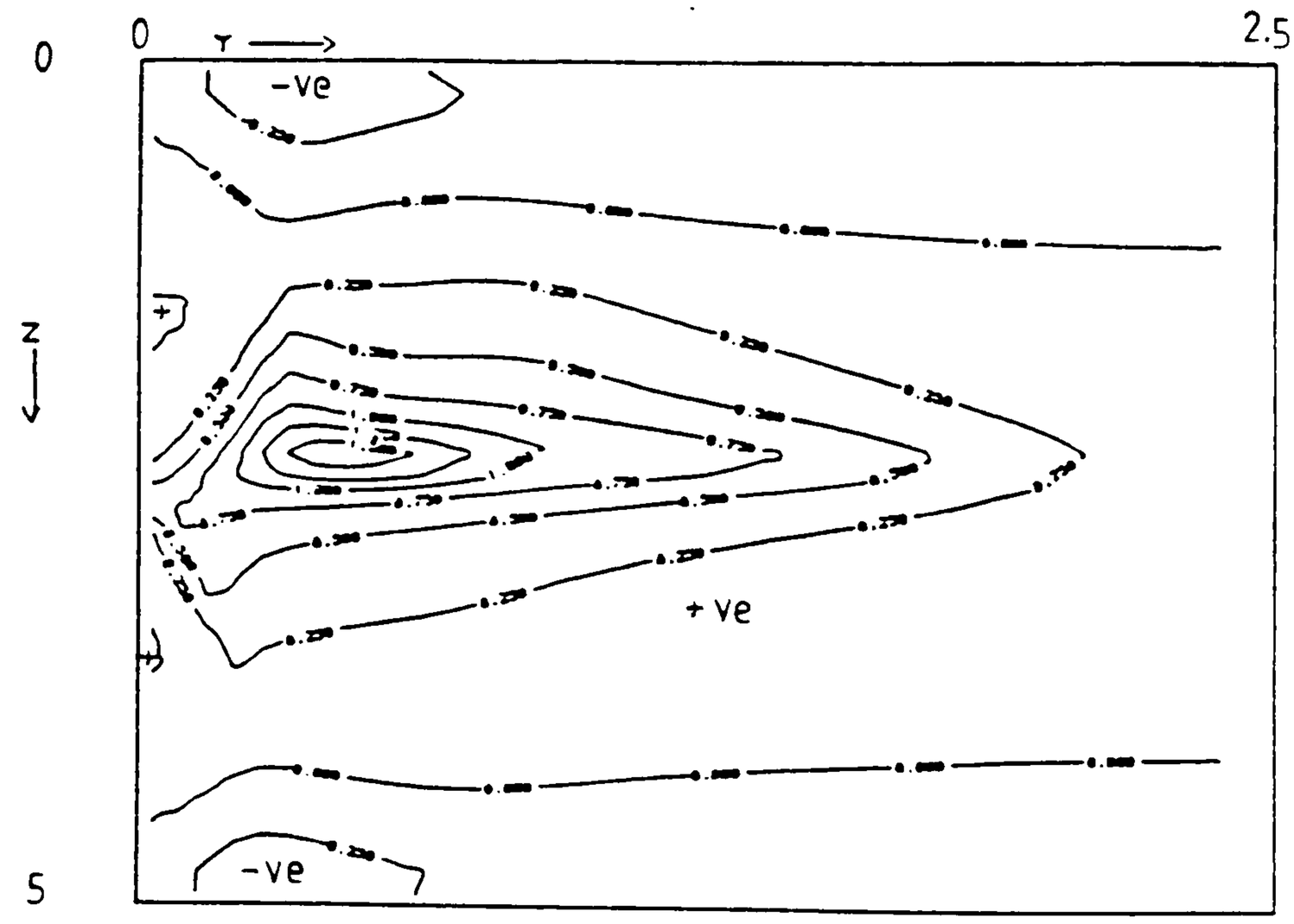

Figure 6.242 Contour plot of ratio R at plane C $(0.5 - hx/2, y, z)$

Fluid = cerrobase, Ra = 10^3, Hy=5, Hz=5, grid=16x40x40

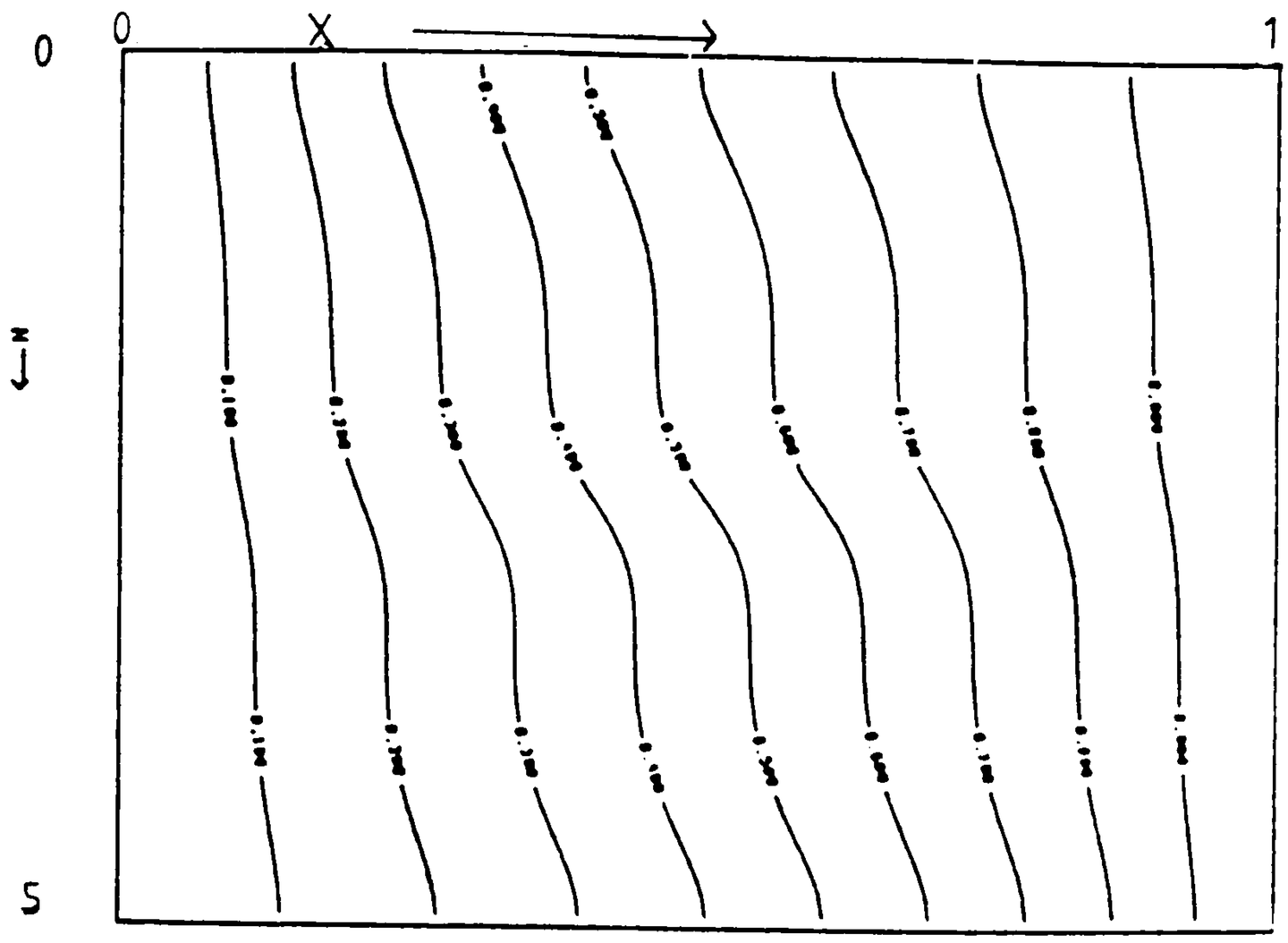

Figure 6.243 Isotherms at plane A, near the end wall

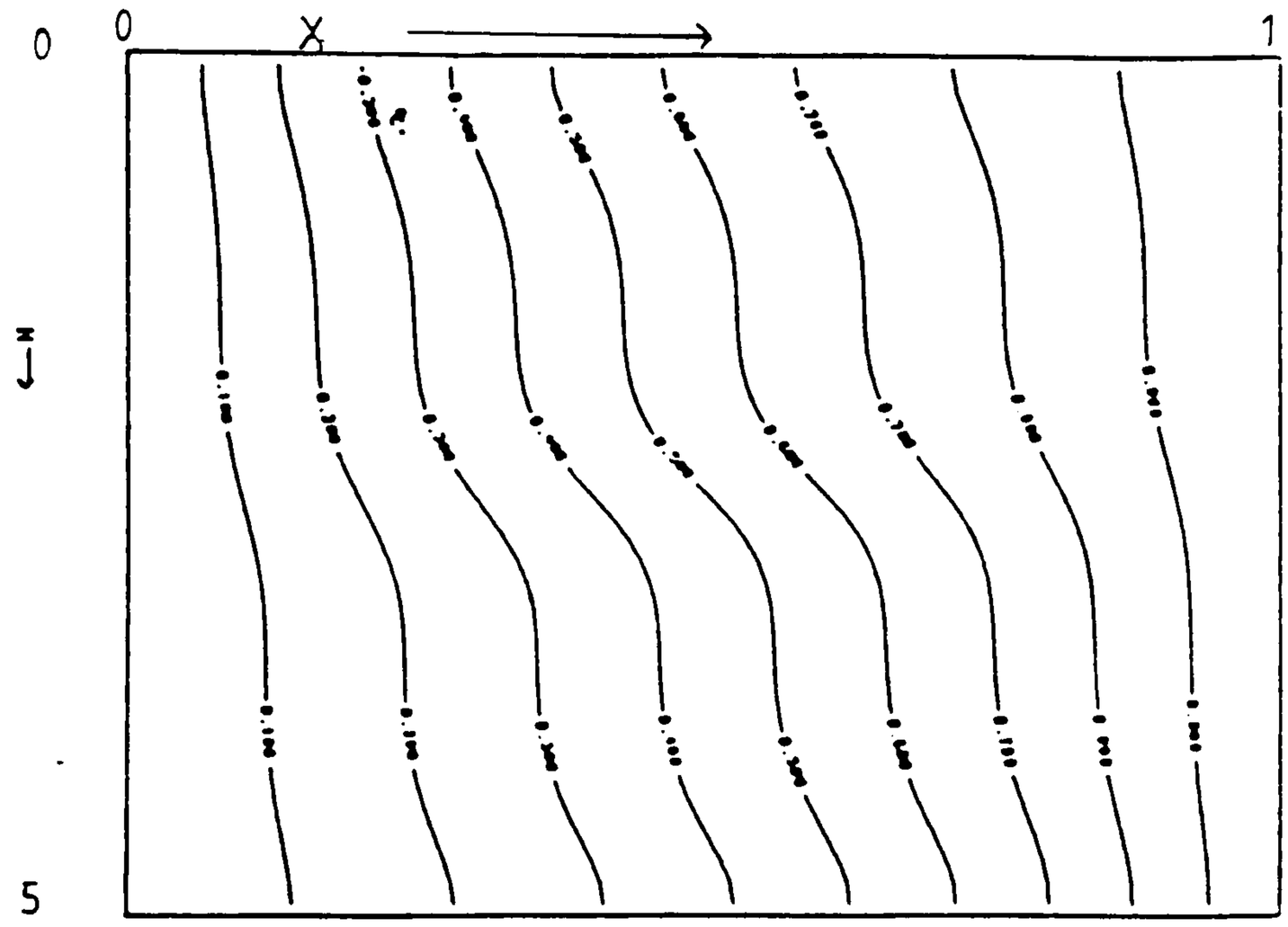

Figure 6.244 Isotherms at plane B, near the symmetry plane

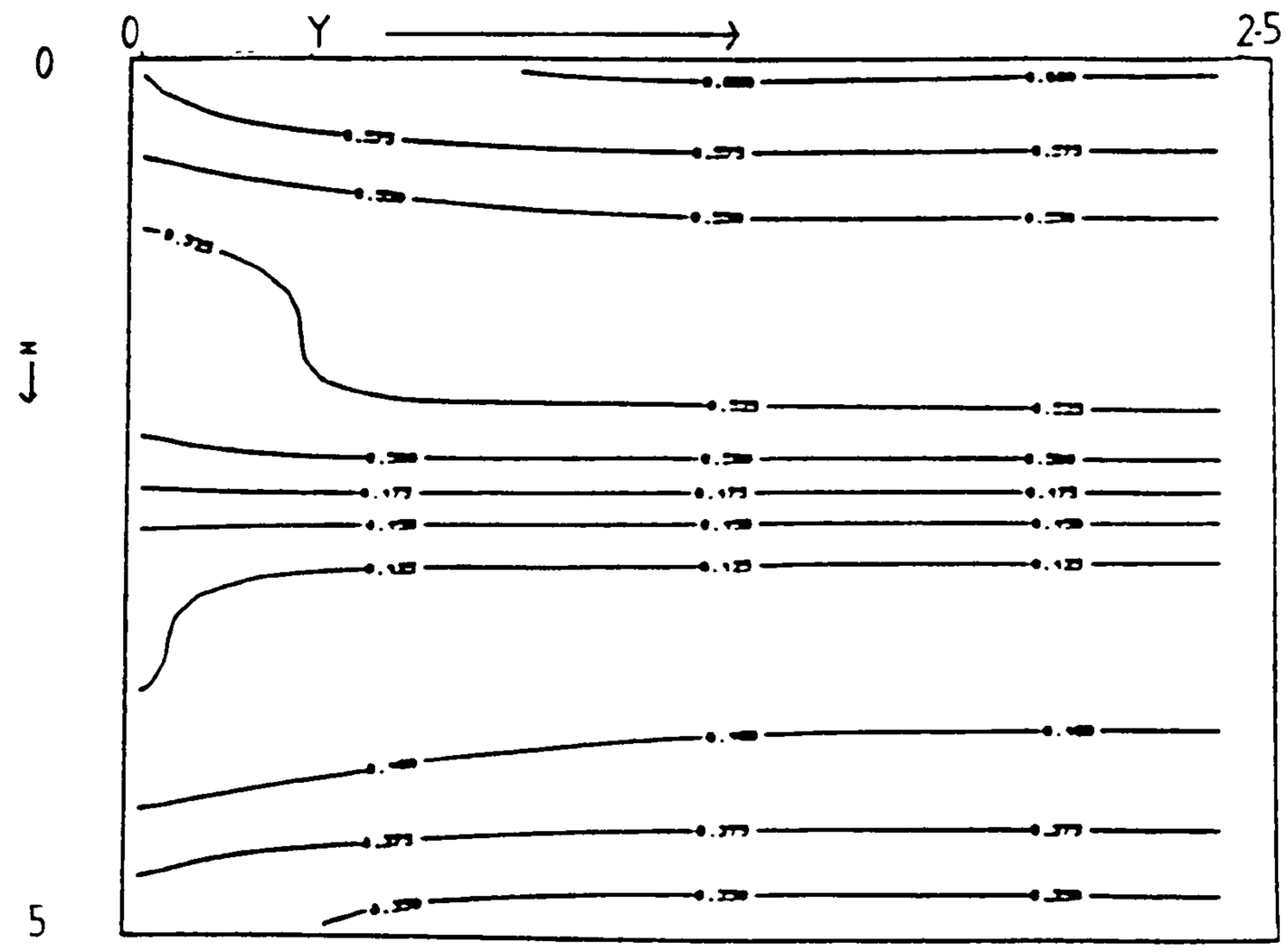

Figure 6.245 Isotherms at plane C, $(0.5 - hx/2, y, z)$

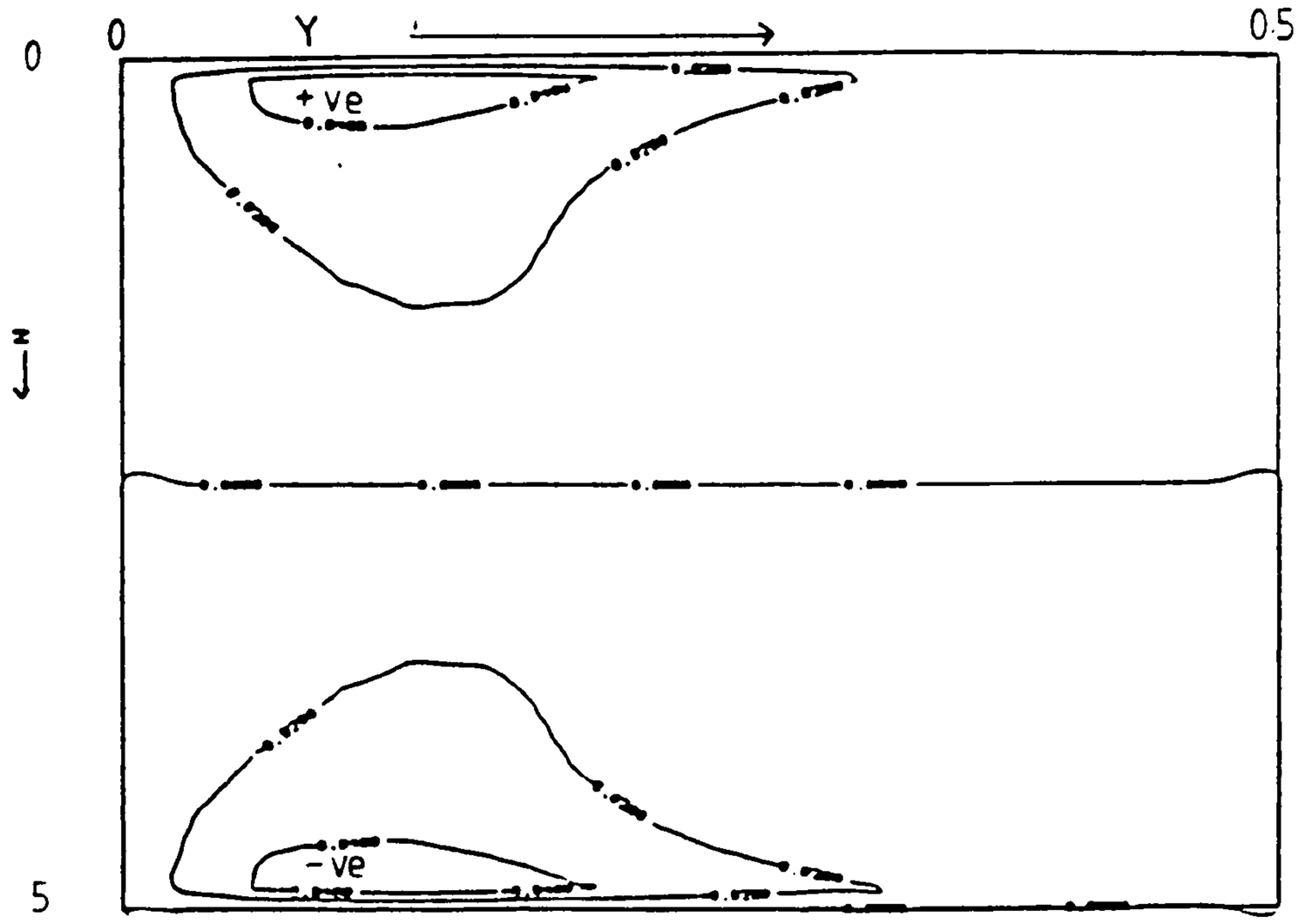

Figure 6.246 $\partial\theta/\partial y$ at plane C, $(0.5 - hx/2, y, z)$, Hy=1

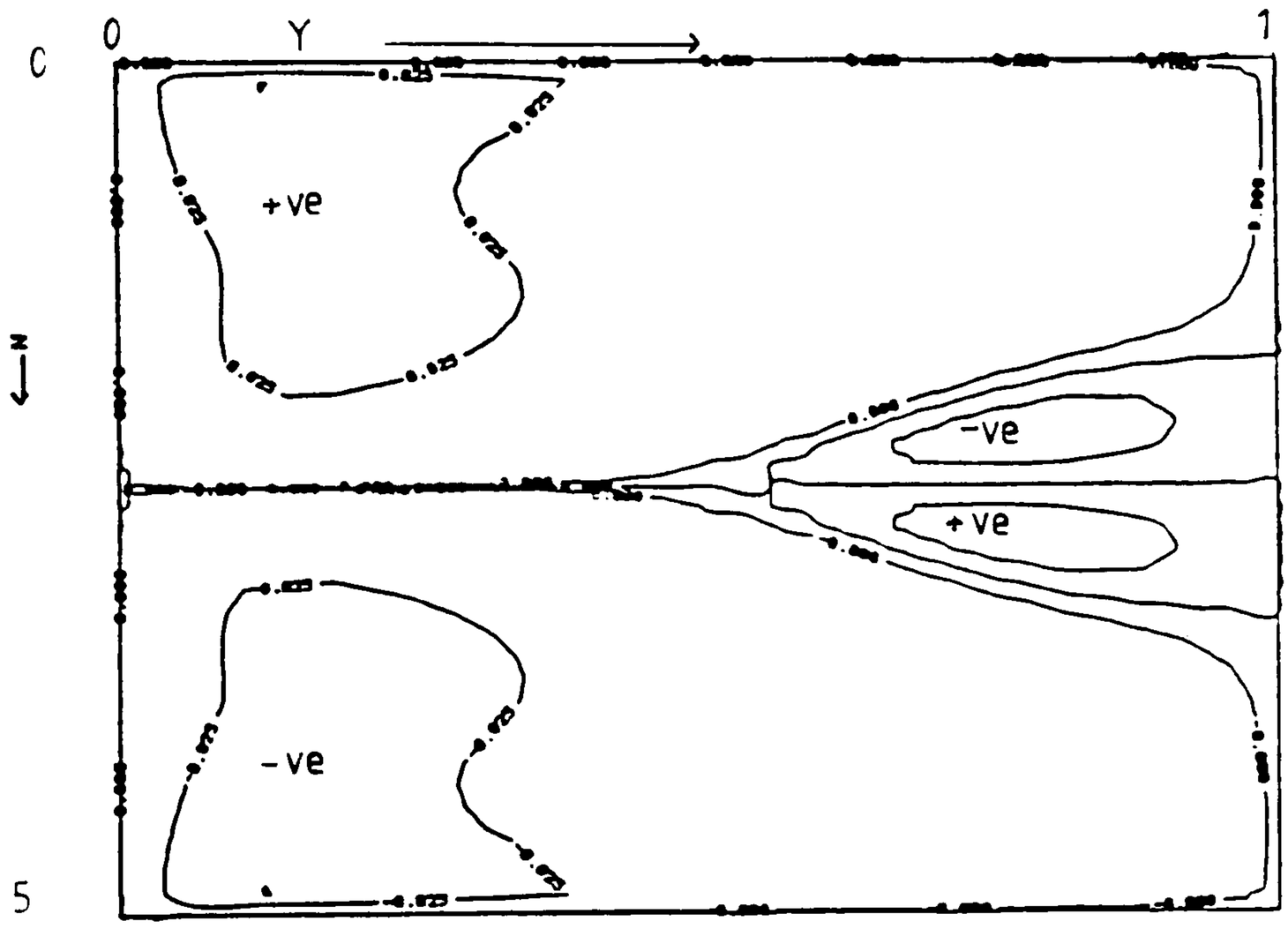

Figure 6.247 $\partial\theta/\partial y$ at plane C, $(0.5 - hx/2, y, z)$, Hy=2

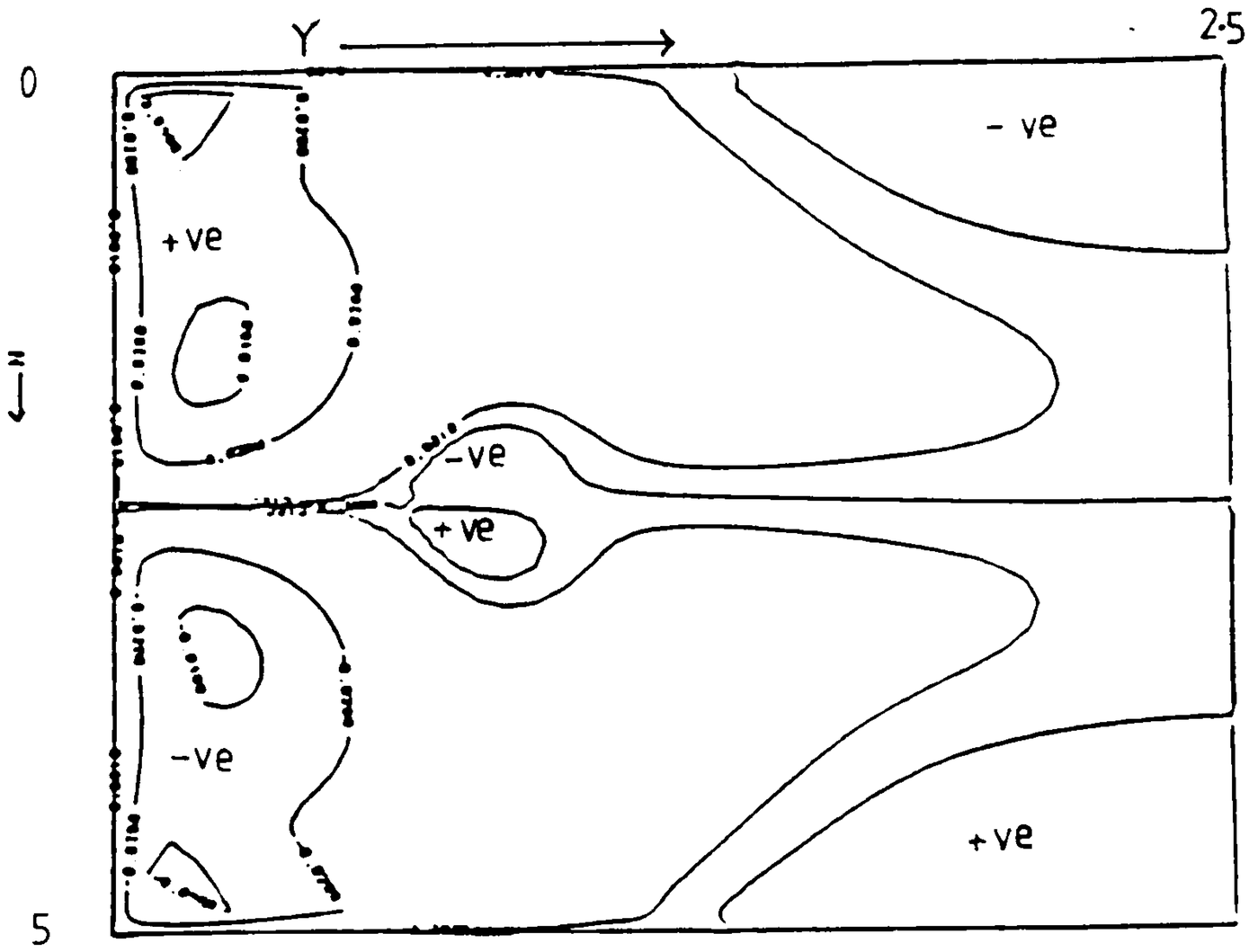

Figure 6.248 $\partial\theta/\partial y$ at plane C, $(0.5 - hx/2, y, z)$, Hy=5

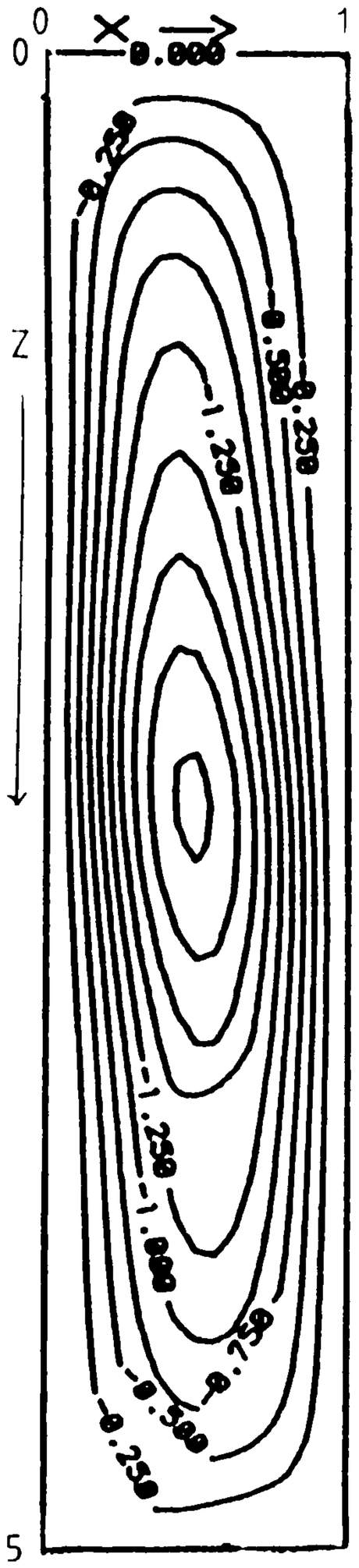

Figure 6.249 Streamlines, Hy=5

Graph A: cerrobase at Ra = 10^3, Hy=1, Hz=5

Graph B: cerrobase at Ra = 10^3, Hy=2, Hz=5

Graph C: cerrobase at Ra = 10^3, Hy=5, Hz=5

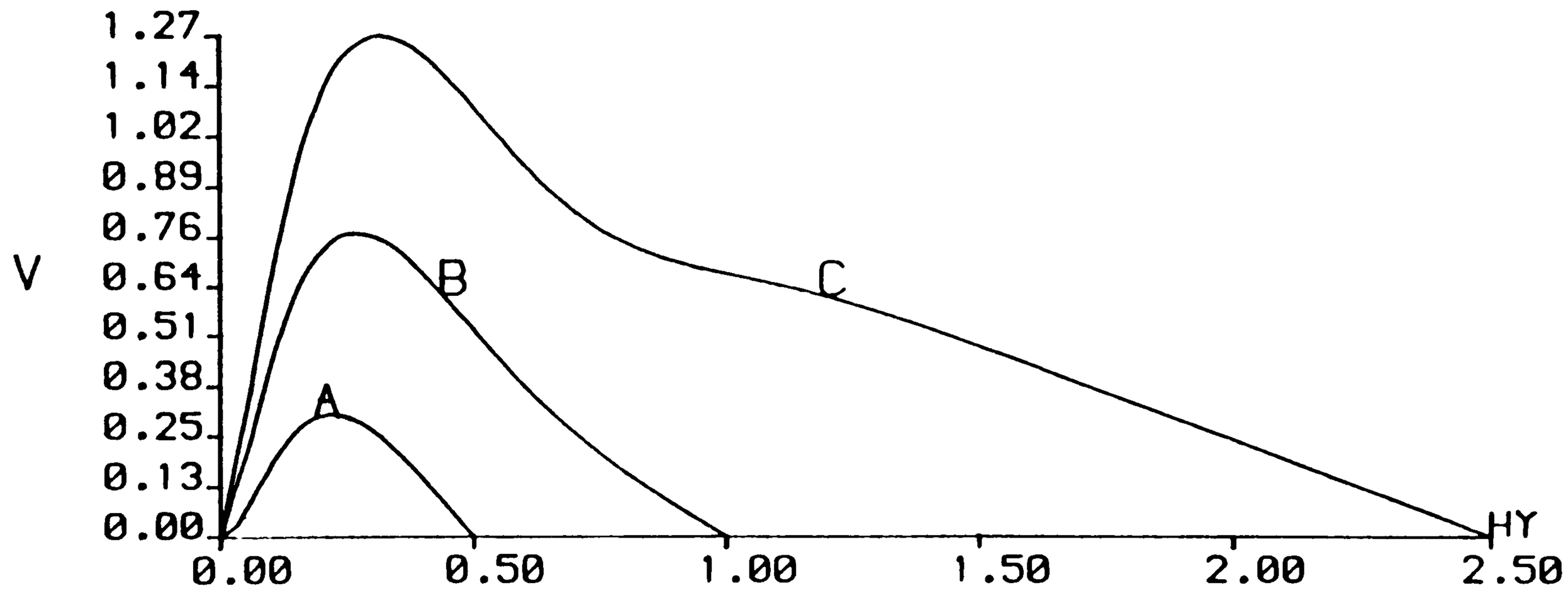

Figure 6.250 Axial-velocity along $(0.5, y, 2.5)$

6.8.4 Results obtained for cerrobase, Ra=5x10^3

The fluid flow behaviour for this case in a cavity with length aspect ratio Hy=1.0 is described by a single forward roll as illustrated in Figure 6.251. In this figure the particle path has been traced from $(0.1, 0.01, 0.1)$.

Figures 6.252-6.254 are contour plots of R at planes A, B and C respectively for Hy=1. There is only one strong region of axial flow in the centre and two weak regions near the upper and lower walls. Positive R contours are attached to the side walls. Strong return flow exists on the right hand corner at the top of the hot wall and the left hand corner at the bottom of the cold wall. Figure 6.255-6.257 are isotherm plots at planes A, B and C respectively for Hy=1.

The fluid flow behaviour in the cavity with aspect ratio Hy=2.0 is described by a single forward roll as illustrated in Figure 6.258. The particle path in this figure has been traced from the point $(.5, .7, 2.0)$. The plot exhibits negative axial velocities near the centre of the cavity and also shows the strong return flow. Figure 6.259 is a view from the point $(-10.0, 0.5, 2.5)$ of the particle path illustrated in Figure 6.258 and exhibits clearly the particle travelling towards the end wall in the inner spiral.

Figures 6.260-262 are contour plots of the ratio R at the planes A, B and C respectively for Hy=2. The contour plots near the end wall indicate a strong inner core with positive R contours attached to the side walls. Figures 6.261 and 6.262 clearly exhibit the reverse axial flow in the forward roll. The region of the reverse axial flow near the centre of the cavity in the upper half appears to be associated with sign changes of $\partial\theta/\partial y$ along the axial direction in the upper half of the cavity, see Figure 6.267. Figures 6.263-6.265 are isotherm plots at planes A, B and C respectively for Hy=2. These are much more convective than those obtained with Hy=1.0.

Figure 6.266 is a contour plot of $\partial\theta/\partial y$ near the plane x=0.5 for Hy=1. $\partial\theta/\partial y$ changes sign once along the centre line. This change appears to be associated with the convection of heat in the inner core. Figure 6.267 is a contour plot of $\partial\theta/\partial y$ near the plane x=0.5 for Hy=2. The lower half of the cavity is dominated by negative $\partial\theta/\partial y$. The upper half of the cavity is dominated by the positive values of $\partial\theta/\partial y$ near the end wall and negative values of $\partial\theta/\partial y$ near the symmetry plane. The change of sign in the upper half of the cavity is possibly due to numerical errors.

Figure 6.268 is a plot of streamlines near the symmetry plane for Hy=2, it reveals a primary recirculating flow.

Figure 6.269 is the axial-velocity profile along the centre line for Hy=1.0 and 2.0.

The flow is restricted in the shorter cavity. A reverse roll or a two-dimensional flow does not exist for Hy $\leq$ 2.0.

Again, Jones [27] obtained two cat's eye cells, one on top of another for this fluid at Ra = $5x10^3$ with the two-dimensional problem. These cells do not appear in the three-dimensional problem as can be see in the streamline plot.

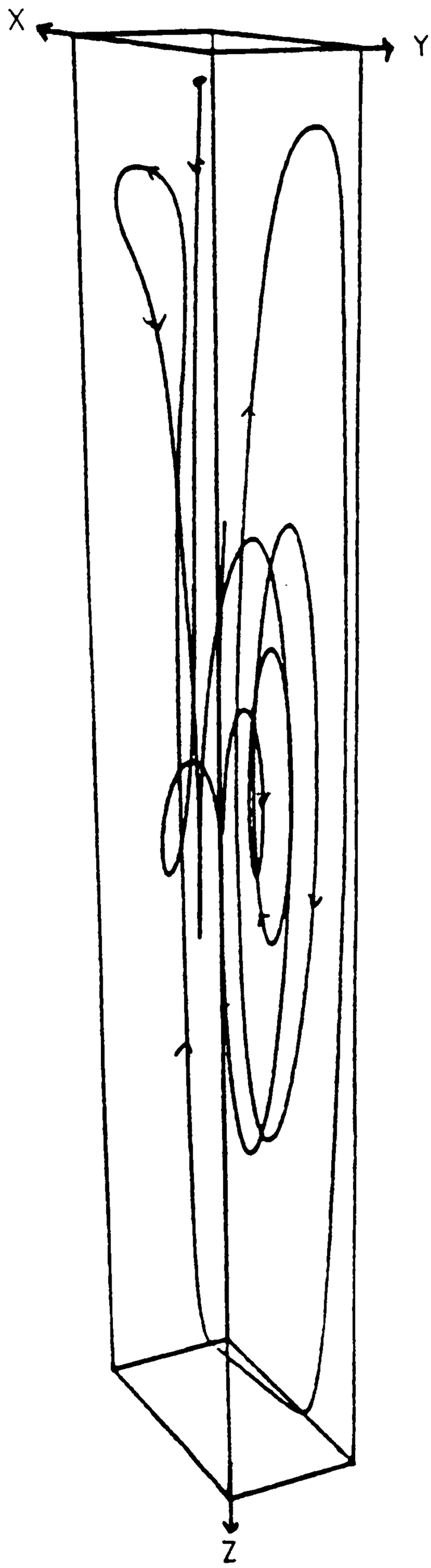

Figure 6.251 Particle track for cerrobase at Ra = 5×10^3,
cavity (1,1,5) grid = 16x16x40

Fluid = cerrobase, Ra = 5×10^3, Hy=1, Hz=5, grid=16x16x40

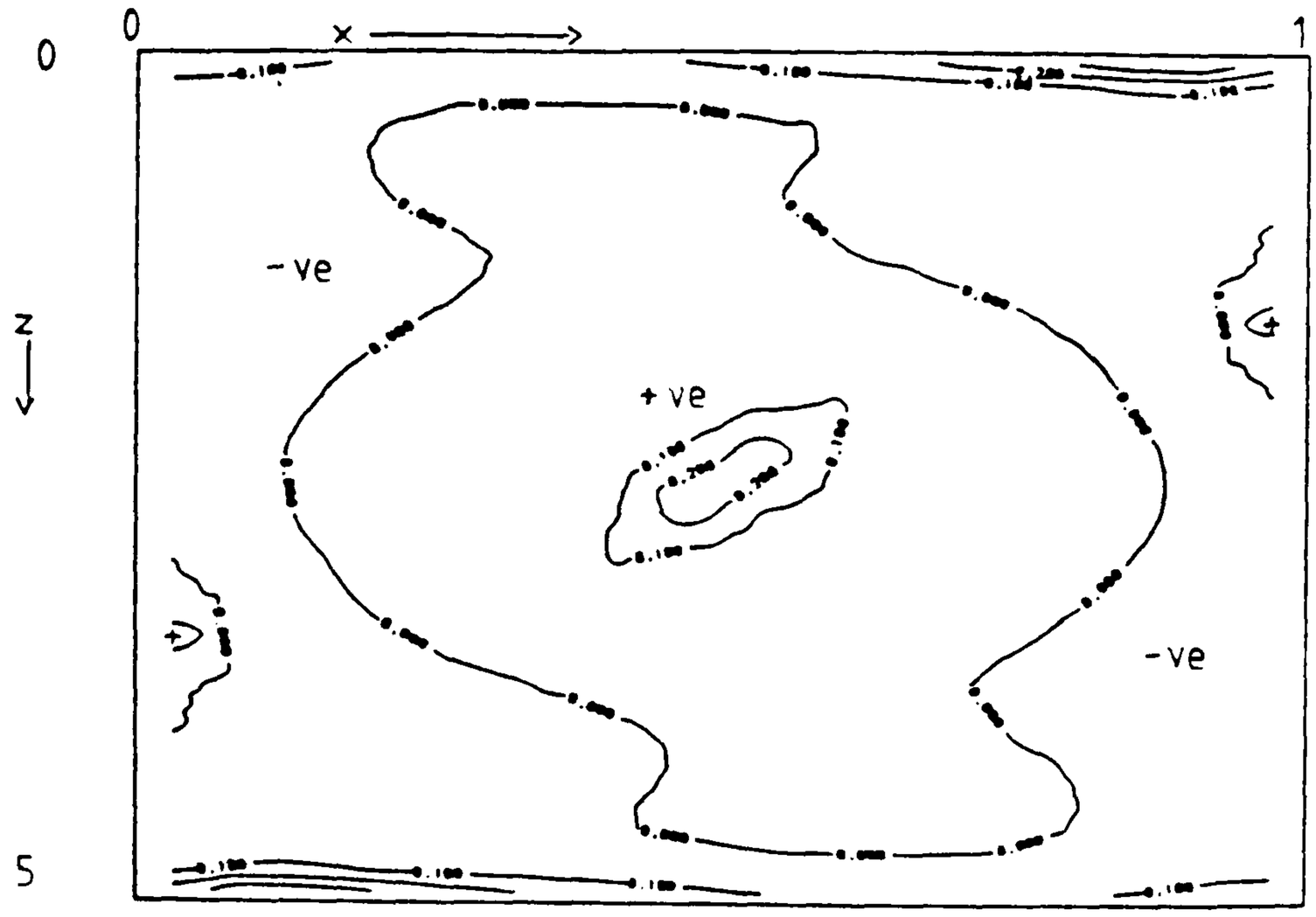

Figure 6.252 Contour plot of ratio R at plane A, near the end wall

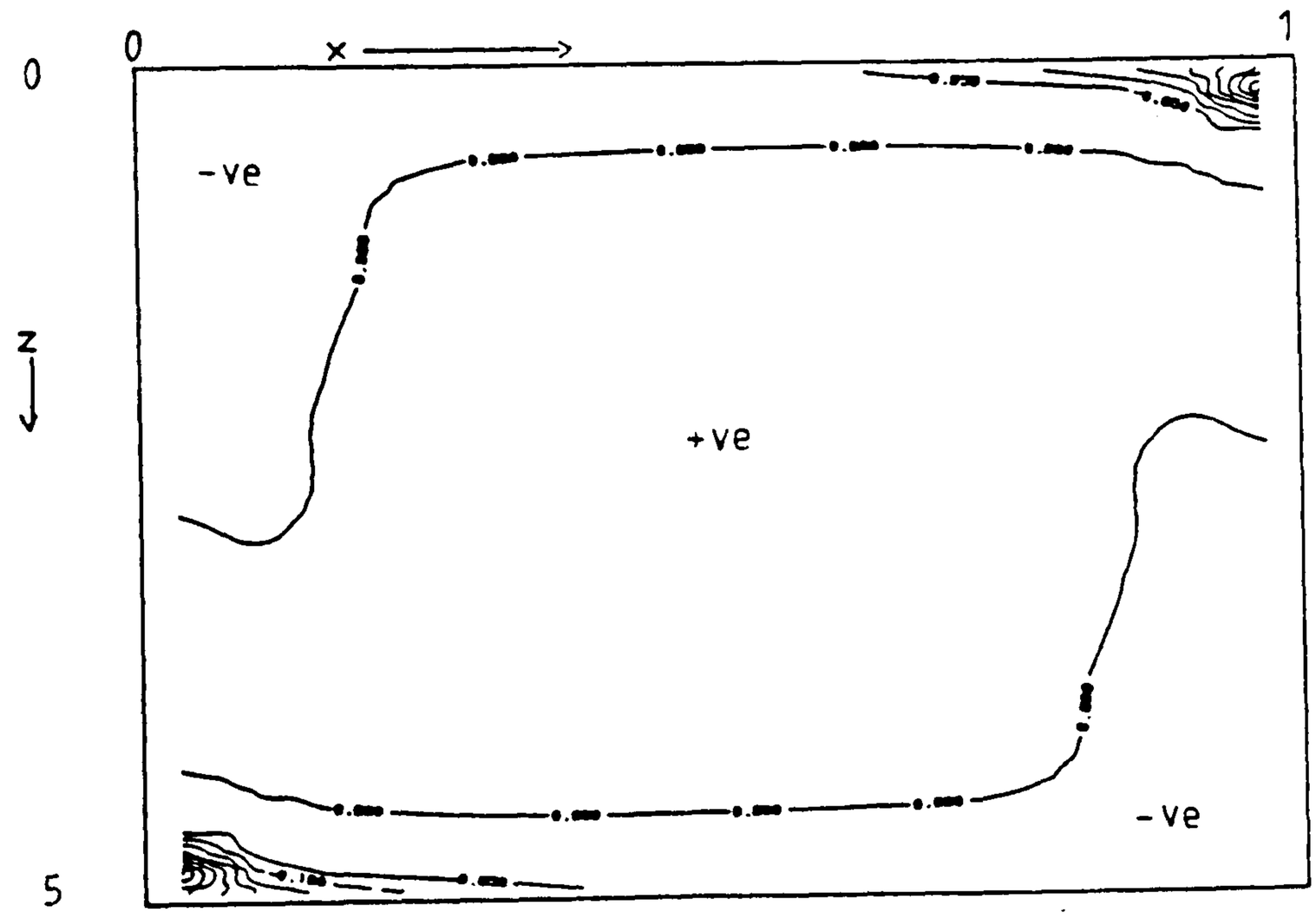

Figure 6.253 Contour plot of ratio R at plane B, near the symmetry plane

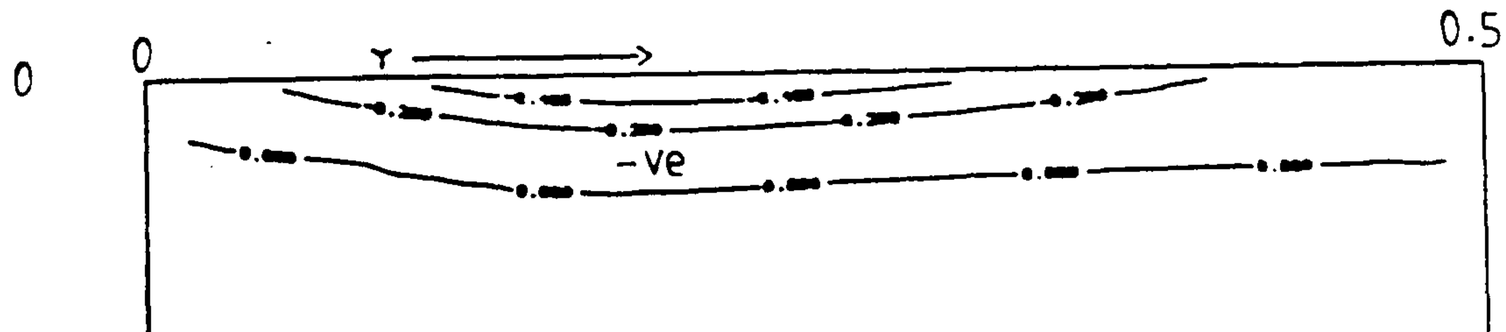

Figure 6.254 Contour plot of ratio R at plane C $(0.5 - hx/2, y, z)$

Fluid = cerrobase, Ra = 5×10^5, Hy=1, Hz=5, grid=16x16x40

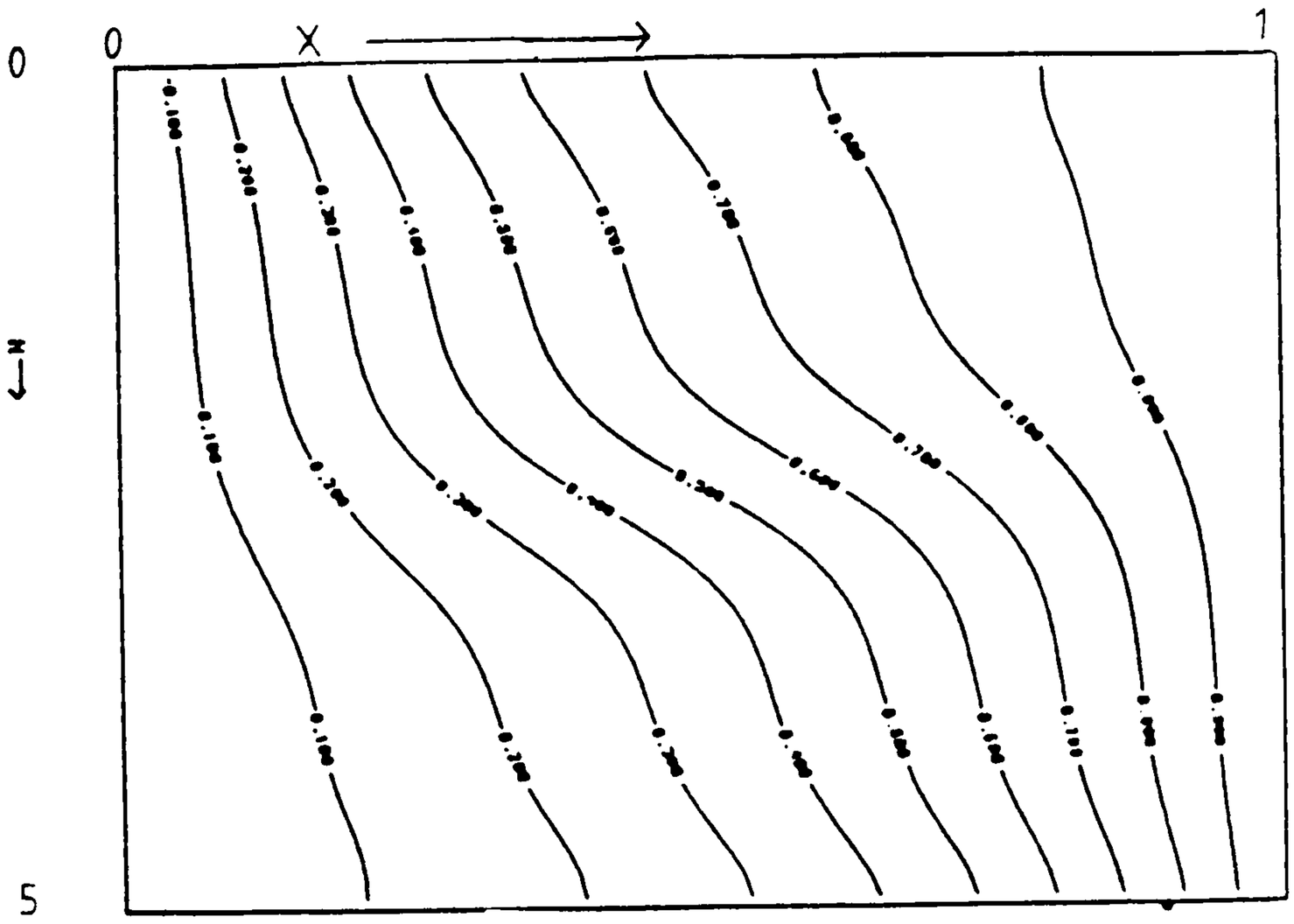

Figure 6.255 Isotherms at plane A, near the end wall

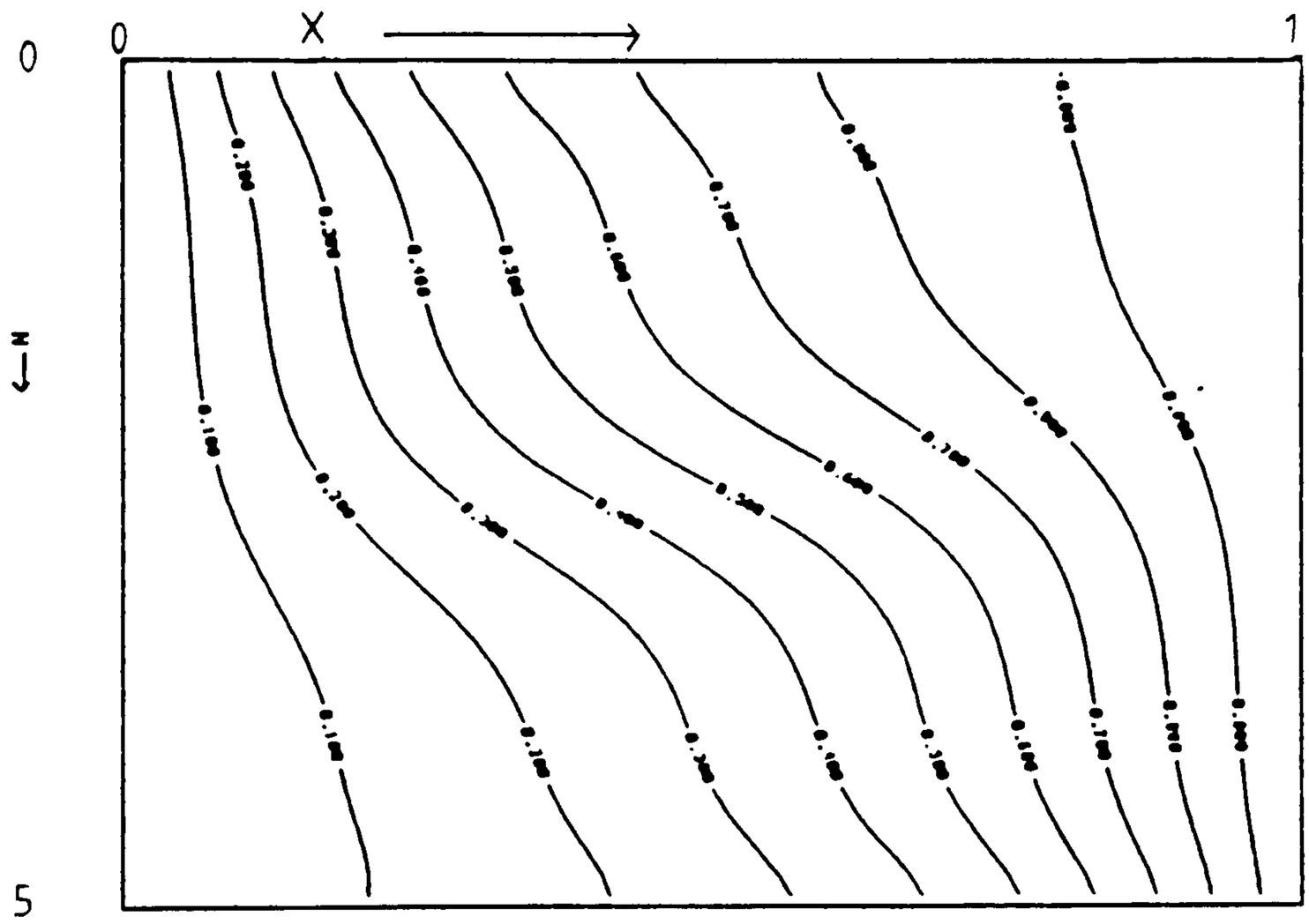

Figure 6.256 Isotherms at plane B, near the symmetry plane

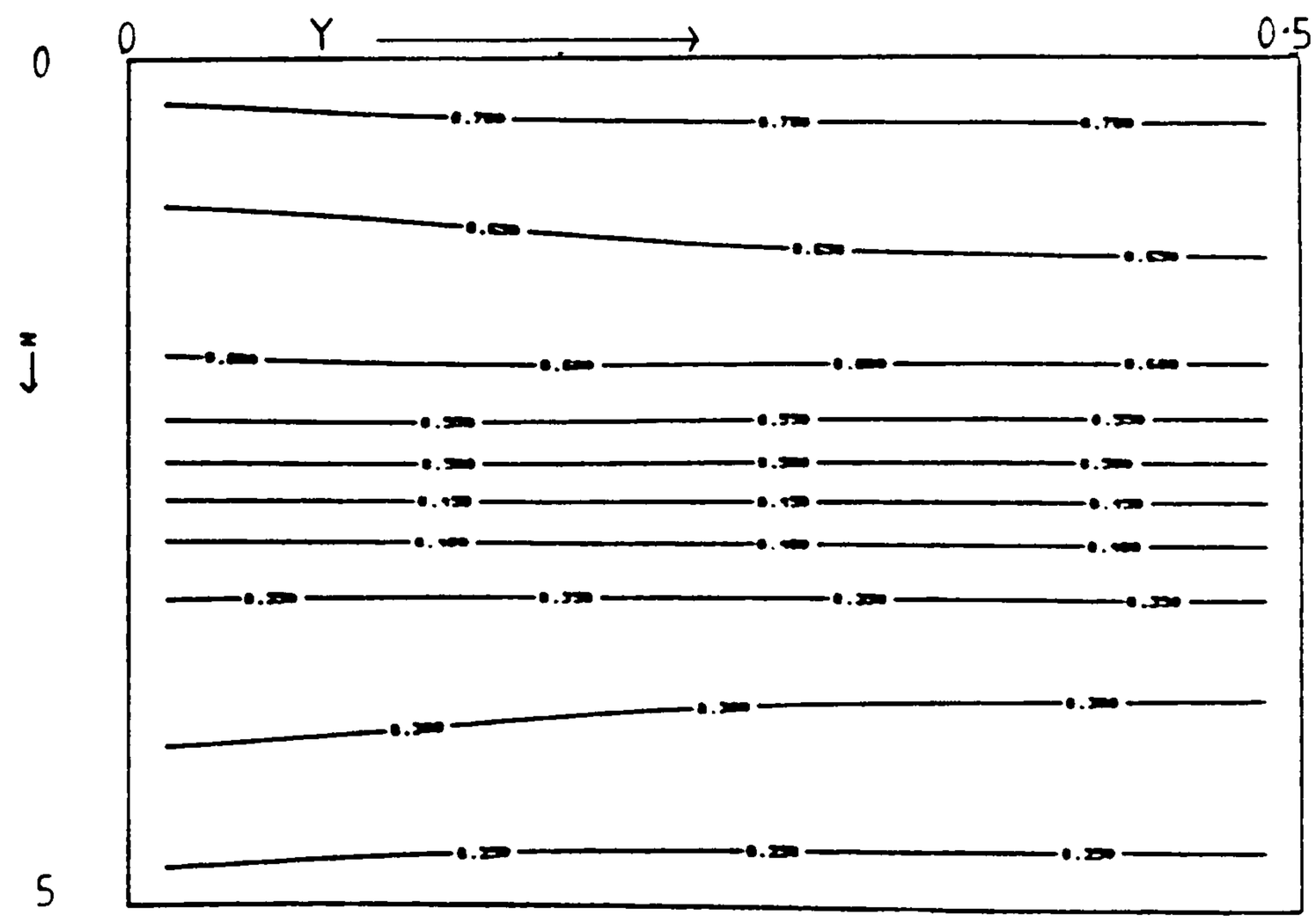

Figure 6.257 Isotherms at plane C, $(0.5 - hx/2, y, z)$

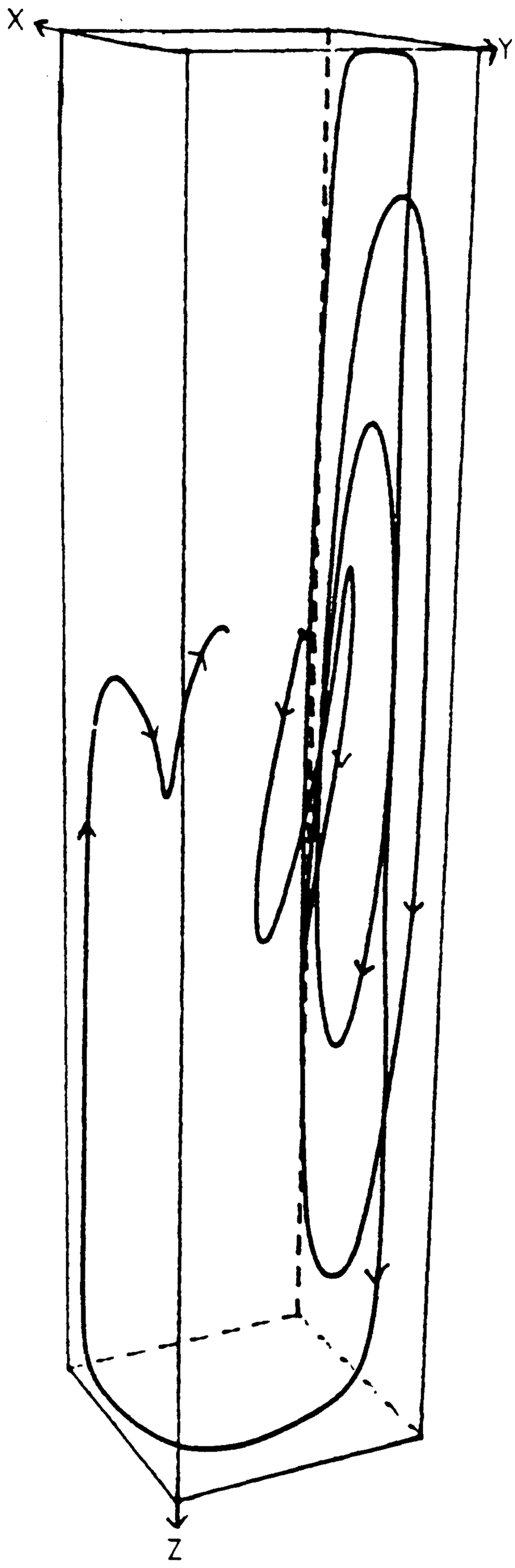

Figure 6.258

Particle track for cerrobase at

$Ra = 5 \times 10^3$, cavity (1,2,5)

grid = 16x16x40

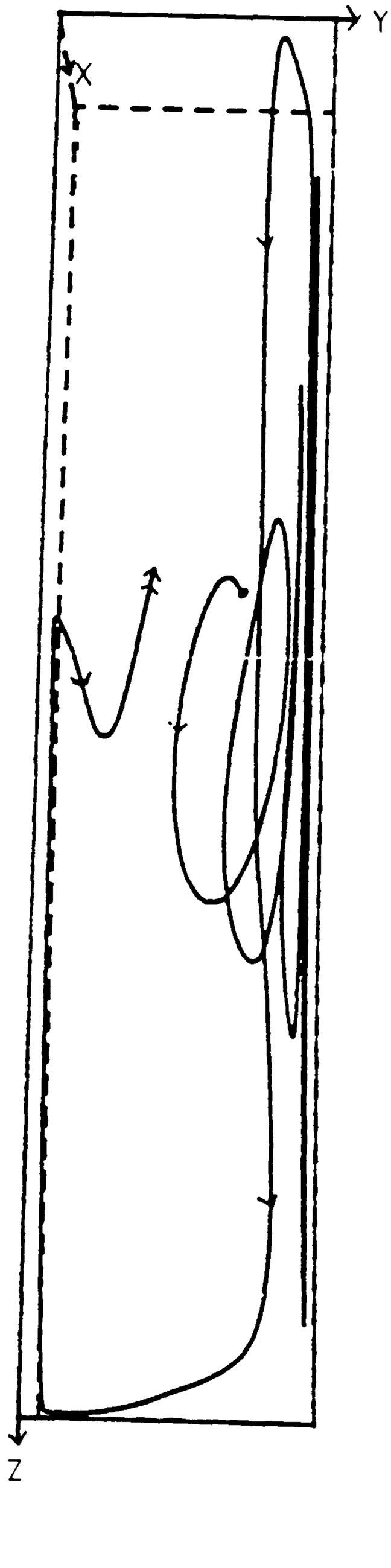

Figure 6.259

Side view of Figure 6.258

Fluid = cerrobase, Ra = 5×10^3, Hy=2, Hz=5, grid=16x16x40

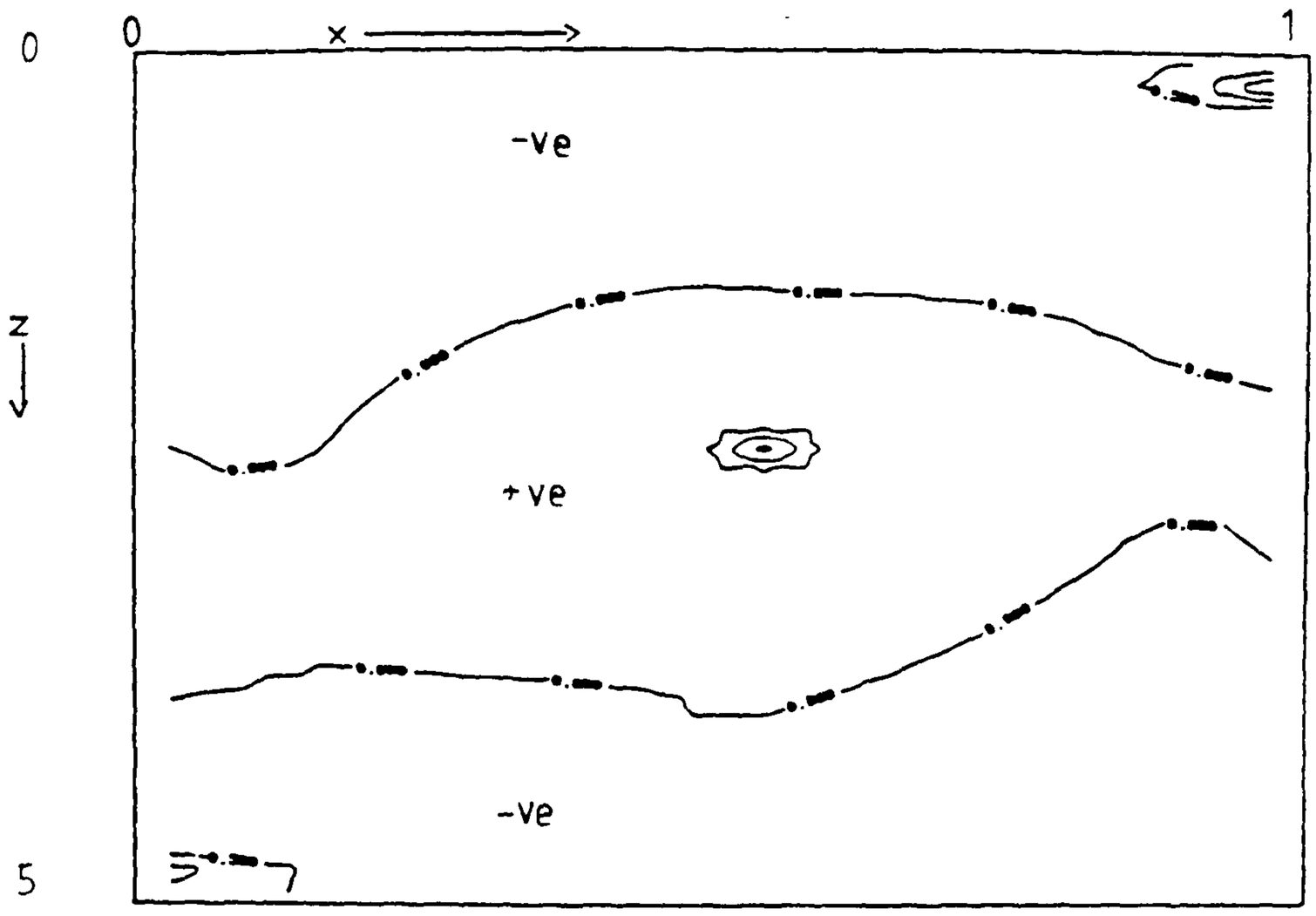

Figure 6.260 Contour plot of ratio R at plane A, near the end wall

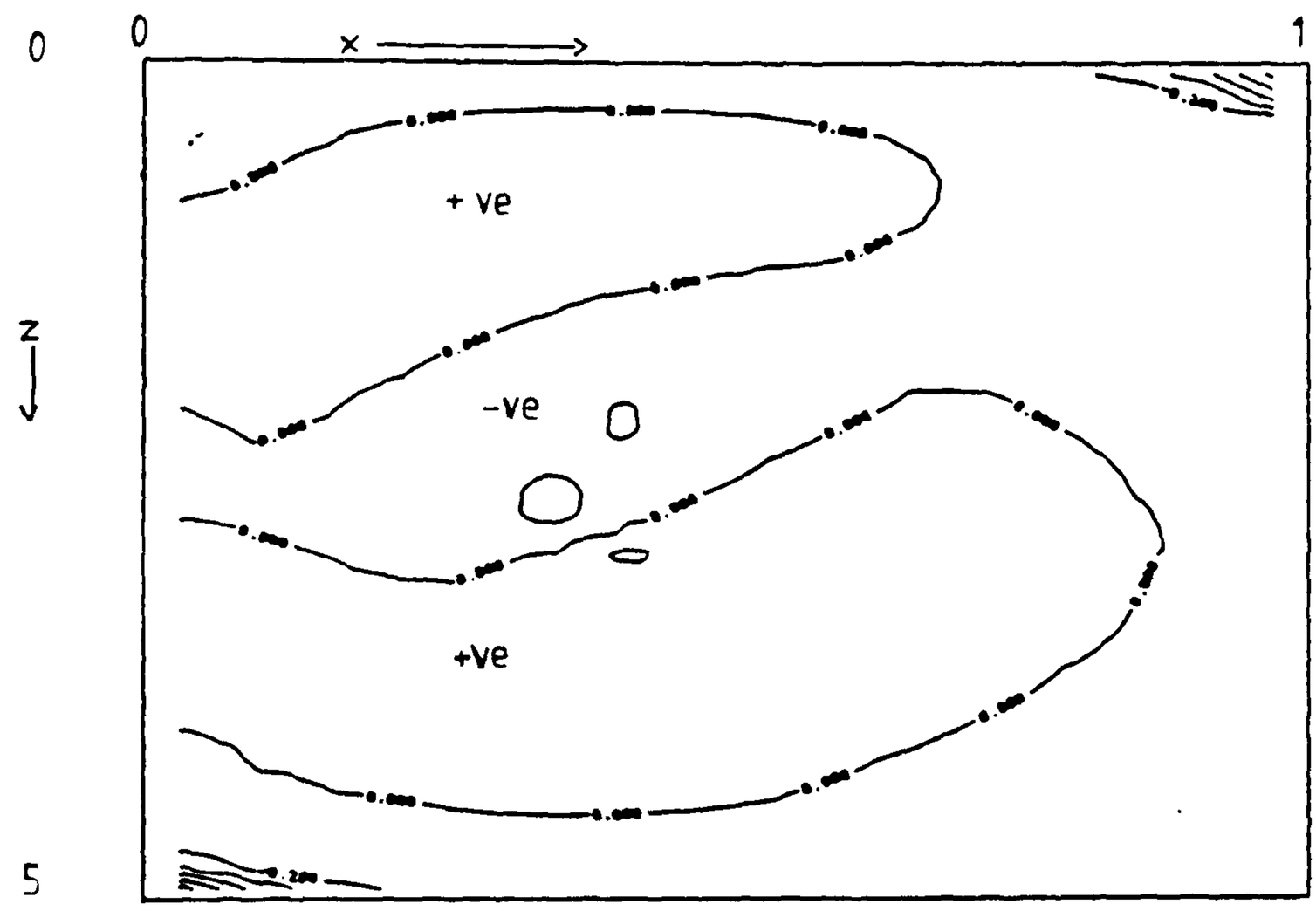

Figure 6.261 Contour plot of ratio R at plane B, near the symmetry plane

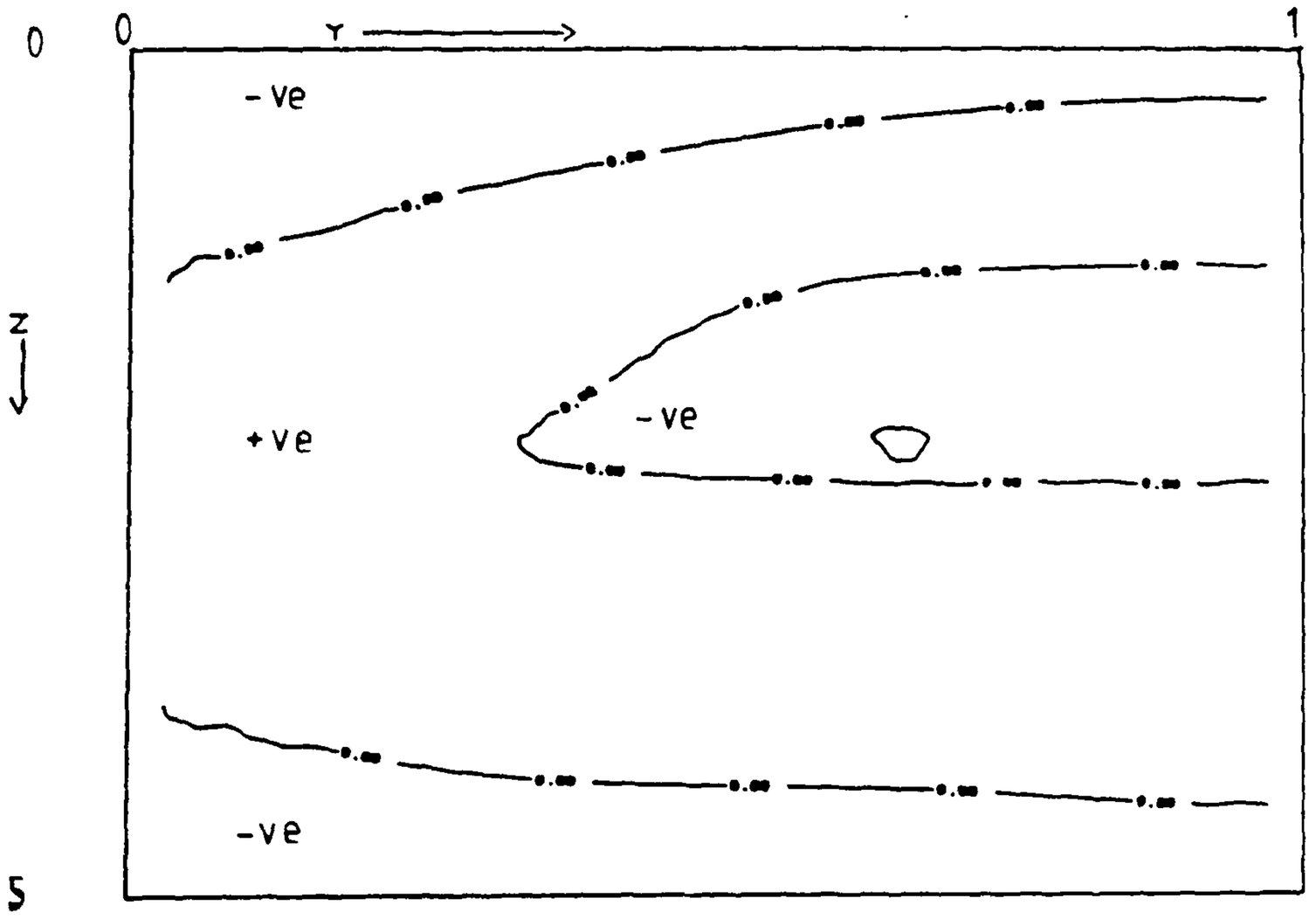

Figure 6.262 Contour plot of ratio R at plane C $(0.5 - hx/2, y, z)$

Fluid = cerrobase, Ra = 5×10^3, Hy=2, Hz=5, grid=16x16x40

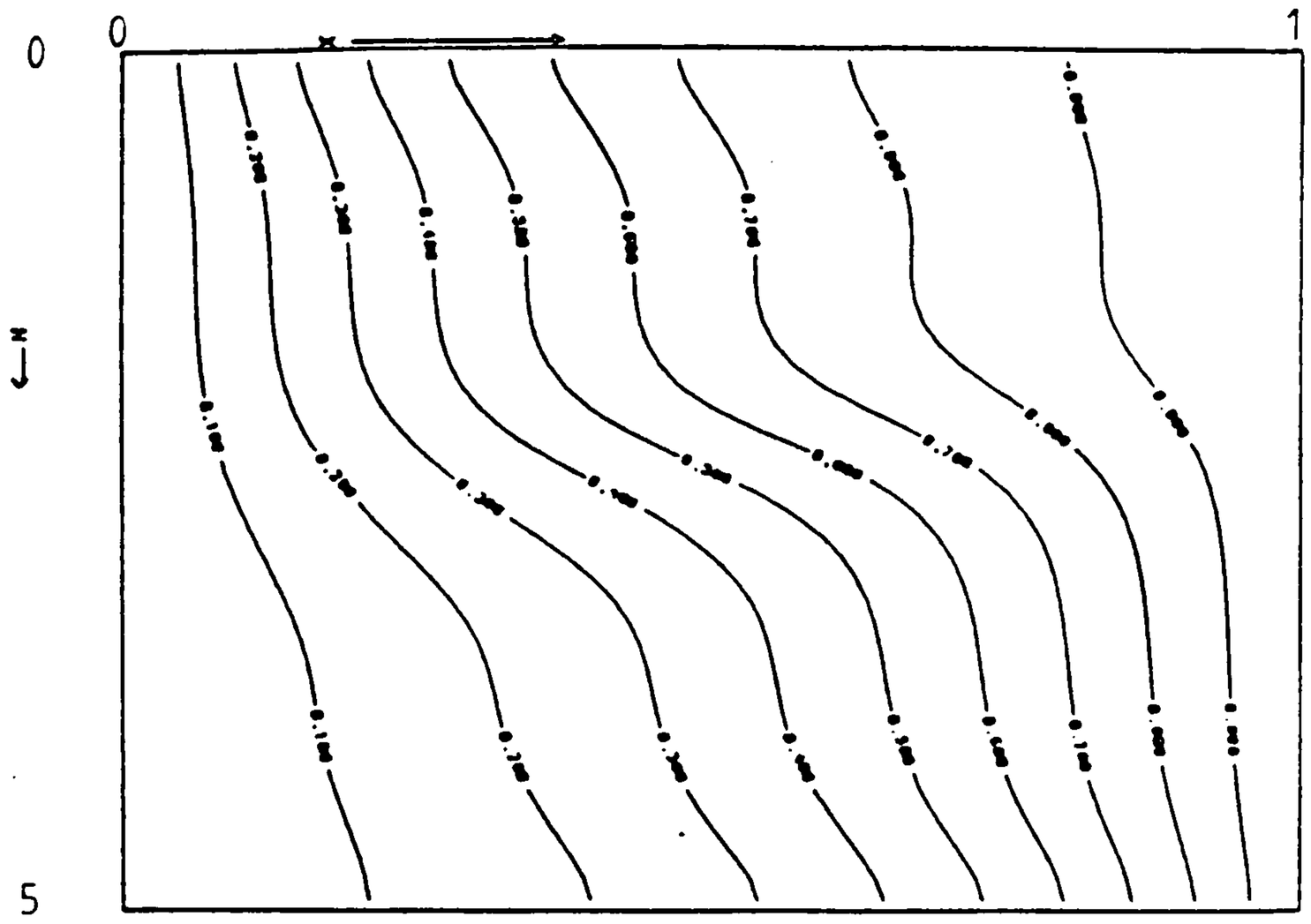

Figure 6.263 Isotherms at plane A, near the end wall

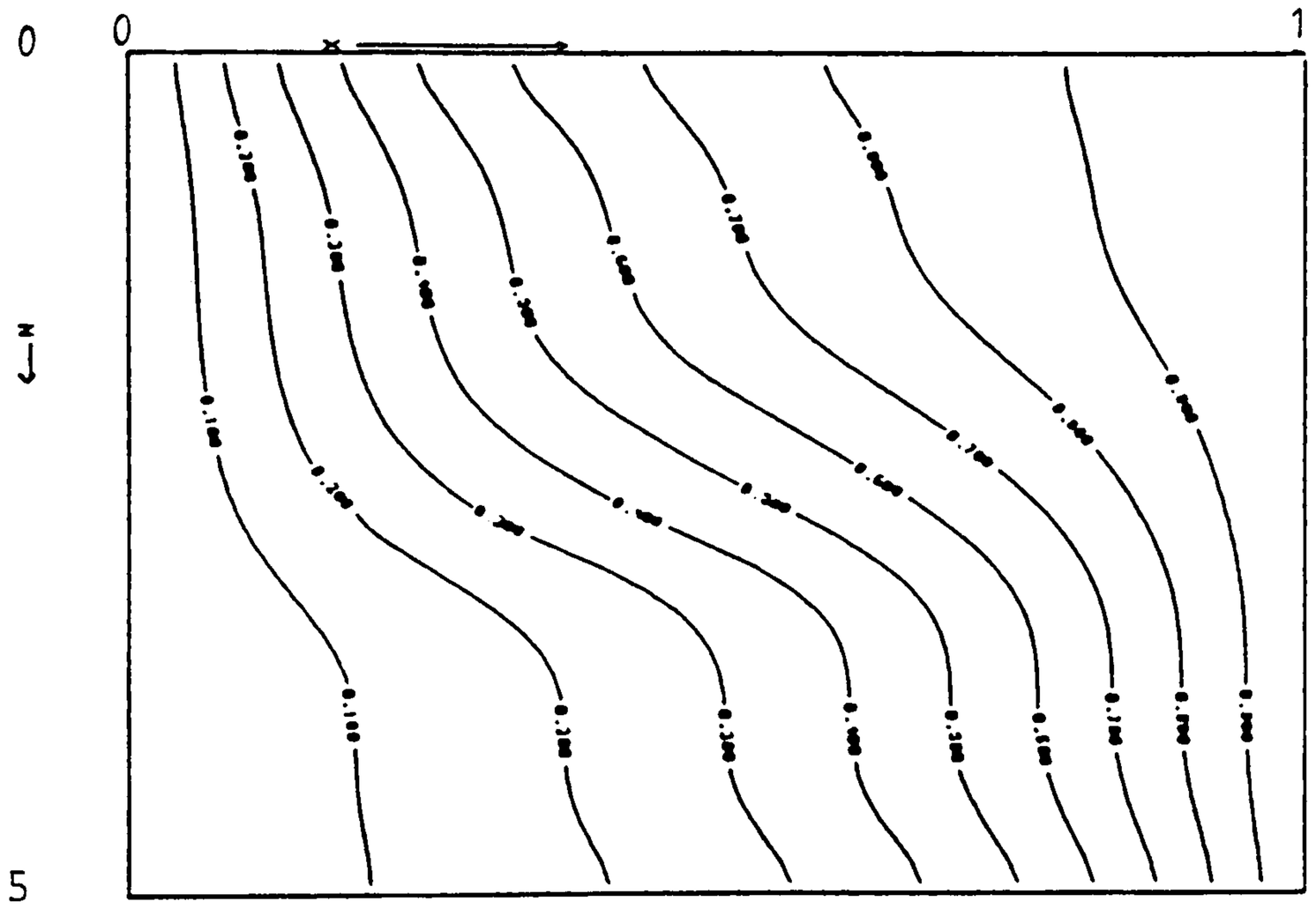

Figure 6.264 Isotherms at plane B, near the symmetry plane

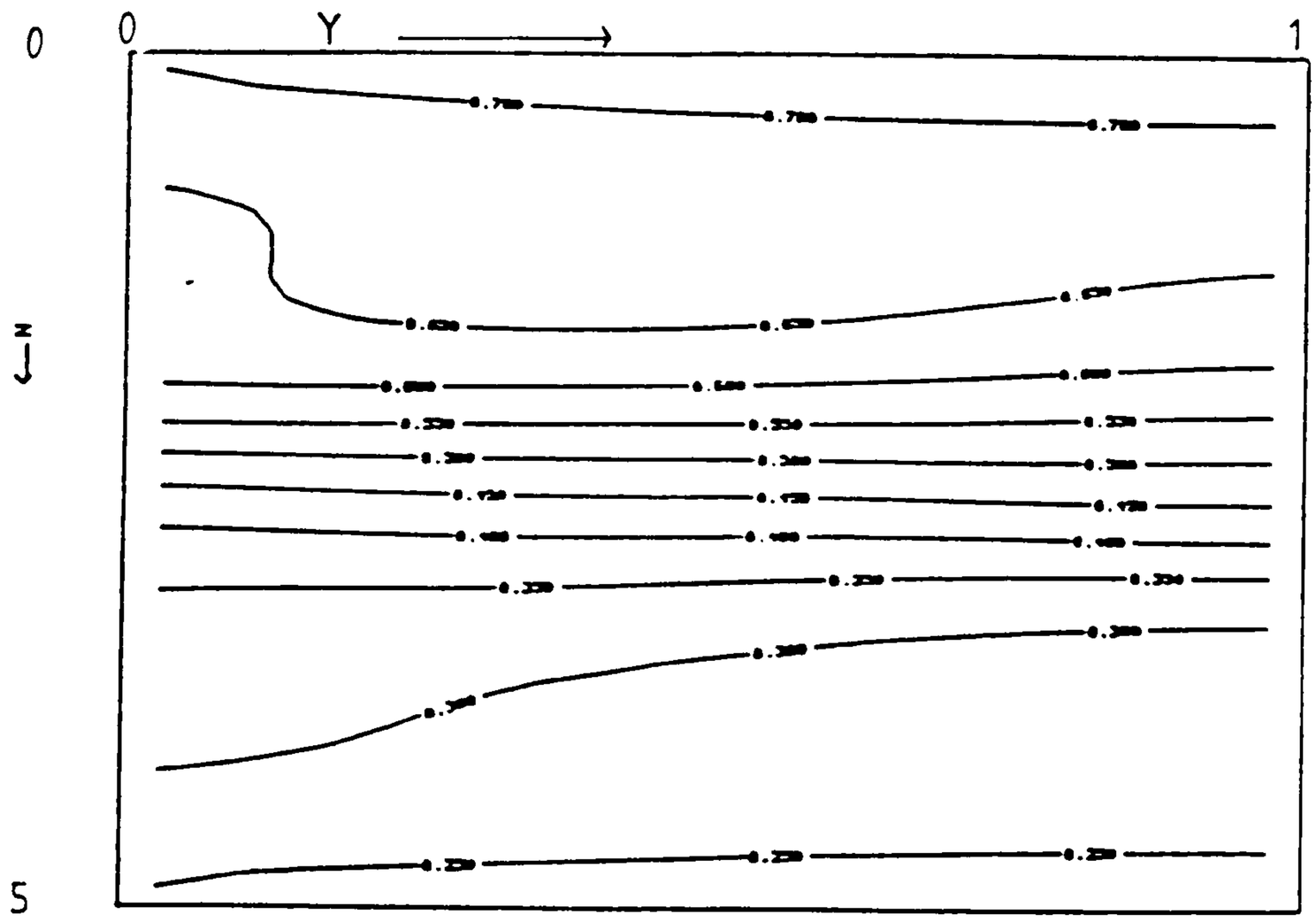

Figure 6.265 Isotherms at plane C, $(0.5 - hx/2, y, z)$

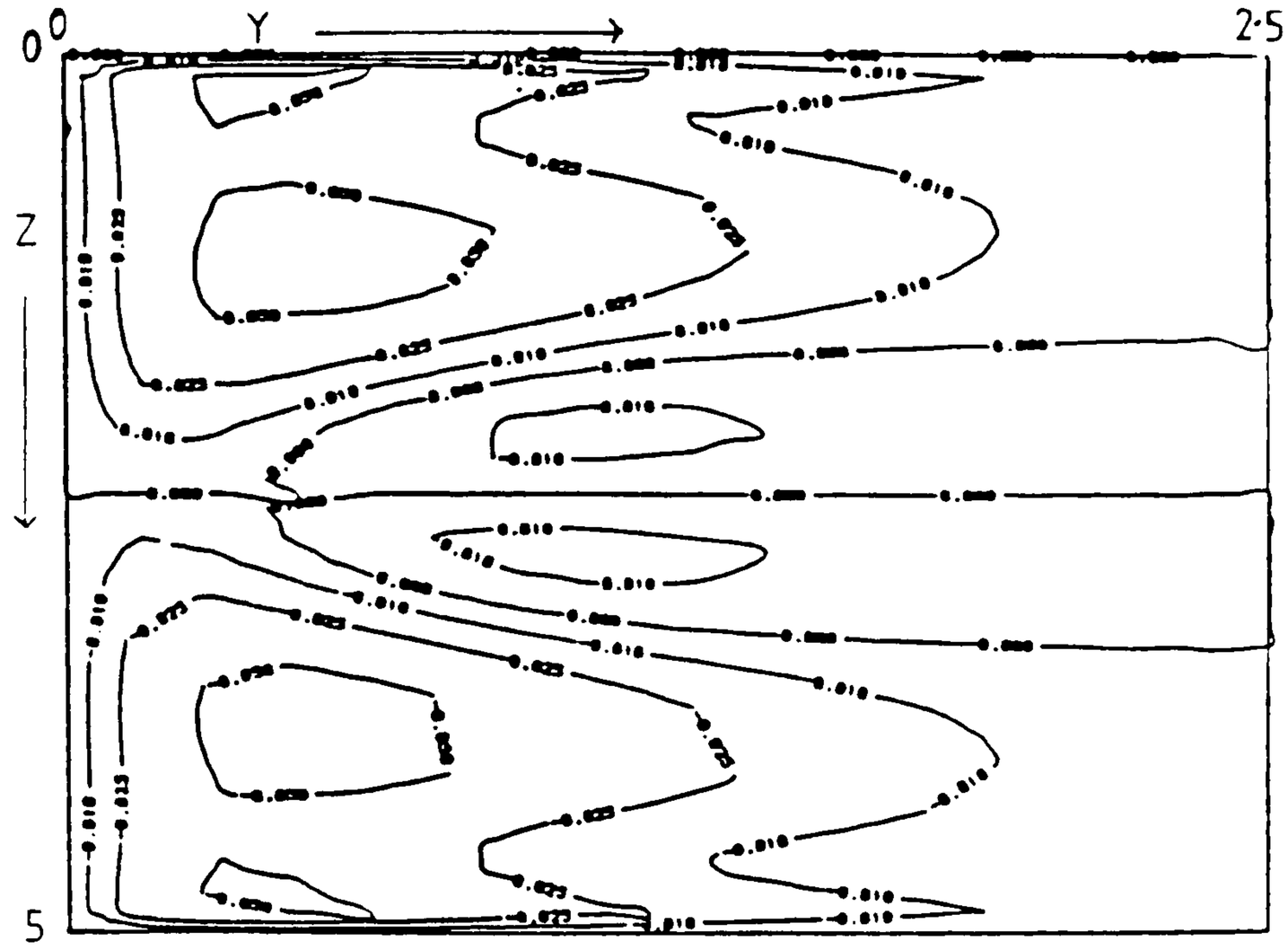

Figure 6.266 $\partial\theta/\partial y$ at plane C, $(0.5 - hx/2, y, z)$, Hy=5

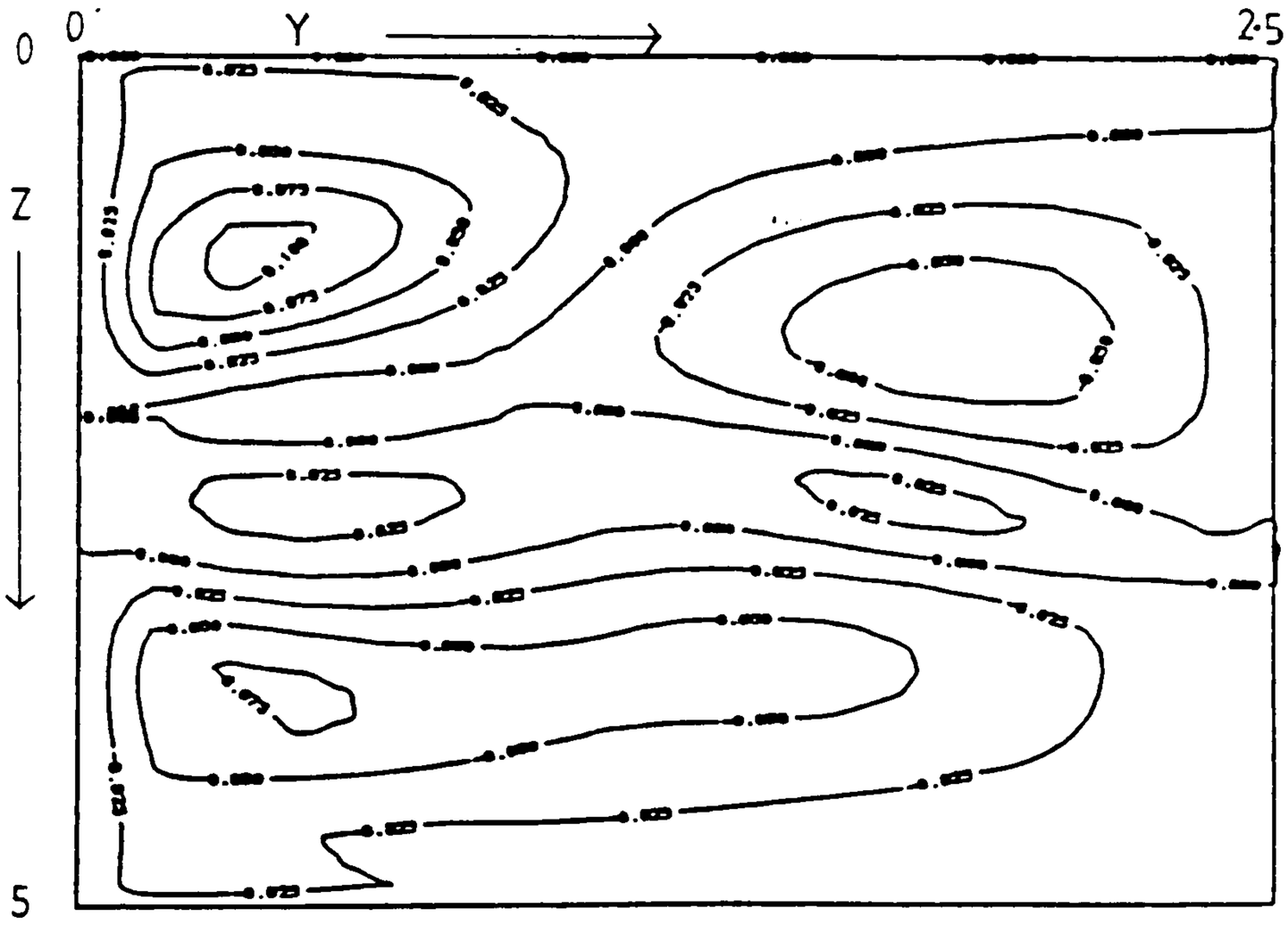

Figure 6.267 $\partial\theta/\partial y$ at plane C, $(0.5 + hx/2, y, z)$, Hy=5

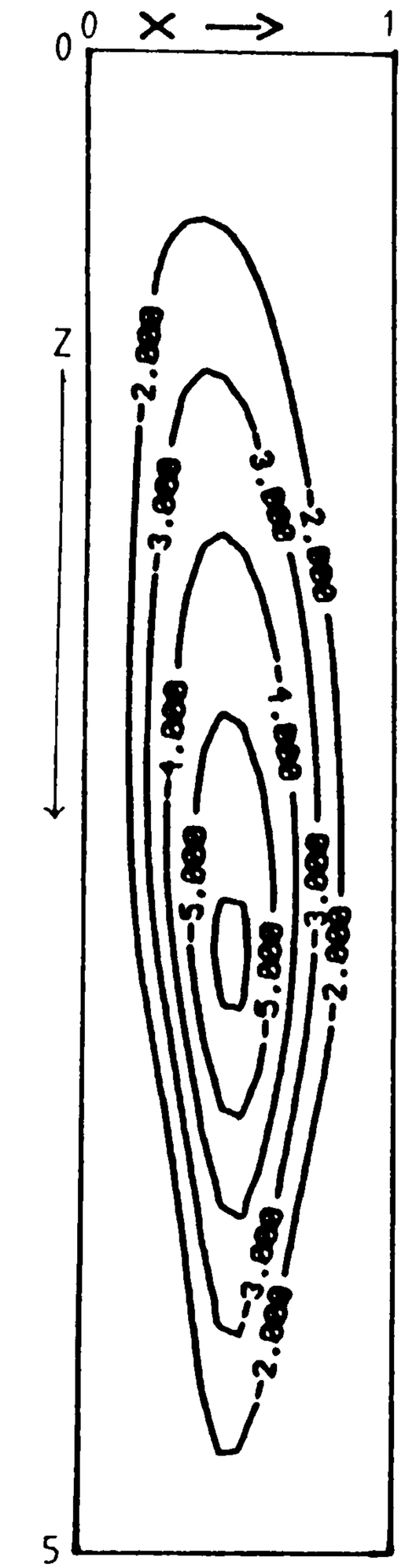

Figure 6.268 Streamlines, Hy=5

Graph A: cerrobase at Ra = 5×10^3, Hy=1, Hz=5

Graph B: cerrobase at Ra = 5×10^3, Hy=2, Hz=5

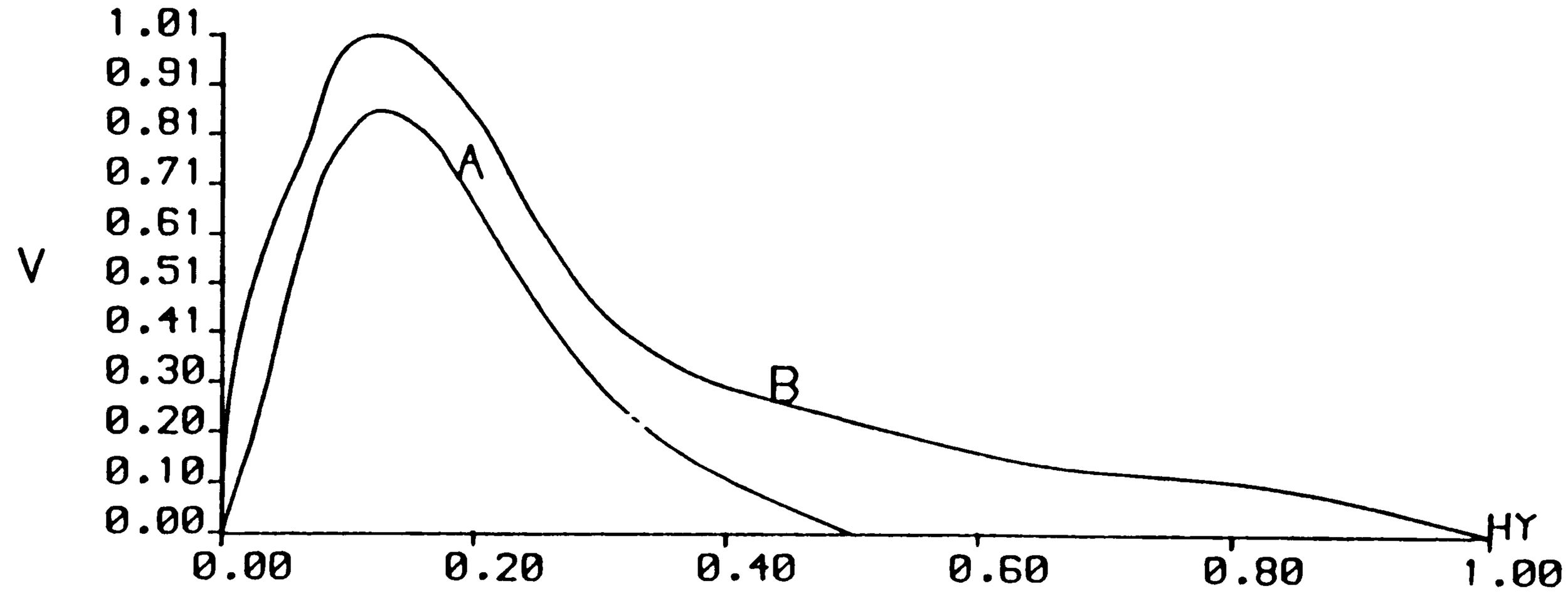

Figure 6.269 Axial-velocity along $(0.5, y, 2.5)$

6.8.5 Heat transfer results for the tall cross section window cavity

Figures 6.270-272 are plots of Nu_v along the isothermal wall x=0 for cavities with length aspect ratio Hy=1, 2 and 5 respectively. Each plot shows Nuv along the isothermal wall for air at Ra = 10^3, cerrobase at Ra = 10^3 and cerrobase at Ra = $5x10^3$. Figure 6.273 is a plot of Nu_v along the isothermal wall, x=0, for air in cavities with length aspect ratio Hy=1, 2 and 5.

$Nu_v(y)$ decreases as the end wall is approached and indicates the extent of the end wall thermal boundary layer in which the convection of heat is reduced. As the Rayleigh number increases the thickness of this layer decreases. With the longer cavity, Hy=5.0, $Nu_v(y)$ increases slightly as $y \rightarrow 0$ until the end boundary layer is reached. The gradual increase results from the increasing magnitude of the axial velocity in the boundary layer as the end wall is approached.

FLUID	CAVITY	Nu_{av}	Nu_{vm}	ψ_{max}	max $\partial\theta/\partial y$
air Ra = 10^3	1x1x5	1.061	1.076	2.50	0.14
	1x2x5	1.082	1.100	2.69	0.15
	1x5x5	1.095	1.104	2.67	0.15
air Ra = 10^5	1x1x5	3.807	4.139	41.67	1.08
	1x2x5	3.923	4.038	35.24	0.94
	1x5x5	3.980	4.019	35.71	0.94
cerrobase Ra = 10^3	1x1x5	1.037	1.046	1.94	0.0736
	1x2x5	1.044	1.054	2.17	0.0691
	1x5x5	1.050	1.057	2.31	0.0670
cerrobase Ra = $5x10^3$	1x1x5	1.223	1.260	5.70	0.154
	1x2x5	1.245	1.302	6.25	0.148

Table 6.6 : Values of Nu_{av} and Nu_{vm}

For air at Ra = 10^5, the Nu_{vm} with the shorter cavity Hy=1 is greater than with Hy=2 or 5 and that with Hy=2 is greater than that with Hy=5. This is due to only forward roll existing in the shorter cavity, Hy=1, which is stronger than the forward roll which coexists with the reverse roll in the cavity with length aspect ratio Hy=2, which in turn is stronger than the forward roll that exists in Hy=5.

The Nusselt number obtained at the symmetry plane for cerrobase at Ra = 10^3 and

$Ra = 5x10^3$ are smaller than those obtained by Jones [27] with his two-dimensional study. This is expected as two-dimensional flow does not exist in the window cavity problem for the length aspect ratios investigated. The values obtained by Jones [27] are 1.08 at $Ra = 10^3$ and 1.53 at $Ra = 5x10^3$.

Graph A: cerrobase at Ra = 10^3, Hy=1, Hz=5

Graph B: cerrobase at Ra = 5×10^3, Hy=1, Hz=5

Graph C: air at Ra = 10^3, Hy=1, Hz=5

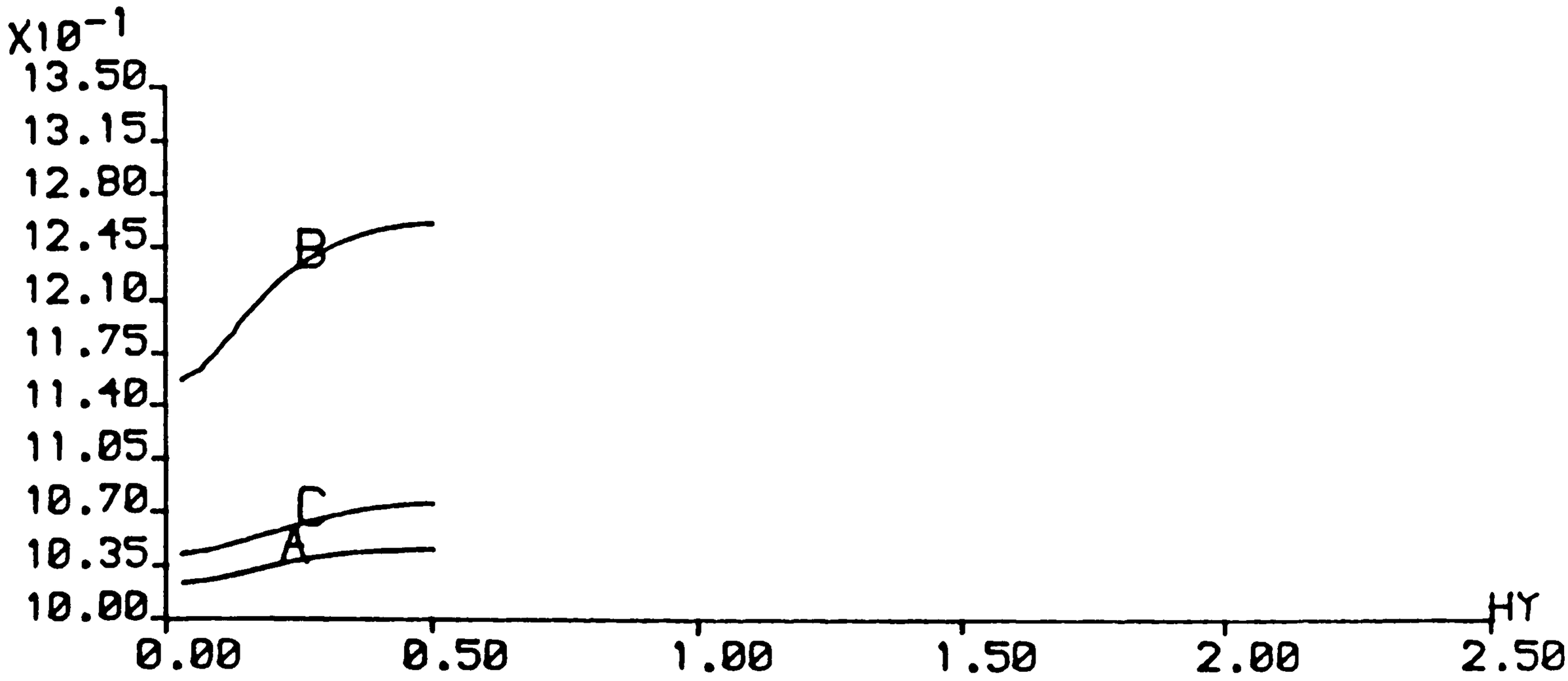

Figure 6.270 Nusselt number along the hot wall

Graph A: cerrobase at Ra = 10^3, Hy=1, Hz=5

Graph B: cerrobase at Ra = 5×10^3, Hy=1, Hz=5

Graph C: air at Ra = 10^3, Hy=1, Hz=5

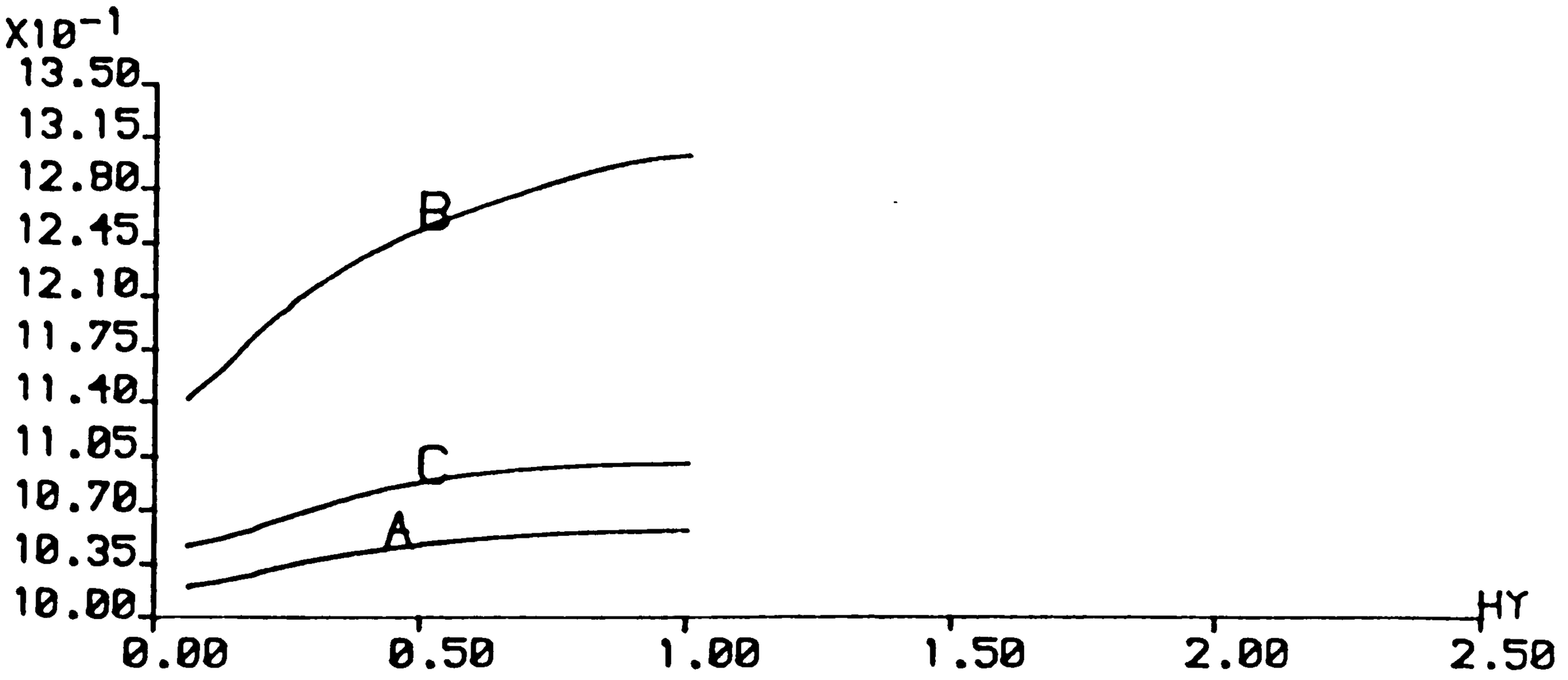

Figure 6.271 Nusselt number along the hot wall

Graph A: cerrobase at Ra = 10^3, Hy=1, Hz=0

Graph B: cerrobase at Ra = 5×10^3, Hy=1, Hz=5

Graph C: air at Ra = 10^3, Hy=1, Hz=5

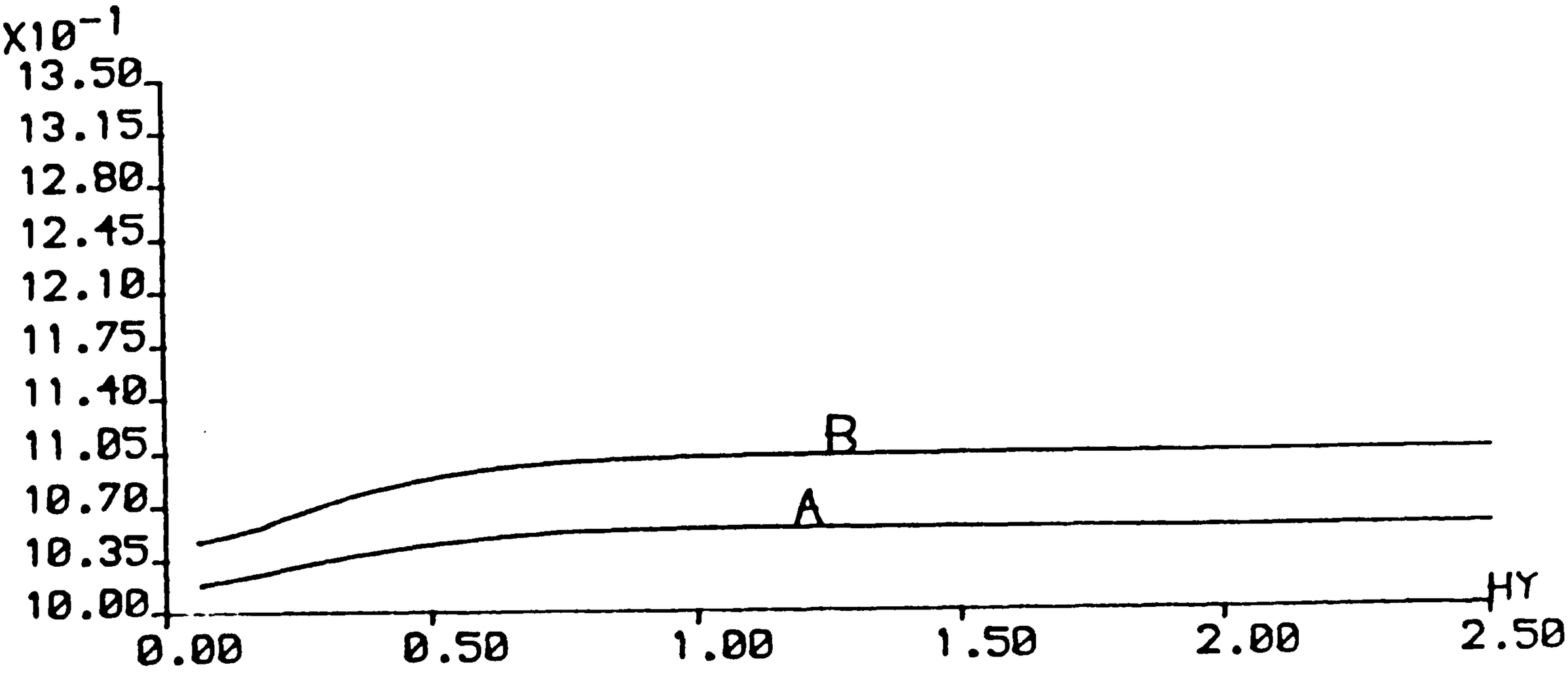

Figure 6.272 Nusselt number along the hot wall

Graph A: air at Ra = 10^5, Hy=1, Hz=5

Graph B: air at Ra = 10^5, Hy=2, Hz=5

Graph C: air at Ra = 10^5, Hy=5, Hz=5

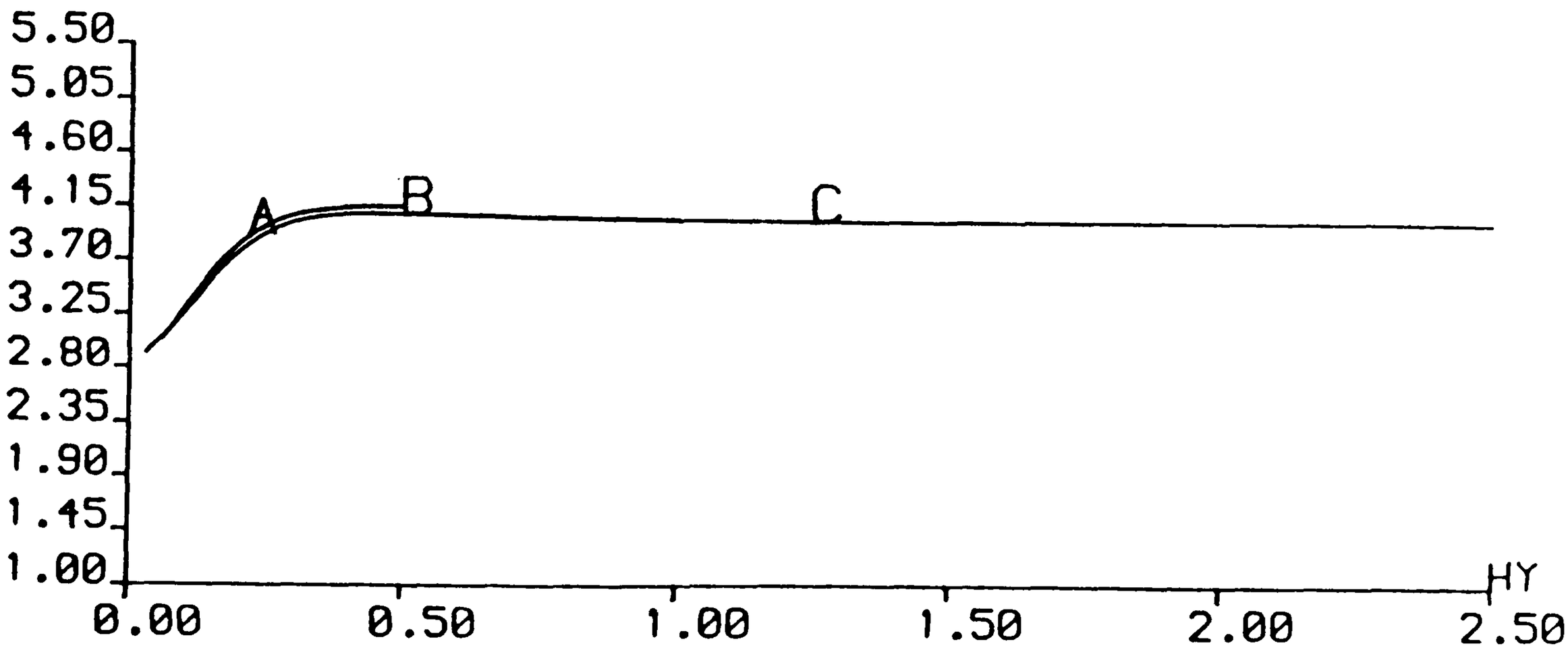

Figure 6.273 Nusselt number along the hot wall

6.8.6 Summary for the tall cross-section window cavity, Hz=5.0

The fluid flow structure at the lower Rayleigh number Ra = 10^3 for air in the tall cross-section window cavity with length aspect ratios, Hy=1, 2 and 5, results in a single forward recirculating roll. The rolls have been illustrated by tracing particle tracks which lie on a torus like surface. The forward roll is generated in the same manner as described for the square cross-section window cavity. The characteristics obtained with the square cross-section window cavity flow also exist here, these being: the magnitude of the cross-sectional velocity being greater near the symmetry plane than near the end wall; the thermal solution being more convective near the symmetry plane than near the end wall; the axial flow being strongest in the vicinity of the end wall and weakest near the symmetry plane, and the strong axial temperature gradients generating vorticity sources that augment the inertial end effect creating undulations in the particle paths.

In the tall cavity, regions of strong axial flow occur near the top and bottom boundaries at the end wall of the cavity, giving an impression that two forward rolls exist, one on top of another, thus implying an existence of two cat's eye cells as found in the two-dimensional problem. This is not the case, as the streamline plot only reveals primary circulation. The regions of strong axial flow near the top and bottom boundaries is due to the greater drag there. Away from the end wall the influence of the drag diminishes and the two regions of strong axial flow amalgamate. Undulations in the particle tracks are also present in this tall cavity flow. The flow appears to be convection dominated near the top and bottom walls, with the flow in the centre conduction-like. Two-dimensional flow does not exist for Hy $\leq$ 5.0 indicating the strength of the axial flow in this tall cavity is greater than that in either the square or the shallow cross-section window cavity.

The fluid flow structure at the lower Rayleigh number (10^3), for cerrobase results in a forward recirculating roll which completely fills the solution cavity for Hy=1, 2 and 5. With this flow, regions of strong axial flow do not exist at the top and bottom boundaries near the end wall. The thermal solution for this flow is conduction-like. The value of $\partial\theta/\partial y$ changes sign along the length of the cavity for Hy=2 and 5 as a result of the contribution of heat from the axial flow. The turning points of the particles do not lie on a cylindrical or elliptic surface and undulations in the particle

tracks exist. Two-dimensional flow does not exist for Hy $\leq$ 5, indicating that the strength of the axial flow in this tall cross-section window cavity is greater than in either the shallow cross-section or the square cross-section window cavity. Streamline plots near the symmetry plane reveal primary circulation. Jones [27] with the two-dimensional problem study obtained secondary flow in the form of two cells, one on top of another, for cerrobase at Ra = 10^3. The three-dimensional flow problem for cerrobase suppresses instabilities obtained with the two-dimensional flow problem. Bergholz [3] indicated that the two-dimensional instabilities in lower Prandtl number flow are shear driven, caused by the interaction of the up and down flowing streams. The considerable drag effect of the end wall slows down the flow and suppresses the instabilities observed in the two-dimensional problem for the length aspect ratios investigated, Hy $\leq$ 5.

The fluid flow structure for cerrobase at the higher Rayleigh number, 5x10^3, results in a single forward recirculating roll completely filling the solution cavity with Hy=1 and 2. The forward recirculating roll in the cavity Hy=2 has negative axial velocity in the inner core, see figure 6.262. It is possible that this could be due to numerical errors as the solution for Hy = 5 was not obtained due to divergence of the solution. Turning points of the particles do not lie on a cylindrical or elliptic surface and undulations in the particle paths exist. Streamline plots for Hy=1 and 2 reveal a primary circulation and not multiple cells as obtained by Jones [27].

The total end wall effect is greater for cerrobase than air with thermal end effect being greater for air than cerrobase and the inertial end effect being greater for cerrobase than air.

The fluid flow structure at the higher Rayleigh number, 10^5, for air results in a forward recirculating roll which fills the solution cavity for Hy=1 and 2. Secondary flow does not exist but two regions of strong axial flow exist in the centre of the cavity due to the convective effects at the higher Rayleigh number, that is, due to the change in the sign of $\partial\theta/\partial x$. Regions of strong axial flow also exist at the end wall near the top and bottom boundaries due to the strong thermal end effect created as a result of extra drag.

The particle paths in the cavity with Hy=2 behave differently to those in Hy=1. For Hy=2, the particles travel forward in the inner core towards the symmetry plane. As they approach the symmetry plane each particle starts to track an uncoiling spiral and begins to move back towards the end wall. After further tracking their respective

spirals they start to move forward towards the symmetry plane until they reach the boundary layer, in which they finally make their journey back towards the end wall. This can be seen in figure 6.210. This behaviour is due to the vorticity generated by the $\partial\theta/\partial y$ not being sufficiently strong to generate a reverse recirculating roll, but yet sufficiently strong to create a reverse flow within the forward recirculating roll.

For the longer cavity, Hy=5, forward and reverse recirculating rolls exist, this is apparent from figure 6.216, which is a contour plot of the ratio R in the plane $(0.5, y, z)$.

Streamline plots for Hy=1, 2 and 5 indicate a primary circulation and not multiple cells. Plots of the axial velocity along the centre line reveal that two-dimensional flow does not exist for Hy $\leq$ 10. The limiting forward (positive) peak axial velocity in the solution cavity is near 1.71. As Hy increases a reverse recirculating roll develops accompanying the forward roll near the end wall. At the same time the forward roll becomes weaker while the reverse roll becomes stronger. An extra study with the longer length aspect ratio Hy=10 has been performed in order to arrive at the above described relationship of the forward and reverse roll with Hy.

The Nusselt number obtained at the symmetry plane for cerrobase with 10^3 and $5x10^3$ are smaller than those obtained by Jones [27] for the two-dimensional problem. This is expected as two-dimensional flow does not exist with the window cavity problem for the length aspect ratios investigated.

6.9 Conclusion of the results obtained for the window cavity problem

Numerical predictions for a low Prandtl number fluid, cerrobase, and a moderate Prandtl number fluid, air, have been presented for window cavities with shallow, square and tall cross sections. All the results presented for cerrobase and those presented for air in the shallow, square and tall cross section window cavities have not, as far as the author is aware, appeared in the literature as yet. The solution to the window cavity problem confirms the existence of a strong three-dimensional effect, the form of which is governed by the height and length aspect ratios, Hz, Hy, the Rayleigh number, Ra, and the Prandtl number, Pr. The three-dimensional motion arises as a result of the end wall effect which is comprised of two mechanisms, the inertial end wall effect and the thermal end wall effect. The inertial end effect for cerrobase is considerably greater than that for air and the thermal end effect for air is generally greater than that for cerrobase, with the overall end wall effect being greater for cerrobase than air. As a result of which the fluid flow behaviour for cerrobase is radically different to that of air. The fact that the nature of the flow for liquid metals is considerably different from that of air needs to be taken into account when simulant fluids such as air and water are used to model liquid metal flows in experiments.

The general structure of the flow near the end wall in the window cavity is like that of two-dimensional problem in the cross-section with axial motion superimposed upon it resulting in a recirculating roll. The recirculating roll can be best described by tracing a particle track, which when traced lies on a toroidal surface.

As mentioned above the three-dimensional flow is dependent on the Rayleigh number, the Prandtl number and the length and height aspect ratios. The table below describes the flow structure that exist for different combinations of the four governing parameters.

A result not included in the table is for air at Ra = 10^5 in the tall cavity with Hy=10. A forward roll exists in the range (0, .6) and a reverse roll exists in the range (.6, 5).

The results show that there are three types of flow depending on the relative values of the parameters. These flows are:

1. a forward roll which occupies the complete half-cavity.

Hz = 0.5	Hy = 1.0	Hy = 2.0	Hy = 5.0
Air Ra = 10^3	Forward roll (0, .5)	Forward roll (0, 1)	Forward roll (0, 1.25) Two-dimensional flow exists in (1.25, 2.5)
Air Ra = 10^5	Forward roll (0, .5)	Forward roll (0, 1)	Forward roll (0, 1.5) Two-dimensional flow exist in (1.5, 2.5)
Cerrobase Ra = 10^3	Forward roll (0, .5)	Forward roll (0, 1)	Forward roll (0, 1.25) Two-dimensional flow exists in (1.25, 2.5)
Cerrobase Ra = $5x10^3$	Forward roll (0, .5)	Forward roll (0, 1)	Forward roll (0, 1.75) Two-dimensional flow exist in (1.75, 2.5)

Hz = 1.0	Hy = 1.0	Hy = 2.0	Hy = 5.0
Air Ra = 10^3	Forward roll (0, .5)	Forward roll (0, 1)	Forward roll (0, 1.5) Two-dimensional flow exist in (1.5, 2.5)
Air Ra = 10^5	Forward roll (0, .5)	Forward roll (0, .7) Reverse roll (.7, 1)	Forward roll (0, .6) Reverse roll (.6, 2.5)
Cerrobase Ra = 10^3	Forward roll (0, .5)	Forward roll (0, 1)	Forward roll (0, 2.5)
Cerrobase Ra = $5x10^3$	Forward roll (0, .5)	Forward roll (0, 1)	Forward roll (0, 2.5)

Hz = 5.0	Hy = 1.0	Hy = 2.0	Hy = 5.0
Air Ra = 10^3	Forward roll (0, .5)	Forward roll (0, 1)	Forward roll (0, 2.5)
Air Ra = 10^5	Forward roll (0, .5)	Forward roll (0, 1)	Forward roll (0, .75) Reverse roll (.75, 2.5)
Cerrobase Ra = 10^3	Forward roll (0, .5)	Forward roll (0, 1)	Forward roll (0, 2.5)
Cerrobase Ra = $5x10^3$	Forward roll (0, .5)	Forward roll (0, 1)	

Table 6.7: Fluid flow structure for the window cavities investigated

2. a forward roll for part of the cavity followed by two-dimensional flow.

3. a forward and reverse roll in the half-cavity.

For Hy=1, the flow is always a forward roll although weak secondary rolls are embedded within the forward roll for air at $Ra=10^5$.

For Hy=2, again the flow is almost always a forward roll. However, for air at $Ra=10^5$, a reverse roll sets in for the square cavity Hz=1. It would be expected that for the tall cavity, Hz=5, a reverse roll would exist for larger values of Hy. This is verified by the results for Hy=5.

For Hy=5, two-dimensional flow can be obtained for shallow cavities (Hz=0.5) and also for the square cavity filled with air provided Ra is low enough.

It is noticeable that cerrobase never produces a reverse roll for the parameters examined but a reverse roll may exist for higher Ra.

In general, the lower the Rayleigh number the shorter the length aspect ratio that is required for two-dimensional flow to exist for a given fluid and height aspect ratio. The end wall effect with the low Prandtl number fluid is greater than that with moderate Prandtl number fluid. In the very short length aspect ratio cavities, for instance Hy=1, the peak axial velocity is not as strong as in the longer cavities. This is due to the end wall drag's influence extending to the symmetry plane. This slows down the cross-sectional flow near the symmetry and thus the difference between the cross-sectional velocity at the symmetry plane and the cross-sectional velocity at the end wall is smaller than that for a longer cavity, where the fluid near the symmetry plane is not influence by the end wall drag. As a result the inertial and the thermal end effects are smaller in the 'short' cavities. The 'short' cavity is defined as the one where the end wall drag can influence the flow at the symmetry plane. The longer the cavity the less influence the end wall effect has on the flow near the symmetry plane. For very long cavities one can expect two-dimensional flow away from the end walls but this may not always be the case. For instance, with the higher Rayleigh number flow convection of heat may create strong axial temperature gradients, which in turn will generate vorticity sources resulting in combinations of forward and reverse recirculating rolls.

The effect of increasing the height of the cavity results in increasing the end wall effect. For instance in the shallow cavity with cerrobase at the low Rayleigh number, $Ra = 10^3$, two-dimensional flow results for $Hy \geq 1.75$ but for the same fluid, two-dimensional flow does not exist in the square or the tall cavities for $Hy \leq 5$. The

maximum value of $\partial\theta/\partial y$, which indicates the strength of the thermal end effect, increases with Hz.

Mallinson and de Vahl Davis [39] regard the reverse roll as being two-dimensional due to it being weak in the square cross-section window cavity. The strength of the reverse roll in the tall cross-section cavity increases with longer cavities, see Figure 6.217 and 6.218. Since the strength of the reverse roll can become comparable to the that of the forward roll, it is thus incorrect to refer to the reverse roll as two-dimensional flow.

The reverse roll results due to the convection effects of the secondary flow which generates vorticity that opposes the forward roll near the symmetry plane. When this vorticity is sufficiently strong it overcomes the forward roll thus producing a reverse roll. The cross section separating the forward and the reverse roll is convex to the end wall and not plane.

For the tall cross-sectional cavity, the streamlines calculated near the symmetry plane exhibit primary recirculating flow and multiple cells do not develop. This contrary to the flow predicted for the two-dimensional double glazing problem, where the flow results into multiple cells. Yet the isotherms obtained for cerrobase in the window cavity problem are very similar to the two-dimensional problem.

Plots of Nusselt number, $\mathrm{Nu}_v(y)$, along the isothermal wall indicates the extent of the thermal boundary layer which decreases as Rayleigh number is increased. The Nusselt number at the symmetry plane, Nu_{vm}, in window cavities where two-dimensional flow does not exist are generally smaller than those obtained with the two-dimensional problem. It is possible for the Nusselt number at the symmetry plane to be larger than that obtained with the two-dimensional problem. This is possible if the contribution to the convection of heat by the axial flow is large. The average Nusselt number along the isothermal wall, Nu_{av}, tends to the that of the two-dimensional problem as Hy increases.

The change of the sign of $\partial\theta/\partial y$ along the axial direction for $\mathrm{Ra} > 10^3$ are associated with the contribution to the convection of heat by the axial flow.

For the shallow and square cross section window cavities, the point at which maximum axial-velocity occurs along the centre line, that is the point at which the end wall has greatest influence, is independent of Hy, occurring at approximately y=0.25 from the end wall.

Turning points of the cerrobase particles in the square cavity lie on a cylindrical

surface but not in the shallow nor the tall cross sectional window cavities. The turning points of the particles with air do not, however, lie on a well defined surface.

The flow in the three dimensional problem is slowed down due to the drag at the end wall, as a result of which instabilities due to the shear driven flow which occur in the two-dimensional problem for low Prandtl number fluid are suppressed. With the flow slowed down, the thermal solution of the flow is less convective, and thus any instabilities that are buoyancy driven, which occur in the two-dimensional problem for moderate Prandtl number fluids, are suppressed too. Of course for very long cavities where the influence of the end wall drag near the symmetry plane is non-existent, two-dimensional flow may occur.

6.10 Appendix A - Computation times for the window cavity problem

The residual of the continuity equation has been used as the convergence criterion. Whilst monitoring the residual of momentum equation and temperature equation. The residual of the continuity equation has been reduced by at least 10^{-6} except for * which has been reduced by 10^{-3}.

FLUID	CAVITY	MESH SIZE	CONT. RES	#ITS	CPU TIME
air Ra = 10^3	1x1x1	16x16x16	0.99x10^{-6}	181	145
	1x2x1	16x16x16	0.36x10^{-6}	340	271
	1x5x1	16x40x16	0.34x10^{-7}	1011	3375
	1x1x1	32x32x32	0.13x10^{-6}	2087	4433
air Ra = 10^5	1x1x1	16x16x16	0.28x10^{-6}	434	348
	1x2x1	16x16x16	0.10x10^{-5}	255	204
	1x5x1	16x40x16	0.76x10^{-6}	1383	4616
cerrobase Ra = 10^3	1x1x1	16x16x16	0.95x10^{-7}	168	135
	1x2x1	16x16x16	0.35x10^{-6}	295	235
	1x5x1	16x40x16	0.32x10^{-7}	295	235
	1x1x1	32x32x32	0.76x10^{-5}	2350	4995
cerrobase Ra = 5x10^3	1x1x1	16x16x16	0.11x10^{-6}	350	280
	1x2x1	16x16x16	0.16x10^{-6}	245	195
	1x5x1	16x40x16	0.15x10^{-6}	715	2386

Table 6.8a: Computer times and the number of iterations taken to converge.

FLUID	CAVITY	MESH SIZE	CONT. RES	#ITS	CPU TIME
air Ra = 10^3	1x1x0.5	16x16x16	0.16x10^{-6}	808	647
	1x2x0.5	16x16x16	0.23x10^{-8}	757	604
	1x5x0.5	16x40x16	0.37x10^{-8}	777	2594
air Ra = 10^5	1x1x0.5	16x16x16	0.15x10^{-6}	544	436
	1x2x0.5	16x16x16	0.22x10^{-6}	674	540
	1x5x0.5	16x40x16	0.36x10^{-6}	721	2408
cerrobase Ra = 10^3	1x1x0.5	16x16x16	0.16x10^{-6}	774	620
	1x2x0.5	16x16x16	0.23x10^{-6}	556	447
	1x5x0.5	16x40x16	0.16x10^{-6}	706	2356
cerrobase Ra = 5x10^3	1x1x0.5	16x16x16	0.78x10^{-6}	677	543
	1x2x0.5	16x16x16	0.78x10^{-6}	677	543
	1x5x0.5	16x40x16	0.18x10^{-6}	568	1900
air Ra = 10^3	1x1x5	16x16x40	0.11x10^{-5}	1060	1875
	1x2x5	16x16x40	0.22x10^{-6}	1424	2547
	1x5x5	16x40x40	0.16x10^{-6}	1494	2682
air Ra = 10^5	1x1x5	16x16x40	0.92x10^{-6}	1520	2720
	1x2x5	16x16x40	0.92x10^{-5}	1589	2842
	1x5x5	16x40x16	0.94x10^{-6}	1492	2670
cerrobase Ra = 10^3	1x1x5	16x16x40	0.28x10^{-7}	1968	3520
	1x2x5	16x16x40	0.15x10^{-6}	1968	3521
	1x5x5	16x40x40	0.20x10^{-6}	1326	2371
cerrobase Ra = 5x10^3	1x1x5	16x16x40	0.68x10^{-6}	1968	3520
	1x2x5*	16x16x40	0.99x10^{-3}	1169	2090
	1x5x5	16x40x40	not converged		

Table 6.8b : Computer times and the number of iterations taken to converge.

6.11 Appendix B

6.11.1 Graphical Output

A major difficulty in interpreting three-dimensional results is the volume of output produced. This problem has been eased by the use of graphical representation. Each solution of the primitive variable formulation is determined by five variables u, v, w, p and θ. The usual approach of displaying the data by contour plots for each slice of the solution variable, hinders the description of the solution due to the large number of plots being generated. The three components of the velocity can be combined and velocity vectors plotted to reduce the amount of output. The structure of the three-dimensional flow is still difficult to understand with the velocity vector plots. Particle paths on the other hand generate the feel of the three dimensional flow extremely well. However, generating particle paths is a long process requiring additional computation time, in the range of 10 to 50 minutes computer time per cavity on an IBM3084. Due to the computational costs some particle paths have not been completed but rather sections of paths have been presented. The coarse interpolation technique of the human eye is used to start each section of the path and of course there is no guarantee that all sections belong to a particular particle. The criterion for choosing the number of path segments is such that the fluid flow in the central and outer longitudinal cores, near the end wall and the symmetry plane can be represented. For clarity the particle paths are only represented in one half of the window cavity, see Figure 6.1. The particle paths are viewed from the point $(-8, -4, -3)$, unless otherwise stated. The faces of the cavity seen from the viewing position are drawn in solid lines and the hidden face are drawn with dashed lines. The mesh size, Rayleigh and Prandtl numbers for the problem are printed at the bottom of each plot.

6.11.2 The particle tracking procedure

In this study a particle tracking procedure developed by Matthews and Wilkes [40] has been used. Since in the pressure-velocity formulation the velocity components lie on a staggered grid they have to be interpolated to obtain the velocity at a point. A method based on tensor product splines is used to interpolate the velocity components to all points of the flow domain. The interpolation automatically generates velocities that satisfy $\nabla.\vec{u} = 0$. Particle paths are drawn by tracking particles for short distances,

proportional to the velocity, in the domain and then stepping forward in time. The forward time stepping integration is performed by using a fourth order Runge-Kutta method with variable time step lengths. Variable time stepping is performed using a back stepping method, that is, after a forward step the velocity components at the new position (P) are interpolated from the staggered grid and reversed. After which another step is performed (effectively a backward step, the new position is now (Q)) which should coincide with the initial position of the particle. However, this may not be the case since more often than not large time steps are chosen. The separation of the new position (Q) from the initial position is used as an error estimate for this time step, which is a user defined acceptable tolerance. From an initial guess, the time steps are slowly decreased till the error estimate is within the bounds of acceptable tolerance.

6.11.3 On the closure of the particle path

The particle paths follow the shape of a double helix with the fluid moving towards the symmetry plane on the inner spiral and returning to the end wall on the outer spiral. The conditions $\nabla.\vec{u} = 0$ and $\partial u/\partial n = 0$ lead to the conclusion that the paths must close, Mallinson and de Vahl Davis [39]. A particle path through a given point may pass near that point before actual closure with all the traverses made to the symmetry plane and back lying on the same toroidal surface, since the velocity is single valued and paths cannot intersect. If each traverse did not lie on the same toroidal surface then it would either lie on a larger (or smaller) toroidal surface which contains (or is contained by) the surface on which the previous traverse was made. In either case it is not possible for the path to return to the original surface without intersection of paths at some point in the cavity. Multiple traverses on the same surface without paths intersecting are however possible and cannot be rejected apriori. Due to the velocity interpolations involved the numerical procedure described above is not capable of the accuracy required to investigate the closure of paths with these coarse grid results (16x16x16).

6.12 APPENDIX C

6.12.1 Key for the velocity vectors

SOLID ARROW implies U-velocity components ≥ 0.0

DASHED ARROW implies U-velocity components < 0.0

ARROW HEAD AT THE TIP OF THE VECTOR implies VELOCITY VECTORS GOING INTO THE PLANE.

ARROW HEAD ON THE VECTOR implies VELOCITY VECTORS COMING OUT OF THE PAPER.

The vectors have only been drawn for every other grid row and column so as not to congest the plot. The velocities have been normalized with respect to the largest occurring velocity in the domain and then with respect to 2x smallest mesh length. This is so that the velocity vectors do not overlap.

6.13 APPENDIX D

This appendix gives a short discussion of published work that appeared during the writing-up of this thesis.

A recent publication by [1c] assesses the suitability of the SIMPLE algorithm as a smoother in a multigrid method using local mode Fourier analysis, as introduced by Brandt [5], the aim being to check if the SIMPLE algorithm can be used as a smoother in a non-linear multigrid algorithm, see [2c]. The SIMPLE algorithm is applied to the shear-driven cavity problem with aspect ratio 1. The theoretical smoothing factor is compared with that obtained in practice for Reynolds number ranging from 1-10000 and is shown to be a pessimistic predictor of the practical smoothing rate. This is because the local mode analysis is based on an idealising assumption that the solution is derived on an infinite grid, see section 2.3. As a result of computational costs the theoretical smoothing factors are obtained over a set of flow directions, eight in all, rather than the overall flow domain, this may also be a contributory factor to the theoretical smoothing factors being pessimistic. The theoretical smoothing factors for Reynolds number from 1 to 10000 range from 0.604 to 0.996 whereas the practical smoothing factors range from 0.478 to 0.910.

Another development has been to use the non-linear multigrid method (FAS) to solve the discrete incompressible Navier-Stokes equations using the SIMPLE algorithm as a smoother, [2c]. The authors, [2c], derive the discretized equation using the control volume approach but perform the multigridding in the finite difference manner. This is apparent from the weighted restriction operator used. This inconsistency would be very apparent for compressible fluid flow problems since the restriction of the residuals are not treated as an integral volume of a source term (see chapters 3 and 4) and hence the coarse grid problem would not be conservative in nature. The weighted restriction operator used is such that it conserves the mass continuity on the coarse grids. The non-linear method as described in chapter 3 is used in V-cycle format. The prolongation process is performed using the bilinear operator. The results obtained with this method for the shear-driven cavity problem over Reynolds number from 1 to 10000 when compared with PACE (SIMPLE algorithm), a fluid flow code developed at Rolls Royce, is extremely efficient. This method appears as if it could very easily be implemented within existing industrial codes that use the SIMPLE algorithm. The method would also be highly desirable for three-dimensional fluid flow problems.

Another non-linear multigrid scheme which is used to solve the Navier-Stokes using a variant of the SIMPLE algorithm as a smoother is that presented in [3c]. Here the non-linear multigrid algorithm is used with the Full Multi-Grid (FMG) method. The smoother applies alternating Gauss-Seidel to the momentum equations (see chapter 2) and distributive point Gauss-Seidel to the pressure-correction as done by Brandt [4]. The discretized incompressible Navier-Stokes are derived using the control volume approach but again the multigridding is done in the finite-difference manner. This is apparent from the weighted restriction operator that is used. This inconsistency would lead to difficulties for compressible fluid flow problems as described above. The restriction is done by weighted averages and no effort is made to conserve the mass-continuity. As a result the FMG algorithm is not much more efficient than an ordinary V-cycle. The author gives a comparison of his non-linear multigrid method to that of SIMPLE algorithm incorporating a linear multigrid algorithm to solve the pressure-correction equation (PC-MG). The test problem treated is that of air flow between two rotating discs, an a 64x64 grid. The non-linear algorithm performs approximately 70% better than PC-MG. Unfortunately this method does not appear to be easily implemented into existing industrial codes that use the SIMPLE algorithm, due to using distributive Gauss-Siedel for solving the pressure-correction. On the other hand such a large saving may make the industry think again about their existing codes.

A recent application of non-linear multigrid method to Navier-Stokes equations discretized using the control-volume in three-dimension is presented in [4c]. The smoother used is BLIMM (Block-Implicit Multigrid Method). BLIMM eliminates the need for a pressure-correction equation by retaining the continuity equation in its primitive form in terms of the velocities. So the finite difference equations on any grid are solved simultaneously by a point Gauss-Seidel procedure, that is, at each node the momentum equations corresponding to the velocities on six faces of a cell and the continuity equation are solved in a coupled manner. Four three-dimensional sudden expansion flows have been treated but none of which are driven by natural convection. The finest grid used is a 16x16x64. FAS has been used in conjunction with FMG and again the weighted restriction reveals that the multigridding has been performed in the finite difference manner. For Reynolds number from 600 to 2400 the smoothing rates range from 0.75 to 0.91.

These recent developments are an extension to the multigrid algorithm presented in this thesis. Only the algorithm of [2c] would satisfy the constraint of modification of

current industrial codes based on the SIMPLE algorithm with minimum costs. Another feature of these latest algorithms is that they do not treat the residuals as integral volume of a source strength, as described in chapters 4 and 5,and as a result the coarse grid problem is no longer in a conservative form. Hence for compressible fluid flow problems these algorithms would experience difficulty in converging. All the non-linear methods discussed here need to be under-relaxed but the avenue of obtaining optimum smoothing rates by using optimum relaxation factors has not been explored.

REFERENCES.

[1c] Shaw, G.J and Sivaloganathan, S. *On the smoothing properties of the SIMPLE pressure-correction algorithm.* Int. Journal for Numerical Methods in Fluids, vol. 8, 1988.

[2c] Sivaloganathan, S. and Shaw, G.J *A multigrid method for recirculating problems.* Int. Journal for Numerical Methods in Fluids, vol. 8, 1988.

[3c] Lonsdale, G. *Solution of a rotating Navier-Stokes problem by a Nonlinear Multigrid algorithm.* Journal of Computational Physics, vol. 74, 1988.

[4c] Vanka, S.P. *Performance of a multigrid calculation procedure in three-dimensional sudden expansion flows.* Int. Journal for Numerical methods in Fluids, vol. 8, 1988.

Bibliography

[1] Aziz. K. Hellums. J. *Numerical solution of the 3-D motion for Laminar Natural Convection.* Physics of Fluid. vol.10 No.2. 1967.

[2] Batchelor. G. K. *Heat transfer by free convection across a closed cavity between vertical boundaries at different temperatures.* Quarterly Jou. of Applied Maths. vol. XII No.3. 1954.

[3] Bergholz. R. F. *Instabilty of a steady natural convection in a vertical fluid flow layer.* Journal of Fluid Mechanics. vol.84 1978.

[4] Brand. K. *Multigrid Bibliography* Ed.3. GMD report Nr.59.

[5] Brandt. A. *Multigrid Solvers on Parallel Computers* Elliptic Problem Solvers (M. H. Schultz,ed) Academic Press. New York. NY. 1981.

[6] Brooks. R. G. *Heat transfer between parallel plates. An Interferometric Investigation.* Journal of Mechanical Eng. Science. vol.14 No.2 1972.

[7] Caretto. L. Gosman. A. D. et al.. *Two calculation procedures for steady three-dimensional flows with recirculation* J. Heat Mass Transfer vol 18. 1978.

[8] Catton. I. *Natural convection in enclosures.* Proc. 6th Int.Heat Transfer Conf.. Toroto,Canada. vol.6 1978.

[9] Churchill. S. W. *Free convection in layers and enclosures.* Single Phase Convective Heat Transfer. Hemisphere Pub. Co. 1983.

[10] Cormack. D.. Leal. L.. Imberger. J.. Seinfield. J. *Natural convection in a shallow cavity with differentially heated end walls* Journal of Fluid Mechanics. vol.65 part 1 and 2. 1974.

[11] de Vahl Davis, G. *Laminar Natural Convection in an enclosed cavity.* Int. Journal Heat Mass Transfer. vol.11 1968.

[12] de Vahl Davies, G., Jones, I. P. *Natural convection in a square cavity. A comparison exercise.* Int. J. Numerical Methods in Fluids. vol.3 1983.

[13] Duxbury, D. *An Interferometric study of Natural Convection in enclosed plane layers.* M.Sc Thesis, Univ. of Salford, England, 1972.

[14] Elder, J. W. *Laminar free Convection in a vertical slot.* Journal of Fluid Mechanics. vol.23 No.1 1965.

[15] Eckert, E. R. G., Carlson, W. *Natural convection in an air layer enclosedbetween two vertical plates with different temperatures.* Int. J. Heat Mass Transfer. vol.2 1961

[16] Foerster, H., Witsch, K. *Multigrid Software for the solution of elliptic problems on a rectangular domain.* G.M.D study Nr.70. 1982.

[17] Ghia, U., Ghia, K., Shin, C. *High-Re Solutions for Incompressible Flow Using the Navier-Stokes Equations and a Multigrid Method.* Journal of Computational Physics. vol.48 No.3 1982.

[18] Gill, A. E., Davey, A. *Instabilities of a buoyancy driven system.* Journal of Fluid Mechanics. vol.35 No.4 1969.

[19] Hackbusch, W. *Multi-grid convergence theory.* Lecture notes in Mathematics, 960, Multigrid Methods, Proceedings, Koln-Porz, 1981, Eds. Hackbusch, W. and Trottenburg D. Springer-Verlag.

[20] Hackbusch, W. *Efficient solutions of elliptic systems.* Proc. GAMM Conference. Jan 1984 Freidr. Vieweg and Sohn. Braunschweig/Wiesbaden.

[21] Hart, J. E. *Low Prandtl Number convection between differentially heated end walls.* Int. J. Heat Mass Transfer. vol.26 No.7 1983.

[22] Hempker, P. *On the comparison of line Gauss-Seidel and ILU relaxation in multigrid algorithms.* Mathematisch Centrum, Amsterdam. 1981.

[23] Hempker, P., Kettler, R., *Multigrid methods: Development of fast solvers.* Applied Maths and Computations 13. 1983.

[24] Hirt, C.W., Nichols, B. D., Romero, N. C. *SOLA - A Numerical Solution Algorithm for Transient Fluid Flows.*

Los Alamos Scientific Laboratory Report LA-5652, New Mexico, April 1975.

[25] Imberger, J. *Natural convection in a shallow cavity with differentially heated end walls.* Experimental results. Journal of Fluid Mechanics. vol.65 part3 1974.

[26] Jones, I. P. *A numerical study of convection in an air filled cavity.* Comparison with experiment. Numerical Heat Transfer. vol.2 1979.

[27] Jones, I. P. *Low Prandtl number free convection in a vertical slot.* AERE Harwell, England. Report AERE-R 10416. 1981.

[28] Jones, I. P. *A comparison problem for numerical methods in fluid dynamics-The double glazing problem.* AERE Harwell, England. Report css-72 1983

[29] Kettler, R. *Analysis and Comparison of Relaxation Schemes in Robust Multigrid and Preconditioned Conjugate Gradient Methods* Lecture Notes in Mathematics, 960, Multigrid Methods, Proceedings, Koln-Porz, 1981, Eds. Hackbusch, W. and Trottenberg D. Springer-Verlag.

[30] Kightley, J. R. *Conjugate Gradient Methods applied to Turbulence Flow Calculations.* 6th Gamm Conerence on Numerical Methods in Fluid Mechanics 1985.

[31] Lee, Y. Korpella, S. *Multicellular natural convection in a vertical slot.* Journal of Fluid Mechanics. August vol.126 1971.

[32] Lillie, A. F., Nottage, H.B. *Some expts. on liquid sodium. Free convection heat transfer across an enclosed gap between vertical layeurs.* Chem. Eng. Progress Symposium Series: Heat Transfer. Seattle, U.S.A. 1968.

[33] Linthorst, S. J. M., Schinkel, W. M. M., Hoogendoorn, C. *Flow structure with natural convection in inclined air filled cavities.* vol.103 1981.

[34] Linthorst, S. J. M. *Natural convection suppresion in solar collectors.* Ph.D Thesis, Univ. of Delft, Holland. 1984.

[35] MacGregor, R. K., Emery, A. F. *Free convection throughvertical plane layers, moderate and high Prandtl number fluids.* Journal of Heat Transfer. vol.91 1969.

[36] MacGregor, R. K., Emery, A. F. *Prandtl number effects on natural convection in an enclosed vertical layer.* Journal of Heat Transfer. May vol.93. 1971.

[37] Mallinson, G. D., Graham, A. D. *Experimental visualization of three-dimensional natural convection.* Proc 5th Australasian Conf. on Hydraulics and Fluid Mechanics, Christchurch, New-Zealand. 1974.

[38] Mallinson, G. D., de Vahl Davis, G. *The method of the false transient for the solution of coupled elliptic equations.* Journal of Comp. Physics. vol.83 1977.

[39] Mallinson, G. D., de Vahl Davis, G. *Three dimensional convection in a box. A numerical study.* Journal of Fluid Mechanics. vol.83 1977.

[40] Mathews, M. D., Wilkes, N. *Particle tracking for3-dimensional fluid flow predictions.* AERE Harwell, England. Report AERE-R 12153, 1986.

[41] Morrison, G. L. L., Tran, Q. *Laminar flow structures in vertical free convective cavities.* Int. J. Heat Mass Transfer. vol.21 1978.

[42] Ortega, J., Voigt, R. *Solution of Partial Differential Equations on Vector and Parallel Computers.*

[43] Ostrach, S., Loka, R. R., Kumar,A. *Natural convection in low aspect ratio rectangular enclosures.* H.T.D. vol.8 ASME 1980.

[44] Ozoe, H. et al. *Natural convection in doubly inclined rectangular boxes.* Heat Transfer Conf. Toronto. Trans. ASME vol.2 1978.

[45] Pao, H. *A numerical computation of a confined rotating flow.* Journal of Applied Mechanics. Trans. ASME June 1970.

[46] Patankar, S. V. Spalding, D. B. *A calculation procedure for heat, mass and momentum transfer in 3-Dimensional Parabolic flows.* J.Heat Mass Transfer. vol 15. 1976.

[47] Patankar, S. V. *Numerical Heat Transfer and Fluid Flow.* Series in Computational Methods in Mechanics and Thermal Sciences. 1980 Hemisphere Publishing Co. McGraw Hill Book Company.

[48] Patankar, S. V. *A Calculation Procedure for 2-D Elliptic Situations* Numerical Heat Transfer, Vol. 4. pp 409-425, 1981.

[49] Pau, V. *Multigrid Methods for the SIMPLE algorithm in 2-Dimensions* Annual Harwell Seminar on Heat Transfer and Fluid Flow, AERE-R12751,1984

[50] Pau, V., Lewis, E. *Application of the Multigrid Method to the Pressure-Correction equation* 2nd European Multigrid Conference, Koln, West Germany, 1984, GMD study No 51.

[51] Pau, V. *Multigrid Methods for 3-Dimensional problems.* Annual Harwell Seminar on Heat Transfer and Fluid Flow, AERE-R14751,1985

[52] Quon, C. *High Ra number convection in an enclosure. A numerical study.* Physics of Fluid. vol.15 No.1 June 1972.

[53] Raithby, G. D., Schneider, G. E. *Numerical Solution of Problems in Incompressible Fluid Flow: Treatment of the Velocity - Pressure Coupling.* Numerical Heat Transfer, Vol. 12. pp 417-440, 1979.

[54] Roache,P. J. *Computational Fluid Dynamics.* 1972, Hermosa Publishers.

[55] Schienkel, W. M. M. *Natural convection in inclined air-filled enclosures.* Ph.D Thesis, Delft University of Technology. Holland. 1980

[56] Schlicting, H. *Boundary Layer Theory.* McGraw-Hill Series in Mech. Eng. 1979.

[57] Shiralkar, G. S., Tien, C. L. *Numerical study of natural convection in a shallow cavities.* Journal of Heat Transfer. vol.103 1981.

[58] Stuben, K., Trottenberg, U. *Software development based on multigrid techniques.* G.M.D. report Nr.84.

[59] Stuben, K., Trottenberg, U. *On the construction of Fast Solvers for Elliptic Equations.* G.M.D Technical report. 26/2/1982

[60] Stuben, K., Trottenberg, U. *Multigrid Methods: Fundamental Algorithms,A Model Problem Analysis and Applications.* G. M. D. Study No. 96, 1984.

[61] Tichy, J., Gadgil, A. *High Ra number laminar convection in low aspect ratio enclosures with adiabatic horizontal walls and differentially heated vertical walls.* Journal of Heat Transfer. vol.104 February 1982.

[62] Tritton, D. J. *Physical Fluid Dynamics.* Van Nostrand Reinhold Pub. Co. 1977

[63] Van Doormal, J. P., Raithby, G. D. *Enhancement of the SIMPLE Method for Predicting Incompressible Fluid Flows.* Numerical Heat Transfer, Vol. 7, pp 147-183, 1984.

[64] Vest, C. M., Arpaci, S.V. *Stability of natural convection in a vertical slot.* *Journal of Fluid Mechanics.* vol.36 1969.

[65] Viskanta, R., Kim, D. M., Gau, C. *Three dimensional natural convection of a liquid metal in a cavity.* Int. J. Heat Masss Transfer. vol.29 No.3 1986.

[66] Wesseling, P. *the rate of convergence of a multigrid method.* Numerical Analysis. G.Watson (ed) Proc. Dundee 1979. Lecture Notes in Maths 1980. Springer Verlag, Berlin 1980.

[67] Wesseling, P. *A Robust and Efficient Multigrid Method.* Lecture notes in Mathematics, 960, Multigrid Methods, Proceedings, Koln-Porz, 1981, Eds. Hackbusch, W. and Trottentag, D. Springer-Verlag.

[68] Wesseling, P. *Theoretical and Practical aspects of a multigrid method.* SIAM. J. SCI. STAT. COMP. vol 3. Nr.4. Dec 1982.

[69] Winters, K. *Laminar natural convection in a partially divided rectangular cavity at high Ra numbers.* AERE Harwell, England. Report TP1118.

[70] Winters, K. H. *A Numerical Study of Natural Convection in a Square Cavity.* AERE Harwell, England. Report AERE R9747, 1980.